VNIVERSITAT DE VALÈNCIA

Departament d'Astronomia i Astrofísica
Programa de Doctorado en Física

Numerical resistive relativistic magnetohydrodynamics

Doctoral Thesis

Sergio Miranda-Aranguren

This work was done under the supervision of

Prof. Dr. Miguel Ángel Aloy Torás

and

Dr. Tomasz Rembiasz

Departament d'Astronomia i Astrofísica
Universitat de València
Burjassot - España

Desembre - 2018

Miguel Ángel Aloy Torás, Profesor Titular del Departamento de Astronomía y Astrofísica de la Universitat de València

y

Tomasz Rembiasz, Investigador Asociado al Departamento de Astronomía y Astrofísica de la Universitat de València

CERTIFICAN:

Que la presente memoria, titulada **Numerical resistive relativistic magnetohydrodynamics**, ha sido realizada bajo su dirección en el Departamento de Astronomía y Astrofísica de la Universitat de València por **Sergio M. Miranda Aranguren**, y constituye su Tesis Doctoral para optar al grado de Doctor en Física.

Y para que conste firman el presente certificado en Burjassot, a 5 de octubre de 2018.

Fdo: Miguel Ángel Aloy Torás

Fdo: Tomasz Rembiasz

Summary

La presente tesis se desarrollada dentro del marco de la Magnetohidrodinámica Resistiva Relativistica (RRMHD; por sus siglas en inglés) y uno de sus principales objetivos es el caracterizar las condiciones físicas que optimizan la disipación de campos magnéticos en plasmas relativistas, especialmente en aquellos que son de interés astrofísico. Para alcanzar este objetivo, realizamos el estudio de los denominados modos de *ruptura* (*Tearing Modes*; TM), bajo condiciones que maximizan sus tasas de crecimiento y los cuales evolucionan en capas de corriente (*current sheets*).

Para lograr este objetivo, piedra angular de la tesis, se construyó un nuevo código RRMHD, apto para ser usado en el estudio de plasmas en el contexto astrofísico. Desde el punto de vista matemático, el sistema de ecuaciones en derivadas parciales que rigen la RRMHD es de tipo hiperbólico. Ello permite plantear problemas *bien puestos* proporcionando datos iniciales sobre una región espacial en un instante dado (instante inicial), es decir, permite plantear problemas de Cauchy con solución única. El hecho de que el sistema de ecuaciones en derivadas parciales sea hiperbólico tiene una consecuencia práctica de gran importancia para diseñar métodos que nos permitan resolver numéricamente problemas de Cauchy, ya que la evolución en el tiempo de cada punto sólo depende de una región espacial limitada por el cono de luz pasado de dicho punto. Ello permite, si así se desea, construir algoritmos de evolución temporal *explícitos*, es decir, algoritmos en los que los datos en un cierto instante temporal (digamos $t = t^n$, siendo $n = 1, 2, \ldots$), son suficientes para conocer el estado del sistema tras un instante (suficientemente breve) de tiempo Δt (es decir, en el instante $t = t^n + \Delta t := t^{n+1}$). Esto es así porque el estado del sistema se propaga de acuerdo con ciertos invariantes a través de las curvas características del sistema de ecuaciones. Por ello, para construir cualquier código numérico que resuelva las ecuaciones de la RRMHD (y el que se ha desarrollado en esta tesis no es una excepción) es preceptivo entender la estructura característica de las ecuaciones que la rigen. Hay que resaltar que esta labor en el sistema de

ecuaciones de la RRMHD ha resultado ser más exigente que aquella para las ecuaciones de la MHD ideal, debido a la existencia de términos fuente *rígidos* en las ecuaciones de Maxwell. La rigidez de este sistema de ecuaciones, es una consecuencia natural del hecho que los efectos debidos a la difusividad tienen lugar en escalas de tiempo que pueden ser muchísimo menores que las escalas de tiempo magnetohidrodinámico cuando nos aproximamos al límite ideal. Dicho límite acontece cuando la resistividad del sistema, η, se hace muy pequeña. De hecho, en unidades de Heaviside-Lorentz y normalizando las velocidades a la velocidad de la luz en el vacío, c (como las adoptadas en este trabajo), la resistividad tiene dimensiones de tiempo. Por ello, cuanto mayor es η, tanto más pequeña es la escala de tiempo de difusión del campo magnético. En la RRMHD, los términos de relajación (rigidez) pueden dominar sobre los términos puramente hiperbólicos, presentando restricciones prohibitivas sobre el paso de tiempo, es decir, restringen la evolución numérica de los datos de tal manera que $\Delta t \sim \eta \ll 1$, si se utilizan algoritmos de integración explícitos para la evolución temporal.

Para emprender la tarea de entender la estructura característica de la RRMHD, primero se calcularon las condiciones de salto a través de choques, incorporando los efectos de la fuente *rígida*, modelada ésta como dos fuentes singulares tipo delta de Dirac (Sec. 3.3). Esta es una manera aproximada y también efectiva para tratar con las modificaciones que pueden aparecer en la solución del problema de Riemann[1] cuando están presentes términos fuentes rígidos en el sistema de ecuaciones. Además de haber calculado tanto las condiciones de salto de Rankine-Hugoniot como la adiabática de Lichnerowicz (*Lichnerowicz adiabat*; Sec. 3.4) para la RRMHD, hemos mostrado que es posible recuperar de estas expresiones, las equivalentes a las condiciones de salto en el caso *ideal* RMHD (Giacomazzo and Rezzolla, 2006; Romero et al., 2005), es decir, cuando la conductividad $\sigma \to \infty$ ($\eta \to 0$).

De igual forma se han estudiado las condiciones que caracterizan la solución a través de rarefacciones. Aunque el las ecuaciones de la RRMHD forman un sistema de leyes de balance y no un sistema de leyes de conservación, realizamos un extensivo trabajo analítico para obtener las soluciones auto-similares en el límite en el cual la conductividad se aproxima a cero (Sec. 3.2). Es en este límite donde las ecuaciones de la RRMHD forman un conjunto de leyes de conservación. Este es también el caso en el límite complementario de altas conductividades, esto es en el límite de la magnetohidrodinámica relativista (RMHD por sus siglas en inglés) ideal, donde las soluciones auto-similares a través de ondas de rarefacción es bien conocido. Aunque nuestros esfuerzos por unir estos dos límites han sido infructuosos, hemos encontrado que la solu-

[1] Un problema de Riemann es un problema de datos iniciales uniformes y discontinuos para una ecuación (o sistema de ecuaciones) en derivadas parciales.

ción auto-semejante en el límite $\sigma \to 0$ es la misma que en el caso RMHD ideal ($\sigma \to \infty$). Entre nuestros resultados, verificamos que cuando el flujo es suave (como en una rarefacción) el sistema de ecuaciones en derivadas ordinarias que permite encontrar soluciones autosemejantes, las cuales no dependen del tiempo, t, y de la posición x por separado, sino de la variable x/t, sólo tiene solución si dicha variable resulta ser igual a alguno de los autovalores de la matriz Jacobiana del sistema de ecuaciones en derivadas parciales de la RRMHD.

Estos dos acercamientos al problema de Riemann (es decir, considerando fuentes singulares en las condiciones de salto o conductividad nula para el estudio de rarefacciones) no permiten obtener una solución exacta y puesto que los resolvedores aproximados de Riemann son utilizados comúnmente en la práctica, desarrollamos como un subproducto de esta tesis, un resolvedor aproximado del tipo HLLC, esto es, un resolvedor de la familia HLL (Harten-Lax-van Leer) en donde se ha introducido una onda de contacto en la solución ("C" denota esta propiedad). El nuevo resolvedor captura de forma exacta discontinuidades de contacto estacionarias, presentando un mejor desempeño que el resolvedor HLL en estos casos. También es importante resaltar que el nuevo resolvedor HLLC no requiere distinguir entre los casos en los cuales el campo magnético perpendicular a la discontinuidad es cero o no, como ocurre en otros resolvedores HLLC (see, e.g. Mignone and Bodo, 2006) y de esta forma, no presenta ninguna patología cuando la componente del campo magnético normal a la discontinuidad inicial se acerca a cero. Diversas pruebas en una y dos dimensiones espaciales, que involucran choques y/o discontinuidades, han mostrado que el esquema HLLC presenta una menor difusividad numérica que el resolvedor aproximado de Riemann HLL. Hemos encontrado que aquellos modelos ejecutados con el resolvedor HLLC son un $\sim 5\% - 20\%$ más costosos en términos de tiempo de computación, que aquellos en los cuales se utilizó HLL (Tab. 5.1). La variación en el tiempo computacional, está relacionada con el número de iteraciones adicionales necesarias para resolver numéricamente la ecuación cuadrática Eq. (5.22). En cuanto al cálculo de errores utilizando la norma L1, los errores medidos son sistemáticamente menores si se emplea el resolvedor HLLC que el HLL. Así, vistas las ventajas en el desempeño numérico del esquema HLLC sobre el HLL, que su costo computacional es modesto en relación al esquema HLL y que su implementación en códigos existentes de la RRMHD es directa, podemos concluir que el nuevo resolvedor HLLC es una alternativa viable al muy ampliamente usado resolvedor HLL.

Este resolvedor aproximado al igual que diversos métodos numéricos incorporados de la literatura o desarrollados por nuestro grupo (CAMAP; *Computer aided modeling of astrophysical plasma*) han sido implementados en el nuevo código Cueva y *verificados* a través de un exhaustivo estudio de errores numéricos demostrado un buen desempeño de estos métodos tanto en el

régimen ideal como en el resistivo. Cueva es un acrónimo de *Computer Unit for EnVironments in Astrophysics*. Con versiones previas de dicho código, se han publicado sendas actas de congresos (Miranda-Aranguren and Aloy, 2013; Miranda-Aranguren et al., 2014), y con la versión actual un artículo en *Monthly Notices of the Royal Astronomical Society* (Miranda-Aranguren et al., 2018). El nuevo código RRMHD está inspirado en una herramienta computacional desarrollada y perfeccionada en el seno del grupo CAMAP (el código Genesis Aloy et al., 1999), que en sus versiones más recientes también resuelve numéricamente las ecuaciones de la RRMHD.

Como se ha comentado más arriba, el sistema de ecuaciones de la RRMHD es rígido y, por tanto, usar métodos de integración temporal explícitos no es posible. Existe una amplia literatura en relación a las diversas alternativas que existen a los métodos explícitos para abordar situaciones en las que el sistema de ecuaciones en derivadas parciales deviene en rígido. Entre las aplicadas a las ecuaciones de la RRMHD, vale la pena resaltar el trabajo de Komissarov (2007), en el cual el tratamiento de los términos fuentes rígidos se lleva a cabo utilizando la técnica de "partición de Strang" (*Strang splitting*) (Strang, 1968). Alternativamente Palenzuela et al. (2009), utiliza por primera vez en el contexto del sistema RRMHD los métodos Implícitos-Explícitos Runge-Kutta (Implicit-Explicit Runge-Kutta methods (RKIMEX; véase, por ejemplo, Sec. 4.2.1)). Aloy and Cordero-Carrión (2016) en un novedoso trabajo, construyen los métodos llamados Mínimamente Implícitos Runge-Kutta (*Minimally Implicit Runge-Kutta*; MIRK, véase Sec. 4.2.2), los cuales han sido diseñados para tratar exclusivamente con la dureza de las ecuaciones de la RRMHD en el régimen de altas conductividades.

Cueva se basa en una formulación conservativa de volúmenes finitos de las ecuaciones de RRMHD. La evolución de un estado inicial dado se realiza mediante la técnica conocida como método de líneas (MoL por sus siglas en inglés). Dicha técnica consiste en discretizar el espacio y el tiempo de manera separada. Tras la discretización de las derivadas espaciales y las fuentes de las ecuaciones de la RRMHD, el conjunto de ecuaciones resultante es un sistema de ecuaciones en derivadas ordinarias, el cual, a priori, puede resolverse con diversos métodos de integración temporal. Sin embargo, dado que el sistema de ecuaciones de la RRMHD es matemáticamente *rígido* en el régimen ideal, la integración temporal se lleva a cabo con métodos parcialmente implícitos. De igual forma, en Cueva se implementan dos familias principales de integradores de tiempo: los métodos RKIMEX y MIRK. En cuanto a la discretización de la parte espacial del sistema de ecuaciones en derivadas parciales, ésta se lleva a cabo mediante métodos conservativos en los cuales el estado de cada celda computacional varía como resultado de los flujos a través de sus fronteras. Los flujos numéricos en las interfases de las celdas se calculan utilizando un resolvedor aproximado del problema de Riemann. En Cueva se implementan los

resolvedores aproximados de Riemann *Local de Lax-Friedrich* (LLF), HLL, así como el resolvedor HLLC del que hemos hablado más arriba y que constituye el capítulo 5 de esta tesis. El código emplea varias técnicas de reconstrucción de los valores de las variables para obtener una precisión mejorada en las interfases entre distintas celdas. La mayoría de esas técnicas de reconstrucción preserva la propiedad conocida como *Total Variation Diminishing* (TVD). Entre ellas, cabe mencionar aquellas que permiten alcanzar segundo orden en la discretización de las derivadas espaciales. Este grado de precisión se alcanza utilizando una interpolación lineal entre los valores promedio de las variables pertenecientes a cada celda. Las pendientes utilizadas en la reconstrucción lineal deben ser *monótonas* par que la antedicha propiedad TVD se cumpla. En Cueva se han implementado los siguientes métodos de reconstrucción espacial de segundo orden: MinMod, MCL y SBL, todos ellos (particularmente los dos primeros) ampliamente utilizados en la literatura. Un mayor orden de precisión espacial también es posible en nuestro código, ya que se han implementado los esquemas de preservación de la monotonicidad de quinto, séptimo y noveno orden, respectivamente conocidos como MP5, MP7 y MP9.

Otro elemento algorítmico clave en un código RRMHD es el tratamiento de las ecuaciones de restricción física (o ligaduras) sobre el campo electromagnético. La ausencia de monopolos magnéticos y el hecho de que la carga eléctrica es el resultado de la existencia de variaciones del campo eléctrico se traducen matemáticamente en sendas ecuaciones elípticas, a saber $\nabla\cdot\mathbf{B}=0$ y $\nabla\cdot\mathbf{E}=q$, donde $\mathbf{B}$, $\mathbf{E}$ son los vectores campo magnético y eléctrico, y q la densidad de carga eléctrica. Estas ligaduras físicas deben ser preservadas numéricamente, lo cual no está garantizado a menos que se implementen métodos específicos para ello, incluso si partimos de datos iniciales donde las antedichas ligaduras se respetan. De entre los posibles métodos existentes en la literatura para tratar con las ecuaciones de ligadura se ha optado en nuestro caso por emplear el método generalizado de multiplicadores de Lagrange (GLM por sus siglas en inglés; Dedner et al., 2002). Eso implica añadir dos ecuaciones diferenciales en derivadas parciales (ecuaciones *telegráficas*), ambas de naturaleza hiperbólica, para incluir la evolución de sendos pseudo-potenciales escalares que controlan que las ligaduras físicas sean respetadas numéricamente con un grado de precisión correspondiente al orden formal de convergencia del método numérico. Por tanto, numéricamente, las ligaduras no son estrictamente satisfechas, solo hasta el nivel de precisión que permite el método. El sistema de ecuaciones de la RRMHD incluyendo estas dos ecuaciones suplementarias suele denominarse sistema RRMHD *aumentado* (Komissarov, 2007). Las nuevas ecuaciones para los pseudo-potenciales escalares tienen una parte parabólica que permite amortiguar el desarrollo de desviaciones con respecto a las ligaduras físicas. Dicha parte parabólica depende de constantes que han de ser ajustadas numéricamente. En el capítulo 4 de la tesis, se muestran di-

versos experimentos numéricos conducentes a obtener valores razonables de las mismas que permitan evolucionar el sistema aumentado de la RRMHD libre de errores.

Para validar el nuevo código RRMHD (objetivo del capítulo 4 de esta tesis), se ha realizado una amplia batería de test estándar en una y dos dimensiones espaciales. Estos tests comprenden desde casos en los que los flujos son suaves hasta casos en los que se generan discontinuidades de diversos tipos (por ejemplo, choques y discontinuidades de contacto). Los tests que no desarrollan choques u otras discontinuidades permiten validar si el código numérico rinde según el orden de convergencia formal de los métodos numéricos empleados. Para afrontar el primero de los casos anteriores (flujos suaves sin discontinuidades), usando los tests conocidos como difusión de una capa de transición autosemejante (*Self-Similar Current sheet*; SCS) o la propagación de ondas de Alfvén circularmente polarizadas (*Circularly Polarized Alfvén Wave*; CPAW), ambos con soluciones analíticas (aproximadas o exactas) conocidas, hemos constatado que nuestro método rinde como se espera y que el orden de convergencia numérico depende ligeramente del resolvedor de Riemann elegido (fijadas el resto de las piezas algorítmicas). Es más, constatamos que el resolvedor LLF es el que desarrolla un menor orden de convergencia (pese a lo cual, dicho orden de convergencia es mayor que la unidad y está cercano a dos cuando se espera que sea de segundo orden), seguido del resolvedor HLL y, finalmente, del HLLC, que es el que mejor rinde de todos. Usando otros tests en los que se plantean problemas de Riemann en una dimensión espacial, constatamos la capacidad de nuestro código para capturar razonablemente bien todas las estructuras características que se desarrollan en dichos problemas de Riemann. Este resultado es notorio, pues según se ha visto en el capítulo 2 de la tesis y, tal como había sido también obtenido previamente en la literatura, el sistema de la RRMHD posee 12 velocidades características de propagación, 8 de ellas iguales a la velocidad de la luz (correspondientes a la propagación de ondas electromagnéticas), 2 a la propagación de ondas acústicas y otras dos a la propagación de la entropía y la carga del sistema. Sin embargo, ni el sistema básico de ecuaciones de la RRMHD ni el aumentado con las ecuaciones de preservación de las restricciones físicas posee como velocidades características ni la de Alfvén ni las ondas magnetosónicas rápidas y lentas. No obstante lo cual, en problemas de Riemann cuya solución desarrolla dichas ondas, y en algunos casos también discontinuidades asociadas a las mismas, nuestro código RRMHD captura razonablemente bien todas las estructuras intermedias del mencionado problema de Riemann, aunque con algo más de difusión que lo que se tendría en un código diseñado para resolver las ecuaciones de la RMHD.

En la tarea de *verificación* del código, hemos comprobado que el mismo ansatz, que caracteriza la dependencia de la difusividad numérica (es decir,

tanto la viscosidad como la resistividad numéricas o combinaciones de ambas) y funciona para códigos Eulerianos MHD, también es razonablemente válido en códigos Eulerianos RRMHD. Esta caracterización es fundamental para distinguir qué aspectos de la solución numérica son debidos a la resistividad física y cuáles son resultado de la resistividad numérica. La verificación del código se encuentra resumida en el Cap. 6, donde a partir de un exhaustivo estudio de los errores numéricos se ha podido comprobar el buen comportamiento de los diversos métodos implementados. Estos errores, que provienen de la discretización de las ecuaciones diferenciales en derivadas parciales, pueden difuminar la solución (*disipación numérica*) o introducir errores de fase (*dispersión numérica*). En términos prácticos nuestro estudio se centró en la disipación numérica, cuyo modo de acción se asemeja al debido a la *viscosidad física* y, para flujos magnetizados, también a la *resistividad física*, este tipo de errores comúnmente son referidos en el campo de la MHD numérica, como *viscosidad numérica* y *resistividad numérica*. La caracterización de la difusividad numérica del código es crucial a fin de interpretar adecuadamente los resultados de modelos numéricos elaborados y complejos. De hecho, el conocer la difusividad numérica es importante para diseñar experimentos computacionales donde el crecimiento de inestabilidades depende críticamente de la resistividad física del sistema de estudio. La resistividad numérica (no física) puede producir fenómenos de reconexión que son de naturaleza enteramente numérica, afectando sustancialmente la exactitud de las simulaciones. Este fenómeno puede ser particularmente severo en el régimen de bajas resistividades, el cual es usualmente el caso presente en el modelado de sistemas físicos reales y los cuales requieren una alta resolución para describir apropiadamente las (pequeñas) escalas espaciales sobre las cuales la resistividad afecta. Uno de los resultados más destacados de nuestro estudio es que la velocidad de la luz es la velocidad característica en cualquiera de los sistemas que hemos usado para caracterizar la difusividad numérica. Esta conclusión contrasta con la que se obtiene en MHD clásica, según la cual, la velocidad característica es, en general, la velocidad magnetosónica rápida, o la del sonido si, en particular, no hay campo magnético en el sistema (Rembiasz et al., 2017).

Después de la extensiva verificación del código Cueva, pudimos *validar* su implementación a través de un modelo más realista, que involucra la rigidez del sistema de ecuaciones RRMHD. Nuestro acercamiento en este contexto fue precisamente el estudio de las inestabilidades de doble ruptura magnética (*Double Tearing Modes*; DTM), en las cuales su desarrollo y crecimiento es consecuencia de la existencia de la resistividad Óhmica. El interés astrofísico en estudiar el crecimiento de estos TMs radica en que las escalas de tiempo para su crecimiento pueden ser, potencialmente, suficientemente pequeñas como para explicar fenómenos de reconexión muy rápidos y violentos en contextos como las magnetosferas de estrellas de neutrones o en chorros relativistas, entre otros.

El campo de la investigación de la reconexión puede verse como una carrera por explicar las altas tasas de reconexión inferidas, por ejemplo, en las erupciones solares más violentas o aquellas que se producen en varios experimentos de reconexión llevados a cabo en laboratorios. Esta carrera investigadora se ha acelerado en los últimos años gracias a las contribuciones de simulaciones numéricas y del análisis de inestabilidades en el régimen linea, las cuales confirman la existencia de modos de reconexión rápidos. En efecto, utilizando la aproximación de un único fluido de la MHD[2] y siempre que el número de Lundquist S_{L}[3] sea suficientemente grande y que la relación de aspecto, L/a (a es el semi-espesor de la capa de corriente magnética) sea también grande, la tasa de crecimiento de los TMs puede aumentar muy significativamente. Incluso bajo las condiciones previas, pueden aparecer eventos secundarios explosivos de reconexión y la producción de cadenas de plasmoides sobre escalas progresivamente menores (estas inestabilidades son usualmente llamadas de *super-ruptura* o *inestabilidades de plasmoides*) que conducen a tasas de reconexión casi independientes de S_{L}. Es de resaltar que incluso hojas de corriente del tipo Sweet-Parker (SP), cuya relación de aspecto cumple $L/a \sim S_{\text{L}}^{1/2}$, llegan a ser inestables frente al desarrollo de TMs y su tasa de crecimiento, γ resulta ser $\gamma t_{\text{A}} \sim S_{\text{L}}^{1/4}$ cuando $S_{\text{L}} > S_{\text{L}}^{\text{thr}} \simeq 10^4$ (Bhattacharjee et al., 2009; Lapenta, 2008; Loureiro et al., 2007; Samtaney et al., 2009).

Las inestabilidades resistivas cuyas tasas de crecimiento se incrementan al aumentar el número de Lundquist, es decir, aquellas en las que $\gamma t_{\text{A}} \propto S_{\text{L}}^{\varrho}$, siendo $\varrho > 0$ resultan paradójicas, puesto que las mismas pueden crecer *infinitamente rápido* en el límite MHD ideal (al cual se tiende cuando $S_{\text{L}} \to \infty$), comportamiento que resulta evidentemente no-físico y no-causal. Se podría argüir que en ese límite, los modos resistivos están prohibidos, pero si ese fuere el caso, las ecuaciones de la MHD tendrían un comportamiento muy singular cuando nos aproximamos al límite de conductividad infinita o equivalentemente en el límite de número de Lundquist infinito. Efectivamente, este no puede ser el caso y debe existir un mecanismo que limite el crecimiento de las inestabilidades, el cual no queda bien descrito en el análisis lineal.

Pucci and Velli (2014), basados en ideas expuestas, en el apéndice D, del artículo seminal sobre los TMs de Furth et al. (1963), encontraron una posibilidad muy sugerente para tratar con el límite paradójico de $S_{\text{L}} \to \infty$. La idea se centra en considerar, que solo sobreviven modos TM "ideales" para números de Lundquist grandes ($S_{\text{L}} \gtrsim 10^6$). El termino *modo de ruptura ideal* (*ideal tearing mode*; ITM) puede parecer una contradicción dado el hecho que los TMs son inestabilidades resistivas (es decir, no ideales). Sin embargo, esta terminología

[2] Existen formulaciones de la MHD de doble fluido, en las cuales, se permite la separación de cargas, de tal manera que las cargas positivas (p.e. iones) y negativas (p.e. electrones) puedan evolucionar de manera separada (aunque no independiente).

[3] $S_{\text{L}} := v_{\text{A}} L/\eta$; donde v_{A} es la velocidad de Alfvén y L la longitud de la capa de corriente.

se usa comúnmente en la literatura debido a que las tasas de crecimiento de los ITMs son independientes del número de Lundquist y, por tanto, *independientes de la resistividad*. Este es el caso, cuando la relación de aspecto, L/a, toma valores críticos tales que escalan con el número de Lundquist elevado a una cierta potencia; concretamente,

$$\frac{L}{a} = S_{\mathrm{L}}^{1/3}.$$

Los resultados teóricos obtenidos por Pucci and Velli (2014) han sido confirmados tanto en simulaciones MHD clásicas en dos dimensiones espaciales en el régimen compresible (Landi et al., 2015) como también en el régimen incompresible (Del Sarto et al., 2016). Más recientemente, Del Zanna et al. (2016) han mostrado que el análisis lineal hecho por Pucci and Velli (2014), sigue siendo valido en la RRMHD pero bajo algunas modificaciones significativas. Es precisamente la primera parte del Cap. 7 en la cual estudiamos, las inestabilidades de ruptura relativistas ideales (*Relativistic Ideal Tearing Modes*; RITMs), bajo las condiciones optimas en las cuales se obtiene las más rápidas tasas de disipación. Puesto que este campo de estudio no es nuevo y existen referencias en la literatura previas (Del Zanna et al. (2016)), nuestro trabajo se centró en reproducir resultados existentes y luego en explorar el espacio de parámetros que conllevan efectos relativistas importantes en la dinámica.

En la segunda parte del Cap. 7 hemos explorado otra posibilidad, también existente en la literatura, ésta es la interacción entre dos (o más) hojas de corriente suficientemente cercanas y que sean inestables frente al crecimiento de TMs. Estas inestabilidades pueden presentar tasas de crecimiento mayores que las correspondientes a los TMs debido a la interacción entre las capas de corriente. La evolución de los TMs en sistemas de múltiples hojas de corriente es diferente de aquellas en una sola hoja de corriente. Varios autores han explorado analíticamente (ver, p.e. Otto, 1991; Otto and Birk, 1992) y numéricamente en la descripción MHD clásica resistiva (ver, p.e. Janvier et al., 2011; T. Birk and Otto, 1991) y en la RRMHD (p.e. Baty et al., 2013). En particular estos estudios se han focalizado en los *modos de ruptura dobles* (*Double Tearing Modes*; DTM) y sus resultados revelan que, en los estados lineales y no lineales, el acoplamiento e interacción de las islas magnéticas puede desestabilizar las hojas de corriente y como resultado es posible que aparezca una *fase explosiva* en cuanto al crecimiento de la inestabilidad (después del final de una fase lineal).

Siguiendo las mismas ideas de escalamiento que en Pucci and Velli (2014) para los ITMs, Baty (2017) encuentra la existencia de modos de ruptura dobles *ideales* (*ideal double tearing modes*; IDTMs), bajo la condición que la relación de aspecto de cada hoja de corriente presente una relación de aspecto que

escale con el número de Lundquist de la siguiente forma

$$\frac{L}{a} = S_{\mathrm{L}}^{9/29}.$$

A fin de comprobar si esta ley de escalamiento es valida también en la RRMHD, hemos realizado simulaciones moderadamente relativistas ($v_{\mathrm{A}} = 0.5$). La elección de este régimen es deliberada, pues nos ha permitido comparar nuestros resultados RRMHD con aquellos de Baty (2017) (clásicos) y, lo que es más importante, verificarlos con otro código construido para tratar problemas MHD clásica viscosa-resistiva (Aenus; Obergaulinger, 2008). De esta forma, hemos confirmado (utilizando tanto el código Cueva como Aenus) que los modos de ruptura doble *ideales* relativistas (*Relativistic Ideal Double Tearing Modes*; RIDTMs) crecen en la RRMHD bajo condiciones similares a las que lo hacen en el caso MHD clásico resistivo. Más aún, las fases evolutivas que sigue el crecimiento de los RIDTMs son cualitativamente los mismos que los descritos por Baty (2017). Primero, existe una fase transitoria donde las perturbaciones iniciales desencadenan (las auto-funciones de) la inestabilidad. Segundo, se establece una fase lineal de crecimiento exponencial de las inestabilidades. Se aprecia en esta fase, por ejemplo, el crecimiento del campo magnético perpendicular a la hoja de corriente (es decir B_x en nuestros modelos numéricos), el cual es inicialmente despreciable comparado con la componente paralela a la hoja de corriente (es decir, B_y). Al mismo tiempo tanto la velocidad en la región afectada por la reconexión del campo magnético, como la energía interna crecen. Tercero, algunos modelos con la adecuada relación de aspecto (L/a) desarrollan una fase explosiva. Nosotros hemos encontrado que modelos en los que $15 \lesssim L/a \lesssim 200$ desarrollan dicha fase explosiva (los límites son sólo aproximados). Una vez que nuestros modelos han entrado en la fase explosiva, el plasma se vuelve súper Alfvénico en ciertas regiones localizadas, que se asemejan a regiones de reconexión de tipo Petscheck (Petschek, 1964). El tiempo en el cual sucede el máximo de amplificación del campo magnético en la fase explosiva, escala aproximadamente como $t_p \propto L_y^{-1/2}$. Cuarto, finalmente el sistema se relaja y B_x decrece a valores que son similares a aquellos que se encuentran al final de la fase lineal.

Comparando con el ritmo de crecimiento de los RITMs, los RIDTMs crecen aún más rápido. Ello los sitúa como una posibilidad muy factible para explicar sucesos astrofísicos que invoquen la disipación ultra-rápida (explosiva) del campo magnético. El hecho de que no sólo desarrollen una fase explosiva los RIDTMs, sino también modos de ruptura doble relativista con relaciones de aspecto cercanos al ideal, dotan a este proceso de gran robustez teórica y práctica. Siguiendo la línea de argumentación de Pucci and Velli (2014) pero aplicada a RIDTMs, nuestros resultados sugieren que en la naturaleza pueden existir sistemas con hojas de corriente cercanas en las cuales, quizá

la relación de aspecto no sea óptima. Típicamente esas hojas de corriente serán excesivamente anchas inicialmente (es decir, L/a será pequeño). Sin embargo, su evolución típica es muy factible que sea la de iniciar un proceso de *adelgazamiento* hasta que, eventualmente se llegue a una relación de aspecto cuasi-óptima ($L/a \sim S_{\rm L}^{9/29}$). En este punto, las hojas de corriente devienen en inestables frente al crecimiento de RIDTMs, los cuales permiten disipar la energía magnética, en una primera fase, de forma que el proceso es exponencial con un ritmo de crecimiento lineal (es decir, $\propto \exp\left(\gamma_{\rm RIDTM} t\right)$), para después desarrollar una fase explosiva, cuya tasa de crecimiento es prácticamente independiente de la resistividad. Dado que este proceso se puede desarrollar en escalas de tiempo de entre ~ 10 y ~ 60 veces el tiempo de cruce de la dimensión longitudinal de la hoja de corriente a la velocidad de Alfvén (es decir, $t_{\rm A}$), el proceso puede ser extremadamente rápido cuando $v_{\rm A} \to 1$. Además, nuestros resultados ponen de manifiesto que los flujos generados como resultado del proceso de reconexión (el cual convierte energía magnética en energía térmica y cinética) pueden ser significativamente relativistas. Cuando $v_{\rm A} = 0.5$ en el medio no perturbado, las capas de corriente pueden llegar a generar canales de plasma con factores de Lorentz máximos $W \sim 1.5 - 2.3$. Nuestros resultados permiten colegir que en modelos en los que $v_{\rm A} \gtrsim 0.65$, $W \gtrsim 10$ puede llegar a alcanzarse. Estos valores del factor de Lorentz están en el intervalo requerido para que el modelo de "chorros-en-un-chorro" (*jets-in-a-jet*) sea viable y permita explicar la rápida variabilidad mostrada por algunas fuentes relativistas (por ejemplo, blazars).

Contents

Summary **i**

1 Introduction **1**
1.1 Overview of numerical methods used in RRMHD 6
1.2 Goals 10
1.3 Plan of the thesis 12

2 The equations of RRMHD **17**
2.1 Maxwell's equations 17
2.1.1 Maxwell field tensor 18
2.1.2 Faraday field tensor 18
2.1.3 Ohm's law 19
2.2 Continuity of charge and current density 20
2.3 Continuity of mass density 21
2.4 Stress-energy tensor 22
2.4.1 Hydrodynamic stress-energy tensor 22
2.4.2 Electromagnetic stress-energy tensor 23
2.5 Conservation Laws 24
2.6 Enforcement of electromagnetic constraints 26
2.7 The augmented RRMHD system of equations 27

3 Characteristic properties of the RRMHD **29**
3.1 Characteristic speeds 31
3.2 Approximate self-similar solution 33
3.3 Jump Conditions across flow discontinuities 36
3.4 Lichnerowicz Adiabat 45

4 Numerical methods **47**
4.1 Spatial Discretization . . . 50
4.1.1 Intercell Reconstruction Methods . . . 50
4.1.2 Approximate Riemann Solvers . . . 53
4.2 Time Integration . . . 57
4.2.1 Implicit-Explicit Runge-Kutta Schemes . . . 58
4.2.2 Minimally Implicit Runge-Kutta Methods . . . 63
4.3 Recovery of the primitive variables . . . 67
4.3.1 Recovery of the Lorentz factor . . . 67
4.3.2 Recovery of the gas pressure . . . 69
4.4 The treatment of the elliptic constraints . . . 70
4.5 Numerical Experiments . . . 71
4.5.1 Resistive Self-similar Current Sheet . . . 72
4.5.2 Large Amplitude CP Alfvén waves . . . 74
4.5.3 Numerical order of accuracy . . . 75
4.5.4 Resistive shock tube . . . 77
4.5.5 Ideal shock tubes . . . 79
4.5.6 Resistive rotor . . . 85
4.5.7 Cylindrical Explosion in the nearly ideal regime . . . 91

5 HLLC Approximate Riemann solver **95**
5.1 HLLC Solver . . . 96
5.1.1 HLLC consistency conditions . . . 97
5.2 Numerical Experiments . . . 102
5.2.1 Contact Wave Discontinuities . . . 102
5.2.2 Rotational Wave . . . 103
5.2.3 Shock Tube Problem 1 (ST1) . . . 105
5.2.4 Shock Tube Problem 2 (ST2) . . . 109
5.2.5 Shock Tube Problem 3 (ST3) . . . 111
5.2.6 Shock Tube Problem 4 (ST4) . . . 111
5.2.7 Shock Tube Problem 5 (ST5) . . . 113
5.2.8 Resistive rotor . . . 116
5.2.9 Cylindrical Explosion . . . 118

6 Numerical dissipation **123**
6.1 Measurement of the numerical viscosity . . . 126
6.1.1 Velocity Shear Layer . . . 127
6.2 Measurement of the numerical resistivity . . . 131
6.2.1 Magnetic Diffusion . . . 132
6.3 Measurement of the numerical diffusivity . . . 138
6.3.1 Circularly Polarized Alfvén Waves . . . 142
6.4 Characteristic scales ($\mathcal{L}$ and $\mathcal{V}$) . . . 160

7 Relativistic *Ideal* Tearing Modes **163**
7.1 Relativistic Ideal Tearing Modes 175
7.2 Relativistic Ideal Double Tearing Modes 181
7.2.1 Dispersion relation of DTMs 182
7.2.2 The non-linear evolution 199

8 Conclusions and outlook **217**

A Cueva code **227**
A.1 Butcher tables 227
A.2 Flowchart 233

B Alternative HLLC solvers **235**
B.1 Hybrid HLLC solver 235

C Collective plasma behaviour **239**

D Heaviside-Lorentz units **243**

E Characteristic velocities **245**

Abbreviations **251**

Acknowledgements **253**

Chapter 1

Introduction

Plasma is the fourth state of matter that results from the ionization of its constituents, whereby electrons and ions dissociate from neutral species, as the temperature in the medium overtakes the ionisation energy. Today we know that plasma is not only a hot and disordered state of matter. Rather, we have learned during the last years that plasma systems can attain gaseous, liquid and even solid phases (as dusty plasma; see e.g. Ishihara (2007)). The plasma state, as an electrically conductive medium, possesses a number of new properties that distinguish it from neutral gases and liquids. Over 99% of the observable matter in the universe is in the plasma state (e.g. Bachynski, 1961).

It was Tonks and Langmuir (1929) who first use the term *plasma* in a physics context to designate that portion of an arc-type discharge in which the densities of ions and electrons are high but substantially equal. It is possible that Tonks and Langmuir use this term in analogy with that introduced in the mid nineteenth century by the Czech physiologist Jan Evangelista Purkinje, who used the Greek word *plasma* (meaning "formed" or "moulded") to denote the clear fluid that remains after removal of all the corpuscular material in blood. However it turned out that, unlike blood where there is a fluid medium carrying the corpuscular material, there actually is no "fluid medium" entraining the electrons, ions, and neutrals in an ionized gas. Actually the term *plasma* is used quite generally to refer a *quasi-neutral* assemblies of charged and neutral particles which exhibits collective behavior, which means that the macroscopic result to an external stimulus is the cooperative response of many plasma particles. It is worth mentioning that plasma physics illustrates how it is possible for matter to behave both as a collection of particles (showing particle-like properties) and as a fluid (showing wave-like properties).

In accordance with Chen (1984) and as explained in App. C, three conditions should be satisfied for collective plasma behaviour and for an ionized gas

to behave as a plasma. These are, first, the time scales of collective oscillatory motion (τ) must be sufficiently short with respect to collision times with neutrals (τ_n), $\tau \ll \tau_n$ (Eq. (C.1)). Second, the length scale of plasma dynamics (λ) must be much larger than the Debye length (λ_D), which is the typical size of a region over which charge imbalance due to thermal fluctuations may occur, $\lambda \gg \lambda_\mathrm{D}$ (Eq. (C.2)). Third, there must be many particles in a Debye sphere, $N_\mathrm{D} \gg 1$ (Eq. (C.3)).

Since the plasma state includes free positive and negative charges, and since movements of these charges produce electrical currents, it is clear that the constituents of the plasma state will be influenced by electric (E) and magnetic fields (B), and that the motion of charged constituents in the plasma can also produce electric and magnetic fields. Hence, in discussing the properties of a plasma, it is essential to regard the electromagnetic field as an integral part of the plasma system.

Following Goedbloed and Poedts (2004), the macroscopic modeling of plasma dynamics can be carried out with three different approaches, namely, the Vlasov theory, the two-fluid theory, and magnetohydrodynamics (MHD). The Vlasov model is the most detailed and characterizes plasma dynamics by following the temporal evolution of electron and ion velocity distribution functions. The two-fluid model is intermediate in complexity and approximates plasma as a system of mutually interacting, finite-pressure electron and ion fluids. The MHD model is the least detailed and approximates plasma as a single, finite-pressure, electrically conducting fluid. For a valid macroscopic model of a particular magnetized plasma, in addition to fulfill the criteria of collective behavior, the time scales and characteristic length, of a particular dynamical configuration, should be much larger than the inverse ion cyclotron frequencies $\Omega_i^{-1} \equiv m_p/|Ze\,B|$ and the ion cyclotron radii $R_i \equiv v_\perp/\Omega_{e,i}$, where m_p is the proton mass, e the electron charge, Z the ion charge number, B the external magnetic field strength and $v_\perp$ the perpendicular component to gyro-radius of velocity. This is possible when the magnetic field is large enough for the plasma volume under consideration to contain many ion gyro radii and when the dynamic phenomena last many ion gyro periods.

As stated in Goedbloed and Poedts (2004), the macroscopic plasma dynamics is driven by the interaction of plasma motion and magnetic field geometry. In order to approach a plasma as a fluid, one shall consider the collective behaviour of electrons and ions under the influence of magnetic fields not as separate species, but as a unique entity. Theoretically, the MHD description is the adequate approximation to describe the interplay between plasma and magnetic field.[1]

[1] We note that there is a fundamental difference between hydrodynamic and MHD fluid models. In the former, the fluid constituents (molecules or atoms) are strongly coupled

Assuming that a *single*-fluid MHD approach is adequate for the purposes of a certain model, relativistic effects can be further considered under some circumstances such as the ones that follow. A relativistic description of the plasma kinematics is needed when the velocities developed by collective (macroscopic) parts of the plasma (or the plasma as a whole) are close to the speed of light in vacuum, c. Likewise, the plasma thermodynamics may become relativistic if the specific internal energy of the plasma constituents is at least of the order c^2. In these cases the appropriate framework to model the fluid is that of either the relativistic MHD (RMHD hereafter), if non-ideal effects are negligible, or the *resistive* relativistic MHD (RRMHD), when (non-ideal) Ohmic dissipation is relevant. Compared to laboratory MHD, astrophysical objects have such large sizes that the electric currents are generated from self-induction rather than electrical resistance (Cowling, 1976). Ideal MHD can be safely adopted for the modeling of most astrophysical plasma, since their conductivity is extremely high. However, the (ideal) limit of *infinite* electric conductivity is only a sound first approximation in many cases, but it is insufficient in many others.

Ohmic dissipation allows for magnetic reconnection, whereby magnetic field lines of oposite polarity *self-destroy* if they are brought in very close contact. The destruction of antiparallel magnetic flux tubes induces a change of topology of magnetic field lines that is prevented in ideal MHD due to flux conservation. Reconnection of the magnetic field typically happens at very small length scales compared with the typical size of the system. In reconnection sites, Ohmic resistivity generates Joule dissipation. The energy generated in this way can be huge in astrophysical contexts. A couple of paradigmatic (though non-relativistic) examples of the previous phenomenology are the heating of the solar corona (Parker, 1983) or solar eruptive events (e.g. Cheng et al., 2017). In both cases the Joule heating is the main driver of the observed dynamics.

In the following, we will introduce a number of astrophysical scenarios where relativistic magnetized plasma is present. In some of these astrophysical contexts Ohmic dissipation is relevant. Thus, hereafter, we will assume that the RRMHD description of the plasma is adequate for the goals pursued in this thesis. Relativistic magnetized plasma is ubiquitously found among the most violent and catastrophic phenomena of the Universe. Active galactic nuclei (AGN) (Blandford, 2002), Gamma-ray bursts (GRBs; Lyutikov and Blandford, 2003), microquasars (McKinney and Gammie, 2004; Meier, 2003), pulsars and magnetars (Bucciantini et al., 2005; Obergaulinger and Aloy, 2017), compact X-ray binaries (Varnière et al., 2002), mergers of binary neutron stars (Fernández and Metzger, 2016; Rezzolla et al., 2011), black holes (Marrone

by means of continuous collisions with their neighbors. Whereas in an ideal plasma its constituents (namely, electrons and ions) do not experience frequent Coulomb collisions with their nearest neighbors. Instead, the charged plasma constituents follow the forces from the average electric and magnetic fields that are produced by many other particles (Piel, 2010).

et al., 2007; Martí-Vidal et al., 2015; Palenzuela et al., 2010), etc., may quite generically be endowed with dynamically relevant magnetic fields. From the dynamical point of view, magnetic fields play a main role in the angular momentum transport required for driving accretion in Keplerian discs girding compact objects. The magnetorotational instability (MRI; Chandrasekhar, 1960; Velikhov, 1959) is likely to be the main mechanism inducing the angular momentum redistribution in accretion discs (e.g. Balbus and Hawley, 1991, 1998). Another context where the MRI seems to be crucial for the magnetic field to reach dynamically relevant strength is stellar core collapse. The post-collapsed core of a massive star develops suitable conditions for the magnetic field to be amplified by the MRI (e.g. Akiyama et al., 2003; Cerdá-Durán et al., 2007; Mösta et al., 2015; Obergaulinger et al., 2006; Sawai and Yamada, 2016; Sawai et al., 2013). In any of these scenarios, the foremost question is not whether MRI may develop, but instead, which is the primarily mechanism quenching the magnetic field growth before it exhausts all the available free energy (namely, differential rotational energy) in the system. Compressibility caused by the magnetic field or parasitic instabilities, which can be strongly affected or even are triggered by non-ideal effects such as resistivity and viscosity (Goodman and Xu, 1994; Latter et al., 2009; Pessah, 2010), are commonly invoked as the main agents setting the termination level of the field growth (but see Rembiasz et al., 2016a,b).

Relativistic jets generated from compact objects are another example where resistive effects may be instrumental to understanding their generation. In one of the most accepted models of jet formation, magnetic field taps a fraction of the rotational energy of a Kerr black hole (BH) and launches a relativistic beam of very magnetized plasma (e.g. Beskin and Kuznetsova, 2000; Blandford and Znajek, 1977; Komissarov, 2004; McKinney, 2006; Okamoto, 2006; Penna et al., 2013; Tchekhovskoy et al., 2010). The global structure of the magnetosphere surrounding either a neutron star (NS) or a BH is reasonably well represented assuming that it is force-free. However, it is unlikely that the force-free conditions hold everywhere. For instance, in the case of NSs, there may exist small regions (gaps) where particles are accelerated by the electric field along the magnetic field lines. These procesesses may explain the magnetospheric emission (Beloborodov, 2013a,b; Beloborodov and Thompson, 2007; Levinson and Segev, 2017). In the case of BH magnetospheres, it is not uncommon that even the simplest topologies of the magnetic field encompass low latitude regions where current-sheets (which are known to be unstable against the tearing mode (TM) instability; Furth et al., 1963) are present, e.g. in split-monopole configurations (Blandford and Znajek, 1977; Contopoulos et al., 2013; Ghosh, 2000; Nathanail and Contopoulos, 2014). They may also develop in the course of the dynamical evolution either arising from the accretion disk (Goodman and Uzdensky, 2008; Parfrey et al., 2015) or due to MHD instabilities of a

Poynting-flux dominated flow (Begelman, 1998; Bromberg and Tchekhovskoy, 2016; Eichler, 1993; Giannios and Spruit, 2006).

Besides the undeniable dynamical influence that non-ideal resistive effects may have on astrophysical sources associated to relativistic outflows, the emission properties of such sources are likely bound to the mechanisms of magnetic field dissipation if the outflows are Poynting-flux dominated (Giannios and Spruit, 2005; Spruit et al., 2001; Thompson, 1994; Zhang and Yan, 2011). The "internal shocks" or "shock-in-jet" model (e.g. Bicknell and Wagner, 2002; Marscher and Gear, 1985; Mimica et al., 2004; Rees, 1978; Rees and Mészáros, 1994; Rueda-Becerril, 2017; Spada et al., 2001) has an important role in the understanding of the blazar spectra and has been very often invoked for explaining many of the features of the blazar variability and flares, as well as the prompt emission of GRBs. For the latter, however, there have been claims that the radiation efficiency is too low (Kumar, 1999; Kumar and Narayan, 2009; Panaitescu et al., 1999), though more detailed numerical models seem to ameliorate this potential drawback (Mimica et al., 2005). Indeed, internal shocks happening in a moderately magnetized plasma can be (much) more efficient converting kinetic energy into thermal *and* magnetic energy than purely hydrodynamic internal collisions (Mimica and Aloy, 2010; Mimica et al., 2007). There are, however, indications that the dissipation of magnetic fields may naturally explain the observed phenomenology as we discuss in the next paragraphs.

First, employing particle-in-cell (PIC) simulations, Sironi et al. (2015) show that magnetic reconnection may deposit more than 50% of the dissipated energy into non-thermal leptons when the magnetic field energy density is larger than the rest-mass energy density. The shock downstream emitting region shows a rough equipartition between magnetic field and radiating particles, accounting naturally for this commonly observed property in blazars. Along the same line, Petropoulou et al. (2016) also conclude that blazar flares naturally result from magnetic reconnection in a magnetically dominated jet.

Second, the lack of a thermal component in the spectrum of some well observed Fermi GRBs (e.g. in GRB 080916C; Zhang and Pe'er, 2009) is taken as an indication of the magnetization of the radiating plasma flow. The photospheric thermal component, which is expected to appear in the standard "fireball" model, can be much dimmer (unobservable in practice) if the outflow is Poynting dominated (Daigne and Mochkovitch, 2002; Zhang and Mészáros, 2002), unless the Poynting flux is directly converted into kinetic energy of the flow below the photosphere (e.g. Vlahakis and Königl, 2003). This means that magnetic dissipation should play a fundamental role shaping the observed spectra.

Third, the short time-scales displayed by the high-energy emission of either GRBs or blazar jets in AGNs have driven the development of various

models where the (*fast*) reconnection of the magnetic field is of paramount importance. Among them, we find the "minijets" or "jets-in-a-jet" model (e.g. Barniol Duran et al., 2016; Giannios, 2013; Giannios et al., 2009, 2010; Nalewajko et al., 2011) and the "fundamental emitters" or "relativistic turbulence" model (e.g. Blandford, 2002; Kumar and Narayan, 2009; Lazar et al., 2009; Lyutikov, 2006; Lyutikov and Blandford, 2003; Narayan and Kumar, 2009; Narayan and Piran, 2012; O'Riordan et al., 2017). The "jets-in-a-jet" model attributes the TeV emission in relativistic AGN jets to blobs of plasma (plasmoids) where the magnetic field dissipates by reconnection (Giannios et al., 2009, 2010). Under certain conditions, the reconnection outflows are moderately relativistic and may efficiently power the observed TeV flares through synchrotron-self-Compton emission. The emission of the outflows generated by episodic reconnection events is Doppler boosted by the relativistic jet beam. The resulting TeV flares timescales may be as short as minutes in the context of AGN jets, consistent with that observed in, e.g. M87 (Acciari et al., 2008; Aharonian et al., 2006; Albert et al., 2008) as well as in the blazars MrK 501 and PKS 2155-304 (Aharonian et al., 2007; Albert et al., 2007). We note, however, that Narayan and Piran (2012) find that the emission properties (variability) of relativistic turbulent motions in a beam with a sufficiently fast jet (with a Lorentz factor $W > 25$) accommodate more easily the TeV light-curve of the blazar PKS 2155-304 than the standard minijets model.

Fourth, models based upon the reconnection of the magnetic field have also become popular to explain the prompt emission of GRBs. For instance, the *Internal Collision-induced Magnetic Reconnection and Turbulence* (ICMART) model (Deng et al., 2015; Zhang and Yan, 2011) assumes that in an intermittent magnetically dominated outflow ($1 \lesssim \sigma_{\rm m} \lesssim 100$),[2] internal collisions take place. Due to the larger magnetization of the flow, the first generation of (weak) internal shocks happening at relatively small distances from the central GRB engine ($\sim 10^{13} - 10^{14}$ cm) distort any large scale magnetic field existing in the flow. The successive generations of shell collisions, which take place at distance scales $\sim 10^{15} - 10^{16}$ cm, trigger fast turbulent reconnection (an ICMART event) that may be observed as a broad pulse in the GRB light curve.

Fifth, for typical long GRB jets, McKinney and Uzdensky (2012) find that magnetic reconnection may be avoided due to the high collisional rate of the plasma deep inside the GRB stellar progenitor, until a "reconnection switch" mechanism proceeds catastrophically near the jet photosphere, where radiation is efficiently released.

[2] In this particular context, the magnetization is defined in Heaviside-Lorentz units as $\sigma_{\rm m} := B^2/(\rho W^2 c^2)$, where B, ρ, W, and c are the magnetic field strength, the rest-mass density, the bulk Lorentz factor of the plasma, and the speed of light in vacuum, respectively. But we note that different definitions of the magnetization are possible (see Eq. (2.25)).

1.1 Overview of numerical methods used in RRMHD

The equations governing the dynamics of either magnetized or unmagnetized fluids are partial differential equations (PDEs). Generically, they express that the balance between fluxes of different physical quantities across the surface of control volumes inside the fluid and the sources or sinks of these quantities yields the evolution of, e.g. mass, momentum, energy, etc. in the system. The possibility that discontinuities (e.g. shocks) appear in a fluid (either magnetized or not) has shaped the development of the numerical methods necessary to evolve mathematically the systems of PDEs mentioned above. Very grossly speaking, the solution of a PDE (or a system of PDEs) should be a differentiable function (or set of functions). However, when shocks or other discontinuities (e.g. contacts) develop in and *inviscid* fluid, the standard methods to integrate PDEs must be cautiously devised. These solutions are provided as the limits of vanishing viscosity and/or resistivity, since finite physical viscosity yields shocks, which do not exhibit infinitely sharp transitions between shocked and unshocked states. Instead, the solutions of PDEs governing MHD, or RMHD display smooth transitions in physical plasmas, even across shocks or current-sheets and the width of the transitions depends on the magnitude of the viscosity and/or the resistivity in the system (the higher the viscosity, the broader the transition layers between shocked and unshocked states; likewise, the higher the resistivity, the broader the transition layer between currents of oposite magnetic polarity). Numerical methods must incorporate suitable recipes to handle the inviscid and the ideal (non-resistive) regimes, since otherwise spurious oscillations develop in the solution, which eventually blow up the overall plasma structure.

As we have argued above, magnetic reconnection is a very important phenomenon in astrophysical plasma. Due to the non-linear character of the dynamics resulting from reconnection events the numerical treatment of most problems of interest has been unavoidable. Though it may seem paradoxical, the effects of magnetic reconnection have been very often approached using ideal MHD or ideal RMHD if relativistic effects shall be incorporated in the numerical modeling. The explanation for this conundrum stems from the fact that even ideal (R)MHD numerical models include *numerical resistivity*, which is obviously unphysical and, in many cases, impossible to control. For this reason, using resistive RMHD is important for understanding reconnection and related phenomena in astrophysical plasma. From a non-relativistic point of view, Ohmic dissipation is accounted for by an additional term $\nabla^2\mathbf{B}/\sigma$ in the induction equation, with σ being the conductivity. This extra term is parabolic from a mathematical point of view and, hence, it may drive non-causal dynamics (as other dissipation terms do in Newtonian theory). As a result, if one takes into account Ohmic dissipation in RMHD using a naive extension of the

aforementioned induction equation, the numerical solution computed in this way is prone to the exponential growth of unphysical modes, and becomes unstable for small perturbations, as was shown for various dissipation processes by Hiscock and Lindblom (1983, 1985). The instabilities (as well as the parabolic term $\nabla^2\mathbf{B}/\sigma$) result from neglecting the time derivative of the electric field in the induction equation with Ohmic dissipation. Thus, a physically consistent numerical evolution of the RMHD equations with Ohmic dissipation must include the time evolution of the electric field, i.e. it must include (the time dependent) Ampere's law. This equation is hyperbolic and satisfies causality.

Most of the methods employed to compute numerical solutions in RRMHD have been inherited from RMHD, though adapted to the possibility that the equations may become stiff in the limit of high conductivity (see below). The evolution of the numerical methods for the integration of the RMHD system of equations can be seen as a continous struggle to apply the minimum amount of *numerical viscosity* to handle properly shocks. The earliest approach to the problem consisted in adding *artificial viscosity* terms to the RMHD equations discretized with finite difference techniques (Wilson, 1975, 1977). With that code, Wilson was able to simulate stellar core collapse and the accretion of magnetized mater onto black holes. However, the use of the early forms of artificial viscosity soon became unsatisfactory, even in relativistic hydrodynamics, as they were not able to handle relativistic regimes with Lorentz factors much larger than 2 (e.g. Centrella and Wilson, 1984). That difficulty led many different groups to adopt alternative strategies. For instance, Dubal (1991) and Yokosawa (1993) employed the so-called flux-corrected transport method (FCT) of Boris and Book (1973) to solve the equation of RMHD. Nonetheless, a fundamental improvement came from the incorporation of high-resolution shock-capturing schemes (HRSC) to the solution of the RMHD equations (e.g. Balsara, 2001; Koide et al., 1996; Komissarov, 1999). Reconnection outflows are bounded by shocks that any numerical code aiming to study them should handle well, in addition to current sheets and filaments in the flow. Thus, HRSC techniques are also a common choice in RRMHD (e.g. Bucciantini and Del Zanna, 2013; Dumbser and Zanotti, 2009; Komissarov, 2007; Palenzuela et al., 2009; Takamoto, 2014; Takamoto and Inoue, 2011).

In recent years, a remarkable progress has been made in numerical methods for RRMHD. The implementation of such numerical methods is chiefly based upon a conservative formulation of the RRMHD system of equations. This requires evaluating either an exact or an approximate solution to the Riemann problem at the interfaces between adjacent computational zones (see, e.g. the excellent review by Martí and Müller 2015). Exact Riemann solvers usually are computationally very expensive. Thus, approximate solvers have been broadly used in classical magnetohydrodynamics (MHD), in RMHD and, more recently, in RRMHD simulations. Among them, the Harten-Lax-van Leer (HLL) solver

(Harten et al., 1983) has been extensively used due to its easy implementation and robustness. Those properties of the HLL solver are based on its Jacobian-free design, which avoids the decomposition of the jumps of the characteristic variables over all right eigenvectors of the system of equations. Instead, a single state that is an average of the solution over the Riemann fan is computed. This single state is bounded by two limiting waves where Rankine-Hugoniot (RH) jump conditions hold. The higher the number of different intermediate states the Riemann problem develops (dictated by the number of different intermediate eigenvalues of the Jacobian), the less accurately the single average state over the Riemann wave structure represents the breakup of the discontinuity (i.e., the more diffusive it is). In its more basic form, the system of RRMHD equations constitutes a hyperbolic system of balance laws with two additional (elliptic) constraint equations that state the solenoidal character of the magnetic field and that the electric charge fixes the divergence of the electric field (Anile, 1989; Dixon, 1978). In the hyperbolic sector of the basic RRMHD system, we find 12 eigenvalues corresponding to electromagnetic waves (6 eigenvalues), fast magnetosonic waves (2 eigenvalues) and entropy, shear and charge waves (4 eigenvalues).[3] In the formulation of Komissarov (2007), the basic RRMHD system is *augmented* with two additional equations, that control the evolution of both scalar potentials, which act as generalized Lagrangian multipliers (GLM; Dedner et al., 2002) to maintain the constraints of the electromagnetic field. In this formulation, the constraints are not elliptic equations but, instead, hyperbolic (telegrapher) equations. Thus, in the augmented system of RRMHD, there are 14 eigenvalues, 8 of which are degenerate and equal to the speed of light (limiting the Riemann fan), in addition to two fast magnetosonic waves and four contact waves moving at the local fluid speed (Cordero-Carrión et al., 2012).

In account of the observations made in the previous paragraph, it turns out that, even in its more basic formulation a RRMHD Riemann problem may breakup in many different intermediate states, rendering (very) inaccurate the HLL single average state approximation. This has motivated us to develop a more accurate (but simple enough) Harten-Lax-van Leer contact wave (HLLC) approximate Riemann solver for the augmented RRMHD system that we discuss in this thesis in Chap. 5, and that has led to a separate publication (Miranda-Aranguren et al., 2018). We note that either HLL or HLLC Riemann solvers applied to RRMHD use the velocity of light as the maximum propagation speed in the solution. Thus, they may suffer from excessive diffusion when one considers problems whose characteristic velocity is much lower than that of light. To ameliorate this problem, Takamoto and In-

[3] In contrast, the system of equations of RMHD has 5 different intermediate eigenvalues (two slow magnetosonic, one Alfvén and one contact) under non-degenerate conditions (Anile, 1989; Antón et al., 2010; Komissarov, 1999).

oue (2011) developed an original technique to integrate the RRMHD equations using the method of characteristics. In their method, different characteristic speeds are employed to evolve the different parts of the fluxes contributing in the RRMHD system. According to Takamoto and Inoue (2011), their method it is capable of accurately solving problems that cannot be approximated as ideal RMHD and whose characteristic velocity is much lower than the velocity of light. However, their method seems to work well only in the regime of relatively low magnetization ($\sigma_{\rm m} \lesssim 1$).[4]

The numerical solution of the augmented system of RRMHD is considerably more challenging than that of the ideal-MHD equations, due to the stiff source terms pressent in Maxwell's equations. The stiffness of the equations is the natural consequence of the fact that the diffusive effects take place on time-scales that are either of the same order of magnitude or much smaller than the dynamical one. In RRMHD, the relaxation terms can dominate over the purely hyperbolic ones, posing prohibitive constraints on the time-step in case that explicit integration algorithms are used for the time evolution. Hence, a number of alternatives to explicit methods have been considered in the literature. Komissarov (2007) treated the potentially stiff source terms with the time-step splitting technique (Strang, 1968). This approach has also been followed by Takamoto and Inoue (2011). Alternatively, Palenzuela et al. (2009), employed Implicit-Explicit Runge-Kutta methods (RKIMEX; see e.g. Sec. 4.2.1) to approach the solution of the augmented system of RRMHD. Aloy and Cordero-Carrión (2016) developed the so-called Minimally Implicit Runge-Kutta methods (MIRK; see e.g. Sec. 4.2.2) to deal with the stiffness of the RRMHD equations in the high conductivity regime. MIRK methods prevent the development of numerical instabilities without increasing the computational costs in comparison with explicit methods, and are algorithmically advantageous with respect to the RKIMEX methods because they are designed to avoid additional iterative loops in order to recover the primitive (physical) variables. We finally note that Marinacci et al. (2018) have introduced novel explicit and implicit numerical schemes for the Ohmic resistivity terms in a moving-mesh code solving Newtonian non-ideal MHD equations.

1.2 Goals

The main goal of this thesis is the study of magnetic reconnection in relativistic plasma of astrophysical interest. Indeed, relativistic reconnection is an active area of research (Del Zanna et al., 2016; Hesse and Zenitani, 2007; Komissarov et al., 2007; Mizuno, 2013; Mohseni et al., 2015; Qian et al., 2017; Takamoto, 2013; Tenbarge et al., 2010; Uzdensky, 2011; Watanabe and Yokoyama, 2006;

[4] The precise definition of the plasma magnetization in RRMHD can be found in Eq. (2.25).

Zenitani and Hesse, 2008; Zenitani et al., 2009, 2010; Zenitani and Hoshino, 2007). Magnetic reconnection is highly dynamic, and it changes magnetic field energy into fluid energy (Li et al., 2007; Zenitani et al., 2009; Zweibel and Yamada, 2009). Thus, our approach to the study is numerical, i.e. we will need to develop numerical models that mimic as closely as possible the physical conditions under which reconnection happens in relativistic astrophysical plasma.

The goals of this thesis can be grouped in two sets: computational and physical. Considering that we aim to obtain physical results (ideally) independent of the numerical methods that we employ, we pursue the development of a new multidimensional RRMHD code for astrophysical applications. The code must include, at least, different numerical algorithms for the time-evolution, for the solution of the Riemann problem and for the intercell reconstruction. Only in this way we may calibrate the impact of the numerical methods on the results. We have several specific and very important partial goals in this realm, namely:

- Understanding the characteristic properties of the RRMHD system, i.e. obtaining some analytic insight on the solution across rarefactions and shocks. For shocks, we are interested in incorporating (at least approximately) the effects of stiff source terms in the jump conditions across them.

- Developing new Riemann solvers either approximate or exact for RRMHD.

- Comparing the performance of different time-integration algorithms to deal with the potential stiffness of the RRMHD equations in the high-conductivity limit.

- Characterizing the numerical methods employed to incorporate Ohmic dissipation in numerical codes. It is of paramount importance to disentangle what aspects of the numerical solution are driven by physical resistivity and which ones result from the numerical resistivity.

As we shall descrive in detail in the introduction of Chap. 7 one of the main difficulties of invoking magnetic reconnection in astrophysical plasma to account for highly variable (or even explosive) events is that, under quite general conditions, the dissipation of magnetic field is a very slow process. An exception to this rule is the regime of fast magnetic reconnection of Petschek type (Petschek, 1964), which may theoretically develop outflows with Lorentz factors] $W \sim \sigma_{\rm m}^{1/2}$ (Lyubarsky, 2005). Only under some special conditions, one expects that the growth of resistive instabilities is fast enough to explain the fast variability of a number of astrophysical sources (e.g. stochastic gamma-ray flares in the Crab nebula Abdo et al., 2011), and quite likely three-dimensional

(3D) effects are required for a very efficient dissipation of the magnetic field (Porth et al., 2014). Therefore, concerning the physics of reconnection in astrophysical plasma, our first and foremost goal is to understand the dependence of the growth rate of resistive instabilities (such as TM instabilities) on the physical properties of the plasma. We shall consider specifically the case of relativistic *ideal* double tearing modes (RIDTMs), where the adjective ideal refers to the fact that the instability develops at a timescale of the order of the MHD timescale (i.e. Alfvén crossing time) and its growth rate is independent of the resistivity (and thus, it does not diverge in the ideal RMHD regime). This is an unexplored and interesting setup where two parallel current sheets may interact as TMs develop yielding an explosive reconnection episode, where the reconnection time scales are so small that may be of interest for explaining a number of astrophysical objects as we have mentioned before. A close previous work in the field (Del Zanna et al., 2016) has extended to the relativistic regime the existing Newtonian studies for relativistic ideal tearing modes (RITMs), i.e. a case in which there is a single (isolated) current sheet, instead of two as we shall consider in the study of RIDTMs. Del Zanna et al. (2016) have shown that RITMs are a very simple physical mode of reconnecting the magnetic field on time scales of the order of the light crossing time of the system within the framework of single-fluid, compressible, RRMHD.

Since the dynamics of the aforementioned instabilities depends on very small length scales compared to the typical size of astrophysical systems, our approach to the problem is by means of *local* numerical simulations of the generic conditions met in *reconnection sites* of relativistic astrophysical sources (see Sec. 1.3). More precisely, our goals are:

- Understanding the growth of relativistic resistive *tearing instabilities* and the optimal conditions to obtain the fastest possible dissipation rate. Since this field is not new and there is already some literature on the subject, our work in this context will consist on first reproducing existing results and, later explore the space of parameters which bring relativistic effects more important in the dynamics.

- Closely related to the previous goal is studying the optimal conditions for the development of *ideal double tearing* modes (IDTMs) in resistive relativistic plasma, since this configuration for resistive sites has been suggested to boost the growth of the dissipation rate in classical resistive MHD (e.g. Baty, 2017).

- Comparing the growth rates of IDTMs in classical resistive MHD and RRMHD.

- Characterizing (numerically) the criteria under which an explosive phase of reconnection may ensue the linear growth phase of RIDTMs. This

is a necessary step to be able to understand whether the conditions for an explosive reconnection phase may happen (at all) in astrophysical plasma.

- One of the foremost questions that the physics of relativistic reconnection rises is the speed at which magnetic energy is converted into other forms of energy (i.e. internal or kinetic). This reconnection speed or reconnection rate typically depends on a few dimensionless parameters of the plasma, such as the Lundquist number. Thus, we shall quantify how fast reconnection outflows may be in the context of RIDTMs. The values of the Lorentz factor obtained may be confronted with the needs of a number of models for reconnection in astrophysical jets (e.g. the jets-in-a-jet model; see above).

In summary, the astrophysical goal of this thesis and also a novelty with respect to what has been done so far in the literature, is extending the characterization of IDTMs to the RRMHD regime. That is, we aim to test whether the (non-linear) explosive reconnection phase observed in classical compressible MHD for IDTMs also holds for RIDTM.

1.3 Plan of the thesis

As stated in the previous section, one of the principal goals of the thesis is characterizing the physical conditions that optimize the resistive dissipation of magnetic fields in relativistic plasma. Thus, we will focus on the development of *tearing* modes in current sheets under conditions that maximize their growth rate in *single-fluid* RRMHD. To arrive to the cornerstone of this thesis (presented in Chapter 7), it is first necessary to accomplish a series of preliminary steps. Among them, we need to build a new RRMHD code for astrophysical plasma applications. We devote Chaps. 4-6 as well as App. A to show all the numerical methods we have incorporated from the literature (or developed by our own), as well as to verify and validate the reliability of the new code Cueva. In order to build the new code, it is mandatory first to derive the equations of RRMHD in *conservation* (or most precisely in *balance*) form, which is best suited for its numerical treatment (Chap. 2). A second basic step is understanding the characteristic structure of the RRMHD equations (Chap. 3).

In order to accomplish the goal of developing a new Riemann solver for RRMHD, we undertake two tasks. Firstly, explicitly compute the jump conditions across shocks when singular source terms are present in the governing equations of the fluid (Sec. 3.3). This is an approximate (yet effective) way of dealing with the modification of the solution of a Riemann problem when

stiff source terms are present in the equations. Furthermore, we shall obtain the *Lichnerowicz adiabat* for RRMHD shocks (Sec. 3.4). Secondly, we study the conditions that characterize the solution across smooth rarefaction fans. Although the system of RRMHD equations is a system of balance laws, and not a system of conservation laws, we have done an extensive analytic work to obtain self-similar solutions for smooth flow in the limit of vanishing conductivity (Sec. 3.2). In the mentioned limit, the RRMHD equations form a set of conservation laws. This is also the case in the complementary limit of very large conductivity (i.e. in the ideal RMHD limit, where self-similar solutions across rarefaction waves are also known). Our efforts to bridge these two limits have been unsuccessful, even if we find that the self-similar solution in the $\sigma \to 0$ limit (under some special configurations of the magnetic field) is the same as in ideal RMHD. However, this is not a practical problem, since the usual application of the exact solution of the Riemann problem in RRMHD serves as a reference for code testing, rather than for computationally intensive experiments.

When the exact solution of the Riemann problem is unavailable or very complex, using approximate Riemann solvers is a common practice. Among these solvers, one the most widely used is the HLL Riemann solver. In order to ameliorate the deficiencies of the HLL-family of approximate Riemann solvers, while at the same time keeping their simplicity and computational efficiency, Toro et al. (1994) proposed a generalisation of the HLL flux for the Euler equations. These authors introduced an additional contact wave in the solution separating two intermediate states and formulated a Harten-Lax-van Leer contact (HLLC) wave approximate Riemann solver. Since then, different HLLC Riemann solvers have been designed for MHD (Gurski, 2004; Li, 2005) and RMHD (Honkkila and Janhunen, 2007; Kim and Balsara, 2014; Mignone and Bodo, 2006).

One of the byproducts of this thesis is the development of a new HLLC-type solver for RRMHD. Due to the importance of this building block of the sought RRMHD code, we have devoted the whole Chap. 5 to delineate its main properties. Indeed, Chap. 5 is an adaptation of our paper Miranda-Aranguren et al. (2018). Employing different numerical experiments we have demonstrated its low computational cost (roughly the same as HLL-type solvers) as well as its capability to deal with large conductivity values in problems involving shocks and other discontinuities.

Besides the Riemann solver, the rest of the technical aspects of the new code that we have named Cueva are described in Chap. 4. Although Cueva is developed from scratch, it has been largely inspired on the finite-volume, conservative, HRSC code MRGenesis (Aloy et al., 1999; Leismann et al., 2005). Thus, Cueva is also based on a finite-volume discretization of the spacetime and splits the spatial integration from the temporal one resorting to the

Method of Lines (MoL). Our new code employs different intercell reconstruction methods of various spatial orders of accuracy (e.g. *minmod*, *monotonised central-difference*, *Monotonicity-Preserving Schemes*, etc.; see Sec. 4.1.1). In addition to the HLLC Riemann solver mentioned above, Cueva also uses, the *Local Lax-Friedrichs* (LLF), and the *HLL* approximate Riemann solvers. To perform the time integration we resort to methods which efficiently deal with stiff sources. For this reason, we have implemented various state-of-the-art Implicit-Explicit Runge-Kutta schemes (RKIMEX; Sec. 4.2.1) and the Minimally Implicit Runge-Kutta methods (MIRK; Sec.4.2.2).

In Chap. 6 we *verify* our code making an exhaustive study of the numerical errors, and demonstrate the good performance of the different methods implemented. These errors, which come from the discretization of the PDEs, can either smear out the solution (*numerical dissipation*) or introduce phase errors (*numerical dispersion*). We concentrate on numerical dissipation, whose mode of action resembles that of a *physical viscosity* and, for magnetized flows, also as *resistivity*, commonly referred in the field of numerical MHD, as *numerical viscosity* and *numerical resistivity*, respectively. In Sec. 6.1 we measured the numerical viscosity by means of the Velocity Shear Layer (VSL) test, in Sec. 6.2 we measured the numerical resistivity with Magnetic Diffusion (MD) test and in Sec. 6.3, the Circularly Polarized Alfvén Wave (CPAW) test, allows us to measure the numerical difussion, i.e. the sum of the numerical viscosity and resistivity. The characterization of the numerical diffusivity of our code is mandatory in order to properly interpret the results of more elaborated numerical models. Indeed, the knowledge of the numerical diffusivity is crucial to design numerical experiments where the growth of instabilities critically depends on the physical resistivity of the system of study. The numerical (non-physical) resistivity may yield to reconnection phenomena that are entirely numerical nature, substantially affecting the reliability of the simulations. This is particularly severe in the low-resistivity regime, which is usually the case in the modelling of real systems and that thus requires very high resolution to properly model the (small) spatial scales over which resistive effects are important.

Thanks to the extensive verification of the Cueva code, we are in optimal conditions to go towards a more realistic modelling of relativistic astrophysical plasmas, dealing with the stiffness of the RRMHD system of equations. Our first approach to this issue is precisely the study of the TM instability. The development of unstable TMs is a consequence of the presence of Ohmic resistivity (Furth et al., 1963). Indeed, TMs are crucial to understand the consequences of resistive processes in astrophysical plasma. This is the reason to devote a full chapter of this thesis to their numerical study (Chap. 7). We study TMs by means of local numerical simulations. This means that we consider computational boxes that represent a relatively small fraction of

the whole astrophysical system in which we may be interested. There, we aim to have sufficient numerical resolution to minimize the unphysical effects of numerical viscosity and resistivity (both are unavoidable in any numerical algorithm for RRMHD). In a long term perspective (which is beyond the scope of this thesis), such detailled local numerical models may serve as a basis of *subgrid models* for the unresolved scales in global numerical simulations (i.e. simulations encompassing the whole astrophysical system of interest). We shall show in Chap. 7 that the development of TMs in systems in which two (or more) initially parallel current sheets may yield the generation of an explosive reconnection phase, where the efficiency of converting magnetic energy into either thermal or kinetic energy is maximum.

Chapter 2

The equations of RRMHD

Into the ideal MHD description, conservation of magnetic flux is directly connected with perfect conductivity, i.e. *zero resistivity*. To complement this point of view, dissipative effects can be included. A straightforward generalization of ideal MHD is resistive MHD which include one form of dissipation, i.e. Ohmic dissipation through the plasma resistivity η. A relativistic non-ideal plasma flow can be described by a system of balance laws (Komissarov, 2007). These equations express the conservation of charge, mass, momentum and energy, together with the Maxwell equations. In what follows we review the set of equations for the electromagnetic field (Maxwell's equations), for the fluid variables (conservation laws) and the Ohm's law that is a constitutive relation between the electromagnetic fields and the currents that generate them. We note that the electromagnetic fields and the fluid variables, are coupled through, e.g. the Lorentz force (per unit volume) acting in the momentum equation. Hereafter, we restrict to applications where General Relativistic effects can be neglected, in which case the metric of the space-time is the Minkowski metric, $\boldsymbol{g} = \mathrm{diag}(-1, 1, 1, 1)$.

2.1 Maxwell's equations

In this thesis, we use the Maxwell's equations in the Heaviside-Lorentz (HL) units, which are the most suitable for numerical treatment. Interested readers may find a conversion from HL units to Gaussian units in App. D.

2.1.1 Maxwell field tensor

The electromagnetic field tensor in matrix form reads (Goedbloed et al., 2010)

$$F^{\alpha\beta} = \begin{pmatrix} 0 & E_x & E_y & E_z \\ -E_x & 0 & B_z & -B_y \\ -E_y & -B_z & 0 & B_x \\ -E_z & B_y & -B_x & 0 \end{pmatrix},$$

In terms of $F^{\alpha\beta}$ the first Maxwell equation, in covariant form, reads, [1]

$$\partial_\beta F^{\alpha\beta} = \frac{1}{c} J^\alpha, \tag{2.1}$$

where J^α is the current density four-vector,

$$J^\alpha = (cq, \mathbf{J})^T, \tag{2.2}$$

with $q = q(\mathbf{x}, t)$ the charge density and $\mathbf{J} = \mathbf{J}(\mathbf{x}, t)$ the current density.

From (2.1) the inhomogeneous Maxwell equations in vector form are

$$\nabla \cdot \mathbf{E} = q,$$
$$\nabla \times \mathbf{B} - \frac{1}{c}\partial_t \mathbf{E} = \frac{1}{c}\mathbf{J},$$

where $\mathbf{E} = (E_x, E_y, E_z)^{\mathrm{T}}$ and $\mathbf{B} = (B_x, B_y, B_z)^{\mathrm{T}}$ are the electric and magnetic three-vectors respectively.

2.1.2 Faraday field tensor

The other two Maxwell equations can be written in terms of the Faraday or the dual field-strength tensor,

$${}^*F^{\alpha\beta} = \frac{1}{2}\epsilon^{\alpha\beta\gamma\delta} F_{\gamma\delta} = \begin{pmatrix} 0 & B_x & B_y & B_z \\ -B_x & 0 & -E_z & E_y \\ -B_y & E_z & 0 & -E_x \\ -B_z & -E_y & E_x & 0 \end{pmatrix},$$

where we made use of the Levi-Civita alternating tensor, i.e.

$$\epsilon_{\alpha\beta\gamma\delta} = \begin{cases} 1 & \text{if } \alpha\beta\gamma\delta \text{ is an even permutation of 0123,} \\ -1 & \text{if } \alpha\beta\gamma\delta \text{ is an odd permutation of 0123,} \\ 0 & \text{if any index is repeated.} \end{cases}$$

[1] In this work we use Greek indices to annotate the (time- or space-like) components of four-vectors or tensors of the whole space time (e.g. $\alpha = 0, 1, 2, 3$), while latin indices (e.g. $i = 1, 2, 3$) are used to denote spatial components of four-vectors, tensors or spatial three-vectors. We adopt Einstein summation convention, whereby repeated indices imply summation.

Using ${}^*F^{\alpha\beta}$, the homogeneous Maxwell equations could be written as

$$\partial_\beta {}^*F^{\alpha\beta} = 0 \tag{2.3}$$

and its vectorial representation, as:

$$\begin{aligned} \nabla \cdot \mathbf{B} &= 0, \\ \nabla \times \mathbf{E} + \frac{1}{c}\partial_t \mathbf{B} &= 0. \end{aligned}$$

2.1.3 Ohm's law

To obtain the covariant generalization of the Ohm's law, we start by considering it in the rest frame,

$$\mathbf{J}' = \sigma \mathbf{E}', \tag{2.4}$$

where σ is the conductivity and primes denote quantities in the rest frame. The electric field four-vector measured by a generic observer is obtained from the projection of the Maxwell field tensor onto the aforementioned observer (e.g. Misner et al. 1973). In the rest frame, the observer four velocity is

$$u^{\alpha'} = (c, \mathbf{0}), \tag{2.5}$$

and, therefore, we find

$$F^{\alpha'\beta'} u_{\beta'} = (0, c\mathbf{E}').$$

Thus the right-hand side of Ohm's law (2.4), can be written as,

$$(0, \sigma \mathbf{E}') = \frac{\sigma}{c} F^{\alpha'\beta'} u_{\beta'}. \tag{2.6}$$

To express the left-hand side of Ohm's law, in four-vector form, its necessary to subtract the charge density q' from the four-current density, this can be done using (2.2), applied in the comoving frame and (2.5) to obtain that $J^{\beta'} u_{\beta'} = -c^2 q'$. Hence,

$$(0, \mathbf{J}') = J^{\alpha'} + \frac{1}{c^2}\left(J^{\beta'} u_{\beta'}\right) u^{\alpha'}. \tag{2.7}$$

Combining (2.6) and (2.7) gives the covariant form of Ohm's law (e.g. Starke and Schober, 2016),

$$J^\alpha = \frac{\sigma}{c} F^{\alpha\beta} u_\beta - \frac{1}{c^2}\left(J^\beta u_\beta\right) u^\alpha, \tag{2.8}$$

where we drop all primes since the equation is in covariant form (frame independent).

To obtain the familiar form of Ohm's law in a general inertial frame, we replace the four-velocity, $u^\alpha = W(c, \mathbf{v})$ (where $W = (1 - (\mathbf{v}/c)^2)^{-1/2}$ is the

Lorentz factor) and the four-current density (2.2) observed in that inertial frame into Eq. (2.8). This allows us to obtain the time component of (2.8),

$$-v^2W^2q + W^2\mathbf{v}\cdot\mathbf{J} = \sigma W\mathbf{v}\cdot\mathbf{E} \tag{2.9}$$

and from the spatial components of (2.8),

$$\mathbf{J} - W^2q\mathbf{v} + \frac{W^2}{c^2}\mathbf{v}\left(\mathbf{v}\cdot\mathbf{J}\right) = \sigma W\left(\mathbf{E} + \frac{1}{c}\mathbf{v}\times\mathbf{B}\right), \tag{2.10}$$

where we have made use of the relation,

$$\frac{1}{c^2}J^\alpha u_\alpha = W\left(-q + \frac{1}{c^2}\mathbf{v}\cdot\mathbf{J}\right).$$

Solving Eq. (2.9) for $\mathbf{v}\cdot\mathbf{J}$ and substituting it into eq. (2.10) gives the formula, usually referred to as the relativistic generalization of Ohm's law in the literature (see e.g. [Rebhan (2011), Section 5.3], [Jackson (1999), Problem 11.16] and [Tsang (1997), Problem 9-15]),

$$\mathbf{J} = \sigma W\left[\mathbf{E} + \frac{1}{c}\mathbf{v}\times\mathbf{B} - \frac{1}{c^2}\left(\mathbf{v}\cdot\mathbf{E}\right)\mathbf{v}\right] + q\mathbf{v}.$$

Hereafter, we will use units in which the speed of light in vacuum $c = 1$. In this units, the Ohm's law reads

$$\mathbf{J} = \sigma W\left[\mathbf{E} + \mathbf{v}\times\mathbf{B} - \left(\mathbf{v}\cdot\mathbf{E}\right)\mathbf{v}\right] + q\mathbf{v}, \tag{2.11}$$

and the Maxwell equations become,

$$\partial_\beta F^{\alpha\beta} = J^\alpha, \qquad \partial_\beta {}^*F^{\alpha\beta} = 0.$$

2.2 Continuity of charge and current density

Following Jackson (1999) (Sec. 11.6), *the four-divergence of a four-vector* (i.e. J^α) *is an invariant*. Provided that $J^\alpha = (q, \mathbf{J})$ is the four-current vector in the laboratory frame and $J^{\alpha'} = (q', \mathbf{0})$ the four-current vector measured in the rest frame, we have,

$$\begin{aligned}\partial_\alpha J^\alpha &= \partial_{\alpha'} J^{\alpha'},\\ \partial_t q + \nabla\cdot\mathbf{J} &= \partial_{t'} q'.\end{aligned}$$

Since in the rest frame we do not have fluxes or sources of charge, its proper temporal variations must be zero. Hence the charge continuity equation reads,

$$\partial_t q + \nabla\cdot\mathbf{J} = 0 \tag{2.12}$$

and its covariant form,

$$\partial_\alpha J^\alpha = 0. \tag{2.13}$$

It is worth noting that charge, but not the charge density, is a Lorentz invariant (Jackson, 1999, see e.g: Sec. 11.9 for an experimental reference).

2.3 Continuity of mass density

The proper density (ρ) measured in the rest frame of the fluid, can be expressed in terms of the number of particles per unit volume (n_0) and its mass (m_0) by,

$$\rho = m_0 n_0.$$

Due to length contraction effect, in the inertial Lorentzian frame, where the fluid is seen to move with velocity $\mathbf{v}$, the particles number density, will be $n = W n_0$. Following Font et al. (1994) (but see also Goedbloed et al., 2010), a convenient way to quantify the "density" in the laboratory frame is,

$$D = \rho W \tag{2.14}$$

and the flux of mass,

$$\mathbf{F}_D = \rho W \mathbf{v}.$$

Then we can define a four-current mass density as,

$$D^\alpha = \rho u^\alpha = (\rho W, \rho W \mathbf{v}), \tag{2.15}$$

which in rest frame it is simply given by,

$$D^{\alpha'} = \rho u^{\alpha'} = (\rho, \mathbf{0}).$$

Consequently with the analysis made in Sec. 2.2 in the derivation of charge continuity expression, the four-divergence of D^α must be an invariant, then,

$$\partial_\alpha D^\alpha = \partial_{\alpha'} D^{\alpha'},$$
$$\partial_t D + \nabla \cdot \mathbf{F}_D = \partial_{t'} \rho'.$$

Using the fact, that in the rest frame there are no fluxes or sources of mass, the temporal variation of the proper density must be zero. Therefore,

$$\frac{\partial D}{\partial t} + \nabla \cdot \mathbf{F}_D = 0 \tag{2.16}$$

and a covariant expression of the mass continuity relation Eq. (2.16), can be expressed as,

$$\partial_\alpha D^\alpha = 0. \tag{2.17}$$

2.4 Stress-energy tensor

2.4.1 Hydrodynamic stress-energy tensor

As stated in, e.g. Rezzolla and Zanotti (2013), energy and momentum in a relativistic framework must be treated as a single physical entity, which is normally expressed through the *energy-momentum tensor*. This tensor, whose contravariant components we denote by $T^{\alpha\beta}_{\rm hyd}$, can be split in different composing parts,

$$T^{\alpha\beta}_{\rm hyd} = \begin{pmatrix} T^{00}_{\rm hyd} & T^{0i}_{\rm hyd} \\ T^{i0}_{\rm hyd} & T^{ij}_{\rm hyd} \end{pmatrix} = \begin{pmatrix} \text{energy density} & \text{energy flux} \\ \text{momentum flux} & \text{stresses} \end{pmatrix}.$$

Since fluxes vanish in the rest frame of the fluid and stresses correspond to the isotropic pressure, $p_{\rm g}$, the components of the energy-momentum in the rest frame read,

$$T^{\alpha'\beta'}_{\rm hyd} = \begin{pmatrix} \mathcal{E}'_{\rm hyd} & 0 & 0 & 0 \\ 0 & p_{\rm g} & 0 & 0 \\ 0 & 0 & p_{\rm g} & 0 \\ 0 & 0 & 0 & p_{\rm g} \end{pmatrix},$$

where $\mathcal{E}'_{\rm hyd}$ is the energy density, which is composed by the sum of the rest mass energy and the internal energy density. The latter quantity reads,

$$\mathcal{E}'_{\rm hyd} = T^{0'0'}_{\rm hyd} = \rho(1+\varepsilon),$$

with ε being the specific internal energy in the fluid frame. Meanwhile, the stresses can be expressed as,

$$T^{i'j'}_{\rm hyd} = p_{\rm g}\mathbf{I},$$

where $\mathbf{I}$ is the identity matrix in three dimensions. To get the hydrodynamic stress-energy tensor in the laboratory frame, where the fluid moves with velocity $\mathbf{v}$, we can make use of a Lorentz transformation of the stress-energy tensor from the rest-frame to the laboratory frame, obtaining

$$T^{\alpha\beta}_{\rm hyd} = (\rho(1+\varepsilon) + p_{\rm g})\, u^\alpha u^\beta + p_{\rm g} g^{\alpha\beta}.$$

Introducing some convenient notation, this tensor can be displayed in matrix form as,

$$\begin{aligned} T^{\alpha\beta}_{\rm hyd} &= \begin{pmatrix} T^{00}_{\rm hyd} & T^{0i}_{\rm hyd} \\ T^{i0}_{\rm hyd} & T^{ij}_{\rm hyd} \end{pmatrix} \\ &= \begin{pmatrix} \rho h W^2 - p_{\rm g} & \rho h W^2 \mathbf{v}^T \\ \rho h W^2 \mathbf{v} & \rho h W^2 \mathbf{v}\mathbf{v} + p_{\rm g}\mathbf{I} \end{pmatrix} \\ &= \begin{pmatrix} \mathcal{E}_{\rm hyd} & \mathbf{F}^T_{\mathcal{E}_{\rm hyd}} \\ \mathbf{S}_{\rm hyd} & \mathbf{F}_{\mathbf{S}_{\rm hyd}} \end{pmatrix}. \end{aligned}$$

Where the relativistic energy density in the laboratory frame is given by,

$$\mathcal{E}_{\rm hyd} = \rho h W^2 - p_{\rm g},$$

the energy flux by,

$$\mathbf{F}_{\mathcal{E}_{\rm hyd}} = \rho h W^2 \mathbf{v},$$

the momentum density,

$$\mathbf{S}_{\rm hyd} = \rho h W^2 \mathbf{v}, \tag{2.18}$$

and the momentum fluxes by,

$$\mathbf{F}_{\mathbf{S}_{\rm hyd}} = \rho h W^2 \mathbf{v}\mathbf{v} + p_{\rm g}\mathbf{I}.$$

In the previous expressions we have introduced the specific enthalpy (h),

$$h := 1 + \varepsilon + \frac{p_{\rm g}}{\rho}. \tag{2.19}$$

For an ideal gas equation of state (EoS) with constant adiabatic index γ,

$$p_{\rm g} = (\gamma - 1)\rho\varepsilon, \tag{2.20}$$

the specific enthalpy can be written as,

$$h(\rho, p_{\rm g}) = 1 + \frac{\gamma}{\gamma - 1}\frac{p_{\rm g}}{\rho}. \tag{2.21}$$

For ulterior reference, we also write explicitly down the expression of the adiabatic, relativistic local sound speed as,

$$c_{\rm s} \equiv \frac{1}{h}\sqrt{\left.\frac{\partial p_{\rm g}}{\partial \rho}\right|_s} = \sqrt{\frac{\gamma p_{\rm g}}{\rho h}}, \tag{2.22}$$

where s is the specific entropy.

2.4.2 Electromagnetic stress-energy tensor

Following Goedbloed et al. (2010) and in analogy with the hydrodynamic case Sec.2.4.1, the stress-energy tensor for the electromagnetic field (in vacuum) can be written as,

$$\begin{aligned} T^{\alpha\beta}_{\rm em} &= \begin{pmatrix} \frac{1}{2}\left(E^2 + B^2\right) & (\mathbf{E}\times\mathbf{B})^T \\ \mathbf{E}\times\mathbf{B} & \frac{1}{2}\left(E^2 + B^2\right)\mathbf{I} - \mathbf{E}\mathbf{E} - \mathbf{B}\mathbf{B} \end{pmatrix} \\ &= \begin{pmatrix} \mathcal{E}_{\rm em} & \mathbf{F}^T_{\mathcal{E}_{\rm em}} \\ \mathbf{S}_{\rm em} & \mathbf{F}_{\mathbf{S}_{\rm em}} \end{pmatrix}. \end{aligned}$$

Where the electromagnetic energy density, is given by,

$$\mathcal{E}_{\rm em} = \frac{1}{2}\left(E^2 + B^2\right),$$

the momentum and energy fluxes are given by the Poynting flux three-vector,

$$\mathbf{S}_{\rm em} = \mathbf{F}_{\mathcal{E}_{\rm em}} = \mathbf{E}\times\mathbf{B}, \tag{2.23}$$

and the contribution of the electromagnetic stresses to the fluxes, in three vectorial notation, reads,

$$\mathbf{F}_{\mathbf{S}_{\rm em}} = \frac{1}{2}\left(E^2 + B^2\right)\mathbf{I} - \mathbf{E}\mathbf{E} - \mathbf{B}\mathbf{B}.$$

For later reference, we write down the expression of the relativistic Alfvén speed following Anile (1989)

$$v_A \equiv \sqrt{\frac{B^2 - E^2}{\rho h + B^2 - E^2}}, \tag{2.24}$$

where in the original definition of Anile (1989) we take into account that the square of the magnetic field four vector corresponds with the squared sum of the magnetic and electric fields in RRMHD brought to the ideal limit (in which $\mathbf{E} = -\mathbf{v}\times\mathbf{B}$ and, thus $B^2 - E^2 = B^2/W^2 + (\mathbf{v}\cdot\mathbf{B})^2$). Alternatively, in terms of the magnetization of the plasma (Appl and Camenzind, 1988; Leismann et al., 2005),

$$\sigma_{\rm m} \equiv \frac{\sqrt{B^2 - E^2}}{\rho}, \tag{2.25}$$

we may also write Eq. (2.24)

$$v_A = \sqrt{\frac{\sigma_{\rm m}}{h + \sigma_{\rm m}}}.$$

2.5 Conservation Laws

The total stress-energy tensor $T^{\alpha\beta}$ describing a perfect fluid coupled to an electromagnetic field is given by the addition of the electromagnetic and hydrodynamic stress-tensors,

$$T^{\alpha\beta} = T^{\alpha\beta}_{\rm em} + T^{\alpha\beta}_{\rm hyd}.$$

In matrix form, this stress-energy tensor becomes,

$$T^{\alpha\beta} = \begin{pmatrix} \frac{1}{2}\left(E^2 + B^2\right) + \rho h W^2 - p_{\rm g} & (\mathbf{E}\times\mathbf{B} + \rho h W^2 \mathbf{v})^T \\ \mathbf{E}\times\mathbf{B} + \rho h W^2 \mathbf{v} & -\mathbf{E}\mathbf{E} - \mathbf{B}\mathbf{B} + \rho h W^2 \mathbf{v}\mathbf{v} + P\mathbf{I} \end{pmatrix} = \begin{pmatrix} \mathcal{E} & \mathbf{F}_{\mathcal{E}}^T \\ \mathbf{S} & \mathbf{F}_{\mathbf{S}} \end{pmatrix},$$

where

$$P = p_{\rm g} + (\mathbf{E}^2 + \mathbf{B}^2)/2,$$

is the total pressure. The total energy density is given by,

$$\mathcal{E} = \mathcal{E}_{\rm em} + \mathcal{E}_{\rm hyd} = \frac{1}{2}(\mathbf{E}^2 + \mathbf{B}^2) + \rho h W^2 - p_{\rm g}. \tag{2.26}$$

The momentum density,

$$\mathbf{S} = \mathbf{S}_{\rm em} + \mathbf{S}_{\rm hyd} = \mathbf{E}\times\mathbf{B} + \rho h W^2 \mathbf{v}, \tag{2.27}$$

the energy fluxes,

$$\mathbf{F}_{\mathcal{E}} = \mathbf{F}_{\mathcal{E}_{\rm em}} + \mathbf{F}_{\mathcal{E}_{\rm hyd}} = \mathbf{E}\times\mathbf{B} + \rho h W^2 \mathbf{v},$$

and the momentum stresses fluxes as,

$$\mathbf{F}_{\mathbf{S}} = \mathbf{F}_{\mathbf{S}_{\rm em}} + \mathbf{F}_{\mathbf{S}_{\rm hyd}} = -\mathbf{E}\mathbf{E} - \mathbf{B}\mathbf{B} + \rho h W^2 \mathbf{v}\mathbf{v} + P\mathbf{I}.$$

In agreement with the treatment made by Rezzolla and Zanotti (2013), to deduce the relativistic hydrodynamics conservation laws. We may enforce the conservation of energy-momentum by imposing that the total net fluxes across a three-surface Σ, vanish. In flat space-time, this condition is expressed in integral form as,

$$\int_{\Sigma} T^{\alpha\beta} l_{\alpha} d^3x = 0,$$

where l_α is a unit normal to the three-dimensional surface Σ. The Gauss divergence theorem permits transforming the surface integral into a volume integral,

$$\int \partial_\beta T^{\alpha\beta} d^4x = 0. \tag{2.28}$$

Since the volume element in the space-time (d^4x) is arbitrary, the integral law Eq. (2.28) is satisfied if,

$$\partial_\beta T^{\alpha\beta} = 0. \tag{2.29}$$

Then the temporal part of this equation, $\partial_\alpha T^{0\alpha} = 0$, yields the *energy conservation equation*,

$$\partial_t \mathcal{E} + \nabla \cdot \mathbf{F}_\mathcal{E} = 0,$$

and the spatial part, $\partial_\alpha T^{i\alpha} = 0$, yields the *momentum conservation law*

$$\partial_t \mathbf{S} + \nabla \cdot \mathbf{F}_\mathbf{S} = 0.$$

2.6 Enforcement of the electromagnetic constraints: the augmented system of Maxwell equations

The time component of the Maxwell equations (obtained for $\beta = 0$ in Eq. (2.3)) are not evolutionary but constraint equations. Thus, in its more basic form, the system of RRMHD equations constitutes a hyperbolic system of balance laws with two additional (elliptic) constraint equations that state the solenoidal character of the magnetic field ($\nabla \cdot \mathbf{B} = 0$) and that the electric charge fixes the divergence of the electric field ($\nabla \cdot \mathbf{E} = q$; Anile, 1989; Dixon, 1978). In the numerical time evolution of the Maxwell equations, violations of the former constraints are unavoidable, unless specific methods are employed to enforce them (Brackbill and Barnes, 1980; Dai and Woodward, 1998). There are two basic possibilities to enforce the constraints. The first one consists on writing down the fluxes of the Maxwell equations in such a way that the elliptic constrains (specially $\nabla \cdot \mathbf{B} = 0$) are enforced down to machine precision. Methods of this kind are generically known as *constraint transport* methods (Evans and Hawley, 1988; Feng and Zhang, 2016; Stone and Norman, 1992; Tóth, 2000), and have been imported also to RRMHD (e.g. Bucciantini and Del Zanna, 2013). The second approach aims to keep numerically the constraints fulfilled not exactly, but to the same formal order of accuracy than the rest of the equations. To undertake this task the Maxwell equations are "augmented" supplementing them with two additional scalar fields (or pseudo-potentials), ψ and ϕ. This formalism was first proposed by Dedner et al. (2002) and used as divergence cleaning strategy, since the new pseudo-potentials enforce the conservation of q and the solenoidal constrain $\nabla \cdot \mathbf{B} = 0$, respectively. Contemporaneously, it was Komissarov (2007), for the first time and Palenzuela et al. (2009), subsequently, who applied this strategy into the equations of RRMHD. The *augmented system of Maxwell equations* can be written as,[2]

$$\begin{aligned} \partial_\beta \left(F^{\alpha\beta} - \psi g^{\alpha\beta} \right) &= J^\alpha - \kappa_\psi \psi n^\alpha \\ \partial_\beta \left({}^*F^{\alpha\beta} - \phi g^{\alpha\beta} \right) &= -\kappa_\phi \phi n^\alpha, \end{aligned} \tag{2.30}$$

[2] We note that there is a typo in one sign of the left-hand side of the augmented Maxwell equations of Palenzuela et al. (2009), which is fixed in Eqs. (2.30).

where n^α is the time-like translational Killing vector, which in a flat Minkowski space-time reads $n_\alpha = (-1, 0, 0, 0)$. We note that in the original formulations of Komissarov (2007) and Palenzuela et al. (2009) a single constant κ was used for both pseudo-potentials. We have generalized the formulation so that each pseudo-potential may be controlled with a different dumping constant. We will take advantage of this fact in some numerical experiments, where the value of the constant employed in the evolutionary equation of ψ will be made larger than that used in the evolutionary equation of ϕ. The set of equations (2.30) can be also written as (Komissarov, 2007),

$$\partial_t \psi = -\nabla \cdot \mathbf{E} \quad + q - \kappa_\psi \psi, \tag{2.31}$$

$$\partial_t \phi = -\nabla \cdot \mathbf{B} \quad - \kappa_\phi \phi, \tag{2.32}$$

$$\partial_t \mathbf{E} = \quad \nabla \times \mathbf{B} - \nabla\psi - \mathbf{J}, \tag{2.33}$$

$$\partial_t \mathbf{B} = -\nabla \times \mathbf{E} - \nabla\phi. \tag{2.34}$$

For any positive κ_ϕ (κ_ψ), the pseudo-potential decays exponentially over a time scale $1/\kappa_\phi$ ($1/\kappa_\psi$) to the trivial solution $\phi = 0$ ($\psi = 0$). We take the time derivative of Eq. (2.32), the divergence of Eq. (2.34) and combining these equations we find that ϕ satisfies the telegraph equation,

$$\partial_{tt}\phi + \kappa_\phi \partial_t \phi = \nabla^2 \phi, \tag{2.35}$$

where $\partial_{tt}\phi$ stands for the second time derivative of ϕ. The telegraph equation is a second-order, partial differential equation of hyperbolic type, which describes waves moving with the speed of light and with decaying amplitude for $\kappa_\phi > 0$. This leads to ϕ evolving towards $\phi = 0$ for suitable boundary conditions.

In the same way, taking the time derivative of Eq. (2.31), the divergence of Eq. (2.33) and using the conservation of charge Eq. (2.12), we get the telegraph equation for ψ,

$$\partial_{tt}\psi + \kappa_\psi \partial_t \psi = \nabla^2 \psi, \tag{2.36}$$

So the behavior of ψ will be the same as ϕ and will tend to zero unless ill-posed boundary conditions are set.

2.7 The augmented RRMHD system of equations

For future reference, we cast all together the equations that form the augmented system of RRMHD. These equations are the Maxwell equations (2.30) and the conservation laws (2.13), (2.17), (2.29), which in three-vectorial form

read,

$$\begin{aligned}
\partial_t q &= -\nabla\cdot\mathbf{J},\\
\partial_t \psi &= -\nabla\cdot\mathbf{E} \quad + q - \kappa_\psi\psi,\\
\partial_t \phi &= -\nabla\cdot\mathbf{B} \quad - \kappa_\phi\phi,\\
\partial_t \mathbf{E} &= \quad \nabla\times\mathbf{B} - \nabla\psi - \mathbf{J},\\
\partial_t \mathbf{B} &= -\nabla\times\mathbf{E} - \nabla\phi,\\
\partial_t D &= -\nabla\cdot\mathbf{F}_D,\\
\partial_t \mathcal{E} &= -\nabla\cdot\mathbf{F}_\mathcal{E},\\
\partial_t \mathbf{S} &= -\nabla\cdot\mathbf{F}_\mathbf{S},
\end{aligned} \tag{2.37}$$

where q, $\mathbf{E}$, $\mathbf{B}$, D, $\mathcal{E}$ and $\mathbf{S}$ stand for the charge density, the electric and magnetic field 3-vectors in the laboratory frame, the relativistic mass-density, the relativistic energy density and the momentum density, respectively. The system of equations is closed with the Ohm's law Eq. (2.8). We restrict to applications in which the thermodynamics is governed by an ideal gas equation of state with constant adiabatic index γ (Eq. (2.20))

In terms of the primitive or physical variables,

$$\mathbf{W} = (\psi, \phi, \mathbf{E}, \mathbf{B}, q, \rho, p_\mathrm{g}, \mathbf{v})^T, \tag{2.38}$$

we gather here the expressions of the fluxes for later easy reference,

$$\begin{aligned}
\mathbf{F}_q &= \mathbf{J},\\
\mathbf{F}_\psi &= \mathbf{E},\\
\mathbf{F}_\phi &= \mathbf{B},\\
F^j_{E^i} &= \delta^j_i\psi - \epsilon_{ijk}B^k,\\
F^j_{B^i} &= \delta^j_i\phi + \epsilon_{ijk}E^k,\\
\mathbf{F}_D &= \rho W\mathbf{v},\\
\mathbf{F}_\mathcal{E} &= \mathbf{E}\times\mathbf{B} + \rho h W^2\mathbf{v},\\
\mathbf{F}_\mathbf{S} &= -\mathbf{E}\mathbf{E} - \mathbf{B}\mathbf{B} + \rho h W^2\mathbf{v}\mathbf{v} + P\boldsymbol{g},
\end{aligned} \tag{2.39}$$

where δ^j_i and ϵ_{ijk} are the Kronecker delta and the spatial Levi-Civita alternating tensor, respectively.

Chapter 3

Characteristic properties of the RRMHD system

The augmented system of the RRMHD equations is a hyperbolic partial differential equations system of balance laws (Cordero-Carrión et al., 2012; Komissarov, 2007). Generically, the set of equations (2.37) can be written as:

$$\partial_t \mathbf{U} + \partial_m \mathbf{F}^m(\mathbf{U}) = \mathbf{\Omega}(\mathbf{U}), \tag{3.1}$$

where $\mathbf{U}$, $\mathbf{F}^m$ $(m = x, y, z)$ and $\mathbf{\Omega}$ are the n-dimensional vectors ($n = 14$ in the augmented RRMHD system) containing the conserved variables, the fluxes and source terms, respectively. Explicitly,

$$\mathbf{U} = (\psi, \phi, \mathbf{E}, \mathbf{B}, q, D, \mathcal{E}, \mathbf{S})^T, \tag{3.2}$$

$$\mathbf{F}^m = (E^m, B^m, \epsilon^{imk} E_k + \psi \delta^{im}, -\epsilon^{imk} B_k + \phi \delta^{im}, F^m_D, F^m_{\mathcal{E}} F^m_{\mathbf{S}})^T,$$

and

$$\mathbf{\Omega} = (q - \kappa\psi, -\kappa\phi, -\mathbf{J}, \mathbf{0}_{1\times 9})^T,$$

where δ^{im} is the Kronecker delta and the latin subscripts take values x, y and z. We note that some variables $(\psi, \phi, \mathbf{E}, \mathbf{B}, q)$ are included in both the conserved set of variables as well as in the primitive set of quantities (compare Eqs. (3.2) and (2.38)). However, numerically, it is fundamental to distinguish between them, since they require differentiated algorithmic treatment.

The system (3.1) may be recast in quasilinear form:

$$\partial_t \mathbf{U} + \mathbf{A}^m(\mathbf{U}) \partial_m \mathbf{U} = \mathbf{\Omega}(\mathbf{U}),$$

where the matrices

$$\mathbf{A}^m = \partial_{\mathbf{U}} \mathbf{F}^m(\mathbf{U}) \tag{3.3}$$

are the Jacobians of the system. In terms of the spectral decomposition of the Jacobians, we say that the system is hyperbolic if it has n real eigenvalues $\lambda_i = \lambda_i(\mathbf{U})$, $i = 1, 2, \ldots, n$, and is strictly hyperbolic if all λ_i are distinct. The λ_i are the wave speeds, or characteristic speeds, that is, they are the propagation velocities of infinitesimal disturbances.

An (approximate) numerical solution of hyperbolic systems of balance laws may be obtained by employing a Godunov-type strategy, i.e., discretizing the system in space employing a tessellation of numerical cells across whose boundaries fluxes are computed. The spatial discretization naturally produces a piecewise discontinuous representation of the physical and numerical quantities, the discontinuities being located at the intercell boundaries. Indeed, Godunov (1959) demonstrated that the time evolution of the complete system can be obtained assembling the solutions of the basic problems set at intercell boundaries, namely, combining the solution of the piecewise discontinuous problems arising at every cell interface. Generically, an initial value problem with discontinuous uniform data of the form,

$$\mathbf{U}_0 = \mathbf{U}(x, 0) = \begin{cases} \mathbf{U}_l & \text{if } x < 0 \\ \mathbf{U}_r & \text{if } x > 0, \end{cases} \tag{3.4}$$

where $\mathbf{U}_l$ and $\mathbf{U}_r$ are uniform vectors of $\mathbb{R}^n$, is called a Riemann problem. Here we have made the simplification that the variables depend on a single spatial direction (x), but the Riemann problem can be cast for arbitrarily spatial orientations.

The solution of the Riemann problem, in RHD and RMHD cannot be obtained analytically in a closed form. Thus, the exact solution may require of the numerical evaluation of complicated algebraic-differential systems, that can be solved up to the sought accuracy (in many cases, up to machine precision). The solution found in this way is referred to as the *exact* solution of Riemann problem, to distinguish it from the *approximate* solution, which is instead obtained when the system of equations is reduced to a locally linear form (see, e.g. Chap. 5).

The first exact solution of the Riemann problem in RHD was proposed by Martí and Müller (1994) for flows without velocities tangential to the initial discontinuity and Pons et al. (2000) extended it to the case where tangential velocities are present. Rezzolla and Zanotti (2001); Rezzolla et al. (2003) improved the solution efficiency employing the relativistic invariant *relative velocity* between two states in order to predict the wave pattern. The work done on the Riemann problem in RMHD began with the first approach made by Romero et al. (2005) for the particular case in which the magnetic field of the initial states is tangential to the discontinuity and orthogonal to the flow velocity. Later, Giacomazzo and Rezzolla (2006) proposed an algorithm to find the exact solution of the Riemann problem in RMHD for generic initial states.

In this chapter we describe the characteristic structure of the of the system of RRMHD equations. We will show the explicitly jump conditions across flow discontinuities (Sec. 3.3). These expressions could be used to assemble a *complete* exact Riemann solver or approximate Riemann solvers like the one we present in Chap. 5. As we shall see, the presence of source terms prevents us from obtaining self-similar solutions across rarefaction waves unless we consider only the homogeneous set of equations of RRMHD, i.e. the source-less system of equations (Sec. 3.2). Unfortunately, we have not found an exact solution of the Riemann problem in RRMHD in the regime of interest for us, namely, when $\sigma \to \infty$. In that regime the current density makes that the sytem becomes stiff and the exact solution of the Riemann problem impractical.

3.1 Characteristic speeds

The breakup of the Riemann problem in the augmented system of RRMHD equations (Eq. (2.37)) produces a set of 14 waves with characteristic speeds,

$$\lambda_{EB_\pm} = \pm 1, \qquad \text{(multiplicity 4)} \tag{3.5}$$

$$\lambda_q = v_x, \qquad \text{(multiplicity 1)} \tag{3.6}$$

$$\lambda_{H_0} = v_x, \qquad \text{(multiplicity 3)}$$

$$\lambda_{H_\pm} = v_x \Delta_H \pm c_\mathrm{s} \sqrt{\frac{\rho h}{\Delta}(1 - v_x^2 \Delta_H)}, \qquad \text{(multiplicity 1)} \tag{3.7}$$

with $\Delta := \rho h W^2 (1 - \mathbf{v}^2 c_\mathrm{s}^2)$, and $\Delta_H := (1 - c_\mathrm{s}^2)/(1 - \mathbf{v}^2 c_\mathrm{s}^2)$. $\lambda_{EB_\pm}$ represent the eight eigenvalues (four times degenerate each) that are equal to the speed of light and limit the Riemann fan. They are associated to the propagation of disturbances in the electromagnetic field, that in the case of the RRMHD system are electromagnetic waves, as well as the velocities of propagation of the scalar potentials. λ_q and λ_{H_0} correspond to the four contact waves moving at the local fluid speed (the former associated to the motion of charge and the latter to the shear and entropy waves). $\lambda_{H_\pm}$ correspond to the two acoustic waves, which in RRMHD are decoupled from the electromagnetic field (Cordero-Carrión et al., 2012).

We point out that the characteristic speeds listed in Eqs. (3.5)-(3.7) are computed, following the standard practice for hyperbolic systems of partial differential equations (e.g., Anile, 1989) as the eigenvalues of the Jacobian matrices of the system of RRMHD equations (Eq. (3.3)). These eigenvalues represent the wave speeds of plasma perturbations only in the cero resistivity limit. This is the reason why Alfvén and slow magnetosonic waves do not explicitly appear among the obtained characteristic speeds. The presence of source terms (the current in Ampere's law; Eq. (2.33) and the GLM scalar potentials in Eqs. (2.31) and (2.32)) alters these signal velocities. Indeed, both the

basic and the augmented RRMHD systems belong to the class of "hyperbolic systems of conservation laws with relaxation" as defined by, e.g., Whitham (1974). The latter term denotes hyperbolic systems of n partial differential equations in conservation form with source terms, which have as a limit a hyperbolic system of M ($M < n$) equations called the equilibrium system as $n - M$ relaxation time parameters $\tau_i \to 0$. In our case, the equilibrium system is the one formed by the equations of (ideal) RMHD and the relaxation parameters are the resistivity, $\eta := 1/\sigma$, and $1/\kappa$ (with k equal to κ_ψ or κ_ϕ from Eq.(2.37)). Following the convention of Pember (1993), the characteristic speeds of the equilibrium and non-equilibrium systems are called *equilibrium* and *frozen* characteristic speeds, respectively.[1]

The equilibrium ($\tilde{\lambda}_j$, $j = 1, \ldots, M$) and frozen (λ_j, $j = 1, \ldots, n$) characteristic speeds satisfy the *subcharacteristic condition* if they are interlaced, i.e. if each $\tilde{\lambda}_j$ lies in the closed interval $[\lambda_k, \lambda_{k+n-M}]$. The previous condition is necessary for the stability of linearized systems with relaxation (Whitham, 1974). The subcharacteristic condition is satisfied by the characteristic speeds of both the basic and the augmented RRMHD systems and the characteristic speeds of the (ideal) RMHD system. Therefore, the numerical solution of the former systems tends to the solution of the equilibrium (ideal RMHD) system as the relaxation time tends to zero (Chen et al., 1994). The eigenspeeds computed by Cordero-Carrión et al. (2012) only apply to the frozen limit where electromagnetic phenomena and matter are completely decoupled. However, the coupling is restored by our method of lines and the application of partly implicit time integration methods (either RKIMEX or MIRK). Takamoto and Inoue (2011) took an alternative approach employing a method of characteristics (MoC) for the integration of the RRMHD equations. Alfvén modes are explicitly restored in their approach (Takamoto and Inoue, 2011) by modifying Ampere's law introducing an effective propagation speed, which depends on the damping rate of electromagnetic modes. That is, when all electromagnetic modes (moving at the speed of light) are damped during one time step of the numerical evolution, Δt, they use appropriate (ideal RMHD) characteristic speeds for their MoC; otherwise, they resort to using the speed of light. In practice, the method of Takamoto and Inoue (2011) only uses characteristic speeds smaller than the speed of light when $\Delta t < \Delta t_{\rm e} := 4\pi/\sigma$. Our partly implicit time integration methods typically provide values of $\Delta t = C_{\rm CFL}\Delta x \gg \Delta t_{\rm e}$[2] for reasonable values of the grid spacing. This means that our algorithm should yield a qualitatively similar restoration of the Alfvén , fast and slow RMHD

[1] One can actually define the concept of stiffness in this framework saying that a system of conservation laws is stiff when at least one of its relaxation times is small compared to the time scale determined by the frozen characteristic speeds of the system and some appropriate length scale.

[2] Where $C_{\rm CFL}$ is the so-called, Courant-Friedrich-Levy (CFL) condition.

modes as that of Takamoto and Inoue (2011) in practical applications.

3.2 Approximate self-similar solution

In this section we seek self-similar solutions of the RRMHD equations, which may be of use to obtain the flow structure across rarefactions. Without lose of generality, we may restrict ourselves to the case where all variables depend on a single spatial coordinate (e.g. x) and on time. In this case, the RRMHD system equations (Eq. 2.37), becomes

$$
\begin{aligned}
\partial_t \psi &= -\partial_x E_x + q - \kappa\psi, \\
\partial_t \phi &= -\partial_x B_x - \kappa\phi, \\
\partial_t E_x &= -\partial_x \psi - \sigma W[E_x + \varkappa_x - \vartheta^{\mathrm{E}}\, v_x] - q v_x, \\
\partial_t E_y &= -\partial_x B_z - \sigma W[E_y + \varkappa_y - \vartheta^{\mathrm{E}}\, v_y] - q v_y, \\
\partial_t E_z &= \partial_x B_y - \sigma W[E_z + \varkappa_z - \vartheta^{\mathrm{E}}\, v_z] - q v_z, \\
\partial_t B_x &= -\partial_x \phi, \\
\partial_t B_y &= \partial_x E_z, \\
\partial_t B_z &= -\partial_x E_y, \\
\partial_t q &= -\partial_x(\sigma W[E_x + \varkappa_x - \vartheta^{\mathrm{E}}\, v_x] - q v_x), \\
\partial_t(\rho W) &= -\partial_x(\rho W v_x), \\
\partial_t(\rho h W^2 + \wp - p) &= -\partial_x(B_z E_y - B_y E_z + \rho h W^2 v_x), \\
\partial_t(\chi_x + \rho h W^2 v_x) &= -\partial_x(-E_x^2 - B_x^2 + \rho h W^2 v_x^2 + \wp + p), \\
\partial_t(\chi_y + \rho h W^2 v_y) &= -\partial_x(-E_x E_y - B_x B_y + \rho h W^2 v_x v_y), \\
\partial_t(\chi_z + \rho h W^2 v_z) &= -\partial_x(-E_x E_z - B_x B_z + \rho h W^2 v_x v_z),
\end{aligned}
\tag{3.8}
$$

where we have introduced the following ancillary quantities,

$$
\begin{aligned}
&\chi_m := (\mathbf{E}\times\mathbf{B})_m, \qquad && \varkappa_m := (\mathbf{v}\times\mathbf{B})_m, \qquad && m = x, y, z, \\
&\vartheta^{\mathrm{E}} := \mathbf{v}\cdot\mathbf{E}, && \vartheta^{\mathrm{B}} := \mathbf{v}\cdot\mathbf{B}, && \wp := \frac{1}{2}\left(E^2 + B^2\right).
\end{aligned}
$$

The initial Riemann problem data in the form (3.4) is invariant under the change of scale, $(x, t) \to (\alpha x, \alpha t)$. However, the RRMHD equations are not invariant under the same transformation unless all the source terms are zero. Therefore, strict self-similar solutions depending on the variable $\xi = x/t$ do not exist in RRMHD. In order to more clearly see the lack of strict self-similarity, let us take ξ as independent variable, in which case the spatial and temporal derivatives can be expressed as,

$$
\partial_x = \frac{1}{t} d_\xi, \qquad \partial_t = \frac{-\xi}{t} d_\xi,
$$

where d_ξ denotes the total derivative with respect to ξ. With this change of variable, the one-dimensional RRMHD system of *partial* differential equations, Eq. (3.8), can be written as an *ordinary* system of differential equations,

$$\xi d_\xi \psi - d_\xi E_x = -t(q - \kappa\psi), \tag{3.9}$$
$$\xi d_\xi \phi - d_\xi B_x = t\kappa\phi, \tag{3.10}$$
$$-d_\xi \psi + \xi d_\xi E_x = t(\sigma W[E_x + \varkappa_x - \vartheta^{\mathrm{E}}\ v_x] + q v_x), \tag{3.11}$$
$$\xi d_\xi E_y - d_\xi B_z = t(\sigma W[E_y + \varkappa_y - \vartheta^{\mathrm{E}}\ v_y] + q v_y), \tag{3.12}$$
$$\xi d_\xi E_z + d_\xi B_y = t(\sigma W[E_z + \varkappa_z - \vartheta^{\mathrm{E}}\ v_z] + q v_z), \tag{3.13}$$
$$-d_\xi \phi + \xi d_\xi B_x = 0, \tag{3.14}$$
$$d_\xi E_z + \xi d_\xi B_y = 0, \tag{3.15}$$
$$-d_\xi E_y + \xi d_\xi B_z = 0, \tag{3.16}$$
$$\tag{3.17}$$

$$\begin{aligned}
&\sigma W(-(1-v_x^2)d_\xi E_x + v_x v_y d_\xi E_y + v_x v_z d_\xi E_z + v_z d_\xi B_y - v_y d_\xi B_z)\\
&+ \left(\sigma W(2E_x v_x + E_y v_y + E_z v_z) - \sigma W^3 v_x(E_x + \varkappa_x - \vartheta^{\mathrm{E}}\ v_x) - q\right) d_\xi v_x\\
&+ \left(\sigma W(E_y v_x - B_z) - \sigma W^3 v_y(E_x + \varkappa_x - \vartheta^{\mathrm{E}}\ v_y)\right) d_\xi v_y\\
&+ \left(\sigma W(E_z v_x + B_y) - \sigma W^3 v_z(E_x + \varkappa_x - \vartheta^{\mathrm{E}}\ v_z)\right) d_\xi v_z\\
&+ (\xi - v_x) d_\xi q \ = \ 0,
\end{aligned} \tag{3.18}$$

$$\begin{aligned}
&\rho W^2 \left(\left(v_x(\xi - v_x) - \frac{1}{W^2} \right) d_\xi v_x + v_y(\xi - v_x) d_\xi v_y + v_z(\xi - v_x) d_\xi v_z \right)\\
&+ (\xi - v_x) d_\xi \rho \ = \ 0,
\end{aligned} \tag{3.19}$$

$$\begin{aligned}
&hW^4 \left(\left(2v_x(\xi - v_x) - \frac{1}{W^2} \right) d_\xi v_x + 2v_y(\xi - v_x) d_\xi v_y + 2v_z(\xi - v_x) d_\xi v_z \right)\\
&+ \left(W^2 \frac{\gamma}{\gamma - 1}(\xi - v_x) - \xi \right) d_\xi p + W^2(\xi - v_x) d_\xi \rho\\
&+ \xi E_x d_\xi E_x + (\xi E_y - B_z) d_\xi E_y + (\xi E_z + B_y) d_\xi E_z + \xi B_x d_\xi B_x\\
&+ (\xi B_y + E_z) d_\xi B_y + (\xi B_z - E_y) d_\xi B_z \ = \ 0,
\end{aligned} \tag{3.20}$$

$$\begin{aligned}
&hW^2 \left(2W^2 v_x^2(\xi - v_x) + (\xi - 2v_x)\right) d_\xi v_x + 2W^4 v_x v_y(\xi - v_x) d_\xi v_y\\
&+ 2hW^4 v_x v_z(\xi - v_x) d_\xi v_z + \left(W^2 v_x \frac{\gamma}{\gamma - 1}(\xi - v_x) - 1 \right) d_\xi p + W^2 v_x(\xi - v_x) d_\xi \rho\\
&+ E_x d_\xi E_x + (\xi B_z - E_y) d_\xi E_y - (\xi B_y + E_z) d_\xi E_z + B_x d_\xi B_x\\
&- (\xi E_z + B_y) d_\xi B_y + (\xi E_y - B_z) d_\xi B_z \ = \ 0,
\end{aligned} \tag{3.21}$$

$$\begin{aligned}
&(E_y - \xi B_z) d_\xi E_x + E_x d_\xi E_y + \xi B_x d_\xi E_z + (\xi E_z + B_y) d_\xi B_x + B_x d_\xi B_y - \xi E_x d_\xi B_z\\
&+ hW^2 v_y \left(2W^2 v_x(\xi - v_x) - 1\right) d_\xi v_x + hW^2(\xi - v_x)\left(1 + 2W^2 v_y^2\right) d_\xi v_y\\
&+ 2hW^4 v_y v_z(\xi - v_x) d_\xi v_z + W^2 v_y \frac{\gamma}{\gamma - 1}(\xi - v_x) d_\xi p + W^2 v_y(\xi - v_x) d_\xi \rho \ = \ 0,
\end{aligned} \tag{3.22}$$

$$
\begin{aligned}
&(E_z+\xi B_y)d_\xi E_x - \xi B_x d_\xi E_y + E_x d_\xi E_z + (B_z-\xi E_y)d_\xi B_x + \xi E_x d_\xi B_y + B_x d_\xi B_z \\
&+ hW^2(\xi-v_x)\left(1+2W^2v_z^2\right)d_\xi v_z + W^2 v_z \frac{\gamma}{\gamma-1}(\xi-v_x)d_\xi p + W^2 v_z(\xi-v_x)d_\xi\rho \\
&+ hW^2 v_z\left(2W^2 v_x(\xi-v_x)-1\right)d_\xi v_x + 2hW^4 v_y v_z(\xi-v_x)d_\xi v_y \;=\; 0.
\end{aligned}
\tag{3.23}
$$

As can been seen, this system is not self-similar, due to the presence of the independent variable t in the source terms of the Maxwell's equations, as well as in the scalar potentials. However, when the source terms vanish (e.g. if $\sigma = 0$), finding self-similar solutions is possible. The exact self-similar solutions in this regime may be used also as *approximate* self-similar solutions if the source terms do not dominate the dynamics (e.g. when the conductivity is sufficiently small and the electric charge is negligible). If these conditions hold, the homogeneous, linear ordinary differential equations system has non-trivial solution if the determinant of the system vanishes. After some algebra and using the notation $v^2 = v_x^2 + v_y^2 + v_z^2$, we can express the determinant of the system (3.9)-(3.23) as,

$$
\begin{aligned}
&\mathrm{Det}[\mathbf{M}] = \frac{-1}{\gamma-1}h^2W^6(v_x-\xi)^4\left(\xi^2-1\right)^4 \\
\times\;& \left[h\left(\gamma-1+v_x^2W^2(\gamma-2)-2v_xW^2\xi(\gamma-2)-\xi^2\left((\gamma-1)-W^2(\gamma-2)\right)\right)\right. \\
+\;& \left.\rho(\gamma-1)\left(-1-v_x^2W^2+2\xi v_xW^2\;-\left(W^2-1\right)\xi^2\right)\right].
\end{aligned}
$$

Non-trivial similarity solutions only exist if $\mathrm{Det}[\mathbf{M}] = 0$, which happens for

$$\xi = 1 \qquad \text{multiplicity 4,} \tag{3.24}$$

$$\xi = -1 \qquad \text{multiplicity 4,} \tag{3.25}$$

$$\xi = v_x \qquad \text{multiplicity 4,} \tag{3.26}$$

$$\xi^{\pm} = \frac{v_x(1-c_\mathrm{s}^2) \pm c_\mathrm{s}\sqrt{(1-v^2)\left[1-v^2c_\mathrm{s}^2-v_x(1-c_\mathrm{s}^2)\right]}}{(1-c_\mathrm{s}^2v^2)}. \tag{3.27}$$

From the spectral analysis done by Cordero-Carrión et al. (2012), the conditions (3.24) and (3.25) are related to either electromagnetic waves or waves associated to the scalar potentials ψ and ϕ propagating at the speed of light along the x-direction in oposite directions. Condition (3.26) corresponds to waves comoving with the fluid (entropy waves). The two solutions displayed in (3.27) correspond to both rarefactions propagating to the left (minus sign) and to the right (plus sign) and correspond to the acoustic waves found in Cordero-Carrión et al. (2012). Differently from the RMHD case (Giacomazzo and Rezzolla, 2006; Romero et al., 2005), these waves are decoupled from the electromagnetic field in our treatment of the homogeneous system of equations. We also note that the two last solutions $\xi^{\pm}$ coincide with the maximum and minimum eigenvalues of the Jacobian matrix associated with the RHD system (Pons et al., 2000).

The homogeneous ODE system (3.9)-(3.23) is still too complex to find analytic solutions to it. Indeed, we have reduced the whole system to a single ODE. However, the solution of the latter equation is not trivial and, since we do not have exact self-similar solutions anyway, to guide our intuition we have resorted to simplifying a bit the problem. We have checked that, under the assumption that the magnetic field is perpendicular to the velocity field, we recover the same self-similarity solution than in Romero et al. (2005) for the ideal RMHD case in the ideal limit of RRMHD. Namely, we can find an expression for the normal velocity behind the rarefaction (v_x^b) in terms of the thermodynamical variables in the state ahead (a) and the total pressure ($\hat{p}^b$) behind the rarefaction wave. This is remarkable in light of the fact that the self-similar solution has been found for the case $\sigma = 0$. We find, therefore, that self-similar solutions are possible in the limits of vanishing conductivity and also, in ideal RMHD, i.e. in the limit of very large conductivities of RRMHD. Unfortunately, in spite of our efforts to bridge the gap between these two limits, we have been unable to find approximate expressions roughly valid in the intermediate regime in which σ is finite.

3.3 Jump Conditions across flow discontinuities

A discontinuous wave is defined as a region of the flow where some of the fluid properties are discontinuous across a surface of infinitesimal width. Shock waves are a discontinuous waves in which, at least, the pressure and the density of a fluid element exhibit jumps. Discontinuities in a fluid flow make the direct solution of the differential version of either the RMHD or RRMHD equations impossible. However, one may always resort to an integral version of the system of equations, where discontinuous solutions are possible. In any case, the fact that the numerical variables display jumps across shocks must be compatible with the continuity of their respective fluxes. The mathematical expression of the previous statement are the RH conditions, which relate the states on both sides of a shock. In the case of PDE systems of balance laws, the presence of source terms may modify the standard RH conditions found in PDE systems of conservation laws. Following Jeffrey and Taniuti (1964) and LeVeque (2002), a scalar, one-dimensional balance law

$$\partial_t U(x,t) + \partial_x F(U(x,t)) = \Omega(x,t), \tag{3.28}$$

can be expressed in integral form as:

$$\begin{aligned}\int_{x_1}^{x_1+\Delta x} U(x,t+\Delta t)\ dx - \int_{x_1}^{x_1+\Delta x} U(x,t)\ dx \\ = \int_{t}^{t_1+\Delta t} F(U(x,t))dt - \int_{t_1}^{t_1+\Delta t} F(U(x+\Delta x,t))dt \\ + \int_{t}^{t_1+\Delta t}\int_{x_1}^{x_1+\Delta x} \Omega(x,t)\ dx\ dt.\end{aligned} \tag{3.29}$$

If the source term $\Omega(x,t)$ were smooth in the integration domain $[t_1, t_1 + \Delta t] \times [x_1, x_1 + \Delta x]$, the contribution of the sources to the RH jump conditions would vanish. However, in RRMHD, the source terms contain the electric currents, which may develop discontinuities and, therefore, the RH conditions must include contributions from the sources. To obtain some insight on how the RH conditions may be modified in the presence of non-regular sources, we model the source term as the combination of two delta functions on each side of the shock front (located at $x_s(t) \in [x_1, x_1 + \Delta x]$; see, e.g. LeVeque 2002)

$$\Omega(x,t) = \Omega_l\ \delta(x - x_s(t)) + \Omega_r\ \delta(x - x_s(t)),$$

then the conservation law reads

$$\begin{aligned}\int_{x_1}^{x_1+\Delta x} U(x,t_1+\Delta t)\ dx - \int_{x_1}^{x_1+\Delta x} U(x,t_1)\ dx \\ = \int_{t_1}^{t_1+\Delta t} F(U(x_1,t))dt - \int_{t_1}^{t_1+\Delta t} F(U(x_1+\Delta x,t))dt \\ + \int_{t_1}^{t_1+\Delta t}\int_{x_1}^{x_s} \Omega_l\ \delta(x - x_s(t))\ dx\ dt \\ + \int_{t_1}^{t_1+\Delta t}\int_{x_s}^{x_1+\Delta x} \Omega_r\ \delta(x - x_s(t))\ dx\ dt.\end{aligned} \tag{3.30}$$

Taking the limit in which both $\Delta x \to 0$ and $\Delta t \to 0$ the equation (3.30) yields

$$\Delta x\ U_r - \Delta x\ U_l = \Delta t\ F(U_l) - \Delta t\ F(U_r) + \Delta t\ (\Omega_l - \Omega_r) + \mathcal{O}(\Delta t^2).$$

Using $\Delta x = -V_s \Delta t$, with V_s the speed of shock front, leads to

$$V_s\,(U_r - U_l) = (F(U_r) - F(U_l)) + (\Omega_r - \Omega_l). \tag{3.31}$$

This is identical to the RH condition for a sourceless balance law (i.e. a conservation law) but with an additional term resulting from the singular source. It expresses the fact that the change in fluxes is, at least partly, compensated by the jump of the source terms.

Note that if the source term $\Omega(x,t)$ were a bounded function rather than a delta function, then the source term in (3.30) would be

$$\int_{t_1}^{t_1+\Delta t}\int_{x_1}^{x_1+\Delta x} \Omega(x,t)\; dx\; dt \approx \Delta t\; \Delta x\; \Omega(x,t),$$
$$\approx \Delta t^2\; V_s\; \Omega(x,t).$$

And after dividing by Δt this would still be $\mathcal{O}(\Delta t)$ and would vanish as $\Delta t \to 0$. Hence a bounded source does not change the RH conditions, but a singular source term makes a non-trivial contribution to them. This is of relevance in our case, since the source terms of the RRMHD are stiff in the ideal limit and, hence, they may behave as non-bounded sources in the RH conditions. On account of this fact, we now proceed to compute the RH conditions for the RRMHD equations in the presence of potentially unbounded source terms in the Maxwell equations.

Let n^α be the unit normal to a hyper-surface (Σ) in Minkowski space-time, across wich, the rest-mass density ρ, the four-velocity u^α, the four-current density J^α, the Maxwell tensor $F^{\alpha\beta}$, the Faraday tensor ${}^*F^{\alpha\beta}$ and the stress-energy tensor $T^{\alpha\beta}$ are discontinuous. In terms of the coordinate velocity of the hyper-surface that defines the position of the shock wave, which we assume for simplicity be moving along the x-direction, we have

$$n^\alpha = W_s(V_s, 1, 0, 0),$$

where W_s is the Lorentz factor of the shock,

$$W_s = \frac{1}{\sqrt{1-V_s^2}}.$$

The RH conditions are based on the continuity of mass flux, energy-momentum flux, current density flux and the electromagnetic fluxes, and we include the possibility that singular sources appear in the (augmented) Maxwell equations. Then, we have

$$\left[\; \rho u^\alpha \;\right] n_\alpha = 0, \tag{3.32}$$
$$\left[\; J^\alpha \;\right] n_\alpha = 0, \tag{3.33}$$
$$\left[\; F^{\alpha\beta} \;\right] n_\beta = \left[\; \tilde{J}^\alpha \;\right], \tag{3.34}$$
$$\left[\; {}^*F^{\alpha\beta} \;\right] n_\beta = \left[\; \hat{J}^\alpha \;\right], \tag{3.35}$$
$$\left[\; T^{\alpha\beta} \;\right] n_\beta = 0, \tag{3.36}$$

where we use the notation:

$$\left[\; G \;\right] = G_a - G_b,$$

with G_a and G_b being the ahead (a) and behind (b) boundary values of G on the two sides of Σ. The source terms in (3.34) and (3.35) respectively read

$$\tilde{J}^\alpha = \begin{pmatrix} q - \kappa\psi \\ J_x \\ J_y \\ J_z \end{pmatrix}, \qquad \hat{J}^\alpha = \begin{pmatrix} \kappa\phi \\ 0 \\ 0 \\ 0 \end{pmatrix}.$$

3.3.0.1 RH condition on the mass density

Developing the RH condition Eq. (3.32), taking into account the definition of D^α (Eq. (2.15)) we have

$$W_s V_s D_a - W_s D_a v_x^a = W_s V_s D_b - W_s D_b v_x^b.$$

Manipulating the previous expression it is possible to introduce the invariant mass flux across the shock,

$$j \equiv W_s D_a (V_s - v_x^a) = W_s D_b (V_s - v_x^b). \tag{3.37}$$

Then the RH condition can be written as in RHD (e.g. Pons et al., 2000):

$$[v_x] = -\frac{j}{W_s}\left[\frac{1}{D}\right].$$

3.3.0.2 RH condition on the current density

The current density four-vector, J^α is given by Eq. (2.2). Using this definition on the RH condition (3.33) and employing the invariant j (3.37), we obtain

$$j\left[\frac{q}{D}\right] = -W_s\left[J_x\right] + W_s\left[q v_x\right].$$

3.3.0.3 RH conditions on the Faraday and Maxwell tensors with source terms

Using the definitions of the Maxwell and Faraday tensors, that is

$$F^{\alpha\beta} = \begin{pmatrix} \psi & -E_x & -E_y & -E_z \\ E_x & -\psi & -B_z & B_y \\ E_y & B_z & -\psi & -B_x \\ E_z & -B_y & B_x & -\psi \end{pmatrix}, \qquad \hat{F}^{\alpha\beta} = \begin{pmatrix} \phi & -B_x & -B_y & -B_z \\ B_x & -\phi & E_z & -E_y \\ B_y & -E_z & -\phi & E_x \\ B_z & E_y & -E_x & -\phi \end{pmatrix}.$$

respectively, we obtain from Eqs. (3.34) and (3.35) and assuming that the source terms may be potentially non bounded as stated at the beginning of this section, we obtain

$$W_s V_s\,[\psi] + W_s\,[E_x] = [q - \kappa\psi]\,, \tag{3.38}$$
$$W_s V_s\,[E_x] + W_s\,[\psi] = -[J_x]\,, \tag{3.39}$$
$$W_s V_s\,[E_y] - W_s\,[B_z] = -[J_y]\,, \tag{3.40}$$
$$W_s V_s\,[E_z] + W_s\,[B_y] = -[J_z]\,, \tag{3.41}$$
$$W_s V_s\,[\phi] + W_s\,[B_x] = -\kappa\,[\phi]\,, \tag{3.42}$$
$$W_s V_s\,[B_x] + W_s\,[\phi] = 0, \tag{3.43}$$
$$W_s V_s\,[B_y] + W_s\,[E_z] = 0, \tag{3.44}$$
$$W_s V_s\,[B_z] - W_s\,[E_y] = 0. \tag{3.45}$$

We can manipulate the previous relations in order to write explicitly down the jumps in the electric field components and the B_x component as,

$$[E_x] = -[\psi] + \frac{1}{W_s(V_s+1)}\left([q-\kappa\psi] - [J_x]\right), \qquad \text{from} \quad (3.38) + (3.39)$$
$$[B_x] = -[\phi] - \frac{\kappa}{W_s(V_s+1)}\,[\phi]\,, \qquad \text{from} \quad (3.42) + (3.43)$$
$$[E_z] = -[B_y] - \frac{1}{W_s(V_s+1)}\,[J_z]\,, \qquad \text{from} \quad (3.41) + (3.44)$$
$$[E_y] = [B_z] - \frac{1}{W_s(V_s+1)}\,[J_y]\,. \qquad \text{from} \quad (3.40) - (3.45)$$

3.3.0.4 RH conditions on the stress-energy tensor

From the temporal ($\beta = 0$) and spatial ($\beta = x, y, z$) parts of Eq. (3.36), we find both conditions for the jumps of the energy density and of the three-momentum density vector, respectively. In order to compare more easily our results with those obtained in ideal RMHD by, e.g. Giacomazzo and Rezzolla (2006) , we introduce the following notation

$$b^2 = B^2 - E^2. \tag{3.46}$$

In the ideal limit $\mathbf{E} = -\mathbf{v}\times\mathbf{B}$ and, consistently, $\mathbf{E}^2 = \mathbf{v}^2\mathbf{B}^2 - (\vartheta^{\rm B})^2$. Thus, Eq. (3.46) becomes equal to the square of the magnetic field four vector, b^μ, i.e. $b^2 = b_\mu b^\mu$. Explicitly

$$b^2 = \frac{\mathbf{B}^2}{W^2} + (\vartheta^{\rm B})^2. \tag{3.47}$$

In terms of b^2 we may express the total specific enthalpy and total pressure (in the ideal RMHD limit) as

$$\hat{h} = h + \frac{b^2}{\rho}, \qquad \hat{p} = p + \frac{1}{2}b^2, \tag{3.48}$$

and, furthermore, we may introduce the conserved energy and momenta densities in the degenerate RMHD limit in which $\vartheta^{\mathrm{B}} = 0$ (i.e. in the case in which the magnetic field is perpendicular to the velocity field)

$$\hat{\mathcal{E}} = \rho\hat{h}W^2 - \hat{p}, \qquad \hat{S}_i = \rho\hat{h}W^2 v_i, \qquad i = x, y, z. \tag{3.49}$$

3.3.0.5 RH condition on the energy density

We can rewrite the conserved energy density (2.26) and the momentum density S_x (2.27) in terms of $\hat{\mathcal{E}}$,

$$\begin{aligned} \mathcal{E} &= \hat{\mathcal{E}} + \mathbf{B}^2 - W^2 b^2, \\ S_x &= \hat{\mathcal{E}} v_x + \hat{p} v_x + \chi_x - W^2\ b^2\ v_x. \end{aligned}$$

Then we obtain from (3.36)

$$\begin{aligned} V_s\big[\mathcal{E}\big] &= \big[S_x\big], \\ \big[(\hat{\mathcal{E}} + \mathbf{B}^2 - W^2 b^2)(V_s - v_x)\big] &= \big[\hat{p} v_x\big] + \big[\chi_x - \mathbf{B}^2 v_x\big], \end{aligned}$$

and making use of the invariant j (Eq. (3.37)), we obtain the RH condition for energy density as,

$$\frac{j}{W_s}\left[\frac{\hat{\mathcal{E}}}{D}\right] = \big[\hat{p} v_x\big] + \big[\chi_x - B^2 v_x\big] - \frac{j}{W_s}\left[\frac{B^2}{D}\right] + \frac{j}{W_s}\left[\frac{W^2\ b^2}{D}\right]. \tag{3.50}$$

We can compare with the ideal RMHD limit considering that for purely inductive electric fields we have, $\chi_x - \mathbf{B}^2 v_x = -B_x \vartheta^{\mathrm{B}}$, which yields the same expression as in Giacomazzo and Rezzolla (2006)

$$\frac{j}{W_s}\left[\frac{\hat{\mathcal{E}}}{D}\right] = \big[\hat{p} v_x\big] - \big[B_x \vartheta^{\mathrm{B}}\big] + \frac{j}{W_s}\left[\frac{W^2 (\vartheta^{\mathrm{B}})^2}{D}\right].$$

3.3.0.6 RH condition on the momentum density x component

Using the definition of $\hat{S}_x$ (3.49), the momentum S_x, can be expressed, as,

$$S_x = \rho h W^2 v_x + \chi_x = \hat{S}_x + \chi_x - W^2\ b^2\ v_x,$$

which allows us to write the RH condition for momentum x component in the following form,

$$\left[(\hat{S}_x + \chi_x - W^2\ b^2\ v_x)(V_s - v_x)\right] = \left[E_y^2 + E_z^2 - B_x^2 + \hat{p} + \chi_x v_x\right].$$

Using the invariant j Eq. (3.37), we obtain the RH condition for $\hat{S}_x$,

$$\frac{j}{W_s}\left[\frac{\hat{S}_x}{D}\right] = [\hat{p}] - \left[B_x^2 - E_y^2 - E_z^2 + \chi_x v_x\right] - \frac{j}{W_s}\left[\frac{\chi_x}{D}\right] + \frac{j}{W_s}\left[\frac{W^2\ b^2\ v_x}{D}\right]. \tag{3.51}$$

In order to recover the ideal RMHD equivalent RH condition, we use the relations,

$$B_x^2 - E_y^2 - E_z^2 + \chi_x\ v_x = \frac{B_x^2}{W^2} + B_x\ v_x\ \vartheta^{\mathrm{B}}$$

and

$$W^2\ b^2\ v_x - \chi_x = B_x\ \vartheta^{\mathrm{B}} + W^2\ v_x\ (\vartheta^{\mathrm{B}})^2,$$

to obtain,

$$\frac{j}{W_s}\left[\frac{\hat{S}_x}{D}\right] = [\hat{p}] - \left[\frac{B_x^2}{W^2}\right] - [B_x \vartheta^{\mathrm{B}} v_x] + \frac{j}{W_s}\left[\frac{B_x \vartheta^{\mathrm{B}}}{D}\right] + \frac{j}{W_s}\left[\frac{W^2 (\vartheta^{\mathrm{B}})^2 v_x}{D}\right].$$

3.3.0.7 RH condition on the momentum y and z components

Using the definition of $\hat{S}_t$, for $t = y, z$ (3.49), the momenta tangential to the shock surface, S_t, can be expressed as

$$S_t = \hat{S}_t + \chi_t - W^2\ b^2\ v_t.$$

Then the corresponding RH conditions may be cast in the form

$$\left[(\hat{S}_t + \chi_t - W^2\ b^2\ v_t)(V_s - v_x)\right] = -\left[E_x E_t + B_x B_t + \chi_t\ v_x\right],$$

and using the invariant j Eq. (3.37), we obtain the RH condition for $\hat{S}_t$

$$\frac{j}{W_s}\left[\frac{\hat{S}_t}{D}\right] = -\left[E_x E_t + B_x B_t + \chi_t\ v_x\right] - \frac{j}{W_s}\left[\frac{\chi_t}{D}\right] + \frac{j}{W_s}\left[\frac{W^2\ b^2\ v_t}{D}\right]. \tag{3.52}$$

In order to recover the ideal RMHD equivalent RH condition, we use the relations,

$$E_x E_t + B_x B_t + \chi_t\ v_x = \frac{B_x B_t}{W^2} + B_x\ v_t\ \vartheta^{\mathrm{B}}$$

and

$$W^2\ b^2\ v_t - \chi_t = B_t\ \vartheta^{\rm B} + W^2\ v_t(\vartheta^{\rm B})^2,$$

to obtain,

$$\frac{j}{W_s}\left[\frac{\hat{S}_t}{D}\right] = -\left[\frac{B_x B_t}{W^2}\right] - [B_x v_t \vartheta^{\rm B}] + \frac{j}{W_s}\left[\frac{B_t \vartheta^{\rm B}}{D}\right] + \frac{j}{W_s}\left[\frac{W^2(\vartheta^{\rm B})^2 v_t}{D}\right],$$

which match the expressions in Giacomazzo and Rezzolla (2006).

3.3.0.8 The normal flow speed in the post-shock state, v_x^b, as a function of the post-shock pressure, $\hat{p}^b$

Once we have formulated the RH conditions, the next step is writing, v_x^b, the normal flow velocity in the post-shock state, as a function of the total post-shock pressure $\hat{p}^b$. Different from the treatment that we have developed for rarefactions (Sec.3.2), where we only consider the case $\mathbf{B} \perp \mathbf{v}$, here we allow for any topology of the magnetic field and relax the previous restriction. We begin by writing Eq. (3.51) in the form

$$\frac{j}{W_s}\left[\frac{\rho\hat{h}W^2 v_x}{D}\right] - \frac{j}{W_s}\left[\frac{W^2 b^2 v_x}{D}\right] + [\chi_x\ v_x] = [\hat{p}] - \left[B_x^2 - E_y^2 - E_z^2\right] - \frac{j}{W_s}\left[\frac{\chi_x}{D}\right],$$

and employ the definition of the invariant j Eq. (3.37) to obtain

$$\begin{aligned} v_x^b\left(\hat{h}_b W_b - \frac{W_b^2(B_b^2 - E_b^2)}{D_b}\right) &= \hat{h}_a W_a v_x^a - \frac{W_a^2(B_a^2 - E_a^2)v_x^a}{D_a} \\ &+ \left(\frac{v_x^a W_s}{j} + \frac{1}{D_a}\right)[\chi_x] \\ &- \frac{W_s}{j}[\hat{p}] + \frac{W_s}{j}\left[B_x^2 - E_y^2 - E_z^2\right]. \end{aligned} \quad (3.53)$$

To simplify the previous expression, we employ Eq. (3.50) in the form,

$$V_s\,[\mathcal{E}] = [S_x]\,,$$

which yields

$$\left[\hat{h}W - \frac{W^2\ b^2}{D}\right] = \frac{V_s W_s}{j}\left[\hat{p} - B^2\right] + \frac{W_s}{j}\left[\chi_x\right].$$

Using Eq. (3.37) we arrive at

$$\hat{h}_b W_b - \frac{W_b^2(B_b^2 - E_b^2)}{D_b} = \hat{h}_a W_a - \frac{W_a^2(B_a^2 - E_a^2)}{D_a} - \left(\frac{v_x^a W_s}{j} + \frac{1}{D_a}\right)\left[\hat{p} - B^2\right] - \frac{W_s}{j}\left[\chi_x\right]. \quad (3.54)$$

Replacing this expression in the left hand side of Eq. (3.53), the normal flow velocity can be written as

$$v_x^b = \frac{\hat{h}_a W_a v_x^a - \frac{W_a^2}{D_a}(B_a^2 - E_a^2)v_x^a + \left(\frac{v_x^a W_s}{j} + \frac{1}{D_a}\right)\left[\chi_x\right]}{\hat{h}_a W_a - \frac{W_a^2}{D_a}(B_a^2 - E_a^2) - \left(\frac{v_x^a W_s}{j} + \frac{1}{D_a}\right)\left[\hat{p} - B^2\right] - \frac{W_s}{j}\left[\chi_x\right]} - \frac{\frac{W_s}{j}\left[\hat{p}\right] + \frac{W_s}{j}\left[B_x^2 - E_y^2 - E_z^2\right]}{\hat{h}_a W_a - \frac{W_a^2}{D_a}(B_a^2 - E_a^2) - \left(\frac{v_x^a W_s}{j} + \frac{1}{D_a}\right)\left[\hat{p} - B^2\right] - \frac{W_s}{j}\left[\chi_x\right]}. \quad (3.55)$$

Next, we check that the previous expression agrees with that in the ideal RMHD case (Giacomazzo and Rezzolla, 2006; Romero et al., 2005). For that we use relations (3.48) (valid in the ideal RMHD limit) to write Eq. (3.55) as

$$v_x^b = \frac{\hat{h}_a W_a v_x^a - \frac{W_s}{j}\left[\hat{p} - \frac{B_x^2}{W^2}\right] - \frac{W_a^2}{D_a}(\vartheta_a^{\rm B})^2 v_x^a + \frac{W_s}{j}B_x^a v_x^a(\vartheta_a^{\rm B})^2 - \left[\frac{B_x\vartheta^{\rm B}}{D}\right]}{\hat{h}_a W_a - \left(\frac{v_x^a W_s}{j} + \frac{1}{D_a}\right)\left[\hat{p}\right] - \frac{W_a^2}{D_a}(\vartheta_a^{\rm B})^2 + \frac{W_s}{j}B_x^a\vartheta_a^{\rm B}}. \quad (3.56)$$

At this point, we straightforwardly recover the expression of Romero et al. (2005) for the particular case $\mathbf{B} \perp \mathbf{v}$ and $B_x = 0$, (see e.g. their Eq. (4.13))

$$v_x^b = \frac{\hat{h}_a W_a v_x^a - \frac{W_s}{j}\left[\hat{p}\right]}{\hat{h}_a W_a - \left(\frac{v_x^a W_s}{j} + \frac{1}{D_a}\right)\left[\hat{p}\right]}.$$

In order to recover the general case in ideal RMHD from equation (3.56) we make use of the invariant j Eq. (3.37) and the relations [(4.10), (4.11), (4.12)] of Giacomazzo and Rezzolla (2006) (only strictly valid in ideal RMHD), as well as the condition $[B_x] = 0$ (i.e. $B_x^a = B_x^b := B_x$), obtaining

$$\frac{W_s}{j}\left[\frac{B_x^2}{W^2}\right] - \left[\frac{B_x\vartheta^{\rm B}}{D}\right] = \frac{W_s}{j}\frac{B_x^2}{W_a^2} - \frac{B_x\vartheta_a^{\rm B}}{D_a} - \frac{W_s}{j}B_x^2(1 - v_y^a v_y^b - v_z^a v_z^b) + \frac{1}{D_a}B_x(B_y^a v_y^b + B_z^a v_z^b) + v_x^b B_x^2\left(\frac{W_s}{j}v_x^a + \frac{1}{D_a}\right).$$

Replacing the latter expression in (3.56) we obtain,

$$v_x^b = \frac{D_a W_s \left\{ B_x v_x^a \vartheta_a^{\mathrm{B}} + \frac{B_x^2}{W_a^2} - [\hat{p}] - B_x^2(1 - v_y^a v_y^b - v_z^a v_z^b) \right\}}{D_a W_s \left\{ B_x \vartheta_a^{\mathrm{B}} - B_x^2 v_x^a - v_x^a [\hat{p}] \right\} - j \left\{ [\hat{p}] + W_a^2 (\vartheta_a^{\mathrm{B}})^2 + B_x^2 - \rho_a \hat{h}_a W_a^2 \right\}}$$
$$+ \frac{j \left\{ B_x (B_y^a v_y^b + B_z^a v_z^b) - B_x \vartheta_a^{\mathrm{B}} - W_a^2 (\vartheta_a^{\mathrm{B}})^2 v_x^a + \rho_a \hat{h}_a W_a^2 v_x^a \right\}}{D_a W_s \left\{ B_x \vartheta_a^{\mathrm{B}} - B_x^2 v_x^a - v_x^a [\hat{p}] \right\} - j \left\{ [\hat{p}] + W_a^2 (\vartheta_a^{\mathrm{B}})^2 + B_x^2 - \rho_a \hat{h}_a W_a^2 \right\}}.$$

Finally, we employ the first of the relations (3.49), introducing a new variable $\hat{\tau} = \rho \hat{h} W^2 - \hat{p} - D$, arriving to the same expression as Giacomazzo and Rezzolla (2006) (their Eq. (4.25))

$$v_x^b = \frac{D_a \left\{ W_s B_x^2 + W_a^2 \left\{ (W_s B_x \vartheta_a^{\mathrm{B}} + j) v_x^a - W_s [\hat{p}] - W_s B_x^2 (1 - v_y^a v_y^b - v_z^a v_z^b) \right\} \right\}}{W_a^2 \left\{ D_a \left\{ j + W_s B_x \vartheta_a^{\mathrm{B}} - W_s (B_x^2 + [\hat{p}]) v_x^a \right\} - j \left\{ B_x^2 - \hat{p}_b + W_a^2 (\vartheta_a^{\mathrm{B}})^2 - \hat{\tau}_a \right\} \right\}}$$
$$+ \frac{j \left\{ B_x (B_y^a v_y^b + B_z^a v_z^b) - B_x \vartheta_a^{\mathrm{B}} + (\hat{\tau}_a + \hat{p}_a - W_a^2 (\vartheta_a^{\mathrm{B}})^2) v_x^a \right\}}{D_a \left\{ j + W_s B_x \vartheta_a^{\mathrm{B}} - W_s (B_x^2 - [\hat{p}]) v_x^a \right\} - j \left\{ B_x^2 - \hat{p}_b + W_a^2 (\vartheta_a^{\mathrm{B}})^2 - \hat{\tau}_a \right\}}.$$

3.3.0.9 The transversal flow speed in the post-shock state, v_t^b, as a function of the post-shock pressure $\hat{p}^b$

Equation (3.52), can be recast in the form

$$\frac{j}{W_s} \left[\frac{\hat{S}_t}{D} \right] = - \left[E_x E_t + B_x B_t + \chi_t \, v_x \right] - \frac{j}{W_s} \left[\frac{\chi_t}{D} \right] + \frac{j}{W_s} \left[\frac{W^2 \, b^2 \, v_t}{D} \right].$$

Employing the definition of j, Eq. (3.37), in the form, $D_b^{-1} = \frac{W_s}{j}(V_s - v_x^b)$, we further obtain

$$v_y^b \left(\hat{h}_b W_b - \frac{W_b^2}{D_b} (B_b^2 - E_b^2) \right) = \hat{h}_a W_a v_y^a - \frac{W_a^2 (B_a^2 - E_a^2)}{D_a} v_y^a$$
$$+ \left(\frac{v_x^a W_s}{j} + \frac{1}{D_a} \right) [\chi_y] + \frac{W_s}{j} \left[E_x E_y + B_x B_y \right].$$

Now applying relation (3.54), the transversal flow speed in the post-shock state v_t^b can be written as

$$v_t^b = \frac{\hat{h}_a W_a v_t^a - \frac{W_a^2}{D_a} (B_a^2 - E_a^2) v_t^a + \left(\frac{v_x^a W_s}{j} + \frac{1}{D_a} \right) [\chi_t] + \frac{W_s}{j} \left[E_x E_t + B_x B_t \right]}{\hat{h}_a W_a - \frac{W_a^2}{D_a} (B_a^2 - E_a^2) - \left(\frac{v_x^a W_s}{j} + \frac{1}{D_a} \right) \left[\hat{p} - B^2 \right] - \frac{W_s}{j} \left[\chi_t \right]}.$$

3.4 Lichnerowicz Adiabat

To derive the Lichnerowicz adiabat, i.e. the final juncture condition for shock waves (Anile, 1989; Taub, 1948), we proceed in the same way as Pons et al. (2000) and Romero et al. (2005), i.e. we begin from the following identity

$$\left[\ T^{\alpha\beta}\ \right] n_\beta \left\{ (\hat{h} u_\alpha)_a + (\hat{h} u_\alpha)_b \right\} = 0, \tag{3.57}$$

which is obtained manipulating by Eq. (3.36), and that is independent of the presence of source terms in the Maxwell equations. Then the jump conditions for shock waves are used in order to obtain the Lichnerowicz adiabat for RRMHD, which is the extension to relativistic magneto-fluid dynamics of the classical Hugoniot adiabat (Anile, 1989).

Gathering the relations that we have derived in the previous sections and making the operation [Eq. (3.50) - Eq. (3.51) - Eq. (3.52)], we can write Eq. (3.57) as

$$\begin{aligned}
\frac{j}{W_s}\left[\hat{h}^2\right] = \frac{j}{W_s}\left(\frac{\hat{h}_a}{\rho_a} + \frac{\hat{h}_b}{\rho_b}\right)[\hat{p}] + \left(\frac{j}{W_s}\left[\frac{B^2}{D} - \frac{W^2 b^2}{D}\right] - \left[\chi_x - B^2 v_x\right]\right)\mathcal{Z}_0 \\
- \left(\frac{j}{W_s}\left[\frac{\chi_x}{D} - \frac{W^2 b^2 v_x}{D}\right] + \left[B_x^2 - E_y^2 - E_z^2 + (\chi_x) v_x\right]\right)\mathcal{Z}_z \\
- \left(\frac{j}{W_s}\left[\frac{\chi_y}{D} - \frac{W^2 b^2 v_y}{D}\right] + \left[E_x E_y + B_x B_y + (\chi_y) v_x\right]\right)\mathcal{Z}_y \\
- \left(\frac{j}{W_s}\left[\frac{\chi_z}{D} - \frac{W^2 b^2 v_z}{D}\right] + \left[E_x E_z + B_x B_z + (\chi_z) v_x\right]\right)\mathcal{Z}_z,
\end{aligned} \tag{3.58}$$

where $\mathcal{Z}_0 := \hat{h}_a W_a + \hat{h}_b W_b$ and $\mathcal{Z}_m := \hat{h}_a W_a v_m^a + \hat{h}_b W_b v_m^b$ $(m = x, y, z)$, or, in terms of the conserved variables as

$$\begin{aligned}
\frac{j}{W_s}\left[\hat{h}^2\right] = & \frac{j}{W_s}\left(\frac{\hat{h}_a}{\rho_a} + \frac{\hat{h}_b}{\rho_b}\right)[\hat{p}] - \left(\frac{j}{W_s}\left[\frac{\hat{\mathcal{E}}}{D}\right] - [\hat{p} v_x]\right)\mathcal{Z}_0 \\
& + \left(\frac{j}{W_s}\left[\frac{\hat{S}_x}{D}\right] - [\hat{p}]\right)\mathcal{Z}_x + \left(\frac{j}{W_s}\left[\frac{\hat{S}_y}{D}\right]\right)\mathcal{Z}_y + \left(\frac{j}{W_s}\left[\frac{\hat{S}_z}{D}\right]\right)\mathcal{Z}_z.
\end{aligned}$$

From expression (3.58) we can recover the Lichnerowicz adiabat for ideal

RMHD, making use the relation Eq. (3.47)

$$\begin{aligned}\left[\hat{h}^2\right] = &\left(\frac{\hat{h}_a}{\rho_a} + \frac{\hat{h}_b}{\rho_b}\right)[\hat{p}] + \left(\left[\frac{W^2(\vartheta^{\mathrm{B}})^2}{D} + \frac{W_s}{j}B_x\vartheta^{\mathrm{B}}\right]\right)\mathcal{Z}_0 \\ &- \left(\left[\frac{B_x\vartheta^{\mathrm{B}}}{D} + \frac{W^2(\vartheta^{\mathrm{B}})^2 v_x}{D}\right] - \frac{W_s}{j}\left[\frac{B_x B_x}{W^2} + B_x v_x \vartheta^{\mathrm{B}}\right]\right)\mathcal{Z}_x \\ &- \left(\left[\frac{B_y\vartheta^{\mathrm{B}}}{D} + \frac{W^2(\vartheta^{\mathrm{B}})^2 v_y}{D}\right] - \frac{W_s}{j}\left[\frac{B_x B_y}{W^2} + B_x v_y \vartheta^{\mathrm{B}}\right]\right)\mathcal{Z}_y \\ &- \left(\left[\frac{B_z\vartheta^{\mathrm{B}}}{D} + \frac{W^2(\vartheta^{\mathrm{B}})^2 v_z}{D}\right] - \frac{W_s}{j}\left[\frac{B_x B_z}{W^2} + B_x v_z \vartheta^{\mathrm{B}}\right]\right)\mathcal{Z}_z.\end{aligned}$$

We can further obtain the particular case, in ideal RMHD, in which $\mathbf{B} \perp \mathbf{v}$ (Romero et al., 2005) since under this restriction, the previous expression reduces to

$$\left[\hat{h}^2\right] = \left(\frac{\hat{h}_a}{\rho_a} + \frac{\hat{h}_b}{\rho_b}\right)[\hat{p}]\,.$$

Chapter 4

Numerical methods

The methods described in this chapter have been implemented in the new code Cueva (see, App. A Miranda-Aranguren et al., 2014), inspired by the Genesis code structure (Aloy et al., 1999). These codes are based on a finite volume discretization of the space-time. This means that the space-time domain, $[t_0, t_\mathrm{f}] \times [a, b]$ [1], where t_0 is the time where the initial data is provided, t_f is the time at which we want to compute the solution and a and b are the lower and upper bounds of the spatial domain, respectively. The space-time domain is tessellated with $n_t \times n_x$ subintervals of the form $\mathcal{C}_i^n := [t^n, t^{n+1}] \times [x_{i-1/2}, x_{i+1/2}]$ ($n = 1, \ldots, n_t$; $i = 1, \ldots, n_x$; $t^1 = t_0$; $t^{n_t} = t_\mathrm{f}$; $x_{-1/2} = a$; $x_{n_x+1/2} = b$). Then a balance law of the form (3.28) is replaced by its integral version for systems of equations[2]

$$\begin{aligned}\int_{x_{i-1/2}}^{x_{i+1/2}} \mathbf{U}(x, t^{n+1})\ dx - \int_{x_{i-1/2}}^{x_{i+1/2}} \mathbf{U}(x, t^n)\ dx \\ = \int_{t^n}^{t^{n+1}} \mathbf{F}(\mathbf{U}(x_{i-1/2}, t))dt - \int_{t^n}^{t^{n+1}} \mathbf{F}(\mathbf{U}(x_{i+1/2}, t))dt \\ + \int_{t^n}^{t^{n+1}} \int_{x_{i-1/2}}^{x_{i+1/2}} \mathbf{\Omega}(x, t)\ dx\ dt,\end{aligned} \tag{4.1}$$

[1] Although we are introducing the definitions for one dimensional cases, they can be easily generalized to multiple spatial dimensions. Here, we restrict to the one dimensional case for simplicity.

[2] For systems of equations, the scalar variables $U(x,t)$, the fluxes $F(U(x,t))$ and the source terms $\Omega(x,t)$ are replaced by the vectors of m components $\mathbf{U}(x,t)$, $\mathbf{F}(\mathbf{U}(x,t))$ and $\mathbf{\Omega}(x,t)$ respectively, with m being the number of unknowns ($m = 14$ in the case of the augmented RRMHD system).

and we define the following averages of the unknown variables on each *numerical cell*:

$$\mathbf{U}_i^n := \frac{1}{\Delta x_i} \int_{x_{i-1/2}}^{x_{i+1/2}} \mathbf{U}(x, t^n) dx, \tag{4.2}$$

with $\Delta x_i = x_{i+1/2} - x_{i-1/2}$. Should the partition of the domain be uniform, all the subintervals have the same width, namely, $\Delta x = (b-a)/n_x$. Likewise, we define spatial averages over the source terms as:

$$\mathbf{\Omega}_i^n := \frac{1}{\Delta x_i} \int_{x_{i-1/2}}^{x_{i+1/2}} \mathbf{\Omega}(x, t^n)\ dx. \tag{4.3}$$

Finally, we define the *numerical fluxes* as

$$\mathbf{F}_{i-1/2} := \int_{t^n}^{t^{n+1}} \mathbf{F}(\mathbf{U}(x_{i-1/2}, t))\ dt. \tag{4.4}$$

In terms of the cell averages defined in Eq. (4.2) and Eq. (4.7) and the numerical fluxes Eq. (4.4), the integral balance law Eq. (4.1) reads

$$\mathbf{U}_i^{n+1} \simeq \mathbf{U}_i^n - \frac{\Delta t}{\Delta x} \left(\mathbf{F}_{i+1/2} - \mathbf{F}_{i-1/2} \right) + \Delta t\ \mathbf{\Omega}_i^n, \tag{4.5}$$

where, for simplicity, we take that the size of the time step, $\Delta t = t^{n+1} - t^n$, is constant hereafter. Certainly, Δt may change from one time step to the next one, as dictated by the Courant-Friedrich-Levy (CFL) condition, namely,

$$\Delta t = C_{\text{CFL}} \frac{\Delta x}{\max\{\lambda\}}, \tag{4.6}$$

where $\max\{\lambda\}$ is the maximum of the eigenspeeds over the whole spatial computational domain (in RRMHD, $\max \lambda = 1$; Sec. 3.1) and $0 < C_{\text{CFL}} \leq 1$ is the CFL factor. Nevertheless, once the dynamics stabilizes, it is usually stable an quite approximately constant. Note that we have already introduced an approximation in Eq. (4.5), namely, that

$$\int_{t^n}^{t^{n+1}} \int_{x_{i-1/2}}^{x_{i+1/2}} \mathbf{\Omega}(x, t)\ dx\ dt \simeq \Delta x\ \Delta t\ \mathbf{\Omega}_i^n. \tag{4.7}$$

In the Eq. (4.5), it clearly stands out that the average values $\mathbf{U}_i^n$ are modified in each time steep by the flux through the spatial boundaries, $x_{i-1/2}$ and $x_{i+1/2}$, of the numerical cell $\mathcal{C}_i^n$, as well as by the action of the source terms.

A conservative method ensures that the integral value of quantities that are conserved in a physical system (like the total mass, energy or momentum) are also conserved in the computational box. An equation is written in

conservation form when the discrete set of algebraic equations obtained after the discretization of the system of PDEs mimics the integral form of the conservation (or balance) laws. In our case, Eq. (3.29) is a method written in conservation form since it mimics the conservation properties of Eq. (4.1). In order to ensure that the method be *conservative*,it is mandatory computing a *single* numerical flux per interface. In this way, we ensure that the same flux that leaves (enters) any spatial grid zone, say $[x_{i-1/2}, x_{i+1/2}]$, through, e.g. the left zone interface, located at $x_{i-1/2}$, enters (leaves) the numerical zone situated to the left of the former, i.e. zone $[x_{i-3/2}, x_{i-1/2}]$. Moreover, the discretization proces unavoidably entails the piecewise continuous representation of the exact solution, which may exhibit jumps of finite size across the interfaces of adjacent numerical zones. The foremost problem in finite volume methods is computing sufficiently accurate numerical fluxes. As we have written in Chap. 3, these numerical fluxes may be obtained exactly solving all the local Riemann problems introduced at each cell interface by the discretization of the numerical solution. This is the approach applied in Godunov methods (Godunov, 1959). However, in general, solving the Riemann problem exactly is not possible (this is the case in RRMHD, so far) or extremely costly from the computational point of view. Alternatively, we may obtain approximate values for the numerical fluxes based on the cell averages Eq. (4.2). Since we limit Δt according to the CFL condition (Eq. (4.6)), which ensures that information arising from the interfaces located at $x_{i-3/2}$ and $x_{i+1/2}$ does not arrive to the interface at $x_{i-1/2}$ within the time interval Δt, it is reasonable to assume, e.g. that we can obtain $\mathbf{F}^n_{i-1/2}$ only from the cell average values $(\mathbf{U}^n_{i-1}, \mathbf{U}^n_i)$ on either side of the interface located at $x_{i-1/2}$, i.e.

$$\mathbf{F}^n_{i-1/2} = \mathcal{F}\left(\mathbf{U}^n_{i-1}, \mathbf{U}^n_i\right), \tag{4.8}$$

where $\mathcal{F}$ is some *numerical flux function*, whose exact form depends on the approximate Riemann solver employed in the method (see Sec. 4.1.2). Regardless of the particular form of the numerical flux function, the *consistency* of the numerical method with the differential form of the balance law (Eq. (3.28)) demands that if the cell averages left, $\mathbf{U}_l := \mathbf{U}^n_{i-1}$, and right, $\mathbf{U}_r := \mathbf{U}^n_i$ to the interface $x_{i-1/2}$ are equal ($\mathbf{U}_l = \mathbf{U}_r := \mathbf{U}$), then

$$\mathcal{F}(\mathbf{U}, \mathbf{U}) = \mathbf{F}(\mathbf{U}).$$

Rather than attempting to discretize simultaneously in space and time, as seems to suggest Eq. (4.5), in the *Method of Lines* (MoL) or semi-discrete approach, we first discretize a PDE, or a system of PDEs, in space alone, obtaining a single or a system of ordinary differential equations (ODEs) for the evolution of cell averages based on instantaneous values of the fluxes through each side. Thus the MoL transforms a set of PDEs, such as Eq. (3.28), into a

set of ODEs called semi-discrete equations. The advantage of the semi-discrete approach is that achieving higher accuracy in space and time are decoupled processes (Schiesser and Griffiths, 2009). Following the MoL procedure, in Sec. 4.1 we describe techniques used to improve the spatial discretization employing high-order intercell reconstruction algorithms, and in Sec. 4.2, we discuss numerical methods used to perform the time integration.

4.1 Spatial Discretization

Using methods in conservation form is particularly important when solving problems with shocks or other discontinuities in the solution (e.g. Rezzolla and Zanotti, 2013). This is because the determination of the correct speeds of propagation of shocks is based on the conservative properties of the original system of PDEs. The presence of discontinuities in a numerical solution must be treated carefully in order to avoid spurious oscillations.

Our approach to solve the equations of RRMHD makes use of Godunov's idea, where the left and right states of the Riemann problem correspond to a first order integration of the balance laws (4.1), which results in a uniform piece-wise representation of the numerical variables at every given discrete value of the time, $\mathbf{U}_i^n$ (Fig. 4.1). In order to improve the spatial accuracy of a Godunov method, one may resort to a piecewise polynomial representation of the conserved quantities within each numerical cell, providing a better estimate of the left and right state, increasing the spatial order of integration. In other words, we resort to a high-order *reconstruction* of the profiles of the numerical variables inside of each numerical zone.

In the following sections, we list the intercell reconstruction methods (Sec. 4.1.1) and the approximate Riemann solvers (Sec. 4.1.2) that we have implemented in our numerical code.

4.1.1 Intercell Reconstruction Methods

In our numerical code, we have implemented linear as well as *monotonicity preserving* (MP) reconstruction methods. The precise implementation details of both types of reconstruction algorithms follow.

4.1.1.1 Linear Reconstruction Methods

From the cell averages $\mathbf{U}_i^n$ we can construct a piecewise linear function of the form

$$\mathbf{U}_i^n(x) = \mathbf{U}_i^n + \boldsymbol{\sigma}_i^n(x - x_i),$$

where $x_i := (x_{i-1/2} + x_{i+1/2})/2$ denotes the coordinate value at the cell center, while $\boldsymbol{\sigma}_i^n$ are the "slopes" (one per each of the components of the vector $\mathbf{U}_i^n$) of

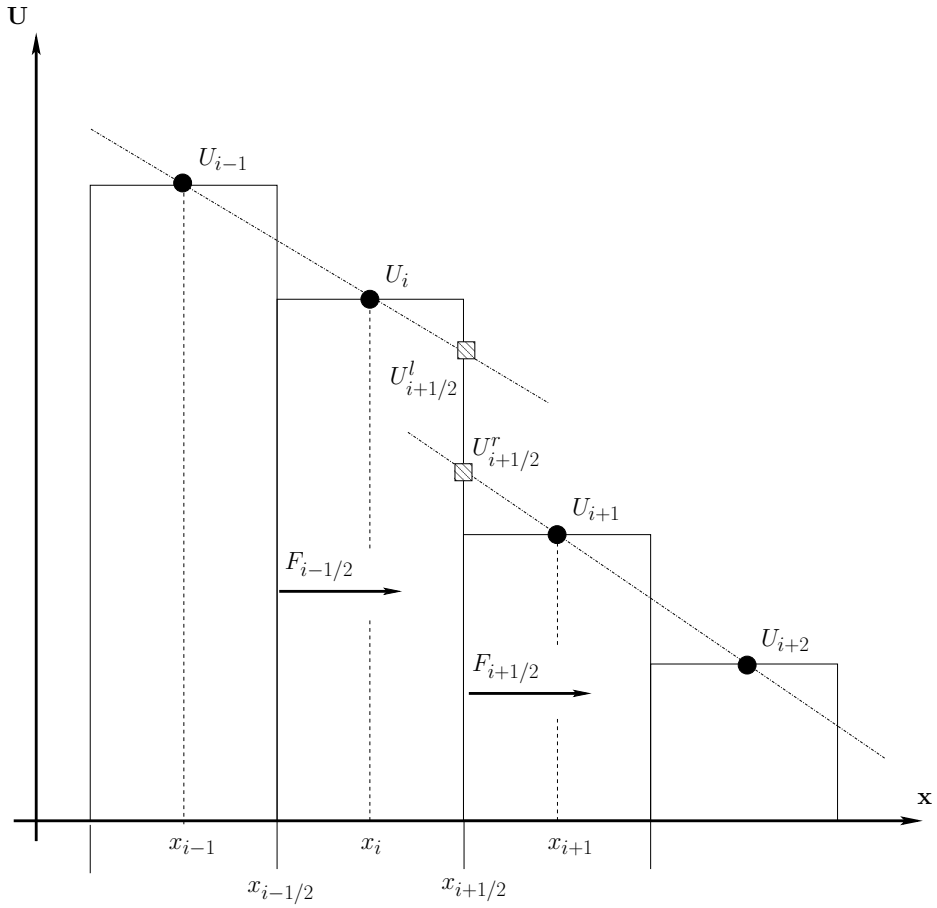

Figure 4.1: Sketch of the discretized numerical solution. We label with $U_{l,i+1/2}$ and $U_{r,i+1/2}$ the locations of the states to the left and to the right of the interface situated at $x_{i+1/2}$. In the figure, these states are built assuming a linear reconstruction method from the values of the variables next to the interface $i + 1/2$.

the linear reconstruction inside the cell (Fig. 4.1). We have implemented three slope limiters that provide a second-order accuracy for smooth solutions and satisfy the *total variation diminishing* (TVD) property, namely:

- *minmod limiter* (MML):

$$\boldsymbol{\sigma}_i^n := \text{minmod}\left(\frac{\mathbf{U}_i^n - \mathbf{U}_{i-1}^n}{\Delta x}, \frac{\mathbf{U}_{i+1}^n - \mathbf{U}_i^n}{\Delta x}\right),$$

where the minmod function of two arguments is defined by (e.g. Kolgan,

1972),

$$\text{minmod}(a,b) := \begin{cases} a & \text{if } |a| < |b| \quad \text{and } ab > 0, \\ b & \text{if } |b| < |a| \quad \text{and } ab > 0, \\ 0 & ab \leq 0. \end{cases}$$

In other words if a and b have the same sign, then the minmod function selects the one with smaller modulus, otherwise it returns zero.

- *monotonised central-difference limiter* (MCL): Sharper resolution of discontinuities can be achieved with other limiters that do not reduce the slope as severely as minmod (MML) near a discontinuity. One popular choice is precisely the monotonised central-difference limiter (van Leer, 1977), in which the slope is limited according to the following criterion

$$\boldsymbol{\sigma}_i^n := \text{minmod}\left(\frac{\mathbf{U}_{i+1}^n - \mathbf{U}_{i-1}^n}{2\Delta x}, 2\frac{\mathbf{U}_i^n - \mathbf{U}_{i-1}^n}{\Delta x}, 2\frac{\mathbf{U}_{i+1}^n - \mathbf{U}_i^n}{\Delta x}\right),$$

where the minmod function of three arguments is defined

$$\text{minmod}(a,b,c) := \begin{cases} \min(a,b,c) & \text{if } a,b,c > 0, \\ \max(a,b,c) & \text{if } a,b,c < 0, \\ 0 & \text{otherwise.} \end{cases}$$

- *superbee limiter* (SBL): Roe (1985) proposed a piecewise linear reconstruction which is less diffusive than minmod (but, by the same token, also more oscillatory) based on the following formula

$$\boldsymbol{\sigma}_i^n := \text{maxmod}\left(\boldsymbol{\sigma}_i^I, \boldsymbol{\sigma}_i^{II}\right),$$

where,

$$\boldsymbol{\sigma}_i^I := \text{minmod}\left(2\frac{\mathbf{U}_i^n - \mathbf{U}_{i-1}^n}{\Delta x}, \frac{\mathbf{U}_{i+1}^n - \mathbf{U}_i^n}{\Delta x}\right),$$
$$\boldsymbol{\sigma}_i^{II} := \text{minmod}\left(\frac{\mathbf{U}_i^n - \mathbf{U}_{i-1}^n}{\Delta x}, 2\frac{\mathbf{U}_{i+1}^n - \mathbf{U}_i^n}{\Delta x}\right),$$

and

$$\text{maxmod}(a,b) := \begin{cases} a & \text{if } |a| > |b| \quad \text{and } ab > 0, \\ b & \text{if } |b| > |a| \quad \text{and } ab > 0, \\ 0 & ab \leq 0. \end{cases}$$

We point out that the maxmod function, in contrast to minmod, selects the largest value in modulus if a and b have the same sign, otherwise it returns zero.

4.1.1.2 Accurate Monotonicity-Preserving Schemes

Suresh and Huynh (1997) presented a new class of high-order MP schemes for the numerical solution of conservation laws, where the interface values are obtained by limiting a polynomial intercell reconstruction of order higher than one. One of the drawbacks of using linear reconstruction schemes is that they tend to clip the extrema of the numerical solution. MP algorithms are designed to preserve accuracy near extrema and to work well with Runge-Kutta (RK) time stepping.

The MP reconstruction is carried out in two steps. In the first step, an accurate and stable interpolant formula is used to compute the interface value. This is called the *original* (or unlimited) value. In the second step, the original value is modified or limited to obtain a final interface value. In the CUEVA code we have implemented the fifth- (MP5), seventh- (MP7) and ninth- (MP9) order accurate schemes for uniform Cartesian discretizations of the spatial domain. Under these conditions, the original interface values on the left of the cell interface $i + 1/2$ (i.e. on the right boundary of the numerical zone i) are respectively given by:

- MP5

$$\mathbf{U}^l_{i+1/2} = \left(2\mathbf{U}_{i-2} - 13\mathbf{U}_{i-1} + 47\mathbf{U}_i + 27\mathbf{U}_{i+1} - 3\mathbf{U}_{i+2}\right)/60, \tag{4.9}$$

- MP7

$$\begin{aligned}\mathbf{U}^l_{i+1/2} = &\left(-3\mathbf{U}_{i-3} + 25\mathbf{U}_{i-2} - 101\mathbf{U}_{i-1}\right.\\ &\left.+319\mathbf{U}_i + 214\mathbf{U}_{i+1} - 38\mathbf{U}_{i+2} + 4\mathbf{U}_{i+3}\right)/420,\end{aligned} \tag{4.10}$$

- MP9

$$\begin{aligned}\mathbf{U}^l_{i+1/2} = &\left(4\mathbf{U}_{i-4} - 41\mathbf{U}_{i-3} + 199\mathbf{U}_{i-2} - 641\mathbf{U}_{i-1}\right.\\ &+ 1879\mathbf{U}_i + 1375\mathbf{U}_{i+1} - 305\mathbf{U}_{i+2} + 55\mathbf{U}_{i+3}\\ &\left.-5\mathbf{U}_{i+4}\right)/2520.\end{aligned} \tag{4.11}$$

The right interface values at $x_{i-1/2}$ are mirror expressions of the above equations. It is essential to clarify that $\mathbf{U}^n_i$ represents a cell average quantity as described in Eq. (4.2) and $\mathbf{U}^l_{i+1/2}$ represents an approximation to the pointwise value $\mathbf{U}(x_{i+1/2}, t^n)$.

The original interface value defined by any of the Eqs. (4.9), (4.10) and (4.11) creates oscillations near a discontinuity. To suppress these oscillations, Suresh and Huynh (1997) suggest that the interface value has to lie inside a certain interval; that is, it must satisfy a certain constraint. The final interface value is obtained by enforcing this constraint on the original interface value. (see the details in Suresh and Huynh, 1997)

4.1.2 Approximate Riemann Solvers

There exists a number of approximate Riemann solvers that can be efficiently implemented in a Godunov scheme. These approximate Riemann solvers just require the knowledge of the characteristic speeds and not the full characteristic decomposition. This is why these solvers are often simply referred to as flux formulae. In this section, we present different approximate Riemann solvers implemented in the Cueva code that provide the numerical flux functions described in Eq. (4.8), which generically follow from the solution of Riemann problems with initial data

$$\mathbf{U}(x,0) = \begin{cases} \mathbf{U}_{l,i+1/2} & \text{if } x < x_{i+1/2}, \\ \mathbf{U}_{r,i+1/2} & \text{if } x > x_{i+1/2}, \end{cases} \tag{4.12}$$

where $\mathbf{U}_{l,i+1/2}$ and $\mathbf{U}_{r,i+1/2}$ are the left and right edge values at the zone interface $i+1/2$.

4.1.2.1 Local Lax-Friedrichs flux formula

The simplest choice for an approximate Riemann solver is the local Lax-Friedrichs (LLF) flux formula. It was used for first time in the field of RRMHD by Palenzuela et al. (2009) who improved it building upon the prescription of Alic et al. (2007) to increase the order of accuracy of the computation of the numerical fluxes.

The original LLF flux function reads

$$\mathbf{F}\left(\mathbf{U}_{l,i+1/2}, \mathbf{U}_{r,i+1/2}\right) = \frac{1}{2}\left[\mathbf{F}_{l,i+1/2} + \mathbf{F}_{r,i+1/2} + c_{i+1/2}\left(\mathbf{U}_{l,i+1/2} - \mathbf{U}_{r,i+1/2}\right)\right],$$

i.e. they are the fluxes of the original balance law computed at the states $\mathbf{U}_{l,i+1/2}$ and $\mathbf{U}_{r,i+1/2}$, respectively. Finally, the coefficient $c_{i+1/2}$ depends on the values of the characteristic speeds at the interface. A suitable choice is:

$$c_{i+1/2} = \max\left(\lambda_{l,i+1/2}, \lambda_{r,i+1/2}\right), \tag{4.13}$$

where the values $\lambda_{l,i+1/2}$ and $\lambda_{r,i+1/2}$ correspond to the absolute values of the maximum signal speeds attainable on the states (left and right) flanking any of the interfaces of the computational domain. In the case of RRMHD, in Cartesian coordinates, $\lambda_{r,i+1/2} = \lambda_{l,i+1/2} = 1$, since the speed of light is the largest possible signal speed. Thus, in practical applications $c_{i+1/2} = 1$.

Instead of obtaining a set of high-order reconstructed values of the states to the left and to the right of every interface, namely of $\mathbf{U}_{l,i+1/2}$ and of $\mathbf{U}_{r,i+1/2}$ and then computing the fluxes $\mathbf{F}_{l,i+1/2}$ and $\mathbf{F}_{r,i+1/2}$, Alic et al. (2007) proposed a different possibility. They first construct ancillary variables:

$$\mathbf{F}_i^{\pm} = \mathbf{F}_i \pm \mathbf{U}_i.$$

Then, using a piecewise linear reconstruction, these ancillary variables are used to obtain first order estimates of their respective values on the left/right side of the interface as,

$$\mathbf{F}^{+}_{l,i} = \mathbf{F}^{+}_{i} + \frac{1}{2}\boldsymbol{\sigma}^{+}_{i} \qquad \mathbf{F}^{-}_{r,i} = \mathbf{F}^{-}_{i+1} - \frac{1}{2}\boldsymbol{\sigma}^{-}_{i+1}, \tag{4.14}$$

where $\boldsymbol{\sigma}^{\pm}_{i}$ are monotonous slopes that can be constructed using any of the linear slope limiters mentioned in Sec. 4.1.1.

Finally, the consistent LLF flux is computed by a simple average (Palenzuela et al., 2009):

$$\mathbf{F}^{\text{llf}}_{i+1/2} = \frac{1}{2}\left(\mathbf{F}^{+}_{l,i} + \mathbf{F}^{-}_{r,i}\right).$$

4.1.2.2 The HLL Approximate Riemann Solver

For the purpose of computing a Godunov flux, Harten et al. (1983) presented a novel approach to solving the Riemann problem approximately. The central idea is to assume that the solution consists of a wave pattern encompassing two waves separating three constant states, as illustrated in Fig. 4.2. The $\mathbf{U}^{\text{hll}}$

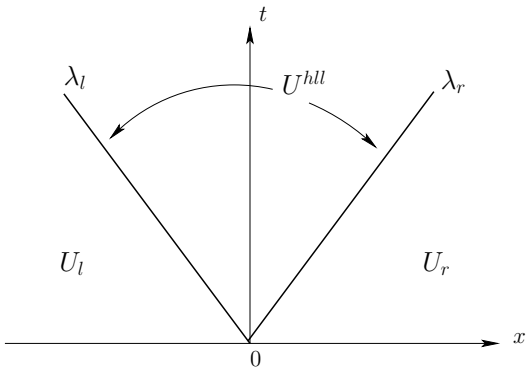

Figure 4.2: Space-time representation of the HLL approximate Riemann solver. The solution in the *star region* consists of a single state $\mathbf{U}^{\text{hll}}$ separated from the initial data by two waves with speeds λ_l and λ_r.

constant intermediate state (see, Fig. 4.2) corresponds to the (HLL) integral average of the solution of the Riemann problem over the wave fan (cf. Toro 1997, § 10.4), and is given by

$$\mathbf{U}^{\text{hll}} = \frac{\lambda_r \mathbf{U}_r - \lambda_l \mathbf{U}_l + \mathbf{F}_l - \mathbf{F}_r}{\lambda_r - \lambda_l}, \tag{4.15}$$

where in the previous expression we have dropped the indices denoting the interface location for simplicity (they are referred to interface $i + 1/2$ unless

stated otherwise). λ_l and λ_r have the same meaning as in the case of the LLF flux formula (4.13), namely, the absolute values of the minimum and maximum signal speeds in the $\mathbf{U}_l$ and $\mathbf{U}_r$ states, respectively. Then, the approximate numerical solution of the initial value problem in each cell interface (generically, in the $x/t = 0$ axis) is computed as

$$\mathbf{U}(0,t) = \begin{cases} \mathbf{U}_l & \text{if } 0 \leq \lambda_l, \\ \mathbf{U}^{\text{hll}} & \text{if } \lambda_l \leq 0 \leq \lambda_r, \\ \mathbf{U}_r & \text{if } 0 \geq \lambda_r. \end{cases}$$

Using the RH conditions, Eq. (3.31) (without the contribution of the source terms), across the left and right waves, we obtain two alternative expressions for the flux integral average of the solution over the Riemann wave structure, $\mathbf{F}^{\text{hll}}$,

$$\mathbf{F}^{\text{hll}} = \mathbf{F}_l + \lambda_l \left(\mathbf{U}^{\text{hll}} - \mathbf{U}_l \right),$$
$$\mathbf{F}^{\text{hll}} = \mathbf{F}_r + \lambda_r \left(\mathbf{U}^{\text{hll}} - \mathbf{U}_r \right).$$

Now, employing Eq. (4.15) and combining the last two RH conditions, one obtains

$$\mathbf{F}^{\text{hll}} = \frac{\lambda_r \mathbf{F}_l - \lambda_l \mathbf{F}_r + \lambda_r \lambda_l (\mathbf{U}_r - \mathbf{U}_l)}{\lambda_r - \lambda_l}. \tag{4.16}$$

The corresponding HLL intercell flux for the approximate Godunov method is selected according to

$$\mathbf{F}^{\text{hll}}_{i+1/2} = \begin{cases} \mathbf{F}_l & \text{if } 0 \leq \lambda_l, \\ \mathbf{F}^{\text{hll}} & \text{if } \lambda_l \leq 0 \leq \lambda_r, \\ \mathbf{F}_r & \text{if } 0 \geq \lambda_r. \end{cases} \tag{4.17}$$

When the values of the maximum and minimum speeds are taken $\lambda_l = -1$ and $\lambda_r = +1$, the RRMHD fluxes are always computed as if the flow was *subsonic* in the equivalent HLL solver for RHD,[3] i.e. the above equation reduces to

$$\mathbf{F}^{\text{hll}}_{i+1/2} = \mathbf{F}^{\text{hll}} = \frac{1}{2}[\mathbf{F}_l + \mathbf{F}_r + (\mathbf{U}_l - \mathbf{U}_r)].$$

[3] In RHD, when the flow is *supersonic*, the HLL solver selects either $\mathbf{F}_l$ or $\mathbf{F}_r$ depending on which is the *upwind* side of the interface. Otherwise, i.e. under subsonic conditions, the central branch of the Eq. (4.17) is selected.

4.1.2.3 The HLLC Approximate Riemann Solver

Resolving the whole Riemann structure arising from every interface assuming that there is *a single* intermediate state as done in the HLL approximate Riemann solver could produce in larger systems, such as the RRMHD system of equations, an inaccurate resolution of physical features such as contact surfaces, shear waves and material interfaces. To remedy the problem of intermediate waves in the HLL approach Toro et al. (1994) proposed the HLLC (C standing for Contact) Riemann solver, as applied to the time-dependent Euler equations. HLLC is a three-wave model, where the missing contact wave is restored, resulting two-star states for the intermediate region of the Riemann fan, as illustrated in Fig. 4.3. Building up a new HLLC approximate Riemann

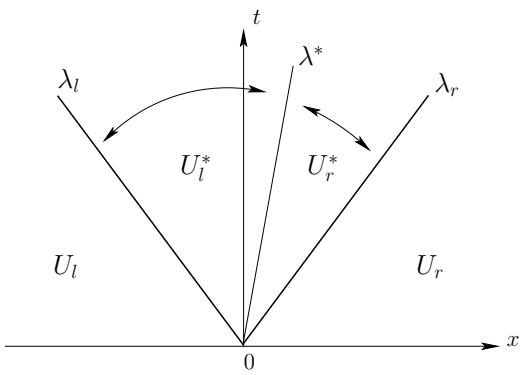

Figure 4.3: Space-time representation of the HLLC approximate Riemann solver. The solution in the *star region* consists of two constant states flanked by two shocks separated by a contact middle wave of speed λ^*.

solver has been one of the main deliverables of this thesis. Thus, we defer to Chap. 5 (see also Miranda-Aranguren et al., 2018) the exhaustive presentation and numerical validation of the new approximate Riemann solver for the augmented system of RRMHD. The new solver captures exactly isolated stationary contact discontinuities, improving on the single state HLL solver. The new HLLC solver we have built does not need to distinguish between the cases in which the magnetic field perpendicular to a discontinuity is zero or not. Thus, it does not suffer from any pathological singularity when the component of the magnetic field normal to a zone interface approaches zero. Discriminating the latter case from the general one has been necessary in HLLC approximate Riemann solvers built for ideal RMHD (Mignone and Bodo, 2005).

4.2 Time Integration

As we have mentioned before, in the MoL the spatial discretization and the time integration are regarded as separated algorithmic pieces. If the source terms in a system of balance laws were regular, bounded and non-stiff, it would be possible to resort to a standard TVD Runge-Kutta (RK) ODE solving scheme to perform the time integration of the MoL. However, the augmented system of RRMHD equations, contains potentially stiff sources and, therefore, a suitable ODE scheme needs to be used. From a mathematical point of view, both the RRMHD and the augmented sytem of RRMHD equations are hyperbolic conservation laws with stiff relaxation terms in the sense of Chen et al. (1994). In order to describe the different time integrators that we have implemented, we notice that the augmented system of RRMHD equations (2.37) has the form (3.1). Since in the RRMHD system there might be source terms which are non-stiff, we split the sources in two parts, one including the potentially stiff source terms, $\mathbf{\Omega}_{\rm s}$, and another one where there are not stiff terms, $\mathbf{\Omega}_{\rm ns}$, so that

$$\partial_t \mathbf{U} + \partial_m \mathbf{F}^m(\mathbf{U}) = \frac{1}{\eta}\mathbf{\Omega}_{\rm s}(\mathbf{U}) + \mathbf{\Omega}_{\rm ns}(\mathbf{U}), \tag{4.18}$$

where we explicitly write down the resistivity, η, which acts as a *relaxation parameter*, in the sense defined by, e.g. Liu (1987), in the limit of infinite conductivity ($\sigma := 1/\eta \to \infty$; ideal limit). In that regime the system is said to be stiff, since the time scale of variation of the relaxation term $\mathbf{\Omega}_{\rm s}\left(\mathbf{U}\right)/\eta$ is in general, much shorter than the time scale of variation of the hyperbolic part of the system, including both the fluxes $\mathbf{F}(\mathbf{U})$ and the non-stiff terms $\mathbf{\Omega}_{\rm ns}$. Usually, the solution of hyperbolic systems with relaxation is well approximated by the solution of a suitable reduced set of conservation laws called the *equilibrium system*, when the source term becomes stiff ($\eta \to 0$). Ideal RMHD is precisely the *equilibrium system* for RRMHD equations for the case of vanishing resistivity, $\eta \to 0$ (or $\sigma \to \infty$).

The problem of developing efficient numerical schemes for hyperbolic system with stiff relaxation terms, has been broadly treated in the literature (e.g. Pareschi and Russo, 2005). In the next sections, we will discuss a couple of possibilities for the time integrators employed for stiff relaxation hyperbolic systems. A very popular choice are the so-called implicit-explicit RK schemes (RKIMEX; Sec.4.2.1). As an alternative, we will show the Minimally Implicit RK (MIRK; Sec.4.2.2) methods.

4.2.1 Implicit-Explicit Runge-Kutta Schemes

RKIMEX schemes, as described by Higueras et al. (2012), were constructed with the aim of optimizing the *region of absolute monotonicity*. This region

characterizes the step-size which is admissible in order to ensure that the total variation of the spatial profile does not increase artificially in the course of time integration. In the case of total-variation vector-norm, this property is usually referred to as TVD, or more generally as *strong stability preserving* (SSP). The TVD or SSP property is essential for a numerical time integrator to be successful in simulations of the problems in our focus, since it allows suppressing spurious oscillations in the spatial discretization (Kupka et al., 2012). Pareschi and Russo (2005) introduce this property by means of the following definition:

Definition 1. *A sequence* $\{\mathbf{U}^n\}$ *is said to be strongly stable in a given norm* $\|\cdot\|$ *if* $\|\mathbf{U}^{n+1}\| \leq \|\mathbf{U}^n\|$ *for all* $n \geq 0$.

The most common norm used in the previous definition is the TV-norm. Moreover, a numerical scheme that maintains *strong stability* at discrete level is called an SSP scheme.

In account of the different stiffness properties of the terms involved in the discretization (4.18), let us consider the following ν-stages RK integration method:

$$\begin{aligned}\mathbf{U}^{(l)} = \mathbf{U}^n &- \Delta t \sum_{j=1}^{l} \tilde{a}_{lj} \left(\partial_m \mathbf{F}^m(\mathbf{U}^{(j)}) - \mathbf{\Omega}_{\mathrm{ns}}(\mathbf{U}^{(j)}) \right) \\ &+ \Delta t \sum_{j=1}^{\nu} a_{lj} \frac{1}{\eta} \mathbf{\Omega}_{\mathrm{s}}(\mathbf{U}^{(j)}), \qquad l = 1, \ldots, \nu \end{aligned} \tag{4.19}$$

$$\begin{aligned}\mathbf{U}^{n+1} = \mathbf{U}^n &- \Delta t \sum_{j=1}^{\nu} \tilde{w}_j \left(\partial_m \mathbf{F}^m(\mathbf{U}^{(j)}) - \mathbf{\Omega}_{\mathrm{ns}}(\mathbf{U}^{(j)}) \right) \\ &+ \Delta t \sum_{j=1}^{\nu} w_j \frac{1}{\eta} \mathbf{\Omega}_{\mathrm{s}} \left(\mathbf{U}^{(j)} \right). \end{aligned} \tag{4.20}$$

The RK method is characterized by the $\nu \times \nu$-matrices $\tilde{A} = (\tilde{a}_{lj})$ and $A = (a_{lj})$ as well as by the coefficient vectors $\tilde{w} = (\tilde{w}_1, \ldots, \tilde{w}_\nu)^T$ and $w = (w_1, \ldots, w_\nu)^T$, which act on the non-stiff and stiff terms of the discretization (4.18), respectively. We say that the RK integration algorithm is an *implicit-explicit* (IMEX) method if the coefficient matrix that controls the non-stiff part satisfies that $a_{lj} = 0$ for $j \geq l$.

The SSP or TVD preserving properties of IMEX methods have been studied by Pareschi and Russo (2005) in the context of hyperbolic systems with relaxation, i.e. the case of RRMHD or the augmented RRMHD system of equations when $\eta \ll 1$. Indeed, Pareschi and Russo (2005) introduce a standard terminology to specify an IMEX method (but see also Higueras et al. (2012) and

App. A for small variants of the standard naming convention). They named an IMEX method as "SSP$k(s, \sigma, p)$" if it encompasses the following properties: k is the order of the method in the stiff limit ($\eta \to 0$), that is characterized by the coefficients for the explicit part. The latter must necessarily be SSP and is commonly referred to as the *asymptotically* SSP scheme. s and σ are the number of stages in the implicit and in the explicit schemes, respectively. p is the global order of the resulting combined method.

The RKIMEX schemes are commonly represented by a double tableau in the usual Butcher notation (e.g. Butcher, 1996),

$$\begin{array}{c|c} \tilde{c} & \tilde{A} \\ \hline & \tilde{w}^T \end{array} \qquad \begin{array}{c|c} c & A \\ \hline & w^T \end{array}$$

where the coefficients $\tilde{c}$ and c used for the treatment of the non-autonomous parts of the systems, must satisfy the consistency conditions:

$$\tilde{c}_i = \sum_{j=1}^{i-1} \tilde{a}_{ij}, \qquad c_i = \sum_{j=1}^{i} a_{ij}.$$

Butcher's tableau for different IMEX schemes implemented in our numerical code are showed in Appendix A.

Note that at each substep an implicit equation for auxiliary intermediate values $\mathbf{U}^{(i)}$ must be solved. The complexity of inverting this equation will clearly depend on the particular form of the operator $\mathbf{\Omega}_{\mathrm{s}}(\mathbf{U})$ and for our particular case, as we will show in the next section, on the inversion of this operator. We notice that if the operator A, acting on the stiff terms of the system, is such that $a_{lj} = 0$ for $j > l$, in which case the method is called diagonally implicit RK (DIRK), then the different stages of the RK scheme can be solved successively (from $j = 1$ to ν) and the explicit part is evaluated only once in each stage (Alexander, 1977; Butcher, 1996). In DIRK methods, one may even avoid the computational cost of the expensive iterative procedures required to apply general fully-implicit methods (Kupka et al., 2012; Pareschi and Russo, 2005).

As can be inferred from its name, in an RKIMEX method the time update of an ODE is split into two parts, one explicit and another one implicit. The non-stiff part of the system is integrated explicitly with a SSP scheme, while the stiff part is treated implicitly with an L-stable (i.e. it satisfies $w^T A^{-1} e = 1$, being e a vector whose components are all equal to 1) DIRK method. These conditions guarantee the *asymptotic preserving property* (i.e. the consistency of the scheme with the equilibrium system) and the *asymptotic accuracy* (i.e. the order of accuracy is maintained in the stiff limit).

4.2.1.1 RKIMEX schemes for RRMHD

Following Palenzuela et al. (2009), the evolution equations for RRMHD (2.37) can be written, taking into account that their global structure is given by (4.18), as:

$$\partial_t \mathbf{Y} = -\partial_m \mathbf{F}_Y^m (\mathbf{X}, \mathbf{Y}) + \mathbf{\Omega}_{\mathrm{ns},\mathbf{Y}} (\mathbf{Y}) , \tag{4.21}$$

$$\partial_t \mathbf{X} = -\partial_m \mathbf{F}_X^m (\mathbf{X}, \mathbf{Y}) + \frac{1}{\eta (\mathbf{Y})} \mathbf{\Omega}_{\mathrm{s},\mathbf{X}} (\mathbf{X}, \mathbf{Y}) + \mathbf{\Omega}_{\mathrm{ns},\mathbf{X}} (\mathbf{X}, \mathbf{Y}), \tag{4.22}$$

where the vector of conserved variables $\mathbf{U}$ is split in two subsets $\{\mathbf{X}, \mathbf{Y}\}$, with $\mathbf{X} = \{\mathbf{E}\}$ containing the unknowns governed by equations with potentially stiff terms and $\mathbf{Y} = \{\mathbf{B}, \phi, \psi, q, \tau, \mathbf{S}, D\}$ the conserved variables whose governing equations do not include stiff sources. As pointed out before, the resistivity (η) plays the role of relaxation parameter and, in order to allow for more general cases, it is allowed to depend on the subset of conserved variables $\mathbf{Y}$, i.e. $\eta (\mathbf{Y})$.

For our particular set of equations, it is convenient to write the stiff part as

$$\mathbf{\Omega}_{\mathrm{s},\mathbf{X}} (\mathbf{X}, \mathbf{Y}) = A(\mathbf{W}) \mathbf{X} + \mathbf{S}_{\mathbf{X}} (\mathbf{Y}, \mathbf{W}), \tag{4.23}$$

where the explicit expression of the matrix $A(\mathbf{W})$ is provided below (Eq. 4.32). $\mathbf{S}_{\mathbf{X}} (\mathbf{Y}, \mathbf{W})$ is the part of the stiff source term of the subset of equations governing the evolution of the $\mathbf{X}$ fields that depends on the variables $\mathbf{Y}$ *and on the primitive variables* ($\mathbf{W}$). The previous remark is relevant since primitive variables in the adequate substep of the numerical method are not necessarily available and, indeed, this fact is one of the motivations to devise MIRK methods (see Sec. 4.2.2).

The procedure to calculate the conserved variables, $\mathbf{U}^{(l)}$, in each stage of the IMEX scheme can be performed in two steps.

- First, we compute the explicit intermediate values $\mathbf{X}^*, \mathbf{Y}^*$ from all the previously known levels,

$$\mathbf{Y}^* = \mathbf{Y}^n - \Delta t \sum_{j=1}^{l-1} \tilde{a}_{lj} \left(\partial_x \mathbf{F}_Y (\mathbf{U}^{(j)}) + \mathbf{\Omega}_{\mathrm{ns},\mathbf{Y}} (\mathbf{U}^{(j)}) \right) , \tag{4.24}$$

$$\mathbf{X}^* = \mathbf{X}^n - \Delta t \sum_{j=1}^{l-1} \tilde{a}_{lj} \partial_x \mathbf{F}_X (\mathbf{U}^{(j)}) + \Delta t \sum_{j=1}^{l-1} \tilde{a}_{lj} \tilde{\mathbf{\Omega}}_X (\mathbf{U}^{(j)}) + \Delta t \sum_{j=1}^{l-1} \frac{a_{lj}}{\eta^j} \mathbf{\Omega}_X (\mathbf{U}^{(j)}). \tag{4.25}$$

- Second, we compute the implicit part, which involves only $\mathbf{X}$, by solving

$$\begin{aligned} \mathbf{Y}^{(l)} &= \mathbf{Y}^*, \\ \mathbf{X}^{(l)} &= \mathbf{X}^* + \Delta t \frac{a_{ll}}{\epsilon^{(l)}} \mathbf{\Omega}_{\mathrm{s},\mathbf{X}}(\mathbf{U}^{(l)}). \end{aligned} \tag{4.26}$$

  Plugging the form of $\mathbf{\Omega}_{\mathrm{s},\mathbf{X}}$ provided in Eq. (4.23), the latter implicit equation for $\mathbf{X}^{(l)}$ can be inverted explicitly,

$$\mathbf{X}^{(l)} = M(\mathbf{W}^*) \left(\mathbf{X}^* + a_{ll} \frac{\Delta t}{\eta^{(l)}} \mathbf{S}_{\mathbf{X}}(\mathbf{Y}^*, \mathbf{W}^*) \right), \tag{4.27}$$

  with,

$$M(\mathbf{W}^*) = \left[I - a_{ll} \frac{\Delta t}{\eta^{(l)}} A(\mathbf{W}^*) \right]^{-1}. \tag{4.28}$$

For the RRMHD system, the explicit expressions for the terms on the left hand side of Eq. (4.23) are

$$\mathbf{\Omega}_{\mathrm{s},\mathbf{E}} = -W\mathbf{E} + W\left(\mathbf{E}\cdot\mathbf{v}\right)\mathbf{v} - W\mathbf{v}\times\mathbf{B}, \tag{4.29}$$

$$\mathbf{S}_{\mathbf{E}} = -W\mathbf{v}\times\mathbf{B} \tag{4.30}$$

and the expression for the non-stiff part of the source term is

$$\mathbf{\Omega}_{\mathrm{ns},\mathbf{E}} = -q\mathbf{v}. \tag{4.31}$$

The matrix $A(\mathbf{W})$ is defined as

$$A(\mathbf{W}) = W \begin{pmatrix} -1+v_x^2 & v_x v_y & v_x v_z \\ v_x v_y & -1+v_y^2 & v_y v_z \\ v_x v_z & v_y v_z & -1+v_z^2 \end{pmatrix}. \tag{4.32}$$

Because of the particular from of the stiff source term (4.29) the matrix $M(\mathbf{W})$ can be computed explicitly from Eq. (4.28)

$$M(\mathbf{W}) = \frac{1}{m} \begin{pmatrix} a+W+aW^2v_x^2 & aW^2v_xv_y & aW^2v_xv_z \\ aW^2v_xv_y & a+W+aW^2v_y^2 & aW^2v_yv_z \\ aW^2v_xv_z & aW^2v_yv_z & a+W+aW^2v_z^2 \end{pmatrix},$$

where $m \equiv W^2a + Wa^2 + W + a$ and $a \equiv a_{ll}\sigma^{(l)}\Delta t$.

Reviewing the procedure to obtain the evolution of the stiff part, first, it is necessary to find the intermediate state $\mathbf{E}^*$ evolving the non-stiff part of the electric field (i.e. using Eq. (4.25) for $\mathbf{E}$ and Eq. (4.24) for the rest of the conserved variables). Then, if the velocity $\mathbf{v}^*$ is known, the value of electric

field in the implicit step (4.27) is actually determined *explicitly* using the matrix M in order to obtain,

$$\mathbf{E}^{(l)} = M\left(\mathbf{v}^{(l)}\right)\left[\mathbf{E}^{*} + a_{ll}\Delta t\sigma^{(l)}\mathbf{S}_{\mathbf{E}}\left(\mathbf{B}^{(l)}, \mathbf{v}^{(l)}\right)\right]. \tag{4.33}$$

As Palenzuela et al. (2009) pointed out, there are two limits in which there exists consistency of the implicit solution of the stiff part. In the ideal limit ($\sigma \to \infty$), the first term of equation (4.33) vanishes, while the contribution of the second term reduces the electric field to be purely inductive as in the ideal MHD limit (i.e. $\mathbf{E} = -\mathbf{v} \times \mathbf{B}$). In the resistive limit (i.e. $\sigma \to 0$), the second term in equation (4.33) vanishes and the matrix reduces to the identity $M(v) = I$. In the latter case, $\mathbf{E} = \mathbf{E}^{*}$ and, therefore, the evolution of the electric field is explicit. It is necessary to highlight that in Eq. (4.33) both $\mathbf{B}^{(l)}$ and $\mathbf{v}^{(l)}$ must be known at the end of the implicit substep (4.27). However, while $\mathbf{B}^{(l)}$ is explicitly provided in the update of the non-stiff set of conserved variables (4.26), the primitive variables (including the velocity field) can be only known after a suitable *recovery* procedure (see Sec. 4.3) following the explicit step that brings the conserved variables from the time level n to the starred state $\mathbf{U}^{*} = (\mathbf{X}^{*}, \mathbf{Y}^{*})$ (Eqs. (4.24) and (4.25)). Thus, in order to fully update the electric field using Eq. (4.33) we need to proceed iteratively, using the latest available value of the velocity, $\tilde{\mathbf{v}}^{(l)}$, to obtain a new update of the electric field $\tilde{\mathbf{E}}^{(l)}$, so that

$$\tilde{\mathbf{E}}^{(l)} = M\left(\tilde{\mathbf{v}}^{(l)}\right)\left[\mathbf{E}^{*} + a_{ll}\Delta t\sigma^{(l)}\mathbf{S}_{\mathbf{E}}\left(\mathbf{B}^{(l)}, \tilde{\mathbf{v}}^{(l)}\right)\right].$$

This fix point iteration is performed without a real mathematical guarantee of convergence. However, in practical applications, numerical experience shows that it converges, though in some cases (e.g. across shocks or discontinuities in the fluid) very slowly and requiring $\sim 10 - 30$ iterations to obtain the electric field components with absolute errors smaller than 10^{-3}. In practice, one may limit the number of iterations to just a few, since the relevant electric field is the one obtained in the final explicit update of the variables.

Because of the coupling between the electric field and the velocity field described in the previous paragraph, the procedure to compute the primitive variables from the conserved ones is more complex in RRMHD than in ideal RMHD. In Sec. 4.3 we describe at length how we have implemented this iterative procedure in the Cueva code.

4.2.2 Minimally Implicit Runge-Kutta Methods

Differently from Palenzuela et al. (2009), we have stressed the fact that matrices A and M depend explicitly on primitive variables (actually, only on the

velocity) and only implicitly on the conserved variables. The dependence on the velocity field in Eq. (4.33) adds an extra iteration loop to recover the primitive variables in RRMHD when using RKIMEX methods for the time update. MIRK methods have been designed to avoid the double iterative procedure to recover primitive variables from the conserved ones. Though the electric field is updated implicitly, the implicit method can be recast in a way that one finds an explicit expression for it.

MIRK schemes were developed by Aloy and Cordero-Carrión (2016) for the system of RRMHD equations (2.37). To build a MIRK scheme, the RRMHD system is split into two subsets of equations, like in the methodology proposed by Palenzuela et al. (2009) for RKIMEX schemes (Eq. (4.22)). In order to simplify the notation, we introduce the following ancillary variables that include the fluxes and the non-stiff source terms of the corresponding equations:

$$\begin{aligned} \mathbf{S}_{\mathbf{Y}} &= -\partial_m \mathbf{F}^m_Y(\mathbf{X},\mathbf{Y}) + \mathbf{\Omega}_{\mathrm{ns},\mathbf{Y}}(\mathbf{Y}), \\ \tilde{\mathbf{S}}_{\mathbf{E}} &= -\partial_m \mathbf{F}^m_{\mathbf{E}}(\mathbf{E},\mathbf{Y}) + \mathbf{\Omega}_{\mathrm{ns},\mathbf{E}}, \end{aligned} \tag{4.34}$$

where $\mathbf{\Omega}_{\mathrm{ns},\mathbf{E}}$ is given by equation (4.31). In terms of these ancillary variables, the two subsets of equations (4.22) read

$$\begin{aligned} \partial_t \mathbf{Y} &= \mathbf{S}_{\mathbf{Y}} \\ \partial_t \mathbf{E} &= \tilde{\mathbf{S}}_{\mathbf{E}} - \sigma \mathbf{\Omega}_{\mathrm{s},\mathbf{E}}. \end{aligned}$$

To illustrate clearly the different steps of the method, Aloy and Cordero-Carrión (2016) define,

$$\begin{aligned} \bar{\sigma} &= \sigma W, \\ \mathbf{S}_{\mathbf{E}} &= \tilde{\mathbf{S}}_{\mathbf{E}} - \sigma W\left(\mathbf{v}\times\mathbf{B} - (\mathbf{E}\cdot\mathbf{v})\,\mathbf{v}\right). \end{aligned} \tag{4.36}$$

MIRK methods avoid numerical instabilities due to the presence of stiff terms without increasing the computational costs in comparison with explicit methods (Aloy and Cordero-Carrión, 2016). MIRK methods reduce to the optimal TVD explicit RK methods of Shu and Osher (1988) for the $\mathbf{S}_{\mathbf{E}}$ and $\mathbf{S}_{\mathbf{Y}}$ operators, and implicitly evolve the stiff source terms as we explain below. In the strategy proposed in MIRK methods, each of the several stages in which they split can actually be viewed as stages from explicit RK methods with an effective time-step.

Then the procedure to evolve the conserved variables from the time level n to the next one, $n+1$, can be cast as a modified s-stage RK method, which are summarized as follows:

1. Set the values of the first intermediate stage according to

$$\begin{aligned} \mathbf{Y}^{(1)} &= \mathbf{Y}^n, \\ \mathbf{E}^{(1)} &= \mathbf{E}^n. \end{aligned}$$

2. The succeeding intermediate stages have the form,

$$\mathbf{Y}^{(l)} = \mathbf{Y}^n + \Delta t \sum_{q=1}^{l-1} \tilde{a}_{lq} \mathbf{S}_{\mathbf{Y}}^{(q)}, \tag{4.37}$$

$$\mathbf{E}^{(l)} = \mathbf{E}^n + \frac{\Delta t}{1+\Upsilon_l} \sum_{q=1}^{l-1} \left(\tilde{a}_{lq} \mathbf{S}_{\mathbf{E}}^{(q)} + \sum_{m=1}^{l-1} a_{lqm} \left(-\bar{\sigma}\right)^{(m)} \mathbf{E}^{(q)} \right),$$

with $l = 2, \ldots, s+1$ and

$$\Upsilon_l = \Delta t \sum_{q=1}^{l-1} b_{lq} \bar{\sigma}^{(q)}.$$

3. The final stage corresponds to

$$\mathbf{Y}^{n+1} = \mathbf{Y}^{(s+1)}, \tag{4.38}$$

$$\mathbf{E}^{n+1} = \mathbf{E}^{(s+1)}, \tag{4.39}$$

where $\tilde{a}_{lq}$ denote the coefficients of the Butcher matrix associated with the explicit RK method from which the MIRK method has been constructed, and a_{lqm}, b_{lq} are the coefficients associated with the implicit part of the method. $\Delta t_{\text{eff}} := \frac{\Delta t}{1+\Upsilon_l}$ can be regarded as an effective time step. It is important to outline that, in contrast with RKIMEX methods, there is no final explicit substep. Indeed, Eqs. (4.38) and (4.39) imply that the updated values of the variables at t_{n+1} are the ones computed after the previous s-substeps of the MIRK algorithm. Equivalently, in the standard notation of Butcher tables (Sec.4.2.1), the coefficients w and $\tilde{w}$ are identically zero (see Eq. (4.20)).

A very interesting property of MIRK schemes is that the time update of the conserved variables is explicit, i.e. all the terms in the right-hand side of the equations are evaluated in time levels of the algorithm that have already been computed. This includes the updated values of the electric field, which depend upon already known values of it and of the primitive variables (know already in a prior stage of the MIRK integration). When applied to the system of RRMHD equations, the latter properties of MIRK schemes avoid the need of performing a double iterative procedure to recover the primitive variables from the conserved ones. This is a clear advantage over the usage of RKIMEX schemes to deal with the stiffness of the RRMHD system. We finally remark that in order to write the implicit scheme in an explicit form with an effective time step Δt_{eff}, a much simpler matrix than $A(\mathbf{W})$ (Eq.(4.32)) has been inverted analytically, since the terms $(\mathbf{E}\cdot\mathbf{v})\,\mathbf{v}$ in the expression for $\mathbf{S}_{\mathbf{E}}$ (Eq.(4.36)) are treated explicitly in MIRK schemes.

Below, we provide the explicit expressions of two MIRK methods: the first and second order MIRK methods devised in Aloy and Cordero-Carrión (2016).

4.2.2.1 First-order MIRK method

The first-order MIRK method (hereafter, MIRK1) corresponds to $s = 1$ in equations (4.37)-(4.39), with all coefficients zero except for

$$\tilde{a}_{12} = a_{211} = 1, \qquad b_{21} = (1 - c_1), \qquad \text{with} \quad (1 - c_1) \neq 0,$$

and c_1 being a real coefficient. This coefficient must be determined to obtain *linear stability* of the scheme. Linear stability is typically coined in terms of the eigenvalues of the matrix $\mathcal{M}_{\Delta t}$ that updates the values of the conserved variables from one time step to next one. However, MIRK schemes adopt another necessary condition to enforce, in practice, linear stability. Namely, it is required that the absolute value of the determinant of the matrix is bounded by 1, i.e. $|\mathcal{M}_{\Delta t}| < 1$. The latter condition is, however, not a sufficient condition to enforce linear stability, but helps to restrict the range of the coefficients of the scheme very efficiently and allows to find values for the coefficient(s) nearly optimally.[4] In the absence of stiff sources, the explicit TVD RK first order scheme is linearly stable and, thus, $|\mathcal{M}_{\Delta t}| < 1$. The choice $c_1 = 0$ yields a determinant of $|\mathcal{M}_{\Delta t}| < 1$ when the stiff source term is included if Δt is sufficiently small. The final expression of the method for this optimal value of the coefficient ($c_1 = 0$) can be written as

$$\begin{aligned} \mathbf{Y}^{n+1} &= \mathbf{Y}^n + \Delta t \mathbf{S}_{\mathbf{Y}}^{(n)}, \\ \mathbf{E}^{n+1} &= \mathbf{E}^n + \frac{\Delta t}{1 + \Delta t \bar{\sigma}^{(n)}} \left(\mathbf{S}_{\mathbf{E}}^{(n)} - \bar{\sigma}^{(n)} \mathbf{E}^n \right). \end{aligned}$$

4.2.2.2 Second-order MIRK method

The second-order MIRK method (hereafter, MIRK2) corresponds to $s = 2$, with all coefficients zero except for

$$\begin{aligned} &\tilde{a}_{21} = a_{211} = 1, && b_{21} = (1 - c_1), && \tilde{a}_{31} = \tilde{a}_{32} = 1/2, \\ &a_{311} = c_1/2, && a_{321} = (1 - c_1)/2, && a_{312} = 1/2, \\ &b_{32} = (c_1/2 - c_2). \end{aligned}$$

The coefficients that satisfy the condition $|\mathcal{M}_{\Delta t}| < 1$ may satisfy any of the following two sets of conditions (Aloy and Cordero-Carrión, 2016)

- $c_2 = \frac{(1-c_1)^2}{2c_1}$ and c_1 satisfies either $c_1 < 0$ or $0.67 < c_1 < 0.75$. Numerical experiments show that only the region $c_1 < 0$ gives stable results, with the optimal value for c_1 located around -0.1.

[4] We shall see in Chap. 6 that, indeed, this condition is not sufficient to guarantee the stability of MIRK schemes in certain circumstances. We take this fact as an indication that additional terms must be treated implicitly in MIRK methods to prevent stability breaches.

- $c_1 = 0$ and $-1 < c_2 < -0.5$. Numerical experiments ascertain that the optimal value for c_2 is located around -0.97.

In order to save RAM memory and improve on computational efficiency, the second-order MIRK scheme can be rewritten as:

$$\begin{aligned}
\mathbf{Y}^{(1)} &= \mathbf{Y}^n + \Delta t \mathbf{S}_{\mathbf{Y}}^{(n)}, \\
\mathbf{E}^{(1)} &= \mathbf{E}^n + \frac{\Delta t}{1 + \Delta t(1-c_1)\bar{\sigma}^{(n)}} \left(\mathbf{S}_{\mathbf{E}}^{(n)} - \bar{\sigma}^{(n)} \mathbf{E}^n \right), \\
\mathbf{Y}^{n+1} &= \frac{1}{2} \left(\mathbf{Y}^n + \mathbf{Y}^{(1)} + \Delta t \mathbf{S}_{\mathbf{Y}}^{(1)} \right), \\
\mathbf{E}^{n+1} &= \mathbf{E}^{(1)} + \frac{\left[-1 + \Delta t \bar{\sigma}^{(1)} (1 - c_1) \right]}{2 \left[1 + \Delta t \bar{\sigma}^{(1)} (c_1/2 - c_2) \right]} \left(\mathbf{E}^{(1)} - \mathbf{E}^n \right) \\
&\quad + \frac{\Delta t}{2 \left[1 + \Delta t \bar{\sigma}^{(1)} (c_1/2 - c_2) \right]} \left(\mathbf{S}_{\mathbf{E}}^{(1)} - \bar{\sigma} \mathbf{E}^{(1)} \right).
\end{aligned}$$

It is remarkable, that written in this form, the second-order MIRK scheme needs the same memory allocation as the corresponding second-order optimal TVD RK scheme.

In the Cueva code we use the first set of values by default, that is, we take $c_2 = \frac{(1-c_1)^2}{2c_1}$ and $c_1 = -0.05$. This selection of values yields stable results under a quite broad range of conditions, as will be shown in Section 4.5. However, even taking these values of c_1 and c_2, the MIRK2 method becomes unstable when the Alfvén velocity is large enough in some tests (see Sec. 6.3.1.3).

4.3 Recovery of the primitive variables

The relation between the vector of conserved variables $\mathbf{U}$ and the vector of primitive variables $\mathbf{W}$ (Eq. (2.38)) is explicit and fully algebraic, through Eqs. (2.14), (2.26) and (2.27). However, there is no *simple* explicit form to express the primitive variables in terms of the conserved ones (Eq. (3.2)). Therefore, the *recovery* of the primitive variables is typically performed numerically, using iterative methods. This situation, which already exists in RHD and RMHD, becomes even more involved in RRMHD, if one uses a standard RKIMEX method for the time integration (Sec. 4.2.1.1). Thus, we have implemented two different algorithms to perform the recovery of the primitive variables. Namely, we compute either the Lorentz factor by solving a quartic equation (Sec. 4.3.1) or the gas pressure solving a non-linear relation (Sec. 4.3.2). We present both alternatives in the following sections assuming that the plasma is governed by an ideal EoS of the form (2.20) (however, the expressions can be extended to more realistic EoSs). We anticipate that,

strictly speaking, solving a quartic equation for the Lorentz factor would provide explicit (analytic) expressions of the primitive variables as a function of the conserved ones. However, the analytic solution computed in this way is often impractical. It becomes extremely complex and it is prone to severe numerical inaccuracies related with the floating point arithmetics. Hence, this analytic solution is, in many cases, taken as an initial guess to compute either the Lorentz factor or the pressure numerically (e.g. using a Newton-Raphson (NR) method).

4.3.1 Recovery of the Lorentz factor

A recovery technique that was first proposed by Dumbser and Zanotti (2009) is based on solving a quartic equation for the Lorentz factor as we shall see. First, from Eq. (2.27), we obtain,

$$(\mathbf{S} - \mathbf{E} \times \mathbf{B})^2 = \rho h^2 W^2 (W^2 - 1). \tag{4.40}$$

From Eq. (2.26) we get the following expression for enthalpy ρh

$$\rho h = \frac{\mathcal{E} - \frac{1}{2}(E^2 + B^2) + p_{\mathrm{g}}}{W^2}. \tag{4.41}$$

Using the definition of the specific enthalpy (Eq. (2.19)) particularized for the case of an ideal gas EoS (Eq. (2.21)) we obtain,

$$p_{\mathrm{g}} = \gamma_1 \, \rho \, (h - 1), \tag{4.42}$$

where $\gamma_1 := (\gamma - 1)/\gamma$. Writing the pressure as a function of the specific enthalpy employing Eq. (4.42) in Eq. (4.41), the enthalpy reads,

$$\rho h = \frac{\mathcal{E} - \frac{1}{2}(E^2 + B^2) - \dfrac{\gamma_1 D}{W}}{W^2 - \gamma_1}. \tag{4.43}$$

We continue by plugging Eq. (4.43) into Eq. (4.40), which yields

$$(\mathbf{S} - \mathbf{E} \times \mathbf{B})^2 = \frac{\left(\mathcal{E} - \frac{1}{2}(E^2 + B^2) - \dfrac{\gamma_1 D}{W}\right)^2}{(W^2 - \gamma_1)^2} W^2 (W^2 - 1). \tag{4.44}$$

Next, from Eq. (2.27) we have, $\mathbf{S}_{\mathrm{hyd}} = \mathbf{S} - \mathbf{E} \times \mathbf{B}$ and from Eq. (2.26) we know that $\mathcal{E}_{\mathrm{hyd}} = \mathcal{E} - \frac{1}{2}(E^2 + B^2)$, which plugged in Eq. (4.44) leads to

$$\mathbf{S}_{\mathrm{hyd}}^2 (W^2 - \gamma_1)^2 = \left(\mathcal{E}_{\mathrm{hyd}} - \frac{\gamma_1 D}{W}\right)^2 W^2 (W^2 - 1).$$

This expression can be cast into the following quartic equation for the unknown Lorentz factor, W,

$$a_4 W^4 + a_3 W^3 + a_2 W^2 + a_1 W + a_0 = 0, \tag{4.45}$$

with coefficients,

$$\begin{aligned} a_4 &= \mathbf{S}_{\rm hyd}^2 - \mathcal{E}_{\rm hyd}^2, \\ a_3 &= 2\gamma_1 \mathcal{E}_{\rm hyd} D, \\ a_2 &= \mathcal{E}_{\rm hyd}^2 - 2\gamma_1 \mathbf{S}_{\rm hyd}^2 - \gamma_1^2 D^2, \\ a_1 &= -2\gamma_1 \mathcal{E}_{\rm hyd} D, \\ a_0 &= \gamma_1^2 (\mathbf{S}_{\rm hyd}^2 + D^2). \end{aligned}$$

The solution of this equation is computed analytically, using the standard Ferrari-Cardano (FC) technique. Once the Lorentz factor is computed by solving the quartic equation (4.45), we choose the correct physical result $W > 1$. The other primitive variables can be computed in a straightforward manner, following this order:

a) Recover the rest-mass density ρ from its conservative counterpart D using Eq. (2.14).

b) Compute the enthalpy (Eq. (4.43)).

c) With the help of Eq. (4.42), we can find the pressure.

d) Next, the velocity components are obtained from Eq. (2.27).

e) Finally, in the case of using an RKIMEX scheme, we can update the electric components by means of Eq. (4.33) and repeat this procedure until the absolute value of the relative difference of the components of $\mathbf{E}$ between two consecutive iterations falls below some prescribed tolerance $\epsilon_{\mathbf{E}}$. Typically, we set $\epsilon_{\mathbf{E}} = 10^{-10}$.

4.3.2 Recovery of the gas pressure

Since $\mathbf{B}$ and $\mathbf{E}$ are both conserved and primitive variables we know the values of $\mathbf{S}_{\rm hyd} = \mathbf{S} - \mathbf{E} \times \mathbf{B}$ (Eq. (2.27)) and $\mathcal{E}_{\rm hyd} = \mathcal{E} - \frac{1}{2}(E^2 + B^2)$ (Eq. (2.26)) at the end of any substage of the time advance algorithm. Hence, the subset of conserved and primitive variables, respectively $(D, \mathbf{S}_{\rm hyd}, \mathcal{E}_{\rm hyd})$ and $(p_{\rm g}, \rho, \mathbf{v})$, is the same as in RHD. Therefore, the same procedures for the recovery of the primitive variables as in RHD can be applied in RRMHD. In particular, one may recover the gas pressure as in Aloy et al. (1999). This technique was first

used in RRMHD by Palenzuela et al. (2009). The procedure can be cast in terms of solving numerically the unique root of the function,

$$f(\bar{p}_{\rm gas}) = p_{\rm g}(\rho, \epsilon) - \bar{p}_{\rm gas}, \tag{4.46}$$

where $p_{\rm g}(\rho, \epsilon)$ is given by the chosen EoS and $\bar{p}_{\rm gas}$ is a guess value for the pressure. In practice, the iterative process to obtain primitive variables from conserved ones proceeds according to the following steps.

a) In the case of recovering the primitive variables in the stage l of an RKIMEX scheme, we use Eq. (4.33) to update the electric field value $\mathbf{E}^{(l)}$ as function of $\mathbf{E}^*, \mathbf{B}^{(l)}$ and the values of velocity at the substep $l-1$, i.e. $\mathbf{v} = \mathbf{v}^{l-1}$.

b) If we have performed step (a) in an RKIMEX scheme, or if we are employing a MIRK scheme (in which case step (a) is not necessary), then the following variables are computed, using as guess for the gas pressure $\bar{p}_{\rm gas} = p_{\rm g}^{(l-1)}$,

$$\begin{aligned}
\mathbf{v} &= \frac{\mathbf{S} - \mathbf{E} \times \mathbf{B}}{\mathcal{E}_{\rm hyd} - D - (E^2 + B^2)/2 + \bar{p}_{\rm gas}}, \\
W &= \frac{1}{\sqrt{1 - \mathbf{v} \cdot \mathbf{v}}}, \\
\rho &= \frac{D}{W}, \\
\epsilon &= \frac{\mathcal{E}_{\rm hyd} - D(1+W) + \bar{p}_{\rm gas}(1 - W^2)}{DW}.
\end{aligned}$$

c) Then we solve Eq. (4.46) by means of an iterative NR solver, so that the solution at the iteration $m+1$ can be computed as

$$\bar{p}_{{\rm gas},(m+1)} = \bar{p}_{{\rm gas},(m)} - \frac{f(\bar{p}_{{\rm gas},(m)})}{f'(\bar{p}_{{\rm gas},(m)})}.$$

The derivative of the function $f(\bar{p}_{\rm gas})$ can be approximated by $f'(\bar{p}_{\rm gas}) \simeq \mathbf{v} \cdot \mathbf{v} c_s^2 - 1$, where c_s is the local sound speed of the fluid (Aloy et al., 1999), given by Eq. (2.22).

d) In a MIRK scheme, the procedure ends at point (c). However, for an RKIMEX scheme, we must update the electric field values, repeating steps (a)-(c) with the newly obtained values for the velocity $\mathbf{v}$ and the pressure $\bar{p}_{\rm gas}$, iterating until the difference between two successive values falls below a specified tolerance.

4.4 The treatment of the elliptic constraints

The preservation of the elliptic constrains in RRMHD can be enforced by a suitable constraint transport method (Evans and Hawley, 1988; Stone and Norman, 1992) as in, e.g. Bucciantini and Del Zanna (2013). Alternatively, as we have seen in Sec. 2.6, the augmented system of RRMHD is built with the purpose of controlling the time evolution of both the solenoidal constraint on the magnetic field ($\nabla \cdot \mathbf{B} = 0$) and the constraint on the divergence of the electric field ($\nabla \cdot \mathbf{E} = q$).

The fulfillment of the constraints is a necessary condition for the accurate solution of the equations of ideal MHD, RMHD or RRMHD. From various numerical techniques that have been devised to ensure that the computed magnetic field is maintained divergence-free throughout the temporal evolution, we have chosen the method of generalized Lagrangian multipliers (GLM; Dedner et al., 2002) to maintain the constraints of the electromagnetic field as in Komissarov (2007) or Palenzuela et al. (2009).

In the GLM formulation, the constraints are not elliptic equations but, instead, hyperbolic (telegraph) equations (see Eqs. (2.35) and (2.36)). From Eq. (2.31), it is easy to check that the magnetic field will be divergence free if it is initially solenoidal, unless ill-posed boundary conditions (which are sources of magnetic monopoles) are set. Taking subsequently the divergence and the time derivative of Eq. (2.34), one can verify that the magnetic field satisfies the same telegraph equation as ϕ (Eq. (2.35))

$$-\partial_{tt}(\nabla \cdot \mathbf{B}) - \kappa \partial_t (\nabla \cdot \mathbf{B}) + \nabla^2 (\nabla \cdot \mathbf{B}) = 0.$$

Consistently, $\nabla \cdot \mathbf{B}$ evolves in the same way as ϕ. Similarly, one finds that $\nabla \cdot \mathbf{E} - q$ also satisfies the telegraph equation

$$-\partial_{tt}(\nabla \cdot \mathbf{E} - q) - \kappa \partial_t (\nabla \cdot \mathbf{E} - q) + \nabla^2 (\nabla \cdot \mathbf{E} - q) = 0,$$

and, therefore, $\nabla \cdot \mathbf{E} - q$ and ψ display parallel evolutions.

Komissarov (2007) discusses the possibility of excluding the electric charge conservation law (Eq. (2.12)) from the set of RRMHD equations and computing the electric charge density enforcing the Gauss law $\nabla \cdot \mathbf{E} = q$. However, this choice would not guarantee that the electric charge distribution be consistent with the evolution of electric current (cf. Komissarov, 2007).

For numerical convenience, the constant $\kappa > 0$, appearing in Eqs. (2.31) and (2.32) is usually defined as $\kappa = c_h^2/c_p^2$, where c_p^2 can be regarded as a diffusion coefficient and c_h as the finite speed at which $\nabla \cdot \mathbf{B}$ errors propagate. For simplicity and not to limit further the time step, we choose this finite speed equal to the speed of light ($c_h = 1$) and following Mignone and Tzeferacos

(2010), we define the dimensionless parameter,

$$\aleph := \Delta h \frac{c_h}{c_p^2}, \tag{4.47}$$

where $\Delta h := \min(\Delta x, \Delta y, \Delta z)$, and Δx, Δy, Δz are the grid spacings in the three Cartesian directions. Thus, in our applications the explicit relation between κ and $\aleph$, for $c_h = 1$ reads

$$\aleph = \Delta h \kappa.$$

According to Mignone and Tzeferacos (2010), the errors associated with the violation of the magnetic field solenoidal constraint are minimised when $\aleph \in [0, 1]$ (but see Sec. 4.5.6). In the numerical experiments presented in this thesis, we set $\aleph = 1$, unless otherwise stated.

4.5 Numerical Experiments

In this section, we present several standard tests implemented in one and two spatial dimensions with which we validate the performance of the numerical algorithms introduced in this chapter. These tests cover different conductivity regimes to assess the validity of our numerical method under different degrees of stiffness of the RRMHD equations. We will compare the various intercell reconstruction schemes, the time advance schemes (RKIMEX and MIRK) and the properties of the divergence cleaning technique to preserve the solenoidal constraint. We defer to Chap. 5 a thorough comparison of the performance of different Riemann solvers. We follow the convention of Higueras et al. (2012) to name RKIMEX schemes as explained in Appendix A.

4.5.1 Resistive Self-similar Current Sheet

Komissarov (2007) proposed a test to probe the resistive regime, i.e., relatively far away from the ideal limit. This is the so-called self-similar current sheet (SCS), where we have a magnetic field $\mathbf{B} = (0, B_y(x,t), 0)$. The magnetic pressure is much smaller than the gas pressure and $B_y(x, 0)$ changes sign within a thin current layer of very small width, a_0, compared with the domain size in the x-direction. Except for the magnetic field, the rest of the primitive variables are set to be constant in the whole domain: $p_{\rm g} = 50$, $\rho = 1$, $\gamma = 2$, $\mathbf{E} = \mathbf{0}$ and $\mathbf{v} = \mathbf{0}$. We furthermore fix $\sigma = 100$. Since the pressure is uniform, the resistivity of the plasma drives a slow diffusive expansion, and the governing equation is the diffusion equation (for more details see Sec. 6.2)

$$\partial_t B_y = \eta \, \partial_x^2 B_y. \tag{4.48}$$

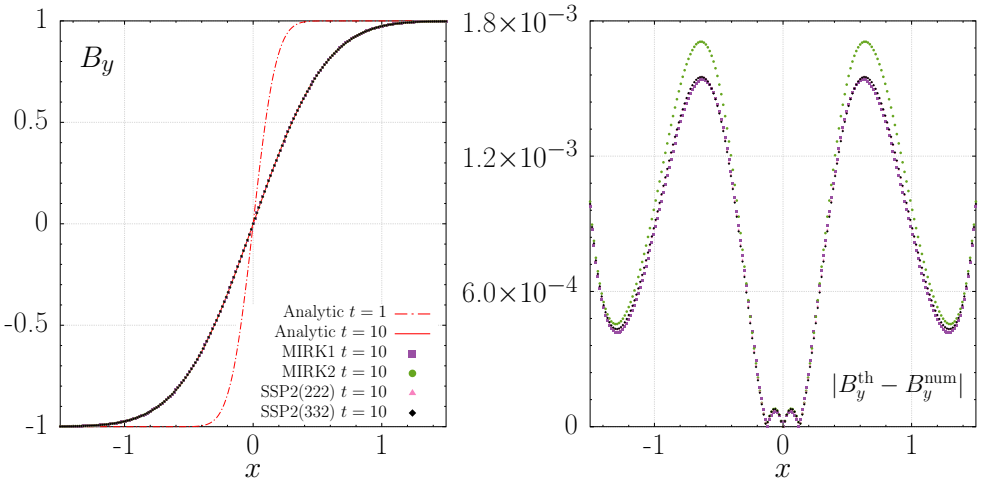

Figure 4.4: Left: Analytic and numeric solution of the self-similar current sheet. The analytic solution is displayed for the initial state at $t = 1$ (red dash-dotted line), and after a time $t = 10$ (red line). The numerical solution is computed with 200 uniform cells at $t = 10$ (see legends), using models with an adiabatic index $\gamma = 2$ and $C_{\rm CFL} = 0.8$. The lines corresponding to the different numerical solutions at $t = 10$ overlap at the scale of this plot. Right: Absolute value of the difference between the approximate analytic solution, $B_y^{\rm th}$ (4.49), and the numerical solution computed with each of the time-integration methods of the left panel.

We highlight that Eq. (4.48) neglects the contributions of the (small) velocities developed in the resistive layer, as well as the action of the (also small) displacement currents. Thus, the solutions to Eq. (4.48) only approximately describe the dynamics of the diffusive expansion in our case. Neglecting all these small effects, after a transitory phase, during which the width of the layer becomes much larger than a_0, the expansion becomes self-similar and adopts the form

$$B_y^{\rm th}(x,t) = B_0\, \texttt{erf}\left(\frac{x - x_0}{2\sqrt{\eta\, t}}\right), \tag{4.49}$$

where the error function is defined in the usual way:

$$\texttt{erf}(x) = \frac{2}{\sqrt{\pi}} \int_0^x e^{-t^2} \mathrm{d}t.$$

Our numerical tests begin from an initial time $t = 1$ and we set $B_0 = 1$ and $x_0 = 0$. We employ 200 computational cells to cover the domain $[-1.5, 1.5]$ with $C_{\rm CFL} = 0.8$. We let the system evolve until $t = 10$ and compare our results with the analytic solution in Fig. 4.4.

While (Aloy and Cordero-Carrión, 2016) use this test to assess the performance of their MIRK methods, we use it here to cross compare the results of different time evolution strategies. For that we fix the Riemann solver (LLF)

and the spatial reconstruction (MML). We observe that in the left panel of Fig. 4.4 all the solutions are very similar after $t = 10$. Only looking at the deviations between the (approximate) analytic solution and the different numerical solutions we identify tiny differences among distinct time integration algorithms (Fig. 4.4 right panel). The solutions found with either the MIRK1 or the second-order RKIMEX methods (SSP2(222) or SSP2(332)-LUM) are almost indistinguishable. However, the MIRK2 solution, computed with the parameters $c_1 = -0.05$ and $c_2 = -6.05$, stands out from the rest, especially for $|x| \gtrsim 0.5$. Variations of the c_1 and c_2 parameters may significantly reduce the gap between the solution obtained with MIRK2 and the other solutions. We point out that in the $\sigma \gg 1$ regime, these discrepancies become much smaller.

In order to validate our numerical code, the SSC test has also been run with other RKIMEX schemes (in addition to the ones whose results we show in Fig. 4.4). Furthermore, we have rotated the initial current sheet to become parallel to the y- and z-directions. The results of these tests are nearly identical to the ones shown in this section. Finally, we point out that this test does not develop shocks or non-smooth regions. Thus it is an excellent candidate to estimate the order of convergence of our algorithm (Sec. 4.5.3).

4.5.2 Large Amplitude CP Alfvén waves

In order to verify that the numerical order of convergence is consistent with the theoretical order of each of our MIRK and RKIMEX methods, we consider the propagation of large amplitude, circularly polarized Alfvén waves (CPAW). We use the same set up as Del Zanna et al. (2007), where the components of $\mathbf{B}$ and $\mathbf{v}$ are given by the ideal RMHD solution,

$$(B_x, B_y, B_z) = B_0(1,\, \epsilon_{\rm am}\cos\left(k(x - v_A t)\right),\, \epsilon_{\rm am}\sin\left(k(x - v_A t)\right), \quad (4.50)$$

$$(v_x, v_y, v_z) = \frac{v_A}{B_0}(0,\, -B_y,\, -B_z) \quad (4.51)$$

$$\rho = \rho_0 \quad (4.52)$$

$$p_{\rm g} = p_{\rm g,0} \quad (4.53)$$

where B_0, k and $\epsilon_{\rm am}$ are, respectively, a normalization value for the magnetic field strength, the wave vector and a small parameter to set the amplitude of the waves. ρ_0 and $p_{\rm g,0}$ are the uniform values of the rest-mass density and of the pressure, respectively. v_A is the Alfvén speed (Eq. (2.24)), which particularized for our set up reads

$$v_A^2 = \frac{2B_0^2}{h + B_0^2(1+\epsilon_{\rm am}^2)}\left(1 + \sqrt{1 - \left(\frac{2\epsilon_{\rm am}B_0^2}{h + B_0^2(1+\epsilon_{\rm am}^2)}\right)^2}\right)^{-1}. \quad (4.54)$$

To our knowledge, there is no exact solution in the RRMHD regime for circularly polarized Alfvén waves, but in the limit of very large conductivity, Eqs. (4.50) and (4.51) are approximately satisfied. Thus, we compute the evolution from the initial state and until the train of waves completes one period. In the ideal limit, the solution should be identical to that in the initial state and we expect that if $\sigma \gg 1$, also the resistive solution shall be quite similar to the initial one.

Figure 4.5 shows the evolution after one period ($t = 2$), with a high uniform value for the conductivity ($\sigma = 10^6$) in a computational domain $x \in [-0.5, 0.5]$. The initial parameters are the same as in Palenzuela et al. (2009), namely, $\rho_0 = p_{\rm g,0} = \epsilon_{\rm am} = k = 1$, $B_0 = 1.1547$, and the initial electric field is obtained from its inductive (ideal) value $\mathbf{E} = -\mathbf{v} \times \mathbf{B}$. The adiabatic index $\gamma = 2$ is fixed. In Figure 4.5 we present the numerical solution for different spatial resolutions, carried out with the MIRK2 time-integrator, the HLL Riemann solver, the MP5 limiter and $C_{\rm CFL} = 0.1$. Numerical solutions computed with

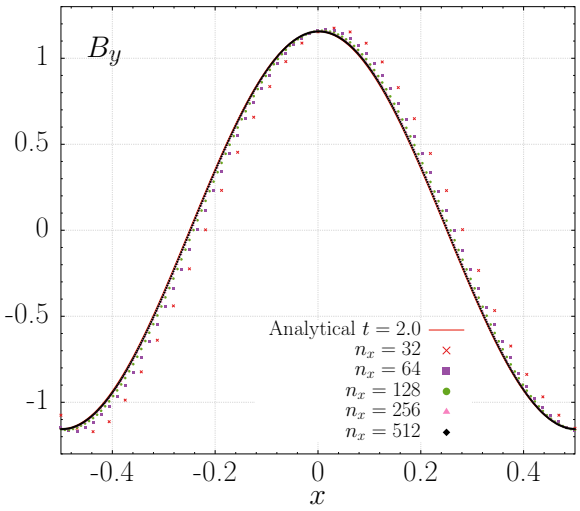

Figure 4.5: Numerical solution for a circularly polarized Alfvén wave after one period of time for different resolutions $n_x = [32, 64, 128, 256, 512]$. The initial parameters for these results are $\rho_0 = p_{\rm g,0} = \epsilon_{\rm am} = k = 1$, $B_0 = 1.1547$.

$n_x \gtrsim 128$ nearly lie on top of the analytic one at the scales shown in Fig. 4.5. At smaller resolutions we find that the numerical train of waves propagates with a group velocity a bit larger than the analytic solution predicts. The result is a small shift (to the right) of the numerical results of the order of the grid size Δx (see, e.g. the shift in the maximum of the solution computed with $\Delta x = 1/32$ - light red- with respect to the maximum of the analytic solution). As the figure shows, this shift becomes smaller with increasing resolution. Besides these small shifts, it is evident that the RRMHD code we use is able to properly

capture the evolution of large amplitude Alfvén waves, without any apparent numerical instability for the resolutions and $C_{\rm CFL}$ factors employed here. We therefore conclude that the results are of the same quality as others presented in the literature (e.g. Palenzuela et al., 2009). In Sec. 6.3.1.3 we will see that this test is, however, very difficult to conduct when $v_A \sim 1$ and, indeed, it becomes an excellent tool to gauge the numerical diffusivity of our algorithms.

4.5.3 Numerical order of accuracy

Since numerical errors, i.e. the difference between the discrete solution and the exact solution, arise both from the spatial (Δx) and from the temporal discretization (Δt) of the solution, these terms should be proportional to powers of the grid size and of the time step, which can be cast formally as (e.g. Rezzolla and Zanotti, 2013, chap. 8; see also Rembiasz et al. (2017) and in Chap. 6, Eqs. (6.1) and (6.2)),

$$E_{\rm disc} = \mathcal{O}\left(\delta_1(\Delta x)^r + \delta_2(\Delta t)^q\right), \tag{4.55}$$

where r and q depend on the order of the numerical schemes, and δ_1 and δ_2 are both functions of the state whose solution we are seeking and the numerical method employed to look for the solution. A thorough treatment of the impact of discretization errors on the amount of numerical viscosity and resistivity of our numerical method is deferred to Chap. 6.

In order to assess the spatial convergence of a simulation it is customary to compare the numerical results obtained with meshes of different sizes, i.e. with different numbers of points. This method is usually referred as *Richardson* test and involves performing the simulation on two or more successively finer grids. As the grid is refined and the time step is refined (reduced) the spatial and temporal discretization errors, respectively, should asymptotically approach zero, excluding computer round-off error (e.g. Roache, 1998).

In order to verify whether the MIRK and RKIMEX schemes perform at the formal orders of convergence for which they are designed, we perform Richardson tests in the cases where the solution is smooth. This is the case of the tests SCS (Sec. 4.5.1) and CPAW (Sec. 4.5.2). For these tests we use the MCL slope limiter for the intercell reconstruction, and compute the numerical fluxes according to the LLF, HLL or HLLC prescriptions. We expect to measure second order of convergence since we are using the MCL slope limiter (second order accurate in space) in combination to the MIRK2 or the SSP2(332)-LUM schemes, which are formally of second order as well.

In Figures 4.6 and 4.7, we display the *local relative errors*, E_{nx}, for SSCS and CPAW tests, respectively, as a function of the grid resolution Δx. We

calculate the local relative error as in Bucciantini and Del Zanna (2013)

$$E_{nx} = \frac{L}{n_x} \sum_{i=0}^{n_x} \left| \frac{U_{\mathrm{ref},i} - U_{\mathrm{num},i}}{\max\{U_{\mathrm{ref}}\}} \right|, \tag{4.56}$$

where L is the size of the computational domain, n_x the grid number points, U_{num} is the numerical solution and U_{ref} is a reference solution computed with the analytical expressions (4.49) and (4.50).

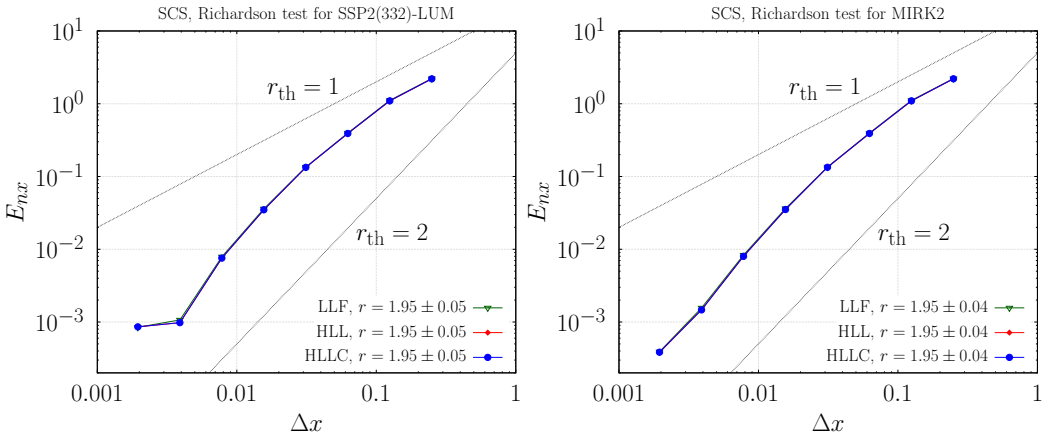

Figure 4.6: Relative error (Eq. (4.56)) vs resolution for SCS test. Left panel: SSP2(332)-LUM time-integrator. Right panel: MIRK2 time-integrator. For reference, we include several dotted lines of the form $E_{nx} \propto (\Delta x)^r$, to mark the first ($r_{\mathrm{th}} = 1$) and second ($r_{\mathrm{th}} = 2$) order accuracy trend lines. All tests are run with $C_{\mathrm{CFL}} = 0.1$.

The order of convergence for the SCS test is $r \simeq 1.95$ (Fig. 4.6). In this test the conductivity is low ($\sigma = 10^2$) and there are not local extrema inside of the region where the action takes place (i.e., in the smooth transition layer). It is remarkable that the numerical results in this test are very insensitive both to the time-integration algorithm and to the exact Riemann solver employed. Both in the case of the MIRK2 time integration or the SSP2(332)-LUM method the order of accuracy is close to 1 for coarser grids and approaches 2 for finer grids.

For the CPAW test, which probes the ideal limit ($\sigma = 10^6$) the order of accuracy is in the range $r \in [1.55, 2.15]$ as we show in Fig. 4.7. These values for r are computed using the data from resolutions $\Delta x = 1/1024$ to $\Delta x = 1/8$, i.e. excluding the models run with $n_x = 4$ uniform numerical zones. Independent of the time integrator, all solvers seem to display a convergence rate $r \simeq 1$ for relatively coarse resolutions $\Delta x \gtrsim 1/8 = 0.125$, which improves towards $r \gtrsim 2$ for finer resolutions. Independently of the time-integrator, we observe larger errors (equivalently, smaller convergence rates) for the LLF solver than for HLL solver, which, in its turn, displays larger errors than the

HLLC solver. The convergence rate has a more monotonic behaviour with resolution for the SSP2(332)-LUM time-integrator than for the MIRK time-integrator. The differences between the convergence rate and the errors of the LLF and HLL solvers are remarkable. We shall consider that, when the maximum signal speeds are limited to $\lambda_l = -1$ and $\lambda_r = +1$, in the absence of any variable or flux reconstruction, HLL and LLF solvers are identical. However, we use the LLF solver employing the flux reconstruction proposed by Alic et al. (2007) (see Eq. (4.14)). In contrast, the HLL and also the HLLC solvers are used computing first the left and right states employing a high-order intercell reconstruction. Although in both cases (LLF and HLL solvers; also in the case of HLLC) we use the same MCL slope limiter, which should result into (formally) second order accurate results, the differences between both procedures of reconstruction are evident in Fig. 4.7. Thus, we conclude that, even if the flux reconstruction may provide stable results when used inside of the LLF solver, it turns out to be more diffusive than reconstructing the primitive variables and then computing the numerical fluxes employing either the HLL or the HLLC solvers.

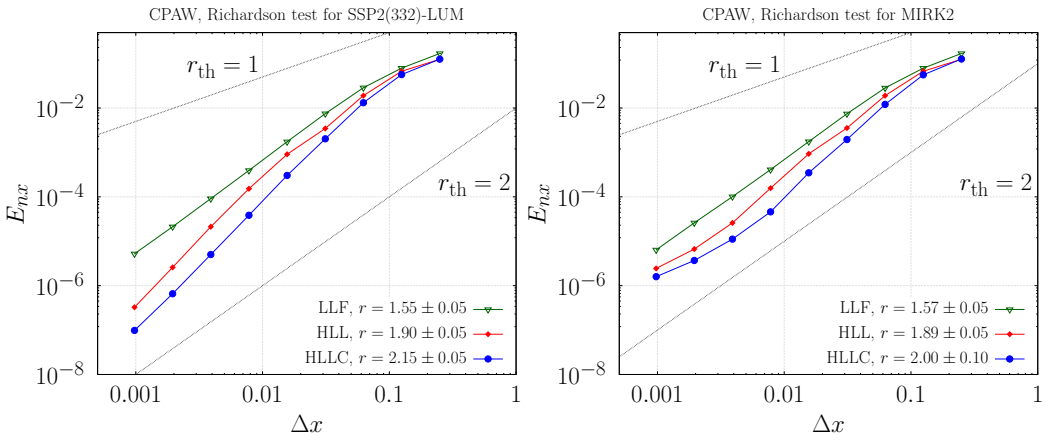

Figure 4.7: Relative error (Eq. (4.56)) vs resolution for CPAW test. Left panel: SSP2(332)-LUM method. Right panel: MIRK2. For reference, we include several dotted lines of the form $E_{nx} \propto (\Delta x)^r$, to mark the first ($r_{\rm th} = 1$) and second ($r_{\rm th} = 2$) order accuracy trend lines. All tests are run with $C_{\rm CFL} = 0.1$.

4.5.4 Resistive shock tube

To demonstrate the shock capturing capabilities of our algorithm, we consider a one-dimensional shock tube (ST0) test with resistivity (dubbed resistive shock tube or RST hereafter) were, the break up of the initial discontinuity develops a Riemann fan with 7 different waves in the ideal limit. We use the same set up as Bucciantini and Del Zanna (2013), where the initial conditions are listed in

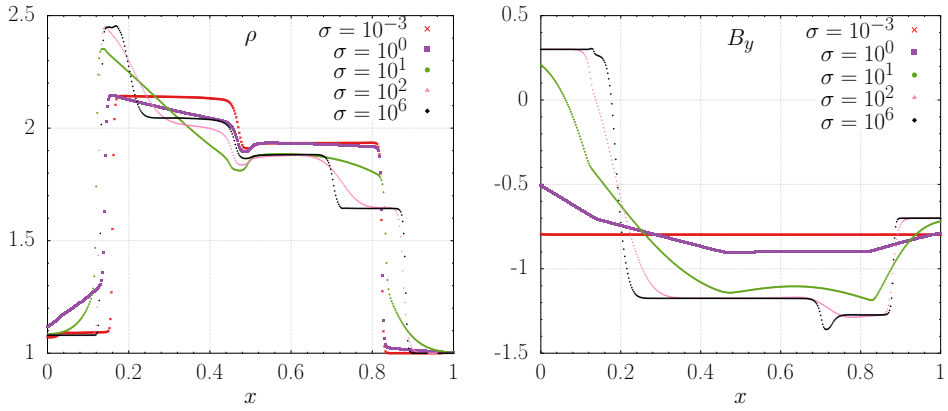

Figure 4.8: Resistive shock tube. Left panel, density ρ and right panel B_y for different regimes of conductivity: 10^6 (red line), 10^2 (orange), 10 (blue), 1 (green) and 10^{-3} (violet).

Tab. 4.1. The computational domain, $x \in [0, 1]$, is covered with a uniform grid of 400 cells, and the test is evolved for various conductivity regimes, from highly conductivity $\sigma = 10^6$ to highly resistive $\sigma = 10^{-3}$, until a final time $t = 0.55$ with adiabatic index $\gamma = 5/3$. In Fig. 4.8 the RKIMEX scheme employed is SSP2(222) with $C_{\rm CFL} = 0.1$ for the highly conductive case and $C_{\rm CFL} = 0.9$ for the highly resistive case. As can be seen, our results are comparable to those existing in the literature. We see that as the conductivity decreases the number of intermediate structures in the Riemann fan resulting from the breakup of the initial discontinuity at $x = 0.5$ decreases. This is related to the fact that in the very resistive regime, only three different eigenspeeds can be differentiated in the system (see Sec. 3.1), instead of the seven different eigenspeeds existing in RHMD. The extremely resistive limit corresponds to the case $\sigma = 10^{-3}$ in Fig. 4.8, where basically a contact wave at $x = 0.5$ flanked by both shocks at $x \simeq 0.016$ and $x \simeq 0.84$ are observable. In contrast, the dynamics close to the ideal RMHD limit is represented by the case with $\sigma = 10^6$ in Fig. 4.8, where we can observe all the ideal RMHD waves. We finally point out that the quantitive results are the same when using a MIRK method for the time integration of the RRMHD equations, as we can see in Sec. 5.2.4.

4.5.5 Ideal shock tubes

In previous test we illustrated the capability of our code to deal with different regimes of conductivity. Here, we perform a comparison of the RKIMEX and MIRK methods to resolve different discontinuities, in situations where the source terms become stiff. To do this, we employ the models listed in Tab. 4.1 seting up $\sigma = 10^6$ (with the exception of models ST0; see Sec. 4.5.4). Model ST1-B0 will be will be a subject of specific study in Sec. 5.2.3.

Table 4.1: Initial conditions for 1D test problems. In all simulations, we set the scalar potentials and the charge density to zero, i.e. $\psi = \phi = q = 0$, and the electric field to its ideal approximation $\mathbf{E} = -\mathbf{v} \times \mathbf{B}$. The computational domain length is $L_x = 1$. The columns give the test name, the state (left; L, set for $x < 0.5$ or right; R, set for $x \geq 0.5$), rest-mass density ρ, gas pressure p, velocity and magnetic field components ($\mathbf{v}$ and $\mathbf{B}$, respectively), the adiabatic index γ, the simulation time t, and the number of zones.

Test	State	ρ	p_g	v_x	v_y	v_z	B_x	B_y	B_z	γ	t	Zones
CW1	L	10.0	1.0	0.0	0.7	0.2	5.0	1.0	0.5	5/3	1.0	40
	R	1.0	1.0	0.0	0.7	0.2	5.0	1.0	0.5			
CW2	L	1.0	1.0	0.2	0.0	0.0	1.0	1.0	0.0	5/3	1.0	40
	R	0.125	1.0	0.2	0.0	0.0	1.0	1.0	0.0			
RW	L	1.0	1.0	0.4	−0.3	0.5	2.4	1.0	−1.6	5/3	1.0	40
	R	1.0	1.0	0.377237	−0.482389	0.424190	2.4	−0.1	−2.178213			
ST0	L	1.08	0.95	0.4	0.3	0.2	2.0	0.3	0.3	5/3	0.4	400
	R	1.0	1.0	−0.45	−0.2	0.2	2.0	−0.7	0.5			
ST1	L	1.0	1.0	0.0	0.0	0.0	0.5	1.0	0.0	2.0	0.4	400
	R	0.125	0.1	0.0	0.0	0.0	0.5	−1.0	0.0			
ST1-B0	L	1.0	1.0	0.0	0.0	0.0	0.0	1.0	0.0	2.0	0.4	400
	R	0.125	0.1	0.0	0.0	0.0	0.0	−1.0	0.0			
ST2	L	1.08	0.95	0.4	0.3	0.2	2.0	0.3	0.3	5/3	0.55	800
	R	1.0	1.0	−0.45	−0.2	0.2	2.0	−0.7	0.5			
ST3	L	1.0	0.1	0.999	0.0	0.0	10.0	7.0	7.0	5/3	0.4	400
	R	1.0	0.1	−0.999	0.0	0.0	10.0	−7.0	−7.0			
ST4	L	1.0	5.0	0.0	0.3	0.4	1.0	6.0	2.0	5/3	0.5	800
	R	0.9	5.3	0.0	0.0	0.0	1.0	5.0	2.0			
ST5	L	1.0	30.0	0.0	0.0	0.0	5.0	6.0	6.0	5/3	0.4	800
	R	1.0	1.0	0.0	0.0	0.0	5.0	0.7	0.7			

4.5.5.1 Shock Tube Problem 1

Balsara (2001) proposed a relativistic extension of the Brio and Wu (1988) test (ST1 hereafter). In this test the initial discontinuity breaks into a left-going fast rarefaction, a left-going compound wave, a contact discontinuity, a right-going slow shock and right-going fast rarefaction wave.

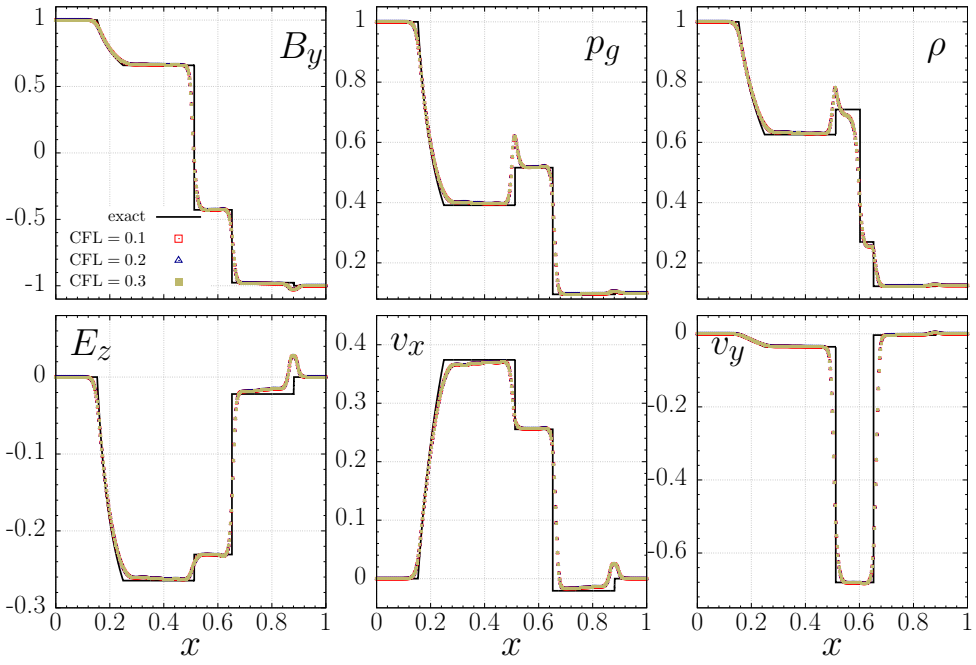

Figure 4.9: ST1: Comparison of the results obtained for different CFL factors ($C_{\rm CFL} = 0.1, 0.2, 0.3$). In all cases we have used the HLL approximate Riemann solver, the MCL intercell reconstruction, and the SSP2(222) time-integration scheme. Upper panels (left to right): B_y component of magnetic field, thermal pressure ($p_{\rm g}$), rest-mass density (ρ). Lower panel: E_z component of electric field, v_x and v_y components of velocity field.

Besides displaying the performance of our numerical scheme to resolve the complex wave pattern generated after the break-up of the initial discontinuity, in this test we also prove the dependency of the results with the $C_{\rm CFL}$ factor. For that, we fix the numerical resolution ($n_x = 400$) the time integration scheme (SSP2(222)), the HLL Riemann solver and the MCL intercell reconstruction and run the test for $C_{\rm CFL} = 0.1, 0.2$ and 0.3. In Fig. 4.9, we observe that all solutions overlap and there is no significant dependence with the $C_{\rm CFL}$ factor. However, values $C_{\rm CFL} > 0.3$ result in the failure of the code. The reason of the failure is the undershooting in the pressure ahead of the right-going slow shock.

4.5.5.2 Shock Tube Problem 2

In the shock tube problem 2 (ST2 hereafter), proposed by Balsara (2001), the transverse magnetic field rotates across the discontinuity by $\simeq 0.55\pi$, and the Riemann fan is composed of three left-going waves (fast shock, Alfvén wave, and slow rarefaction), a contact discontinuity (at $x \simeq 0.475$ when $t = 0.55$), and three right-going waves (slow shock, Alfvén wave, and fast shock).

This test is rather demanding, because of the small relative velocity of the different waves emerging from the break-up of the initial discontinuity, which generates extremely narrow structures. The performance of our methodology to deal with this shock tube in the absence of any high-order intercell reconstruction method is deferred to Sec. 5.2.4. Here we compute numerical solutions using different time integrator schemes, namely, MIRK2, SSP2(332)-LUM and SSP3(443). In all the cases we use the HLL Riemann solver, the MP9 intercell reconstruction and we fix $C_{\rm CFL} = 0.1$, as well as $n_x = 800$.

All time-integration methods faithfully reproduce the analytic solution for the ideal RMHD case. The very high-order of the intercell reconstruction lessens the differences among the numerical solutions computed with any of the time-integrators (Fig. 4.10). However, small scale oscillations are noticeable in the rest-mass density (Fig. 4.11, right panel) in the region flanked by the two fast shocks that delimitate the whole Riemann fan. These oscillations are also present in other variables, though their amplitude is smaller (e.g. Fig. 4.11, left and mid panels). These oscillations arise because of the high-order of the reconstruction, but are bounded because we employ an MP scheme.

4.5.5.3 Shock Tube Problem 3

In shock tube problem 3 (ST3 hereafter), two relativistic plasma streams collide producing two strong relativistic fast shocks propagating symmetrically and a higher rest-mass density region around $x = 0.5$ flanked by another two (slow) shocks. This test was computed using MIRK2 time-integration scheme until a time $t = 0.4$, for the HLL and LLF approximate Riemann solvers. The prescription of Alic et al. (2007) for the LLF solver (Sec. 4.1.2.1) obtains formal second order of spatial accuracy (but see the discussion in Sec. 4.5.3). Our implementation of the HLL solver (Sec. 4.1.2.2) combined with the MCL reconstruction of the primitive variables is also (formally) second-order accurate for smooth flows. Furthermore, since the, maximum and minimum speeds that we implement in the HLL solver are $\lambda_l = -1$ and $\lambda_r = +1$, the flux formula employed in the HLL solver (Eq. 4.1.2.2), reduces to the LLF flux formula (Eq. 4.1.2.1) without the further improvement suggested by Alic et al. (2007) to obtain second-order estimates of the interface fluxes.

The results of both solvers in this test basically overlap, indicating that in

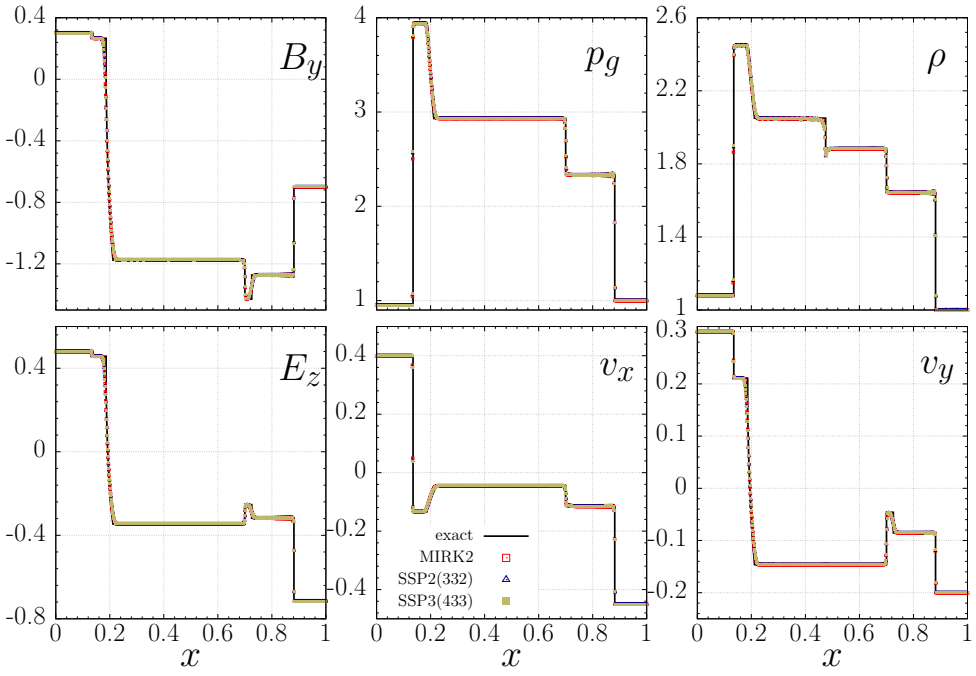

Figure 4.10: ST2: Comparison of the results obtained with different time-integration schemes: MIRK2, SSP2(332)-LUM and SSP3(443). In all cases we use, the HLL approximate Riemann solver, with MP9 spatial reconstruction and a CFL factor $C_{\rm CFL} = 0.1$. Upper panels: B_y component of the magnetic field, thermal pressure ($p_{\rm g}$), rest-mass density (ρ). Lower panels: E_z component of the electric field, v_x and v_y components of the velocity field.

situations where the dynamics is dominated by shocks or other discontinuities, the effective response of the two alternative methods described above is nearly the same. This is in contrast to the case studied for a smooth flow as that of Sec. 4.5.3, where the actual order of convergence of our method employing the LLF solver was significantly lower than that obtained with the HLL solver.

4.5.5.4 Shock Tube Problem 4

Here we explore the effects that the MP5, MP7 and MP9 reconstruction schemes have on the overall solution of a problem. In order to highlight the importance of the reconstruction, we consider the shock tube problem 4 (ST4) with a reduced number of points, $n_x = 100$, with respect to the *standard* value employed in the literature (Tab. 4.1; see also Sec. 5.2.6). We fix in this test the integration algorithm (SSP2(332)-LUM) and the HLL solver.

For this test, the initial discontinuity results into a contact discontinuity, which separates a fast rarefaction wave (at $x \simeq 0.05$ in Fig. 4.13), a rotational wave (at $x \simeq 0.44$), and a slow shock (at $x \simeq 0.46$), from a slow shock (at $x \simeq 0.56$), an Alfvén wave (at $x \simeq 0.57$) and a fast shock (at $x \simeq 0.97$). This

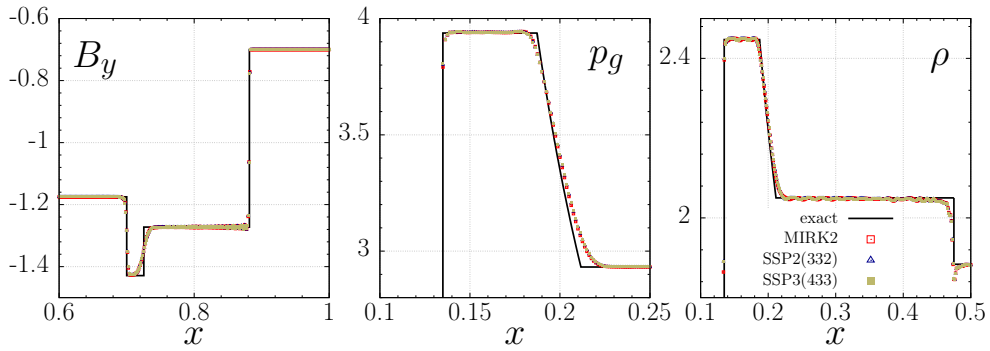

Figure 4.11: ST2: Zoom of several regions of interest in Fig. 4.10. From left to right: y component of the magnetic field (B_y), thermal pressure ($p_{\rm g}$) and mass density (ρ).

test shows the performance of the algorithm at resolving narrow structures. As can be seen in Fig. 4.14 none the implemented MP intercell reconstructions can satisfactory resolve the very narrow structures developed by some of the primitive variables displayed with the working resolution in this test. The small amplitude oscillations present in the uniform states of the Riemann fan typically develop when MP reconstructions are used. In the zoomed plots of Fig. 4.14, we note that the amplitude of the oscillations is slightly smaller for the MP9 reconstruction than for the other two cases considered (MP5 and MP7). A smaller CFL may ameliorate (but not eliminate) these oscillations.

4.5.5.5 Shock Tube Problem 5

In the shock tube problem 5 (ST5 hereafter), after a time $t = 0.4$, left-going fast (at $x \simeq 0.16$) and slow (at $x \simeq 0.53$) rarefaction waves are separated by a contact discontinuity (at $x \simeq 0.76$) from two right-going slow (at $x \simeq 0.86$) and fast (at $x \simeq 0.9$) shocks waves (see also Sec. 5.2.7).

We employ this test to show whether there are differences between the two algorithms we employ to recover the primitive variables from the conserved ones (Sec. 4.3). Thus, we compute the numerical solution using both, the FC analytic procedure to compute the Lorentz factor (Sec. 4.3.1) and the NR iterative algorithm to recover the thermal pressure (Sec. 4.3.2). We fix the time-integrator (SSP2(332)-LUM), the Riemann solver (HLLC), and the spatial reconstruction (MCL). In both cases the test is performed with $C_{\rm CFL} = 0.1$.

At the scale displayed in Fig. 4.15, we do not find significant differences between the two recovery algorithms tested. With both recovery methods our code captures the analytic solution reasonably well, at the same qualitative level as in other papers where this test has been performed (e.g. Del Zanna et al., 2003), though the capturing of the narrow structure between the two

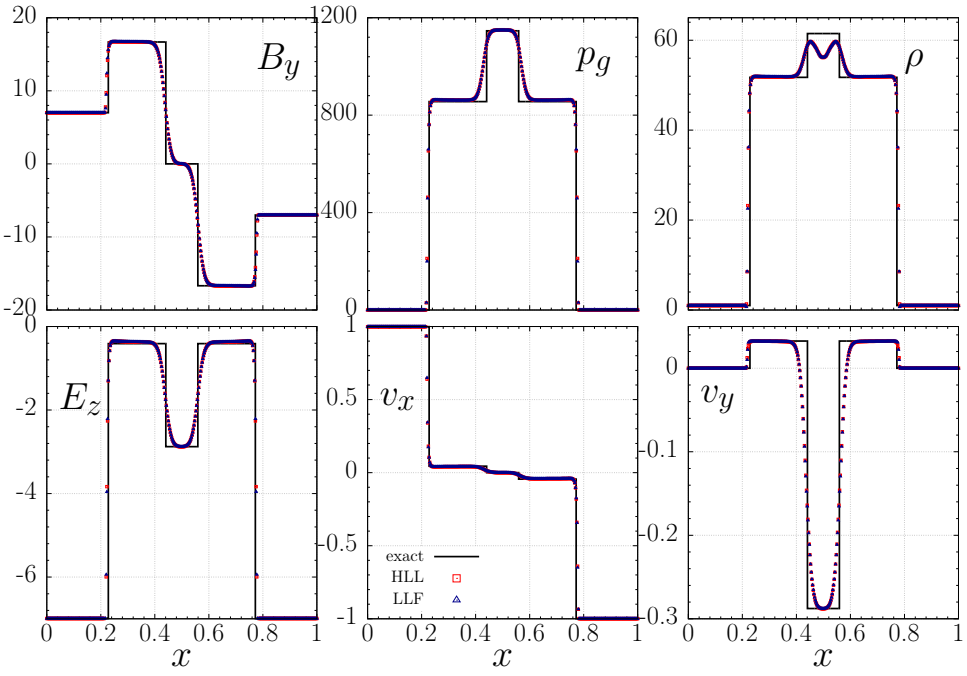

Figure 4.12: ST3: Comparison of the results obtained with the HLL and LLF solvers. This test has been executed with SSP2(332)-LUM time integrator scheme, the MCL intercell reconstruction on a grid of $n_x = 400$ points with a CFL factor $C_{\text{CFL}} = 0.1$. Upper panels: B_y component of the magnetic field, thermal pressure (p_{g}), rest-mass density (ρ). Lower panels: E_z component of the electric field, v_x and v_y components of the velocity field.

right going shocks is not as good as in RMHD (compare Fig. 2 Balsara (2001) with our Fig. 4.15). A more thoughtful examination of the data reveals tiny differences at the level of the relative tolerance of the iterative NR algorithm (in our case set to 10^{-10}). These differences are irrelevant for the ST5 Riemann test. They are, however, important in other more complex tests in which different waves may interact on a single numerical zone. Indeed, Dumbser and Zanotti (2009) point that the accuracy of the analytic FC procedure tends to be insufficient for practical RRMHD applications and, it is often employed to obtain initial (seed) values for an iterative solution of the same equation.

4.5.6 Resistive rotor

The relativistic ideal MHD version of this test was initially proposed by Del Zanna et al. (2003), while a resistive version has been introduced by Dumbser and Zanotti (2009), to which we hereby refer as resistive rotor (RR). We implement the resistive version in the form presented by Bucciantini and Del Zanna (2013), according to which, a circular region with radius $r = 0.1$, with high density, $\rho = 10$, and rotating at high relativistic angular velocity $\Omega = 8.5$

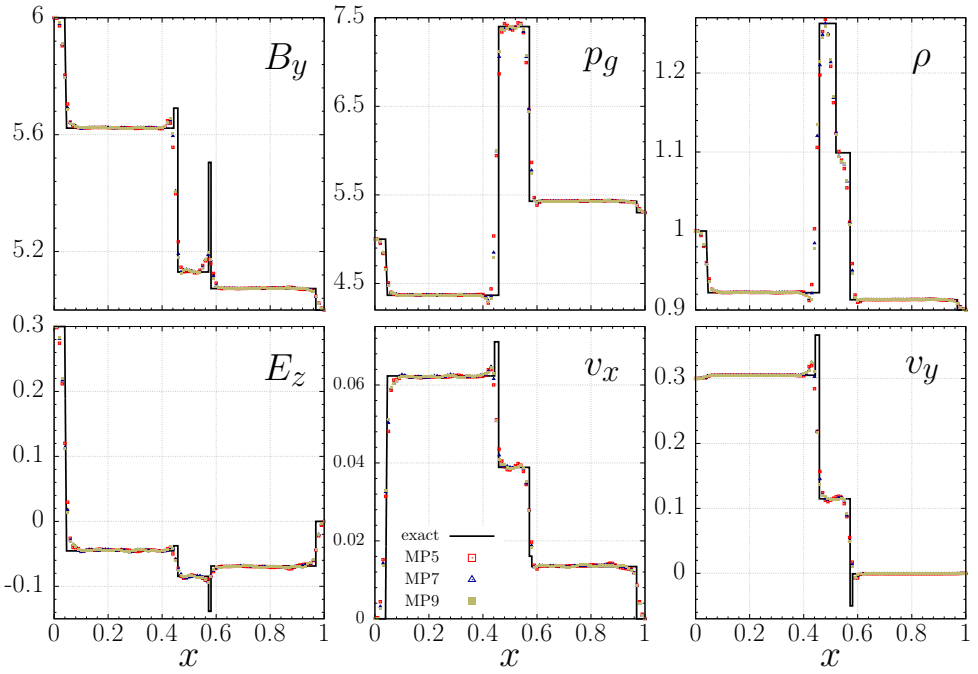

Figure 4.13: ST4: We show in a reduced grid of $n_x = 100$ points the performance of MP5, MP7 and MP9 spatial reconstruction schemes. We use the RKIMEX time-integration algorithm SSP2(332)-LU and the HLL solver with a CFL factor $C_{\rm CFL} = 0.1$. Upper panels: B_y component of the magnetic field, thermal pressure ($p_{\rm g}$), rest-mass density (ρ). Lower panels: E_z component of the electric field, v_x and v_y components of the velocity field.

is located within a medium at rest, with a lower density $\rho = 1$. The pressure $p_{\rm g} = 1$ and the magnetic field $(B_x, B_y, B_z) = (1, 0, 0)$ are uniform in the whole domain. The initial electric field is set like in ideal RMHD, and the adiabatic index is $\gamma = 4/3$.

Figure 4.16 shows a snapshot and Fig. 4.17 the profile in $x = 0$, for the gas pressure $p_{\rm g}$ and the electric field component E_z at $t = 0.3$, in different conductivity regimes. The results in the figures are computed on a grid of 300×300 numerical zones and with $C_{\rm CFL} = 0.1$. We observe that the numerical solution in the high conductivity regime presents all the morphological properties characteristic of the ideal RMHD limit, with a central region of low thermal pressure and torsional Alfvén waves adopting a spiral pattern. The outgoing propagation of the torsional Alfvén waves is bounded by a fast shock with a quasi-elliptical structure slightly elongated along an axis that forms an angle of $\sim 35^\circ$ with respect to the vertical direction. As the conductivity decreases, the eccentricity of the limiting outer shock decreases until it adopts an almost circumferential shape for $\sigma = 10$. This transition of the structural shape is induced by the progressive degeneration of Alfvén waves into electromagnetic

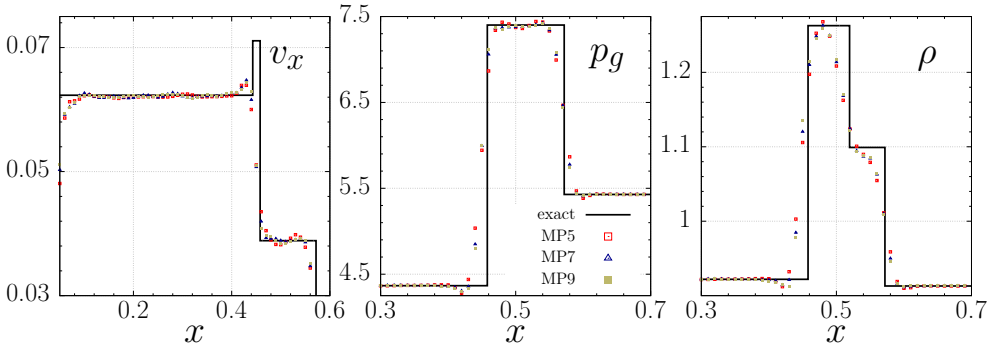

Figure 4.14: ST4: Zoomed image of several regions of interest of Fig. 4.13. From left to right: v_x component of the velocity field, thermal pressure (p_g) and rest-mass density (ρ).

waves, which propagate almost isotropically at the speed of light. Another relevant difference in the low-σ regime is that the acoustic waves propagate at a fraction of the speed of light, and thus, the pressure front (Fig. 4.16 top right) is left behind the electromagnetic front (Fig. 4.16 bottom right).

Figure 4.16 can be directly compared with Fig. 5.17, where a higher order reconstruction (MP5) and a different Riemann solver (HLLC) are employed. As we discuss in Sec. 5.2.8, the high-order reconstruction drives some small scale oscillations at the tail of the rarefaction wave that generates as the central core expands nearly isotropically in the case of $\sigma = 10$. These oscillations are absent using an MCL intercell reconstruction.

Since there is not analytic solution for the RR test, we have repeated it employing a few different time integration algorithms fixing the numerical resolution (300×300), the CFL factor, the Riemann solver (HLL) and the spatial reconstruction (MCL). The results are displayed in Fig. 4.17. Though some of the time-advance methods allow for a larger CFL factor, others fail even for $C_{\rm CFL} = 0.15$. Thus, for the sake of comparison, we fix in all cases $C_{\rm CFL} = 0.1$. The similarity of all the results in the nearly ideal regime ($\sigma = 10^6$) is an excellent validation of the numerical methods we are using. Only the MIRK2 time-integrator seems to slightly clip the extrema of E_z (Fig. 4.17 bottom left panel) at the same time that yields thermal pressure maxima that slightly overshoot the ones computed with the other methods of time-integration. This trend to clip the E_z extrema and overshoot the pressure maxima exacerbates as the conductivity decreases. Obvious discrepancies with the other methods are visible for $\sigma = 10$ in the right panels of Fig. 4.17. In practice, the differences shown by the MIRK2 method are not relevant, as we are more interested in the high-conductivity regime (which is relevant for most astrophysical applications). However, this is another hint pointing towards the (very likely repairable) deficiencies of the MIRK methods as implemented in Aloy and Cordero-Carrión (2016).

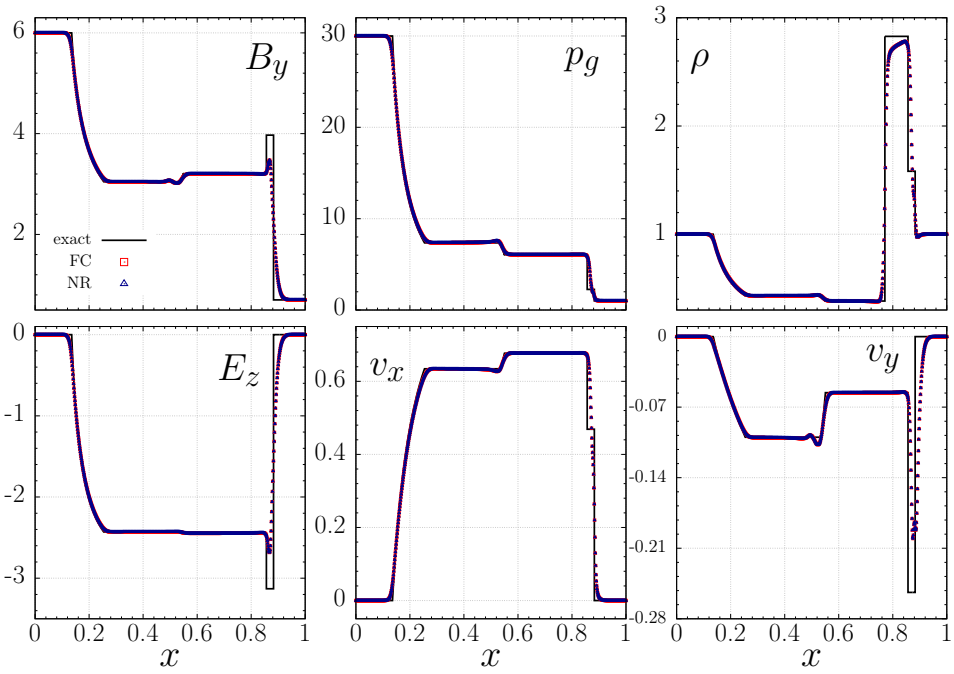

Figure 4.15: ST5: Comparison of the FC and NR primitive variables recovery techniques for a time integration scheme SSP2(332)-LUM and MCL slope limiter. Upper panels: B_y component of magnetic field, thermal pressure (p), mass density (ρ). Lower panels: E_z component of electric field, v_x and v_y components of velocity field.

We have also employed this multidimensional test to calibrate the influence of the different parameters employed in the divergence cleaning method implemented in our code (Sec. 4.4). Using the same three values of the conductivity as above and fixing the time-integration scheme (MIRK2), the Riemann solver (HLL), and the spatial reconstruction (MCL), we display the values of the scalar potential ϕ in Fig. 4.18 along the line $x = 0$, $y > 0$. The different symbols and colors correspond to different values of the parameter $\aleph_\phi$ (Eq. 4.47). We note that $v_z = B_z = 0$, thus, the only non zero component of the electric field is E_z. As the test is two-dimensional and we assume that the z-derivatives of all variables vanish (in particular $\partial_z E_z = 0$), the value of the scalar potential ψ is zero. According to Mignone and Tzeferacos (2010), the errors associated with the violation of the $\nabla \cdot \mathbf{B} = 0$ constraint are minimised when $\aleph_\phi \in [0, 1]$. Komissarov (2007) argues that having two different parameters controlling the solenoidal magnetic field constraint and $\nabla \cdot \mathbf{E} = q$ is unnecessary, but note that he employs κ as a parameter (see the relation between κ and $\aleph$ in Eq. 4.4). We, however, find that using two different values for $\aleph_\phi$ and $\aleph_\psi$ is worth in some cases (see below). Empirically, we find that $\aleph_\phi \gtrsim 1$ yields the best results. Furthermore, in some cases it is useful to employ values as large as $\aleph_\phi \simeq 10$ to

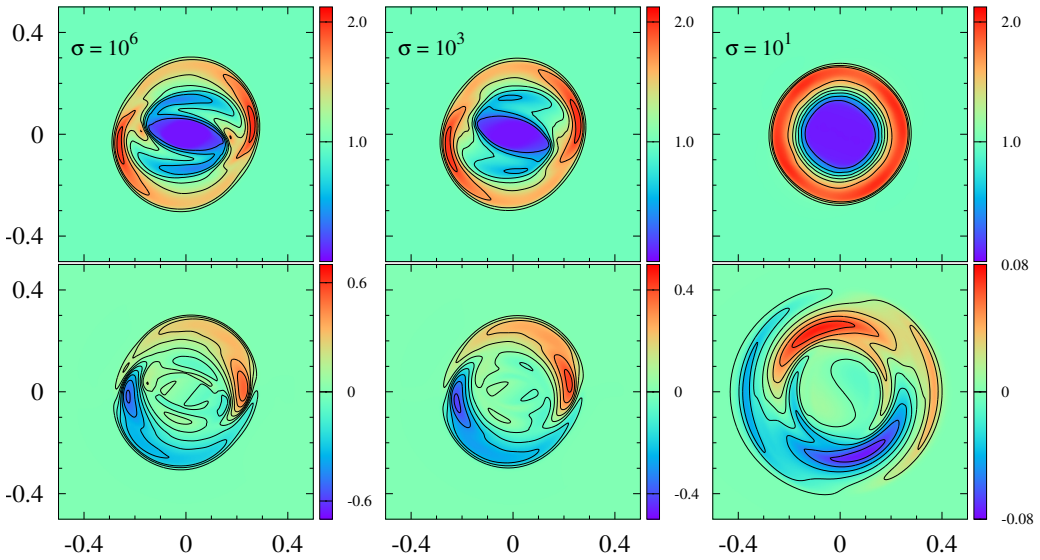

Figure 4.16: Snapshots of the pressure (upper panels) and of E_z (lower panels) for the resistive rotor computed with a grid of 300×300 uniform zones at $t = 0.3$. The spatial reconstruction, Riemann solver and time-integrator are MCL, HLL and MIRK2, respectively. We show different values of conductivity, the nearly ideal case $\sigma = 10^6$ (left panel), $\sigma = 10^3$ (central panel) and the resistive case $\sigma = 10$ (right panel). Note the change in the color scale of the lower panels to adapt to the progressively decreasing electric field strength in the low-conductivity regime.

avoid code failures. However, values $\aleph > 100$ result in bizarre dynamics and yield catastrophic numerical errors. To a large extent this is due to the fact that the equations of the scalar potentials also become stiff if $\aleph \gg 1$.

Focusing on the high conductivity regime (Fig. 4.18 left panel) and comparing the cases in which $\aleph_\phi = 0.1$ and $\aleph_\phi = 10$, we observe a significant decrease of the magnitude of ϕ (approximately, by a factor of 3 to 5 at the maxima located at $y \simeq 0.07$). Furthermore, the region where the most significant deviations from zero occur is more narrowly focused in the parts of fluid with the largest gradients (i.e. associated to the regions crossed by torsional Alfvén waves). We observe a reduction of the magnitude of ϕ and, hence, the errors induced by the violation of the solenoidal constraint, for increasing values of $\aleph_\phi$. This trend is qualitatively independent of the value of σ, but for the low-sigma regime (Fig. 4.18 right panel), the differences in the magnitude of ϕ for values of $\aleph_\phi \in [1, 10]$ are small and there is not obvious reason to choose a particular value of $\aleph_\phi$ in the aforementioned interval. However, since larger values of $\aleph_\phi$ yield better results in the nearly ideal limit, we tend to use in our simulations values $\aleph_\phi \in [1, 10]$. We anticipate that we have risen the values of the previous parameter $\aleph_\phi = 15$ in some applications of Chap. 7 since, otherwise, our code failed to compute any solution when the Alfvén velocity of the

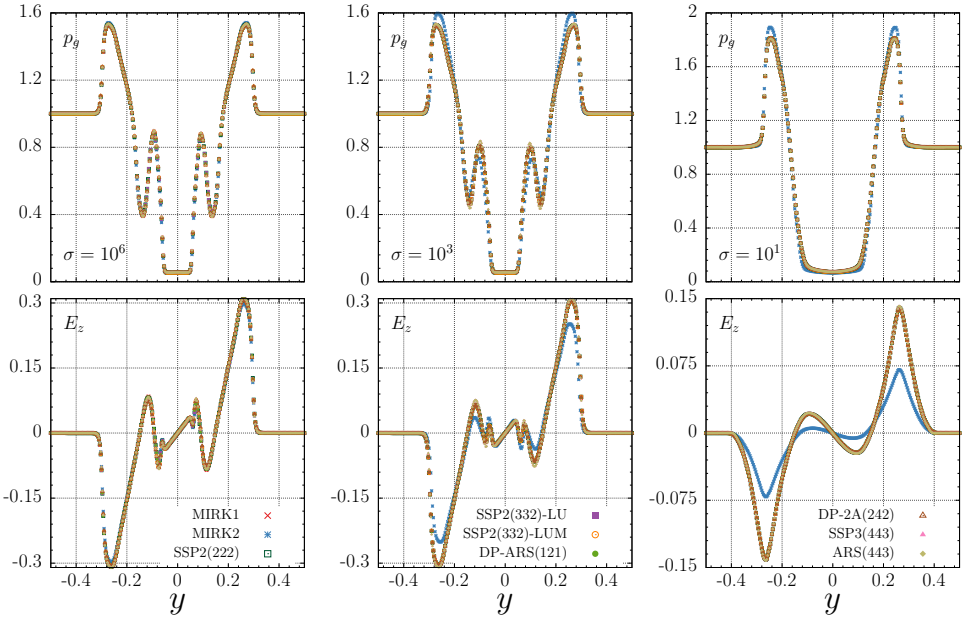

Figure 4.17: Profiles of Fig. 4.16 at $x = 0$ of the gas pressure (top panels) and of E_z (bottom panels) at $t = 0.3$. We show different values of conductivity $\sigma = 10^6$ (left panels), $\sigma = 10^3$ (central panels) and $\sigma = 10$ (right panels).

background medium is large (e.g. when $v_A \gtrsim 0.75$; see Sec. 7.2).

In order to test the performance of the scalar potential ψ at controlling the constraint $\nabla \cdot \mathbf{E} = q$, we have implemented a variant of the standard RR test that we call *modified* RR test. The physical and numerical setup It is exactly like the RR test, but with an additional magnetic field component perpendicular to the plane of rotation, i.e., $(B_x, B_y, B_z) = (1, 0, 10^{-2})$.

We observe in Fig. 4.19 similar qualitative trends as found in the case of the variation in the $\aleph_\phi$ parameter. Rising the value of $\aleph_\psi$ lowers the absolute value of ψ. This trend in independent of the conductivity. However, the magnitude of ψ is significantly smaller in the low-sigma regime (compare the left and right panels of Fig. 4.19). Another important conclusion we draw is that the parameters $\aleph_\phi$ and $\aleph_\psi$ are completely independent in their impact on the control of each of the constrains they have to deal with. Note that in simulations with the same $\aleph_\psi$ but different $\aleph_\phi = 1$ and $\aleph_\phi = 10$, the scalar potential ψ is the same (Fig. 4.19).

4.5.7 Cylindrical Explosion in the nearly ideal regime

The cylindrical explosion (CE) test probes the capabilities of a numerical scheme to deal with strong shocks propagating into a magnetically dominated

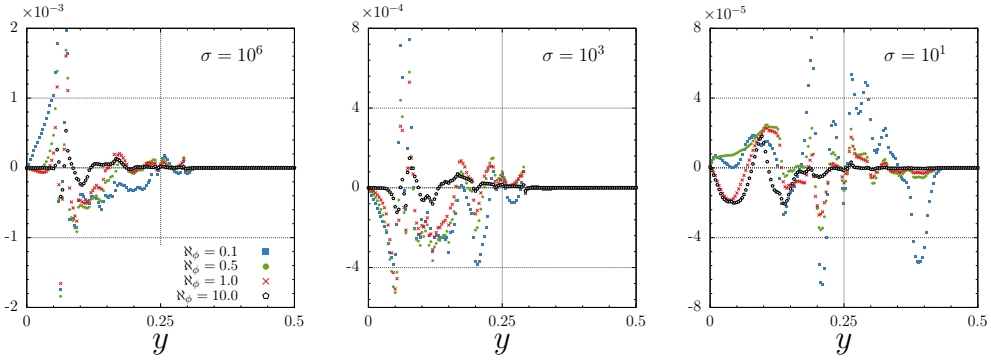

Figure 4.18: Profiles at $x = 0$ of the scalar potential ϕ for the standard RR test. Because of the symmetry of the test, only values $y \geq 0$ are displayed. The profiles at $t = 0.3$ are showed for distinct values of the paramater $\aleph_\phi$ and fixed $\aleph_\psi = 10$. From left to right we display distinct values of the conductivity, from the nearly ideal case $\sigma = 10^6$ (left panel), to the resistive regime $\sigma = 10$ (right panel). This test has been made with the HLL Riemann solver, the MIRK2 time-integrator, the MCL spatial reconstruction and $C_{\rm CFL} = 0.1$. Note the differences in the vertical scales among the three panels.

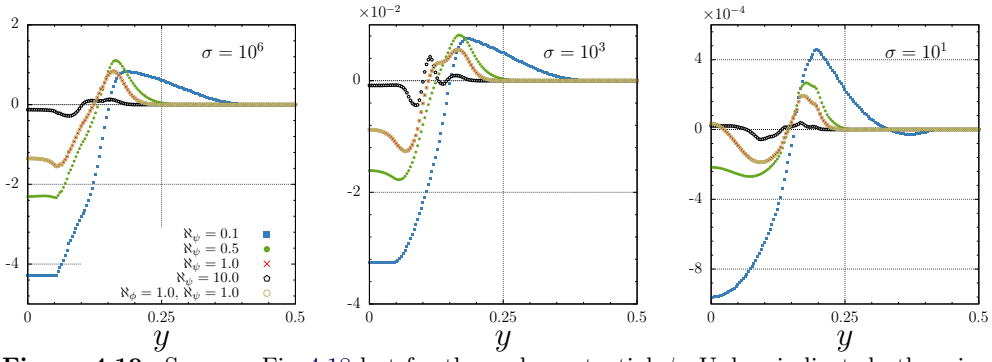

Figure 4.19: Same as Fig. 4.18 but for the scalar potential ψ. Unless indicated otherwise in the legends, we fix $\aleph_\phi = 10$ and vary $\aleph_\psi$.

medium. In the 2D version of this test a uniform magnetic field $(B_x, B_y, B_z) = (B_0, 0, 0)$ is set up in a computational domain $-6 \leq x \leq 6$, $-6 \leq y \leq 6$, which is at rest. The central region $r := \sqrt{x^2 + y^2} < 1$ is filled with a gas pressure ($p_{\rm g,c}$) and rest-mass density $\rho_{\rm c}$ (much) higher than elsewhere in the (x, y) plane, where the values of the pressure, $p_{\rm g,b}$, and rest-mass density, $\rho_{\rm b}$, are such that $\xi_{\rm p} := p_{\rm g,c}/p_{\rm g,b} \gg 1$ and $\xi_\rho := \rho_{\rm c}/\rho_{\rm b} \gg 1$. The strength of the shock developed from this initial state depends on the ratios $\xi_{\rm p}$ and ξ_ρ. The larger their values, the stronger the fast-magnetosonic shocks that develop. Typically central values are $p_{\rm g,c} = 1$ and $\rho_{\rm c} = 0.01$, whereas the values elsewhere are very small, e.g., $p_{\rm g,b} = 3 \times 10^{-5}$ and $\rho_{\rm c} = 10^{-4}$. The shape of the shock depends on B_0. Larger values of B_0 yield more elongated (eventually jet-like) structures.

To ameliorate the numerical difficulty of resolving the initial pressure and density jump between the region $r < 1$ and the rest of the domain, a smooth

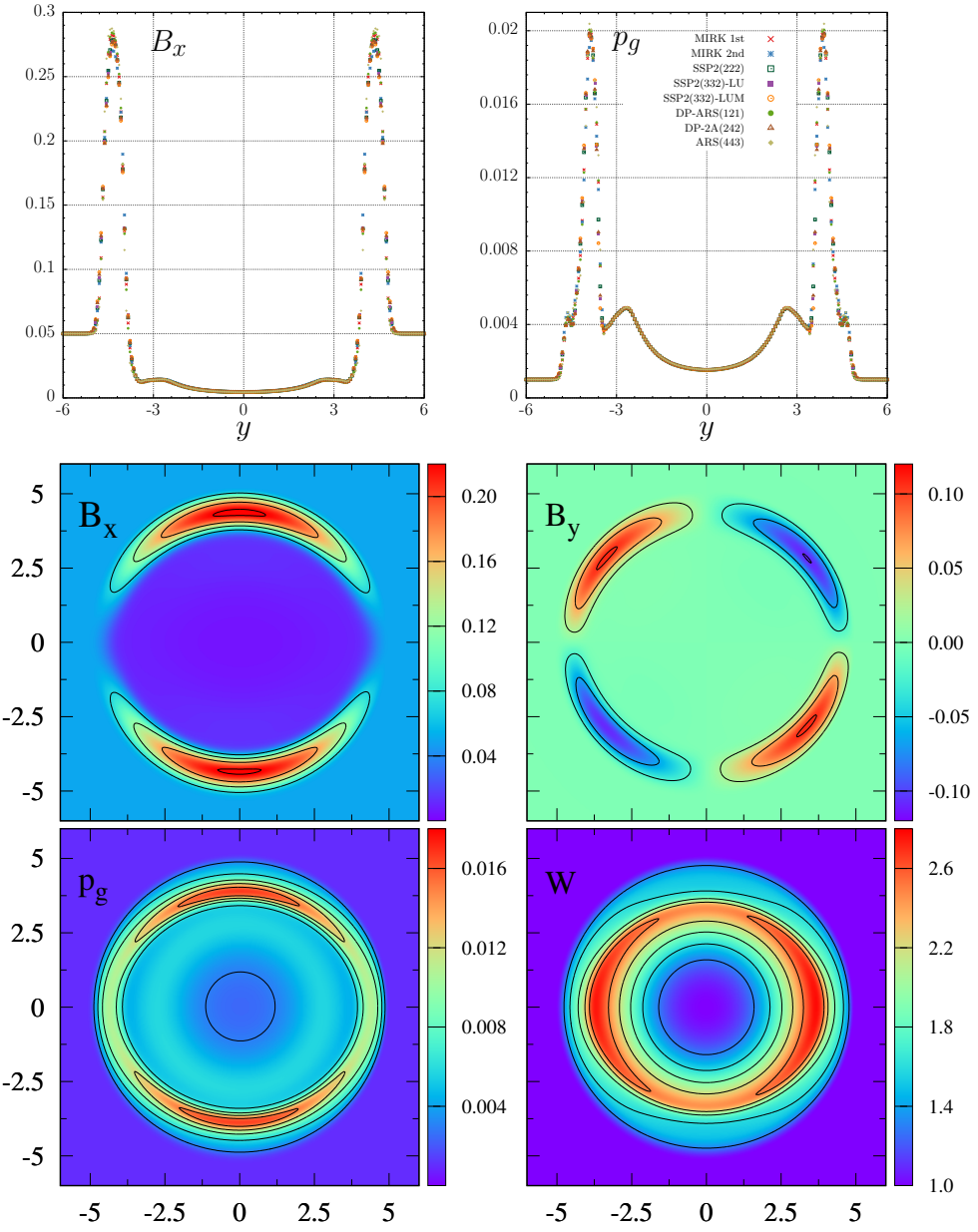

Figure 4.20: Upper panels: profiles at $x = 0$ of B_x (left) and $p_{\rm g}$ (right) for a variety of time integration schemes (see legends). Middel row: snapshots of B_x (left) and B_y (right). Lower panels: gas pressure (left) and Lorentz factor (right), at time $t = 4$. In all panels, we fix the Riemann solver (HLL), the intercell reconstruction (MCL) and $C_{\rm CFL} = 0.1$.

transition layer is customarily set up. Very large values of $\xi_{\rm p}$ and ξ_ρ combined with large values of $B_0 \simeq 1$ typically require special methods to deal with

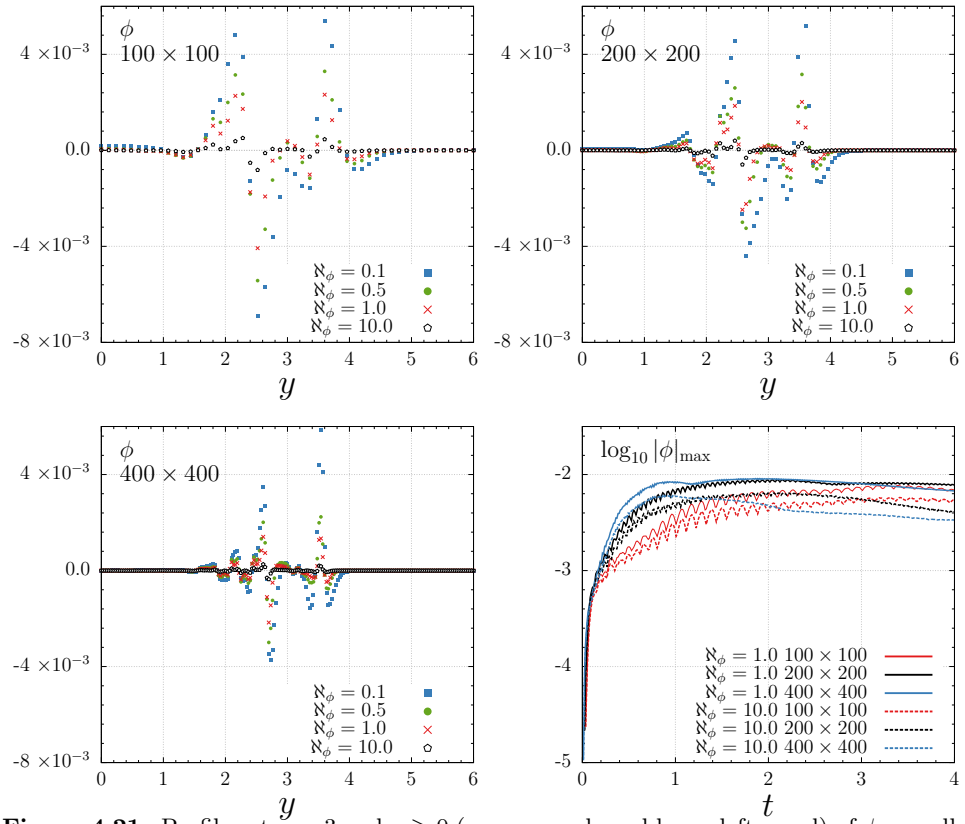

Figure 4.21: Profiles at $x = 3$ and $y \geq 0$ (upper panels and lower left panel) of ϕ as well as the time evolution of the logarithm of the maximum absolute value of ϕ (lower right panel) using different resolutions in the CE test. The profiles at $t = 4.0$ are shown for distinct values of the paramaters $\aleph_\phi$ (see legend) and fixed $\aleph_\psi = 1$. In all the tests we fix the Riemann solver (HLL), the time-integration scheme (MIRK2), the intercell reconstruction (MCL) and $C_{\rm CFL} = 0.1$. The numerical resolutions employed are 100×100, 200×200 and 400×400 cells for the upper left, upper right and lower left panels, respectively.

strong shocks in extremely magnetized media (see,e.g. Martí, 2015). Since we have not implemented these special methods and in order to reduce the numerical difficulty of the problem, we consider a milder version of the CE, similar to that of Palenzuela et al. (2009), in which $B_0 = 0.05$, and the pressure and rest-mass density are distributed according to

$$p_{\rm g} = \begin{cases} 1 & r \leq 0.8 \\ e^{-\alpha_1 (r - 0.8)} & 0.8 < r < 1.0 \\ 10^{-3} & 1.0 < r \end{cases} , \tag{4.57}$$

$$\rho = \begin{cases} 10^{-2} & r \leq 0.8 \\ 10^{-2}\ e^{-\alpha_2 (r - 0.8)} & 0.8 < r < 1.0 \\ 10^{-3} & 1.0 < r \end{cases} , \tag{4.58}$$

with $\alpha_1 = -\ln(0.1)/0.2$ and $\alpha_2 = -\ln(10^{-3})/0.2$. The test is performed in the nearly ideal limit ($\sigma = 10^6$) and we set $\gamma = 4/3$. The reference numerical grid consists of 200×200 uniform cells, but other grid spacings have been considered (100×100 and 400×400 zones). Our code may handle larger values of B_0 and also larger pressure and density jumps from the central core to the background medium (for instance, we show in Sec. 5.2.9 the CE test with $B_0 = 0.1$). However, this requires lowering the $C_{\rm CFL}$ and increasing the resolution to values which are prohibitive to perform the diversity of algorithmic tests we have done here. Indeed, as shown in the upper panels of Fig. 4.20, we have tested many different RKIMEX time-integrators, in addition to the two MIRK schemes we have implemented in our code. Remarkably, all of them yield very similar results, both quantitatively and quantitatively and the solutions are regular everywhere. Furthermore, they are quantitatively and qualitatively the same as in Palenzuela et al. (2009). In all these tests, we have fixed the MCL intercel reconstruction and the HLL Riemann solver (testing of the HLLC Riemann solver in this test is deferred to Sec. 5.2.9).

Figure 4.21 shows the profiles of the scalar potential ϕ for different values of the parameter $\aleph_\phi$. As in the case of the RR test, we observe that $\aleph_\phi \geq 1$ (especially $\aleph_\phi = 10$) significantly reduce the errors associated with the violations of the solenoidal constraint. Compared with Fig. 4.18, the values of ϕ in the CE test are of the same order of magnitude as in the RR test (i.e. $\phi \sim 10^{-3}$).

It is instructive to look at the time evolution of the maximum values of the logarithm of $|\phi|$ displayed in the lower right panel of Fig. 4.21. We observe that the magnitude of ϕ is larger for finer grids than for coarser ones during a relatively short initial period ($0.3 \lesssim t \lesssim 2$). Afterwards, the maximum magnitude of ϕ decreases faster for finer grids than for coarser ones. This is related to the initial transient during which the full set of Riemann structures (shocks, contacts, rarefactions, etc.) develops and separate from each other by more than a few numerical zones as they move away from the center of the domain. Furthermore, looking at the profiles of ϕ at different resolutions shown in Fig. 4.21 (upper panels and lower left panel), we conclude that $|\phi|_{\rm max}$ is determined by the amplitude of the constraint violation in the transition region between the central cylindrical (high-pressure, high-density) region. Everywhere else, increasing the resolution reduces the magnitude of ϕ. As expected, this means that the violation of the solenoidal constraint are reduced for finer grids. The only exception is the, somewhat artificial, transition region between the central exploding core and the rest of the domain. Since there is no further physical interest in improving this transition region, we have not investigated more closely the effect of other transition models different from the exponential shape used in the initialization of this test (Eqs. (4.57) and (4.58)).

Chapter 5

An HLLC Approximate Riemann solver for RRMHD

The numerical solution of the Riemann problem is one of the building blocks of any Godunov-type method for the solution of either conservation or balance laws. In these methods the spatial discretization of the problem solution yields jumps of different variables at every cell interface in a computational grid. In Chap. 3, we have seen that the existence of source terms in the system of equations has impeded us to find an exact solution of the Riemann problem in RRMHD. However, the exact solution of the Riemann problem is not usually of interests for practical numerical applications due to its (typically) large computational cost. Also, the potential benefit of knowing the exact solution of the Riemann problem is reduced by its necessary time averaging through any time step of a simulation. This averaging is needed to obtain the *integral effect* of the fluxes of the equations on a time step. For these reasons, constructing robust *approximate* Riemann solvers is a common and very widespread practice to numerically solve hyperbolic systems of conservation laws.

Approximate Riemann solvers of Godunov-type have proven their computational efficiency in classical magnetohydrodynamics (MHD) and RMHD simulations. Among them, the HLL solver, Harten et al. (1983), has been commonly used due to its ease implementation and robustness. However, the HLL formulation cannot resolve isolate contact discontinuities and is more diffusive than other approximate solvers. Toro et al. (1994) corrected this deficiency by designing an HLLC solver, for Euler equations, by introducing in the Riemann fan two intermediate states, separated by a contact wave ("C" denotes this special feature) in contrast to the single average state of the HLL solver. Since then, different HLLC Riemann solver have been designed for MHD (Gurski (2004); Li (2005)) and RMHD (Honkkila and Janhunen (2007); Kim and Bal-

sara (2014); Mignone and Bodo (2006)).

In this chapter we present our work published in MNRAS (Miranda-Aranguren et al., 2018) on a new approximate Riemann solver for the augmented system of equations of RRMHD that belongs to the family of HLLC Riemann solvers. In HLLC solvers, the solution is approximated by two constant states flanked by two shocks separated by a contact wave. The format and the contents of the paper Miranda-Aranguren et al. (2018) have been adapted to the ones in this thesis. In particular, the introduction and the section on equations of Miranda-Aranguren et al. have been removed, since they have been incorporated in the previous chapters. Furthermore, the discussions on the characteristic properties of the augmented system of RRMHD equations and on bounded source terms have been included in Secs. 3.1 and 3.3, respectively. Finally, the conclussions of Miranda-Aranguren et al. (2018) have been joined with the global conclusions of this thesis in Chap. 8. The RRMHD system of equations was implemented in the Cueva code (App. A) using the numerical method that we descrive in Chap. 4.

The solver is obtained in Sec. 5.1 for Resistive Special Relativistic MHD, but can be used also in applications involving General Relativistic gravitational fields resorting to the methodology devised in Pons et al. (1998). The accuracy of the new approximate solver is calibrated through standard one-dimensional (1D) and two-dimensional (2D) numerical test performed in Sec. 5.2. We point out that a more extended testing and validation of the Cueva code is presented in Chap. 4. Here, we restrict to the tests that show specifically the performance of the HLLC solver over other solvers like, e.g. the HLL solver. In Sec. 7.1, we present the simulations of relativistic TMs originally included in our paper Miranda-Aranguren et al. (2018), in addition to further models which were not included in our paper. These models serve us for the twofold purpose of validating our models against existing results in the literature for relativistic TMs and, also to a lesser extent, to calibrate the benefits of the new HLLC solver in practical astrophysical plasma applications.

5.1 HLLC Solver

As we have already done in Sec. 4.1.2, we consider for simplicity a Riemann problem along the $x-$coordinate direction set at the location $x_{i+1/2}$, i.e. the interface between two consecutive cells, i and $i+1$ as in Eq. (4.12). An HLLC approximate Riemann solver avoids the full characteristic decomposition of all the wave pattern in the Riemann fan by only introducing a contact wave with constant speed, λ^*, which separates two intermediate states $(\mathbf{U}_l^*, \mathbf{U}_r^*)$ bounded by two fast shocks. More explicitly, the solution of the initial value problem

(Eq. (4.12)) in each cell interface is written as

$$\mathbf{U}(0,t) = \begin{cases} \mathbf{U}_l & \text{if } \lambda_l \geq 0, \\ \mathbf{U}_l^* & \text{if } \lambda_l < 0 \leq \lambda^*, \\ \mathbf{U}_r^* & \text{if } \lambda^* < 0 \leq \lambda_r, \\ \mathbf{U}_r & \text{if } \lambda_r < 0, \end{cases} \tag{5.1}$$

where λ^* is the propagation velocity of the contact wave and λ_l, λ_r are estimates of the maximum signal speeds propagating to the left and to the right of the initial discontinuity, respectively. Since in RRMHD the electromagnetic fields propagate at the speed of light Eq. (3.5), we set (in most cases) $\lambda_l = -1$ and $\lambda_r = 1$, but for the sake of clarity, we maintain the notation λ_l, λ_r throughout the chapter. There is also another reason why it is interesting keeping explicitly the values of λ_l and λ_r, namely, the possibility of *increasing* the diffusivity of the solver in case of numerical need. This can be done by rising the absolute values of λ_l and λ_r.

The numerical fluxes corresponding to the assumed solution (5.1) are:

$$\tilde{\mathbf{F}} = \begin{cases} \mathbf{F}_l & \text{if } \lambda_l \geq 0, \\ \mathbf{F}_l^* & \text{if } \lambda_l < 0 \leq \lambda^*, \\ \mathbf{F}_r^* & \text{if } \lambda^* < 0 \leq \lambda_r, \\ \mathbf{F}_r & \text{if } \lambda_r < 0, \end{cases} \tag{5.2}$$

with $\mathbf{F}_l = \mathbf{F}(\mathbf{U}_l)$ and $\mathbf{F}_r = \mathbf{F}(\mathbf{U}_r)$ and $\mathbf{F}_l^*$, $\mathbf{F}_r^*$ the intermediate flux functions, whose expressions will be found in the next subsections. As we have remarked in Sec. 4.1.2.2, the fact that we typically take $\lambda_l = -1 < 0$ and $\lambda_r = +1 > 0$, makes that in most applications only the two central branches of Eq. (5.2) are used. Thus, the augmented RRMHD fluxes are always computed as if the flow was *subsonic* in the equivalent HLLC solver for RHD.[1]

5.1.1 HLLC consistency conditions

As we have argued in Sec. 3.3, a bounded source term does not change the RH conditions at a discontinuity and, thus, we can use the following set of RH conditions for the shocks and the contact wave in the HLLC solution:

$$\lambda_l(\mathbf{U}_l^* - \mathbf{U}_l) = \mathbf{F}_l^* - \mathbf{F}_l, \tag{5.3}$$

$$\lambda^*(\mathbf{U}_r^* - \mathbf{U}_l^*) = \mathbf{F}_r^* - \mathbf{F}_l^*, \tag{5.4}$$

$$\lambda_r(\mathbf{U}_r - \mathbf{U}_r^*) = \mathbf{F}_r - \mathbf{F}_r^*. \tag{5.5}$$

[1] See footnote 3 in Sec. 4.1.2.2

Following Mignone and Bodo (2006), we find the consistency conditions for conserved intermediate variables by adding the tree equations in (5.3)-(5.5),

$$\frac{(\lambda^* - \lambda_l)\,\mathbf{U}_l^* + (\lambda_r - \lambda^*)\,\mathbf{U}_r^*}{\lambda_r - \lambda_l} = \mathbf{U}^{\rm hll}, \tag{5.6}$$

where $\mathbf{U}^{\rm hll}$ is given by Eq. (4.15). Likewise, dividing each equation in (5.3)-(5.5) by their corresponding λ on the left-hand sides and adding all the resulting expressions one finds

$$\frac{(\lambda^* - \lambda_l)\,\lambda_r\mathbf{F}_l^* + (\lambda_r - \lambda^*)\,\lambda_l\mathbf{F}_r^*}{\lambda_r - \lambda_l} = \lambda^*\mathbf{F}^{\rm hll}, \tag{5.7}$$

with $\mathbf{F}^{\rm hll}$ obtained from Eq. (4.16) as a function of $\mathbf{U}_r$, $\mathbf{U}_l$, λ_r and λ_l. We point out that employing the (global) values for the system limiting speeds $\lambda_l = -1$ and $\lambda_r = +1$, the HLL flux (4.16) reduces to the Local Lax-Friedrich flux.

Building an HLLC solver for the RRMHD system of equations ultimately consists in obtaining the expressions for $\mathbf{F}_l^*$ and $\mathbf{F}_r^*$ in (5.2). In general, $\mathbf{F}_l^* \neq \mathbf{F}(\mathbf{U}_l^*)$ and $\mathbf{F}_r^* \neq \mathbf{F}(\mathbf{U}_r^*)$. Instead, the RH jump conditions (5.4) provide a set of relations between the starred numerical fluxes and the corresponding state vectors $\mathbf{U}_l^*$ and $\mathbf{U}_r^*$. More precisely, if $\mathbf{U}_l^*$ and $\mathbf{U}_r^*$ are known, from Eqs. (5.3) and (5.5), we have

$$\begin{aligned}\mathbf{F}_l^* &= \mathbf{F}_l + \lambda_l(\mathbf{U}_l^* - \mathbf{U}_l),\\ \mathbf{F}_r^* &= \mathbf{F}_r + \lambda_r(\mathbf{U}_r^* - \mathbf{U}_r).\end{aligned} \tag{5.8}$$

If each state vector has n components ($n = 14$ in the augmented RRMHD system of equations (2.37)), the problem at hand has $4n+1$ unknowns, i.e. $\mathbf{F}_l^*$, $\mathbf{F}_r^*$, $\mathbf{U}_l^*$, $\mathbf{U}_r^*$, and λ^*. In addition, there are four ancillary variables, $v_{x,r}^*$, $v_{x,l}^*$, P_r^* and P_l^*, originating from the fact that the fluxes, Eq. (2.39), cannot be expressed in closed form only as a function of the conserved variables. However, if we include these ancillary variables as a part of our problem, the momentum in the $x-$direction is not an independent variable, since using Eqs. (2.26) and (2.27), it can be written as

$$S_{x,a}^* = (\mathbf{E}_a^* \times \mathbf{B}_a^*)_x + (\mathcal{E}_a^* + P_a^* - (\mathbf{E}_a^*)^2 - (\mathbf{B}_a^*)^2)v_{x,a}^*, \tag{5.9}$$

where the subscript $a = l, r$ refers to each of the two states to the left and to the right of the contact wave. Thus, we have to find $4n+5$ relations among the unknowns. Two of them are provided by Eq. (5.9). There are $2n$ consistency relations (5.6) and (5.7). We advance that part of the n RH conditions across the middle wave, Eq. (5.4), become trivially satisfied (and thus replaced) by the subsequent assumptions that we employ to find the remaining $2n+3(= 31)$ equations. We chose these additional equations in the following way. First, we

assume the continuity of a subset of the conserved variables and of the four ancillary variables. Second, we assume the functional dependence of the fluxes in the starred regions with the conserved and ancillary variables. Specifically, we impose continuity of the charge density, of the scalar potentials ϕ and ψ as well as of the magnetic and electric field components across the contact wave,

$$\begin{aligned} &q^*_r = q^*_l := q^*, \quad B^*_{i,r} = B^*_{i,l} := B^*_i, \quad E^*_{i,r} = E^*_{i,l} := E^*_i, \\ &\phi^*_r = \phi^*_l := \phi^*, \quad \psi^*_r = \psi^*_l := \psi^*, \end{aligned} \tag{5.10}$$

where $i = x, y, z$. For the ancillary variables, we impose continuity of the total pressure and of the normal component of the velocity, i.e.

$$P^*_r = P^*_l := P^*, \quad v^*_{x,r} = v^*_{x,l} = \lambda^*. \tag{5.11}$$

Notice that in the above equation, we have assumed that the speed of the contact wave is equal to the (average) normal velocity over the Riemann fan. We point out that one may choose different sets of variables to be continuous across the contact wave. Our choice is similar (but not equal) to that of Mignone and Bodo (2006). However, we do not impose continuity of the components of the velocity parallel to the contact wave. In this sense, our approach is similar to that of Li (2005) in classical MHD or to the one of Honkkila and Janhunen (2007) or Kim and Balsara (2014) in RMHD. Instead, we impose continuity of the electric field due to its duality with respect to the magnetic field in RRMHD.

We have also imposed continuity of the scalar potentials ϕ^*_a and ψ^*_a and left unspecified the form of their corresponding fluxes, $F^*_{\phi,a}$ and $F^*_{\psi,a}$, respectively, which are unknowns of the problem. If we did not assume continuity of ϕ^* and ψ^*, this would be incompatible with the RH conditions across the middle wave (Eq. (5.4)) if we also enforced that $F^*_{\phi,a} = B^*_x$ and that $F^*_{\psi,a} = E^*_x$. Alternatively, we could relax the conditions $\phi^*_r = \phi^*_l$ and $\psi^*_r = \psi^*_l$ and assume that $F^*_{\phi,a} = B^*_x$ and $F^*_{\psi,a} = E^*_x$, but then the resulting system of equations becomes overdetermined. In the practical applications where we have used the new HLLC sover, this is not a problem though. The reason is that if we assume that the form of the fluxes of ϕ^*_a and ψ^*_a is $F^*_{\phi,a} = B^*_x$ and $F^*_{\psi,a} = E^*_x$, we obtain from the RH conditions across the middle wave that $\phi^*_r = \phi^*_l$ and $\psi^*_r = \psi^*_l$. But then, we have two alternative expressions for the fluxes of the latter variables: from the consistency relations across the outermost waves, Eqs. (5.6) and (5.7), we have $F^*_{\phi,a} = F^{\rm hll}_\phi$ and $F^*_{\psi,a} = F^{\rm hll}_\psi$, while from the assumed form of the fluxes, we obtain $F^*_{\phi,a} = B^{\rm hll}_x$ and $F^*_{\psi,a} = E^{\rm hll}_x$, respectively. These alternative expressions for the fluxes are in general incompatible. There is, however, a possibility to make all these alternative expressions of the fluxes in the starred region compatible if and only if $\lambda_l = -1$ and $\lambda_r = +1$. Fortunately, this is

the default choice that we make for the bounds on the limiting speeds of the RRMHD system. However, this procedure leaves no choice on the selection of λ_l and λ_r, as it is typically the case in other HLLC solvers. Another way to circumvent the incompatibility found above (if we do not enforce $\phi^*_r = \phi^*_l$ and $\psi^*_r = \psi^*_l$) is to assume that the fluxes of ϕ^* and ψ^* are free variables. However, to close the system of equations, we would need to impose two additional relations among the fluxes of ϕ^* and ψ^* on each side of the middle wave. In this regard, two considerations are in order. First, the scalar potentials are introduced in the algorithm to preserve the constraints $\nabla \cdot \mathbf{E} = q$ and $\nabla \cdot \mathbf{B} = 0$ and, second, we assume that both $\mathbf{E}$ and $\mathbf{B}$ are continuous across the middle wave. Taking into account these two considerations, we have not found satisfactory alternatives to the assumption of continuity of the ϕ^* and ψ^* across the contact wave in the standard framework of an HLLC solver for *the whole* set of conserved variables. More details on alternative formulations of the HLLC solver can be found in App. B.

The conditions imposed on the conserved variables, Eq. (5.10), provide 9 relations among the unknowns of our problem, to which we add the 9 non-trivial RH conditions across the middle wave corresponding to the same subset of conserved variables (i.e. q^*, ϕ^*, ψ^*, $\mathbf{E}^*$ and $\mathbf{B}^*$), as well as the additional three conditions, Eq. (5.11), on the ancillary variables. Therefore, there are still 10 additional missing equations to set a well posed problem, which come from assuming that the form of the fluxes $\mathbf{F}^*$ formally is the same as that of Eq. (2.39) in the x-direction for the following set of variables $(D^*, S^*_x, S^*_y, S^*_z, \mathcal{E}^*)$. More precisely, we assume that the starred fluxes relate to the starred variables through

$$F^*_{D,a} = D^*_a \lambda^*, \tag{5.12}$$

$$F^*_{\mathcal{E},a} = S^*_{x,a}, \tag{5.13}$$

$$F^*_{S_x,a} = -E^*_x E^*_x - B^*_x B^*_x + [S^*_{x,a} - (\mathbf{E}^* \times \mathbf{B}^*)_x]\lambda^* + P^*, \tag{5.14}$$

$$F^*_{S_y,a} = -E^*_x E^*_y - B^*_x B^*_y + [S^*_{y,a} - (\mathbf{E}^* \times \mathbf{B}^*)_y]\lambda^*, \tag{5.15}$$

$$F^*_{S_z,a} = -E^*_x E^*_z - B^*_x B^*_z + [S^*_{z,a} - (\mathbf{E}^* \times \mathbf{B}^*)_z]\lambda^*. \tag{5.16}$$

The assumed dependence of the fluxes on the conserved variables and on the λ^* and P^* makes that 5 RH conditions across the contact wave Eq. (5.4) corresponding to the subset of variables $(D^*, S^*_x, S^*_y, S^*_z, \mathcal{E}^*)$ become trivially satisfied. Hence, these equations are replaced by Eqs. (5.12)-(5.16).

For the subset of conserved variables for which we have assumed continuity across the contact wave, Eq. (5.10), the consistency condition (5.6) yields:

$$\begin{aligned} &q^* = q^{\rm hll}, \quad B^*_i = B^{\rm hll}_i, \quad E^*_i = E^{\rm hll}_i, \\ &\phi^* = \phi^{\rm hll}, \quad \psi^* = \psi^{\rm hll}. \end{aligned} \tag{5.17}$$

The fluxes corresponding to the conserved variables given in (5.17) are readily found applying Eqs. (5.8):

$$\begin{aligned} F^*_{q,a} &= F^{\rm hll}_q, \quad F^*_{\phi,a} = F^{\rm hll}_\phi, \quad F^*_{\psi,a} = F^{\rm hll}_\psi, \\ F^*_{B_i,a} &= F^{\rm hll}_{B_i}, \quad F^*_{E_i,a} = F^{\rm hll}_{E_i}. \end{aligned} \tag{5.18}$$

The flux of $\mathcal{E}^*_a$ is exactly $S^*_{x,a}$ (Eq. (5.13)) and, hence, employing the consistency relations (5.7) and (5.6), we find

$$S^*_{x,a} = \frac{\lambda_a S^{hll}_x - \lambda^* F^{hll}_{\mathcal{E}}}{\lambda_a - \lambda^*}. \tag{5.19}$$

Similarly, the especially simple form of the flux of D, Eq. (5.12), inserted in any of the Eqs. (5.8), yields:

$$D^*_a = \frac{\lambda_a - v_{x,a}}{\lambda_a - \lambda^*} D_a.$$

Using relation (5.7) for the $y-$ and $z-$momentum density fluxes, Eqs. (5.15) and (5.16), combined with Eq. (5.6) for S^{hll}_y and S^{hll}_z yields

$$\begin{aligned} S^*_{y,a} &= \frac{\lambda_a S^{hll}_y - F^{hll}_{S^y} - \lambda^*(\mathbf{E}^* \times \mathbf{B}^*)_y - E^*_x E^*_y - B^*_x B^*_y}{\lambda_a - \lambda^*}, \\ S^*_{z,a} &= \frac{\lambda_a S^{hll}_z - F^{hll}_{S^z} - \lambda^*(\mathbf{E}^* \times \mathbf{B}^*)_z - E^*_x E^*_z - B^*_x B^*_z}{\lambda_a - \lambda^*}. \end{aligned}$$

Applying the consistency relation (5.6) to the x component of the momentum density, we find

$$S^{hll}_x = \lambda^*[\mathcal{E}^{hll} + P^* - (\mathbf{E}^*)^2 - (\mathbf{B}^*)^2] + (\mathbf{E}^* \times \mathbf{B}^*)_x. \tag{5.20}$$

Likewise, applying the consistency relation (5.7) to the x component of the momentum density flux (5.14) and to the energy density flux (5.13) leads to

$$\lambda^* F^{hll}_{S^x} = (\lambda^*)^2[F^{hll}_{\mathcal{E}} - (\mathbf{E}^* \times \mathbf{B}^*)_x] + \lambda^*[P^* - (E^*_x)^2 - (B^*_x)^2]. \tag{5.21}$$

Subtracting Eq. (5.21) from Eq. (5.20) we arrive at a quadratic equation for λ^*

$$a(\lambda^*)^2 + b\lambda^* + c = 0, \tag{5.22}$$

whose coefficients are

$$\begin{aligned} a &= F^{hll}_{\mathcal{E}} - (\mathbf{E}^* \times \mathbf{B}^*)_x, \\ b &= (\mathbf{E}^*_\perp)^2 + (\mathbf{B}^*_\perp)^2 - \mathcal{E}^{hll} - F^{hll}_{S^x}, \\ c &= S^{hll}_x - (\mathbf{E}^* \times \mathbf{B}^*)_x, \end{aligned} \tag{5.23}$$

where $(\mathbf{B}^*_\perp) = (0, B^*_y, B^*_z)^T$ and $\mathbf{E}^*_\perp = (0, E^*_y, E^*_z)^T$.

In the ideal limit, in which the electric field simply is $\mathbf{E} = -\mathbf{v}\times\mathbf{B}$, the coefficients of the quadratic equation (5.23) reduce to the expressions in Mignone and Bodo (2006). Thus, employing the same arguments as in the former paper (see also Mignone and Bodo, 2005), of the two roots of Eq. (5.22), only the one with the minus sign is compatible with $\lambda_l \le \lambda^* \le \lambda_r$ and, therefore, it is the physically admissible solution.

If the solution resulting from Eq. (5.22) is $\lambda^* \neq 0$, then P^* can be recovered from Eq. (5.21)

$$P^* = F^{hll}_{S^x} + (E^*_x)^2 + (B^*_x)^2 - \lambda^*[F^{hll}_{\mathcal{E}} - (\mathbf{E}^*\times\mathbf{B}^*)_x].$$

In the complementary case that $\lambda^* = 0$, using the second RH condition of (5.4) together with the flux consistency condition (5.7) allows us to express all the fluxes in terms of the HLL flux (i.e. in terms of the variables in the left and right states):

$$\mathbf{F}^*_r = \mathbf{F}^*_l = \mathbf{F}^{hll} \quad (\text{if } \lambda^* = 0), \tag{5.24}$$

and the calculation of P^* is not necessary to obtain the numerical fluxes.

The energy density $\mathcal{E}$, Eq. (2.26), can also be expressed as

$$\mathcal{E} = (S_x - (\mathbf{E}\times\mathbf{B})_x)/v_x - P + \mathbf{E}^2 + \mathbf{B}^2,$$

if $v_x \neq 0$. In any of the intermediate states, using Eq. (5.19), we find:

$$\mathcal{E}^*_a = \frac{1}{\lambda^*}\left[\frac{\lambda_a S^{hll}_x - \lambda^* F^{hll}_{\mathcal{E}}}{\lambda_a - \lambda^*} - (\mathbf{E}^*\times\mathbf{B}^*)_x\right] - P^* + (\mathbf{E}^*)^2 + (\mathbf{B}^*)^2,$$

if $\lambda^* \neq 0$. The complementary case ($\lambda^* = 0$) makes use of Eq. (5.24), and the evaluation of $\mathcal{E}^*_a$ is not needed.

5.2 Numerical Experiments

In this section, we demonstrate the performance of the new HLLC solver in a number of 1D Riemann problems and 2D standard (R)RMHD tests. To compare our results with the ones in the ideal limit, we set the conductivity to a large constant value, i.e. $\sigma = 10^6$ (see the discussion in Sec. 5.2.4 as well as Fig. 5.10). A more through study of the non-ideal, low-σ regime is considered in Chap. 4. All 1D test problems are performed in a computational domain $x \in [0, 1]$ and with the CFL factor $C_{\text{CFL}} = 0.1$. The initial discontinuity is placed at $x = 0.5$. RRMHD equations are integrated using the second order MIRK method (Aloy and Cordero-Carrión, 2016, see also Sec. 4.2.2). However, we note that most of the results presented in this paper are computed

employing a (globally) 1st-order accurate scheme, resulting from not applying any intercell reconstruction to the numerical variables (Godunov method). In this way, a comparison of the performance of the HLL and HLLC Riemann solvers can be shown more clearly. The initial conditions for 1D tests are summarized in Tab. 4.1 (Chapter 4).

5.2.1 Contact Wave Discontinuities

Contact wave discontinuity tests (CW1 and CW2 in Tab. 4.1) consist in simulating an isolated contact discontinuity with a jump only in the mass density ρ. In the CW1 test, where $v_x = 0$, the HLLC solver does not show any smearing of the initial profile, as for this particular case, HLLC resolves the discontinuity (Fig. 5.1 left panel) exactly. This behaviour is expected for the HLLC solver, which is specifically built to include a contact wave in the numerical solution. In the CW2 test, whose setup was proposed by Honkkila and Janhunen (2007), there is a smearing of the contact wave, which is smaller for the HLLC solver than for the HLLC solver (Fig. 5.1 central panel). The smearing of the contact wave is a result of two facts: (*i*) the non-Lorentzian invariance of the numerical viscosity added by the HLL and HLLC solvers; (*ii*) an inherent numerical diffusion of shock-capturing methods of Godunov-type (unless specific techniques to track internal interfaces dynamics are employed; see, e.g. Abgrall and Karni, 2001).

We have considered several variants of the CW2 test where progressively larger values of v_x are taken. As $v_x \to 1$, the diffusion of the contact discontinuity becomes larger in both approximate Riemann solvers and the differences between them reduce (yet the HLLC solver always displays smaller smearing than the HLL solver). This is due to the degeneration of the Riemann structure when any of the components of the 3-velocity is close to the speed of light. Under such conditions, all eigenvalues of the system of RRMHD equations approach the speed of light and the contact wave is resolved as a shock by the

Table 5.1: Mean ratios of CPU running time between the HLLC solver and the HLL solver, $t_{\rm hllc}/t_{\rm hll}$. To compute the mean ratios in 1D tests (ST1 to ST5), we first measure the ratio of CPU running times for each of the working resolutions employed in this paper, $t_{\rm hllc}/t_{\rm hll}(n_{x,i})$, $n_{x,i} = \{50, 100, 200, 400, 800, 1600, 3200\}$, and then average over all of these results (i.e. $t_{\rm hllc}/t_{\rm hll} := \frac{1}{7}\sum_{i=1}^{7} t_{\rm hllc}/t_{\rm hll}(n_{x,i})$). Likewise, for the 2D tests (RR and CE) the average of ratios of CPU time is computed performing them with resolutions of 50×50, 100×100, 200×200 and 400×400.

CPU running times

test	ST1	ST1-B0	ST2	ST3	ST4	ST5	RR	CE
$t_{\rm hllc}/t_{\rm hll}$	1.06	1.06	1.06	1.13	1.18	1.15	1.05	1.18

algorithm (thus, unphysical numerical dissipation is added).

5.2.2 Rotational Wave

Following (Mignone et al., 2009), we set up an isolated rotational wave (RW) like in their ideal RMHD test. Across a rotational wave, the components of vector fields exhibit jumps (yet their moduli are preserved), while scalar quantities (e.g. rest-mass density, total pressure, etc.) are continuous. We show in Fig. 5.2 the variation of B_y across the rotational wave. Neither the HLL nor the HLLC solver is able to capture the initially specified jump (see Tab. 4.1) and both smear the solution (the HLL solver slightly more than the HLLC solver). As noted in Antón et al. (2010), in practical applications, the numerical diffusion is not as large as one may infer from the results of Fig. 5.2 (upper panel). To ameliorate the problem, a high-order spatial interpolation (instead of using simply the Godunov method) is advisable. Thus, we have repeated both the RW and also the CW2 tests employing an MP5 intercell reconstruction (see Sec. 4.1.1.2 and Suresh and Huynh, 1997). The results are shown in Figs. 5.1 (right panel) and 5.2 (bottom panel). In both cases, only 4 numerical zones are needed to resolve the isolated discontinuities.

5.2.3 Shock Tube Problem 1 (ST1)

The test of Balsara (2001) (which is a relativistic extension of the test proposed by Brio and Wu, 1988) has been used by a number of practitioners in the RMHD field (e.g. Antón et al., 2010; Del Zanna et al., 2003; Leismann et al., 2005; Mignone and Bodo, 2006; Mignone et al., 2009). It considers a fluid with adiabatic index $\gamma = 2$. The initial discontinuity breaks into a left-going fast rarefaction, a left-going compound wave, a contact discontinuity, a right-going slow shock and a right-going fast rarefaction wave (Fig. 5.3). According to the analytic solution (Giacomazzo and Rezzolla, 2006)[2], the contact discontinuity must be located at $x \approx 0.6$. The structure of the contact is more accurately resolved by the HLLC solver than by the HLL solver as can be seen in the zoomed Fig. 5.4.

Both solvers are slightly more diffusive in this test than their ideal RMHD counterparts (compare our Fig. 5.4 to, e.g. Fig. 4 of Mignone et al. (2009) or to Fig. 4 of Antón et al. (2010), where the test is shown with the same resolution). This extra diffusivity comes from two sources. First, our estimates for the limiting speeds of the approximate Riemann solvers ($\lambda_r = +1$, $\lambda_l = -1$; Sec. 5.1)

[2]The solution of Giacomazzo and Rezzolla (2006) is built explicitly neglecting compound waves. Besides their physical or unphysical nature, numerically the compound wave shows up at $x \simeq 0.5$, inducing the seemingly large deviation of the numerical solution from the analytic one in the vicinity of its location.

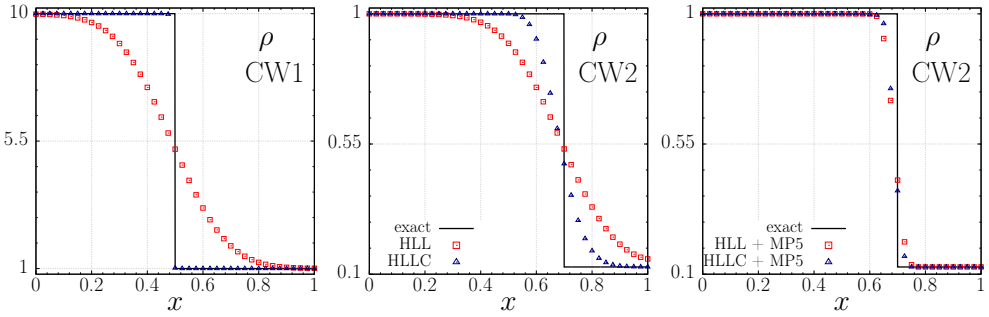

Figure 5.1: CW: Rest-mass density at $t = 1.0$ in contact wave discontinuity tests CW1 (left panel) and CW2 (central and right panels; see Tab. 4.1) performed with the HLL (red squares) and the HLLC (blue triangles) approximate Riemann solvers. The analytical solution is depicted with a black solid line. In the simulation presented in the right panel, the MP5 scheme is used, whereas in the other simulations the piecewise constant reconstruction (Godunov) is employed.

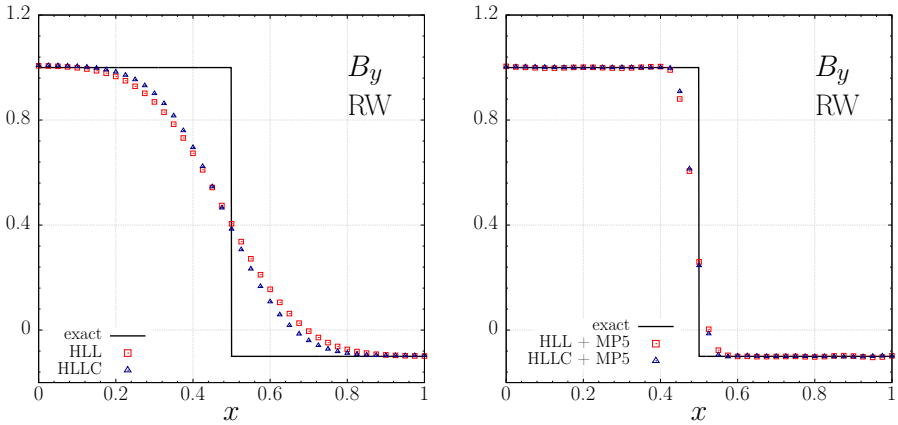

Figure 5.2: RW: Magnetic field (B_y component) for an isolate rotational wave at $t = 1$. The solid line stands for the analytic solution, blue triangles and red squares symbols show the solution with the HLLC and HLL solvers, respectively. The upper panel is computed without employing any high-order intercell reconstruction (Godunov), while the lower panel corresponds to the same test using the MP5 reconstruction.

are larger in absolute value than the fast magnetosonic waves for this test in ideal RMHD. The latter are commonly employed as estimators of the fastest signal speeds in HLL and HLLC approximate Riemann solvers for RMHD. Note, however, that fast-magnetosonic waves propagate at the speed of light in RRMHD. Second, the notorious degeneracy of the eigenfields limiting the Riemann fan Eq. (3.5) increases the amount of numerical dissipation added to characteristic variables corresponding to eigenvalues without jumps for certain electromagnetic configurations.

To quantify the accuracy of the HLL and HLLC solvers, we use the discrete L1-norm error, in the form:

$$\varepsilon_{\rm L1} = \frac{1}{n_x}\sum_{i=1}^{n_x}\left|U_i^{\rm ref} - U_i\right|, \tag{5.25}$$

where $U_i^{\rm ref}$ is a reference solution computed with the exact solver of Giacomazzo and Rezzolla (2006) on the same grid as the numerical solution U_i. n_x is the number of numerical grid zones in the $x-$direction. For the 1D tests, we evaluate the L1-norm errors of the B_y component of the magnetic field and display them as a function of the number of numerical zones in Fig. 5.5. The measured errors for the ST1 test are $\sim 20\%$ smaller using the HLLC solver than using the HLL solver for $n_x > 100$ (Fig. 5.5, top left panel), reflecting that the HLLC solutions are closer to the exact ones than the HLL numerical approximations.

Differently from the ideal RMHD implementation of the HLLC solver by Mignone and Bodo (2006), our approximate Riemann solver does not need to distinguish between the cases $B_x = 0$ and $B_x \neq 0$ (see Sec. 5.1). To demonstrate this, we consider the ST1-B0 test (see Tab. 4.1), which is like the ST1 test, but with $B_x = 0$. The structure of the solution to this test only contains two fast waves, a rarefaction moving to the left and a shock moving to the right with a tangential discontinuity between them. In contrast to the standard ST1 test, compound waves are not present in ST1-B0. The new HLLC solver can deal with this setup at the same quantitative level as in the case with $B_x \neq 0$ (Fig. 5.6). A small overshooting in the thermal pressure across the tangential discontinuity (at $x \simeq 0.63$) is present in both approximate Riemann solvers, but the contact wave is more sharply resolved with the HLLC than with the HLL solver (Fig. 5.7). Discrete L1-norm errors of the magnetic field B_y component, computed for the ST1-B0 test, are plotted in the upper mid panel of Fig. 5.5. In this case the difference between L1-norm errors for the HLL and HLLC solvers reduces substantially as compared to the ST1 test. This happens because the jump accros the contact wave is zero in this test and, as a result, the potential advantage of the HLLC solver with respect to the HLL solver drastically reduces. Anyway, the HLLC L1-norm errors are a bit smaller than

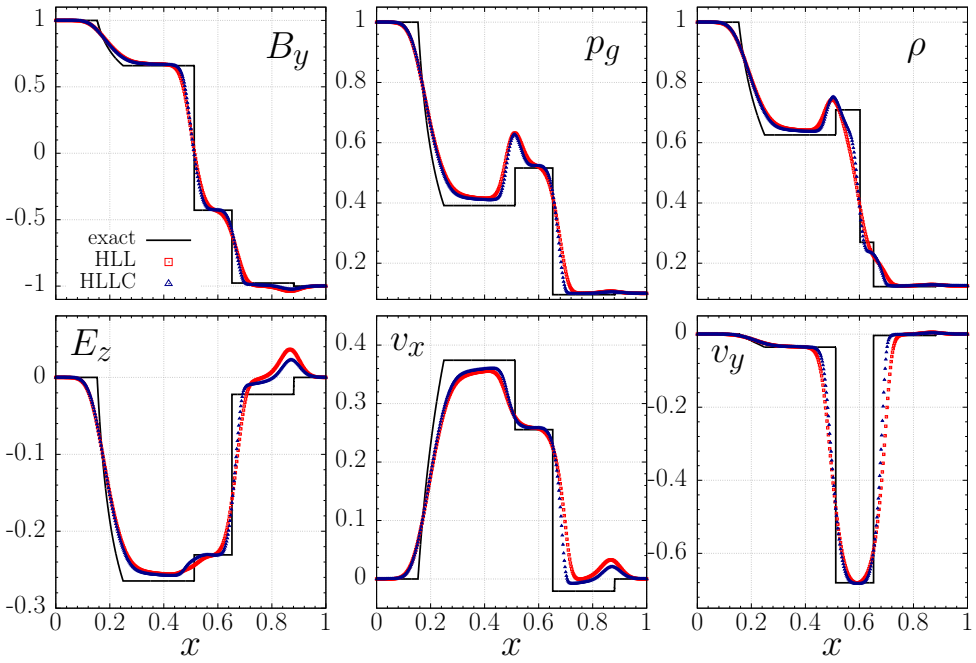

Figure 5.3: ST1: Relativistic Brio-Wu shock tube test at t=0.4. The calculations are performed with a 1$^{\rm st}$-order accurate scheme on a grid of 400 zones employing the HLL (red symbols) and HLLC (blue symbols) Riemann solvers. The analytic solution of this test in ideal RMHD is displayed with black solid line. Upper panel: magnetic field (B_y component), thermal pressure ($p_{\rm g}$), rest-mass density (ρ). Lower panel: electric field (E_z component), velocity field (v_x and v_y components).

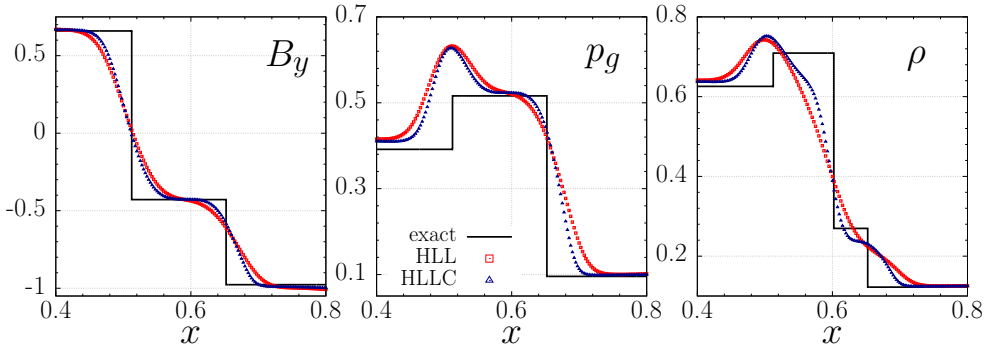

Figure 5.4: ST1: Zoom of Fig. 5.3 on the region where the contact discontinuity is located. From left to right: magnetic field (B_y component), thermal pressure ($p_{\rm g}$) and rest-mass density (ρ).

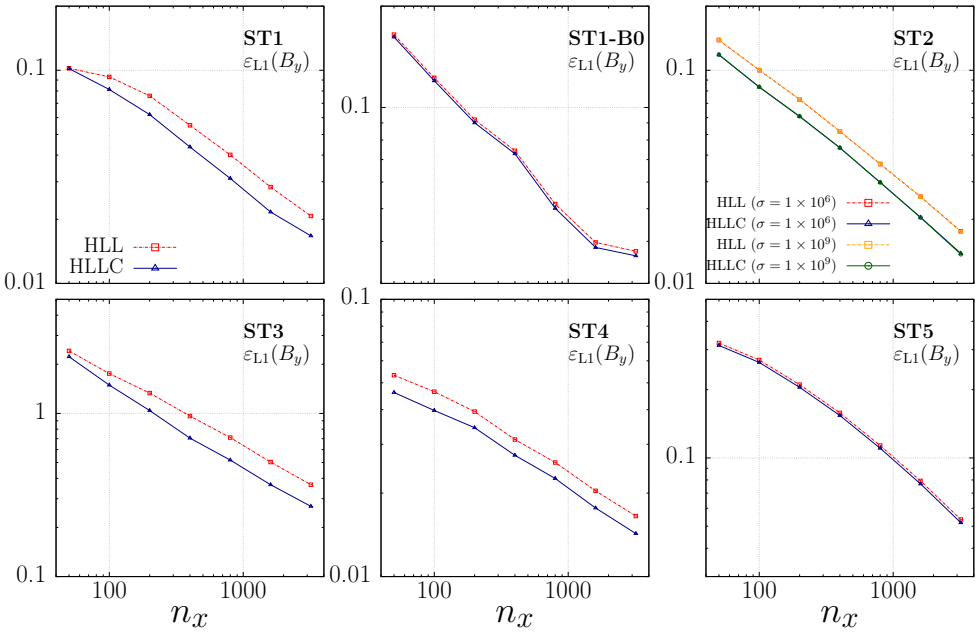

Figure 5.5: L1-norm errors (Eq. (5.25)) of B_y magnetic field component in six shock tube problems presented in Tab. 4.1. All tests were performed with resolutions of $n_x = 50, 100, 200, 400, 800, 1600$, and 3200 grid zones, and a small $C_{\rm CFL} = 0.1$ to avoid contributions of the error arising from the time discretization (see more details on Chap. 6). The numerical solutions computed with the HLL and HLLC solvers are displayed with red and blue symbols, respectively, in all panels except in the upper right panel (see the corresponding legends there).

the corresponding HLL L1-norm errors at all resolutions. We observe that the computational overhead of the HLLC solver with respect to the HLL solver is very modest (Tab. 5.1). On average, employing the former solver takes only $\sim 6\%$ more time to compute the solution in the ST1 and ST1-B0 tests.

5.2.4 Shock Tube Problem 2 (ST2)

In this shock tube problem, the break up of the initial discontinuity develops a Riemann fan with 7 different waves in the ideal limit. We use the same set up as Antón et al. (2010) (in RMHD) or as Dumbser and Zanotti (2009) or Bucciantini and Del Zanna (2013) in RRMHD, where the computational domain, $x \in [0, 1]$, is resolved with a uniform grid of 400 cells and the test is evolved until a final time $t = 0.55$. The HLLC solver attains a sharper representation of the entropy wave located at $x \simeq 0.48$ than the HLL solver (Fig.5.8). Nonetheless, an undershooting ahead of the entropy wave is evident in the HLLC solution. The state between the right-going slow shock ($x \simeq 0.7$) and the right-going Alfvén wave at $x \simeq 0.73$ is smeared by both solvers albeit

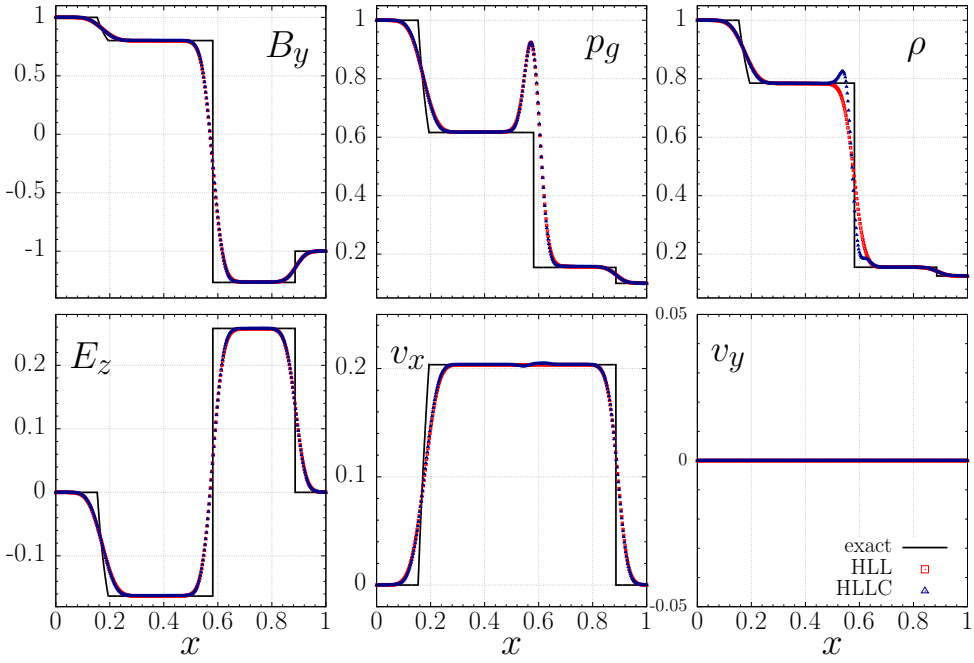

Figure 5.6: ST1-B0: Variant of the relativistic Brio-Wu shock tube test at t=0.4 when the longitudinal magnetic field is zero ($B_x = 0$). The panels, lines and symbols are the same as in Fig. 5.3.

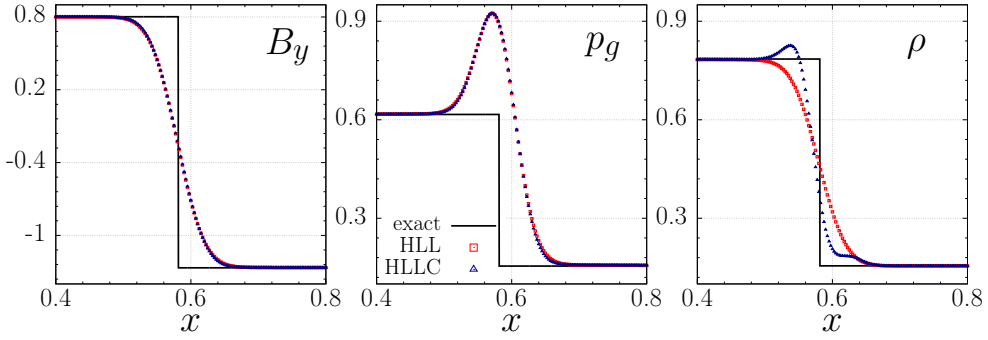

Figure 5.7: ST1-B0: Same as Fig. 5.4 but for test ST1-B0.

the HLLC solution is slightly closer to the analytical one also in that region (Fig. 5.9). It is also the case for the state between the left-going Alfvén wave ($x \simeq 0.185$) and the left going slow rarefaction at $x \simeq 0.19$. In the latter case, the two waves are so close to each other that none of the approximate Riemann solvers can resolve them. Indeed, this is to be expected, since resolving this region is a challenge even for the exact solver of Giacomazzo and Rezzolla (2006), which cannot obtain a solution for this test with an accuracy better than 3.4×10^{-4}.

The L1-norm errors in this test (Fig. 5.5 upper right panel) show again a larger accuracy of the solutions computed with the HLLC solver. These errors are $\sim 10\%$ lower than for equivalent tests performed with the HLL solver, almost independently of the resolution employed. Remarkably, for the ST2 test, the computational cost to obtain the solution employing the HLLC solver is only a $\sim 6\%$ larger than using the HLL solver (Tab. 5.1).

In Fig. 5.10, we explore the dependence of the results on the conductivity σ analogously to the studies done by Dumbser and Zanotti (2009) and Bucciantini and Del Zanna (2013).[3] Resistive versions of the shock tube problem ST2 display smoother profiles of B_y with decreasing conductivity. Noteworthy, the cases with $\sigma = 10^9$ and 10^6 basically overlap at a resolution of $n_x = 800$ zones. From this fact, we draw two conclusions. First, since the results basically are insensitive to the exact value of the conductivity, when it is large enough, we can assess that for $\sigma \gtrsim 10^6$ the *numerical* resistivity is larger than the physical one in this particular set up.[4] Second, the *proximity* of the results to the analytic solution justifies our choice of $\sigma = 10^6$ as a conductivity value close enough to the ideal RMHD limit. This result is expressed more quantitatively in Fig. 5.5 (upper right panel; orange and green lines). For both solvers, the L1-norm errors are basically the same in tests set up with $\sigma = 10^6$ and $\sigma = 10^9$.

5.2.5 Shock Tube Problem 3 (ST3)

In this test, two relativistic, magnetized streams collide producing two "reverse" strong relativistic fast shocks propagating symmetrically from the mid point of the computational domain (see, e.g. Antón et al., 2010; Balsara, 2001; Del Zanna et al., 2003; Leismann et al., 2005; Mignone and Bodo, 2006; Mignone et al., 2009). Following the fast shocks, a pair of symmetric slow shocks further thermalize the plasma in the state delimited by them, converting all the remaining kinetic energy into thermal energy and leaving the fluid at rest (Fig. 5.11). In this test there is no jump of the variables across the

[3] We explore the non-resistive regime with a different time-evolution scheme in Sec. 4.5.4.

[4] An extensive discussion of the numerical resistivity and viscosity of our algorithms is deferred to Chap. 6

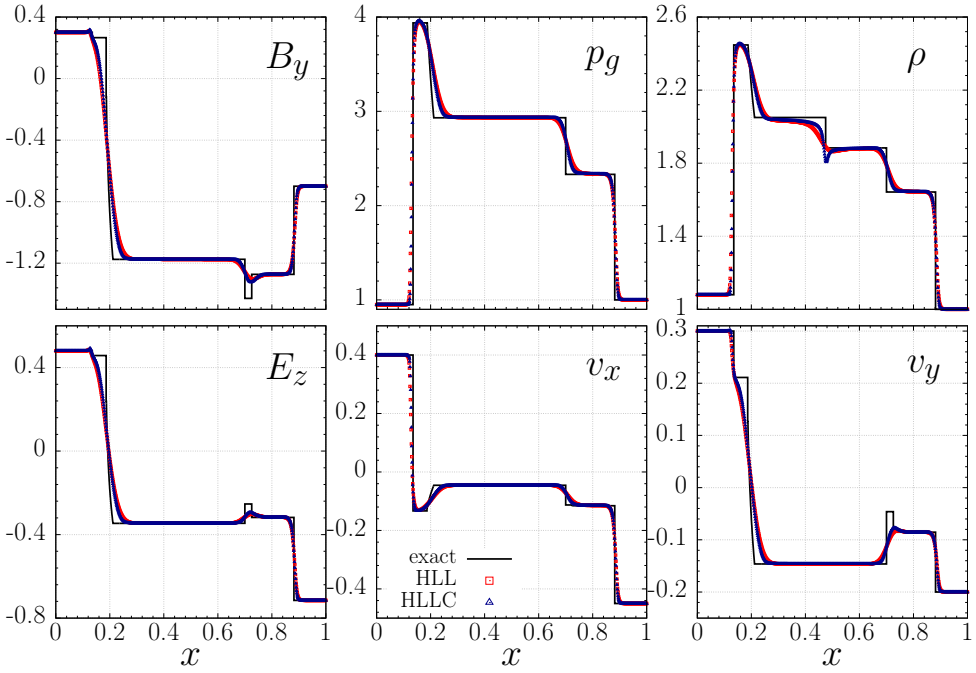

Figure 5.8: ST2: Second 1D Riemann problem (Tab. 4.1) after $t = 0.55$ and using 400 numerical zones. The variables displayed and the meaning of the symbols and lines is the same than in Fig. 5.3.

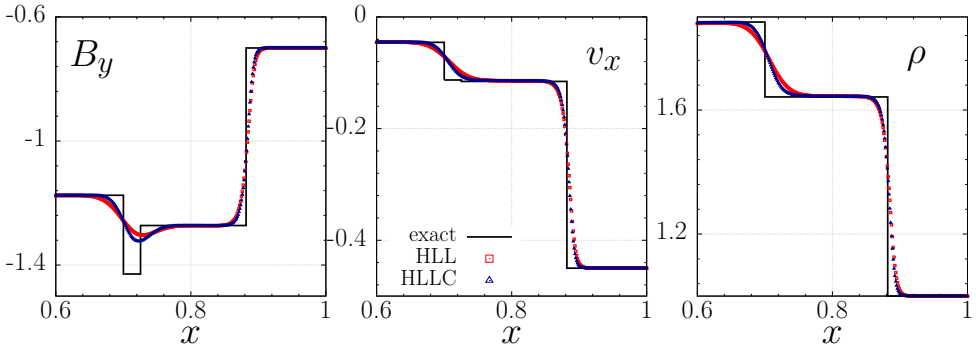

Figure 5.9: ST2: Zoom of some of the variables displayed in Fig. 5.8 focusing on the right-going slow shock ($x \simeq 0.7$), Alfvén wave ($x \simeq 0.73$) and fast shock ($x \simeq 0.88$). From left to right: magnetic field (B_y component), velocity (v_x component) and rest-mass density (ρ).

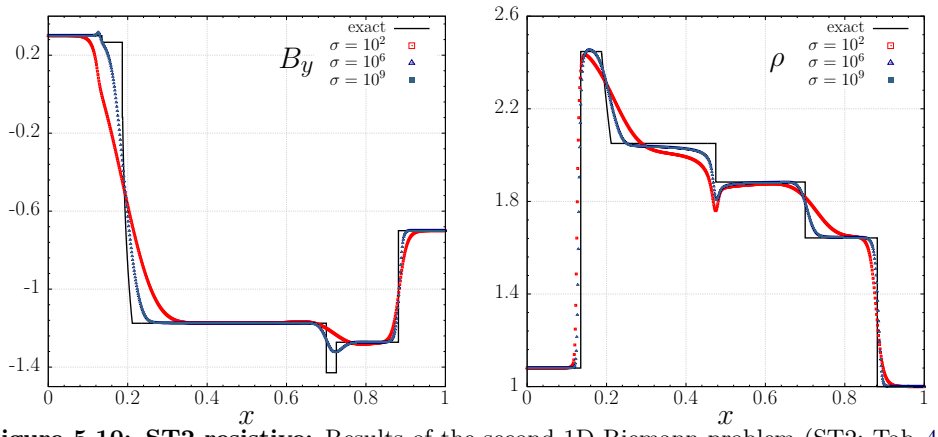

Figure 5.10: ST2-resistive: Results of the second 1D Riemann problem (ST2; Tab. 4.1) after $t = 0.55$ and using 800 numerical zones, but for different conductivities $\sigma = 10^9, 10^6$, and 10^2, and the HLLC solver. Note that the lines and symbols corresponding to the case $\sigma = 10^9$ overlap with the case $\sigma = 10^6$.

contact wave (standing at $x = 0$) and, therefore, the differences between HLL and HLLC are rather small. However, the HLLC approximate Riemann solver produces a slightly sharper representation of the intermediate discontinuities (slow shocks).

Even though both solvers display a pathological undershooting of the density at the grid center, the density decrease for the HLLC solver is substantially larger than for the HLL solver. This is a well know pathology of many Godunov-type schemes know as "wall heating" problem (Noh, 1987), which is more stringent for approximate solvers possessing smaller numerical dissipation. Hence, the HLL solver displays a much smaller undershooting than the HLLC solver at $x = 0.5$ (Fig. 5.12). The slightly higher quality of the HLLC solution is quantified by the smaller L1-norm errors obtained with the latter solver in comparison to the HLL solver (Fig. 5.5 bottom left panel). At the maximum resolution employed ($n_x = 3200$) the errors made with the HLLC solver are $\sim 26\%$ smaller than the ones made with the HLL solver. For the ST3 test, the computational cost to obtain the solution employing the HLLC solver is $\sim 13\%$ larger than using the HLL solver (see Tab. 5.1).

5.2.6 Shock Tube Problem 4 (ST4)

Giacomazzo and Rezzolla (2006) refer to this Riemann problem as "Generic Alfvén " test, which is very challenging for ideal RMHD as well as RRMHD codes, as it encompasses all seven possible waves in the Riemann fan it develops. It has been adopted as a benchmark by, e.g. Mignone et al. (2009) and Antón et al. (2010). For this setup, the initial discontinuity results into

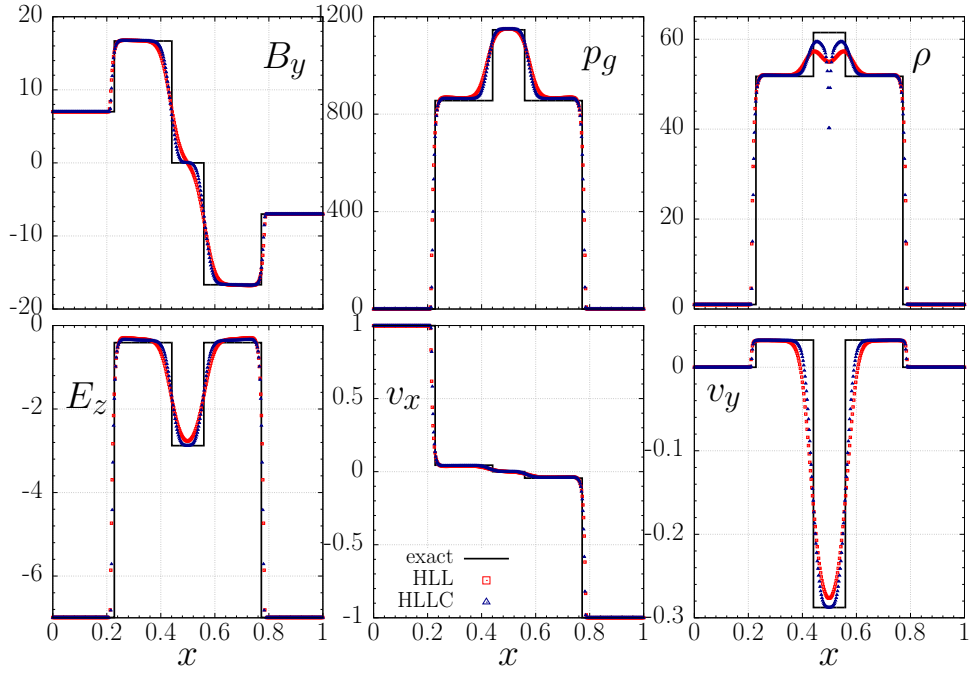

Figure 5.11: ST3: Collision of two oppositely moving streams of plasma after $t = 0.4$ computed with 400 numerical zones. Upper panels (from left to right): magnetic field (B_y component), thermal pressure ($p_{\rm g}$), rest-mass density (ρ). Lower panels (from left to right): electric field (E_z component), velocity (v_x and v_y components).

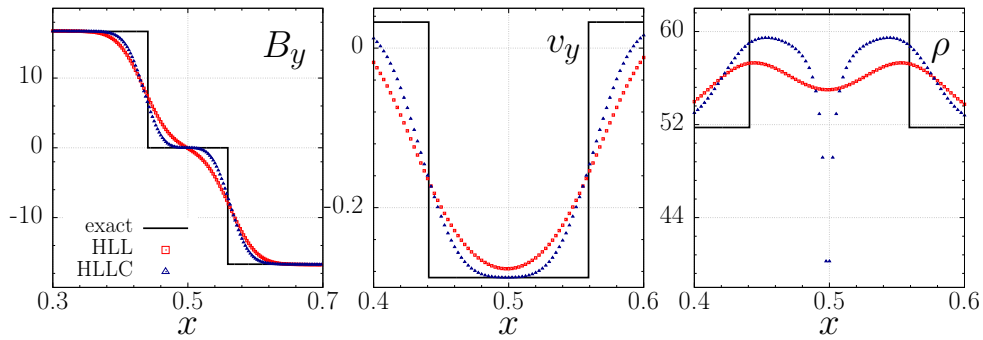

Figure 5.12: ST3: Magnification of the central region of the ST3 test encompassing the two slow shocks located at $x \simeq 0.44$ and $x \simeq 0.56$. From left to right: magnetic field (B_y component), velocity (v_y component) and rest-mass density (ρ).

a contact discontinuity which separates a fast rarefaction wave (at $x \simeq 0.05$), a rotational wave (at $x \simeq 0.44$), and a slow shock (at $x \simeq 0.46$), from a slow shock (at $x \simeq 0.56$), an Alfvén wave (at $x \simeq 0.57$) and a fast shock (at $x \simeq 0.97$). The exact solution of this test, together with the results at $t = 0.4$ for the HLLC and HLL solvers, are shown in Fig. 5.13. The finest structures in this test, associated with the rotational discontinuities travelling very close to the slow shocks, are hardly resolved by the 1$^{\rm st}$-order scheme using any of the approximate Riemann solvers employed in this paper at the working resolution of 800 uniform numerical zones (Fig. 5.14).

The L1-norm errors of this test (Fig. 5.5 bottom mid panel) show the same qualitative trend like those of the ST2 test (Fig. 5.5 upper right panel). The HLLC numerical solution yields L1-norm errors $\sim 13\%$ smaller than the HLLC counterpart almost independently of the numerical resolution. For the ST4 test, the computational cost to obtain the solution employing the HLLC solver is $\sim 18\%$ larger than using the HLL solver (Tab. 5.1). This represents the largest computational overhead of all the 1D tests presented in this section. The larger computing time is explained in terms of the challenging nature of the ST4 test, that develops several regions where very fine structures are attempted to be resolved by the HLLC solver (while they are completely smeared out by the HLL solver).

5.2.7 Shock Tube Problem 5 (ST5)

The relativistic blast wave test problem with a moderate initial pressure difference was proposed by (Balsara, 2001). The Riemann problem develops a left-going fast rarefaction wave (at $x \simeq 0.16$) and slow rarefaction fan (at $x \simeq 0.53$) are separated by a contact discontinuity (at $x \simeq 0.76$) from two right-going shocks waves, a slow (at $x \simeq 0.86$) and fast (at $x \simeq 0.9$) one. The overal structure of the solution can be found in Fig. 5.15, where the inability of either HLLC or HLL to properly capture the finest structure left to the right-going slow shock wave is evident. The contact wave is slightly better resolved with the HLLC solver than with the HLL solver, as can be seen in Fig. 5.16. The marginally better performance of the HLLC solver at all the resolutions considered is quantified in terms of the L1-norm errors of the rest-mass density (Fig. 5.5 bottom right panel). The proximity of the L1-norm errors obtained with the HLLC and HLL solver is due to the fact that the contact discontinuity in this test is moving faster than in any other 1D tests shown in this section. This reduces the sharpness with which the contact wave is captured by the HLLC scheme, as discussed for the CW2 test in Sec. 5.2.1.

Finally, we have measured a mean computational overhead of $\sim 15\%$ using the HLLC solver in the ST5 test with respect to the corresponding models employing the HLL solver (Tab. 5.1).

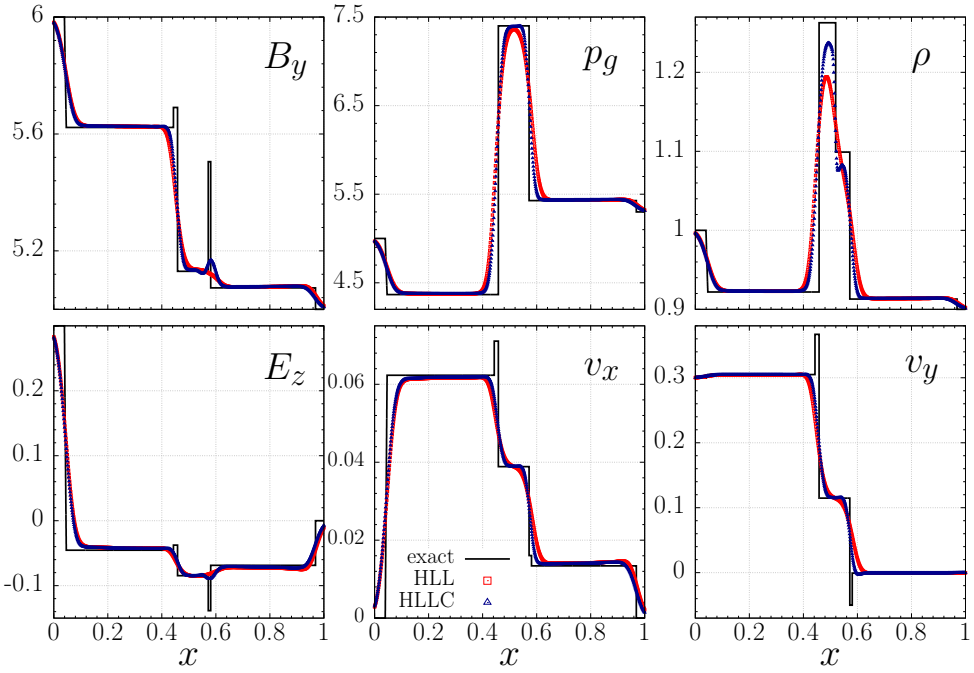

Figure 5.13: ST4: Numerical results for the generic Alfvén test problem ST4, after $t = 0.4$ on a grid with 800 numerical zones. Upper panels (from left to right): magnetic field (B_y component), thermal pressure (p_g), rest-mass density (ρ). Lower panels (from left to right): electric field (E_z component), velocity (v_x and v_y components).

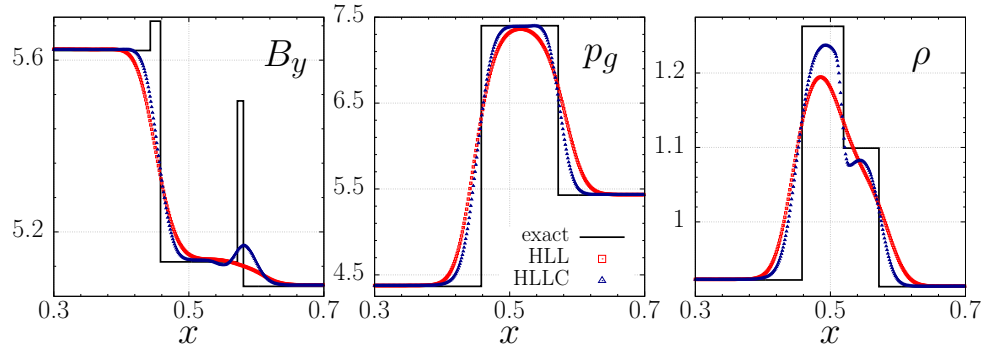

Figure 5.14: ST4: Enlargement of the central region of Fig. 5.13. From left to right: magnetic field (B_y component), thermal pressure (p_g) and rest-mass density (ρ).

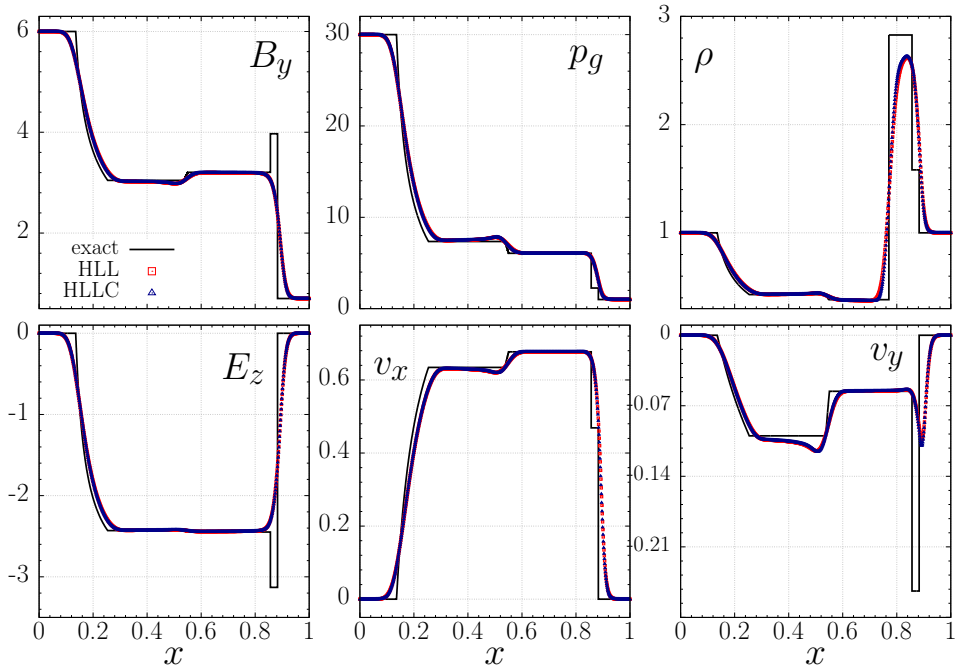

Figure 5.15: ST5: Numerical and exact solutions for the ST5 test at $t = 0.4$. Upper panel: magnetic field (B_y component), thermal pressure (p_g), rest-mass density (ρ). Lower panel: electric field (E_z component), velocity (v_x and v_y components).

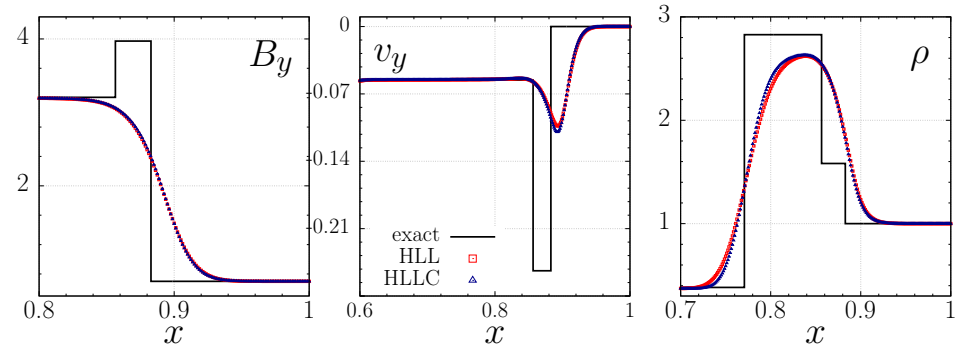

Figure 5.16: ST5: Magnification of a region of interest in Fig. 5.15. From left to right, magnetic field (B_y component), velocity (v_y component) and rest-mass density (ρ).

5.2.8 Resistive rotor

The resistive rotor (see, e.g. Bucciantini and Del Zanna, 2013; Dumbser and Zanotti, 2009) is of interest not only as a calibration test for resistive as well as ideal MHD numerical multidimensional codes, but also because of its connection to the problem of angular momentum loss through torsional Alfvén waves in star formation (Mouschovias and Paleologou, 1980). It consists of an initial 2D state where in a region of radius $r \leq 0.1$ around the domain center, the density is $\rho = 10$, and the fluid rotates with a constant angular velocity $\Omega = 8.5$. Outside this region ($r > 0.1$) the medium at rest is uniform ($\rho = 1$). Both the thermal pressure ($p_{\rm g} = 1$) and the magnetic field $\mathbf{B} = (1, 0, 0)$ are uniform in the whole computational domain, a unit square covering the range $-0.5 \leq x \leq 0.5$, $-0.5 \leq y \leq 0.5$. The initial electric field is set like in ideal RMHD, and the adiabatic index is $\gamma = 4/3$. Figure 5.17 shows snapshots of the thermal pressure $p_{\rm g}$ and of the electric field component E_z at $t = 0.3$, in different conductivity regimes (cases with $\sigma = 10^6$, 10^3 and 10 are considered). The model was obtained using the second order MIRK scheme, the MP5 intercell reconstruction, with a CFL factor $C_{\rm CFL} = 0.1$, the HLLC approximate Riemann solver and a grid of 300 zones per dimension.

Our results agree relatively well with those of Dumbser and Zanotti (2009) and Bucciantini and Del Zanna (2013) for intermediate ($\sigma = 10^3$) or almost ideal ($\sigma = 10^6$) regimes. In the resistive regime ($\sigma = 10$), the differences are more obvious though. The interface between the high-density, rotating central cylinder and the external medium develops small amplitude instabilities in our case (visible in the upper right panel of Fig. 5.17). Also the two dimensional distribution of E_z (Fig. 5.17 lower right panel) *seems* more circularly symmetric in our case. We note, however that the vertical scale of Bucciantini and Del Zanna (2013) is compressed with respect to the horizontal one in their Fig. 3. Hence all the structures look more oblate than what they actually are in our figures, where the vertical and horizontal scales are isotropic. The differences beween our approach and those of Dumbser and Zanotti (2009) and Bucciantini and Del Zanna (2013) likely stem from the distinct numerical methods employed. For instance, Bucciantini and Del Zanna (2013) employ a *fully constrained* scheme, i.e. they do not have an explicit equation for the charge conservation as we do, but instead impose $\nabla \cdot \mathbf{E} = q$. Furthermore, they enforce the magnetic solenoidal constraint, $\nabla \cdot \mathbf{B} = 0$ via the upwind constrained transport method employing staggered grids (Del Zanna et al., 2003), while we resort to the hyperbolic divergence cleaning method of Dedner et al. (2002). However, we find that the spatial reconstruction is one of the most relevant differences to explain the discrepancies in the low-σ regime. In such a resistive regime the wave structure changes drastically, with a faster expanding electric field, which is no longer inductive (see also the transverse profile of the solution

along the $x = 0$ axis in Fig. 5.18 lower panels). We have employed the $5^{\rm th}$-order accurate reconstruction scheme MP5, while Bucciantini and Del Zanna (2013) resort to a $3^{\rm rd}$-order accurate Central Essentially Non-Oscillatory spatial reconstruction with a Monotonised Center (MC) limiter. We have repeated the resistive rotor test reducing the order of the spatial reconstruction. For that we have employed a $2^{\rm nd}$-order MC intercell reconstruction, finding that the differences with respect to Bucciantini and Del Zanna (2013) for the case $\sigma = 10$ are significantly reduced (see, Fig. 4.16 in Sec. 4.5.6). In particular, we observe a reduction of the perturbations in the pressure at the transition layer between the central, rotating cylinder and the initially static outer medium. Our results hint towards an excessive dissipation of the algorithms, both of Bucciantini and Del Zanna (2013) and ours, for low-order spatial reconstructions. The differences in the resistive regime with respect to Dumbser and Zanotti (2009) can also be attributed to the usage of a lower order scheme (P_0P_2 in their case) compared to ours. Figure 5.18 shows a more quantitative comparison between the HLLC and HLL solvers with different spatial reconstructions. The smaller numerical resistivity of the HLLC solver stands out in the nearly-ideal regime ($\sigma = 10^6$; Fig. 5.18 left panels) for tests with a $1^{\rm st}$-order (Godunov) spatial reconstruction. The HLLC solver captures very well the sharp, small scale variations in the solution, which almost overlaps with that of models using the MP5 spatial reconstruction (compare the green line -HLLC- with the solutions using MP5 and either HLLC or HLL in the lef panels of Fig. 5.18). At intermediate values of the conductivity ($\sigma = 10^3$) the solutions using the HLL and HLLC solvers are nearly overlapping, and the $1^{\rm st}$-order schemes smear out the torsional Alfvén waves (small scale structure) flanking the central core of the rotor (Fig. 5.18 central panels).

In this 2D test, the models run with the HLLC solver need $\sim 5\%$ larger computational time than those computed with the HLL solver.

5.2.9 Cylindrical Explosion

The cylindrical explosion test develops a strong shock propagating into a magnetically dominated medium. Results for different cylindrical explosion problems in RMHD (e.g. Del Zanna et al., 2003; Komissarov, 1999; Leismann et al., 2005; Martí, 2015; Mignone and Bodo, 2006) as well as in the RRMHD regime (e.g. Komissarov et al., 2007; Palenzuela et al., 2009) have been published. We have chosen a setup similar to that in Palenzuela et al. (2009). It consists of a square covering the domain $-6 \le x \le 6$, $-0.5 \le y \le 0.5$, having a central circular region with a radius $r = \sqrt{x^2 + y^2} \le 0.8$, where the thermal pressure ($p_{\rm g,c} = 1$) and the rest-mass density ($\rho_{\rm c} = 0.01$) are higher than elsewhere ($p_{\rm g,b} = \rho_{\rm b} = 0.001$; $r > 1$). We note that these values of the thermal pressure and of the rest-mass density are larger than the *standard* ones in RMHD

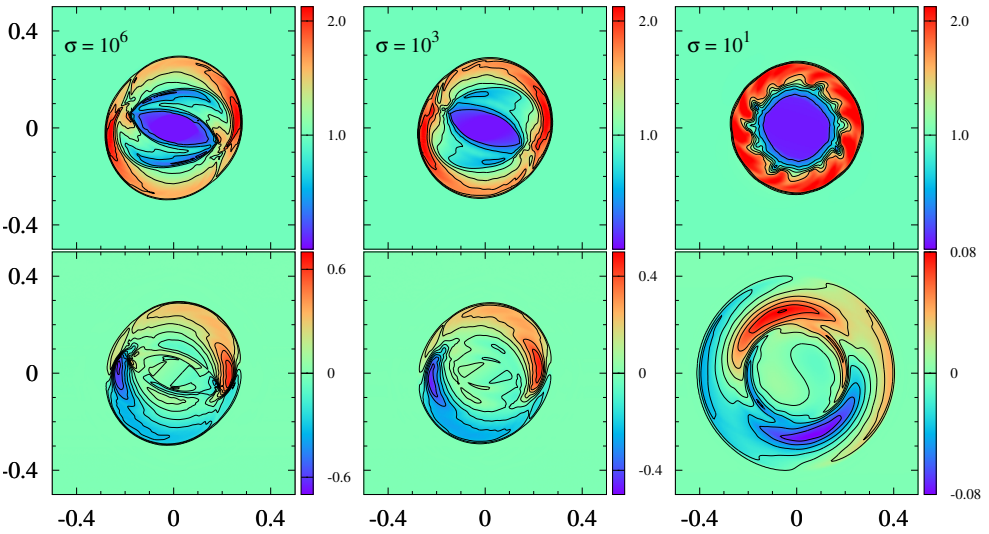

Figure 5.17: Resistive Rotor computed with a second order MIRK scheme, MP5 intercell reconstruction and a grid of 300×300 zones evolved up to a time $t = 0.3$. Upper panels: snapshots of the gas pressure. Lower panels: snapshots of E_z. We show the evolution for different values of the conductivity: the nearly ideal case $\sigma = 10^6$ (left panels), an intermediate or semi-resistive case $\sigma = 10^3$ (central panels) and a resistive case $\sigma = 10$ (right panels).

benchmarks, where $p_{\rm g,b} = 3 \times 10^{-5}$ and $\rho_{\rm b} = 10^{-4}$ for $r > 1$ are adopted. Our RRMHD code is unable to handle such extreme conditions, where the magnetization of the outer medium is 50 times larger than assumed here, unless a prohibitively small CFL factor or extremely fine grids are employed. The central region is continuously connected with the surroundings using an exponentially decreasing pressure and density in the region $0.8 \leq r \leq 1$. Everywhere in the computational domain, the magnetic field, $\mathbf{B} = (0.1, 0, 0)^T$,[5] is uniform, $\mathbf{v} = (0, 0, 0)^T$ and the adiabatic index is $\gamma = 4/3$. The initial data are evolved until $t = 4$. This test is used to validate the new resistive code in 2D and in the ideal limit (a uniform conductivity $\sigma = 10^6$ is set everywhere), in a situation where strong shocks develop (in contrast to the resistive rotor shown in Sec. 5.2.8).

A direct comparison with an analytic solution is not possible in this case. We note, however, that our results (Fig. 5.19) compare fairly well with the those obtained with our ideal RMHD code (Antón et al., 2010; Leismann et al., 2005), as well as with the same setup in Palenzuela et al. (2009). As in the latter reference, our solution is also regular everywhere and similar results can be obtained with smaller values of the conductivity, namely with $\sigma \gtrsim 10^4$.

[5] Palenzuela et al. (2009) employ a weaker magnetic field $\mathbf{B} = (0.05, 0, 0)^T$ in this test.

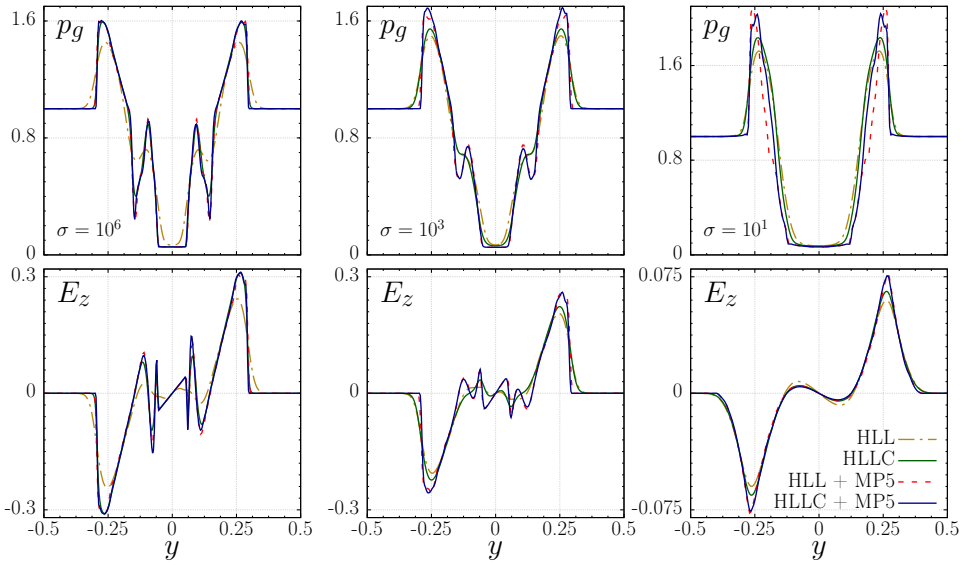

Figure 5.18: Profile along the $x = 0$ axis of the gas pressure (upper panels) and E_z (lower panels) for different values of the conductivity (labeled in each panel) at $t = 0.3$. Dash-dotted brown and solid green lines show the 1^{st}-order schemes employing HLL and HLLC solvers, respectively. Dashed red and solid blue lines show the cases in which we combine the MP5 intercell reconstruction with either the HLL solver or the HLLC solver, respectively.

The largest discontinuities in this test are the shocks delimiting the fast expanding shell, whose profiles at $x = 0$ are displayed in Fig. 5.19 (bottom panels). Thus, resolving the contact waves does not play a major role in the overall dynamics. As a result, the advantage of using the HLLC solver with respect to employing the HLL solver is significantly decreased. Indeed, for this test, the HLLC and HLL solutions basically overlap independently of the spatial reconstruction employed. This fact is evident in Fig. 5.19 (bottom panels). The solutions computed without any spatial reconstruction are nearly coincident, with tiny discrepancies in the pressure on the central evacuated area of the domain (see yellow and green lines in Fig. 5.19 bottom panels). The results of simulations employing a 2^{nd}-order MCL reconstruction and the HLL or the HLLC solver are almost indistinguishable.

The CE tests performed with the HLLC solver require $\sim 18\%$ larger computational time than those computed with the HLL solver, i.e. in this 2D test the computational overhead of using the HLLC solver is a bit larger than for the RR test. However, looking at the variations of the overheads displayed in Tab. 5.1, we may conclude that the computational time needed by the HLLC solver is $\sim 5 - 20\%$ larger than with the HLL solver, independently of the dimensionality of the problem.

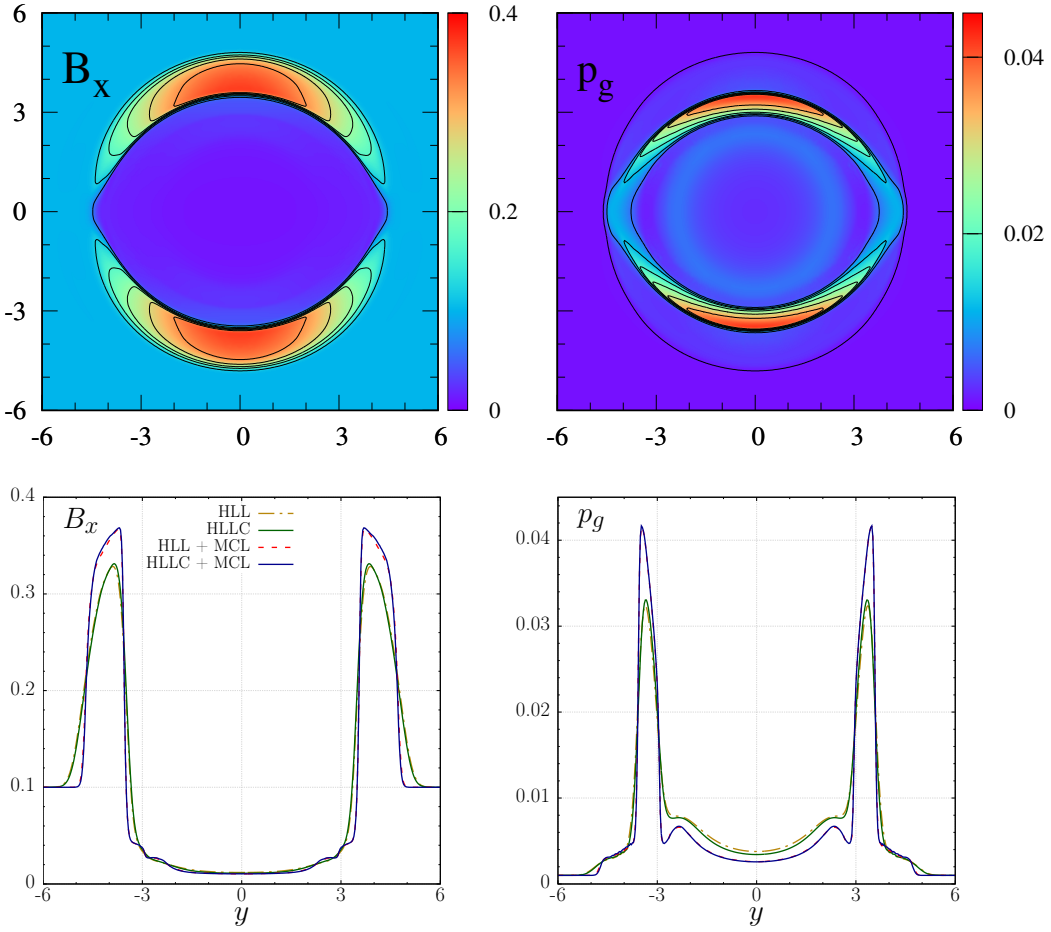

Figure 5.19: Upper panel: snapshots at $t = 4$, of the magnetic field (B_x component; left) and thermal pressure $p_{\rm g}$ (right), for the CE test computed with a uniform grid of 400×400 cells, CFL factor $C_{\rm CFL} = 0.1$, employing the IMEX-RK scheme SSP2(332)-LUM and a MCL intercell reconstruction. Lower panel: profiles along $x = 0$, for B_x (left) and $p_{\rm g}$ (right). Dash-dotted brown and solid green lines show the $1^{\rm st}$-order HLL and HLLC schemes, respectively. Dashed red and solid blue lines show the second order case using the MCL spatial reconstruction in combination with the HLL and the HLLC solvers, respectively.

Chapter 6

Numerical dissipation

To evaluate if a numerical simulation is accurate and reliable, we must perform verification and validation tests. Following (Roache, 1997), we understand verification as *solving the equations right* and validation as *solving the right equations*. That is *verification* allow us to find the order of accuracy of a numerical solution and *validation* tell us if that solution is consistent with the physical problem of interest. While in the Chaps. 4 and 5 we have been more concerned about the *validation* of our methodology, in this chapter our main focus is on the *verification* procedure.

We compute the numerical solution of the PDEs that form the system governing equations of RRMHD performing a finite volume discretization of the space-time and employing a MoL, whereby the spatial and temporal discretization of the equations are undertaken in different steps (see Chap. 4). The spatial discretization of the governing equations subdivides the spatial domain of the problem into cells of finite size, Δx.[1] Likewise, for the temporal discretization, the interval of time in which the equations are evolved is also tessellated with a number of sub-intervals of size Δt, which we assume to be all of the same size to simplify the ensuing discussion (see the discussion on the validity of this assumption in the text between Eqs. (4.6) and (4.7) in Chap. 4). The discretized set of equations are no longer PDEs, but their algebraic analogues. The solution to the discretized equations, is not the same as the exact solution, i.e. the solution to the system of PDEs, though it approximates the latter. The difference between the two solutions is called the *discretization error*. Discretization methods are consistent if the discretization error goes to zero as $\Delta x \to 0$ and $\Delta t \to 0$. The rate at which the error decreases to zero is called the order of accuracy. The spatial and temporal orders of accuracy do

[1] For the purpose of this explanation, we may restrict to one spatial dimension, but the discussion that follows is valid in any number of spatial dimensions.

not need to be the same, as we have anticipated in Sec. 4.5.3. For example, a discretization method for a PDE (or a system of PDEs) is said to be second order accurate in space if the discretization error goes to zero as $\delta_1(\Delta x)^2$, while simultaneously, it could be first order accurate in time if the discretization error goes to zero as $\delta_2(\Delta t)^1$, where δ_1 and δ_2 are quantities that depend on the typical time and length scales of the problem whose solution we are seeking and the numerical method employed to look for the solution. The overall order of accuracy of such a method will depend on the regime where we are seeking the solution and on the particular spatial and temporal integration methods used, i.e. it does not necessarily have to be the lowest order of all the approximations (first-order in the previous example; e.g. Rembiasz et al., 2017). This fact can be easily understood since, formally, we may write the total discretization error as the sum of the spatial and of the temporal discretization errors like in Eq. (4.55). Hence, depending on the relative values of $\delta_1(\Delta x)^r$ and $\delta_2(\Delta t)^q$ (where r and q are the spatial and temporal orders of accuracy, respectively), either discretization errors of spatial origin are negligible $\delta_1(\Delta x)^r \ll \delta_2(\Delta t)^q$ or, otherwise $\delta_2(\Delta t)^q \ll \delta_1(\Delta x)^r$.[2] In the former case the order of the method will be determined by the accuracy of the temporal discretization, while in the latter case it will be given by the accuracy of the spatial discretization. Discretization errors can manifest themselves in two ways. They can either smear out the solution (*numerical dissipation*) or introduce phase errors (*numerical dispersion*). In the study of numerical errors carried out in this chapter, we assume that spatial discretization errors and time integration errors contribute only to numerical dissipation. As the mode of action of the numerical dissipation, introduced during the numerical integration of an hydrodynamic flow, resembles that of a *physical viscosity* and, for magnetized flows, also a *physical resistivity*, they are commonly referred to as *numerical viscosity* and *numerical resistivity*, respectively (see, e.g. Laney (1998), Chap. 14, and Bodenheimer et al. (2006), Chap. 8.3).

If the errors introduced by numerical viscosity and resistivity are not sufficiently small, they lead to discrepancies from the genuine physical solutions. As an example (out of many) of the previous situation we refer to the case of Obergaulinger et al. (2009), who found a development of the TM instability (Furth et al., 1963) in their 2D *ideal* MHD simulations of the MRI (Balbus and Hawley, 1991), in spite of the fact that TM instabilities can only grow in resistive MHD. Thus Obergaulinger et al. presumed that TM instabilities in their simulations grew due to numerical resistivity. Indeed, in most scientific papers where dissipative effects are claimed as responsible for the dynamics found, the governing equations employed were not the Navier-Stokes equations or the

[2]Intermediate regimes where both kinds of errors are comparable exists, in which case, the lowest of the two orders of accuracy determines the global order of accuracy.

equations of resistive (relativistic) MHD. Two examples of the previous papers (again out of many others) follow. Aloy et al. (2000) find evidences of jet stratification due to the *viscous* shearing of parsec-scale relativistic jets with the medium flanking them using and inviscid RHD code, which means that the viscosity they find is of numerical origin. Bromberg and Tchekhovskoy (2016), claim that magnetic field reconnection plays a fundamental role to explain the formation of dissipative regions in the evolution of relativistic magnetized jets, on the basis of numerical models where they solve for the equations of General Relativistic MHD (i.e. without accounting for the physical resistivity).

In order to estimate the importance of the numerical errors that we make in the discretization of the RRMHD equations, we follow the approach of Rembiasz et al. (2017). These authors discussed in depth the expected *functional* dependence of the numerical viscosity and of the numerical resistivity in an Eulerian MHD code. Both physical viscosity and resistivity may have very involved tensor character, inherited from the action on the plasma of the viscosity and resistivity tensors (see, e.g. Landau and Lifshitz, 1986). However, we will assume that the fluid is isotropic, in which case both the viscosity and the resistivity can be cast in the form of scalar coefficients (Landau and Lifshitz, 2013). Since both resistivity and kinematic viscosity have dimensions of $[\mathrm{cm}^2\,\mathrm{s}^{-1}]$, a possible assumption, e.g. for the numerical shear viscosity is that it is proportional to $\nu^* \propto \mathcal{V}\mathcal{L}$, where $\mathcal{V}$ and $\mathcal{L}$ are the characteristic velocity and length scale of a simulated system, respectively. We note that the previously assumed form is natural in Newtonian fluid dynamics, but may look inadequate in a relativistic context. The relativistic analog of a characteristic speed could be the corresponding four-velocity $\mathcal{U} := \mathcal{V}/\sqrt{1-\mathcal{V}^2}$, and the analog of the characteristic length could be the proper length, $\tilde{\mathcal{L}} := \mathcal{L}\sqrt{1-\mathcal{V}^2}$. In such a case, we would find again that $\nu^* \propto \mathcal{U}\tilde{\mathcal{L}} \propto \mathcal{V}\mathcal{L}$. Other corrections related to relativistic kinematics could be important in shaping the form of the numerical viscosity and resistivity, but we opt for not complicating the assumed dependence in the light of the results we will show in this chapter.

Given the origin of the numerical viscosity and resistivity (i.e. stemming from discretization errors), it is natural to assume that they depend on Δx and Δt in a similar way as any other discretization error, namely, similarly to Eq. (4.55). Hence, these errors should be proportional to $(\Delta x)^r$ and $(\Delta t)^q$. Since Δx has dimensions of length and since Δt has dimensions of time, and as in Eq. (4.55) we have formal dependences $(\Delta x)^r$ and $(\Delta t)^q$, each of these terms should be multiplied by $\mathcal{L}^{-r}$ and by $(\mathcal{V}/\mathcal{L})^{-q}$, respectively, in order to have the expressions for the numerical viscosity and resistivity with the correct dimensions. Furthermore, in either MHD or RRMHD, the time step is not independent of the spatial discretization if the integration method is either explicit or partly implicit, i.e. the CFL stability condition (Eq. (4.6)) holds. Therefore, following the steps of Rembiasz et al. (2017) for Newtonian

MHD, we propose to test their ansatz for the numerical shear viscosity ν^* in RRMHD, namely, that the numerical viscosity has the following dependences

$$\nu^* = \mathfrak{N}_\nu^{\Delta x} \mathcal{V} \mathcal{L} \left(\frac{\Delta x}{\mathcal{L}} \right)^r + \mathfrak{N}_\nu^{\Delta t} \mathcal{V} \mathcal{L} \left(\frac{C_{\rm CFL} \Delta x}{\mathcal{L}} \right)^q , \tag{6.1}$$

where, $\mathfrak{N}_\nu^{\Delta x}, \mathfrak{N}_\nu^{\Delta t}, r$ and q are constants for a given numerical scheme. An identical premise could be imposed for the numerical resistivity, η^*, but changing the coefficients $\mathfrak{N}_\nu^{\Delta x}$ and $\mathfrak{N}_\nu^{\Delta t}$ by other (different) ones $\mathfrak{N}_\eta^{\Delta x}$ and $\mathfrak{N}_\eta^{\Delta t}$, namely

$$\eta^* = \mathfrak{N}_\eta^{\Delta x} \mathcal{V} \mathcal{L} \left(\frac{\Delta x}{\mathcal{L}} \right)^r + \mathfrak{N}_\eta^{\Delta t} \mathcal{V} \mathcal{L} \left(\frac{C_{\rm CFL} \Delta x}{\mathcal{L}} \right)^q . \tag{6.2}$$

Once the unknown coefficients $\mathfrak{N}$, r and q are determined, the above ansatzes can be used to estimate the numerical resistivity and viscosity of any Eulerian (RR)MHD code, employed in a different physical setup but with the same method (i.e. using the same Riemann solver, reconstruction scheme and time integrator). We stress that the different coefficients $\mathfrak{N}$ (to first approximation) should be problem independent and their values may be computed in relatively simple tests problems (as we shall do in the following sections).

The expressions for our ansatzes of the numerical viscosity (Eq. 6.1) and resistivity (Eq. 6.2) depend on two parameters which *are* problem dependent: $\mathcal{L}$ and $\mathcal{V}$. However, as we shall conclude in Sec. 6.4, one of the biggest differences between classical Eulerian MHD codes and RRMHD codes is that the characteristic speed is always the speed of light in the case of RRMHD (i.e. , $\mathcal{V} = 1$). In contrast, the characteristic length depends on the problem and we will set up simple cases (damping of the amplitude of propagating waves or diffusion of shear layers)[3] where, for numerical convenience, the sought characteristic length is set equal to the computational box.

6.1 Measurement of the numerical viscosity

Although the system of RRMHD equations (Eq. 2.37) does not include shear viscosity explicitly, any numerical method employed to integrate it will include some amount of numerical viscosity. In the following, we will measure ν^* resorting to wave damping tests. In the absence of any dissipation (either numerical or physical), small amplitude velocity waves should maintain their amplitude at any time. In practice, the presence of numerical dissipation damps these waves and we may obtain a direct measurement of the numerical

[3]Hereafter, a shear layer describes a region of a flow where there is a significant velocity gradient and shear stresses are proportional to this velocity gradient and to the shear viscosity. Also, we refer to a magnetic shear layer as the region of the plasma where the magnetic gradients are significant.

viscosity from the determination of the damping rates. This is the procedure we follow in the 1D shear layer test (Sec. 6.1.1).

To determine the dissipative effects into the shear layer simulations is instructive to generalize the equation of motion including viscous effects (i.e. examining the Navier-Stokes equations), ignoring the complexity of plasma transport coefficients in presence of magnetic fields and just exploit the scalar character of the kinematic viscosity coefficient (ν). Then the *(near) conservation of momentum* can be expressed in ideal MHD as, (Goedbloed and Poedts, 2004, see e.g. Eq.(4.136))

$$\rho\left(\partial_t + \mathbf{v}\cdot\nabla\right)\mathbf{v} = -\nabla p_{\rm g} + \frac{1}{\mu_0}\left(\nabla\times\mathbf{B}\right)\times\mathbf{B} + \mathbf{F}_{\rm visc},$$

with the viscous force given by,

$$\mathbf{F}_{\rm visc} \approx \rho\nu\left(\nabla^2\mathbf{v} + \frac{1}{3}\nabla\nabla\cdot\mathbf{v}\right).$$

In order to simplify the measurement of the numerical viscosity, we restrict to a numerical setup which is incompressible ($\nabla\cdot\mathbf{v}=0$), non magnetized ($\mathbf{B}=0$), isobaric ($p_{\rm g}=p_{\rm g,0}$) and uniform ($\rho=\rho_0$). Under these conditions the (near) conservation of momentum, looks like a *dissipation equation* of the form,

$$\left(\partial_t + \mathbf{v}\cdot\nabla\right)\mathbf{v} = \nu\nabla^2\mathbf{v}. \tag{6.3}$$

For sufficiently small velocities and specific enthalpies, Eq. (6.3) also describes the damping of small amplitude waves in RRMHD.

6.1.1 Velocity Shear Layer

test	$p_{\rm g,0}$	ρ_0	B_0	v_0	$\epsilon_{\rm am}$	$v_{\rm A}$	$c_{\rm s}$	$v_{\rm fms}$
VSL	10^{-4}	1	0	10^{-5}	–	0	1.41×10^{-2}	1.41×10^{-2}
MD	10^{-4}	1	10^{-2}	0	–	10^{-2}	1.41×10^{-2}	1.70×10^{-2}
CPAW-cla	10^{-4}	1	10^{-4}	10^{-9}	10^{-5}	10^{-4}	1.41×10^{-2}	1.41×10^{-2}
CPAW-rel	10^{-2}	1	10^{-1}	10^{-1}	1	10^{-1}	1.40×10^{-2}	1.67×10^{-1}

Table 6.1: Parameters of the models considered in this chapter. The columns list (from left to right): the generic model name, the thermal pressure, $p_{\rm g,0}$, the rest-mass density, ρ_0, the magnetic field strength, B_0, the velocity, v_0, the Alfvén speed, $v_{\rm A}$ (Eq. (4.54)), the sound speed, $c_{\rm s}$ (Eq. (2.22)) and the fast magnetosonic speed, $v_{\rm fms}$ (Eq. (6.18)). The subscript "0" refers to the background state. By default for all simulations in this chapter, if not otherwise stated, we set the characteristic velocity to $\mathcal{V}=1$, the box length to $L_x=\mathcal{L}=1$ (see Sec. 6.4), the wavevector to $k=2\pi$, the physical resistivity to $\eta=10^{-9}$ and we use an ideal EoS with adiabatic index $\gamma=2$.

Following the guidelines of the previous section, we set up a uniform and isobaric medium, where the velocity profile displays a shear layer:

$$\begin{aligned} v_y &= v_0 \ \sin(kx), \\ \rho &= \rho_0, \\ p_{\rm g} &= p_{{\rm g},0}, \end{aligned}$$

with k the x-component of the wave vector.[4] We will refer to the previous problem setup as velocity shear layer (VSL) test.

The exact solution of the *dissipation equation* (hereafter denoted with an "(ex)" subscript), Eq. (6.3), for the velocity field, v_y, reads

$$v_{y,({\rm ex})}(x,t) = v_0 \exp\left(-\mathfrak{D}_{\rm SL}\, t\right) \sin\left(kx\right), \tag{6.4}$$

where the damping coefficient, $\mathfrak{D}_{\rm SL}$, as a function of k, is defined as

$$\mathfrak{D}_{\rm SL} = k^2 \nu.$$

To estimate the numerical viscosity ν^*, first we compute the kinetic energy, integrating the (exact) value of the velocity (Eq. (6.4)) to compute the (analytic) value of the kinetic energy (note that we assume $\rho_0 = 1$) in the whole spatial domain. The expression obtained can be cast in the form

$$\ln\left(\int v^2_{y,({\rm ex})}(x,t)\ dx\right) \quad = \quad \ln\left(\frac{v_0^2 L_x}{2}\right) - 2\,\mathfrak{D}_{\rm SL}\, t.$$

This expression serves as a linear model for the numerical data, which can be fitted to a straight line of the form $y = b + at$, where $y = \ln\left(\int v_y^2(x,t)\ dx\right)$ is computed from the numerical distribution of the velocity in the whole computational domain. From the slope of the linear fit, we find

$$\nu^* = -\frac{a}{2k^2}.$$

According to our ansatz (Eq. (6.1)), the numerical viscosity depends on both Δx and Δt. In order to compute the dependence of the numerical viscosity on the grid resolution minimizing the contribution of the time integration errors we set $C_{\rm CFL} = 0.01$,[5] so that Eq. (6.1) approximately reads

$$\nu^* \ \simeq \ \mathfrak{N}_\nu^{\Delta x}\ \mathcal{V}\ \mathcal{L}\ \left(\frac{\Delta x}{\mathcal{L}}\right)^r. \tag{6.5}$$

[4] For brevity, we will sometimes refer to the scalar value of k as a "wave vector", even though the strictly speaking, the wave vector should denote $\mathbf{k} = (k_x, k_y, k_z)$. However, in all 1D problem, we assume that $k = k_x$, $k_y = k_z = 0$.

[5] We have also considered a larger value of the CFL ($C_{\rm CFL} = 0.1$) finding no significant differences in the quantitative values of the numerical viscosity for this problem.

Equation (6.5) does not only allow us to infer the behavior of the numerical viscosity in terms of the grid resolution, but also provides us a way to measure the order of convergence of the scheme. For that, we take logarithms in Eq. (6.5) and compute a linear regression $\ln(\nu^*)$ vs $\ln(\Delta x)$ of the form

$$\ln(\nu^*) = d + r \ln(\Delta x), \tag{6.6}$$

where r is the estimated order of convergence of the scheme and

$$d := \ln\left(\mathfrak{N}_\nu^{\Delta x}\, \mathcal{V}\, \mathcal{L}^{1-r}\right). \tag{6.7}$$

In the following, we show the results obtained for the numerical viscosity as a function of the grid resolution for a set of 1D experiments where, we adjust a single wave in a box of length $L_x = 1$ (see e.g. Fig. 6.1), with amplitude $v_0 = 10^{-5}$ and wave number $k = 2\pi/L_x$, within a homogeneous medium of uniform density $\rho_0 = 1$ and thermal pressure $p_{\mathrm{g},0} = 10^{-4}$ (see Tab. 6.1).

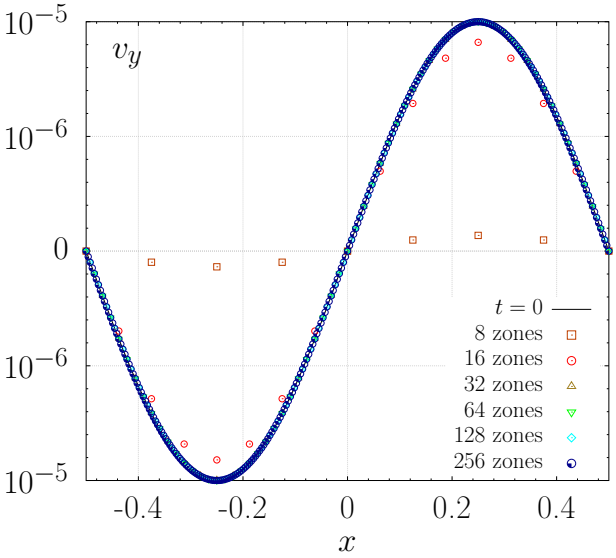

Figure 6.1: VSL. Velocity field v_y profile at $t = 100$ for different number of grid zones. The simulations were performed with the MIRK2 time-integrator, the HLL Riemann solver and the MP5 reconstruction algorithm. The solutions with more than 32 zones per wavelength nearly overlap each other and can hardly be distinguished at the scale of the plot.

Figure 6.1 depicts the numerical results after a time $t = 100$, where we observe the evident amplitude damping when the resolution is coarser (i.e. the domain is discretized in fewer number of zones). This is the qualitative behavior to be expected from Eq. (6.6). For finer resolutions ($n_x \geq 32$) there is a tiny numerical damping and the solution looks very much the same as in the inviscid limit. It should be noted that, for the spatial reconstruction schemes used,

MP5, MP7 and MP9, the measured orders of convergence (r) are very close to the theoretical ones ($r_{\rm th}$), as can be seen in Tab. 6.2 (see also Fig. 6.2). Furthermore, the computed numerical orders of accuracy are weakly dependent on the choice of time-integration scheme and Riemann solver. This result is consistent with the fact that, for the small values of the CFL factor employed, spatial errors are the dominant contribution to the numerical viscosity. Table 6.2 also shows the value of the parameter $\mathfrak{N}_\nu^{\Delta x}$ that we obtain from the constants of the fits, for simulations where we use our code employing MIRK1, MIRK2, SSP2(332)-LUM or SSP3(433) as time-integrators, HLL or HLLC as Riemann solvers and three different choices for the spatial reconstruction scheme (MP5, MP7 or MP9). We notice that, in order to compute $\mathfrak{N}_\nu^{\Delta x}$ from d (Eq. (6.7)) it is necessary to make assumptions on the values of $\mathcal{V}$ and $\mathcal{L}$. As we will justify in Sec. 6.4, we use $\mathcal{V} = \mathcal{L} = 1$. It can be seen in Tab. 6.2 that, within the margins set by the statistical errors of the fit, the computed parameter $\mathfrak{N}_\nu^{\Delta x}$ only depends on the order of the spatial reconstruction, and it is insensitive to the employed approximate Riemann solver and time integration scheme, when used in combination with the MP5 and MP7 reconstructions. Employing the MP9 reconstruction, we observe some dependence with the time-integrator as well as with the Riemann solver, though rather moderate.

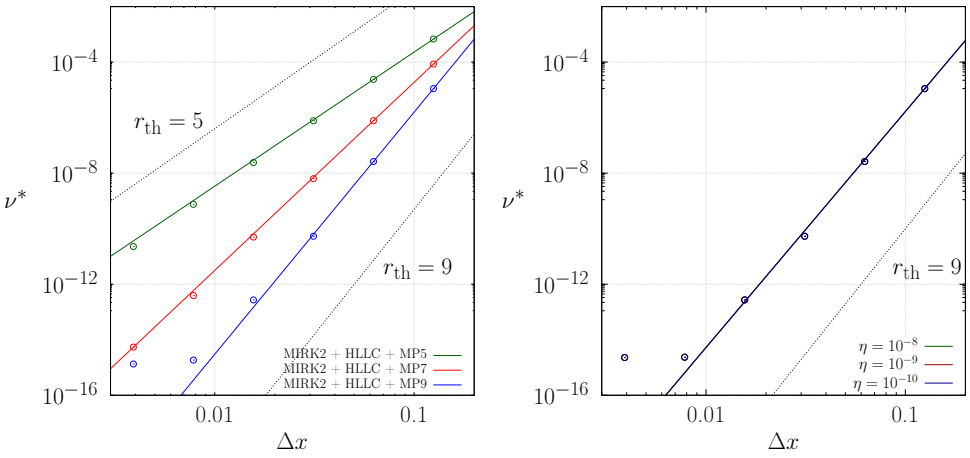

Figure 6.2: VSL. *Left panel*: Numerical viscosity (circles), ν^*, as a function of the grid resolution (Δx) for the MIRK2 time integration scheme, using the HLLC solver and different MP schemes (corresponding to the different colors; see plot legends). These simulations were also performed with another time integration scheme (SSP2(332)-LUM) in combination with HLL or HLLC solvers and different MP schemes, resulting in qualitatively and quantitatively similar results. The integration order measured (r) and the parameter $\mathfrak{N}_\nu^{\Delta x}$ are shown in Tab. 6.2. In the figure we also show with solid lines of the same colors as the symbols the fits to the numerical results. Several dotted lines are included to display the theoretical order of accuracy ($r_{\rm th}$). *Right panel*: Behavior of numerical viscosity for different resistivity values (η) using MIRK2, HLL, and MP9.

time-integrator	solver	reconstruction	r	$\mathfrak{N}_\nu^{\Delta x}$
MIRK1	HLL	MP5	4.971 ± 0.015	22 ± 2
MIRK1	HLL	MP7	6.98 ± 0.03	190 ± 24
MIRK1	HLL	MP9	8.88 ± 0.04	830 ± 170
MIRK1	HLLC	MP5	4.963 ± 0.014	21.8 ± 1.3
MIRK1	HLLC	MP7	6.83 ± 0.06	120 ± 30
MIRK1	HLLC	MP9	8.88 ± 0.04	1230 ± 170
MIRK2	HLL	MP5	4.971 ± 0.017	22.3 ± 1.5
MIRK2	HLL	MP7	6.90 ± 0.03	153 ± 17
MIRK2	HLL	MP9	8.48 ± 0.21	400 ± 300
MIRK2	HLLC	MP5	4.971 ± 0.017	22.3 ± 1.5
MIRK2	HLLC	MP7	6.83 ± 0.06	120 ± 30
MIRK2	HLLC	MP9	8.47 ± 0.21	400 ± 300
SSP2(332)-LUM	HLL	MP5	4.971 ± 0.017	22.3 ± 1.5
SSP2(332)-LUM	HLL	MP7	6.91 ± 0.03	152 ± 17
SSP2(332)-LUM	HLL	MP9	8.51 ± 0.19	500 ± 300
SSP2(332)-LUM	HLLC	MP5	4.971 ± 0.017	22.3 ± 1.5
SSP2(332)-LUM	HLLC	MP7	6.91 ± 0.03	152 ± 17
SSP2(332)-LUM	HLLC	MP9	8.51 ± 0.19	500 ± 300
SSP3(433)	HLL	MP5	4.971 ± 0.017	22.3 ± 1.5
SSP3(433)	HLL	MP7	6.82 ± 0.06	120 ± 30
SSP3(433)	HLL	MP9	8.51 ± 0.19	500 ± 300
SSP3(433)	HLLC	MP5	4.971 ± 0.017	22.3 ± 1.5
SSP3(433)	HLLC	MP7	6.82 ± 0.06	120 ± 30
SSP3(433)	HLLC	MP9	8.88 ± 0.04	1230 ± 170

Table 6.2: VSL. Spatial integration order of accuracy, r, and coefficient $\mathfrak{N}_\nu^{\Delta x}$, for numerical schemes including as time-integrators MIRK1, MIRK2, SSP2(332)-LUM or SSP3(433), using HLL or HLLC as approximate Riemann solvers in combination with different reconstruction schemes (MP5, MP7 or MP9). In order to estimate $\mathfrak{N}_\nu^{\Delta x}$ we assume $\mathcal{V} = \mathcal{L} = 1$ (see Sec. 6.4).

We shall notice that in order to obtain the numerical order of accuracy when using the MP9 reconstruction, we have excluded the point computed with the grid consisting of $n_x = 256$ cells, since it is clearly out of the trend of the values computed at coarser resolutions. The reasons for this behaviour are multiple. First, the MP9 reconstruction produces values of the numerical viscosity extremely small ($\eta^* < 10^{-15}$) as $\Delta x < 1/128$. For such tiny values round-off errors in the (double precision) floating point arithmetics compromise the accuracy of the evaluation of η^* from the fits and, indeed, the accuracy of the numerical scheme becomes comparable to the limits that the floating point system may resolve. In practical applications this is not a limitation, since one *never resolves* a single sinusoidal variation of the data with more

than a few (typically $\lesssim 10$ numerical zones). Increasing the resolution in such a regime (i.e. using finer grids) with MP9 reconstruction practically results in a 9th order accurate improvement of the results. Second, the assumption made on the negligible value of the contributions arising from the time discretization errors to the numerical viscosity breaks down. Equation (6.5) does not strictly hold and the numerical viscosity should adopt the form of our full ansatz expressed in Eq. (6.1), which is not a power-law in logarithmic scale but a smoothly broken power-law with two different slopes.

As a final comment, we point out that we have performed a *sanity check* in order to verify that the numerical viscosity that we have measured is independent of the physical resistivity. This must be the case from the physical point of view, since there the magnetic field is zero in this test. We find that this is also the case numerically (Fig. 6.2; right panel).

6.2 Measurement of the numerical resistivity

In the following, we focus on the behavior of plasma subject to pure resistive diffusion of a magnetic field in the absence of a plasma flow. This means that the magnetic field changes in time due to resistive effects and that the evolution in time of the magnetic field is governed by a diffusion equation. In the particular case, in which the magnetic diffusivity, owing to resistivity (η), is uniform in space and the plasma is at rest ($\mathbf{v} = 0$), the current density Eq. (2.11) reduces to $\mathbf{J} = \mathbf{E}/\eta$ and the Faraday's equation (Eq. (2.3)) to

$$\partial_t \mathbf{B} = -\eta \, \nabla \times \mathbf{J}. \tag{6.8}$$

If we set up a problem such that the currents are divergence free ($\nabla \cdot \mathbf{J} = 0$) in a macroscopically neutral plasma ($q = 0$), then we may neglect the displacement currents ($\partial \mathbf{E}/\partial t$) in Maxwell's equations and the current density is related to the magnetic field simply by the time-independent Ampère's law

$$\mathbf{J} = \nabla \times \mathbf{B}. \tag{6.9}$$

Combining Faraday's equation in the form of Eq. (6.8) with Ampère's law as in Eq. (6.9), we obtain the diffusion equation

$$\partial_t \mathbf{B} = \eta \, \nabla^2 \mathbf{B}. \tag{6.10}$$

6.2.1 Magnetic Diffusion

In order to measure the numerical resistivity of our algorithm, we propose a new test, which has a number of advantages over the existing self-similar diffusion test proposed by Komissarov (2007) (see Sec. 4.5.1), as we shall explain below.

In simple numerical applications consisting in the diffusion of a one dimensional magnetic layer as we show in this section, the total resistivity (η_t), driving the diffusive evolution of the magnetic field, contains the contribution of both physical (η) and numerical (η^*) resistivity, and we shall assume that it has the form[6]

$$\eta_t = \eta + \eta^*. \tag{6.11}$$

In order to *verify* the ability of our method to properly resolve simple diffusion problems, we set up series of 1D problems whose initial conditions are given by

$$\begin{aligned} B_y &= B_0 \ \sin(kx), \\ B_z &= B_0 \ \cos(kx), \\ \rho &= \rho_0, \\ p_{\rm g} &= p_{\rm g,0}. \end{aligned} \tag{6.12}$$

We refer to the numerical experiments using this generic setup as magnetic diffusion (MD) tests.

For these initial conditions, the solution of the diffusion equation (Eq. (6.10)), for the magnetic field components is

$$B_{y,(\rm ex)}(x,t) = B_0 \exp\left(-\mathfrak{D}_{\rm MD}\, t\right) \sin\left(kx\right), \tag{6.13}$$

$$B_{z,(\rm ex)}(x,t) = B_0 \exp\left(-\mathfrak{D}_{\rm MD}\, t\right) \cos\left(kx\right), \tag{6.14}$$

where the damping coefficient $\mathfrak{D}_{\rm MD}$ is defined as

$$\mathfrak{D}_{\rm MD} := k^2 \eta. \tag{6.15}$$

This setup (6.12) is in the *force-free* equilibrium, not only initially, but at any time of the evolution. It is so becasue the magnetic field components, according to Eqs. (6.13) and (6.14), and the magnetic pressure (although decreasing with time) stays uniform. In contrast, the system is not initially in equilibrium in the self-similar current sheet setup (Sec. 4.5.1). The absence of a force-free equilibrium triggers the motion of the plasma, making the "analytic" solution provided in Eq. (4.49) only approximate. The setup (6.12) is an exact solution of the diffusion equation and the diffusion of the two magnetic field components happens at the same rate (see Eq. (6.14)), so that the system is (at least analytically) evolving under force-free conditions at all times. Besides, the approximate solution given by Eq. (4.49) strictly holds if the domain is infinitely long. Numerically, we are forced to take a finite extension of the computational domain and impose boundary conditions at the two ends of

[6] More complex (tensor-like) relations could hold between the total resistivity and η and η^*, but we restrict to the functional (additive) form of Eq. (6.11) for simplicity.

the 1D region covering the magnetic shear layer. In the setup of Komissarov (2007), the boundary conditions at a finite distance (precisely, at $x = \pm 1.5$) are imperfect and do necessarily influence the numerical solution, which may differ from the approximate analytic solution with boundaries set at infinity. For the setup (6.12), periodic boundary conditions permit to set the same boundaries both numerically and theoretically (and at a final distance). Thus, the influence on the solution of the boundary conditions is absent in our setup.

Integrating $B^2_{y,(\mathrm{ex})}(x,t)$ over all the spatial domain (L_x) and taking logarithms, we obtain

$$\ln\left(\int B^2_{y,(\mathrm{ex})}(x,t)\ dx\right) = \ln\left(\frac{B_0^2 L_x}{2}\right) - 2\mathfrak{D}_{\mathrm{MD}} t.$$

As in Sec. 6.1.1, the previous expression serves as a linear model for the numerical data, which can be fitted to a straight line of the form $y = b + at$, where $y = \ln\left(\int B^2_y(x,t)\ dx\right)$ is computed from the numerical distribution of the magnetic field in the whole computational domain.

Numerical resistivity can be determined from the slope of the linear fit and using Eqs. (6.11) and (6.15) as:

$$\eta^* = -\frac{a}{2k^2} - \eta.$$

According to the ansatz (Eq. (6.2)), the numerical resistivity depends on both Δx and Δt. In order determine the dependence of the numerical viscosity on the grid resolution, we minimize the contribution of the time integration errors setting $C_{\mathrm{CFL}} = 0.01$.

$$\eta^* \simeq \mathfrak{N}_\eta^{\Delta x}\ \mathcal{V}\ \mathcal{L}\ \left(\frac{\Delta x}{\mathcal{L}}\right)^{-r}. \tag{6.16}$$

Equation (6.16) allows us to infer the behavior of the numerical resistivity in terms of the grid resolution and provides us a way to measure the order of convergence of the scheme. For that, we take logarithms in Eq. (6.16) and compute a linear regression $\ln(\eta^*)$ vs Δx of the form

$$\ln(\eta^*) = d + r\ln(\Delta x), \tag{6.17}$$

where r is the estimated order of convergence of the scheme and

$$d := \ln\left(\mathfrak{N}_\eta^{\Delta x}\ \mathcal{V}\ \mathcal{L}^{1-r}\right).$$

In the following, we show the results obtained for the numerical resistivity as a function of the grid resolution for a set of 1D experiments where, we

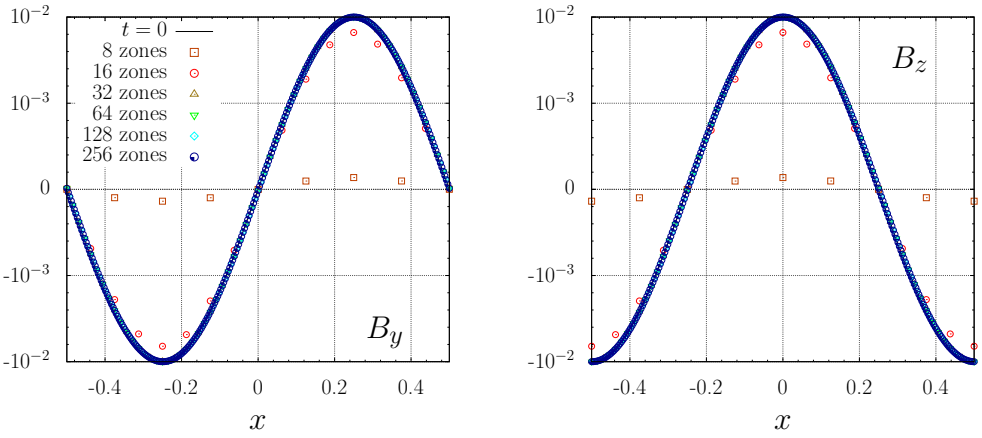

Figure 6.3: MD. Profiles of B_y (left) and B_z at $t = 100$ for different grid resolutions. The simulations have been performed with the MIRK2 time-integrator, the HLL Riemann solver and the MP5 reconstruction algorithm. The solutions with more than 32 zones per wavelength fall nearly on top of each other as well as the solution at $t = 0$ (black solid line) and, thus, they can hardly be distinguished at the scale of the plot.

set a magnetic shear layer (given by Eq. (6.12); see Fig. 6.3), with amplitude $B_0 = 10^{-2}$ in a box of length $L_x = 1$, within a homogeneous medium of uniform density $\rho_0 = 1$ and thermal pressure $p_{g,0} = 10^{-4}$ as in the VSL test (see Tab. 6.1). For this setup, the sound speed (Eq. (2.22)) is $c_s = 1.4 \times 10^{-2}$, the Alfvén velocity (Eq. (4.54)) $v_A = 10^{-2}$ and the fast magnetosonic velocity $v_{fms} = 1.7 \times 10^{-2}$, where the latter velocity is defined as (e.g. Leismann et al., 2005)

$$v_{fms} = \frac{v_x(1-w^2)}{1-v^2w^2-R} \pm \frac{\sqrt{\left((v^2-1)w^2+R\right)\left((v^2-v_x^2)w^2+v_x^2-1+R\right)}}{1-v^2w^2-R}, \tag{6.18}$$

with $R = c_s^2(\mathbf{v}\cdot\mathbf{B})^2/(\rho\hat{h}W^2)$, $w^2 = c_s^2+v_A^2-c_s^2v_A^2$, and $\hat{h}$ being the total specific enthalpy (Eq. 3.48). In order to complete the numerical setup for RRMHD, we assume that the charge density and both scalar potentials (ϕ and ψ) are zero everywhere in the computational domain.

The left panels of Fig. 6.4 represent the dependence of the numerical resistivity on the spatial resolution for two different time integrators (MIRK2 and SSP2(332)-LUM), delineating relation (6.17). As in the VSL test (Sec. 6.1.1) the calculated order of convergence (r) is very similar to the theoretical one (r_{th}), for the different MP schemes with distinct orders of accuracy. As we have mentioned in Sec. 6.1.1 (and for the same reasons as argued there), in order to obtain the fit to the data using the MP9 reconstruction, we do not include the value of η^* computed for the grid with $n_x = 256$ numerical zones.

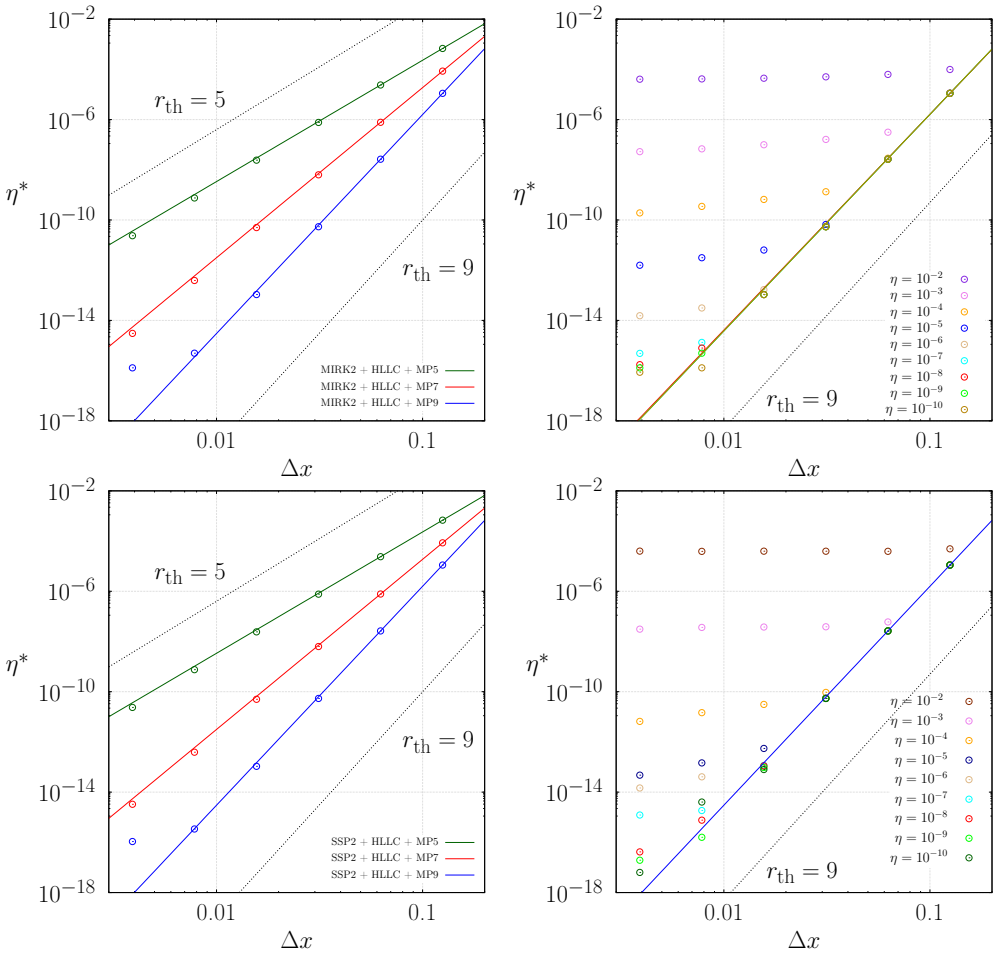

Figure 6.4: MD. *Upper left panel*: Numerical resistivity, η^*, as a function of the grid resolution (Δx), for the MIRK2 time integration scheme, using the HLLC solver and different MP schemes (corresponding to the different colors; see plot legends). All the models are run with the same physical resistivity, $\eta = 10^{-9}$. The integration order measured (r) and the coefficient $\mathfrak{N}_\eta^{\Delta x}$ are listed in Tab. 6.3. We show with solid lines of the same colors as the symbols the fits to the numerical results. Dotted lines are included to display the theoretical order of accuracy ($r_{\rm th}$). *Upper right panel*: Behavior of numerical resistivity for different physical resistivity values (η) using MIRK2, HLLC, and MP9. In both panels, we have set $C_{\rm CFL} = 0.01$. *Lower panels:* Same as upper panels but for SSP2(332)-LUM time integrator.

Table 6.3 shows the integration order (r) and the parameter $\mathfrak{N}_\nu^{\Delta x}$ measured in the different numerical experiments.

Time integrator	flux solver	reconstruction	r	$\mathfrak{N}_\eta^{\Delta x}$
MIRK1	HLL	MP5	4.963 ± 0.014	21.8 ± 1.3
MIRK1	HLL	MP7	6.941 ± 0.017	169 ± 12
MIRK1	HLL	MP9	8.84 ± 0.03	1100 ± 130
MIRK1	HLLC	MP5	4.963 ± 0.014	21.8 ± 1.3
MIRK1	HLL	MP7	6.941 ± 0.017	169 ± 12
MIRK1	HLLC	MP9	8.84 ± 0.03	1100 ± 130
MIRK2	HLL	MP5	4.963 ± 0.014	21.8 ± 1.3
MIRK2	HLL	MP7	6.951 ± 0.019	174 ± 14
MIRK2	HLL	MP9	8.88 ± 0.04	1220 ± 160
MIRK2	HLLC	MP5	4.963 ± 0.014	21.8 ± 1.3
MIRK2	HLLC	MP7	6.951 ± 0.019	174 ± 14
MIRK2	HLLC	MP9	8.88 ± 0.04	1220 ± 160
SSP2(332)-LUM	HLL	MP5	4.963 ± 0.014	21.8 ± 1.3
SSP2(332)-LUM	HLL	MP7	6.935 ± 0.017	166 ± 11
SSP2(332)-LUM	HLL	MP9	8.78 ± 0.07	910 ± 220
SSP2(332)-LUM	HLLC	MP5	4.963 ± 0.014	21.8 ± 1.3
SSP2(332)-LUM	HLLC	MP7	6.935 ± 0.017	166 ± 11
SSP2(332)-LUM	HLLC	MP9	8.78 ± 0.07	910 ± 220

Table 6.3: MD. Spatial integration order, r, and coefficient $\mathfrak{N}_\eta^{\Delta x}$, for numerical schemes including as time integrators either MIRK2 or SSP2(332)-LUM, using HLL or HLLC as approximate Riemann solvers in combination with different reconstruction schemes (MP5, MP7 or MP9). In order to estimate $\mathfrak{N}_\eta^{\Delta x}$ we assume $\mathcal{V} = \mathcal{L} = 1$ (see Sec. 6.4).

As we have observed in the VSL test for $\mathfrak{N}_\nu^{\Delta x}$, in the case of the MD test the value of the coefficient $\mathfrak{N}_\eta^{\Delta x}$ mostly depends on the order of the spatial reconstruction, and it is insensitive (within the statistical errors) to the employed approximate Riemann solver and time integration scheme (see Tab. 6.3). Furthermore, for all reconstructions $\mathfrak{N}_\eta^{\Delta x} \simeq \mathfrak{N}_\nu^{\Delta x}$ within the limits set by the statistical errors of the fits.

The right panels of Fig. 6.4 show the dependence of the numerical resistivity on the physical resistivity in the particular case in which we use either MIRK2 (upper right panel) or SSP2(332)-LUM (lower right panel) as time integration method in combination with the HLLC solver and the MP9 reconstruction. These simulations were also performed with the HLL Riemann solver, resulting into qualitatively and quantitatively similar results. We perform the study considering cases from highly resistive plasma $\eta = 10^{-2}$ to the almost ideal MHD limit ($\eta = 10^{-10}$). The behaviour that we observe in this set of experiments is different than in the previous one. Instead of a single power-law dependence of the numerical resistivity with the grid resolution (Eq. (6.16)),

we observe (in most cases) an smoothly broken power-law, in qualitative agreement with the dependence assumed in Eq. (6.2). Below a certain grid size, the contribution of the time-discretization errors becomes dominant. The value of Δx below which the break in the power-law is observed at smaller values of Δx happens depends on the physical resistivity. The smaller the physical resistivity, the smaller the resolution below which the time-discretization errors dominate. Indeed, for the larger values of $\eta \gtrsim 10^{-2}$, time-discretization errors dominate the numerical resistivity and $\eta^* \sim 10^{-4}$ is nearly independent of Δx. For all other values of the physical resistivity ($10^{-10} \lesssim \eta \lesssim 10^{-3}$), the slope of the dependence of η^* with Δx assumes values between ~ 0.8 and ~ 1.5, depending on the time-integrator and the resistivity. More precisely, the slopes for the MIRK2 time-integrator in region where temporal errors dominate are (where the dependence is $\eta^* \propto (C_{\rm CFL}\Delta x)^q$ holds), $q = 0.98 \pm 0.02$ for resistivities in the interval $10^{-10} \lesssim \eta \lesssim 10^{-4}$ and $q = 0.82 \pm 0.07$ for $\eta = 10^{-3}$. In contrast, for SSP2(332)-LUM time-integrator, the slopes are $q = 1.6 \pm 0.3$ for resistivities in the interval $10^{-10} \lesssim \eta \lesssim 10^{-4}$ and $q = 0.8 \pm 0.3$ for $\eta = 10^{-3}$. This is not expected from our ansatz (Eq. (6.2)), which predicts that when the time discretization errors dominate, $\eta^* \propto (\Delta x)^2$ for a second order time integration method (as it is the case for MIRK2). The observed behaviour at large values of η can be partly understood since MIRK methods are optimized to yield first (MIRK1) or second (MIRK2) order accuracy when η is sufficiently small. The power-law index, q, of the dependence $\eta^* \propto (C_{\rm CFL}\Delta x)^q$ grows progressively, but does not reach the theoretically expected value $q = 2$ in the regime of conductivities $10^{-10} \lesssim \eta \lesssim 10^{-3}$. We understand this trend because as we approach the ideal limit, the formal order of convergence of MIRK2 *tends* to be recovered. Qualitatively similar comments hold for the SSP2(332)-LUM time integrator, which suffers a degradation of the order of convergence as η grows. The loss of temporal order of accuracy is more moderate than for MIRK2 though. We shall come back to this problem of the degradation of the order of accuracy in the region dominated by temporal discretization errors in Sec. 6.3.1.1.

We finally point out that we have run several models for a much longer time ($t = 10000$), but we have found no trace of any transitory behaviour in the magnetic field diffusion and, hence, our numerically computed damping rates are very robust for this test.

6.3 Measurement of the numerical diffusivity

In the previous sections, we have employed tests in which either numerical viscosity (Sec. 6.1.1) or numerical resistivity (Sec. 6.2.1) may operate in the simulated system. However, in practical applications, both effects act together

resulting in a total numerical diffusivity, which we aim to assess in this section. In order to measure it, we perform tests involving CPAWs. Alfvén waves are waves in an ionized fluid (i.e., plasma), for which the only restoring force is provided by the magnetic field. This magnetic field causes a tension that tends to restore the initial shape. In the propagation of CPAWs plasma moves in the direction perpendicular to the wave propagation. Hence, viscous effects may damp the amplitude of the velocity field, while simultaneously, resistive diffusion may damp the amplitude of the magnetic field.

Up to our best knowledge, there is no known solution of the diffusion equation in RRMHD. Thus, we need to resort to Newtonian resistive MHD in order to proceed further. To proceed with the derivation of the diffusion equation (for Newtonian resistive MHD), in a homogeneous, incompressible ($\nabla \cdot \mathbf{v} = 0$) plasma (Campos, 1999), the state of the fluid is assumed to be, the contribution of an homogeneous mean state at rest (which we annotate with a "0" subscript), plus an unsteady and non-uniform perturbation (annotated with a "1" subscript), namely,

$$\{\mathbf{v}, \mathbf{B}, \rho, p_{\mathrm{g}}\}(\mathbf{x}, t) = \{\mathbf{0}, \mathbf{B}_0, \rho_0, p_{\mathrm{g},0}\} + \{\mathbf{v}_1, \mathbf{B}_1, \rho_1, p_{\mathrm{g},1}\}(\mathbf{x}, t). \tag{6.19}$$

For small perturbations of the velocity field ($\mathbf{v}_1 \ll v_{\mathrm{A}}^2$) or of the magnetic field ($||\mathbf{B}_1|| \ll ||\mathbf{B}_0||$), the diffusion equation for transverse motions (e.g. like Alfvén waves) reads (see, e.g. Campos, 1999, Eq. (18)):

$$\left\{ \frac{\partial^2}{\partial t^2} - v_A^2 \frac{\partial^2}{\partial l^2} - (\nu + \eta) \frac{\partial}{\partial t} \nabla^2 + \nu\, \eta\, \nabla^4 \right\} \begin{pmatrix} \mathbf{v}_1(\mathbf{x}, t) \\ \mathbf{B}_1(\mathbf{x}, t) \end{pmatrix} = 0, \tag{6.20}$$

where $\mathbf{l} \equiv \mathbf{B}_0 / B_0$ is the unit vector in the direction of the background magnetic field $\mathbf{B}_0$ and $\partial / \partial l = \mathbf{l} \cdot \nabla$ is the derivative along magnetic field lines. The transversality condition requires that

$$\mathbf{l} \cdot \mathbf{v}_1 = 0. \tag{6.21}$$

Inserting plane wave solutions, for the velocity and the magnetic field perturbations, characterized by a wave vector $\mathbf{k}$ and an angular frequency ω, in Eq. (6.20), with corresponding amplitudes, $\tilde{\mathbf{v}}_1$ or $\tilde{\mathbf{B}}_1$, i.e. having the form,

$$\begin{pmatrix} \mathbf{v}_1(\mathbf{x}, t) \\ \mathbf{B}_1(\mathbf{x}, t) \end{pmatrix} = \begin{pmatrix} \tilde{\mathbf{v}}_1 \\ \tilde{\mathbf{B}}_1 \end{pmatrix} \exp\left[i(\mathbf{k} \cdot \mathbf{x} - \omega t) \right], \tag{6.22}$$

gives the required dispersion relation, $\omega = \omega(\mathbf{k})$ (see, e.g. Campos, 1999, Eq. (28b)),

$$\omega^2 - v_{\mathrm{A}}^2 (\mathbf{k} \cdot \mathbf{l})^2 + i\omega k^2 (\nu + \eta) - k^4 \nu \eta = 0. \tag{6.23}$$

The roots of the previous second order equation are (see, e.g. Campos, 1999, Eq. (35a))

$$\omega = -ik^2 \xi / 2 \pm \left| v_{\mathrm{A}}^2 k_{\parallel}^2 - \left(k^2 (\eta - \nu)/4 \right)^2 \right|^{1/2}, \tag{6.24}$$

with $k_\parallel := \mathbf{k}\cdot\mathbf{l}$, and $\xi := \nu + \eta$ being the total diffusivity, i.e. the sum of resistivity and shear viscosity.[7]

If $\eta \neq \nu$ and $\left(k^2(\eta-\nu)/(2v_{\rm A}k_\parallel)\right)^2 \ll 1$ (moderate dissipation), the approximate solutions of Eq. (6.24) are (see, e.g. Campos, 1999, Eq. (36a))

$$\omega = \pm v_{\rm A}k_\parallel\left(1 - k^4(\eta-\nu)^2/(8v_{\rm A}^2k_\parallel^2)\right) - ik^2(\nu+\eta)/2, \tag{6.25}$$

which shows that the phase velocity (real part of ω) changes only due to second order terms in the diffusivities.

Often, we are interest in the case in which both η and ν are small and we can neglect their product, $\nu\eta$, in Eq. (6.23), which yields a simplified version of the dispersion relation in the regime of small dissipation

$$\omega^2 + i\omega k^2\xi - v_{\rm A}^2k_\parallel^2 = 0. \tag{6.26}$$

The roots of the quadratic equation Eq. (6.26) are

$$\omega = -ik^2\xi/2 \pm \left|v_{\rm A}^2k_\parallel^2 - \left(k^2\xi/2\right)^2\right|^{1/2}. \tag{6.27}$$

Depending on the ratio

$$\mathcal{H}_{\rm A} := \left(k^2\xi/(2v_{\rm A}k_\parallel)\right)^2, \tag{6.28}$$

we can distinguish two damping regimes, namely, *weak* and *strong* damping regimes. The weak damping regime holds for $\mathcal{H}_{\rm A} \ll 1$, in which case the roots of Eq. (6.27) simplify to (see, e.g. Campos, 1999, Eq. (34a))

$$\omega = \pm v_{\rm A}k_\parallel - ik^2(\nu+\eta)/2. \tag{6.29}$$

Comparing Eq. (6.29) with Eq. (6.25), we observe that in the weak damping regime the phase velocity of the different modes becomes independent of the diffusivities and, hence, it does not change due to viscous or resistive effects.

If we define the Alfvén damping rate, $\mathfrak{D}_{\rm A}$, as (see, e.g. Rembiasz et al., 2017, Eq. (43))

$$\mathfrak{D}_{\rm A} := \frac{k^2}{2}\left(\nu+\eta\right), \tag{6.30}$$

we obtain the evolution of the velocity and of the magnetic field perturbations plugging the roots of the dispersion relation (Eq. (6.29)) in Eq. (6.22) and expressing the imaginary part of ω in terms of the Alfvén damping rate (Eq. (6.30)), i.e.

$$\mathbf{v}_1(\mathbf{x},t) = \tilde{\mathbf{v}}_1 \exp\left[i(\mathbf{k}\cdot\mathbf{x} \mp v_{\rm A}k_\parallel t)\right]\exp\left[-\mathfrak{D}_{\rm A}\ t\right],$$

[7] For easy comparison, we warn the reader that the symbol ξ denotes the bulk viscosity in Rembiasz et al. (2017).

and

$$\mathbf{B}_1(\mathbf{x},t) = \tilde{\mathbf{B}}_1 \exp\left[i(\mathbf{k}\cdot\mathbf{x} \mp v_{\rm A} k_\parallel t)\right] \exp\left[-\mathfrak{D}_{\rm A}\, t\right], \tag{6.31}$$

respectively. These relations show that in the weak damping approximation, the amplitude of vector fields decays exponentially with time, on a characteristic time scale inversely proportional to the Alfvén damping rate.

In the *strong damping* regime, i.e. for $\mathcal{H}_{\rm A} \gg 1$ (Eq. (6.28)), the roots of Eq. (6.23) are

$$\omega = -i\frac{k^2}{2}\xi\left(1 \pm \left[1 - \frac{4(\nu\eta + v_{\rm A}^2 k_\parallel^2/k^4)}{\xi^2}\right]^{1/2}\right),$$

To obtain further insight in the obtained frequencies, we shall note that the factor $4\nu\eta/\xi^2$ has a maximum value equal to 1 when $\eta = \nu$ and becomes smaller than 1 when the magnitudes of $\eta \neq \nu$ (e.g. when $\nu \simeq 0$ and $\eta \neq 0$, a case of interest in the following sections). In these two cases, we find

$$\omega = \begin{cases} \pm v_{\rm A} k_\parallel/2 - ik^2\eta & \eta = \nu, \\ -i\dfrac{k^2\xi}{2}\left(1 \pm 1 \mp \dfrac{2v_{\rm A}^2 k_\parallel^2}{k^4\xi^2}\right) = \begin{cases} -ik^2\eta \\ -i\dfrac{k_\parallel^2 v_{\rm A}^2}{k^2\eta} \end{cases} & 0 \simeq \nu \ll \eta, \end{cases} \tag{6.32}$$

or, equivalently, the corresponding damping rates are

$$\mathfrak{D}_{\rm A} := k^2\eta, \quad (\eta = \nu), \tag{6.33}$$

$$\mathfrak{D}_{\rm A}^{+} := k^2\eta, \quad 0 \simeq \nu \ll \eta, \tag{6.34}$$

$$\mathfrak{D}_{\rm A}^{-} := \frac{k_\parallel^2 v_{\rm A}^2}{k^2\eta} \quad 0 \simeq \nu \ll \eta. \tag{6.35}$$

Remarkably, in the strong damping regime, there exist non-propagating modes (i.e. the real part of ω is zero) when $\nu \simeq 0$ (and η is finite). Due to the strong damping condition, when $\omega = -ik_\parallel^2 v_{\rm A}^2/(k^2\eta)$ (third branch of Eq. (6.32)), the imaginary part of ω (i.e. the damping rate; Eq. (6.35)) is very small. Indeed,

$$\frac{\mathfrak{D}_{\rm A}^{-}}{\mathfrak{D}_{\rm A}^{+}} = \left(\frac{k_\parallel v_{\rm A}}{k^2\eta}\right)^2 \ll 1,$$

because of the strong damping condition. Furthermore

$$\mathfrak{D}_{\rm A}^{-} = v_{\rm A}^2/\eta \qquad (k_\parallel = k),$$

which shows that $\mathfrak{D}_{\rm A}^{-}$ is independent of the wavenumber if $k_\parallel = k$.

We also note that in the case $\eta = \nu$, the damping rates corresponding to either the weak (Eq. (6.30)) or strong (Eq. (6.33)) damping regimes are equal,

in spite of the differences in the damping regimes. In the case in which $\nu \simeq 0$ and η is finite, one of the two modes corresponding to the strong damping regime (Eq. (6.34)) has a damping rate that that is twice higher than the one in the weak damping regime (Eq. (6.30)).

Finally, we derive here dispersion relation for the case of incompressible plasma ($\nabla \cdot \mathbf{v} = 0$) but relaxing the transversality condition (Eq. (6.21)). Strictly speaking, such a dispersion relation does not correspond to Alfvén waves, which are transverse by definition. However, it is of numerical interest, since we shall see that because of numerical inaccuracies, the transversality condition is breached in some of our numerical models. For concreteness, and in the view of the numerical experiments that we shall present in the following sections, we consider the case in which $\mathbf{l} = (1, 0, 0)$. If $\mathbf{l} \cdot \mathbf{v}_1 = v_{1,x} \neq 0$ the only change with respect to the transverse case is that Eq. (6.20) holds for all perturbed quantities (Eq. (6.19)) except for the x-component of the perturbed velocity ($v_{1,x}$), for which the diffusion equation reads

$$\left\{ \frac{\partial^2}{\partial t^2} - v_A^2 \left(\frac{\partial^2}{\partial l^2} - \nabla \frac{\partial}{\partial l} \right) - (\nu + \eta) \frac{\partial}{\partial t} \nabla^2 + \nu \, \eta \, \nabla^4 \right\} v_{1,x}(\mathbf{x}, t) = 0. \quad (6.36)$$

Inserting plane wave solutions of the form of Eq. (6.22) into Eq. (6.36), we obtain the following dispersion relation

$$\omega^2 - v_{\mathrm{A}}^2 k_{\parallel}^2 (1 - k/k_{\parallel}) + i\omega k^2 (\nu + \eta) - k^4 \nu\eta = 0. \quad (6.37)$$

Again, driven by the set up of our numerical experiments, we consider the case $k_{\parallel} = k$ in Eq. (6.37), that yields the following purely imaginary frequencies:

$$\omega_{\mathrm{nt}} = -ik^2 \left(\xi \pm |\eta - \nu| \right) /2. \quad (6.38)$$

Thus, the non-transverse case behaves as a non-propagating slow magnetosonic mode (Campos, 1999), i.e. a mode with zero phase speed.

We notice that the case $\eta = \nu$, Eq. (6.38) yields the same damping rate as for transverse modes in the weak damping regime (Eq. (6.30)). Likewise, if $0 \simeq \nu \ll \eta$, only one of the two modes of Eq. (6.38) survives (has a non-zero frequency)

$$\omega_{\mathrm{nt}}^{+} = -ik^2\eta, \qquad \omega_{\mathrm{nt}}^{-} \simeq 0. \quad (6.39)$$

The damping rate corresponding to ω_{nt}^{+} that is twice higher than that of the transverse modes in the weak damping regime (Eq. (6.30)).

6.3.1 Circularly Polarized Alfvén Waves

The initial data for setting up CPAWs in a homogeneous medium are given by Eqs. (4.50), (4.51), (4.52) and (4.53). For this setup, we have that the wave

vector and unit vector along the direction of the background magnetic field ($\mathbf{B}_0 = (B_0, 0, 0)$) are $\mathbf{k} = (k, 0, 0)$ and $\mathbf{l} = (1, 0, 0)$. Thus, $k_\parallel = \mathbf{k} \cdot \mathbf{l} = k$. As expected for Alfvén waves, the transversality condition (Eq. (6.21)) holds, since the velocity oscillations (Eq. (4.51)) happen in a plane perpendicular to $\mathbf{l}$. The scalar potentials and the charge density are set to zero, and the electric field is computed from its ideal expression $\mathbf{E} = -\mathbf{v} \times \mathbf{B}$.

In the weak damping regime, using Eq. (6.31), the temporal evolution of the magnetic field components, can be written as

$$\begin{aligned} B_{y,(\mathrm{ex})}(x,t) &= B_0\ \epsilon_{\mathrm{am}}\ \exp(-\mathfrak{D}_{\mathrm{A}}\ t)\ \cos(kx), \\ B_{z,(\mathrm{ex})}(x,t) &= B_0\ \epsilon_{\mathrm{am}}\ \exp(-\mathfrak{D}_{\mathrm{A}}\ t)\ \sin(kx). \end{aligned}$$

To measured the numerical diffusion term ($\xi^* := \nu^* + \eta^*$), we integrate the square of the magnetic field strength over the whole spatial domain,

$$\int B^2_{(\mathrm{ex})}(x,t)\ dx\ =\ B_0^2\,\epsilon^2_{\mathrm{am}}\,L_x\ \exp(-2\,\mathfrak{D}_{\mathrm{A}} t).$$

Taking logarithms in the previous expression

$$\ln\left(\int B^2_{(\mathrm{ex})}(x,t)\ dx\right)\ =\ \ln\left(B_0^2\,\epsilon^2_{\mathrm{am}}\,L_x\right)\ -\ 2\,\mathfrak{D}_{\mathrm{A}}\ t, \tag{6.40}$$

we obtain a linear relation to which the computed data can be fitted. This relation is of the form $y = at + b$, with $y = \ln\left(\int B^2(x,t)\ dx\right)$, and the damping rate can be measured from the slope (a) of the linear fit as

$$\mathfrak{D}_{\mathrm{A}} = -\frac{a}{2}.$$

We note that, in order to accurately measure the damping rate, it is necessary to compute the CPAW evolution for, at least, one full period ($T = 1/v_{\mathrm{A}}$). This is because the damping of the CPAWs does not proceed monotonically in our numerical models, but it is modulated by variations with a frequency $\simeq 2kv_{\mathrm{A}}$ (see Sec. 6.3.1.2), which may induce a false determination of the damping rate and, thereby, of the numerical diffusivity. Even in some cases instead of damping, one could measure amplification of the CPAWs (corresponding to negative numerical diffusivities). We explicitly point out the difference in the behaviour of the damping rate in this test and in the previous ones, where the damping proceeds monotonically in time. As we shall see, the non-monotonicity of the damping rate hinders the accuracy with which we can measure it from fits to our numerical data.

Once the damping coefficient has been found, we can obtain the numerical diffusion (ξ^*) from its definition (Eq. (6.30)), but replacing the physical viscosity and resistivity by the total (including numerical) viscosity and resistivity,

respectively,

$$\mathfrak{D}_{\rm A} \;=\; \frac{k^2}{2}\left[(\eta+\eta^*)+(\nu+\nu^*)\right].$$

Since in our formalism the physical viscosity is set to zero ($\nu = 0$), then the numerical diffusivity is given by,

$$\xi^* = \nu^* + \eta^* = \frac{2\,\mathfrak{D}_{\rm A}}{k^2} - \eta.$$

Following the same methodology as in the previous sections, in order to find the dependence of the diffusivity with the grid resolution, we have run a series of simulations maintaining a fixed setup given in Eqs. (4.50)-(4.53) and varying Δx. In addition, as we employ a small $C_{\rm CFL} = 0.01$, so that we would expect to be dominated by the spatial-discretization errors, in which case, considering Eq. (6.5) and Eq. (6.16), we would have

$$\xi^* = \nu^* + \eta^* = \mathfrak{N}_{\xi}^{\Delta x}\;\mathcal{V}\;\mathcal{L}\;\left(\frac{\Delta x}{\mathcal{L}}\right)^{-r}, \tag{6.41}$$

where $\mathfrak{N}_{\xi}^{\Delta x} := \mathfrak{N}_{\nu}^{\Delta x} + \mathfrak{N}_{\eta}^{\Delta x}$.

Provided that the previous power-law dependence of ξ^* on Δx holds, the simulation results could be fitted to the function

$$\ln\left(\xi^*\right) = d \;+\; r\;\Delta x, \tag{6.42}$$

where r is the numerically measured order of accuracy and d the fit parameter that allows us to determine the coefficients $\mathfrak{N}_{\xi}^{\Delta x}$ from the relation

$$\mathfrak{N}_{\xi}^{\Delta x} = \frac{\exp(d)}{\mathcal{V}\mathcal{L}^{1-r}}. \tag{6.43}$$

In the strong damping regime, when $\eta = \nu$, the measurement of the numerical diffusivity is completely analogous to the weak damping case. Thus, we focus on the two cases corresponding to the (nearly) inviscid regime ($\nu \simeq 0$). Firstly, in the case in which the damping rate is $\mathfrak{D}_{\rm A}^{+}$ (Eq. (6.34)),

$$\xi^* = \eta^* = \frac{\mathfrak{D}_{\rm A}^{+}}{k^2} - \eta. \tag{6.44}$$

Secondly, the case in which the damping rate is $\mathfrak{D}_{\rm A}^{-}$ (Eq. (6.35)),

$$\xi^* = \eta^* = \frac{v_{\rm A}^2}{\mathfrak{D}_{\rm A}^{-}} - \eta. \tag{6.45}$$

In both cases, considering the different expressions for ξ^* (Eqs. (6.44) and (6.45)) we may resort to Eq. (6.16) in order to measure the numerical diffusivity (in these two cases $\xi^* = \eta^*$) as a power-law function of the grid spacing Δx, by means of a least squares fit analogous to that of Eq. (6.42).

Since the solution to the dissipation equation found by Campos (1999) is valid in the Newtonian regime, in the following subsections we consider two series of CPAW tests. In the first one (Sec. 6.3.1.1), called *classical* CPAW, the Alfvén speed and the flow velocities are *strictly* Newtonian ($v_\mathrm{A} = 10^{-4}$). In the second one (Sec. 6.3.1.1), called *relativistic* CPAW the Alfvén velocity is much larger than in the previous case ($v_\mathrm{A} = 10^{-1}$), though still small enough that the Newtonian solution derived by Campos (1999) holds. We probe numerically the relativistic regime considering tests in which the Alfvén speed is larger than in the previous cases in Sec. 6.3.1.3. As we shall see there, the dependence found by Campos (1999) between the damping rate and the diffusivity still holds in the relativistic regime, though numerical difficulties prevent our code from reaching values $v_\mathrm{A} \gtrsim 0.76$.

6.3.1.1 Classical CPAW

In this series of simulations, we consider a single wave in the 1D numerical box of length $L_x = 1$, the homogeneous environment has a background magnetic field set to $B_0 = 10^{-4}$, a constant density $\rho_0 = 1$ and a thermal pressure $p_{\mathrm{g},0} = 10^{-4}$. The amplitude of the wave perturbations takes the value $\epsilon_\mathrm{am} = 10^{-5}$ (see Tab. 6.1).

Figure 6.5 represents the dependence of the numerical diffusion as a function of the spatial resolution. For the chosen reference value of the resistivity ($\eta = 10^{-9}$), and the set up value $v_\mathrm{A} = 10^{-4}$, $\mathcal{H}_\mathrm{A} \simeq 10^{-9} \ll 1$ (Eq. (6.28)), hence this series of models evolve in the weak damping regime. For the small value of the Alfvén velocity chosen, one full period of time evolution ($T = 1/v_\mathrm{A} = 10^4$), needs of 2.56×10^8 time steps at the maximum numerical resolution ($n_x = 256$) and CFL number ($C_\mathrm{CFL} = 0.01$) making these models relatively expensive, in spite of the fact that they are one-dimensional. The expected dependence expressed by Eq. (6.41) only holds for small values of n_x (i.e. for coarse resolutions). The threshold n_x^thr above which the numerical diffusivity does not follow Eq. (6.41) depends on the order of the reconstruction and on the time-integration scheme, but in all the cases under study, $n_x^\mathrm{thr} > 16$. For the MIRK2 time-integrator (Fig. 6.5; upper left panel), the diffusion saturates at a value $\xi^* \approx 2 \times 10^{-9}$. However, this seems to be a numerical pathology specific to the MIRK2 method. For the MIRK1 (Fig. 6.5; lower left panel), SSP2(332)-LUM and RK36$\mathcal{S}_E$ time integrators (Fig. 6.5; right panels), the subsequent dependence goes as $\xi^* \propto (C_\mathrm{CFL}\Delta x)^q$, though with significantly different values of q. These temporal orders of accuracy are $q = 1.24 \pm 0.02$, $q = 0.52 \pm 0.07$ and

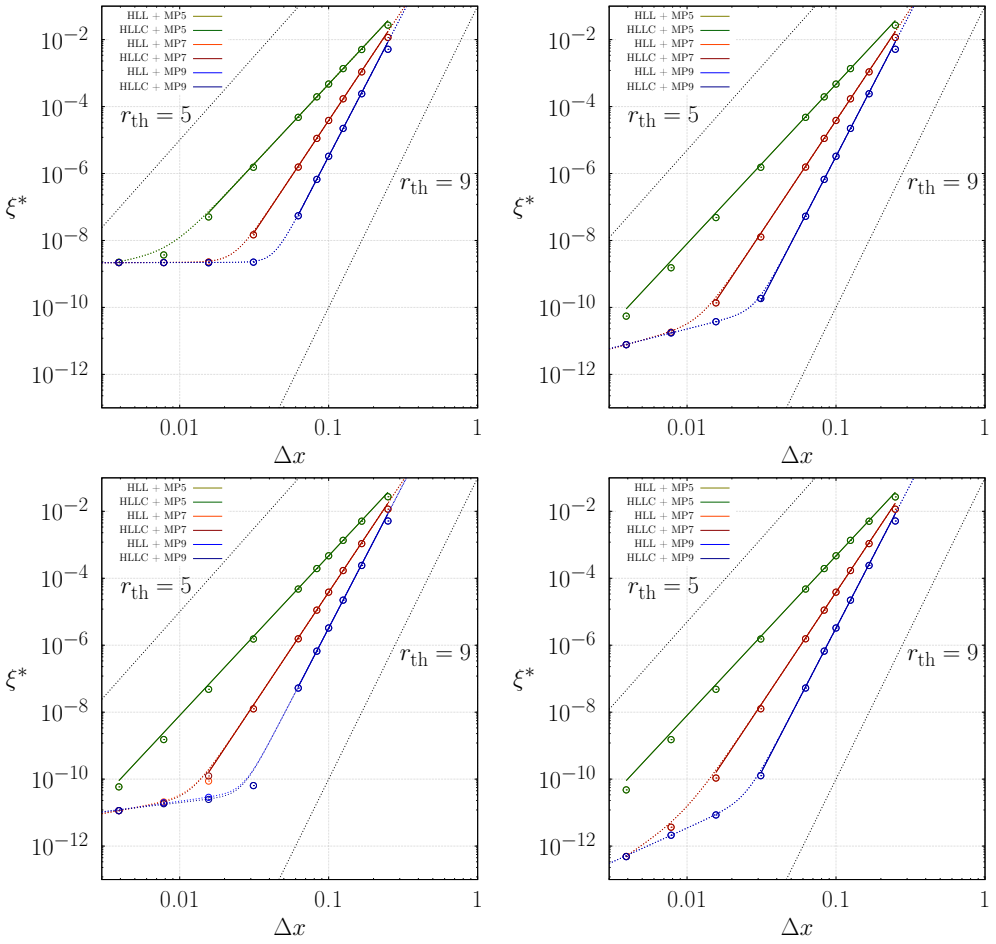

Figure 6.5: Classical CPAW. *Left panels*: Numerical diffusion, $\xi^*_{\rm cla}$, as a function of the grid resolution (Δx) for a fixed value of the physical resistivity ($\eta = 10^{-9}$). The different values of Δx are obtained by fixing L_x and varying $n_x = 4, 5, 6, 8, 10, 12, 16, 32, 64, 128,$ and 256. This series of simulations are made with the MIRK2 (upper panel) and MIRK1 (lower panel) time-integrators in combination with either the HLL or the HLLC solvers with different MP schemes. The results are nearly independent of the Riemann solver employed and, thus, the values for HLL or the HLLC nearly overlap for each intercell reconstruction. In all cases $C_{\rm CFL} = 0.01$. Several dotted lines are included to show the theoretical order of convergence ($r_{\rm th}$). *Right panels*: Same as the left panels but for the SSP2(332)-LUM (upper right) and the RK36$\mathcal{S}_E$ (lower right) time-integrators.

$q = 2.02 \pm 0.02$ for the SSP2(332)-LUM, MIRK1 and RK36$\mathcal{S}_E$ time-integrators, respectively.

The existence of this break in the power-law dependence (Eq. (6.41)) is due to the fact that temporal errors begin to dominate the total diffusivity and, when this happens, one expects to measure an order of convergence governed

time-integrator	solver	reconstruction	r	$\mathfrak{N}^{\Delta x}_{\xi,\mathrm{cla}}$
MIRK1	HLL	MP5	4.87 ± 0.03	31 ± 4
MIRK1	HLL	MP7	6.80 ± 0.09	210 ± 50
MIRK1	HLL	MP9	8.77 ± 0.20	1500 ± 700
MIRK1	HLLC	MP5	4.87 ± 0.03	31 ± 3
MIRK1	HLLC	MP7	6.70 ± 0.07	170 ± 30
MIRK1	HLLC	MP9	8.77 ± 0.20	1500 ± 700
MIRK2	HLL	MP5	4.81 ± 0.06	27 ± 4
MIRK2	HLL	MP7	6.44 ± 0.11	102 ± 25
MIRK2	HLL	MP9	8.29 ± 0.13	600 ± 170
MIRK2	HLLC	MP5	4.81 ± 0.06	27 ± 4
MIRK2	HLLC	MP7	6.44 ± 0.11	102 ± 25
MIRK2	HLLC	MP9	8.29 ± 0.13	600 ± 170
SSP2(332)-LUM	HLL	MP5	4.90 ± 0.04	33 ± 4
SSP2(332)-LUM	HLL	MP7	6.74 ± 0.08	180 ± 40
SSP2(332)-LUM	HLL	MP9	8.48 ± 0.11	880 ± 230
SSP2(332)-LUM	HLLC	MP5	4.90 ± 0.04	33 ± 4
SSP2(332)-LUM	HLLC	MP7	6.74 ± 0.08	180 ± 40
SSP2(332)-LUM	HLLC	MP9	8.48 ± 0.11	880 ± 230

Table 6.4: Classical CPAW. Same as Tab. 6.3 but for the classical CPAW test. $\mathfrak{N}^{\Delta x}_{\xi,\mathrm{cla}}$ (Eq. (6.43)) is the parameter measured for the relation Eq. (6.41) in this test ($v_\mathrm{A} = 10^{-4}$).

by the time-integration scheme (and not by the spatial intercell reconstruction method). In our case, however, all schemes tested (regardless of the order of accuracy of the time-integrator) seem to perform below the theoretical order of accuracy. However, the degradation of the order of convergence is not equally severe in all cases. We remark that the MIRK1 time-integrator, performs closer to its theoretical convergence rate than any of the RKIMEX schemes used. Nevertheless, the RK36$\mathcal{S}_E$ method is the one which performs best in the regime dominated by time-discretization errors, though at a computational cost $\sim 3-5$ times larger than that of the MIRK1 time-integrator.

The fact that RKIMEX schemes, which are not specifically tailored to display a uniform convergence rate with the stiffness parameter ϵ_stiff (η in our case), suffer (severe) degradation of their order of convergence is well known (e.g. Boscarino and Russo, 2007, 2009; Hundsdorfer and Ruuth, 2007; Izzo and Jackiewicz, 2017, 2018). The degradation of the order of convergence is not necessarily monotonically dependent on the stiffness parameter (e.g. Boscarino and Russo, 2007, 2009) and may be problem and variable dependent. Indeed, Hundsdorfer and Ruuth (2007) considered several problems of advection-reaction and advection-diffusion type (RRMHD could be clas-

sified as a generalized advection-reaction problem) and the convergence order of RKIMEX schemes such as SSP2(222) or SSP3(433) degraded to $q \simeq 1$ (like it happens in our case), even for linear advection reaction problems with constant coefficients and stiffness parameters $\simeq 10^{-6}$ (we are taking here a much smaller stiffness parameter $\eta = 10^{-9}$). Employing suitable Chapman-Enskog expansions of the solution in terms of the stiffness parameter, Boscarino (2007) finds that the global error of a number of RKIMEX schemes depends on the time step and on the stiffness parameter as $\mathcal{O}(\Delta t^q)+\mathcal{O}(\Delta t^s \epsilon_{\rm stiff}^m)$, if $\Delta t \epsilon_{\rm stiff} < 1$, and $s + m \leq q$. Moreover, the order of the global error depends on whether it is measured for the variables governed by the stiff equations (set of variables $\mathbf{X} = \{\mathbf{E}\}$ in Eqs. (4.21)-(4.22)) or for variables governed by equations without stiff sources (set of variables $\mathbf{Y}$ in Eqs. (4.21)-(4.22)). For instance, for the SSP3(433) time-integrator, the error goes as $\mathcal{O}(\Delta t)$ for the variables governed by stiff source terms and as $\mathcal{O}(\Delta t^3)+\mathcal{O}(\Delta t \epsilon_{\rm stiff})$ for the rest of the variables in a particular set of equations (see Boscarino, 2007, Tab. 1). If this is the form of the error, our ansatz for the numerical resistivity (Eq. (6.2)) is not optimal. It has been directly taken from Rembiasz et al. (2017), who obtained it for explicit time integration schemes. We are using partly implicit time integration methods and our results suggest that in this case the dependence of the time discretization errors with the numerical resolution is not well captured by Eq. (6.2). Unfortunately, due to the time limitations of this thesis, it has not been possible to find other ansatzes that explain better the observed behaviour. However, in the realm of coarse enough resolutions ($\Delta x \gtrsim 0.03$) we are dominated by spatial discretization errors, where the ansatz of Rembiasz et al. (2017) (applied to RRMHD) is clearly correct. For practical applications this is not a limitation since one can afford resolving simple waves with more than ~ 30 cells per wavelength very rarely.

In the previous sections, we observed that the value of the coefficient $\mathfrak{N}^{\Delta x}$ only depended on the order of the spatial reconstruction (see Tabs. 6.3 and 6.2). In the present test, we also find a mild dependence on the time integration scheme employed (Tab. 6.4). The value of $\mathfrak{N}^{\Delta x}_{\xi_{\rm cla}}$ for MIRK2 is slightly smaller than for other time integrators, but compatible with the them within the accuracy of the results. This is also the case for the measured integration order (r), but to a lesser extent. The differences are related to the transition from numerical diffusivities dominated by spatial errors to being dominated by temporal errors (Fig. 6.5). The point at the finest resolution for which the power-law dependence (Eq. (6.41)) is considered in the fit may be slightly out of the trend of the points at coarser resolutions for MIRK2. The effect of this transition to saturation at higher values of ξ^* is to reduce slightly the measured integration order. The large dependence of $\mathfrak{N}^{\Delta x}_{\xi_{\rm cla}}$ on r (Eq. (6.43)) explains the observed variations of the former coefficient as a result of the (small) changes of the latter when the time integration scheme is varied. Thus, we may con-

clude that in the regime of models dominated by spatial discretization errors, the value of the coefficient $\mathfrak{N}^{\Delta x}_{\xi\mathrm{cla}}$ depends fundamentally on the order of the spatial reconstruction method.

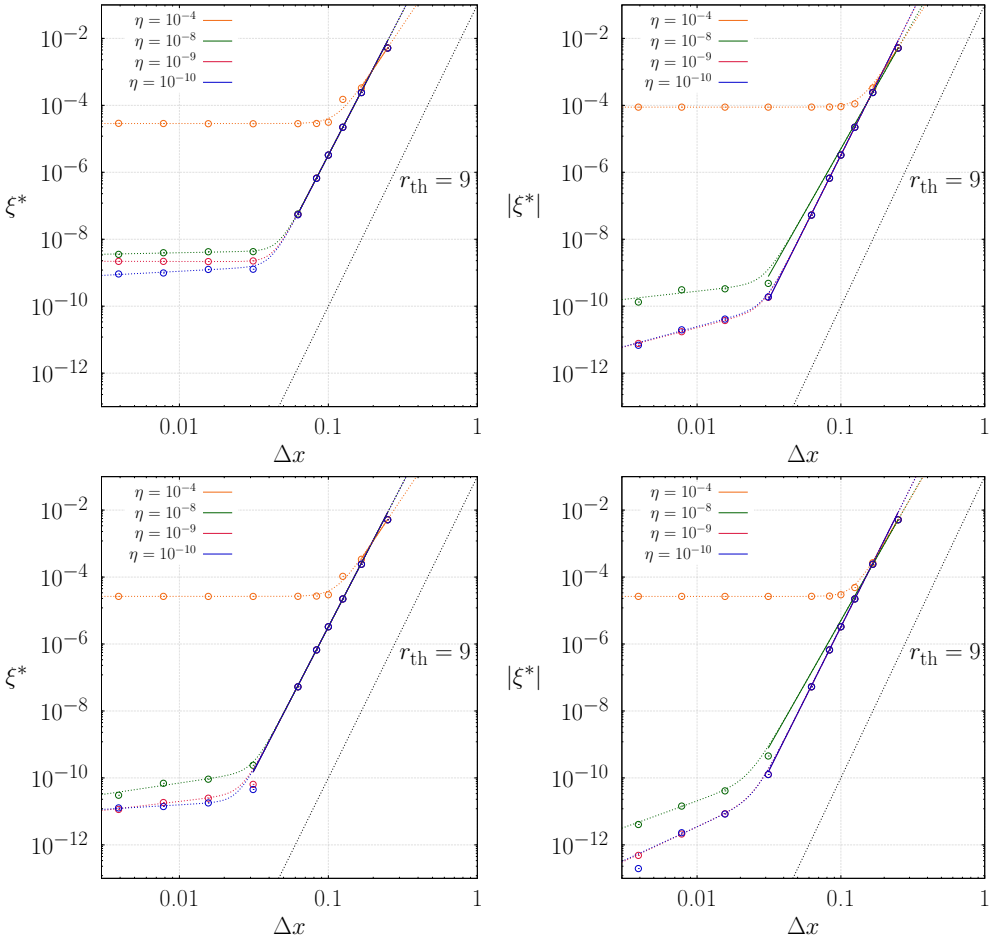

Figure 6.6: Classical CPAW. *Left panels*: Numerical diffusivity as a function of the resolution for different physical resistivities (see legends), in models where the time integration method are MIRK2 (upper left) and MIRK1 (lower left). *Right panels*: Same as the left panels but for the SSP2(332)-LUM (upper right) and the RK36$\mathcal{S}_E$ (lower right) time-integrators. We use HLL and MP9 in all cases shown in the figure.

In Fig. 6.6, we also explore the dependence of the numerical diffusion on the physical resistivity, using various time-integrators, the HLL flux formula and the MP9 spatial reconstruction. We find that for $\eta \leq 10^{-8}$, the numerical diffusion follows the same qualitative behaviour described in Fig. 6.5 (right panels). Indeed, the results obtained with $\eta = 10^{-9}$ nearly fall on top of the data for $\eta = 10^{-10}$ for most of the time-integrators used, with the exception

of MIRK2, where smaller values of $|\xi^*|$ are observed at the finest resolutions as the resistivity decreases (Fig. 6.6 upper left panel). For $\eta = 10^{-8}$, in the regime dominated by temporal discretization errors, the power-law index q ($|\xi^*| \propto (C_{\rm CFL}\Delta t)^q$) has a smaller value than in the previous case (for MIRK time-integrators the order degradation is significantly larger than for RKIMEX schemes). The degradation of the order of convergence is more severe for larger values of η than for smaller ones. This trend is exacerbated at high resistivities ($\eta = 10^{-4}$), where the numerical diffusivity saturates at a constant value $|\xi^*| \lesssim \eta$. An important physical difference happens for this particular value $\eta = 10^{-4}$, namely, that the dissipation of the CPAWs develops in the strong damping regime. This is the case since $\mathcal{H}_{\rm A} \simeq 10$ (Eq. (6.28)). Hence, the damping rate given by either $\mathfrak{D}_{\rm A}^+$ (Eq. (6.34)) or $\mathfrak{D}_{\rm A}^-$ (Eq. (6.35)), can be twice faster than in the weak damping regime. We note that $\mathfrak{D}_{\rm A}^+ = k^2\eta = 4\pi^2 10^{-4}$ and $\mathfrak{D}_{\rm A}^- = v_{\rm A}^2/\eta = 10^{-4}$ for $v_{\rm A} = 10^{-4}$ and $\eta = 10^{-4}$.

For resolutions $\Delta x \geq 1/32$ and small resistivity ($\eta \leq 10^{-8}$), the measured ξ^* saturates at a value which depends on the physical resistivity for the MIRK2 time-integrator (Fig. 6.6 upper right panel). The saturation value is below the physical resistivity ($\xi^* \simeq \eta$) if $\eta = 10^{-8}$ or 10^{-9}, but is larger than the physical resistivity if $\eta = 10^{-10}$. The behaviour of the MIRK1 time-integrator differs significantly from that of the MIRK2 scheme in the regime dominated by time discretization errors. Firstly, for $\eta = 10^{-8}$, the numerical diffusivity still decreases at a rate $q = 0.7 \pm 0.2$, while this rate decreases significantly ($q = 0.53 \pm 0.07$) for $\eta \leq 10^{-9}$. Secondly, the resolution below which time discretization errors dominate is $\Delta x < (\Delta x)_{\rm th} \simeq 1/64$, i.e. time discretization errors dominate the numerical diffusivity for MIRK1 at resolutions about twice finer than for MIRK2. The threshold $(\Delta x)_{\rm th}$ found for the MIRK1 time integrator is effectively the same as in the RKIMEX schemes. These results are a first hint suggesting the possibility that more terms need to be treated implicitly in MIRK methods of second or higher order. In the following section, we will show further hints pointing in that direction.

Among the RKIMEX schemes, RK36$\mathcal{S}_E$ performs closer to its theoretical order of convergence in the region dominated by time discretization errors. In this regime, the power-law indices q ($\xi^* \propto (C_{\rm CFL}\Delta x)^q$) are $q = 2.02 \pm 0.02$ and $q = 1.2 \pm 0.1$ for the RK36$\mathcal{S}_E$ and SSP2(332)-LUM time-integrators, respectively.

An important conclusion that holds independently of the damping regime (weak or strong), and of the time-integrator used, is that we can always select a resolution such that the numerical diffusivity is smaller than the physical resistivity for CPAWs in the Newtonian regime. Thus, more physically interesting numerical models (see, e.g. Chap. 7) may not be biased by numerical diffusivity if we suitably choose the working resolution.

6.3.1.2 Relativistic CPAW

The *relativistic* setup differs from the *classical* CPAW case, by a larger background magnetic field set to $B_0 = 10^{-1}$ a greater thermal pressure, $p_{g,0} = 10^{-2}$, and a also bigger amplitudes of the wave perturbations, $\epsilon_{am} = 1$ (see Tab. 6.1). For the chosen value of the resistivity ($\eta = 10^{-9}$), and the set up value $v_A = 10^{-1}$, $\mathcal{H}_A \simeq 10^{-15} \ll 1$ (Eq. (6.28)) and, therefore, this series of models evolves in the weak damping regime.

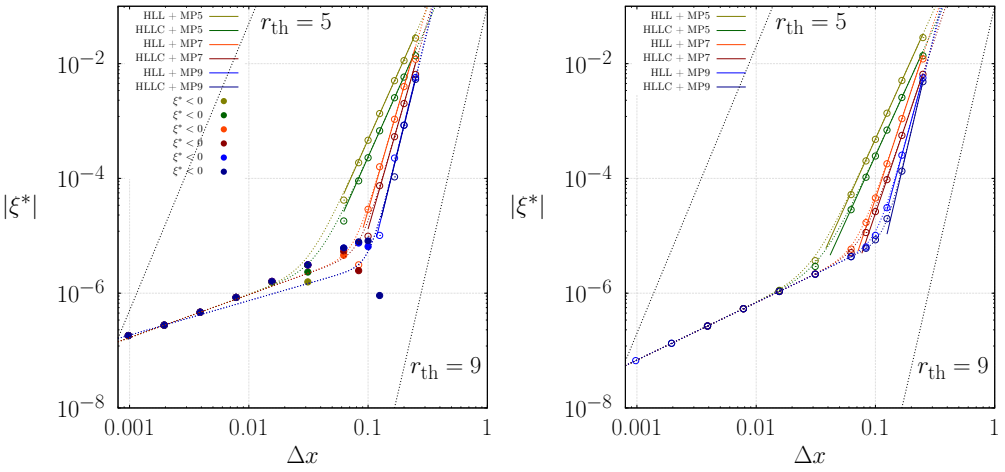

Figure 6.7: Relativistic CPAW. *Left panel*: Numerical diffusion, ξ^*_{rel}, as a function of the grid resolution (Δx), for a number cells $n_x = 4$, 5, 6, 8, 10, 12, 16, 32, 64, 128, 256, 512 and 1024. A fixed value of the physical resistivity ($\eta = 10^{-9}$) is used in all the cases. This series of simulations made with the MIRK2 time-integrator using either the HLL or the HLLC Riemann solvers with different accurate reconstruction schemes. The integration order measured (r) and the coefficient $\mathfrak{N}^{\Delta x}_{\xi rel}$ are listed in Table. 6.5. Dotted lines are included to show the theoretical order of accuracy (r_{th}). *Right panel*: Same as the left panel but for SSP2(332)-LUM time-integrator. Filled colored circles show the negative values of ξ^*.

Figure 6.7 shows the dependence of the numerical diffusivity as a function of the spatial resolution delineating the relation of Eq. (6.41). Since the results are only dominated by the contributions of spatial discretization errors for $\Delta x \geq 1/8$, the fits only include models with $n_x \leq 8$. It is important to note that for the MIRK2 time-integrator (Figure 6.7; left panel), we find negative values of the diffusivity (drawn as filled colored circles in the figure). These negative values appear for both HLL and HLLC Riemann solvers. The exact resolution below which negative diffusivity values appear depends on the spatial reconstruction employed in a non-obvious way. For MP5 they are present when $\Delta x < 1/16$, for MP7, when $\Delta x < 1/10$ and for MP9 reconstruction when $\Delta x > 1/8$. The presence of values $\xi^* < 0$ is an indication of numerical instability, since the CPAWs grow in amplitude with time (very slightly

time-integrator	solver	reconstruction	r	$\mathfrak{N}_{\xi\mathrm{rel}}^{\Delta x}$
MIRK1	HLL	MP5	4.76 ± 0.12	23 ± 6
MIRK1	HLL	MP7	7.0 ± 0.4	250 ± 190
MIRK1	HLL	MP9	7.8 ± 1.9	300 ± 900
MIRK1	HLLC	MP5	4.99 ± 0.20	18 ± 7
MIRK1	HLLC	MP7	6.8 ± 0.4	90 ± 60
MIRK1	HLLC	MP9	10.0 ± 1.1	6000 ± 10000
MIRK2	HLL	MP5	4.69 ± 0.08	21 ± 4
MIRK2	HLL	MP7	6.6 ± 0.3	140 ± 70
MIRK2	HLL	MP9	9.1 ± 0.5	1800 ± 1700
MIRK2	HLLC	MP5	4.77 ± 0.12	12 ± 3
MIRK2	HLLC	MP7	7.1 ± 0.4	150 ± 100
MIRK2	HLLC	MP9	9.6 ± 0.9	4000 ± 5000
SSP2(332)-LUM	HLL	MP5	4.56 ± 0.05	17.0 ± 2.0
SSP2(332)-LUM	HLL	MP7	6.03 ± 0.06	52 ± 7
SSP2(332)-LUM	HLL	MP9	7.0 ± 0.4	80 ± 60
SSP2(332)-LUM	HLLC	MP5	4.48 ± 0.05	7.4 ± 0.9
SSP2(332)-LUM	HLLC	MP7	5.85 ± 0.14	20 ± 6
SSP2(332)-LUM	HLLC	MP9	7.0 ± 0.8	60 ± 90

Table 6.5: Relativistic CPAW. Spatial integration order (r) and parameter $\mathfrak{N}_{\xi\mathrm{rel}}^{\Delta x}$, for time-integrators MIRK2 and SSP2(332)-LUM, using HLL and HLLC approximate Riemann solvers with MP5, MP7 and MP9 reconstruction schemes.

though). The negative value of the diffusivity on sufficiently fine grids for the MIRK2 time-integrator is another hint (which should be added to fact that the saturation value of ξ^* is nearly independent of η found in Sec. 6.3.1.1) pointing towards the possibility that more terms in the stiff sources must be treated implicitly in this algorithm. A technical remark is in order here. Measuring the values of ξ^* is hampered in the MIRK2 method by the small ($\lesssim 2.5\%$) periodic modulations of the variable $y = \ln\left(\int B^2(x,t)\,dx\right)$ in Eq. (6.40), where we replace the exact values of the magnetic field by the numerical values of $B^2(x,t) = B_y^2(x,t) + B_z^2(x,t)$. These modulations are also present in other variables and have in common a frequency $\simeq 2kv_{\mathrm{A}}$, i.e. a frequency that is half the frequency of the CPAWs set up in the computational domain ($\omega = kv_{\mathrm{A}}$).

The growth of the aforementioned *numerical* instabilities resembles the growth of parametric (*physical*) instabilities in periodic MHD shear flows. Parametric instabilities develop unstable modes with a frequency, ω, equal to twice the external (periodic) force frequency, ω_{ext}, i.e. when $\omega = \omega_{\mathrm{ext}}/2$ (e.g.

Zaqarashvili et al., 2004).[8] We identify the origin of and *external fictitious force* in the breaching of the transversality condition Eq. (6.21), for numerical and physical reasons (see below). The transversality condition is broken once $v_x \neq 0$ is generated in our models. To see this point, assume that there were an actual periodic force density acting on the system along the x-axis of the form

$$\mathbf{F}(t) = (F_x(t), 0, 0),\ F_x(t) = \rho a_{\rm ext} \cos(\omega_{\rm ext} t), \tag{6.46}$$

where $a_{\rm ext}$ is the amplitude of the acceleration. The force density of Eq. (6.46) would drive a velocity field directed along the x-axis too,

$$\mathbf{V}(t) = (v_x(t), 0, 0),\ v_x(t) = \frac{a_{\rm ext}}{\omega_{\rm ext}} \sin(\omega_{\rm ext} t).$$

Reversing the argument, if we have a periodic modulation of the v_x component, we may regard it as produced by an external fictitious force with the same frequency. The strength of the effective force grows as v_x grows, something that (numerically) happens when we increase either the Alfvén speed or the resistivity in our tests (but, the break up of the transversality condition does not yield an unstable result for all time-integrators and all possible -relativistic- Alfvén speeds). We notice this effect in Fig. 6.9, where we display the time evolution of

$$\mathcal{V}_x^2 := \frac{1}{L_x} \int v_x^2 dx. \tag{6.47}$$

The integral in Eq. (6.47) extends over the whole computational domain. For pure CPAWs in ideal RMHD, $v_x = 0$ holds at any time, and hence, $\mathcal{V}_x^2 = 0$. However, this is no longer true in RRMHD. First, because of (physical) resistive effects, as larger values of η drive larger values of $\mathcal{V}_x^2$ (compare the left and right panels of Fig. 6.9 for the same values of $v_{\rm A}$). Second, because of the impact of the numerical floating point accuracy on our method.

To understand the correlation between the growth of v_x and the increase of the Alfvén velocity, we point out that, besides the effects of the physical resistivity, another numerical source of $v_x \neq 0$ is the very different magnitude of the x-component of the Poynting flux (Eq. (2.23)), $S_{{\rm em},x} = (\mathbf{E} \times \mathbf{B})_x \simeq B_0^2 v_{\rm A} \epsilon_{\rm am}^2$, and the x-component of the hydrodynamic momentum density (Eq. (2.18)), $S_{{\rm hyd},x} = \rho h W^2 v_x$ as the magnetization (Eq. (2.25)) grows. Increasing $v_{\rm A}$, the ratio $S_{{\rm em},x}/S_{{\rm hyd},x} \propto v_{\rm A} \epsilon_{\rm am}^2$ grows. Indeed, in the classical CPAW test $v_{\rm A} = 10^{-4}$, $B_0 = 10^{-4}$ and $\epsilon_{\rm am} = 10^{-5}$, while in the relativistic cases $\epsilon_{\rm am} = 1$ and $B_0 \gtrsim 1$, so that the ratio $S_{{\rm em},x}/S_{{\rm hyd},x}$ is, at least 21 orders of magnitude smaller in the classical CPAW test than in the mildest relativistic CPAW test

[8] A simple physical example of parametric instability is found in a mathematical pendulum with periodically varying length. Note that parametric instabilities differ from direct resonances precisely in that the resonance in a physical system happens when the driving frequency, $\omega_{\rm ext}$, equals that of some of the eigenmodes of the system, ω, i.e. when $\omega = \omega_{\rm ext}$.

($v_{\rm A} = 0.1$). Such a huge difference of the numerical values of electromagnetic and hydrodynamic fluxes in the relativistic regime (compared to the classical one) renders a (much) larger loss of floating point accuracy in the operations related to the recovery of the primitive variables (Sec. 4.3). Prior to the recovery, we obtain $\mathbf{S}_{\rm hyd} = \mathbf{S} - \mathbf{S}_{\rm em}$ (Eq. (2.27)) and, also, $\mathcal{E}_{\rm hyd} = \mathcal{E} - \mathcal{E}_{\rm em}$ (Eq. (2.26)) and use these values to compute the primitive variables and, in particular v_x. Since the Poynting flux is positively set up in CPAW tests, our code tends to develop positive values of v_x. After a quick initial transient (lasting only a few time steps), v_x builds up to finite values. This transient is much faster when using a MIRK2 method, in which v_x almost immediately grows to reach a steady value (Fig. 6.9, lower panels) which is larger than the value reached in, e.g. the SSP2(332)-LUM time-integrator by the end of the computed time (Fig. 6.9, upper panels). In the classical case, the values reached by v_x in the computed time are tiny (see blue lines in Fig. 6.9) and the transversality condition is (basically) maintained. In the relativistic regime (especially, when $v_{\rm A} \gtrsim 0.1$), the transversality condition is only marginally fulfilled. When this happens, the damping rate acting on v_x ($\Im(\omega^+_{\rm nt})$; Eq. (6.39)) is twice larger than that of the rest of the variables, which tends to inhibit the further growth of v_x (in most of the time-integrators used). Indeed, we observe in Fig. 6.9 (especially in the upper panels) that the growth of v_x tends to saturate with time as a result of the counter-balancing effects of the damping of non-transverse modes and the growth of v_x instigated by the finite floating point accuracy. This is not the case for MIRK2 once the Alfvén speed is large enough ($v_{\rm A} \gtrsim 0.76$) and the growth of v_x renders the failure of our code.

From the data represented in Fig. 6.9, it is only possible to notice the temporal modulation of $\mathcal{V}_x^2$ in the case of the MIRK2 time integrator (see the inset in Fig. 6.9 in the lower left panel showing the case of $v_{\rm A} = 0.1$ as an example). In the rest of the models, it is nearly impossible to notice the modulations of $\mathcal{V}_x^2$ because of the large vertical range needed for a common representation of several cases corresponding to distinct Alfvén speeds and, most notably, because $\mathcal{V}_x^2$ grows by many orders of magnitude in a single CPAW period. Thus, we have represented in Fig. 6.10 the first and second time derivatives of $\mathcal{V}_x^2$, for the exemplary case of $v_{\rm A} = 0.1$ (similar plots can be produced for other values of $v_{\rm A}$). For the MIRK2 time-integrator we can clearly observe the modulations of $d\mathcal{V}_x^2/dt$, as well as of $d^2\mathcal{V}_x^2/dt^2$, with approximately constant amplitudes of the order of 10^{-12}. In contrast, the modulations cannot be noticed in $d\mathcal{V}_x^2/dt$ for the SSP2(332)-LUM time integrator, because they are tiny at the scale of the plot ($\sim 10^{-14}$). However, these oscillations, with growing amplitude at scales $\sim 10^{-15}$, are evident in $d^2\mathcal{V}_x^2/dt^2$ (Fig. 6.10 bottom left panel). Remarkably, in all the cases, the oscillation frequency is $2kv_{\rm A}$, i.e. twice the frequency of the CPAWs. This fact reinforces our interpretation of the growth of the velocity v_x due to a periodic effective (numerical) force that gives rise to a paramet-

ric resonance. The resonance renders the instability of the MIRK2 scheme at $v_A \gtrsim 0.76$ because the amplitude of the generated v_x is several orders of magnitude larger than for the SSP2(332)-LUM time-integrator.[9] However, we notice that the fact that the oscillations in the SSP2(332)-LUM scheme are growing with time (the amplitude doubles in a single period), suggests that also the previous RKIMEX scheme may become unstable if either (much) longer time integrations are carried out or sufficiently large Alfvén velocity is considered. Actually, for values $v_A > 0.91$, this is the case and most time-integrators we have used fail to compute the evolution of ultrarelativistic CPAWs.

We find that, for $n_x \gtrsim 16$, the diffusivity values for SSP2, are fit to a line whose slope ($q = 1.6 \pm 0.1$) is roughly compatible with the theoretical temporal integration order $q \simeq q_{\rm th} = 2$, indicating that for the finer resolutions we are dominated by the temporal discretization errors. For the MIRK2 scheme, the negative values of the diffusivity follow a power-law dependence with a power-law index $q = 0.91 \pm 0.01$. Once again, we believe that this means that the MIRK2 method needs some additional theoretical development to be fully competitive with other RKIMEX schemes.

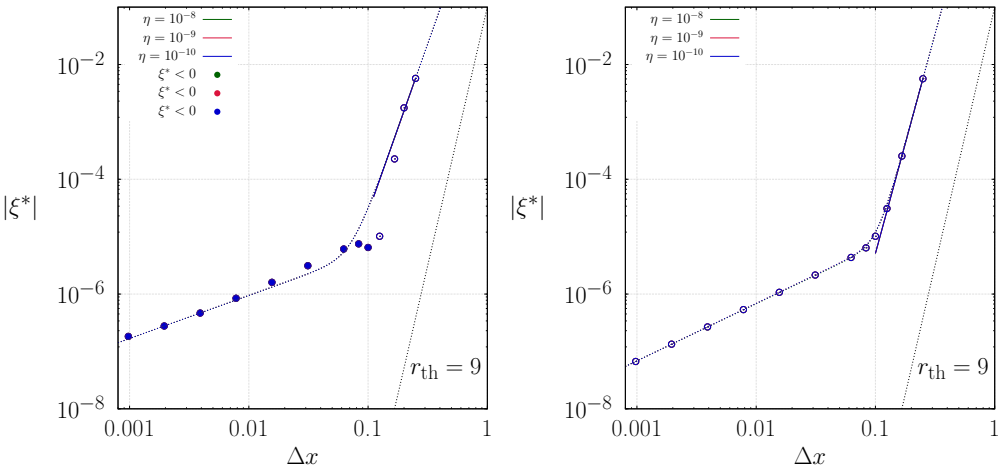

Figure 6.8: Relativistic CPAW. Same as Fig. 6.7 but for different values of η. Since the results are nearly independent of η, all three cases represented are almost indistinguishable.

In Figure 6.8 we explore the dependence of the numerical diffusivity on the physical resistivity for both time integration schemes using the HLL flux formula and the MP9 spatial reconstruction. We find that it is nearly independent of η, something qualitatively different from the classical CPAW tests, where for $\eta > 10^{-9}$ there is a clear difference between distinct values of η (more

[9] For the case of $v_A = 0.1$, the values of $\mathcal{V}_x^2$ and of the amplitudes of their oscillations are ~ 3 orders of magnitude larger for the MIRK2 time-integrator than for the SSP2(332)-LUM time integrator. For larger values of v_A the oscillations are larger.

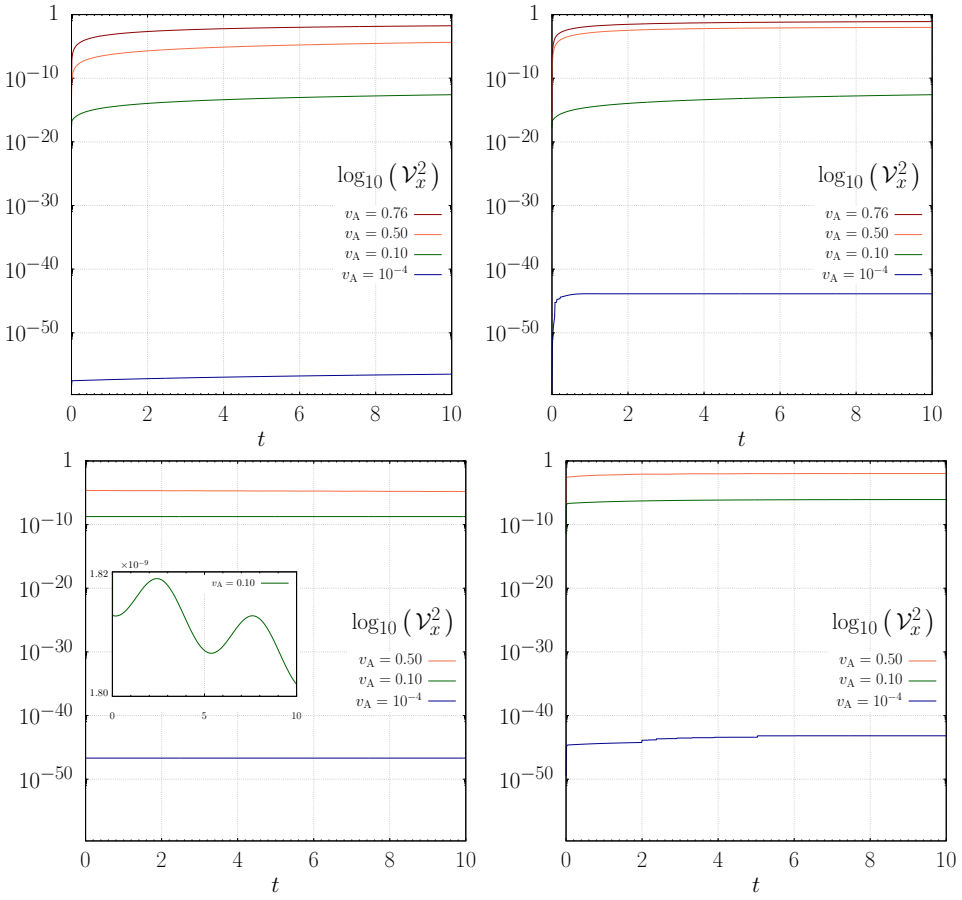

Figure 6.9: Growth of v_x for different Alfvén speeds. The variable represented is $\mathcal{V}_x^2 := 1/L_x \int v_x^2 dx$. Different color lines correspond to distinct values of v_A (see legends). *Left panels*: Cases with $\eta = 10^{-9}$. *Right panel*: Cases with $\eta = 10^{-2}$. The upper (lower) panels have been computed with the SSP2(332)-LUM (MIRK2) time-integrator, the MP9 reconstruction and the HLL Riemann solver and $n_x = 256$. The case with $v_A = 0.76$ yields a code failure when using the MIRK2 time-integrator.

evidently for the SSP2(332)-LUM time-integrator; see Fig. 6.6, left panel). We have performed simulations of relativistic CPAWs with larger values of the Alfvén speed, $0.1 < v_A < 0.76$, to understand better the differences found between the relativistic CPAW test and its classical counterpart (see Sec. 6.3.1.3). When trying to perform the same exercice for $0.76 < v_A < 1$, our code crashed for most of the cases with the finests grids and the results cannot be used to verify our extrapolation of the observed behaviour of ξ^* as a function of η in the nearly ideal regime ($\eta \ll 10^{-6}$).

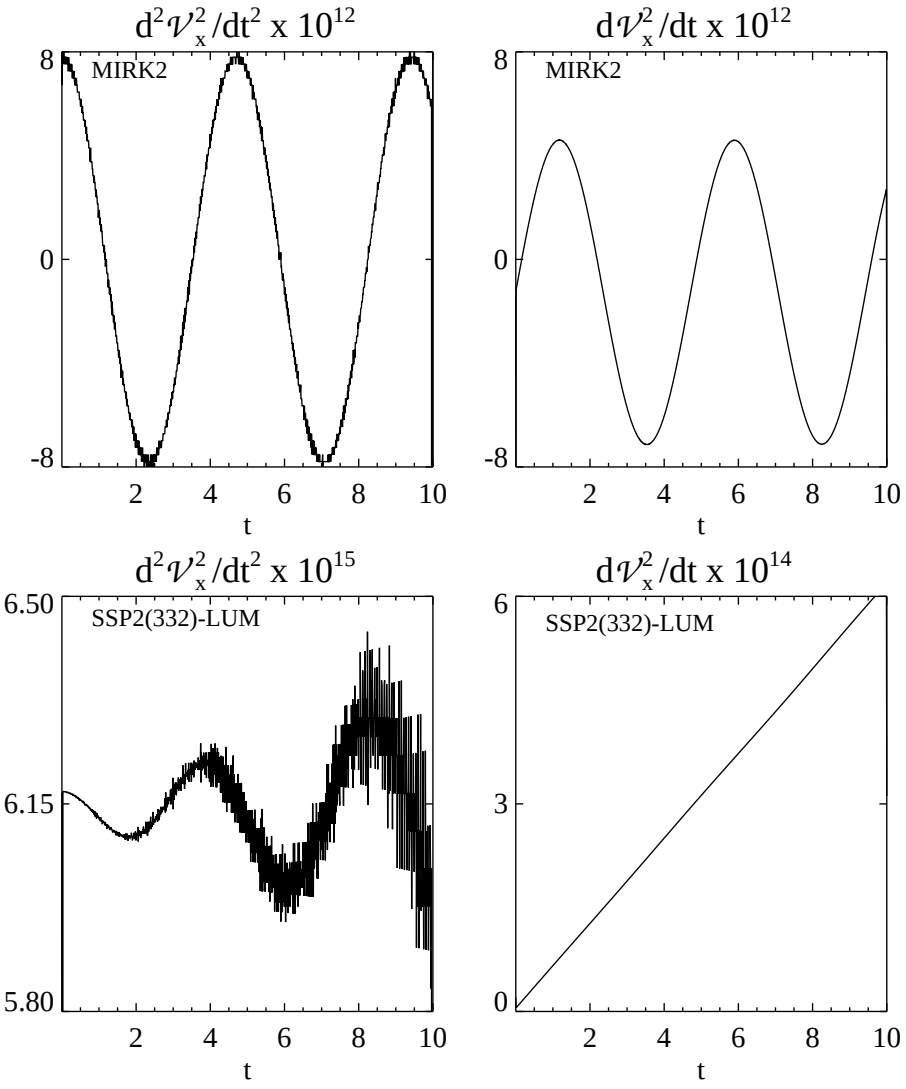

Figure 6.10: Evolution of $d\mathcal{V}_x^2/dt$ and of $d^2\mathcal{V}_x^2/dt^2$ in one period of the CPAWs. The variables represented are the first and second time derivatives of $\mathcal{V}_x^2 := 1/L_x \int v_x^2 dx$ for fixed values of $\eta = 10^{-9}$, $v_{\rm A} = 0.1$, $n_x = 256$, $C_{\rm CFL} = 0.01$, as well as the same Riemann solver (HLL) and intercell reconstruction (MP9). *Upper panels*: MIRK2 time-integrator. *Bottom panel*: SSP2(332)-LUM time-integrator. Notice the different vertical scales of each panel (see the corresponding panel titles).

6.3.1.3 Validity of the Newtonian relations for CPAWs in RRMHD

In Section 6.3.1, we have shown the functional form of the damping rate (Eq. (6.30)) obtained by Rembiasz et al. (2017), from the results of Campos (1999). We have used the previous functional form for CPAWs in RRMHD

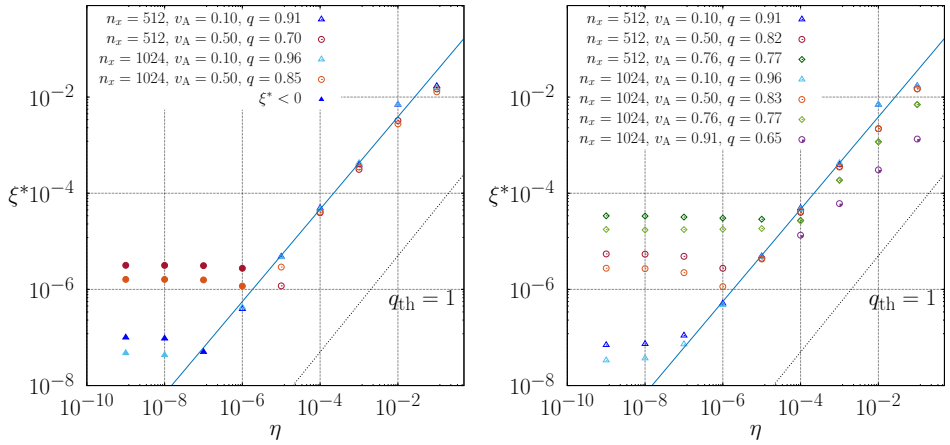

Figure 6.11: Damping rate of CPAWs as a function of the physical resistivity. *Left panel*: The values computed for ξ^* result from numerical models combining the MIRK2 time-integrator, the HLL Riemann solver, the MP9 reconstruction scheme and a $C_{\rm CFL} = 0.01$. Two different number of zones have been used ($n_x = 512$ and $n_x = 1024$) combined with two different values of the Alfvén speed ($v_{\rm A} = 0.1$ and $v_{\rm A} = 0.5$). Note that filled symbols are used in the cases in which the numerically computed damping rate is negative. *Right panel*: The same as the left panel but with the SSP2(332)-LUM time-integrator. With this time integrator, we can also display the results with a larger Alfvén speed ($v_{\rm A} = 0.76$) for all values of η, and even we show results for $v_{\rm A} = 0.91$ for $\eta > 10^{-4}$.

though, admittedly, it is only strictly valid in the Newtonian resistive MHD. In this section we aim to test numerically the validity of the dependence of the diffusivity as a function of the resistivity as we enter in the relativistic regime. For that, we have set up several series of CPAWs tests with a broad range of resistivity values ($\eta \in [10^{-9}, 0.1]$) Alfvén speeds $v_{\rm A} = 0.1$ and $v_{\rm A} = 0.76$ and rather high resolution (we will show results for $n_x = 512$ and $n_x = 1024$) in order to minimize the numerical diffusivity as much as possible. We note that at the previous resolutions our results are likely dominated by time discretization errors. But even if this is the case, for the relativistic CPAW test we observed a decrease of the numerical diffusivity $|\eta^*| \propto (\Delta x)^q$ ($q \simeq 0.91 - 1.6$) in the range of high resolutions (see, e.g. Fig. 6.8). Values $v_{\rm A} \gtrsim 0.91$ are achievable by our code only for relatively large resistivities $\eta \gtrsim 10^{-4}$ and only if we use some RKIMEX time integration schemes (e.g. the SSP2(332)-LUM or the RK36$\mathcal{S}_E$ time-integrators). Smaller values of the physical resistivity lead to code failures associated to the fact that we are in a regime in which numerical parametric instabilities quickly develop (see discussion in Sect. 6.3.1.2).

In Fig. 6.11 we show the diffusivity for CPAWs as a function of resistivity for two different time-integrators, SSP2(332)-LUM (right panel) and MIRK2 (left panel). Both cases show qualitatively similar trends, as we have found in the previous sections in the case of the tests with $v_{\rm A} = 0.1$. Indeed, for the previous

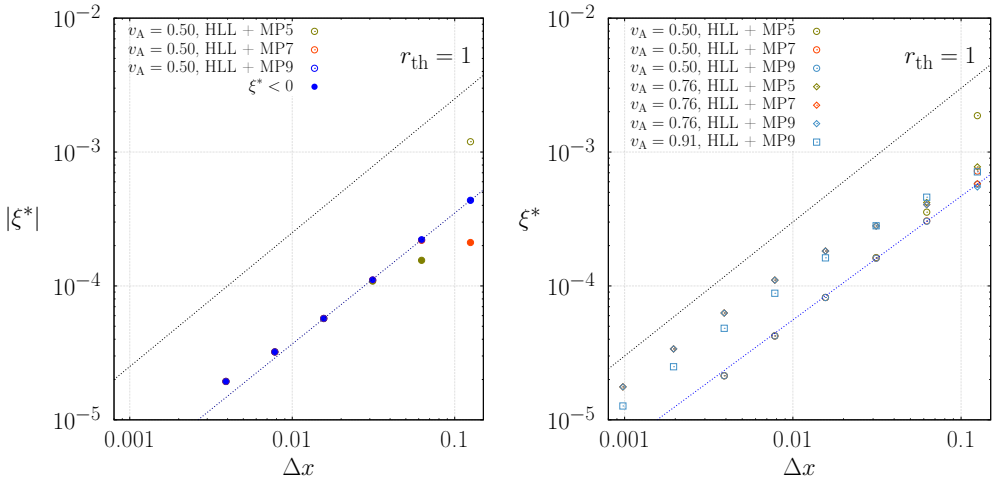

Figure 6.12: Ultrarelativistic CPAW. Same as Fig. 6.7, but showing the dependence of the numerical diffusivity with the grid spacing Δx for various values of the Alfvén speed (see legends). Qualitatively similar results have been obtained using the HLLC Riemann solver.

Alfvén speed, these test are the same as those set up in Sec. 6.3.1.2. The two left-most blue triangles symbols (corresponding to $\eta = 10^{-8}$ and $\eta = 10^{-9}$) have already been presented in Fig. 6.8. As it happened for relativistic CPAWs with $v_A = 0.1$, also for $v_A = 0.5$ we have negative diffusivity values when using the MIRK2 time-integrator (filled symbols in Fig. 6.11, left panel). However, this is a problem which does not show up with the SSP2(332)-LUM time-integrator and, for this reason we may draw some conclusions about the validity of the dependence of the damping rate of CPAWs on the diffusivity. From Fig. 6.11 and regardless of the time-integrator, we observe that there is a range in which $|\xi^*| \simeq \eta$ above a certain value of the resistivity, $\eta_{\rm thr}$, that depends on the Alfvén speed. $\eta_{\rm thr}$ grows with increasing v_A. Physics wise, we expect that $\xi = \eta + \nu \simeq \eta$ is valid in the limit of negligible shear viscosity for any value of η. Numerically, this proportionality is restricted to $\eta > \eta_{\rm thr}$. The previous range of validity of the relation corresponds to the region of values of Δx in which we are dominated by spatial discretization errors. This can be seen in Fig. 6.12, where we observe that the range of Δx in which we are dominated by spatial discretization errors decreases for the larger values of v_A regardless of the time-integrator employed. More explicitly, for $\Delta x < 1/10$, the results are dominated by time discretization errors when $v_A \gtrsim 0.5$. Indeed, the reduction of the order of accuracy is rather severe for $v_A \gtrsim 0.5$, and even a method like the SSP2(332)-LUM, which has been designed to have a uniform order of accuracy reduces its convergence rate to $q \lesssim 1$.[10] We must point out that the optimization of

[10]Note the "U" in the name given by Higueras et al. (2012) to denote that the SSP2(332)-LUM time-integrator is uniformly convergent; see Eq. (A.1) in App. A.1.0.3.

the coefficients in the SSP2(332)-LUM method, so that it becomes uniformly convergent, is done for relatively simple scalar ODEs (Higueras et al., 2012) and not for the more complex case of systems of PDEs (our case). Thus, it is not totally surprising that the order of accuracy of the SSP2(332)-LUM method, applied to RRMHD may be degraded in some circumstances. As we have commented in the previous sections, when this happens, our ansatz for the numerical resistivity (Eq. (6.2)) is imperfect since it does not account for the fact that we employ a partly implicit time integration scheme. This means that the estimation of η^* becomes unreliable and we cannot use it to asses the validity of the dependence of the damping rate on the diffusivity. Besides this numerical subtleties, which require a deeper study, it is clear that the damping rate dependence on the diffusivity obtained in the Newtonian MHD limit by Campos (1999) can be cautiously used in the RRMHD limit.

6.4 Characteristic scales ($\mathcal{L}$ and $\mathcal{V}$)

With the aim of assessing which are the characteristic length and speed in our code, we make a series of numerical tests involving the diffusion of shear layers or the propagation of Alfvén waves in an homogeneous medium, i.e. these are the same tests as presented in the previous sections. These tests include neither an initial discontinuity nor discontinuities (i.e. shocks) developing in the course of the time evolution. Hence, they allow us to assess whether the algorithms implemented in our numerical code perform at the formal (theoretical) order of accuracy. In these first exploratory tests, we restrict to one spatial dimension. Two tests adress the numerical diffusion of either velocity (VSL test; Sec. 6.1.1) or magnetic field (MD test; Sec. 6.2.1) shear layers. In another test, we consider the numerical diffusion experienced by relatively small amplitude, circularly polarized Alfvén waves (CPAW test; Sec. 6.3.1).

Following Rembiasz et al. (2017), we explore the dependence of ν^* and η^* on the characteristic length of systems, $\mathcal{L}$, which should be proportional to the wavelength, λ in tests involving a wave propagation. In order to make the study simpler, we set the wavelength equal to the size of the numerical domain, L_x, i.e. $L_x = \lambda$. In this form a single wave is contained in the computational domain and suitable periodic boundary conditions can be applied at the two ends of the numerical box. For each kind of wave considered, we perform a series of tests in which we only modify the numerical resolution by changing the domain size L_x (we take $L_x = \lambda = 1, 2, 3, 4$ and 5), but fixing the number of grid zones ($n_x = 32$). We remind that varying $L_x = \lambda$, we also change $k = 2\pi/\lambda$ in each of the tests. We choose $n_x = 32$ because this is a value *significantly larger* than the typical number of zones employed in realistic (global) simulations to

resolve a *single* wavelength with a high order accurate method.[11] If we neglect the errors due to time discretization and in accordance with, e.g. Eq. (6.1), the results of these series of simulations can be fit to

$$\ln(\nu^*) = \ln\left(\mathfrak{N}_\nu^{\Delta x} \mathcal{V} n_x^{-r}\right) + \alpha \ln(\lambda)\,. \tag{6.48}$$

test	α
VSL	0.999997 ± 0.000001
MD	0.999998 ± 0.000001
CPAW-cla	1.013 ± 0.003
CPAW-rel	0.99976 ± 0.00004

Table 6.6: Values of α (Eq. (6.48)) computed in order to identify the characteristic length of the system. All simulations have been performed with the MP5 reconstruction scheme, the HLL Riemann solver, and the MIRK2 time-integrator. In order to compute the fit, λ has been varied in the interval $[1, 5]$. The CPAW-rel test has been computed with $v_{\rm A} = 0.1$.

For all the wave damping problems studied in this chapter (see Tab. 6.6), we find that the measured fit parameter is $\alpha \simeq 1$, as expected, confirming that $\mathcal{L} = \lambda (= L_x)$. In Fig. 6.13 (upper left panel) we display the results computed for ξ^* in the MD test (in which case $\xi^* = \eta^*$), confirming that the wave length is the characteristic length of the different wave systems $\mathcal{L} = \lambda$. Figures similar to Fig. 6.13 computed for all the other tests (VSL and classical and relativistic CPAW) can be found in App. E.

To determine the characteristic velocity of the different systems we explore the dependence of ξ^* as a function of the various potentially relevant propagation velocities in these problems, namely, the sound, Alfvén and fast magnetosonic speeds. As an example, we show in Fig. 6.13 the case of the MD test (other cases can be found in App. E). We observe in the bottom panels as well as in the upper right panels of that figure that the diffusivity is independent of any of the possible eigenspeeds of the system (similar results hold for other tests problems; see App. E). This independence of ξ^* on $c_{\rm s}$, $v_{\rm A}$ or $v_{\rm fms}$ (or combinations thereof) suggests, by discard, that the characteristic speed in those systems is the light speed, i.e. $\mathcal{V} = 1$. This seems to be the only possible alternative and, therefore, we have assumed it to be the characteristic speed for all simulations in this chapter. This result is in clear contrast with the findings of Rembiasz et al. (2017) in Newtonian MHD, where the characteristic velocity is always equal to the fast magnetosonic speed. This constitutes a novelty that, to our best knowledge, has been only found in this thesis.

[11] This procedure differs from the one followed in the previous sections, in which we considered a series of simulations, for which we kept constant L_x (and hence λ by construction) and changed the number mesh points in order to measure the numerical diffusivity.

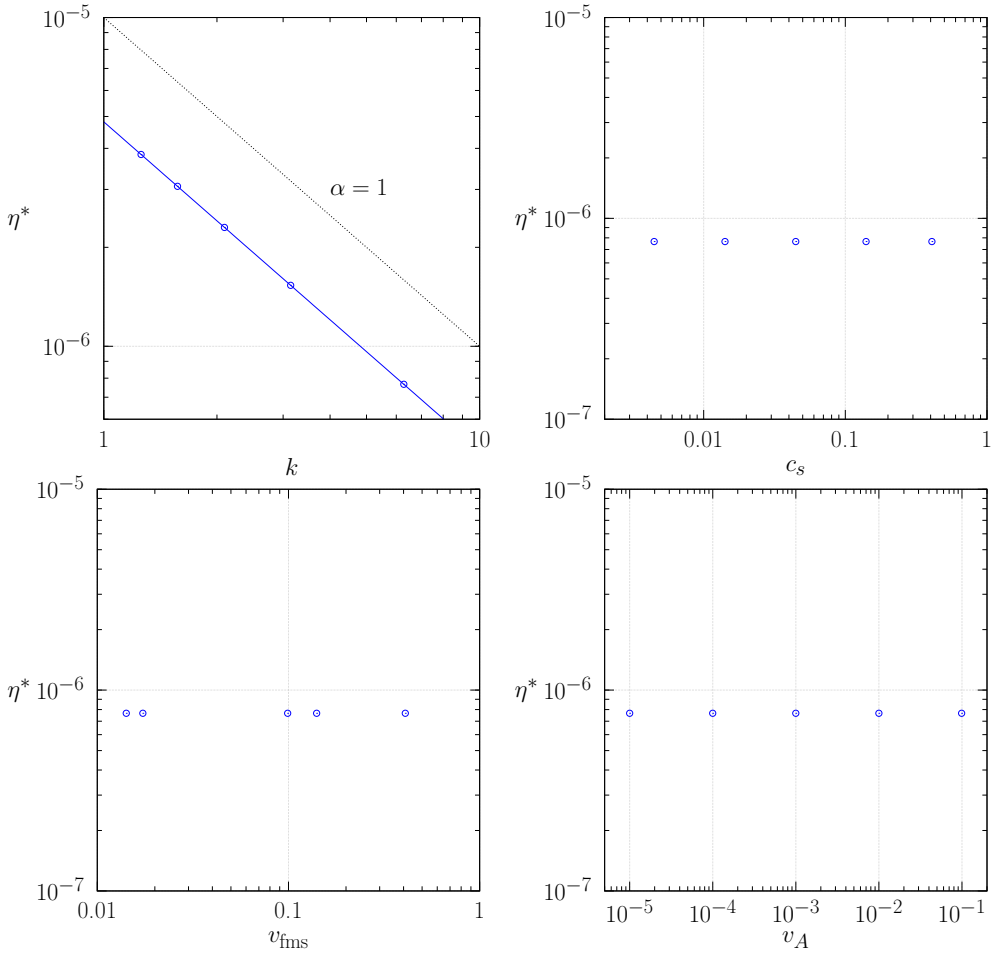

Figure 6.13: Numerical diffusivity for the **MD** test. *Upper left panel*: dependence on the wavenumber $k = \pi/\lambda$, i.e. on the box size since we fix $L_x = \lambda$. *Upper right panel*: dependence on the sound speed ($c_{\rm s}$). The different values of $c_{\rm s}$ are set keeping the background density, ρ_0, constant and varying the background pressure, $p_{\rm g,0}$. *Lower left panel*: dependence on the fast magnetosonic speed ($v_{\rm fms}$). The variation of $v_{\rm fms}$ with respect to the standard set up of this test is obtained varying the background magnetic field strength, B_0, and the background pressure, $p_{\rm g,0}$. *Lower right panel*: dependence on the Alfvén speed ($v_{\rm A}$). We modify the Alfvén speed varying only the background magnetic field strength and maintain constant the remaining parameters. All the values displayed in this figure are computed using a MIRK2 time-integrator, the HLL Riemann solver and MP9 reconstruction.

Chapter 7

Relativistic *Ideal* Tearing Modes in single and double current sheets

Almost everywhere in the universe the magnetic Reynolds number, $R_m \equiv \mathcal{L}\mathcal{V}/\eta$ ($\mathcal{L}$ and $\mathcal{V}$ are the characteristic length scale and typical velocity of the system, respectively), is so much larger than unity that the magnetic field is attached very effectively to the plasma. Only in minuscule regions, the magnetic gradients are typically million times or more stronger than in other regions, and therefore the magnetic field can slip through the plasma and reconnect (c.f. Priest and Forbes, 2000).

Sweet (1958) and Parker (1957) devised a seminal model to understand magnetic reconnection in a steady state regime. The Sweet-Parker (SP) model assumes the existence of a magnetic diffusion layer along *the whole boundary* between regions of opposite polarity magnetic fields. The length of the diffusion layer (L) equals the global external length scale ($\mathcal{L}$), and the reconnection rate equals to the speed with which the magnetic flux enters the diffusion region. Magnetic reconnection timescales are typically expressed in terms of dimensionless numbers, generically called Lundquist numbers, $S_{\rm L}$, defined as[1]

$$S_{\rm L} := \frac{v_{\rm A} L}{\eta}. \tag{7.1}$$

In astrophysical or laboratory highly conducting plasmas, typically, $S_{\rm L} \gg 1$, e.g. $S_{\rm L} \sim 10^{12}$ in the solar corona. In terms of $S_{\rm L}$, the typical time scale, $t_{\rm SP}$, in which the basic SP mechanism operates reconnecting magnetic field along

[1] In Eq. (7.1), the definition of the Lundquist number is *associated* to a length scale, L, that in the SP model coincides with the global external length scale, $\mathcal{L}$. However, it is possible to define analogous dimensionless numbers associated to other length scales of the problem, as we shall see later.

the magnetic diffusion layer is

$$t_{\mathrm{SP}} = t_{\mathrm{A}} S_{\mathrm{L}}^{1/2}, \tag{7.2}$$

where

$$t_{\mathrm{A}} := \frac{L}{v_{\mathrm{A}}} \tag{7.3}$$

is the Alfvén crossing time of the system whose length scale is L. Since in most plasmas of astrophysical interest $\eta \ll 1$, the Lundquist number is huge and the resulting time scale for the reconnection is much too slow to explain, e.g. the energy released in a solar flare or in disruptive events in a tokamak. Remarkably, t_{SP} is a fraction of t_{A}, but still, it is (much) shorter than the (extremely slow) diffusion time scale of the magnetic field,

$$t_{\mathrm{d}} := \frac{L^2}{\eta}. \tag{7.4}$$

Indeed, from the definitions given in Eqs. (7.3) and (7.4), we may interpret the Lundquist number as the ratio of diffusion-to-Alfvén time scales (i.e. $S_{\mathrm{L}} = t_{\mathrm{d}}/t_{\mathrm{A}}$). Furthermore, it turns out that the SP time scale is the geometric mean of previous time scales, namely, $t_{\mathrm{SP}} = (t_{\mathrm{A}} t_{\mathrm{d}})^{1/2}$.

In order to circumvent the problem of the very long time scales implied by the SP reconnection mechanism, Petschek (1964) suggested that the SP diffusion region could be limited to a small region $L \ll \mathcal{L}$, i.e. much smaller than the macroscopic (global) size of the system. Under this assumption, not only the diffusion region (of size L) is shorter, but also thinner, and the reconnection process may proceed faster. For typical astrophysical systems, the time scale for the Petschek reconnection is $\sim 0.01 t_{\mathrm{A}} - 0.1 t_{\mathrm{A}}$ (Priest and Forbes, 2000). Other possibilities to enhance the *steady* reconnection rate of the basic SP mechanism have been suggested and the interested reader is referred to the excellent book of Priest and Forbes (2000).

The reconnection modes previously considered (SP and Petschek) are steady reconnection mechanisms. However, unsteady reconnection processes exist and may operate on significantly shorter time scales. Hence, they are of great interest to understand fast, time-dependent flaring activity associated to the reconnection of magnetic field in astrophysical systems. The development of resistive instabilities in a plasma depends on the local relaxation of the constraint that the fluid must remain attached to the magnetic field. The TM instability is a resistive MHD instability that can develop in current sheets and dissipates magnetic energy into kinetic energy and subsequently into thermal energy. Current sheets naturally form when there is magnetic shear as a consequence of the Ampère's law, since every spatial change of the magnetic field direction drives a current.

A typical current sheet tends to diffuse at a slow rate with a time-scale of

$$\tau_{\rm d} := \frac{a^2}{\eta}, \tag{7.5}$$

where $2a$ is the width of the current sheet, whose typical (macroscopic) length is L. While the magnetic field is diffusing, magnetic energy is converted ohmically into thermal energy at the same slow rate. Even if typically $a < L$ (or even $a \ll L$) and therefore, $\tau_d < t_{\rm d}$ (or sometimes $\tau_d \ll t_{\rm d}$; compare Eqs. (7.4) and (7.5)), τ_d is typically huge in cosmic processes and, therefore, the magnetic diffusion of (*thin*) current sheets cannot be invoked to explain the time-scale of dynamical cosmic processes. However, magnetic diffusion may drive three distinct resistive instabilities in a current sheet, namely, *gravitational* and *rippling* modes, as well as TMs (Furth et al., 1963). The growth rates of these modes (especially of the TMs) are often fast enough to be physically significant These instabilities develop when the sheet is sufficiently wide and the following relation holds: $\tau_{\rm d} \gg \tau_{\rm A}$, where

$$\tau_{\rm A} := \frac{a}{v_{\rm A}}, \tag{7.6}$$

is the Alfvén crossing time of the current sheet width.[2] The instabilities have the effect of creating in the sheet many small-scale magnetic loops. The magnetic energy is released because resistive instabilities produce current filaments in current sheets (even more generally, in any sheared structure), which diffuse away. The resistive instabilities found by Furth et al. (1963) occur on time-scales $\tau_{\rm d}(\tau_{\rm A}/\tau_{\rm d})^{\lambda} = \tau_{\rm d} S_a^{-\lambda}$, where $0 < \lambda < 1$, and

$$S_a = \frac{a v_{\rm A}}{\eta} \tag{7.7}$$

is the Lundquist number *associated* to the width of the magnetic shear (to be compared with the Lundquist number $S_{\rm L}$ defined in Eq. (7.1)).

As other resistive processes, TMs disconnect and rejoin magnetic field lines, thereby changing the topology of the magnetic field. TMs are of great relevance in astrophysics, (e.g. in the magnetopause or magnetotail of the solar wind, in flares or coronal loops of the Sun, and in the flares of the Crab pulsar; cf. Priest and Forbes 2000). They have been also suggested to be a terminating agent of the MRI (Balbus and Hawley, 1991; Latter et al., 2009; Pessah, 2010, but

[2] Note the difference between the Alfvén crossing times associated to the crossing of the current sheet width (Eq. (7.6)) and that associated to the length of the diffusion layer in, e.g. the SP mechanism (Eq. (7.3)). While the latter time scale may be very small if the current sheet is *thin*, the former one may be rather large if the current sheet has a length comparable to the global (macroscopic) length scale of the system, i.e. when $L \sim \mathcal{L}$.

see Rembiasz et al. 2016a who observed an MRI termination by the Kelvin-Helmholtz instability in their 3D MRI simulations).

A finite conductivity allows an initial background field with a shear of a width a, (typically, $\mathcal{L} \gg a$) to relax to a less energetic (topologically different) configuration. If the conductivity is infinite, lines of force that are initially different must remain so during a perturbation. When a TM is excited, lines of force that are initially distinct, link up as a result of the perturbation. Therefore, these modes do not exist in the infinite-conductivity limit or, stated alternatively, their growth time becomes infinite when $\sigma \to \infty$.

The linear theory of TMs was extensively studied, in the context of plasma fusion physics, in a seminal paper of Furth et al. (1963), and has been very throughly tested against numerical simulations (see, e.g. Rembiasz et al., 2017, and references therein). Among the most salient results of Furth et al. (1963) we find the theoretical prediction for the growth rate, γ, and the corresponding wave number, k, of the tearing instability under a number of simplifying assumptions. Since our focus are not TMs, we will not derive here the linearized equations and the corresponding dispersion relation (interested readers are referred to the original reference or to Rembiasz, 2013, Sec. 3.4). However, we shall briefly recap the basic assumptions under which the linear theory holds for later reference:

1. It is assumed that the plasma is subsonic, $|\mathbf{v}| \ll c_\mathrm{s}$, which can be equivalently stated as that the plasma is incompressible ($\nabla \cdot \mathbf{v} = 0$). It must be noticed that TMs also grow in the compressible regime as was demonstrated in the App. A of Furth et al. (1963).

2. The magnetic shear of the initial configuration is in mechanical equilibrium. Since in a magnetic shear the gradient of magnetic pressure is finite, one needs to balance it out by either a suitable gas pressure gradient (*pressure equilibrium* configuration) or by an additional magnetic field component (*force-free* configuration).

3. The perturbations considered by the linear theory have a wavelength, at most, comparable to the shear width, i.e.

$$k \lesssim a^{-1}.$$

   This is in contrast to the other two instabilities studied by Furth et al. (1963). Gravitational and rippling modes develop when the density or η varies in the direction across the sheet. However, these modes produce small-scale structure in the current sheet (Fig. 7.1(b)) and, therefore their ability to destabilize the large-scale structure of the sheet is limited, although they may feed a turbulent diffusivity. We note that the tearing

instability is likely the most important of the three instabilities described by Furth et al. (1963), since requires neither a gravitational force nor a resistivity gradient to develop.

4. The growth time of the resistive modes is small compared with the diffusive timescale of the system, namely,

$$\frac{a^2}{\eta} \gg \gamma^{-1}. \tag{7.8}$$

For practical purposes, this condition means that the background magnetic field can be treated as constant.

5. The Alfvén crossing time must be much shorter than the instability time scale. This happens when the Alfvén speed is sufficiently large, that the following condition holds:

$$\frac{\mathcal{L}}{v_{\rm A}} \ll \gamma^{-1}. \tag{7.9}$$

The conditions expressed by Eqs. (7.8) and (7.9) can be combined to

$$\frac{\mathcal{L}}{v_{\rm A}} \ll \gamma^{-1} \ll \frac{a^2}{\eta}.$$

Under the former assumptions, Furth et al. (1963) find (see their Fig. 3) that the growth rate of TMs is (c.f. Priest and Forbes, 2000)

$$\gamma \simeq (\tau_{\rm d}^3 \tau_{\rm A}^2 (ka)^2)^{-1/5}, \qquad \text{if } S_a^{-1/4} \lesssim ka \lesssim 1. \tag{7.10}$$

We may gain some additional physical insight into the meaning of Eq. (7.10) by noting that the shortest allowed wavelengths grow in a time $\tau_{\rm d}^{3/5}\tau_{\rm A}^{2/5}$, or equivalently, with a growth rate

$$\gamma_{\rm TM} \simeq \tau_{\rm d}^{-3/5}\tau_{\rm A}^{-2/5} = \tau_{\rm A}^{-1} S_a^{-3/5} \qquad \text{for} \qquad k_{\rm TM} a \simeq 1,$$

whilst the longest wavelengths grow at rates

$$\gamma_{\rm TM} \simeq (\tau_{\rm d}\tau_{\rm A})^{-1/2} = \tau_{\rm A}^{-1} S_a^{-1/2} \qquad \text{for} \qquad k_{\rm TM} a \simeq S_a^{-1/4}.$$

Remarkably, the longest wavelengths at which TMs grow are such that $aS_a^{1/4} \gg a$, i.e. their scales are much larger than the width of the current sheet. In spite of the larger growth rate of TMs compared to, e.g, the growth rate of SP-steady reconnection, still for the large values of the Lundquist number expected in astrophysical contexts, classical models of the TM instability fail to predict the observed time variability exhibited by, e.g. solar flares or tokamak disruptions.

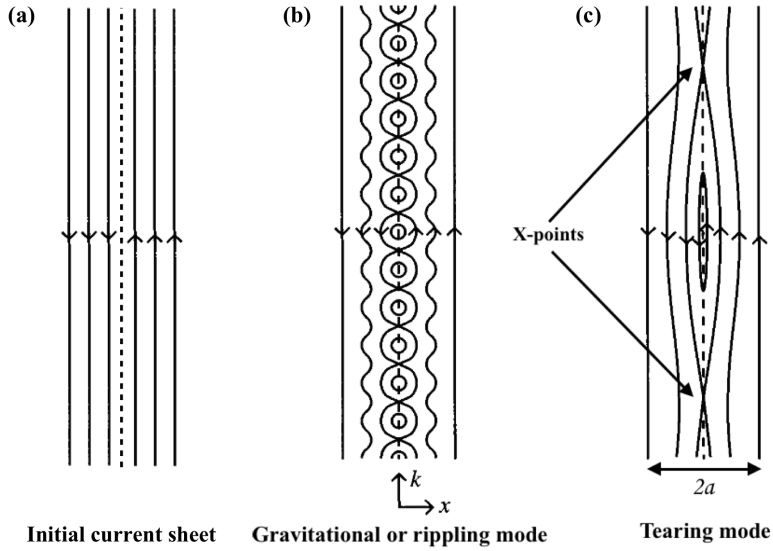

Figure 7.1: Sketch of the resistive instabilities found by Furth et al. (1963). (a) Initial configuration of the magnetic field. (b) Small-wavelength and (c) long-wavelength instabilities in a resistive curent sheet or sheared magnetic field. The coordinate x grows in the direction across the equilibrium magnetic field. The figure is adapted from Fig. 6.1 of Priest and Forbes (2000).

The previous phenomenology happens on a non-negligible fraction (namely, not less than 10%; Del Zanna et al., 2016) of the ideal (Alfvénic) time scales.

As we have already mentioned, TMs are resistive instabilities which require a finite resistivity to develop, at least in a narrow (resistive) layer, whose width is $L_{\mathrm{R}} \simeq (ka)^{-3/5} S_a^{2/5}$ (c.f. Priest and Forbes, 2000). Inside the resistive layer, the magnetic field vanishes and may slip quickly through the plasma. In order to understand the growth mechanism of the TMs, consider a 2D current sheet with magnetic field parallel to the sheet (Fig. 7.1(a)). We perturb this configuration and end up with a geometry similar to that of Fig. 7.1(c). In that configuration, the magnetic tension pulls the new loops away from the "X-points" in the vertical direction, while simultaneously the magnetic pressure gradient pushes the plasma sidewise (along the horizontal direction) towards the X-points. As a result of this force imbalance, the perturbation grows. In the process, the magnetic field lines are bent, generating a restoring tension force, which is minimized at the longest wavelengths.

The velocity of the outflow generated in a current sheet as sketched in Fig. 7.1(c) is schematically displayed in Fig. 7.2. The resistive layer is flanked by the extrema of the velocity field. These extrema are stationary and may be very narrow and, therefore, very difficult to resolve numerically.

The (research) field of reconnection can be regarded as a continuous race

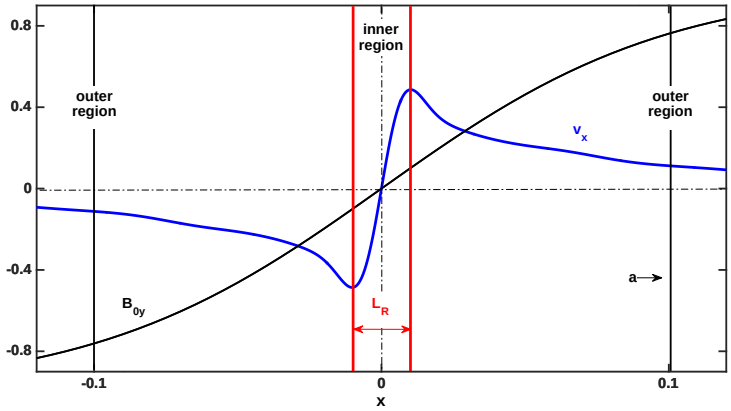

Figure 7.2: Sketch of the 1D flow structure and magnetic field after the development of TMs. Background magnetic field B_{0y} (black) and the amplitude (rescaled for a better visibility) of the velocity perturbation v_x (brown) at a vertical location half-way between two consecutive X-points (see Fig. 7.1(c)).The vertical scale is arbitrary. Only the region in the vicinity of the central part of the current sheet is shown. Black and red vertical lines respectively mark, the shear width a and the width of the resistive layer $L_{\rm R}$. The inner region is determined the local extrema of the velocity v_x. The outer region is represented to be sufficiently far way from the resistive viscous layer.

to find ways to overcome the slowness of steady state reconnection and even of unsteady reconnection. This race has accelerated in the last years with contributions from numerical simulations and linear instability analyses that confirm the existence of fast reconnection modes. Indeed, using single-fluid MHD, provided that $S_{\rm L}$ is sufficiently large and that the current sheet aspect ratio (L/a) is also large, the TM growth rate may significantly raise. Actually, in the previous conditions, there can appear explosive secondary reconnection events and the production of plasmoid chains on progressively smaller scales (these instabilities are often called *super-tearing*, or *plasmoid* instabilities), which lead to reconnection rates almost independent of $S_{\rm L}$. Interestingly, if $L/a \sim S_{\rm L}^{1/2}$ even the SP current sheet becomes TM unstable and its growth rate becomes $\gamma t_{\rm A} \sim S_{\rm L}^{1/4}$ when $S_{\rm L} > S_{\rm L}^{\rm thr} \simeq 10^4$ (Bhattacharjee et al., 2009; Lapenta, 2008; Loureiro et al., 2007; Samtaney et al., 2009). Qualitatively similar results in the RRMHD regime have been found in a number of previous studies in 2D (e.g. Watanabe and Yokoyama, 2006; Zenitani et al., 2010) even in 3D (Zanotti and Dumbser, 2011).

Resistive instabilities whose growth rate increases with increasing Lundquist number (as stated in the previous paragraph) are paradoxical. Their modes

would grow *infinitely* fast in the ideal MHD limit (something evidently unphysical and non-causal). One may argue that in that limit, resistive modes are prohibited, but if that were the case, the MHD equations would have a very singular behaviour as we approach the infinite conductivity limit or, equivalently, in the infinite Lundquist number limit. Certainly, this cannot be the case and there exist mechanisms to limit the growth of instabilities, which cannot be captured in a linear analysis. Pucci and Velli (2014), based on ideas already sketched out in the appendix D of Furth et al. (1963), found a very appealing possibility to deal with the paradoxical $S_{\rm L} \to \infty$ limit. The idea is that for large enough Lundquist numbers ($S_{\rm L} \gtrsim 10^6$) only and "ideal" TM survives. The term "ideal tearing mode" (ITM) may seem an oxymoron given the fact that TMs are resistive (i.e. non-ideal) instabilities. However, their name was coined because *the growth rate of ITMs is independent of the Lundquist number* and, hence, independent of the resistivity. This is the case for *critical* values of the aspect ratio of the current sheet, L/a, such that they scale with the macroscopic Lundquist number, namely,

$$\frac{L}{a} = S_{\rm L}^{1/3}. \tag{7.11}$$

As a consequence of this critical scaling of the sheet aspect ratio, the growth time of the TMs becomes optimal, namely, a fraction (of the order of unity) of $t_{\rm A}$. To see this point, using the critical scaling of Eq. (7.11), we rewrite Eq. (7.10) in terms of the sheet length and the macroscopic Lundquist number *rescaling* the Lundquist number associated to the current sheet width $S_a = (a/L)S_{\rm L}$ (see Eqs. (7.1) and (7.7)) and $t_{\rm A} = (L/a)\tau_{\rm A}$, which for critical sheet aspect ratios (Eq. (7.11)) become $S_a = S_{\rm L}^{2/3}$ and $t_{\rm A} = S_{\rm L}^{1/3}\tau_{\rm A}$, respectively. One readily obtains

$$\gamma \simeq (\tau_{\rm d}^3 \tau_{\rm A}^2 (kL)^2)^{-1/5} S_{\rm L}^{2/15}, \qquad \text{if } S_{\rm L}^{1/6} \lesssim kL \lesssim S_{\rm L}^{1/3}.$$

For the modes of shortest wavelengths, the growth rate is

$$\gamma_{\rm ITM} \simeq \tau_{\rm A}^{-1} S_{\rm L}^{-2/5} \simeq t_{\rm A}^{-1} S_{\rm L}^{-1/15} \qquad \text{for} \qquad k_{\rm ITM} L \simeq S_{\rm L}^{1/3}. \tag{7.12}$$

Likewise, for the modes of longest wavelengths (which are the fastest growing ones), the growth rate is

$$\gamma_{\rm ITM} \simeq \tau_{\rm A}^{-1} S_{\rm L}^{-1/3} \simeq t_{\rm A}^{-1} \qquad \text{for} \qquad k_{\rm ITM} L \simeq S_{\rm L}^{1/6}. \tag{7.13}$$

Thus, we can see from Eq. (7.13) that $\gamma_{\rm ITM} t_{\rm A} \simeq 1$, i.e. the growth time of the ITMs with the longest wavelengths is of the order of the macroscopic Alfvén crossing time, independently of the Lundquist number (equivalently, independently of the resistivity). For the shortest wavelengths, Eq. (7.12) states that

$\gamma_{\rm ITM} t_{\rm A} \simeq S_{\rm L}^{-1/15}$, also displaying a very weak dependence on the Lundquist number. From Eq. (7.2), it is evident that the growth rate of TMs in an SP reconnection layer is

$$\gamma_{\rm SP} = t_{\rm A}^{-1} S_{\rm L}^{-1/2}, \tag{7.14}$$

that can be compared to the fastest growth rate of ITMs, Eq. (7.13), letting us conclude that $\gamma_{\rm ITM}/\gamma_{\rm SP} = S_{\rm L}^{1/2} \gg 1$ for the typical (large) Lundquist numbers to be expected in astrophysical systems.

The *rescaling* procedure employed by Pucci and Velli (2014) is more general than assuming that the sheet aspect ratio is exactly as in Eq. (7.11). They proceed heuristically and assume that the aspect ratio of the sheet may generically scale as $L/a = S^{\alpha}$, concluding that if $\alpha > 1/3$ the growth rate of TMs exhibits an unphysical divergence with increasing $S_{\rm L}$. Only for $\alpha = 1/3$ the growth rate becomes independent of $S_{\rm L}$, which means that as we approach the ideal limit, current sheets can, at most, become as thin as $a/L \sim S_{\rm L}^{-1/3}$. This conclusion let Pucci and Velli (2014) argue that as the current sheet slims down from a macroscopic thickness, the value of the power-law index α would evolve from about 0 to 1/3 as $S_{\rm L} \to \infty$. Indeed, $\alpha = 1/3$ is a critical exponent that separates *slowly unstable* sheets (hence, with a relatively slow dynamics) from reconnection instability modes that grow on an *ideal* time scale, leading eventually as the thinning process sets $a/L \sim S_{\rm L}^{-1/3}$ to fast magnetic dissipation and, eventually to flaring events. Since for ITMs growing at the fastest rates we have (Eq. (7.13)) $k_{\rm ITM} L \simeq S_{\rm L}^{1/6}$, the expectation is the number of magnetic islands grows with increasing $S_{\rm L}$. These heuristic arguments have been tested in the linear regime by Pucci and Velli (2014) solving numerically the dispersion relation for different values of α, finding that if $S_{\rm L} \geq 10^7$,

$$\gamma_{\rm TM} t_{\rm A} \simeq 0.6 S_{\rm L}^{(3\alpha-1)/2} \qquad \text{for} \qquad k_{\rm TM} L \simeq 1.4\ S_{\rm L}^{(1-5\alpha)/4}, \tag{7.15}$$

which for the critical value $\alpha = 1/3$ becomes

$$\gamma_{\rm ITM}\ t_{\rm A} \simeq 0.6 \qquad \text{for} \qquad k_{\rm ITM} L \simeq 1.4 S_{\rm L}^{1/6}, \tag{7.16}$$

and if the case $\alpha = 1/2$ is found during the thinning process of SP current sheets, one recovers the growth rate of TMs in an unstable SP current sheet with a critical aspect ratio $L/a \sim S_{\rm L}^{1/2}$ (Eq. (7.14)). Therefore, the ITM instability solves simultaneously two problems (and both in the framework of single-fluid resistive MHD). Firstly, the paradox of *super-tearing* instability in SP current sheets. Secondly, it gives an elegant solution to the quest for (spontaneous) fast magnetic reconnection that may account for flaring events occurring in astrophysical plasmas.

The theoretical results obtained by Pucci and Velli (2014) solving numerically the dispersion relation of ITMs have been confirmed numerically with

2D compresible classical MHD simulations by Landi et al. (2015) as well as in incompressible, electron MHD (Del Sarto et al., 2016). Tenerani et al. (2015) have furthermore found that in models with a critical aspect ratio, once the (induced) collapse of current sheets proceeds, fast reconnection is triggered avoiding the formation of a SP-type current sheet configuration. Already in the linear stage, plasmoids grow in a few Alfvén times when the predicted ITM threshold $S_{\rm L}^{-1/3}$ is approached. More recently, Del Zanna et al. (2016) have shown that the linear analysis made by Pucci and Velli (2014), still holds in RRMHD but with some (significant) modifications. Also in the relativistic force-free electrodynamics or magnetodynamics (MD), the same result holds for generic TMs (Komissarov et al., 2007, but note that these authors did not consider the case of ITMs in MD). Both Komissarov et al. (2007) and Del Zanna et al. (2016) are able to reduce the linearized equations of either MD or RRMHD to a set of equations that is formally the same as in incompressible MHD and, hence, the dispersion relation is formally the same as in the latter case. The key to understand this is the fact that in any of the cases it is assumed that the velocities of the background plasma (or the drift velocity of charged particles across the magnetic field, $\mathbf{E}\times\mathbf{B}/B^2$, in the case of MD) are very small (non-relativistic for practical purposes) and, hence, the electric field and the displacement current can be neglected in the RRMHD equations. In that limit, the Maxwell equations reduce to the same ones as in non-relativistic MHD. The largest difference is that in either MD or RRMHD, there is a new time scale, the light crossing time of the sheet length,

$$t_c := \frac{L}{c}, \tag{7.17}$$

where we explicitly write the speed of light (c) to make the comparison with the Newtonian MHD case simpler. The new time scale defined in Eq. (7.17) replaces the Alfvén crossing time of the sheet length, $t_{\rm A}$ in all expressions. This is not easy to understand since both in RRMHD (see Sec. 3.1) and MD (Komissarov, 2002)) Alfvén waves do not explicitly appear as eigenvalues of the former equations, but in the RRMHD case, Alfvén waves do exist and propagate along the magnetic field lines with the speed $v_{\rm A}$. Nevertheless, $v_{\rm A}\to c$ in the relativistic limit and, hence, it does not seem unlikely that the Alfvén time scale becomes replaced by the light time scale in the (ultra-)relativistic regime. Then, the maximum growth rate expected for RITMs can be obtained from Eq. (7.16), writing it in terms of t_c (see Eq. (32) in Del Zanna et al., 2016)

$$\gamma_{\rm RITM}\; t_c \simeq 0.6\frac{v_{\rm A}}{c} \qquad \text{for} \qquad k_{\rm RITM}\; L \simeq 1.4 S_{\rm L}^{1/6}. \tag{7.18}$$

The wavenumber in Eq. (7.18) can also be expressed normalized to a, resulting

$$k_{\rm RITM}\; a \simeq 1.4 S_{\rm L}^{-1/6}. \tag{7.19}$$

In this previous expression the location of the peak of the dispersion relation $\gamma(ka)$ is expected to decrease with increasing values of $S_{\rm L}$ (a result consistent with Pucci and Velli 2014).[3] The growth rates obtained by Del Zanna et al. (2016) imply that RITMs may grow on light crossing time scales corresponding to the macroscopic scale, L, if the Alfvén speed is relativistic (i.e. $v_{\rm A} \to c$) as it is the case of strongly magnetized plasmas. We note that to formally reproduce the incompressible MHD growth rates and wavelengths of ITMs (also of *standard* TMs), one must use the correct expression of the Alfvén velocity in RMHD (Eq. (2.24)). This must be compared to the classical MHD result, in which ITMs may develop on Alfvén crossing time scales. Hence, RITMs open new possibilities to reconcile the observed time scales for bursty activity in many astrophysical relativistic sources.

So far we have focused on the different studies performed in single-fluid MHD or RMHD of the TM instability, noting that the growth rate of the instability maximizes and becomes independent of the resistivity when current sheets reach critical aspect ratios $L/a \sim S_{\rm L}^{1/3}$ and sufficiently large macroscopic Lundquist numbers (these are ITMs in the classical MHD case or RITMs in the RRMHD case). There is, however, another possibility that has also been explored in the literature that could enhance the growth rate of the TM instability, namely the interaction between two (or more) sufficiently close TM-unstable current sheets. This scenario is not merely academic, but it has a deeper physical motivation. For instance, the topology of the magnetic field in pulsar magnetospheres involves the presence of a current sheet wobbling around the equatorial plane if the rotational and magnetic axes of the neutron star are misaligned Coroniti (1990). In laboratory magnetic confinement systems, it has been observed that such configurations are unstable to TMs (see, e.g. Bierwage et al., 2005).

The evolution of TMs in multiple current sheet systems is rather different from that in one single current sheet. Many authors have explored analytically (see, e.g. Otto, 1991; Otto and Birk, 1992) and numerically in the non-relativistic resistive MHD regime (see, e.g. Janvier et al., 2011; T. Birk and Otto, 1991) and in the RRMHD regime (e.g. Baty et al., 2013) the double tearing mode (DTM) instability and their results revealed that, in the linear and nonlinear stages, the coupling and interaction of the magnetic islands might destabilize the current sheets and result in a phase of explosive evolution (after the linear phase and other intermediate phases end). Remarkably, the time scale of DTMs in the explosive phase is only weakly dependent on the Lundquist number, scaling as $S_{\rm L}^{\varsigma}$ with $0 \lesssim \varsigma \lesssim 0.2$, once the onset of instability is reached (Wang et al., 2007). Janvier et al. (2011), using an incompressible,

[3] However, if the dispersion relation was built as a function of kL (Eq. (7.18)) it would be an increasing function of $S_{\rm L}$.

reduced-MHD numerical method, find that the free energy for the DTM instability is related to the 2D asymmetry of the magnetic islands, which explains why the growth rate is weakly dependent on the Lundquist number.

In analogy to the single TM instability, where there exist ITMs feeding off current sheets with a critical aspect ratio and such that the growth rate is maximized and, at the same time, is independent of η (for $S_{\rm L} \gg 1$), one may question whether there are optimal aspect ratios for two current sheets interacting in a DTM experiment. This is potentially very relevant for astrophysical plasmas because DTMs may develop explosive phases, where magnetic energy is quickly released. In the classical resistive MHD case, Baty (2017) has recently found that this is the case by extending the linear stability analysis of ITMs to double-current layer systems, where two identical layers of oppositely directed current density are separated by a distance $2l$ (see Fig. 7.6). This system is characterized by different spatial scales: the half-length along the current sheet, L, the half-thickness of the sheets, a, and the half-separation of the sheets, l. Due to the symmetry properties of the DTM, there are two types of unstable modes: symmetric and anti-symmetric. The latter ones are dominant in a broad range of values of l, a and L (indeed, the symmetric mode is stabilized when $l \simeq a$; Birk et al., 1997). Assuming periodicity in the direction normal to the current sheets (which actually means considering a case of an infinitely set of parallel current sheets; e.g. Otto and Birk 1992) and a linear profile for the magnetic field component that reverses polarity across the sheet (instead of the prototypical *Harry's profile* based upon hyperbolic tangent functions) Birk et al. (1997) obtained the corresponding analytic dispersion relation, which Baty (2017) solves numerically for a number of values of the ratio $l/a \in [1.25, 250]$ and several values of S_a (this Lundquist number relative to the current sheet width has the same definition as for single sheets; Eq. (7.7)). Following the same rescaling ideas delineated in Pucci and Velli (2014) for ITMs, Baty (2017) also finds the existence of *ideal* double tearing modes (IDTMs), provided that the aspect ratio of each individual current sheet scales as

$$\frac{L}{a} = S_{\rm L}^{9/29}, \tag{7.20}$$

where we note the similarity with the critical scaling needed for maximum growth in ITMs (Eq. (7.11)). If the aspect ratio is fixed by the optimal relation (7.20), then the Lundquist numbers relative to a and L are not independent but follow the relation,

$$S_{\rm L} = S_a^{29/20}. \tag{7.21}$$

For the optimal scaling of the aspect ratio Baty (2017) finds for the maximum growth rate and wavenumber of IDTMs

$$\gamma_{\rm IDTM} t_{\rm A} \simeq \alpha_{\rm IDTM} \qquad \text{for} \qquad k_{\rm IDTM} L \simeq \beta_{\rm IDTM} S_{\rm L}^{6/29}, \tag{7.22}$$

where $\alpha_{\rm IDTM} \in [0.5, 0.8]$ and $\beta_{\rm IDTM} \in [0.35, 077]$ are both numerical factors (which depend on l) of the order of unity. Eq. (7.22) for IDTMs must be compared with Eq. (7.16) for ITMs, which allows one to conclude that also for IDTMs one may find a growth rate independent of $S_{\rm L}$, hence the instability can grow on the Alfvén crossing time of the current sheet length. The comparison of the wave numbers in both cases shows some (significant) differences regarding the dependence of $k_{\rm IDTM}$ on $S_{\rm L}$ as compared to $k_{\rm ITM}$. The former results (based on the rescaling obtained for the numerical solutions of the DTM dispersion relation) have been confirmed using 2D compressible MHD simulations also by Baty (2017). He finds in these numerical models a double cascade process beyond the initial linear phase in which the evolution is dominated by the linearly fastest (from the excited ones) mode. As a result, explosive reconnection is triggered, as in standard DTMs, which can be triggered for double current sheets with smaller aspect ratios (of the order of 2π) than those of IDTM (e.g. Janvier et al., 2011; Wang et al., 2007), but on shorter timescales (by factors ~ 4) than in equivalent DTM models with the same ratio l/a.

The goal of this chapter and also a novelty with respect to what has been done so far in the literature, is the extension of the study of IDTMs to RRMHD in both the linear and in the non-linear regime of the instability. Baty (2017) obtained his scaling laws for DTMs which he used to predict the properties of IDTMs by numerically solving the dispersion relation for a somewhat different system that he actually used in his 2D simulations. Therefore, in the linear regime, we plan to compare our simulations done in a mildly relativistic (Alfvén velocity $v_{\rm A} = 0.5$) regime with simulations obtained with another numerical code Aenus (Just et al., 2015; Obergaulinger, 2008; Obergaulinger and Aloy, 2012; Obergaulinger et al., 2014), which solves with the classical MHD equations. In this way, we can determine whether potential discrepancies with respect to the results of Baty (2017) come from the simplifications made by him or rather are of a relativistic origin. In the non-linear regime, we aim to test whether the (non-linear) explosive reconnection phase observed in classical compressible MHD for IDTMs also holds for RIDTMs (Sec. 7.2). In order to reach these goals, we first validate the methodology developed in Chaps. 4-6 in this specific context by reproducing previous results of Del Zanna et al. (2016) for the growth of TMs in a single current sheet with a critical aspect ratio scaling as $S_{\rm L}^{1/3}$ (Eq. (7.11)), i.e. in the regime in which RITMs grow (Sec. 7.1). These results along with our exhaustive study on the numerical diffusivity of our algorithm (Chap. 6), allows us to find out the minimal resolution needed to properly capture the expected (analytic) growth rate of the ITM instability, and to understand the systematics driven on the numerical dispersion relation by the new HLLC solver.

7.1 Relativistic Ideal Tearing Modes

RITMs have very recently attracted the attention of the scientific community (Del Zanna et al., 2016). The main reason for this interest is because they are a very simple physical mode of reconnecting the magnetic field on time scales of the order of the light crossing time of the system within the framework of single-fluid, compressible, RRMHD. Furthermore, RITMs as well as their classical counterparts (ITMs), aid to resolve the paradox set by standard TMs whose growth rate depends on Lundquist number and therefore diverges in the low-resistivity limit (or, equivalently, high $S_{\rm L}$ limit). As mentioned in the previous section, ITMs and RITMs are based upon setting an aspect ratio with a precise dependence on the Lundquist number, namely $L/a = S_{\rm L}^{1/3}$.

Here, we validate our numerical methodology employing a numerical set up that follows closely the pioneer paper of Del Zanna et al. (2016). We simulate a RITM in a 2D domain of $[-20a, 20a] \times [0, L_y]$, where the Lunsquist number is $S_{\rm L} = 10^6$, $a = S_{\rm L}^{-1/3} L = 0.01L$, $L_y = 2\pi/k$, and we further set $L = 1$ and $k = 12$. We use copying and periodic boundary conditions in the directions x and y, respectively, for all variables but B_x. The boundary values of the latter variable in the x direction are computed from the solenoidal constraint $\nabla \cdot \mathbf{B} = 0$.

To trigger the TM instability, we perturb the initial background magnetic field

$$\begin{aligned} B_{0y} &= B_0 \tanh(x/a), \\ B_{0z} &= B_0 \ \mathrm{sech}(x/a), \end{aligned} \tag{7.23}$$

with

$$\begin{aligned} B_{1x} &= \epsilon_{\rm ritm} B_0 \cos(ky) \ \mathrm{sech}(x/a), \\ B_{1y} &= \epsilon_{\rm ritm} (ka)^{-1} B_0 \sin(ky) \tanh(x/a) \ \mathrm{sech}(x/a). \end{aligned} \tag{7.24}$$

We set $B_0 = \rho_0 = 1$, $p_0 = 0.5$, $\eta = 5 \times 10^{-7}$, and $\epsilon_{\rm ritm} = 10^{-4}$, so that the (classical) magnetization is $\sigma_{\rm m} := B_0^2/\rho_0 = 1$, the ratio of magnetic-to-thermal pressure is $\beta_0 := 2p_0/B_0^2 = 1$,[4] and the resulting Alfvén speed is $v_{\rm A} = 0.5$. Since we fix the Lundquist number and the Alfvén velocity, the resistivity is not a free parameter anymore. For this set up we have $\eta = L v_{\rm A} S_{\rm L}^{-1} = 5 \times 10^{-7}$. We note that the initial setup of this test yields a *force free* configuration, the

[4] In RRMHD, the definition of the magnetization of the fluid should be given by Eq. (2.25). Likewise, the ratio of magnetic-to-thermal pressure should be defined as $\beta_{\rm m} := 2p_0/(B_0^2 - E_0^2)$. However, to be consistent with the classical definition of these quantities and, specially, to compare more directly with (Del Zanna et al., 2016), we employ the definitions in the text. Note that since $E_0 = 0$ in this set up, both definitions are equal.

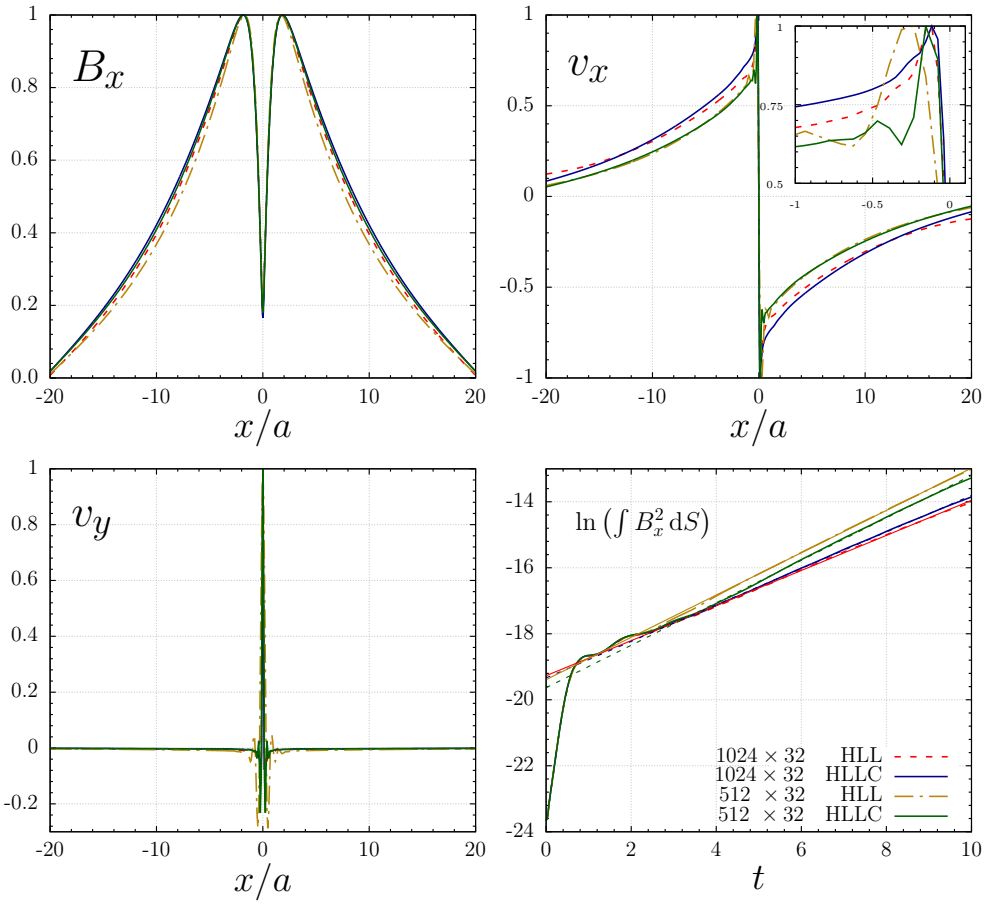

Figure 7.3: 2D simulations of TMs performed with the HLL and HLLC Riemann solvers, MP9 reconstruction scheme and resolution of 512×32 and 1024×32 zones. All quantities (but in bottom right panel) are presented at $t = 10t_c$ and normalized for a better comparison. *Upper left*: $x-$component of magnetic field (B_x) at $y = 0$. *Upper right*: $x-$component of velocity (v_x) at $y = 3L_y/4$. *Bottom left*: $y-$component of velocity (v_y) at $y = 0$. *Bottom right*: Time evolution of $\ln(\int B_x^2\,\mathrm{d}S)$. The TM growth rate is determined from a linear fit (solid and dashed lines of the corresponding colors for the HLL and HLLC solvers, respectively) to this quantity for $t \in [4, 10]$ (see Tab. 7.1).

standard employed by Del Zanna et al. (2016). Though, in principle the growth rate should not be affected by the initial equilibrium conditions, in practice, using a *pressure equilibrium* (with the participation of the gas pressure) may bring a variation in the growth rate of the TMs which yields a small delay in the appearance of the final explosive phase (e.g. Del Zanna et al., 2016). They attribute the delay in the explosive phase to the enhanced compressibility effects in the pressure equilibrium initial configuration.

For this Lundquist number ($S_{\mathrm{L}} = 10^6$), Del Zanna et al. (2016) used a

resolution of 2048×512 zones, finding numerically $\gamma_{\rm RITM} t_c = \gamma_{\rm RITM} = 0.27$.[5] This choice for the numerical resolution was driven by the fact that for the default one chosen by those authors (1024×512), numerical resistivity was higher than the physical one and strongly affected their simulation results. However, in our studies, we used lower resolutions of 512×32 and 1024×32 zones for the following reasons. First, because we employ the MP9 ultrahigh-order spatial reconstruction scheme (Sec. 4.1.1.2; see also Suresh and Huynh, 1997) whose numerical dissipation is much lower than that of other lower order schemes (see Chap. 6 and the extensive studies of Rembiasz et al., 2017), in particular of MP5, which is the reconstruction used by Del Zanna et al. (2016). Second, as we are only interested in the linear phase of the TM instability, we can use a much lower resolution in the y-direction where all perturbed quantities exhibit a (co-)sinusoidal variation. Hence, the characteristic length of the system (Sec. 6.4; see also Rembiasz et al., 2017) in this direction is equal to the box length, L_y, and it can be very well resolved with 32 zones using the MP9 scheme as we have demonstrated with the MD test in Sec. 6.2.1.

A possible tracer for the growth of the TM instability is the induced growth of the magnetic field component B_x, which after the initial transient phase grows as $B_x(x, y, t) = B_{1x}(x, y) e^{\gamma_{\rm TM} t}$, where $B_{1x}(x, y)$ is a time independent eigenfunction of the TM. In order to have a positively defined global quantity[6] we compute the integrated value in the whole computational domain of B_x^2,

$$\tilde{\mathcal{B}} := \int B_x^2(x, y, t) \, \mathrm{d}S.$$

Then, we take the logarithm of $\tilde{\mathcal{B}}$,

$$\ln \tilde{\mathcal{B}} = 2\gamma_{\rm TM} t + \ln \left(\int B_{1x}^2(x, y) \, \mathrm{d}S \right), \tag{7.25}$$

and obtain $\gamma_{\rm TM}$ from the slope of the linear fit $\ln \tilde{\mathcal{B}}$ vs t in the time interval $t \in [4, 10]$.

Our simulation results (Fig. 7.3 and Tab. 7.1) are very similar to those obtained by Del Zanna et al. (2016; Figs. 1, 3 and 4, therein). The TM instability sets in after $t \approx 2$ and its growth rate (which can be inferred from the bottom right panel of Fig. 7.3) is close to $\gamma_{\rm RITM} = 0.3$, which Del Zanna et al. (2016) obtained both analytically as well as with their numerical code for solving the linearized MHD equations (but note that, as stated above, the numerically computed value was $\gamma_{\rm RITM} = 0.27$). In our simulations performed with the lower resolution (512×32 zones), the TM growth-rate is very similar but

[5] For our choice of L, $t_c = 1$ (Eq. (7.17)) in our default system of units, where $c = 1$.

[6] Alternatively, one may use $\max_{x,y} |B_x(x, y, t)|$ (e.g. this is the choice of Del Zanna et al., 2016) or other tracers of the magnetic field growth from a tiny value at $t = 0$.

higher than theoretically expected, i.e. $\gamma_{\rm TM} \approx 0.32$ independently of the Riemann solver employed. We attribute this discrepancy to numerical resistivity. In the simulations performed with 1024×32 zones, the TM growth-rate is lower than theoretically expected, i.e. $\gamma_{\rm TM} \approx 0.27$. This can be explained by the resistive dissipation of the background magnetic field (as pointed out by Del Zanna et al., 2016, who obtained the same value) as well as by numerical viscosity present in the simulations, since viscosity is known to reduce the TM growth rate (Furth et al., 1963; Rembiasz et al., 2017). The $x-$components of the magnetic field, B_x (see the upper left panel of Fig. 7.3), are similar in all four simulations, however, there are visible differences in the $x-$ and $y-$components of the velocity. In Fig. 7.4 we show a snapshot of the distribution of B_x and v_x at the end of the computed time, which is in the middle of the linear growth phase. The figure shows that the excited mode with the set up perturbations (Eq. (7.27)) is preserved in shape (note the co-sinusoidal modulation of the amplitude of B_x whose wavelength exactly fits L_y) all over the linear phase, as it corresponds to a TM eigenfunction. In the simulation performed with the HLL solver and the resolution of 512×32 zones, the (characteristic for the TM instability) velocity peaks of the v_x component (Fig. 7.3, upper right panel) are located farther away from $x = 0$ than in the other simulations. We attribute this difference to a higher numerical viscosity (and resistivity) of the HLL solver, as the distance between these peaks is proportional to certain (not necessarily equal) powers of viscosity and resistivity (see Rembiasz et al., 2017, for a detailed discussion for a different TM setup).

By performing a set of 2D simulations (employing the HLL and the HLLC Riemann solvers) of RITMs with different k and measuring their growth-rate in each of them, we have obtained the dispersion relation (Fig. 7.5) In the figure, we display the results of simulations performed with $k = \{8, 10, 12, 14, 16, 18, 20\}$. The growth rate is lower in the simulation performed with 512×32 zones and the HLL solver than in the one with the HLLC solver. Besides the differences in the exact value of $\gamma_{\rm RITM}$ with respect to the theoretical prediction, we also note that the peak of the numerical dispersion relation is at $k_{\rm RITM} a \simeq 0.12$, in relatively good agreement with the theoretical value (Eq. (7.19)) $k_{\rm RITM} a \simeq 0.14$.

Table 7.1: TM growth rate determined from a linear fit of $\ln \tilde{\mathcal{B}}$, Eq. (7.25), in the time interval $t \in [4, 10]$ (see bottom right panel of Fig. 7.3) in simulations performed with the HLLC (second column) and HLL (third column) approximate Riemann solvers and the MP9 spatial reconstruction scheme.

Growth rate		
resolution	HLLC	HLL
512×32	0.322	0.321
1024×32	0.276	0.265

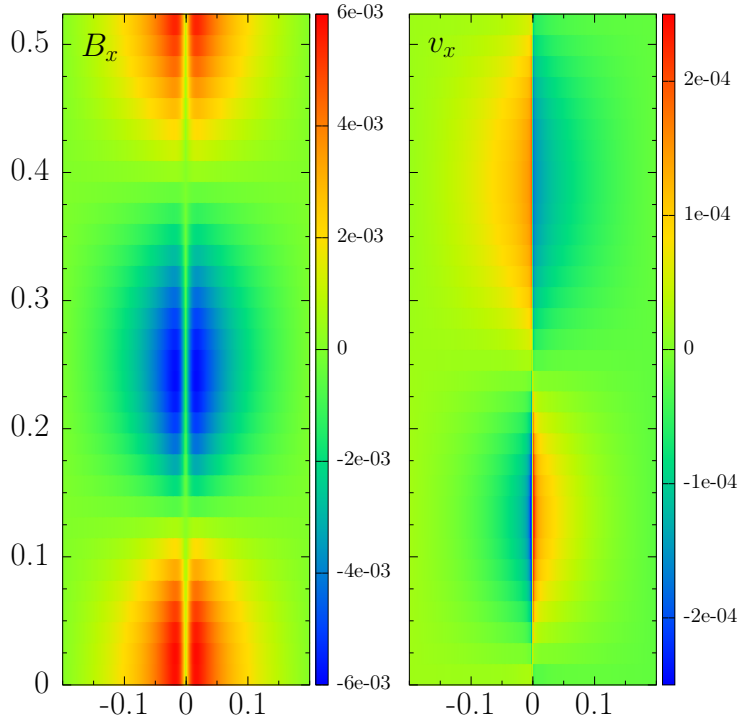

Figure 7.4: Snapshots at $t = 10t_c$ (i.e. an intermediate time within the linear phase of the RITM evolution) for the B_x magnetic field component (*left panel*) and v_x velocity field (*right panel*). The models here displayed are run with the MIRK2 time-integrator, the HLLC Riemann solver, the MP9 reconstruction method, a $C_{\rm CFL} = 0.1$ and a resolution of 512×32 zones. For better visualization the scale is expanded along the horizontal direction.

For comparison, Del Zanna et al. (2016) also obtain numerically $k_{\rm RITM}a \simeq 0.12$ (but with 4 times larger numerical resolution in the x direction). The small differences that we obtain for the numerical dispersion relation ($\gamma(ka)$) using the HLL and the HLLC solvers originate from a different amount of numerical diffusivity they have. In order to assess the differences in the quality of the solution obtained with both Riemann solvers, we may compare solutions computed at the two different resolutions used in these series of tests. Looking at the profiles of both v_x and v_y, their resemblance in the case of models run with the HLLC solver is greater than when using the HLL solver. Since the higher resolution models are closer to the actual solution of the problem, this means that tests conducted with the HLLC solver are closer to a converged state than the same models run with the HLL solver.

We may conclude that with as few as 32 zones in the vertical direction is possible to reproduce accurately enough the analytic growth rate of the RITMs in the linear phase of its evolution. The wavenumber at which the maximum

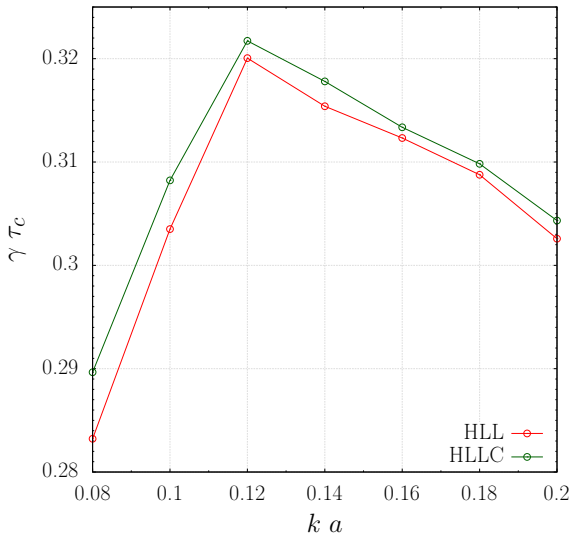

Figure 7.5: Dispersion relation obtained from numerical simulations with the HLL and the HLLC Riemann solvers in RITM simulations, with a resolution of 512×32 zones, where $v_{\rm A} = 0.5$ and we use the scale relation $a = S_{\rm L}^{-1/3} L$, with $L = 1$ and $S_{\rm L} = 10^6$.

growth rate develops is slightly shifted (by $\sim 14\%$) below the theoretical expectations ($k_{\rm RITM} a \simeq 0.14$). However, this is consistent with previous RRMHD models of Del Zanna et al. (2016) and, like in their case, one of the most important reasons to drive this discrepancy is the diffusion of the initial background field B_0. The theoretical derivations are done under the assumption that the initial background magnetic field changes at a timescale much larger than the RITM timescale (Eq. (7.8)) and therefore is assumed to be constant. However, this approximation is only valid for such small values of η that are unachievable in numerical simulations (without being completely dominated by numerical resistivity). Therefore, one typically either performs numerical simulations in the parameter space regime where condition (7.8) is not strictly valid or resorts to *artificial* modifications of the magnetic field induction equation (see,e.g., Landi et al., 2015; Rembiasz et al., 2017).

7.2 Relativistic Ideal Double Tearing Modes

As we have pointed out in the introduction of this chapter, in analogy with the existence of a critical aspect ratio for individual current sheets (Eq. (7.11)), which brings the existence of ITMs (or RITMs in the relativistic realm), when there are two parallel current sheets both with half-width, a, and the same half-length, L, there also exists a critical aspect ratio of the sheets (Eq. (7.20)) for which the instability growth rate becomes independent of $S_{\rm L}$, provided $S_{\rm L} \gg 1$.

Since the growth rate in this regime is independent of the resistivity, and since it becomes the maximum possible growth rate for the instability, one refers to the growth of TMs in these conditions as IDTMs. Baty (2017) has shown in the classical, compressible MHD regime that IDTMs grow at the rate predicted by the linear theory also in numerical simulations. But more importantly, Baty (2017) has shown that, depending on the separation between the two current sheets, there is an explosive phase of the instability growth ensuing after the linear phase or after a secondary phase of relatively slow (linear) growth (the Rutherford phase). In this section we aim to prove the existence of IDTMs in the relativistic regime (RIDTMs). To our best knowledge, this is a novelty in the field and deserves a careful study since it may bring an elegant, yet simple explanation of the existence of extremely violent reconnection regimes in a number of objects of interest for Relativistic Astrophysics. We note that the closest work on this subject is that of Baty et al. (2013), who considered relativistic double tearing modes (RDTMs), but without accounting for the possibility that critical aspect ratios may yield optimal conditions for TM growth at Alfvénic time scales.

We achieve this goal in two steps. First, in Sec. 7.2.1 we numerically test whether the scaling laws obtained by Baty (2017) in Newtonian MHD for a somewhat different setup (i.e. the background magnetic field and boundary conditions), give correct predictions of the dominant DTMs both in the Newtonian MHD and mildly relativistic resistive MHD. Second, we use these scalings to set up simulations of RITMs, and study their properties both in the linear and non-linear regime with our RRMHD code.

7.2.1 Dispersion relation of DTMs

As already mentioned in the introduction of this Chapter, Baty (2017) numerically solves the dispersion relation of Birk et al. (1997) to find dominant DTMs. Based on those results, he predicts scaling laws for the dominant IDTMs, which he then uses to set up his numerical simulations. However, the setup considered by Birk et al. (1997) in their analytical derivations is different from the one used by Baty (2017) (both being more suitable for the respective studies). Nonetheless, as shown by the latter author, there is an agreement within $\sim 10\%$ (when it comes to the general properties of DTMs), between both setups which was good enough for the purposes of that author. Moreover, that comparison was not done rigorously enough, as that was not the main goal of the studies of Baty (2017). This precision is not sufficient for a part of our studies, however. As we are going to mostly concentrate on mildly relativistic simulations ($v_{\rm A} = 0.5$), we may expect relativistic corrections to be of the same order (or perhaps somewhat larger) than the discrepancies between the analytic and the numeric results in the classical MHD regime for

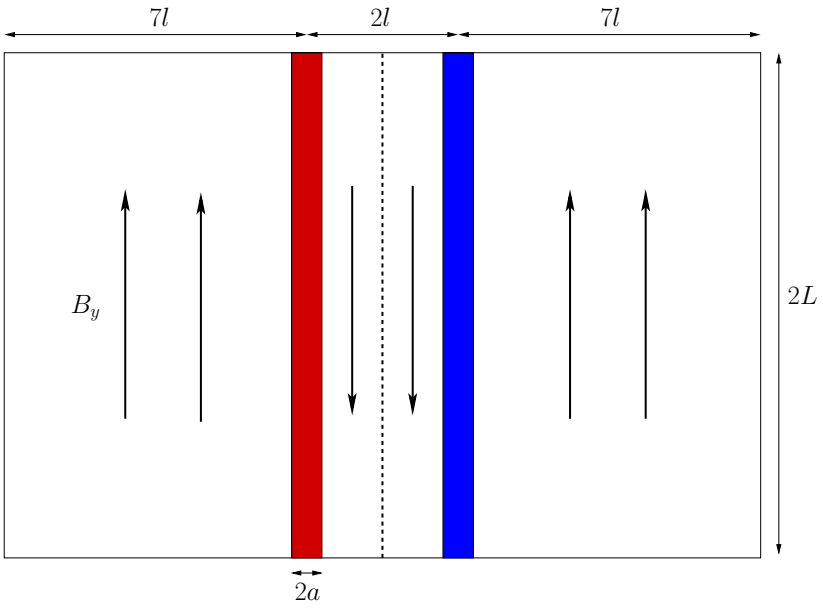

Figure 7.6: Sketch of the initial configuration of the RIDTM computational box. We set up an unidirectional magnetic field, with a component $B_{0y}(x)$ (see Eq. (7.26)) displaying two reversals and producing two current layers of negative and positive current density of half-thickness a (regions with a red and blue colors). The variation of the magnetic field $y-$component is equilibrated with a suitably chosen $B_{0z}(x)$ component, which results in a *force-free* initial data. A distance $2l$ separates the two current sheets of vertical length $2L$.

the linear phase. Therefore, the only way to detect them is by comparing our results with simulations done with exactly the same physical setup and a Newtonian code employing the same numerical methods. Fortunately, to this end, we could use the classical version of the MHD code Aenus (Just et al., 2015; Obergaulinger, 2008; Obergaulinger and Aloy, 2012; Obergaulinger et al., 2014). However, even though simulations performed with Aenus are computationally much less expensive, using it to reproduce all scaling laws obtained by Baty (2017) in his Fig. 4 would not be feasible. This is not a big problem though, as our main goal is not reproducing (or testing) the results of Baty (2017), but simply checking how much they deviate for one particular choice of S_a. In the case of a reasonable agreement, one can sufficiently rely on his results to use them to set up simulations, which are done for the main goal of this chapter, that is, the study of IDTMs in the relativistic regime (hence RIDTMs).

Following Baty (2017), we set a double Harris-like current sheet configuration, with a magnetic field parallel to the y-axis and varying with x. Unlike in his setup, this field is supplemented with an additional z-component tailored to produce a *force-free* equilibrium (note that with the ensuing setup

$\mathbf{B}^2 = B_0^2 =$ uniform):

$$B_{0y} = B_0 \left[1 + \tanh((x-l)/a) - \tanh((x+l)/a)\right], \tag{7.26}$$
$$B_{0z} = \sqrt{B_0^2 - B_{0y}^2}.$$

We point out that Baty (2017) employs an initial mechanical equilibrium with the contribution of the thermal pressure, which balances out the gradients of magnetic pressure generated by the assumed x-dependence of B_{0y}. We will comment on the consequences of that later. We further set $a = 0.05$, and a half-separation between the currents $l = 5a$. To compare our results with Baty (2017), in both codes (Aenus and Cueva), we set the magnetic field amplitude, the background density and the thermal pressure to $B_0 = 1.0$, $\rho_0 = 1$, $p_{\rm g} = B_0^2/2$, respectively, and the adiabatic index to $\gamma = 5/3$. In the Newtonian code, this corresponds to $v_{\rm A} = 1$ (in dimensionless units), whereas in the relativistic one to $v_{\rm A} = 0.5$ (i.e. $0.5c$). The difference results from different definitions of the Alfvén velocity in both regimes (in RRMHD, it is given by Eq. (2.24)). Note that Baty (2017) also used the same values of the magnetic field, thermal pressure and rest-mass density. We stress, however, that in the RRMHD case, our intention was not performing simulations with the same B_0, ρ_0, and $p_{\rm g}$, but setting a mildly relativistic $v_{\rm A} = 0.5$ (i.e. $0.5c$), and these parameters coincide. In RRMHD, for this setup, the plasma magnetization and plasma beta are $\sigma_{\rm m} = 1$, and $\beta_0 = 1$, respectively. We perform numerical simulations in a 2D domain of $[-40a, 40a] \times [0, L_y]$ with $L_y = 2\pi/k$ (see Fig. 7.6). In all (Newtonian and relativistic) simulations presented in this subsection, we set $S_a = 5000$. To achieve the same value of the Lundquist number (necessary for a proper comparison), we set different values of physical resistivity ($\eta = 10^{-5}$ and $\eta = 5 \times 10^{-6}$ in the Newtonian and relativistic case, respectively), since the values of the Alfvén velocity are different in the Newtonian and relativistic experiments. We use periodic boundary conditions in the directions x and y. We notice that employing periodic boundary conditions in the x direction differs from the treatment of Baty (2017), who used copying boundaries in the horizontal direction. However, several considerations are in order here. Firstly, the dispersion relation that Baty (2017) solves numerically to obtain the fastest growing mode was obtained by Birk et al. (1997) for a *periodic* profile of the magnetic field, where all the currents are equidistant (note the difference with respect to our periodic setup, where there are two currents separated by a distance $2l$ and each of them is located at a distance $7l$ from the closest boundary in the x direction; Fig. 7.6). Secondly, the profile of the background magnetic field in Birk et al. (1997) was a *periodic* sequence of piecewise constant values of the magnetic field (with alternating polarity) linearly connected across the current sheets (the shape is like that of a saw with truncated -flat- extrema; see Fig. 1 of Otto and Birk 1992). In contrast,

Baty (2017) sets up a double Harris-like current sheet configuration with B_{0y} as in Eq. (7.26). Therefore, both initial kinds of boundary conditions (either periodic or copying) as well as the background initial field do not exactly match the analytic set up employed to derive the dispersion relation for IDTMs. Since periodic boundaries introduce much less numerical noise than copying boundaries and since they are closer to the conditions employed for the derivation of the analytic dispersion relation, we have decided to use them, even if in this point we depart a bit from Baty's setup.

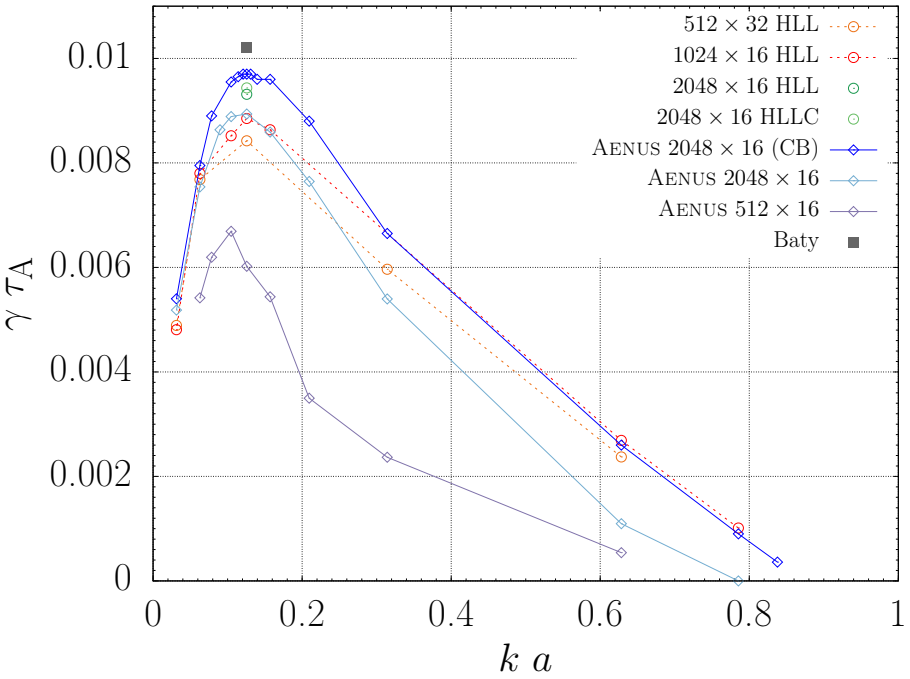

Figure 7.7: Dispersion relation for RIDTMs computed for different resolutions of a computational box with $n_x \times n_y$ cells (see legends). Simulations were preformed with the RRMHD code Cueva (circles) and the classical MHD code Aenus (diamonds; explicit name in the legend). The maximum dimensionless growth rate computed by Baty (2017) for $l/a = 5$ and $S_a = 5000$ (data extracted from Fig. 4 therein) is marked with the black square.

In order to trigger the instability, the initial equilibrium configuration is perturbed at $t = 0$ with a single mode by, if $x < 0$,

$$B_{1x} = \epsilon_{\text{ridtm}} B_0 \cos(ky)\ \text{sech}((x+l)/a), \tag{7.27}$$
$$B_{1y} = \epsilon_{\text{ridtm}} \bar{k}^{-1} B_0 \sin(ky) \tanh((x+l)/a)\ \text{sech}((x+l)/a),$$

and if $x \geq 0$,

$$B_{1x} = \epsilon_{\rm ridtm} B_0 \cos(ky)\ \mathrm{sech}((x-l)/a), \tag{7.28}$$
$$B_{1y} = \epsilon_{\rm ridtm} \bar{k}^{-1} B_0 \sin(ky) \tanh((x-l)/a)\ \mathrm{sech}((x-l)/a),$$

where $\bar{k} = ka$. The small (divergence free) perturbations added to the background magnetic field have an amplitude $\epsilon_{\rm ridtm} = 10^{-5}$. Furthermore, the perturbations have spatial dependences similar to the initial state in RIDTMs (Eq. (7.27)) and follows the functional dependence employed by Del Zanna et al. (2016). For comparison, Baty (2017) imposes a set of 10 modes with different values of k.

We begin our analysis with the simulations done with Aenus, MP9 reconstruction, RK3 time integrator and 2048×16 zones (dark blue diamonds in Fig. 7.7; which converge with simulations done with 4096×64 zones, not presented here) and an artificially subtracted diffusion of the background magnetic field (like in, e.g. Landi et al., 2015; Rembiasz et al., 2017). We find that the growth rate of the dominant DTM (measured as described in Sec.7.1) agrees within $5 - 10\%$ with the predictions of Baty (2017) and the (dimensionless) wave vector ka within 5%. The obtained dispersion relation is also very similar to that in Fig. 2 therein (note that obtained for $S_a = 10^6$, however; such high Lundquist numbers would require a prohibitively high resolution even in Newtonian 2D simulations). Baty (2017) reports that double current sheets are stable against DTMs with $ka \lesssim 0.75$, however, we can observe unstable modes even for $ka \approx 0.84$. We also note the smooth, (nearly) concave shape of the dispersion relation around its maximum values using 2048×16 uniform zones. We take it as one of the requirements to state that the models have sufficient numerical resolution in the linear phase, precisely, the smoothness of the numerical dispersion relation around its peak.

Next, to investigate the influence of the diffusion of the background magnetic field on the DTM growth-rate, we repeat the same series of simulations (Aenus with 2048×16 zones), but with unmodified (i.e. correct) MHD equations. As can be seen in Fig. 7.7 (light blue diamonds), the growth rate of the DTM instability is decreased by some $\sim 10\%$ w.r.t. the analogous simulations but without the artificial removal of the background magnetic field diffusion.

To finish the 'Newtonian part' of the studies, we performed a series of simulations with a much lower resolution of 512×16 zones (purple diamonds in Fig. 7.7). It is clear that because of numerical resistivity (enhancing the diffusion of the background field) and numerical viscosity (known to reduce the TM growth rate, Furth et al., 1963; Rembiasz et al., 2017), the DTM growth rate is reduced by some $\sim 50\%$. Moreover, the dominant mode is shifted to smaller values of ka.

As RRMHD simulations are computationally much more demanding than

the Newtonian ones, we could not perform such extensive studies with Cueva. With the highest resolution of 2048×16 zones, we performed only two RRMHD simulations with $ka \approx 0.126$ ($L_y = 2.5$), the MP9 reconstruction, and the HLL and HLLC Riemann solvers (dark green and light green circles, respectively, in Fig. 7.7). Regarding the choice of resolution in the vertical direction for our RRMHD models, we point out that all variables experience periodic (co-)sinusoidal variations in the vertical direction (in the linear phase of the instability). Thus, as we have demonstrated in Sec. 6.2.1, $n_y = 16$ zones per wavelength suffice, at least during the linear phase of the evolution, to properly capture the growth rate of the instability,[7] unless we use first order or MIRK2 time integration schemes. Therefore, we decided to use the SSP2(332)-LUM time integrator. The growth rates in RRMHD simulations using different Riemann solvers are very similar, but the one obtained with the HLLC solver being slightly larger. We attribute this tiny difference to a lower numerical viscosity of the HLLC solver. More importantly, both results differ some 5% from the corresponding Newtonian simulation (light blue diamonds). However, we are unable to definitively conclude whether this difference is due to relativistic corrections or, e.g. to a different numerical treatment of the solenoidal constraint of the magnetic field. To enforce $\nabla \cdot \mathbf{B} = 0$, Cueva employs a divergence cleaning technique, whereas Aenus uses constraint transport method. Furthermore, Cueva uses partly implicit time-integrators to account for the stiffness of the RRMHD system in the limit of large conductivity, while Aenus resorts to an explicit RK time-integrator, since the classical MHD system of equations is not stiff even if $\sigma \to \infty$.

In a series of RRMHD simulations done with 1024×16 zones and the HLL Riemann solver (red circles in Fig. 7.7), we explore the DTM growth-rate dependence on ka. We observe that around the dominant mode with $ka \approx 0.12$, the growth rate is very similar to the Newtonian simulations done with 2048×16 zones with the diffusion of the background magnetic field (light blue diamonds), whereas for modes $ka \gtrsim 0.25$ to Newtonian simulations done with 2048×16 zones without diffusion of the background magnetic field (dark blue diamonds). It is beyond the scope of this section, as well as difficult to test, whether these differences are of numerical origin or truly correspond to relativistic effects. However, initially, and throughout the linear growth of DTMs, neither the fluid velocities are close to the speed of light nor the magnetic fields are strong enough for the Alfvén velocity to be close to the speed of light. Hence, we tentatively presume that these differences originate from the different numerical algorithms used in Cueva and Aenus. There is one more argument supporting our hypothesis. Komissarov et al. (2007)

[7] The measurement of the damping rate in a magnetic diffusion layer (Sec. 6.2.1) can be regarded as the same procedure as the measurement of the growth rate in RIDTMs.

and Del Zanna et al. (2016) obtain that the linearized equations in MD or RRMHD are formally the same as in incompressible MHD and, hence, the dispersion relation for single TMs is formally the same as in the latter case. The basic reason is that for TMs one assumes that the background velocity of the unperturbed state is zero ($\mathbf{v}_0 = \mathbf{0}$), and the velocity perturbations on that background state ($\mathbf{v}_1$) are very small (non-relativistic) and, thus, the electric field and the displacement current can be neglected from the RRMHD equations. Another condition that must hold to formally recover the classical MHD dispersion relation in RRMHD is that one of the two terms arising from the linearization of the Pointing flux ($B_0^2\mathbf{v}_1$) is much larger than the other one ($-(\mathbf{v}_1 \cdot \mathbf{B}_0)\mathbf{B}_0$), so that the latter can be neglected and only the former is kept (Del Zanna et al., 2016). We also expect it to be the case in RDTM simulations. Indeed, as we show in the next section, in simulations of RIDTMs, which we analyse in much more detail, the condition $B_0 v_1 \gg (\mathbf{v}_1 \cdot \mathbf{B}_0)$ holds.

Finally, in a series of RRMHD simulations done with 512×16 zones (orange circles in Fig. 7.7), we note the much less smooth shape of the peak of the dispersion relation. As stated above, we take this fact as a hint that 512×16 zones is the absolute minimum acceptable resolution to explore the linear growth of DTMs with our RRMHD code and for the considered value of the Lundquist number (as we shall in the following sections for higher values of S_{L} finer numerical resolutions are required to obtain *sufficiently* converged results). In Fig. 7.7, we observe a DTM growth rate somewhat lower than in the higher resolution simulations, but the general shape of the dispersion curve is the same. This difference can be once again attributed to a higher numerical resistivity and viscosity of the code in simulations with a lower resolution. It is also worthwhile mentioning that in the analogous Newtoninan MHD simulations (purple diamonds), the DTM growth rate is some 50% lower. We see that the discrepancy between under-resolved simulations is larger. Therefore, we presume that also in the simulations with the best resolution, the differences in the DTM growth rates are mainly of numerical origin (yet very small, as both types of simulations should already converge, but not necessarily to the same value).

Let us summarize our results without losing the big picture in technical details. For practical applications, we are interested in the dominant DTMs and their general properties. The growth rates and wave vectors of dominant DTMs obtained by Baty (2017) and both the Newtonian and RRMHD codes (for a somewhat different physical setup) are very similar (differences of the order of 10%). Therefore, we conclude that the scaling laws obtained by Baty (2017) (see Fig. 4 therein) are good enough for our purposes (astrophysical applications), and can be used for designing an initial setup of our simulations presented in Sec. 7.2.1.1. The differences between the background magnetic fields used in our numerical simulations and the analytical calculations of Baty

(2017) are of a secondary importance. We remind the reader that realistic current sheets in relativistic astrophysical scenarios will not be in a *perfect* equilibrium to begin with.

7.2.1.1 Linear phase of dominant RIDTMs

We have tested in the previous section, that the dispersion relation, numerically solved by Baty (2017) to find the dominant DTMs (even though for a slightly different setup, and in classical MHD) can be used to choose the initial setup of our RIDTMs simulations and study their evolution both in the linear and non-linear phase.

In the RRMHD simulations presented in this section, we (typically) employ a resolution of $n_x = 1024$ uniform cells in the direction perpendicular to the current sheet and $n_y = 32$ cells per dominant mode fit in the direction parallel to the current sheet. Since we normally fit two dominant modes ($n = 2$), a typical resolution that we use is $n_x \times n_y = 1024 \times 64$ uniform numerical cells. We use by default the SSP2(332)-LUM time-integrator, the HLL Riemann solver, and the MP9 reconstruction. For some special cases (with large Alfvén speed) some models have also been run with the RK36$\mathcal{S}_E$ time-integrator, in order to verify the numerical results. The utilization of the MP9 (to be compared with the Koren and van der Maarel (1993) 2^{nd}-order method used by Baty 2017), allows us to employ many less points in both spatial dimensions than Baty (2017), who used 1920×480 uniformly distributed spatial grid points.

Baty (2017) uses a box length in the *periodic* direction $L_y = 2L$, following the standard conventions employed to study SP resistive layers. For this vertical dimension Baty selects the wave numbers of his perturbations to satisfy $k_n = 2\pi n/L_y = \pi n/L$, with $n = 1, \ldots, 10$. Taking into account the critical aspect ratio necessary to obtain dominant IDTMs (Eq. (7.20)) and the scaling law for the wavenumber corresponding to the fastest growing mode (Eq. (7.22)), we obtain a condition for the *discrete* values of S_{L} that can be used to fit n equal (dominant) modes in the vertical direction, namely

$$S_{\text{L}}(n) \approx \left(\frac{n\pi}{\beta_{\text{IDTM}}} \right)^{29/6} . \tag{7.29}$$

As we can see, by construction, the dominant IDTM mode can appear only for a few S_{L}. However, Baty (2017), does not restrict to the discrete values of $S_{\text{L}}(n)$ resulting from Eq. (7.29), which implies that only subdominant modes (i.e. growing at a lower rate) can be excited in his computational domain. We have carefully selected box-periodic modes in Eqs. (7.27) and (7.28), which coincide with the fastest growing mode expected theoretically.

We must also take into account that from the definition of the Lundquist number relative to a (Eq. (7.7)) and the relation between S_a and S_{L} (Eq. (7.21)),

which holds for the critical aspect ratio (Eq. (7.20)), we obtain a restriction on the (discrete) values of the conductivity for given a, $v_{\rm A}$ and n, namely

$$\sigma(n) \approx \frac{1}{a v_{\rm A}} \left(\frac{n\pi}{\beta_{\rm idtm}} \right)^{10/3} . \tag{7.30}$$

Likewise, using the critical aspect ratio (Eq. (7.21)) for the discrete values of $S_{\rm L}(n)$ resulting from Eq. (7.29), together with the fact that $L_y = 2L$, we obtain the following discrete values of L_y that fit an integer number of dominant modes in the vertical direction:

$$L_y(n) \approx 2a \left(\frac{n\pi}{\beta_{\rm IDTM}} \right)^{3/2} . \tag{7.31}$$

Table 7.2: Discrete values of $S_{\rm L}(n)$ (Eq. (7.29)), S_a (Eq. (7.21)), $\sigma(n)$ (Eq. (7.30)) and $L_y(n)$ (Eq. (7.31)) that ensure fitting an integer number of dominant modes (n; first column) in the vertical direction of the computational box for a given Alfvén speed $v_{\rm A}$ and $\beta_{\rm idtm} = 0.45$ (suitable for the case in which $l/a = 5$; Baty, 2017).

n	$v_{\rm A}$	$S_{\rm L}(n)$	$S_a(n)$	$\sigma(n)$	$L_y(n)$
1	0.50	1.20×10^4	6.50×10^2	2.60×10^4	1.85
2	0.50	3.42×10^5	6.56×10^3	2.62×10^5	5.22
3	0.50	2.43×10^6	2.53×10^4	1.01×10^6	9.59
4	0.50	9.75×10^6	6.61×10^4	2.64×10^6	14.8
1	0.82	1.20×10^4	6.50×10^2	1.59×10^4	1.85
2	0.82	3.42×10^5	6.56×10^3	1.61×10^5	5.22
3	0.82	2.43×10^6	2.53×10^4	6.20×10^5	9.59

We summarize in Tab. 7.2 the possible discrete values of various parameters in order to properly set up an integer number of dominant modes in the vertical direction of the computational domain for fixed values of $v_{\rm A}$ and $l/a = 5$. We note that for each value of n, $S_{\rm L}(n)$, $S_a(n)$ and $L_y(n)$ are the same, independently of the value of $v_{\rm A}$. Even though the cases $n = 3$ and $n = 4$ are closer to the asymptotic regime $S_{\rm L} \gg 1$, necessary for the scaling relations of Eq. (7.22) to hold, we cannot perform a detailed analysis of them, as they require larger computational domains, which imply models with many more numerical zones in the vertical direction and very likely also increasing by another factor $\sim 2-4$ the number of zones in the horizontal direction, as simulations with the Aenus code have empirically shown. This is because the conductivity increases with n (Eq. (7.30)), and we have already show in Chap. 6 that to avoid being dominated by numerical diffusivity finer grids are needed. Instead, we will focus on the $n = 1, 2$ cases. In the comparison with the classical results of Baty (2017) we will take $n = 2$, unless otherwise stated.

In order to analyze the numerical results (also the non-linear phase of the evolution in the next subsection), we define the following quantities:

$$\mathcal{B}(t) := \sqrt{\frac{1}{\mathcal{S}} \int B_x^2 \, \mathrm{d}S}, \tag{7.32}$$

where $\mathcal{S} := \int \mathrm{d}S$ is the surface of the computational domain where most of the dynamics develops (in our case the rectangle defined by $-1 \leq x \leq 1$, $0 \leq y \leq L_y$), and

$$\mathcal{A}_{\mathcal{B}}(t) := \frac{\mathcal{B}(t)}{B_0}. \tag{7.33}$$

The quantities defined in Eqs. (7.32) and (7.33) shall grow as the RIDTM instability develops. Note that at $t = 0$, the magnetic field x-component is tiny, as it has a value given by the perturbations (Eqs. (7.27) and (7.28)). In order to quantify the effective instantaneous amplification of the magnetic field x-component computed numerically, we define

$$\mathcal{A}_{B_x}(t) := \max_S |B_x/B_0|. \tag{7.34}$$

We also define the maximum value of $\mathcal{A}_{\mathcal{B}}(t)$ (Eq. (7.33)) and of $\mathcal{A}_{B_x}(t)$ (Eq. (7.34)) over the whole time evolution as

$$\tilde{\mathcal{A}}_{\mathcal{B}} := \max_t(\mathcal{A}_{\mathcal{B}}(t)), \tag{7.35}$$

and

$$\tilde{\mathcal{A}}_{B_x} := \max_t(\mathcal{A}_{B_x}(t)), \tag{7.36}$$

respectively. Likewise, we define the instantaneous maximum value of the velocity modulus in the computational domain as

$$v_p(t) := \max_S(v), \tag{7.37}$$

and the maximum value of the velocity throughout the evolution as

$$\tilde{v}_p := \max_t(v_p(t)). \tag{7.38}$$

We further define the maximum instantaneous value of the ratio of p_{g}/ρ in the computational domain

$$\xi_p(t) := \max_S(p_{\mathrm{g}}/\rho), \tag{7.39}$$

and its global maximum in the whole computed evolution

$$\tilde{\xi}_p := \max_t(\xi_p(t)). \tag{7.40}$$

In the upper left panel of Fig. 7.8 (blue line), we show the evolution of $\mathcal{A}_{\mathcal{B}}(t)$ for models with $n = 2$ dominant modes in the vertical computational box (Tab. 7.2), computed with the box having $L_y \simeq 5.22$, which optimizes the aspect ratio L/a to (theoretically) maximize the growth rate (solid blue line). Other cases with $n = 2$ and different values of L_y are also displayed. We note that for cases with $5 \lesssim L_y \lesssim 5.5$, our models eventually fail at the default resolution employed in this section (namely, when $n_x \times n_y = 1024 \times 64$). This is not the case at lower resolution (e.g. employing $n_x \times n_y = 512 \times 128$ or even smaller values $n_y = 64$). The reasons for this behaviour will be commented in Sec. 7.2.2, but for the qualitative description of the temporal evolution phases that follows, this is irrelevant. Firstly, because these phases are common to all models satisfying certain optimality conditions and, secondly, because at lower resolutions we also observe the same qualitative behaviour for models with a vertical computational domain with length $L_y \simeq 5.22$. The last comment can also be extended to other lower resolution models with computational domains with $5 \lesssim L_y \lesssim 5.5$. Thus, to exemplify the discussion, we refer to a model with $L_y = 5.5$, which is sufficiently close to $L_y \simeq 5.22$ (Fig. 7.8 blue dash-dotted line), although the aspect ratio of that model is not the optimal one. The system exhibits an initial, transitory, purely numerical phase (a) where the initial conditions settle (during this time the numerical solution *adjusts* to the eigenfunctions). Afterwards, once the eigenmodes are properly developed in the system, the physical evolution follows and we observe three clearly identifiable phases. The linear phase (b), in which the TMs (and hence, B_x) grow exponentially, as it is predicted by the theory. Later, we find an explosive, non-linear growth phase (c), which finishes after having reached the maximum value of the amplification factors $\mathcal{A}_{\mathcal{B}}(t)$ and $\mathcal{A}_{B_x}(t)$. The evolution ends with a relaxation phase (d) where the field decays, though to a value which is non-zero and close to that reached by the end of the linear amplification phase.[8] Thus, the time evolution displayed in our Fig. 7.8 (upper left panel) is qualitatively identical to that shown in Fig. 7 of Baty (2017) for his models 1, 2 and 3, serving this fact as a first validation of our numerical strategy. The similarities of our results are not restricted to the evolution of global (integrated) variables, but also extend to the morphology of the magnetic field distribution as we shall see later.

In order to check whether the linear evolution phase is dominated by the growth of the linearly fastest mode, we have again computed numerically the dispersion relation $\gamma(ka)$, but this time using $n = 2$ dominant modes prop-

[8] Some of our models, especially those having the larger computational domains in the vertical direction, are not run for sufficiently long time to observe the full relaxation of the system. However, the trends are clear and the assessment of the relaxation phase is not our primarily target of study. Instead, here we focus more on the linear and on the explosive phases.

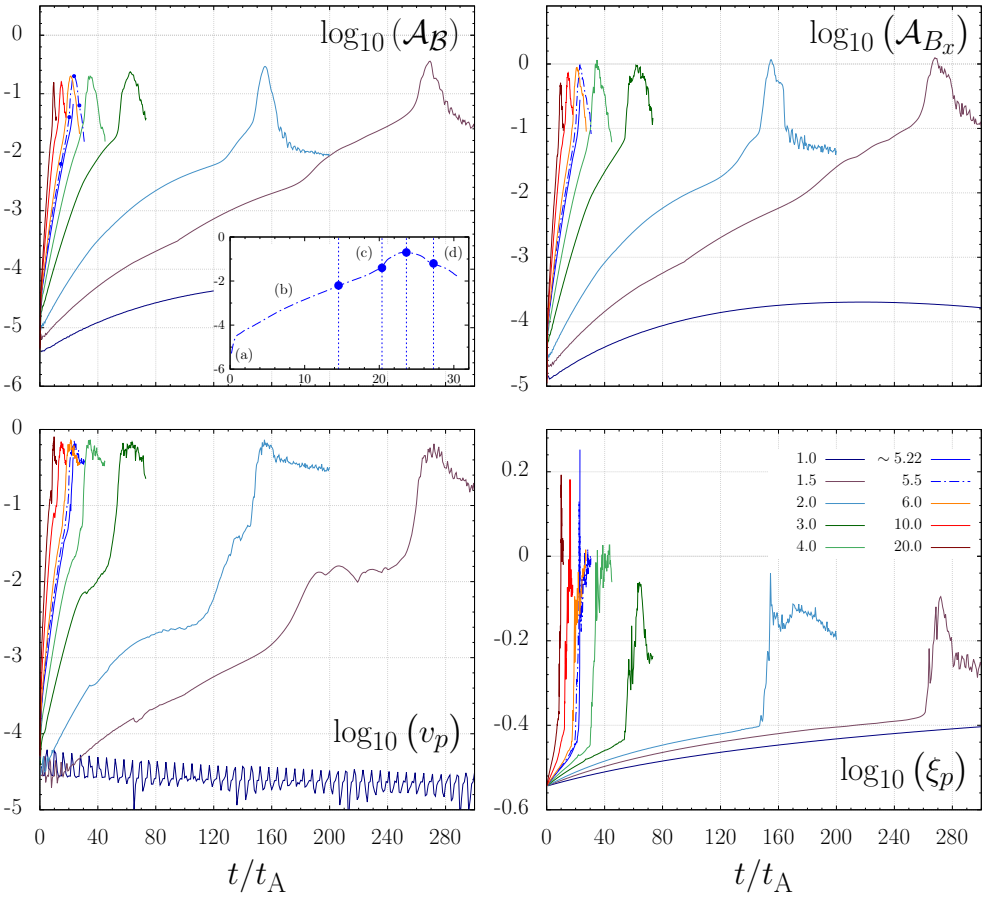

Figure 7.8: Temporal evolution (normalized to the Alfvén crossing time of the current sheets half-length (Eq. (7.3)) of several quantities for models with different L_y (see legends) in which $n = 2$ dominant modes are set up. In all cases $S_a \simeq 6.56 \times 10^3$. *Upper left panel*: Evolution of $\mathcal{A}_{\mathcal{B}}(t)$ (Eq. (7.33)) for different box lengths (see legends) employing a grid of 1024×64 uniform zones. In the inset labels (a), (b), (c) and (d) identify four distinct evolutionary phases for the setup with $L_y = 5.5$. The blue circles correspond to the times displayed in the snapshots of Figs. 7.12, 7.13 and 7.14. *Upper right panel*: Same as the upper left panel for $\mathcal{A}_{B_x}(t)$ (Eq. (7.34)). *Lower left panel*: Same as the upper left panel for v_p (Eq. (7.37)). *Lower right panel*: Same as the upper left panel for ξ_p (Eq. (7.39)).

erly quantized in the vertical direction (Fig. 7.9). We select different values of k varying L_y and keeping all other parameters, as well as the numerical resolution fixed. For a resolution of 512×64 uniform zones (Fig. 7.9; red circumferences), the numerical dispersion relation peaks at $k_{\rm RIDTM}^{\rm num} a \simeq 0.10$, roughly in agreement with the theoretical prediction for normalized half separation $l/a = 5$ and $S_a(2) = 6555$, namely $k_{\rm RIDTM} a \simeq 0.45 S_a^{-3/20} \simeq 0.12$ (Baty, 2017). This is also the case for models with a resolution of 1024×64 zones,

Table 7.3: Measured properties of various models set up with $\gamma = 5/3$, $l/a = 5$, and different values of the number of dominant modes n (first column) in the vertical direction. Columns (from left to right): number of dominant modes in the vertical direction, Alfvén velocity, vertical size of the computational domain, number of zones in the grid, conductivity ($\sigma_5 = \sigma \times 10^5$), growth rate in the linear phase corresponding to a value ka where the peak of the dispersion relation is theoretically expected (e.g. $k_{\rm RIDTM}a \simeq 0.12$ for $n = 2$ and $v_{\rm A} = 0.5$), time at which the peak of the explosive phase happens normalized to $t_{\rm A}$ ($t_p/t_{\rm A}$; measured as the time by which the quantity $\mathcal{A}_{B_x}(t)$ (Eq. (7.34)) is maximum, i.e. when $\mathcal{A}_{B_x}(t_p) = \tilde{\mathcal{A}}_{B_x}$), amplification factor for the magnetic field measured in two different ways, either as $\tilde{\mathcal{A}}_{\mathcal{B}}$ (Eq. (7.35)), or as $\tilde{\mathcal{A}}_{B_x}$ (Eq. (7.36)), maximum value of the velocity $\tilde{v}_p$ (Eq. (7.38)) and maximum value of $\tilde{\xi}_p$ (Eq. (7.40)). The models run with $v_{\rm A} = 0.82$, as well as models with $v_{\rm A} = 0.5$, $n = 2$ and $n_x = 1024$ uniform zones, have failed at about the beginning of the explosive phase. Thus, we cannot measure the values of t_p, $\tilde{\mathcal{A}}_{\mathcal{B}}$, $\tilde{\mathcal{A}}_{B_x}$, $\tilde{v}_p$ and $\tilde{\xi}_p$. In such cases, we provide between parenthesis the values measured by the last computed time (listed in the column t_p) of the previous quantities. Since all these quantities grow until $t = t_p$, they correspond to their respective maxima in the computed evolution.

n	$v_{\rm A}$	L_y	$n_x \times n_y$	σ_5	$t_p/t_{\rm A}$	$\gamma^{\rm num}_{\rm RIDTM}$	$\tilde{\mathcal{A}}_{\mathcal{B}}$	$\tilde{\mathcal{A}}_{B_x}$	$\tilde{v}_p$	$\tilde{\xi}_p$
1	0.50	1.84	512×32	0.26	56.9	0.11 ± 0.05	0.28	1.04	0.48	0.80
1	0.50	1.84	512×64	0.26	58	0.11 ± 0.05	0.28	1.05	0.56	0.80
1	0.50	1.84	512×128	0.26	57.5	0.12 ± 0.05	0.27	1.22	0.58	0.72
1	0.50	1.84	768×32	0.26	45.54	0.124 ± 0.011	0.26	0.85	0.39	0.83
1	0.50	1.84	1024×32	0.26	(27.1)	0.133 ± 0.009	(0.14)	(0.41)	(0.31)	(0.44)
2	0.50	5.22	512×32	2.62	31.2	0.0470 ± 0.0016	0.22	0.83	0.52	0.69
2	0.50	5.22	512×64	2.62	29.7	0.053 ± 0.004	0.24	1.04	0.52	0.61
2	0.50	5.22	512×128	2.62	28	0.052 ± 0.004	0.21	1.05	0.73	0.70
2	0.50	5.22	768×64	2.62	22.5	0.0698 ± 0.0004	0.24	1.05	0.49	0.84
2	0.50	5.22	1024×32	2.62	(23)	0.0703 ± 0.0017	(0.04)	(0.23)	(0.35)	(2.48)
2	0.50	5.22	1024×64	2.62	(25.3)	0.0704 ± 0.0016	(0.22)	(0.92)	(0.50)	(0.74)
2	0.50	5.22	1024×128	2.62	(23)	0.0704 ± 0.0021	(0.06)	(0.28)	(0.43)	(1.79)
2	0.50	5.50	1024×32	2.62	27.09	0.076 ± 0.003	0.19	0.67	0.62	0.87
2	0.50	5.50	1024×64	2.62	23.64	0.0759 ± 0.0015	0.21	0.84	0.71	0.77
2	0.50	5.50	1024×128	2.62	22.36	0.077 ± 0.003	0.23	1.09	0.66	0.85
3	0.50	9.59	512×96	10.1	13.25	0.061 ± 0.003	0.21	0.95	0.79	0.92
3	0.50	9.59	512×128	10.1	14.7	0.055 ± 0.003	0.22	1.20	0.65	0.73
3	0.50	9.59	768×96	10.1	15.34	0.0513 ± 0.0024	0.18	0.82	0.56	0.71
3	0.50	9.59	1024×96	10.1	(15.5)	0.051 ± 0.012	(0.05)	(0.28)	(0.46)	(80000)
4	0.50	14.8	512×128	26.4	8.67	0.054 ± 0.003	0.18	0.93	0.73	0.74
4	0.50	14.8	768×128	26.4	10.7	0.0444 ± 0.0023	0.19	0.87	0.92	0.87
4	0.50	14.8	1024×128	26.4	(5.01)	0.046 ± 0.020	(0.0009)	(0.02)	(0.18)	(1.1)
2	0.82	5.22	512×32	1.61	(24.1)	0.089 ± 0.004	(0.05)	(0.16)	(0.43)	(46.4)
2	0.82	5.22	512×64	1.61	(23.5)	0.090 ± 0.004	(0.06)	(0.20)	(0.63)	(1.89)
2	0.82	5.22	512×128	1.61	(22.8)	0.090 ± 0.003	(0.03)	(0.13)	(0.45)	(2.18)
2	0.82	5.22	512×256	1.61	(22.5)	0.092 ± 0.003	(0.04)	(0.21)	(0.71)	(2.07)
4	0.82	14.8	512×128	16.2	(9.96)	0.060 ± 0.005	(0.06)	(0.34)	(0.79)	(4537)

although, within the numerical accuracy of the determination of the growth rate, the values at $ka \simeq 0.10$ and $ka \simeq 0.12$ are nearly the same. The numerical growth rate of the fastest growing mode, $\gamma^{\rm num}_{\rm RIDTM}\tau_{\rm A} \simeq 0.0066$ for a resolution 512×64 ($\gamma^{\rm num}_{\rm RIDTM}\tau_{\rm A} \simeq 0.0075$ for a resolution 1024×64) is smaller than the value obtained from the scaling relations provided by Baty (2017) from fits

to the theoretical values computed solving numerically the dispersion relation, i.e. $\gamma_{\rm IDTM}\tau_{\rm A} \simeq 0.55 S_a^{-9/20} \simeq 0.0105$. For the value at which the theoretical peak of the dispersion relation should be found, we provide the growth rate in Tab. 7.3 (note that at a resolution of 512×64 the value in the table is smaller than the numerical maximum growth rate located at $k_{\rm RIDTM}a \simeq 0.12$). Certainly, our models are influenced by the fast diffusion of the magnetic field background, which is assumed to be constant on the RIDTM timescale, but in our simulations it is not. Since we do not (artificially) prevent the diffusion of the background magnetic field (as, e.g. Landi et al. 2015; Rembiasz et al. 2017), we do not expect to obtain the *exact* theoretical growth rate in our numerical models, but (typically) smaller values. Furthermore, the boundary conditions in the horizontal direction are not exactly as assumed to derive the theoretical dispersion relation. Added to these effects, the resolution in the x-direction may also change the maximum growth rate modulating it within relative variations $\lesssim 25\%$ (note the slightly larger values of $\gamma\tau_{\rm A}$ for resolutions 1024×64 compared to the cases computed with 512×64 uniform cells). The numerical resolution in the y-direction produces a relatively smaller change in the values of $\gamma\tau_{\rm A}$. For the theoretical value of the peak location ($ka = k_{\rm RIDTM}a \simeq 0.12$), using a grid twice finer in the vertical direction modifies by $\lesssim 2\%$ the value of $\gamma^{\rm num}_{\rm RIDTM}\tau_{\rm A}$ (compare the cases run with resolutions of 512×64 and 512×128 in Fig. 7.9 and see the exact values of the growth rate for $ka \simeq 0.12$ in Tab. 7.3 -rows corresponding to $n = 2$ and $v_{\rm A} = 0.5$). Indeed, using a grid of $1024 \times n_y$ zones, with $n_y = 32$, 64 and 128 yields the same growth rate ($\gamma^{\rm num}_{\rm RIDTM} \simeq 0.070$) within the accuracy of our measurement method.

We observe that for a fixed value of n_x (say $n_x = 512$), n_y has a relatively small impact on the evolution as can be seen in Fig. 7.10. We note that even using $n_y = 32$ (i.e. 16 zones per dominant wavelength) the linear phase and the evolution prior to the explosive phase (namely, up to $t/t_{\rm A} \lesssim 24$) is nearly identical, and so are the measured growth rates in the linear phase. However, the number of zones in the horizontal direction is much more important to properly obtain the growth of B_x (or any other quantity) in the linear phase. This is because properly resolving the current sheets half-width is the key to prevent an excessive diffusion of the background magnetic structure due to the numerical diffusivity. Increasing n_x from 512 to 1024 the growth rate in the linear regime slightly increases, which yields a factor ~ 4 larger amplification factor $\mathcal{A}_{\mathcal{B}}(t)$ by the end of the linear phase ($t/t_{\rm A} \simeq 24$). Later, by the peak of the explosive phase this diference almost disappears, and the resulting amplification factors are quite robustly estimated independently of the numerical resolution employed (though the location of the peak time sensitively depends on the chosen resolution), as we shall see in Sec. 7.2.2.1.

Also for the value $ka = 0.12$, we have computed models with the RK36$\mathcal{S}_E$ ti-

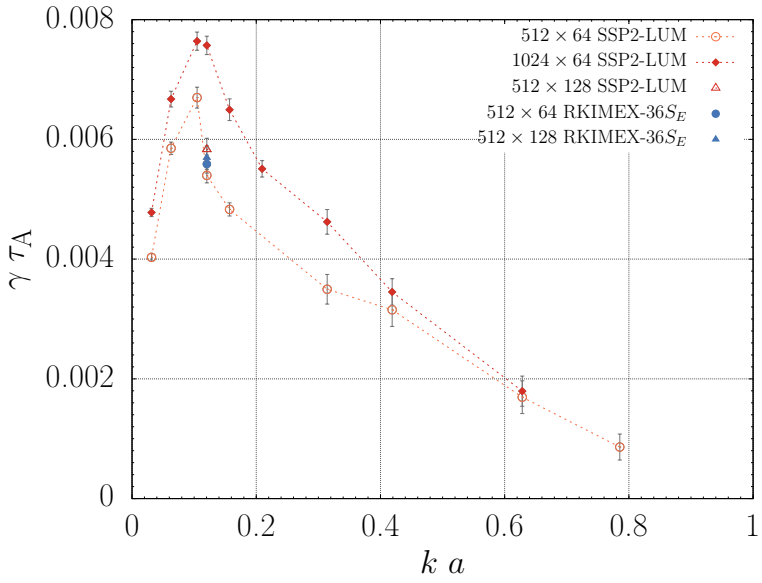

Figure 7.9: Dispersion relation for $n = 2$ modes in RIDTMs computed for different computational box and numerical resolutions (see legends). Two different time-integrators (SSP2(332)-LUM and RK36$\mathcal{S}_E$) are used in Cueva to obtain this numerical dispersion relation. The Alfvén velocity and the current sheet width are equal in all cases, $v_A = 0.5$ and $a = 0.05$, respectively. The resistivity and S_a can be found in Tab. 7.2 (case $n = 2$). In order to measure the different growth rates, we have considered cases with $L_y = 0.8, 1, 1.5, 2, 3, 4, 5.22, 6, 10$ and 20. Exact values of the maximum growth rate and the corresponding wavenumber can be found in Tab. 7.3.

me-integrator (orange symbols in Fig. 7.9). We find that at a resolution of 512×128 cells the results are nearly identical as with the SSP2(332)-LUM time-integrator with a resolution 512×64, while using 512×64 zones the growth rate for $ka = 0.12$ changes by less than $\sim 5\%$ with respect to the same resolution but run with a different time-integrator. The summary of these results is that using, at least, $n_x = 512$ and 32 uniform zones per dominant mode (e.g. 512×64 cells for $n = 2$), the growth rate is numerically converged within a relative accuracy of $\sim 10\%$, regardless of the time-integrator employed.

Although our reference models contain $n = 2$ dominant modes, we have also considered the variations induced in the growth rate by the change of n. Since increasing n increases L_y (Eq. (7.31)), in order to have a fair comparison among models, we run them all with different resolutions in the horizontal direction ($n_x = 512,\ 768$ and 1024), and we use 32 uniform cells per dominant mode in the vertical direction. We may compare the numerically obtained maximum growth rate with the theoretical expectation in the classical MHD regime (columns headed with $\gamma^{\rm num}_{\rm RIDTM}$ and $\gamma_{\rm IDTM}$ in Tab. 7.4). We observe that

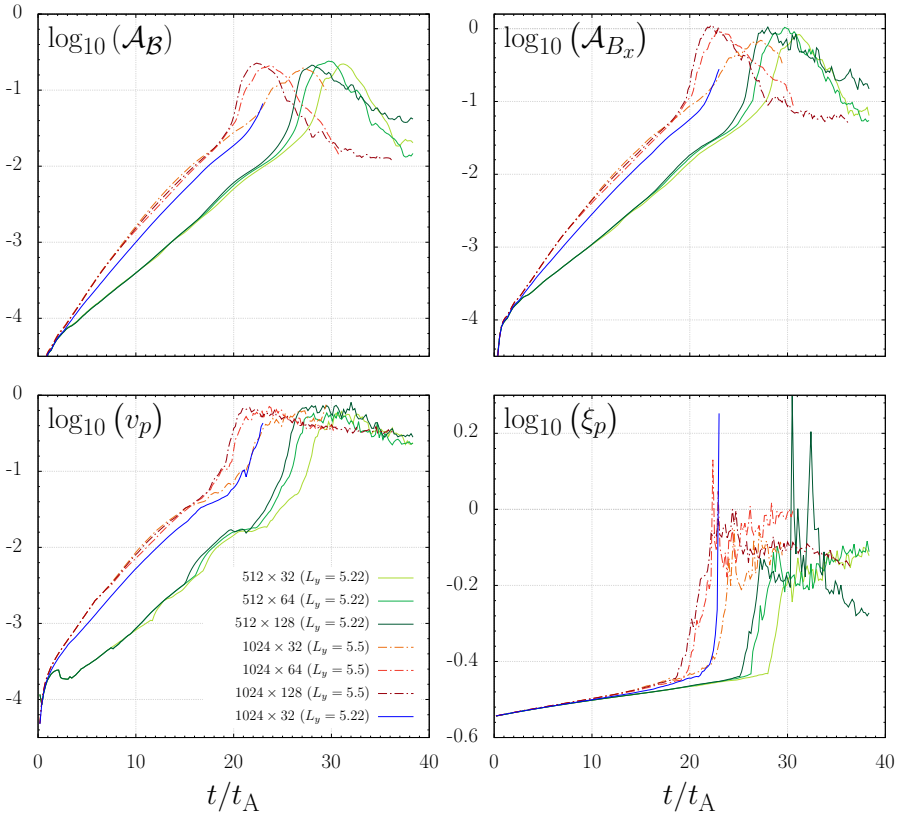

Figure 7.10: Dependence of various quantities with the resolution. The setup and the quantities displayed are the same as in Fig. 7.8, i.e. there are $n = 2$ dominant modes in the vertical direction. Several values of $n_x \times n_y$ have been considered (see legends). The results are computed with the SSP2(332)-LUM time integrator, the HLL Riemann solver and the MP9 intercell reconstruction. The models computed with 1024×64 zones are the same as in Fig. 7.8. With solid lines we show models with $L_y \simeq 5.22$ and dot-dashed lines correspond to models with $L_y = 5.5$. While the former model fails before reaching the maximum of the explosive phase if $n_x = 1024$ zones are used, the latter ones run without difficulties.

.

the growth rate tends to decrease as n increases. Theoretically, we expect a decrease of the growth rate for increasing values of n (see column headed with $\gamma_{\rm IDTM}$ in Tab. 7.4). Only for $n = 3$, $\gamma^{\rm num}_{\rm RIDTM} \simeq \gamma_{\rm IDTM}$, whereas the values for $n = 1$ are $\gamma^{\rm num}_{\rm RIDTM} \simeq 0.5\gamma_{\rm IDTM}$. For $n = 2$, the numerical growth rate is $\lesssim 35\%$ smaller than the theoretical one, as it is inferred from the values computed with the larger horizontal resolutions ($n_x = 768$ and 1024). We atribute this discrepancy to the diffusion of the background magnetic field, which is significant for the smaller values of the conductivity (i.e. for $n = 1$ and -to a smaller extent- for $n = 2$; see Tab. 7.4). For $n = 4$ the IDTM growth rate is somewhat enhanced by the numerical resistivity which becomes

Table 7.4: Several quantities for models where $n = 1, 2, 3$ and 4 dominant modes are set up in the vertical direction of the computational box. In all cases, the resolution employed is such that we have 32 cells per dominant mode in the vertical direction and the background Alfvén speed is $v_{\rm A} = 0.5$, corresponding to $\tau_{\rm A} = 0.1$. The values $\gamma_{\rm IDTM}$ are computed from Eq. (7.22), using $\alpha_{\rm IDTM} = 0.55$, whereas the values of $\gamma_{\rm RITM}$ are computed from Eq. (7.18) for reference. Since the growth rate is not numerically constant during the whole linear phase, we make several measurements of γ in various time intervals with a common origin ($t = 150\tau_{\rm A}$) selected to avoid (as much as possible) the influence of the initial (purely numerical) phase. The errors in the determination of $\gamma^{\rm num}_{\rm RIDTM}$ correspond to three times the standard deviation of measurements of the growth rate performed in the following intervals $t/\tau_{\rm A} \in [150, t_{\rm max}/\tau_{\rm A}]$, with $t_{\rm max}/\tau_{\rm A} = 250, 400, 500, 600, 700$ and 800.

$n_x \times n_y$	n	σ_5	$\gamma^{\rm num}_{\rm RIDTM}$	$\gamma_{\rm IDTM}$	$\gamma_{\rm RITM}$	$k^{\rm num}_{\rm IDTM}$	L_y
512×32	1	0.26	0.11 ± 0.05	0.2982	0.3252	3.4062	1.85
512×64	2	2.62	0.053 ± 0.004	0.1054	0.1150	2.4086	5.22
512×96	3	10.1	0.061 ± 0.003	0.0575	0.0626	1.9666	9.59
512×128	4	26.4	0.054 ± 0.003	0.0373	0.0407	1.7031	14.8
768×32	1	0.26	0.124 ± 0.011	0.2982	0.3252	3.4062	1.85
768×64	2	2.62	0.0698 ± 0.0004	0.1054	0.1150	2.4086	5.22
768×96	3	10.1	0.0512 ± 0.0008	0.0575	0.0626	1.9666	9.59
768×128	4	26.4	0.0422 ± 0.0018	0.0373	0.0407	1.7031	14.8
1024×32	1	0.26	0.133 ± 0.009	0.2982	0.3252	3.4062	1.85
1024×64	2	2.62	0.0704 ± 0.0016	0.1054	0.1150	2.4086	5.22
1024×96	3	10.1	0.0438 ± 0.0006	0.0575	0.0626	1.9666	9.59
1024×128	4	26.4	0.0331 ± 0.0003	0.0373	0.0407	1.7031	14.8

comparable to the physical one (when acting on the characteristic scale of the IDTMs; but is negligible when it comes to the diffusion of the background magnetic field, as this scale is well resolved). To see this point, note that for $\sigma(n = 4) = 2.64 \times 10^6$ ($\eta \simeq 3.79 \times 10^{-7}$), $\xi^* \simeq \eta$ when $v_{\rm A} = 0.5$, as can be seen in Fig. 6.11 (note in the figure that for the resistivity used in the case $n = 4$ our models would be very close to the transition region between the region dominated by spatial discretization errors and that dominated by time discretization errors). We observe, however, that using $n_x = 1024$ zones in the horizontal direction the numerical diffusivity decreases sufficiently and the numerical growth rate approaches the theoretical one.

As anticipated in Sec. 7.2.1, we have tested in our numerical simulations that $B_0 v_1 \gg (\mathbf{v}_1 \cdot \mathbf{B}_0)$, something theoretically necessary to obtain the same dispersion relation in MHD than in RRMHD or MD. For this end, we computed the integrated value of both terms in the whole computational domain (we take absolute values to avoid cancellation of terms with different signs in the integrals), and display its ratio in Fig. 7.11 (right panel). There, we show that $\int B_0 |v_1| {\rm d}S / \int |\mathbf{v}_1 \cdot \mathbf{B}_0| {\rm d}S \ll 1$ during most of the evolution (including the linear

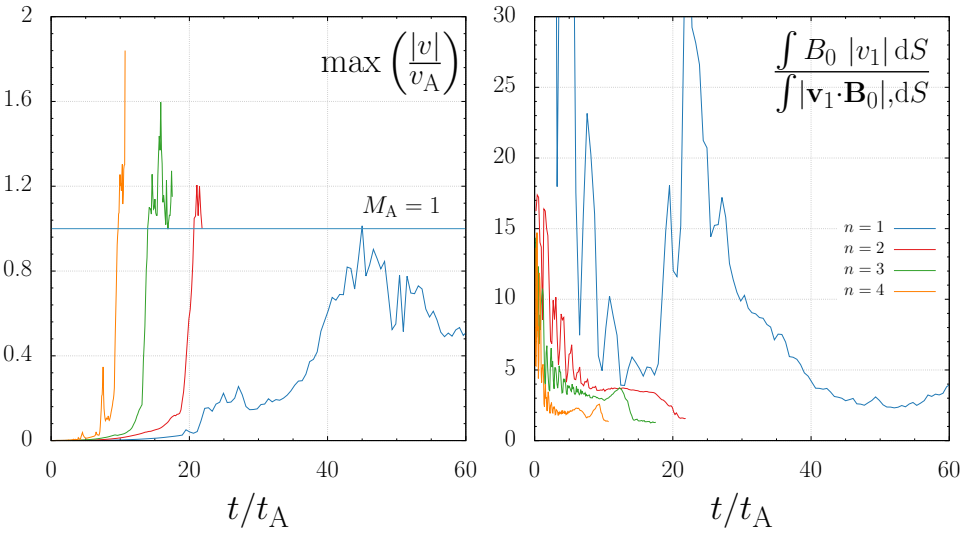

Figure 7.11: *Left panel*: Temporal evolution of the maximum Alfvén number computed over the whole spatial domain $M_A = |\mathbf{v}|\,/v_A$ for models with different number of dominant modes in the vertical direction (see legends) in computational domains whose lengths, $L_y(n)$, are set up using Eq. (7.31). Above the horizontal blue line parts of the flow become super-Alfvénic. *Right panel*: Time evolution of the ratio $\int B_0\ |v_1|\ \mathrm{d}S\,/\ \int |\mathbf{v}_1 \cdot \mathbf{B}_0|\ \mathrm{d}S$. The plot shows that the term in the numerator is (much) larger than that in the denominator throughout most of the evolution until we reach the explosive phase. Both terms arise from the linearization of the Poynting flux used to obtain the dispersion relation for RIDTMs. All the models have been run with $n_x = 768$ and 32 uniform zones per dominant wavelength in the vertical direction (i.e. for $n = 1, 2, 3$ and 4, we have $n_y = 32, 64, 96$ and 128 cells).

phase) except during the explosive phase, where $\int B_0 |v_1| \mathrm{d}S \gtrsim \int |\mathbf{v}_1 \cdot \mathbf{B}_0| \mathrm{d}S$. These results are independent of the number of dominant modes computed in the domain, as can be seen from the fact that the aforementioned ratio is significantly larger than 1 in all the cases shown in the figure ($n = 1, \ldots, 4$).

We finally note that the fluid velocities are subalfvénic ($M_A = |v|/v_A \lesssim 1$) in the linear phase (Fig. 7.11 left panel), as well as throughout most of the computed evolution.

7.2.2 The non-linear evolution

As we have commented in the previous section, models run with a grid of $n_x = 1024$ zones in the horizontal direction and vertical sizes in the range $5 \lesssim L_y \lesssim 5.5$ fail to reach the peak of the explosive phase. This is not the case at lower resolutions. The cause of this failure is the development of very hot regions in the sites of most active reconnection. We observe how the variable $\xi_p(t)$ blows up at $t/t_A \gtrsim 23$ in the lower right panel of Fig. 7.8 (solid blue line). Other models run with the same resolution but nearly the optimal value of the aspect ratio (especially the model with $L_y = 5.5$) also display an abrupt increase of

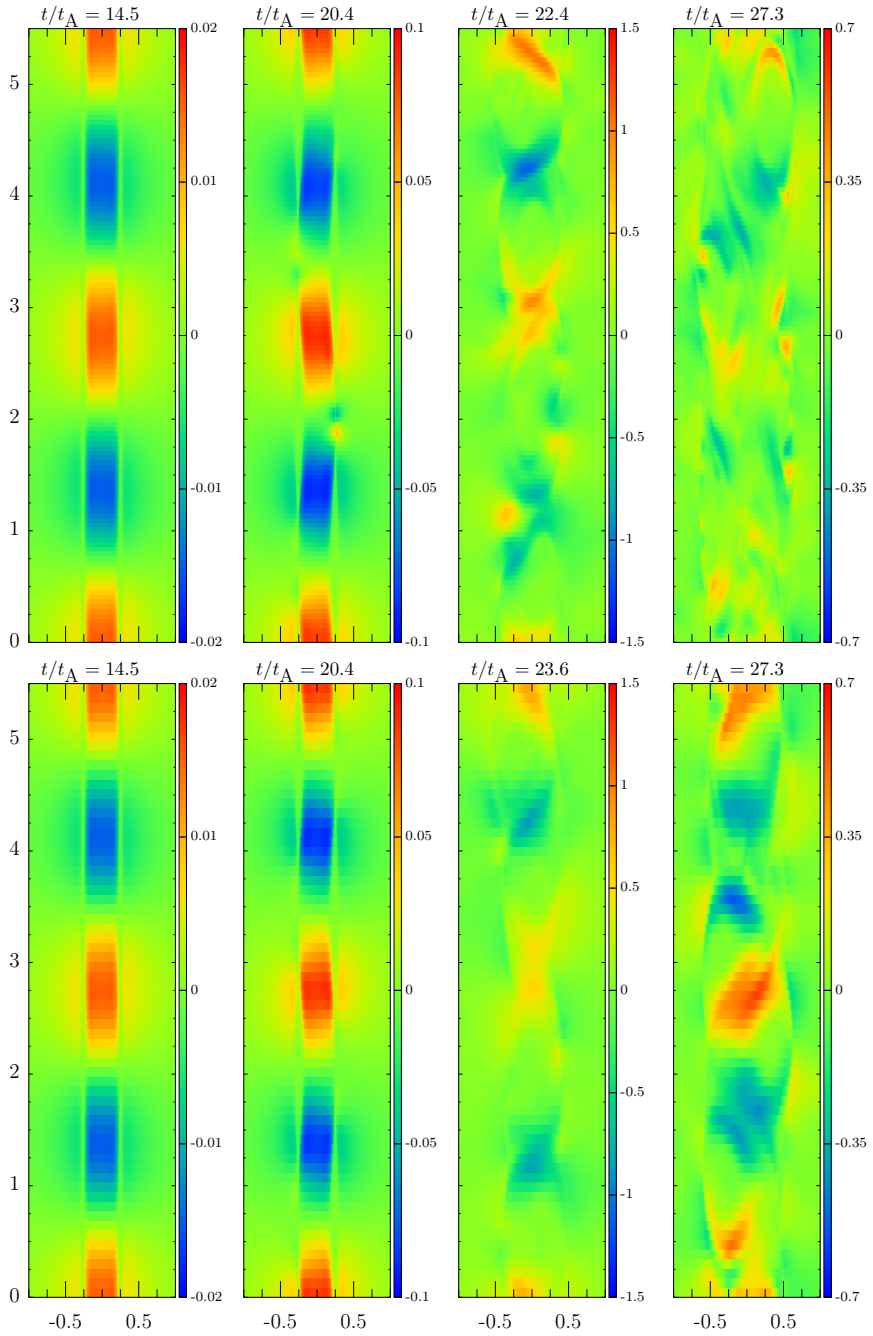

Figure 7.12: B_x component of the magnetic field at four different times and two different resolutions (*upper panels*: 1024×128; *lower panels*: 1024×64), representative of the different phases illustrated in the left panel of Fig. 7.8. Only a part of the whole x-range is shown ($x \in [-1 : 1]$). The whole domain in the vertical direction is displayed $[0 : L_y]$ (the vertical and horizontal scales are not homogeneous). For readability, the color scales are different in every panel because the values of B_x have very different magnitudes.

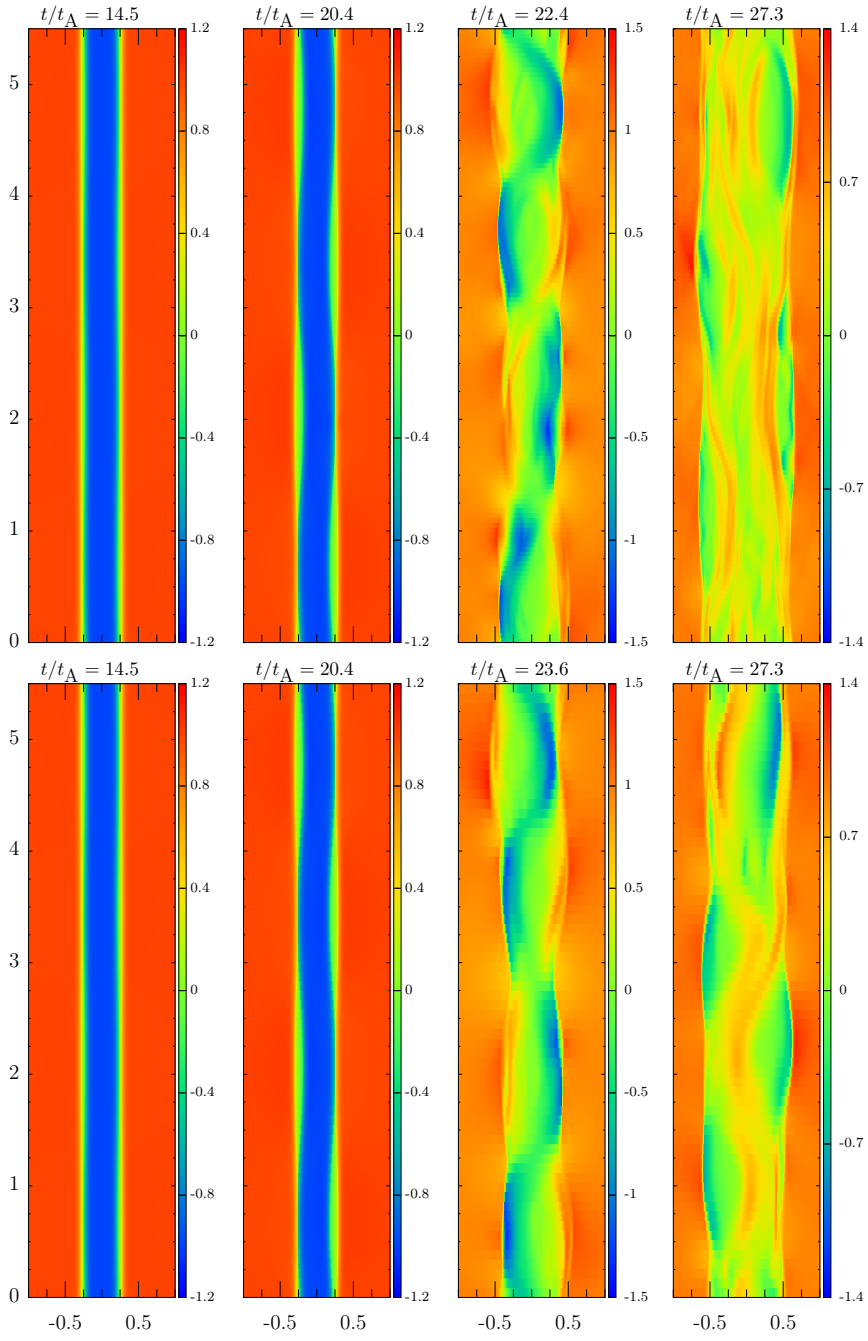

Figure 7.13: Same as Fig. 7.12 but for B_y.

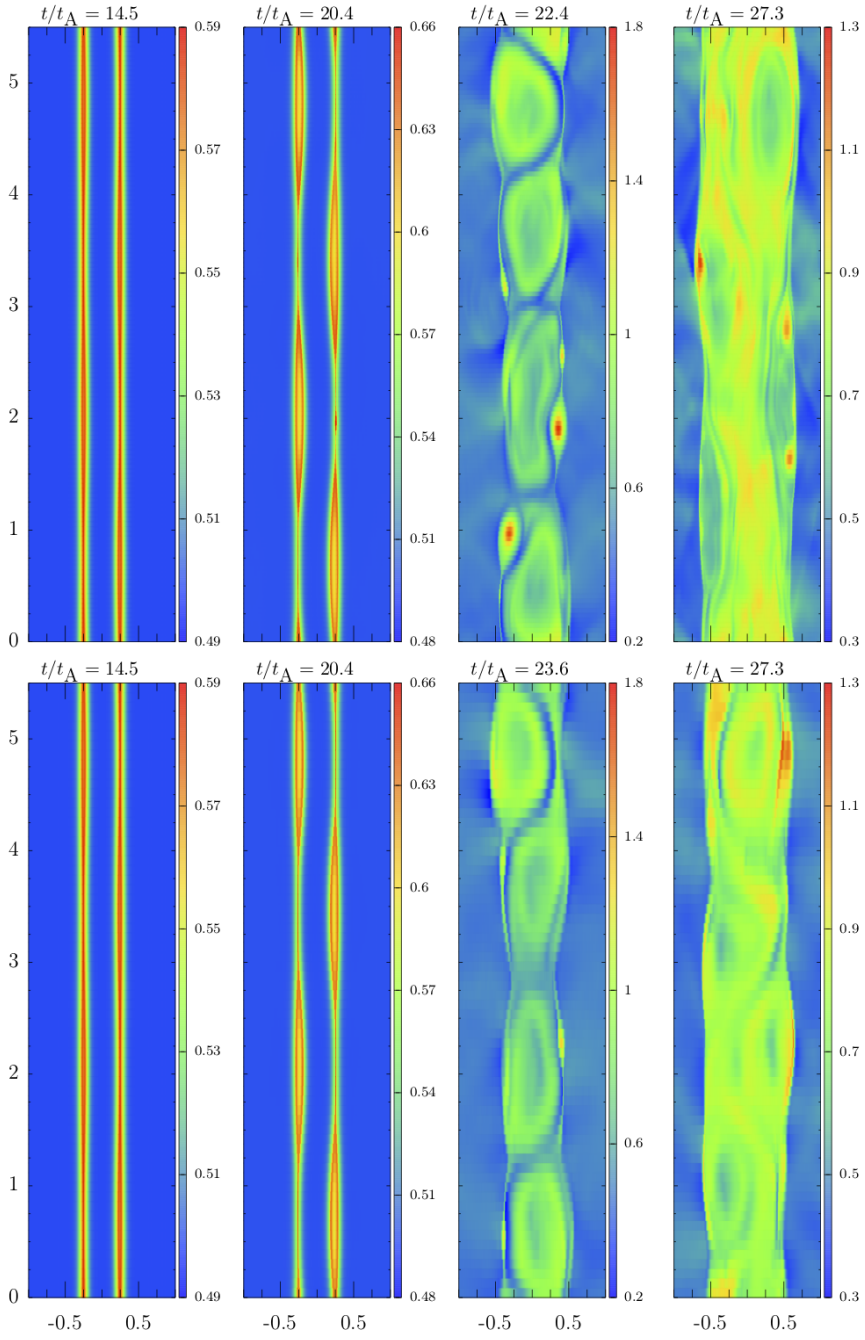

Figure 7.14: Same as Fig. 7.12 but for the thermal pressure.

$\xi_p(t)$, which quickly decais after having reached the first local maximum in the evolution. We have tried to explore this phase with an even larger resolution and the RK36$\mathcal{S}_E$ time-integrator but with unsatisfactory results. We believe that this behavior is associated to the loss of numerical accuracy when the density drops very significantly in the vicinity of X-points. We note that all other quantities associated to the time evolution of the model with $L_y \simeq 5.22$ in Fig. 7.8 behave qualitatively like in other models with explosive phase but different values of L_y. We have not been able to explore more carefully the reasons of this failure in the time frame of this thesis. However, since the dynamics of all models that display an explosive phase is qualitatively similar, we address the non-linear evolution of the model set up with $L_y = 5.5$ and $n = 2$ dominant modes hereafter instead of taking the model with $L_y \simeq 5.22$ and $n = 2$. The properties that we discuss for this model are qualitatively rather similar to the ones of the model with the optimal box ($L_y \simeq 5.22$), which would have been our reference model to assess the dynamics in the non-linear phase.

We show the evolution of the case with $n = 2$ dominant modes in a box with $L_y \simeq 5.5$ considering several 2D snapshots of B_x, B_y and p_g in Figs. 7.12, 7.13 and 7.14, respectively. The snapshots are selected to be representative of the evolutionary phases shown in Fig. 7.8 or at the interface between them (marked in Fig. 7.8 with blue circles). In all these figures, we focus on the central part of the domain, omitting the regions $|x| > 1$, to clearly display the most dynamical part of the computational box.

The evolution ensuing the linear phase results from the competing effects of a double cascade process (cf. Baty, 2017). On the one hand, new secondary sheets with smaller half-length, $L^* < L$ and half-width, $a^* < a$ form (see, e.g. Fig. 7.13 lower left and central panels and the upper panels of Fig. 7.15) and, eventually, their aspect ratios reach critical values $L^*/a^* \simeq S_{L^*}^{1/3}$, characteristic of ITMs (and of RITMs). Once these *ideal* (optimal) conditions are met, fast reconnection on Alfvénic time scales $\tau_A^* = L^*/v_A < \tau_A$ proceeds. The previous process repeats down to ever smaller length scales and, on correspondingly smaller time scales driving the explosive phase. On the other hand, there is an inverse cascade proceeding towards larger scales. This inverse cascade is driven by the merger of small-scale plasmoids into larger scales ones. The dynamics observed during the non-linear phase looks like an accelerated version of what happens in RDTMs (Baty et al., 2013). For comparison, reaching the peak of the explosive phase takes $\sim 100t_c - 120t_c$ in our RIDTM models with $4 \lesssim L_y \lesssim 20$, instead of $\sim 1000t_c - 2000t_c$ in the RDTMs of (Baty et al., 2013).

In the final phase observed ((d) in Fig. 7.8), B_x (and also v_x) decays and relaxes towards a new stable state in which current sheets and plasmoids are nearly absent or reduce to very small scales (Fig. 7.12, right panels). A broad

layer, with a much smaller magnetic field than in the adjacent regions (see the right panels of Figs. 7.13 and 7.14), forms in the region $x \in [-0.65, 0.65]$, i.e. with a width $\sim 25a$, that is more than twice the initial current sheet separation. The previous model dynamics bears many qualitative similarities with the non-relativistic DTMs of, e.g. Janvier et al. (2011); Zhang and Ma (2011) and IDTMs (Baty, 2017).

We do not observe a clearly identifiable *Rutherford* phase (Rutherford, 1973) in most of our models as in some classical MHD models (e.g. Baty, 2017; Janvier et al., 2011). We note that using the Aenus code, we neither clearly observe the aforementioned Rutherford phase in models that are classical counterparts of ours. This is because its appearance and duration sensitively depend on the parameters of the models. The Rutherford phase is characterized by a slower growth of the magnetic field B_x than dictated by the fastest growing RIDTM, with $\gamma \sim \eta^1$, and may appear at the end of the of the linear phase, connecting it with the explosive phase observed afterwards. The only models which seem to (approximately) undergo a Rutherford phase are the ones with $L_y = 2$ and 3, within the respective intervals $40 \lesssim t/t_\mathrm{A} \lesssim 120$ and $32 \lesssim t/t_\mathrm{A} \lesssim 46$, where we observe an small reduction of the growth rate of B_x (Fig. 7.8 upper panels; solid dark green and light blue lines) that happens contemporaneously with a more significant reduction of the growth rate of the velocity (Fig. 7.8 lower left panel). We note, however, that the velocity growth does not completely stop for the model with $L_y = 3$ in this phase prior to the explosive one, as it would be formally required to completely identify the observed behaviour with that of a Rutherford phase (compare our model with $L_y = 3$ to the models of, e.g. Fig. 9 in Baty, 2017). The model with $L_y = 1.5$ is a borderline between cases developing an explosive phase and cases which do not develop it. In the interval $170 \lesssim t/t_\mathrm{A} \lesssim 240$ the growth of the velocity field ceases, but the growth of B_x remains nearly unchanged. Hence, the aforementioned time interval may also marginally be considered as a Rutherford phase for the model with $L_y = 1.5$ (Fig. 7.8). Our results suggest that models with a vertical length sufficiently smaller than the optimal one (namely, $L_y \lesssim 3$) but eventually displaying an explosive phase (i.e. with $L_y \gtrsim 2$; see Sec. 7.2.2.2) may develop a Rutherford phase if we evolve them for a sufficiently long time. Furthermore, if our identification of the Rutherford phase is correct, it appears later and lasts longer if the vertical domain length is smaller.

Even if it may seem paradoxical, the growth of TMs (including also ITMs) produces a growth of the magnetic field component perpendicular to the current sheet. This growth comes at the expense of the decrease of the (dominant) magnetic field component ($B_y \propto B_0$), which is parallel to the current sheets. Thus, the growth of B_x (and of other quantities which are initially very small or even zero) is a good tracer for the development of the instability, as well as to discuss its eventual saturation. The mentioned saturation of B_x shall

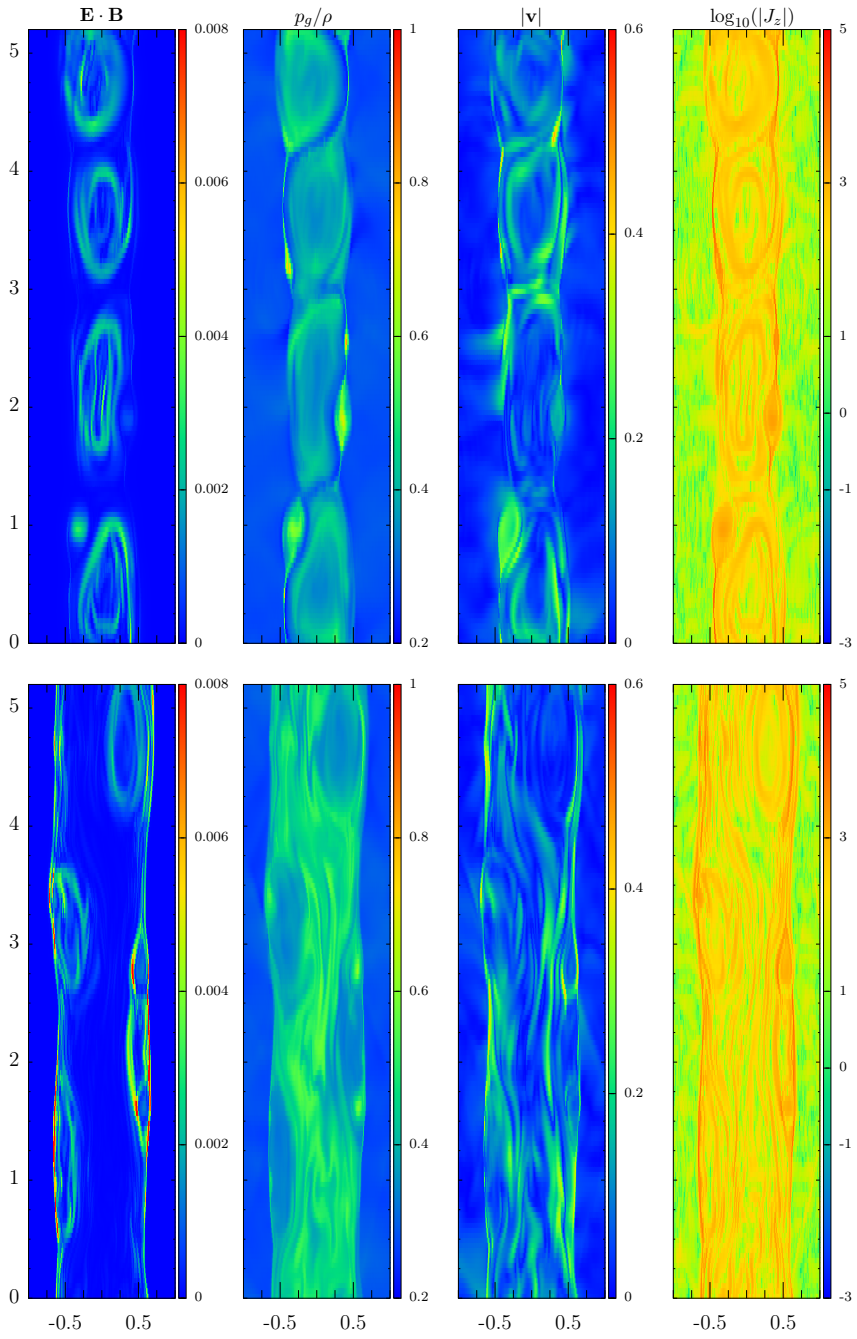

Figure 7.15: *Upper panels*: Snapshots of $\mathbf{E}\cdot\mathbf{B}$, p_g/ρ, $|\mathbf{v}|$, J_z (from left to right) at the maximum of the explosive phase at $t/t_{\rm A} \simeq 22.4$, for a grid with 1024×128 zones. *Lower panels*: The same but in the relaxation phase at $t/t_{\rm A} \simeq 27.3$.

happen, at most, when it arrives to a value $B_x \lesssim B_0$. Actually, since a fraction of the magnetic energy in the current sheets is transformed into heat and kinetic energy, we expect that B_x reaches, at most, a fraction of the order of unity of B_0 (under *ideal* conditions, i.e. if the aspect ratio of the current sheet is not arbitrary but scales with a certain power of the Lundquist number). We may quantify this effect evaluating the ratio B_x/B_0. For that, the quantities $\mathcal{A}_{\mathcal{B}}(t)$ (Eq. (7.33)) or $\mathcal{A}_{B_x}(t)$ (Eq. (7.34)) are well suited. We note that $\mathcal{A}_{B_x}(t)$ may take values (slightly) larger than 1 because of the growth of B_x in very localized regions of the reconnection layer. Before discussing the amplification factors for B_x or v, some considerations are in order. As we observe in Fig. 7.8 (upper right panel), the growth of $\mathcal{A}_{\mathcal{B}}(t)$ (and more evidently of $\mathcal{A}_{B_x}$) once the explosive phase begins is not totally smooth and, hence, it can possess several local maxima. If we use a different value to trace the growth of B_x, e.g. $\mathcal{A}_{B_x}(t)$, the time at which the peak of the latter variable happens does not exactly coincide with the peak time for the former one. The difference between the times at which the global maxima of $\mathcal{A}_{\mathcal{B}}(t)$ and of $\mathcal{A}_{B_x}(t)$ happen is small though. Thus, we define t_p as the time at which the global maximum of $\mathcal{A}_{B_x}(t)$ is measured, i.e. when $\mathcal{A}_{B_x}(t_p) = \tilde{\mathcal{A}}_{B_x}$. Likewise, the values of $\tilde{v}_p$ and $\tilde{\xi}_p$ may happen at times slightly different from t_p, but these differences are small and we discuss the results in the following assuming that all these quantities were roughly measured simultaneously, unless otherwise stated. In Table 7.3, we observe that for $n = 2$ and $v_{\rm A} = 0.5$, $\tilde{\mathcal{A}}_{B_x} \sim 1$, meaning that for models which undergo an explosive phase, B_x is amplified to values $\sim B_0$ from its initially negligible seed value. This is a very important result indicating that the reconnection proceeds very efficiently (nearly optimally) for RIDTMs.

In order to discuss whether relativistic outflows result from the models of RIDTMs, we track the evolution of $v_p(t)$ (Fig. 7.8 lower left panel). We can observe in that figure that around $t \simeq t_p$ also the velocities in the computational domain reach their maxima. Maximum values $\tilde{v}_p \simeq 0.7$ are reached for the model with $L_y \simeq 5.5$, which means that the fluid becomes superalfvénic for $t < t_p$. These qualitative results confirm what has been found in previous RRMHD simulations regarding the ability of producing high-speed channels, where plasma may flow at relativistic speeds (e.g. Baty et al., 2013; Del Zanna et al., 2016; Watanabe and Yokoyama, 2006; Zanotti and Dumbser, 2011; Zenitani et al., 2010).

We observe that in all models where an explosive phase takes place, the flows become superalfvénic during a time interval of variable duration, significantly depending on the value of n (Fig. 7.11 right panel). The maximum Alfvén number, attained during the explosive phase roughly at t_p, increases with increasing n (i.e. decreasing resistivity). Whereas for $n = 1$ the fluid becomes marginally superalfvénic at $t/t_{\rm A} \simeq 46$, maximum values $M_{\rm A} \lesssim 1.8$ are reached for $n = 4$, signaling the fact that Lorentz factors ~ 2.3 are locally

developed even in cases in which the Alfvén speed is moderately relativistic. It is interesting to notice that for all the cases with $n > 2$ the maximum Alfvén number attained by our RIDTM models is $M_{\rm A} \gtrsim 1.5$, whereas the RITM models of Del Zanna et al. (2016) yield $M_{\rm A} \lesssim 1.1$ for the same Alfvén speed of the background state (see Fig. 7 in Del Zanna et al., 2016). This is an indication that RIDTMs are more efficient in accelerating the fluid at superalfvénic speeds than RITMs. The places where superalfvénic conditions are met correspond to the twin channels emerging (almost vertically and in oposite directions) from the X-points formed in the course of the evolution. Actually, four main structures (relevant in terms of the dynamics of the reconnection process) form throughout the evolution (two per current sheet) following the vertical pattern observable in, e.g. the pressure distribution (Fig. 7.14 second column of panels). These structures look like Petschek-type profiles connecting X- and O-points (Petschek, 1964). After the linear phase, all these X- and O-points interact very strongly reaching the entangled configuration displayed in the upper panels of Fig. 7.15. There, we observe the thin sheets along with the larger velocities develop at a time $t \simeq t_p$. The velocity structure resembling a "Y" in the region $3.5 \lesssim y \lesssim 4.5$ and $0.25 \lesssim x \lesssim 0.5$, where the velocity maximum is attained is reminiscent from the previous Petschek-like structures.

In ideal (R)MHD, $\mathbf{E}\cdot\mathbf{B} = 0$, while resistive effects produce non-zero values of this quantity. In the left panels of Fig. 7.15, we show the magnitude of $\mathbf{E}\cdot\mathbf{B}$, which becomes significantly different from zero as the explosive phase proceeds and is also becomes even larger in the relaxation phase that follows (Fig. 7.15 lower left panel). The largest resistive effects in the explosive phase develop inside of O-points, which interact with their cousin structures in the adjacent current sheet (e.g. notice the two green-red ribbons in the region $0.5 \lesssim y \lesssim 3$; each of the two structures has grown from an O-point in a different current sheet). Regions of high current density map the structures where $\mathbf{E}\cdot\mathbf{B} \neq 0$ (compare left and right upper panels of Fig. 7.15). These regions are potential sites for particle acceleration by non-ideal electric fields along magnetic field lines (cf. Del Zanna et al., 2016). Looking at the current density component J_z (the dominant one), we observe that potential particle acceleration is more likely to happen along the channels of high-speed plasma and inside the larger plasmoids (where both the current density and $\mathbf{E}\cdot\mathbf{B}$ are larger). Interestingly, in the relaxed state, both the currents and the locations where $\mathbf{E}\cdot\mathbf{B} \neq 0$ run nearly parallel to the vertical direction and delimit the broad layer left after the explosive episode has taken place (Fig. 7.15 lower left and right panels).

In the explosive phase, the ratio $p_{\rm g}/\rho$ may develop peaks where it becomes larger than 1, i.e. where the thermodynamics is relativistic. We observe in Fig. 7.8 (lower right panel) that this is the case for all models that develop an explosive phase without a Rutherford phase ($L_y \gtrsim 4$), but not for other models (this is more clear in the model with $L_y = 3$). After peaking at $t \simeq t_p$,

the value of $\xi_p(t)$ lowers and sets to a value $\xi_p \sim 0.1 - 1$, rather independently of the vertical box size (if $L_y \gtrsim 3$). During the process of reconnection, plasma is heated up slightly during the linear phase, and very abruptly in the explosive phase. In Fig. 7.15 (second column, upper panel) we observe that there are several hot spots (dominating the evolution of $\xi_p(t)$) where plasma is significantly heated. These hot spots occupy a relatively small fraction of the total domain. Later, in the relaxation phase, there are nearly vertical filaments with the largest values of $p_{\rm g}/\rho$, occupying the broad central layer where $p_{\rm g}/\rho$ is $\sim 2 - 3$ times larger than in the background (initial) medium.

7.2.2.1 Dependence on the numerical resolution

In Sec. 7.2.1 we have shown that either using resolutions of 512×32 or 1024×16 uniform zones was sufficient to capture the growth rate of the RIDTM instability with an accuracy $\lesssim 10\%$ when we set up a single dominant mode in the computational box. Similar results hold for cases when $n = 2$ modes are considered (see, e.g. Tab. 7.3). However, the subsequent non-linear phase involves resolving smaller aspect ratios as a consequence of the cascade towards lower scales we mentioned at the beginning of Sec. 7.2.2. Typically, one expects to require higher numerical resolution to resolve the non-linear evolution of exponentially growing instabilities. However, we shall see that if we are interested in obtaining a *sufficiently accurate* value of the amplification factor of the magnetic field B_x or of the velocity field, the resolution that we have already used is high enough.

We show in Fig. 7.10 the evolution of $\mathcal{A}_{\mathcal{B}}(t)$ for our reference model with $n = 2$ modes, $L_y \simeq 5.22$ and $v_{\rm A} = 0.5$ run at different resolutions. Since models with $n = 2$ and the optimal vertical length fail before reaching the peak of the explosive phase (Fig. 7.10 blue solid line), we display, instead, the evolution of the models with $L_y = 5.5$ and $n_x = 1024$ (dot-dashed lines) for reference. These tests show that fixing the number of zones in the x-direction to a given value (e.g. $n_x = 512$) the maximum amplification during the explosive phase is properly captured with as little as $n_y = 32$ zones per dominant mode, if the numerical code uses the MP9 reconstruction algorithm. The value of t_p, is more sensitive to both the vertical resolution, but it is well captured for $n_y = 32$ zones per mode with an accuracy of $\lesssim 10\%$. This is also the trend found for other models including different number of dominant modes in the vertical direction (see the values of $\mathcal{A}_{B_x}$ in Tab. 7.3). Similar conclusions can be found for $\tilde{\xi}_p$. This is not the case for t_p, which happens $\sim 5\%$ earlier for a resolution of 512×64 uniform zones. For the model with 1024×64 uniform zones and $L_y = 5.5$, the results are very similar to those obtained for 512×128 cells and $L_y \simeq 5.22$. We must notice the slightly larger growth rate in the linear phase seems to bring the results run with 1024×64 zones

far from those computed with 512×128 zones due to the representation in logarithmic scale. However, the amplification factors are $\tilde{\mathcal{A}}_{\mathcal{B}} \simeq 0.21$ in both cases (regardless the differences in resolution and L_y; see Tab. 7.3). Among the models with $L_y = 5.5$ and $n_x = 1024$ zones and, at least 32 zones per dominant mode in the vertical direction, the amplification factors for B_x differ by less than $\sim 10\%$. Restricting to the case with $L_y = 5.5$, the values of $\tilde{v}_p$ seem to agree, within a $\sim 10\%$ accuracy when $n_x = 1024$ and n_y varies from 32 to 128 zones (Tab. 7.3). Since we do not aim to measure $\tilde{v}_p$ with a large accuracy, considering all the previous evidences, resolutions of 1024×64 (and even 512×128) suffice for the purpose of computing the amplification factors and t_p with accuracies $\lesssim 15\%$.

In the upper and lower rows of panels of Figs. 7.12, 7.13 and 7.14, we show the same model (corresponding to $L_y = 5.5$ and $n = 2$) but with different numerical resolutions in the vertical direction ($n_y = 64$ and 128). The third column of these figures is selected to coincide with the peak of the explosive phase. Since the value of t_p is slightly sensitive to the numerical resolution (see above), the times represented are not exactly the same. At first glance, it is evident that the gross morphology is already well captured in models with 1024×64 numerical cells, though finer structure shows up at higher resolution. Again, this hints that our reference numerical grid (1024×64 cells) is enough to describe the dynamics within an accuracy $\sim 10\% - 20\%$.

7.2.2.2 Dependence on the aspect ratio

We have also checked the dependence of the results on the vertical box size, L_y (fixing all other parameters, including a, S_a and l). In the simulations performed to compare closely with Baty (2017), the growth rate in the linear phase decreases as the vertical size of the computational domain is changed (either increasing or decreasing it) from the optimal value obtained for an optimal scaling (Eq. (7.20)) necessary to make the growth rate independent of $S_{\rm L}$. As a result, the growth rate is no longer *ideal* but smaller. This confirms the ideas of Pucci and Velli (2014) regarding ITMs, but applied to the case of DTMs. As already explained (see text above Eq. (7.15)) Pucci and Velli (2014) have suggested that current sheets may need to thin from aspect ratios $L/a \sim S^{\tilde{\alpha}}$ with $\tilde{\alpha} \simeq 0$ initially, to $\tilde{\alpha} = 9/29$ in order to yield a finite growth rate (i.e. $\gamma \tau_{\rm A} \sim \eta^0$) in the ideal (R)MHD regime. In classical incompressible MHD (Janvier et al., 2011) as well as in classical compressible MHD (Baty, 2017) a similar qualitative behaviour has been found.

Qualitatively similar results are obtained when we use a properly quantized computational domain to include an integer number of dominant modes in the vertical direction. We note, however, that the numerical dispersion relation displayed in Fig. 7.9 displays a relatively broad peak, implying that slightly

different values of ka close to the fastest growing mode basically have the same growth rate. Indeed, the cases $ka = 0.10$ and $ka = 0.12$, corresponding to $L_y = 6$ and $L_y \simeq 5.22$, nearly have identical growth rates within the measurement errors. This translates into a very similar evolution during the initial and linear phases of both models (compare the blue and yellow lines in Fig. 7.8). Likewise, the evolution in the non-linear phase is very similar.

There are small differences in the values of t_p (measured in units of t_c) that correlate with the exact time by which the explosive phase begins, which in turn depends on how far the model setup from the optimal (theoretical) value of $k_{\mathrm{RIDTM}}a \simeq 0.12$ is. However, when we measure t_p in units of t_{A} (as it is shown in Fig. 7.8), the differences are significant. For instance, when increasing the box length from $L_y = 1.5$ to $L_y = 20$ the peak shifts from $t_p \simeq 270t_{\mathrm{A}}$ to $t_p \simeq 10t_{\mathrm{A}}$ (Tab. 7.5), and we find that

$$t_p/t_{\mathrm{A}} \sim 8.5 + 23L_y^{-1/2}. \tag{7.41}$$

This approximate scaling relation suggests that making $L_y \gg 1$, the explosive phase may take place, at most, after $\sim 8.5t_{\mathrm{A}}$. But even this last result must be taken cautiously, since the scaling of Eq. (7.41) has only been tested for a single value $v_{\mathrm{A}} = 0.5$ and it is likely that relativistic effects modify this relation if $v_{\mathrm{A}} \to 1$.

Another important point is the fact that for aspect ratios sufficiently smaller than the critical one (reached for $L_y \simeq 5.22$), the explosive phase is absent in our models with $n = 2$. This can be seen in the time evolution of any of the quantities displayed in Fig. 7.8. For $L_y < 1.5$, the RDTM growth rate tends to decrease and there is no explosive phase (at least, not in the computed interval of time). The non-existence of the explosive phase for L_y smaller than a critical threshold was also found in classical incompressible MHD by Janvier et al. (2011) and also observed in compressible MHD by Baty (2017). Janvier et al. (2011) finds that the critical box size below which DTMs saturate and do not develop an explosive phase depends on the current sheets half-separation, l. From their Fig. 2, it is possible to find the following empirical function for the vertical box size that separates explosive from non explosive phases: $L_y \simeq 5.15l$. For the chosen value of $l = 5a = 0.25$ in our experiments, the result of Janvier et al. (2011) would imply that for vertical sizes $L_y \lesssim 1.3$, the explosive phase should be absent. Indeed, we observe the explosive phase for $L_y = 1.5$, but not for $L_y = 1$ in the simulated time. Taking into account that our RRMHD models are affected by the numerical diffusion of the background field (absent by construction in the models of Janvier et al., 2011), we conclude that our results in the relativistic regime are consistent with those in the classical MHD regime.

Whereas B_x decays after the explosive phase (Fig. 7.8 upper panels), the peak velocities are nearly sustained (Fig. 7.8 lower left panel) and superalfvénic

(Fig. 7.11 left panel) during a significant amount of time of the order of $t/t_{\rm A} \sim 4-8$ for models with $3 \lesssim L_y \lesssim 6$. As the vertical length increases, the peak velocities are sustained for shorter periods after t_p (see, e.g, the cases of $L_y = 10$ and, especially $L_y = 20$ in the lower left panel of Fig. 7.8).

The plasma heating in the explosive phase, traced by $\xi_p(t)$ (Fig. 7.8 lower right panel), displays a faster growth than $\mathcal{A}_{\mathcal{B}}(t)$, $\mathcal{A}_{B_x}(t)$ or $v_p(t)$ in the first part of the explosive phase, until the peak is reached. This initial growth rate in the explosive phase is smaller for the longer computational domains in the vertical direction. After the peak, there is also a fast decrease for models with $L_y \gtrsim 5.22$,[9] while it levels off for models with $L_y \lesssim 4$. The growth previous to the peak of $\xi_p(t)$ is faster for nearly optimal aspect ratios than for aspect ratios differing more from the optimal one. Indeed, the much faster growth of $\xi_p(t)$ is evident in Fig. 7.8 (lower right panel; solid blue line) in the model with $L_y \simeq 5.22$ prior to the peak of the explosive phase, and the reason for its numerical failure in models with $n_x = 1024$ zones.

We represent in Fig. 7.16 the amplification factors $\tilde{\mathcal{A}}_{\mathcal{B}}$, $\tilde{\mathcal{A}}_{B_x}$, $\tilde{v}_p$ and $\tilde{\xi}_p$ (the exact values can be found in Tab. 7.5). For $ka \gtrsim 0.42$ the explosive phase is absent in our experiments, while for $ka \lesssim 0.31$, corresponding to a model with $L_y = 2$, we observe such a phase (see the discussion on the reasons for this phenomenon in Sec. 7.2.2.2). For $ka \lesssim 0.31$, amplification factors $0.15 \lesssim \tilde{\mathcal{A}}_{\mathcal{B}} \lesssim 0.29$ and $0.51 \lesssim \tilde{\mathcal{A}}_{B_x} \lesssim 1.15$ are observed for the magnetic field component B_x (Tab. 7.5). As we have discussed before, the fact that $\tilde{\mathcal{A}}_{\mathcal{B}} \lesssim 1$ and also $\tilde{\mathcal{A}}_{B_x} \sim 1$ are clear indicators of saturation of the TM growth. It is important that these amplification factors do not only happen for the optimal aspect ratio but for a relatively wide range of aspect ratios about the optimal one namely, within a factor of ~ 10, since we observe the explosive phase for $2 \lesssim L_y \lesssim 20$ (corresponding to $0.03 \lesssim ka \lesssim 0.31$). The exact range of values of L_y (equivalently, of the aspect ratio) that yield an explosive phase has only been approximately computed. Both the lower and upper bounds of L_y are approximate, since for $L_y = 1.5$ there is no explosive phase (at least, in the computed time interval), but there may be values $1.5 < L_y < 2$ for which the explosive phase may also develop (perhaps, also for $L_y = 1.5$ if we wait long enough, i.e. for a time $t/t_{\rm A} \gtrsim 150$). Likewise, we have not explored values $L_y > 20$, which perhaps may also develop an explosive phase, but if they do, the amplification factors will be smaller than the ones found here. We note that $\tilde{\mathcal{A}}_{\mathcal{B}}$ and $\tilde{v}_p$ decrease with increasing L_y (i.e. decreasing values of ka). In contrast, the values of $\tilde{\xi}_p$ display a maximum around the critical aspect ratio of the computational domain, corresponding to $ka \simeq 0.12$ (Fig. 7.16 yellow symbols). Likewise, the values of $\tilde{\mathcal{A}}_{B_x}$ show a maximum at $ka \simeq 0.16$, but this

[9] For the optimal computational box we do not have data for high resolution grids with $n_x = 1024$, but the behaviour can be observed in models with 512×128 zones in Fig. 7.10.

quantity displays a rather variable behaviour around the peak of the explosive phase (see Fig. 7.8 upper left panel; solid green line), the accuracy with which it can be measured should not be taken to be better than $\sim 10\%$.

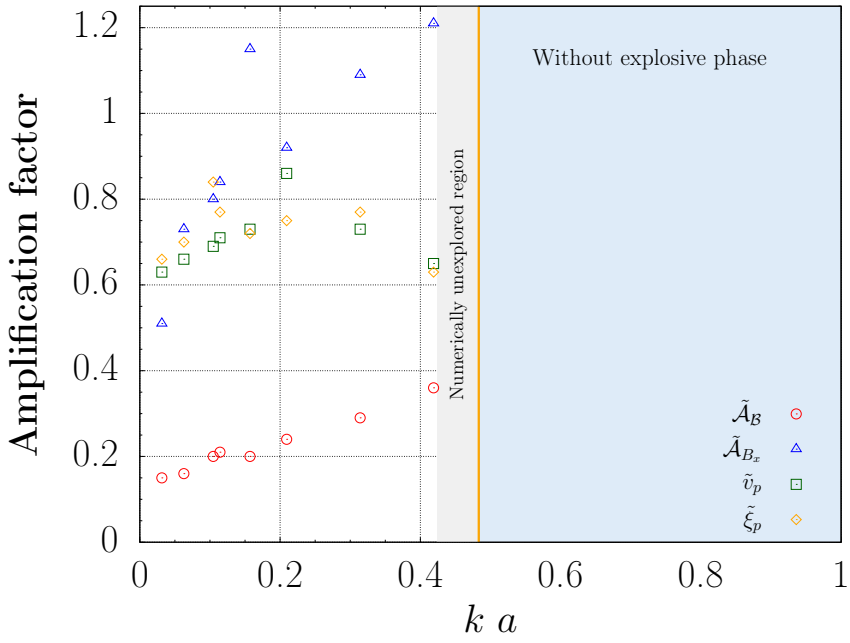

Figure 7.16: Magnetic field amplification in the explosive phase: Values of $\tilde{\mathcal{A}}_{\mathcal{B}}$, $\tilde{\mathcal{A}}_{B_x}$, $\tilde{v}_p$ and $\tilde{\xi}_p$ as a function of ka for models where we set $n = 2$ dominant modes in the vertical direction of the computational domain. The region filled with a blue background shows the set of values of ka for which the explosive phase is not present in our numerical models. All models are computed with a grid of 1024×64 uniform zones.

7.2.2.3 Dependence on $v_{\rm A}$

In the previous sections we have explored in detail models in which $v_{\rm A} = 0.5$. This is a moderately relativistic speed that permits comparing our results to preexisting ones in the literature for IDTMs in classical MHD, as well as to another code (Aenus) that we have available. Although the time restrictions to finish this Ph.D. prevent us to perform a through analysis of the results in the ultrarelativistic regime ($v_{\rm A} \simeq 1$), we can advance some relevant features we have found for the case in which $v_{\rm A} = 0.82$. For a later reference, we write down the parameters of the model with $v_{\rm A} = 0.82$, where we have taken $B_0 = \sqrt{10}$, $p_0 = 1$, $\rho_0 = 2.5$ and $\eta = 8.17 \times 10^{-6}$, which yields $\sigma_0 = 4$, $\beta_0 = 0.2$ and $S_a = 5000$. We note that we use again a setup similar to that employed to compare with Baty (2017). This is because it easies the comparison of our results with the ones obtained with the Aenus code.

Table 7.5: Several quantities characterizing the dependence of our models with the aspect ratio L/a. For fixed $a = 0.05$, we vary $L_y = 2L$ obtaining distinct values of L/a. From left to right the columns list, L_y, the peak time for $\mathcal{A}_{\mathcal{B}}$ normalized to $t_{\rm A}$, $t_p/t_{\rm A}$, the peak time for $v_p(t)$ (Eq. (7.37)) normalized to $t_{\rm A}$, $t_p^*/t_{\rm A}$, the growth rate in the linear phase, γ, $\tilde{\mathcal{A}}_{\mathcal{B}}$ (Eq. (7.35)), $\tilde{\mathcal{A}}_{B_x}$ (Eq. (7.36)), $\tilde{v}_p$ (Eq. (7.38)), $v_p(t_p^*)$ and $\tilde{\xi}_p$ (Eq. (7.40)). In all models we set up $n = 2$ dominant modes, $v_{\rm A} = 0.5$ and the a grid of 1024×64. The results within parenthesis are shown for the model with $L_y \simeq 5.22$, since it fails before reaching the peak of the explosive phase. Thus, the amplification factors are lower bounds of the ones corresponding to that vertical computational box length.

L_y	$t_p/t_{\rm A}$	$t_p^*/t_{\rm A}$	γ	$\tilde{\mathcal{A}}_{\mathcal{B}}$	$\tilde{\mathcal{A}}_{B_x}$	$\tilde{v}_p$	$\tilde{v}_p(t_p^*)$	$\tilde{\xi}_p$
1.5	269.3	272	0.0345 ± 0.0015	0.36	1.21	0.57	0.65	0.63
2	155.5	155	0.0462 ± 0.0018	0.29	1.09	0.62	0.73	0.77
3	62.7	63	0.0551 ± 0.0014	0.24	0.92	0.62	0.86	0.75
4	34.8	34.8	0.0649 ± 0.0016	0.20	1.15	0.73	0.73	0.72
5.22	(25.3)	(25.3)	0.0704 ± 0.0016	(0.22)	(0.92)	(0.50)	(0.50)	(0.74)
5.5	24.9	24.9	0.0759 ± 0.0015	0.21	0.84	0.71	0.71	0.77
6	21.2	21.3	0.0764 ± 0.0015	0.20	0.80	0.69	0.72	0.84
10	14.8	14.7	0.0667 ± 0.0013	0.16	0.73	0.66	0.69	0.70
20	9.6	9.8	0.0478 ± 0.0007	0.15	0.51	0.63	0.80	0.66

Table 7.6: Properties of various models set up with $l/a = 5$. From left to right the columns list the Alfvén velocity, the number of grid cells, the Lundquist number relative to L ($S_{\rm L,5} = S_{\rm L} \times 10^5$), the Lundquist number relative to a ($S_{a,3} = S_a \times 10^3$), the conductivity ($\sigma_5 = \sigma \times 10^5$), the maximum growth rate, the maximum growth multiplied by the light crossing time of the sheet length ($\gamma_{\rm RIDTM} t_c$), the maximum growth multiplied by the Alfvén crossing time of the sheet length ($\gamma_{\rm RIDTM} t_{\rm A}$) and the combination $\gamma_{\rm RIDTM} t_{\rm A} W_{\rm A}^{1/2}$.

L	$v_{\rm A}$	$n_x \times n_y$	$S_{\rm L,5}$	$S_{a,3}$	σ_5	$\gamma_{\rm RIDTM} t_c$	$\gamma_{\rm RIDTM} t_{\rm A}$	$\gamma_{\rm RIDTM} t_{\rm A} W_{\rm A}^{1/2}$
1.25	0.50	512×32	2.3	5.0	2.00	0.111 ± 0.014	0.22 ± 0.03	0.24 ± 0.03
1.25	0.50	512×64	2.3	5.0	2.00	0.111 ± 0.011	0.22 ± 0.023	0.238 ± 0.024
1.25	0.82	512×32	2.3	5.0	1.23	0.143 ± 0.003	0.174 ± 0.003	0.230 ± 0.004
1.25	0.82	512×64	2.3	5.0	1.23	0.143 ± 0.004	0.174 ± 0.005	0.230 ± 0.006
2.61	0.50	512×128	3.4	6.6	2.62	0.068 ± 0.005	0.136 ± 0.010	0.146 ± 0.011
2.61	0.50	1024×64	3.4	6.6	2.62	0.091 ± 0.008	0.183 ± 0.016	0.196 ± 0.017
2.61	0.82	512×128	3.4	6.6	1.61	0.117 ± 0.004	0.143 ± 0.005	0.189 ± 0.006
2.61	0.82	512×256	3.4	6.6	1.61	0.120 ± 0.004	0.146 ± 0.005	0.193 ± 0.006

Running our models with higher values of $v_{\rm A}$ turned out to be problematic with the typical resolutions employed in the previous sections. We have tried to run cases with $0.5 \lesssim v_{\rm A} \lesssim 0.82$, but all these models tend to fail when arriving to the explosive phase. The amount of time in the explosive phase that we have been able to compute is larger as the value of $v_{\rm A}$ decreases. For the particular case of $v_{\rm A} = 0.82$, we have been able to run our models only for $\sim 2t_c$ after entering in the explosive phase. Contrarily, for $v_{\rm A} \simeq 0.7$ we

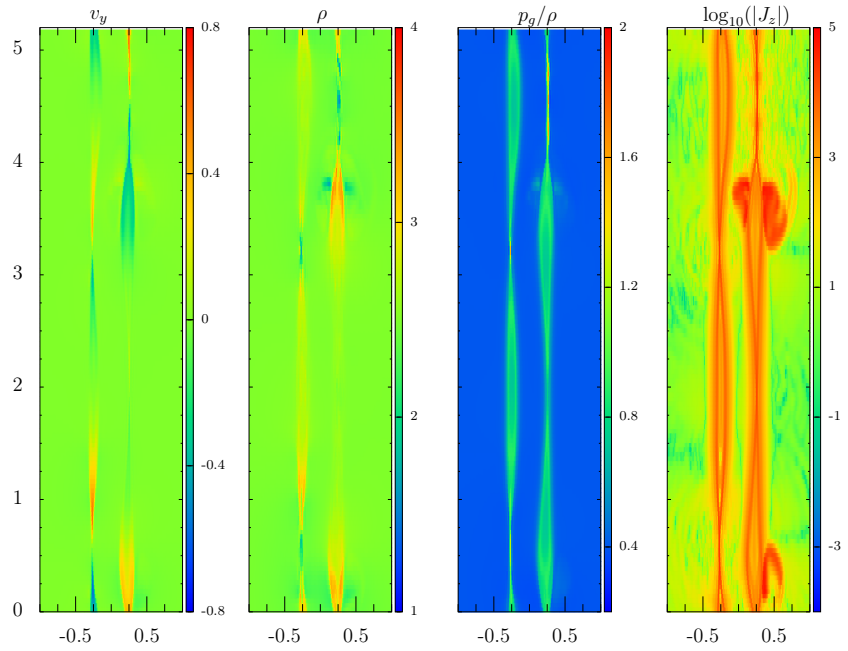

Figure 7.17: From left to right, snapshots of v_y, ρ, p_g/ρ and $\log_{10}(|J_z|)$ for a model run with $v_A = 0.82$, $n = 2$ dominant modes and employing a grid of 512×128 uniform cells right before code failure at the beginning of the explosive phase ($t/t_A \simeq 23$).

have been able to run for $\sim 10t_c$ after the beginning of the explosive phase, namely, *nearly* up to the peak of the explosive phase (we cannot be totally sure because the growth of the various quantities used to track the evolution of the models may show various local maxima in that phase). The numerical problems that we face arise from the plasma starvation at X-points. There, we may recognize dynamics which shares some similarity to that of Petscheck reconnection (Petschek, 1964). In Figure 7.17 (left panel), we observe almost twin high-speed jets originating from a couple of X-points (each in a different current sheet). The plasma flows mainly vertically along both narrow exhausts while, at the same time, the outflows are constituted by two parallel streams of oposite charge flowing along the vertical electric field (E_y), that also displays a similar dual structure with antiparallel components on both half-sides of the streaming jets. The influx of mass from the sides is insufficient to compensate the mass flux along the jets and the X-points begin a phase of progressive rarefaction (both rest-mass density -see Fig. 7.17; second panel on the left-, and thermal pressure become very small). At the same time, the current flowing from the X-points to the O-points rises very steeply (Fig. 7.17 right panel) and, since the flux of current is so large, it accumulates on the lateral boundaries of some of the O-points. Eventually, the current density is so large that it leads

our RRMHD code to fail. Significantly, in classical resistive MHD, this effect does not happen or, at least, it is not so intense to bring the Aenus code to fail. We have tried several strategies to cure this pathology (e.g. using density and pressure *floors*, employing higher order partly implicit time-integrators -e.g. the third-order RK36$\mathcal{S}_E$ time-integrator-), but only increasing sufficiently the resolution seems to ameliorate the problem. We estimate that larger values of $v_{\rm A}$ require grids which are, at least, 10 times finer in the horizontal direction and about 4 times finer in the vertical direction. Such simulations require ~ 80 times more computational time than the ones with the previous resolution and, hence, they are prohibitive (so far) for a carefull parameter exploration. Thus, the rest of this section must be taken as preliminary results, which need confirmation once new higher resolution models are available.

The first relevant question to address is whether in the relativistic regime the IDTM independence of the growth rate on the Lundquist number still holds, i.e. $\gamma_{\rm RIDTM} t_{\rm A} \simeq \alpha_{\rm ridtm}$ (in analogy to Eq. 7.22) or, whether $\gamma_{\rm RIDTM} t_c \simeq 0.27$, as proposed by Del Zanna et al. (2016) for single RITMs.[10] A preliminary answer to this question can be deduced from Tab. 7.6, where the value of $\gamma_{\rm RIDTM} t_{\rm A} \simeq 0.2$ with an accuracy of $\sim 35\%$. This would mean that we find that $\gamma_{\rm RIDTM} t_{\rm A} \simeq$ constant as Baty (2017), but our constant is about twice smaller than in that publication. We cautiously notice that our results may be dominated by the numerical diffusion of the background field, especially important when the Alfvén velocity approaches the speed of light, as it has been shown in Sec. 6.3.1.3. Thus, we repeat that our conclusions are preliminary.

The alternative possibility, suggested by Del Zanna et al. (2016) (but in a different physical experiment) would be that $\gamma_{\rm RIDTM} t_c \simeq 0.27$. In view of the data of Tab. 7.6, our results suggest

$$\gamma_{\rm RIDTM} t_c \simeq 0.1. \tag{7.42}$$

The scaling of Eq. (7.42) estimates the maximum growth rate with an accuracy $\lesssim 35\%$. Alternatively, looking at the last column of Tab. 7.6, we may suggest

$$\gamma_{\rm RIDTM} t_{\rm A} W_{\rm A}^{1/2} \simeq 0.2, \tag{7.43}$$

where $W_{\rm A} = 1/\sqrt{1 - v_{\rm A}^2}$. The accuracy of Eq. (7.43) is $\lesssim 25\%$. Indeed, the accuracy is probably better ($\sim 5\%$) if we take into account only the values provided by the simulations with the finer resolutions (1024×64), which possess the smaller numerical diffusion of the background magnetic field. However, Eq. (7.43) does not have an easy physical interpretation and is based on relatively few observations. We defer to a future study exploring the relevance of the scaling suggested by our data.

[10] Del Zanna et al. (2016) also find that the scaling law of Baty (2017) approximately holds, since they conclude that $\gamma_{\rm RIDTM} t_{\rm A} \simeq 0.6$ (note that $\alpha_{\rm IDTM} \simeq 0.55$).

Chapter 8

Conclusions and outlook

In this thesis, we have tried to accomplish two types of goals that we have outlined in Sec, 1.2, namely, computational and astrophysical ones. For this end, we have developed a new code (Cueva), based upon state-of-the-art numerical methods, to deal with the stiffness of the balance laws of the *augmented* system of equations of RRMHD (the most salient features of the new code are summarized in App. A). This code is based on a finite volume method for discretization of the space-time and incorporates the approximate Riemann solvers, LLF, HLL, and HLLC, as well as intercell reconstruction methods like MML, MCL, MP5, MP7 and MP9. The time integration techniques implemented deal with the stiffness of the RRMHD system, present in the limit of infinite conductivity, i.e. in the ideal regime. These time-integrators belong to the families of RKIMEX and MIRK methods. In Chap. 4, we have presented a series of 1D and 2D standard numerical experiments in which we validate the numerical algorithms implemented, exploring different conductivity regimes from a (strongly) resistive ($\sigma = 10$) to an almost ideal one ($\sigma = 10^9$). Also, we have demonstrated the shock capturing capabilities of our algorithm in 1D shock tube tests. In the same way we study the properties of the divergence cleaning technique in the 2D tests (RR and CE) by examining different values of the two parameters that control the solenoidal magnetic field and $\nabla \cdot \mathbf{E}$ constraints, that is for $\aleph_\phi$ and $\aleph_\psi$ (Eq. (4.47)) finding empirically that values of $\aleph \gtrsim 1$ yield the best results. However, values $\aleph \gg 100$ result in fatal numerical errors providing wrong dynamics. This is mainly due to the fact that the equations of the scalar potentials also become stiff if $\aleph \gg 1$.

With the goal of improving one of the most important building blocks of RRMHD codes (i.e. the Riemann solver), we have studied the characteristic properties of the augmented RRMHD system (Chap. 3), obtaining a self-similar solution for smooth flows inside of rarefaction waves in the limit of vanishing

conductivity (Sec. 3.2), i.e. for the homogeneous set of RRMHD equations. For this system of homogeneous equations, we have also recovered the characteristic speeds for RRMHD, which coincide with the ones found by Cordero-Carrión et al. (2012). We have further computed the RH jump conditions across generic shocks in RRMHD, the modifications included in the previous jump conditions by the presence of singular source terms, as well as the Lichnerowicz adiabat. We have shown that it is possible to recover the equivalent jump conditions in ideal RMHD (Giacomazzo and Rezzolla, 2006; Romero et al., 2005), i.e. when $\sigma \to \infty$, from the ones obtained in RRMHD.

Although we plan to use the obtained RH conditions to develop an approximate two-shock Riemann solver for the augmented RRMHD system in a future work, in this thesis we have developed a new approximate HLLC solver for RRMHD (Chap. 5). The new solver exactly captures isolated stationary contact discontinuities, improving on the single state HLL solver, which in RRMHD reduces to a LLF Riemann solver. The new HLLC solver does not need to distinguish between the cases in which the magnetic field perpendicular to a discontinuity is zero or not (differently from other HLLC solvers in RMHD; see, e.g. Mignone and Bodo, 2006) and thus it does not suffer from any pathological singularity when the component of the magnetic field normal to a zone interface approaches zero. Several test problems in 1D and 2D show that the HLLC scheme displays a smaller numerical diffusion than the HLL approximate Riemann solver in tests involving shocks or contact discontinuities. The computational overhead with respect to the simpler HLL solver is very modest and its implementation in existing RRMHD codes is straightforward.

The new HLLC solver has shown its capability to resolve strong shocks in 2D tests and a good behavior in different conductivity regimes. For most of the numerical experiments including discontinuities (i.e. Riemann problems) in the plasma, the results are insensitive to the exact value of the conductivity when $\sigma \gtrsim 10^6$ for a large enough resolution. We take this as an indication of the fact that the numerical resistivity of our algorithm is $\lesssim 10^{-6}$ if the grid spacing is $\Delta x \lesssim 1/400$ in the typical 1D Riemann problems usually taken as tests beds for RMHD. Also, this result justifies our choice of a default conductivity ($\sigma = 10^6$) to address the ideal RMHD regime in most of the numerical benchmarks that we have conducted involving shocks or other flow discontinuities.

We find that the models run with the HLLC solver are $\sim 5\% - 20\%$ computationally more expensive than those employing the HLL solver (Tab. 5.1). These results hold for both 1D and 2D simulations. The variations in the computational time are closely related to the different number of iterations necessary to solve numerically the quadratic equation Eq. (5.22). In view of the fact that the L1-norm errors are systematically smaller employing the HLLC solver than the HLL solver, and also considering the small computational overhead that the HLLC solver introduces, we conclude that the new HLLC solver is a

viable alternative to the very broadly used HLL solver.

Moreover, we have assessed the performance of different time-integration algorithms to deal with the potential stiffness of the RRMHD equations in the high-conductivity limit. When spatial discretization errors dominate the global error (when either the resolution is coarse or when the intercell reconstruction algorithms are of low numerical accuracy, e.g. for MLL or MCL, which are second order accurate), most partly implicit time-integrators are adequate for the numerical solution of the RRMHD equations (even up to $\sigma \gtrsim 10^6$). This means that all the tested time-integrators tend to converge under grid refinement roughly at the formal order of accuracy with which they are designed. However, in the cases, when time discretization errors dominate the global error, which is the usual situation when we either have fine numerical resolutions or employ high order methods for the intercell reconstruction, a diversity of results has been found (Chap. 6). When the Alfvén speed is non-relativistic, the smaller the physical resistivity, the smaller the resolution below which the time-discretization errors dominate. Furthermore, the slope of the (assumed) power-law dependence (q) of the numerical resistivity on resolution ($\eta^* \propto (C_{\rm CFL}\Delta x)^q$) is smaller than the theoretical order of accuracy of the time-integrators employed. Among all the methods used, the RK36$\mathcal{S}_E$ time-integrator is the one that has the largest values of q, even though in this RKIMEX scheme, we observe a degradation of the theoretical order of convergence ($q_{\rm th} = 3$) by one unit (i.e. $q \simeq 2$ in the regime dominated by time-discretization errors). We notice this degradation of the order of convergence also employing RKIMEX methods specifically tailored to be uniformly convergent in (much) simpler systems of stiff ODEs (e.g. the case of the SSP2(332)-LUM time-integrator). Given the larger numerical cost of the RK36$\mathcal{S}_E$ time-integrator in comparison with the SSP2(332)-LUM time-integrator, we have used the latter by default in astrophysical applications, reserving the former for special cases.

We have found some hints pointing towards the possibility that the MIRK2 time-integrator can be improved. First, the decrease of the errors in the CPAW test run with the MIRK2 time-integrator and second-order accurate intercell reconstruction is less monotonic than when performing the same test with the RKIMEX SSP2(332)-LUM time-integrator (Fig. 4.7). Second, the significantly larger amount of dissipation of some electric field components in the RR test for intermediate to large resistivity regime ($10^{-3} \lesssim \eta \lesssim 0.1$; Fig. 4.17 lower panels). Third, the degradation of the method-order (w.r.t. the theoretical value), q, ($\eta^* \propto (C_{\rm CFL}\Delta x)^q$) is higher for MIRK2 than for MIRK1 or any other RKIMEX method for intermediate to small values of the resistivity $10^{-10} \lesssim \eta \lesssim 10^{-4}$ in the MD test (Fig. 6.4 upper right panel). Fourth, the asymptotic (i.e. for very high resolutions) value of the numerical diffusivity $\xi^* \lesssim \eta$ found in the classical CPAW test at the finer grid resolutions (Fig. 6.5

upper left panel). Fifth, the negative values of the numerical diffusivity found in the relativistic CPAW test (e.g. Fig. 6.7 left panel), which may eventually lead to a code failure for moderately relativistic values of the Alfvén speed ($v_\mathrm{A} \gtrsim 0.5$; e.g. Fig. 6.11 left panel) as a result of the amplification of numerical errors, which render the method unstable to (numerical) perturbations that seem analogous to (physical) parametric instabilities (Fig. 6.10).

To characterize the numerical methods employed, we study the dependence of the numerical diffusivity on the grid resolution. For that, we make an ansatz about how the numerical diffusivity depends on Δx, on the order of accuracy of the spatial intercell reconstruction and of the time-integrators employed, as well as on the characteristic velocity and length scale of the system (Eqs. (6.1), (6.1)). This ansatz is the same as proposed by Rembiasz et al. (2017) in classical, Eulerian, resistive-viscous MHD using explicit time-integrators. Our main finding in this context is that the same ansatz also mostly works for Eulerian RRMHD codes. The deviations from the ansatz stem from the fact that we need to use partly implicit methods in RRMHD due to the stiffness of the system of equations as $\sigma \to \infty$. These partly implicit methods may suffer a degradation of the order of convergence depending on the value of the stiffness parameter (η in the case at hand), which can be problem- and variable-dependent (e.g. Boscarino and Russo, 2007, 2009). The ansatz for the numerical diffusivity proposed in Chap. 6 does not include such a degradation of the order of convergence. However, the ansatz proposed by Rembiasz et al. (2017) is presumably universal for time-integration methods that minimize the degradation of the order of accuracy in the regime dominated by time discretization errors. This makes us confident that it can be used to estimate dissipation coefficients for other flows.

In the study of numerical errors carried out in Chap. 6, we focus on those that manifest smearing out the solution, known as *numerical dissipation* and we neglect the effects of phase errors or *numerical dispersion*. The importance of these studies lies in the ability to discern what aspects of the numerical solution are driven by physical dissipation and which ones result from the numerical dissipation (i.e. numerical resistivity or numerical viscosity). Although the system of RRMHD equations does not include physical shear viscosity explicitly, the numerical methods used, introduce some amount of numerical viscosity. In fact, we found through the VSL test (Sec. 6.1.1) that the intrinsic numerical viscosity (i.e. using the MIRK2 time-integrator, the HLLC Riemann solver and the MP9 intercell reconstruction) is $\nu^* \lesssim 10^{-5}$ and $\nu^* \lesssim 10^{-10}$ for grid resolutions $\Delta x \lesssim 1/16$ and $\Delta x \lesssim 1/128$, respectively, if we use any of the monotonicity preserving intercell reconstruction algorithms (MP5, MP7 or MP9). Indeed, the VSL test clearly shows the advantage of employing the MP9 intercell reconstruction, since the numerical viscosity measured is as small as $\nu^* \sim 10^{-8}$ already for grids with $\Delta x \lesssim 1/16$.

To determine the numerical resistivity of the implemented methods, we consider the MD test (Sec. 6.2.1), where a pure resistive diffusion process is present in the absence of a plasma flow. The intrinsic numerical resistivity when using the MIRK2 time-integrator, the HLLC Riemann solver and the MP9 intercell reconstruction is smaller than the physical resistivity if $\eta \gtrsim 10^{-2}$. For smaller values $\eta \lesssim 10^{-2}$, we can always find a grid resolution, $(\Delta x)_{\rm o}$ such that $\eta^*(\Delta x \leq (\Delta x)_{\rm o}) < \eta$. In practical terms, this means that for resistivities smaller than 10^{-6}, using a grid resolution $\Delta x \lesssim 1/16$, the numerical resistivity is sufficiently small to not affect significantly the computational results (if the MP9 intercell reconstruction is used).

For the determination of the numerical diffusion, which we assume (as a simple working hypothesis) that it is the sum of the numerical viscosity and resistivity ($\xi^* = \nu^* + \eta^*$), we perform the CPAW tests for different values of the Alfvén speed (Sec. 6.3.1). Two prototype cases have been considered, a *classical* one, corresponding to a low Alfvén velocity ($v_{\rm A} = 10^{-4}$) and a *relativistic* case with a moderate Alfvén velocity ($v_{\rm A} = 10^{-1}$). We have also explored larger values of Alfvén velocity (i.e. $v_{\rm A} \lesssim 0.91$), which only work without code failures using selected RKIMEX time-integrators and relatively large resistivity alues ($\eta \gtrsim 10^{-4}$. The purpose of choosing these moderate Alfvén speeds (compared to the speed of light) was to be either clearly in the Newtonian regime (the case of the classical CPAW tests of Sec. 6.3.1.1) or in the mildly relativistic regime (the case of the relativistic CPAW tests of Sec. 6.3.1.2), with the aim of using the Newtonian results of Campos (1999) for the damping rate (Eq. (6.30)). As a byproduct of our work, we have assessed the functional dependence of the damping rate of Alfvén waves on the resistivity obtained by Campos (1999) in the relativistic regime (Sec. 6.3.1.3). We have obtained a power-law dependence of ξ^* as a function of the physical resistivity whose power-law slope is $a \simeq 1$ (Fig. 6.11), at least when the physical resistivity is large enough, demonstrating the validity of the damping rate of Campos in the relativistic regime.

The CPAW tests have turned out to be the more demanding ones when the Alfvén velocity becomes relativistic. They reveal that with the current numerical methods and formulation of the RRMHD equations, approaching the limit $v_{\rm A} \sim 1$ is only possible if the physical resistivity is moderate (e.g. $\eta \gtrsim 10^{-5}$) and the time-integrator possesses sufficiently high order or it is uniformly convergent. In this regard, the SSP2(332)-LUM time-integrator (which is uniformly convergent) provides relatively good results when the Alfvén speed is (ultra-)relativistic. This is also the case of the RK36$\mathcal{S}_E$ time-integrator due to its formal third-order accuracy.

An interesting result of the code verification is that the characteristic velocity of all the systems that we have explored is the light speed in RRMHD (i.e. $\mathcal{V} = 1$; Sec. 6.4 and App. E). This is significantly different from classical resistive MHD (Rembiasz et al., 2017), where either $\mathcal{V} = c_{\rm s}$, for tests in which

the magnetic field is zero (e.g. the damping of sound waves), or $\mathcal{V} = v_{\rm fms}$, in the rest of the cases (even in tests involving the damping of Alfvén waves, for which a naive expectation would be that $\mathcal{V} = v_{\rm A}$). The practical consequence of this finding is that the numerical diffusivity becomes larger in a RRMHD code than in a purely classical MHD code (especially in systems, in which all fluid and wave velocities are much smaller than the speed of light). We shall notice that η^* and ν^* are both proportional to the characteristic speed, i.e. $\nu^* \propto \mathcal{V}$ and $\eta^* \propto \mathcal{V}$, as indicated by the proposed ansatzs for each of these numerical diffusivities, Eq. (6.1) and Eq. (6.2), respectively. In the cases in which the fast magnetosonic speed is relativistic (either because the sound speed, or the Alfvén velocity or both $c_{\rm s}$ and $v_{\rm A}$ are close to the light speed), the difference between having $\mathcal{V} = 1$ or $\mathcal{V} = v_{\rm A}$ makes a small contribution to the numerical diffusivity. However, if either $c_{\rm s} \ll 1$ or $v_{\rm A} \ll 1$, the numerical diffusivity of a RRMHD code may be huge compared with an equivalent code in classical MHD.

The so far discussed studies (worth a separate publication in the nearest future) were a necessary step toward the main goal of this thesis, which is numerical studies of resistive plasma instabilities in astrophysical plasmas.

Looking for a possible mechanism that accelerates the reconnection rate in plasma of astrophysical interest, in the framework of single fluid RRMHD, we have studied in detail RIDTMs. These TMs can grow in two (or more) close enough parallel current sheets with *critical* aspect ratios $L/a = S_{\rm L}^{9/29}$ at a rate that is independent of the resistivity if $S_{\rm L} \gg 1$. Similarly, TMs can grow at a rate that is independent of the resistivity in a single current sheet with an aspect ratio $L/a = S_{\rm L}^{1/3}$. While the latter possibility has already been addressed by means of RRMHD numerical simulations (Del Zanna et al., 2016), the former has only received some attention in the classical MHD case (e.g. Baty, 2017).

One may wonder whether this is simply an academic problem as requiring that the aspect ratio of a current sheet is exactly set by the power of the Lundquist number stated above seems somewhat *ad hoc*. However, Pucci and Velli (2014) argue that the natural evolution of a current sheet drives a *thinning* process whereby the aspect ratio, initially likely independent of the Lundquist number or, perhaps being $L/a \sim S_{\rm L}^{\alpha}$, with $\alpha \gtrsim 0$ grows (i.e. the current half-thickness a decreases and, hence, α grows). In the absence of any ideal aspect ratio, the current sheet would thin until, $L/a \sim S_{\rm L}^{1/2}$, i.e. until the current sheet adopts the classical SP aspect ratio. *Before* thinning that much, the current sheet may develop aspect ratios $L/a \sim S_{\rm L}^{\alpha}$, with $\alpha \sim 1/3$. This means that the ideal conditions for the growth of TMs are reached *before* SP reconnection may set in. To see clearly this point, we note that the Lundquist number in many astrophysical environments may be as large as 10^{12}. Thus, $S_{\rm L}^{1/3} \sim 10^4$, while

$S_{\rm L}^{1/2} = 10^6$, meaning that current sheets 100 times thicker than needed for the initiation of the reconnection due to the SP mechanism become unstable to ITMs. In the relativistic regime, the same process explains why either RITMs or RIDTMs are so interesting, since conditions for the growth of ITMs should set in as current sheets shrink from their initially large aspect ratios well before other, much slower, reconnection mechanisms take place in the system.

In Chap. 7 we have first calibrated our RRMHD code comparing the results of our simulations of RITMs to those of Del Zanna et al. (2016). The obtained dispersion relation (Fig. 7.5) is fully compatible with that of Del Zanna et al. (2016). Both, the peak of the numerical dispersion relation and the dimensionless wavenumber at which the maximum growth rate is found are consistent with the theoretical solution of the dispersion relation, if we take into account the (physically unavoidable) numerical diffusion of the background magnetic field.

The reassuring results obtained for RITMs allow us to face the study of RIDTMs with confidence. As mentioned before, the growth rate of IDTMs becomes independent of the resistivity in classical resistive MHD (Baty, 2017). In order to test whether this is also the case in RRMHD, as a first step, we have set up models which are moderately relativistic ($v_{\rm A} = 0.5$), thus allowing us to compare our RRMHD results with those of Baty (2017) and, more importantly, to cross check them with a different classical viscous-resistive code (Aenus). We confirm (using both Cueva and Aenus codes) that RIDTMs grow in RRMHD under similar conditions like in classical resistive MHD. Moreover, the evolution proceeds in roughly the same stages as found by (Baty, 2017). First, there is a transitory phase where the initial perturbations trigger (the eigenfunctions of) the instability. Second, a linear phase of exponential growth of the instability sets in. We observe in this phase, e.g. the growth of the magnetic field component perpendicular to the current sheets (namely, B_x), which is initially negligible compared with the magnetic field component parallel to the current sheet. At the same time also the velocity in the region affected by the magnetic field reconnection, as well as the internal energy grow. Third, some models with adequate aspect ratios (L/a) develop an explosive phase. As our models enter the explosive phase, the plasma becomes superalfvénic in a number of localized regions, which resemble the typical sites of Petschek reconnection. The time at which the maximum amplification of the magnetic field happens in the explosive phase scales, roughly as $t_p \propto L_y^{-1/2}$. Fourth, the system relaxes and B_x decreases to values which are similar to those reached by the end of the linear amplification phase. In our models, a Rutherford phase bridging the end of the linear phase and the beginning of the explosive phase is not clearly identifiable, with the exception of models with an aspect ratio in the borderline between developing or not developing an explosive phase.

Baty (2017) finds that the growth rate of the dominant IDTMs is $\gamma_{\rm IDTM} t_{\rm A} \simeq \alpha_{\rm IDTM}$ with $\alpha_{\rm IDTM}$ being a constant that mostly depends on the initial separation of the current sheets, precisely, on the ratio l/a (for our models, $l/a = 5$, $\alpha_{\rm IDTM} \simeq 0.55$). Our preliminary results are compatible with the possibility that $\gamma_{\rm IDTM} t_{\rm A} \sim \alpha_{\rm RIDTM}$, with $\alpha_{\rm RIDTM} \sim 0.2$, with a moderate accuracy $\lesssim 35\%$. This means that RIDTMs grow on time scales $\sim 5 t_{\rm A}$, i.e. extremely rapidly, opening the prospects for potential applications in astrophysical systems where explosive reconnection dynamics is invoked. Our results may (to some extent) be influenced by the unavoidable numerical diffusivity present in all simulations. To further reduce the numerical diffusivity we would need to perform additional very high resolution simulations. Unfortunately, this was not possible because of limited computational resources and a limited time frame in which this thesis had to be finished (but see below in the outlook). This means that, very likely, the growth of RIDTMs is possible on time scales of $\sim t_{\rm A}$ or, perhaps, even smaller.

We have also preliminary found that $\gamma_{\rm RIDTM} t_c \simeq 0.1$, to be compared with $\gamma_{\rm RITM} t_c \simeq 0.27$ found by Del Zanna et al. (2016) for RITMs. The accuracy with which our result holds is somewhat large ($\lesssim 35\%$) if we consider globally our results at various numerical resolutions. However, restricting to the cases with the finer grids (i.e. the more reliable cases), the accuracy of the prediction is likely larger ($\sim 5\%$).

We have characterized numerically the criteria under which an explosive phase of reconnection may ensue the linear growth phase of RIDTMs. This is a necessary step to be able to understand whether the conditions for an explosive reconnection phase may happen (at all) in astrophysical plasma. We find that an explosive phase develops for computational boxes with $1.5 < L_y < 20$ (corresponding to current sheets aspect ratios $15 < L/a < 200$ (see Fig. 7.6) or, equivalently for $0.03 \simeq ka \simeq 0.42$). Both the lower and upper limits of the values of L_y that yield an explosive phase are only upper and lower bounds, respectively, of the true values. It is likely that an explosive phase may also develop in boxes with $1 < L_y < 1.5$ (the case $L_y = 1$ does not develop an explosive phase, at least, during the interval of time we have followed this model) and, likewise, for $L_y > 20$ the explosive phase may also take place, though the amplification factors of the magnetic field tend to decrease with increasing L_y. From the astrophysical perspective, the fact that explosive phases may happen on a very broad range of current sheets aspect ratios (say $L/a \gtrsim 15$) is very important. It means that one may very commonly find current sheets which aspect ratios suitable for the development of the explosive growth of RIDTMs. It is roughly required that these structures be ~ 15 times longer than thiner.

One of the foremost questions that the physics of relativistic reconnection rises is the speed at which magnetic energy is converted into other forms

of energy (i.e. internal or kinetic). All our models that develop an explosive phase generate superalfvénic streams of plasma. Typically, $M_{\rm A} \gtrsim 1.5$ for models with $v_{\rm A} = 0.5$. This means that as the Alfvén speed of the background (unperturbed) plasma grows, very relativistic velocities can be reached. Unfortunately, our models with $v_{\rm A} \geq 0.82$ have run into numerical difficulties that prevented us from quantifying the exact Lorentz factor that may be attained in this reconnection episodes. Extrapolating our results obtained with $v_{\rm A} = 0.5$, for which fluid Lorentz factors arrive to $W \approx 1.5 - 2.3$, we predict that in models with $v_{\rm A} \gtrsim 0.65$, $W \gtrsim 10$ could be achieved. This is in the ballpark of the values required for the jets-in-a-jet model to work and explain the fast variability displayed in some relativistic sources.

Regarding the future work to be done after this thesis, we have a few straightforward continuation lines that we aim to follow. In Chap. 7, we have started, but not finished a complete exploration of the relativistic regime of RIDTMs. We have seen that, like in the classical resistive MHD regime, after the linear growth, TMs develop at the *optimal* rate, i.e. on time scales of the order of the $\sim 10t_{\rm A} - 60t_{\rm A}$. Indeed, the fact that the time scale over which RIDTMs decreases with increasing Lundquist number (i.e. decreasing resistivity) is an indication that the time scale of their growth is close to (perhaps even smaller than) the Alfvén crossing time of the current sheet length ($t_{\rm A}$). Limited by the resolution (and hence the computational cost) that we can realistically use to be able to conduct a sufficiently comprehensive parameter scan, we have restricted to models where $S_{\rm L} \lesssim 10^7$ ($S_{\rm L} \lesssim 2.4 \times 10^6$ for our reference models with $n = 2$). The results are encouraging, suggesting that RIDTMs grow fast enough to be relevant in astrophysical scenarios where fast (explosive) reconnection is invoked to explain the observed phenomena. However, the truly relativistic regime $v_{\rm A} \sim 1$ has only been partly explored because of the huge numerical resolutions needed and the time limitations of this thesis. Hence, we have not been able to test throughly whether there exist scaling relations for the growth rate of RIDTMs akin to those found, e.g. for RITMs. The numerical constraints we have found seem to be related to the stiffness of the RRMHD system of equations. As we have shown in Sec. 6.3.1.3, in principle, it is possible to run Cueva (even for very long times) and $v_{\rm A} \sim 1$, but using relatively large values of η. Thus, a future line of work will be to improve the partly implicit methods that we use, probably incorporating even higher order, uniformly converging RKIMEX methods or improved versions of MIRK time-integrators.

Another possible lines of work are the parametric study of the influence of the separation between the initial currents (l/a) and the carefull exploration of the relaxation phase after the explosive one. The latter study requires (much) using finer resolutions, since the current sheets left in that phase are much thinner (by factors ~ 5) than the initially set up current sheets half-width.

In a broader astrophysical context, there are two possible scenarios where the developments done in this thesis are relevant. Firstly, the study of the growth of MRI including relativistic effects in the context of core-collapse supernove. In the last decade, the basic models for magnetic field saturation have been probed by based on numerical simulations and simplified analytic estimations in different physical regimes including viscosity and resistivity (e.g., Guilet and Müller, 2015; Guilet et al., 2015; Rembiasz et al., 2016a,b), though none of them has treated the problem in the framework of RRMHD. Secondly, we are interested in the study of the dissipation of magnetic field in the internal shocks model for blazars and GRBs. As pointed out in Mimica and Aloy (2010); Mimica et al. (2007); Rueda-Becerril (2017); Rueda-Becerril et al. (2017), the efficiency in converting the kinetic and magnetic energy of the beam of a magnetized relativistic jet in radiation energy depends on the resistive dissipation of the magnetic energy, among other factors. This dissipation is very likely concentrated in a relatively small region of interaction between *shells* of plasma moving in the beam of the jet with different velocities. A fundamental factor determining the relevance of this process is the rate at which magnetic field may reconnect. If the reconnection is too slow, it cannot participate in the explanation of the observed variability in blazars or in the prompt phase of GRBs. Both of these mid-term goals are under study at the time of submission of this thesis.

Appendix A

CUEVA code

CUEVA an acronym for **C**omputer **U**nit for **E**n**V**ironments in**A**strophysics, is a new code developed for the purpose of this thesis. Preliminary versions of CUEVA have been used in a pair of publications on the code status (Miranda-Aranguren and Aloy, 2013; Miranda-Aranguren et al., 2014). It is inspired in GENESIS code (Aloy et al., 1999), with the aim to solve numerically the relativistic non-ideal magnetohydrodynamic (RRMHD) system of equations.

Time integration is carried out with partly implicit methods in order to deal with the stiffness of the RRMHD equation in the ideal regime. Two main families of time-integrators are implemented in CUEVA: the RKIMEX methods (Sec. 4.2.1) as well as the MIRK schemes (MIRK, see Sec. 4.2.2). CUEVA is based on a conservative, finite-volume formulation of the RRMHD equations in which numerical fluxes at cell interfaces are calculated using either the LLF (Sec. 4.1.2.1), the HLL (Sec. 4.1.2.2) or the HLLC approximate Riemann solver presented in Chap. 5. The code employs various reconstruction techniques, most of which preserving the TVD property. The slopes used in piecewise-linear reconstruction (second order of accuracy) are any of the following: MinMod, MCL or SBL (Sec. 4.1.1.1). We have also implemented the monotonicity-preserving schemes MP5, MP7 and MP9 (Sec. 4.1.1.2).

In the ensuing sections, we provide the Butcher tables for the different RKIMEX time-integrators (Sec. A.1) and the flow chart of the code (Sec. A.2).

A.1 Butcher tables

As we have mentioned in Sec. 4.2.1, for RKIMEX schemes we use the standard notation NAME(s, σ, p) where s and σ are, respectively, the number of function evaluations of the explicit and the implicit methods and p is the combined order of the scheme. The field NAME of the schemes is composed of the initials of the

authors or the scheme type. In the case of *strong stability preserving* schemes denoted as SSP$k(s,\sigma,p)$-LUM, where k represent the order of the SSP scheme and the letters have the following meaning: (Higueras et al. (2012))

- 'L': L-stable;
- 'U': the IMEX method features uniform convergence;
- 'M': the IMEX method has a nontrivial region of absolute monotonicity.

In this appendix, we present the RKIMEX schemes in the double table notation introduced by Butcher (1996):

$$\begin{array}{c|c} \tilde{c} & \tilde{A} \\ \hline & \tilde{w}^T \end{array} \qquad \begin{array}{c|c} c & A \\ \hline & w^T \end{array}.$$

where $\tilde{A}$, A and $\tilde{w}$, w are the matrix and vector coefficients for the explicit and implicit parts, respectively, while $\tilde{c}$ and c are the coefficients used for the treatment of non-autonomous systems, as mentioned in Sec. 4.2.1.

A.1.0.1 SSP2(222)

The most basic second-order RKIMEX scheme has the following Bucher representation:

$$\begin{array}{c|cc} 0 & 0 & 0 \\ 1 & 1 & 0 \\ \hline \tilde{A} & 1/2 & 1/2 \end{array} \qquad \begin{array}{c|cc} \gamma & \gamma & 0 \\ 1-\gamma & 1-2\gamma & \gamma \\ \hline A & 1/2 & 1/2 \end{array}$$

Where the constant $\gamma := 1 - 1/\sqrt{2}$ (e.g. Kupka et al., 2012).

A.1.0.2 SSP2(332)-LU

$$\begin{array}{c|ccc} 0 & 0 & 0 & 0 \\ 1/2 & 1/2 & 0 & 0 \\ 1 & 1/2 & 1/2 & 0 \\ \hline \tilde{A} & 1/3 & 1/3 & 1/3 \end{array} \qquad \begin{array}{c|ccc} 1/4 & 1/4 & 0 & 0 \\ 1/4 & 0 & 1/4 & 0 \\ 1 & 1/3 & 1/3 & 1/3 \\ \hline A & 1/3 & 1/3 & 1/3 \end{array}$$

A.1.0.3 SSP2(332)-LUM

0	0	0	0
1/2	1/2	0	0
1	1/2	1/2	0
$\tilde{A}$	1/3	1/3	1/3

1/5	1/5	0	0
3/10	1/10	1/5	0
1	1/3	1/3	1/3
A	1/3	1/3	1/3

Note that this method is uniformly convergent and, thus, it satisfies that

$$w^T A^{-1} c = 1 \tag{A.1}$$

A.1.0.4 SSP3(433)

0	0	0	0	0
0	0	0	0	0
1	0	1	0	0
1/2	0	1/4	1/4	0
$\tilde{A}$	0	1/6	1/6	2/3

α	α	0	0	0
0	$-\alpha$	α	0	0
1	0	$1-\alpha$	α	0
1/2	β	η	$1/2-\beta-\eta-\alpha$	α
A	0	1/6	1/6	2/3

and

$$\alpha \equiv 0.24169426078821, \qquad \beta \equiv 0.06042356519705,$$
$$\gamma \equiv 1 - 1/\sqrt{2}, \qquad \eta \equiv 0.12915286960590.$$

A.1.0.5 DP1-A(242)

The following two schemes of Dimarco and Pareschi (2013) are named after their authors (DP) trailed with a number (1 or 2) indicating the global order of accuracy of the scheme.

0	0	0	0	0
1/3	1/3	0	0	0
1	1	0	0	0
1	1/2	0	1/2	0
$\tilde{A}$	1/2	0	1/2	0

1/2	1/2	0	0	0
2/3	1/6	1/2	0	0
1/2	−1/2	1/2	1/2	0
1	3/2	−3/2	1/2	1/2
A	3/2	−3/2	1/2	1/2

A.1.0.6 DP2-A(242)

0	0	0	0	0
0	0	0	0	0
1	0	1	0	0
1	0	1/2	1/2	0
$\tilde{A}$	0	1/2	1/2	0

γ_{dp}	γ_{dp}	0	0	0
0	$-\gamma_{dp}$	γ_{dp}	0	0
1	0	$1-\gamma_{dp}$	γ_{dp}	0
1	0	1/2	$1/2-\gamma_{dp}$	γ_{dp}
A	0	1/2	$1/2-\gamma_{dp}$	γ_{dp}

To ensure absolute monotinicity the coefficient γ_{dp} must satisfy $\gamma_{dp} > (2+\sqrt{2})/2$. In our case we find that the scheme is most stable, for RRMHD system of equations, if this coefficient is choosen as $\gamma_{dp} = (3+\sqrt{2})/2$.

A.1.0.7 ARS(443)

This scheme of Ascher et al. (1997) is named after its authors. Like the SSP3(433) scheme, ARS(443) is a third order IMEX-RK scheme.

0	0	0	0	0	0
1/2	1/2	0	0	0	0
2/3	11/18	1/18	0	0	0
1/2	5/6	−5/6	1/2	0	0
1	1/4	7/4	3/4	−7/4	0
$\tilde{A}$	1/4	7/4	3/4	−7/4	0

0	0	0	0	0	0
1/2	0	1/2	0	0	0
2/3	0	1/6	1/2	0	0
1/2	0	−1/2	1/2	1/2	0
1	0	3/2	−3/2	1/2	1/2
A	0	3/2	−3/2	1/2	1/2

A.1.0.8 RK36$\mathcal{S}_E$

This scheme of Izzo and Jackiewicz (2017), there named IMEX-RK36$\mathcal{S}_E$, has a global third-order accuracy and needs to perform 6 sub-stages to update the variables to the following time step. The explicit method of this RKIMEX time-integrator is not SSP, but the area of the stability region is maximal and the implicit part of the method is A-stable (that is the the region of absolute stability contains the set $\{z \in \mathbb{C} | \mathrm{Re}(z) < 0\}$, i.e. the left half complex plane). The corresponding Butcher tables are

0	0	0	0	0	0	0
$\frac{83}{242}$	$\frac{83}{242}$	0	0	0	0	0
$\frac{1537}{4715}$	$\frac{249}{15377}$	$\frac{307}{991}$	0	0	0	0
$\frac{2171}{2565}$	$-\frac{239}{1758}$	$\frac{1080}{1687}$	$\frac{737}{2154}$	0	0	0
$\frac{846}{683}$	$-\frac{220}{5231}$	$\frac{524}{793}$	$-\frac{1579}{4141}$	$\frac{810}{809}$	0	0
$\frac{667}{602}$	$\frac{701}{7073}$	$-\frac{861}{1844}$	$\frac{1487}{1433}$	$\frac{809}{1433}$	$-\frac{135}{1132}$	0
$\tilde{A}$	$-\frac{181}{5045}$	$\frac{3288}{4885}$	$\frac{247}{1657}$	$\frac{231}{1684}$	$\frac{513}{3415}$	$-\frac{238}{3231}$

$\frac{1247}{2772}$	$\frac{1247}{2772}$	0	0	0	0	0
$\frac{885}{5722}$	$-\frac{405}{1372}$	$\frac{1247}{2772}$	0	0	0	0
$\frac{166}{129}$	$\frac{1715}{1951}$	$-\frac{784}{18635}$	$\frac{1247}{2772}$	0	0	0
$\frac{1039}{866}$	$\frac{651}{866}$	$-\frac{346}{1555}$	$\frac{4367}{19788}$	$\frac{1247}{2772}$	0	0
$\frac{943}{512}$	$-\frac{59}{1491}$	$\frac{947}{1201}$	$-\frac{235}{343}$	$-\frac{288}{1999}$	$\frac{1247}{2772}$	0
$\frac{1159}{415}$	$\frac{635}{1659}$	$-\frac{163}{829}$	$\frac{1027}{1136}$	$\frac{1103}{1620}$	$\frac{565}{988}$	$\frac{1247}{2772}$
A	$-\frac{181}{5045}$	$\frac{3288}{4885}$	$\frac{247}{1657}$	$\frac{231}{1684}$	$\frac{513}{3415}$	$-\frac{238}{3231}$

A.2 Flowchart

Next we present the flowchart of the CUEVA code for future reference.

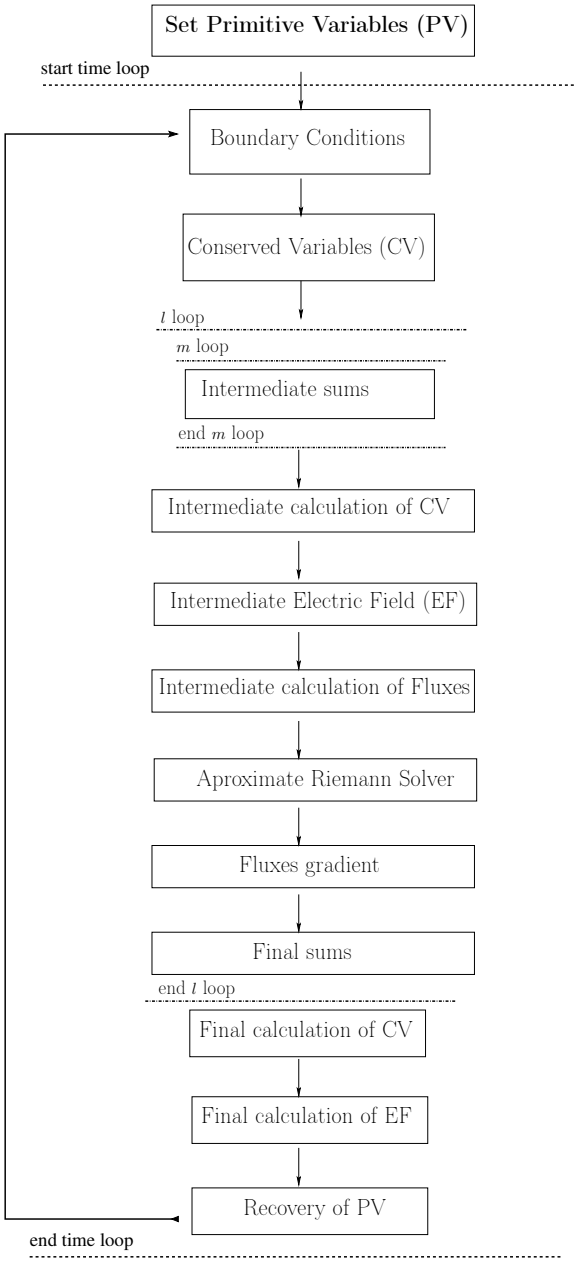

Figure A.1: l and m represent the loop counters for implicit and explicit intermediate values, usually $m = l - 1$. Intermediate variables are calculated as in Eq. (4.19) and final variables by means of Eq. (4.20).

Appendix B

Alternative HLLC solvers

B.1 Hybrid HLLC solver (HLLC1)

Here, we explore alternatives to the assumption made in Sec. 5.1, Eq. (5.17), on the continuity of the electromagnetic variables. For that, we may generalize the approach of Mignone and Tzeferacos (2010) for RRMHD in combination with the GLM method. When solving a one dimensional Riemann problem at a zone interface (e.g., in the $x-$direction as we are assuming), the following 2×2 linear hyperbolic sub-systems arise:

$$\begin{cases} \partial_t B_x = -\partial_x \phi, \\ \partial_t \phi = -\partial_x B_x, \end{cases} \tag{B.1}$$

$$\begin{cases} \partial_t E_x = -\partial_x \psi, \\ \partial_t \psi = -\partial_x E_x, \end{cases} \tag{B.2}$$

$$\begin{cases} \partial_t B_y = +\partial_x E_z, \\ \partial_t E_z = +\partial_x B_y, \end{cases} \tag{B.3}$$

$$\begin{cases} \partial_t B_z = -\partial_x E_y, \\ \partial_t E_y = -\partial_x B_z. \end{cases} \tag{B.4}$$

We note that in the systems (B.3) and (B.4) the electric current and the source terms for the GLM scalar potentials are not included since they are treated either implicitly or in a different algorithmic substep by our time integration schemes (either MIRK or RKIMEX). For generic pairs of left and right states $(B_{x,l}, \phi_l)$, $(B_{x,r}, \phi_r)$; $(E_{x,l}, \psi_l)$, $(E_{x,r}, \psi_r)$; $(B_{y,l}, E_{z,l})$, $(B_{y,r}, E_{z,r})$, and

$(B_{z,l}, E_{y,l})$, $(B_{z,r}, E_{y,r})$, the Godunov flux of the systems (B.1), (B.2), (B.3) and (B.4) can be exactly computed as

$$\begin{cases} \hat{B}_x = \dfrac{B_{x,l} + B_{x,r} - (\phi_r - \phi_l)}{2}, \\ \hat{\phi} = \dfrac{\phi_{x,l} + \phi_{x,r} - (B_{x,r} - B_{x,l})}{2}, \end{cases} \tag{B.5}$$

$$\begin{cases} \hat{E}_x = \dfrac{E_{x,l} + E_{x,r} - (\psi_r - \psi_l)}{2}, \\ \hat{\psi} = \dfrac{\psi_{x,l} + \psi_{x,r} - (E_{x,r} - E_{x,l})}{2}, \end{cases} \tag{B.6}$$

$$\begin{cases} \hat{B}_y = \dfrac{B_{y,l} + B_{y,r} + (E_{z,r} - E_{z,l})}{2}, \\ \hat{E}_z = \dfrac{E_{z,l} + E_{z,r} + (B_{y,r} - B_{y,l})}{2}, \end{cases} \tag{B.7}$$

$$\begin{cases} \hat{B}_z = \dfrac{B_{z,l} + B_{z,r} - (E_{y,r} - E_{y,l})}{2}, \\ \hat{E}_y = \dfrac{E_{y,l} + E_{y,r} - (B_{z,r} - B_{z,l})}{2}. \end{cases} \tag{B.8}$$

Therefore, we may obtain the solution of the 2×2 linear Riemann problems separately before using a standard Riemann solver for the remaining set of one-dimensional equations. The electric and magnetic field components as well as the scalar potentials ϕ and ψ precomputed with Eqs. (B.5), (B.6), (B.7) and (B.8) enter as constant parameters in the computation of the numerical Riemann fluxes. Our choice is to employ an HLLC approximate Riemann solver built as in Sec. 5.1. In this case, the only numerical fluxes that need to be computed are the ones corresponding to $(q, D^*, S_x^*, S_y^*, S_z^*, \mathcal{E}^*)$.

We note that the numerical fluxes of the conserved variables $(\phi, \psi, B_x, B_y, B_z, E_x, E_y, E_z)$ corresponding to the exact solutions written in Eqs. (B.5), (B.6), (B.7) and (B.8) are $(\hat{B}_x, \hat{E}_x, \hat{\phi}, -\hat{E}_z, \hat{E}_y, \hat{\psi}, \hat{B}_z, -\hat{B}_y)$, respectively. It turns out that, if we fix $\lambda_l = -1$ and $\lambda_r = +1$, the expressions for these fluxes coincide with those that we obtained for the HLLC solver described in the Sec. 5.1, Eq. (5.18). Remarkably, the numerical fluxes of Eq. (5.18) result from the assumption that the conserved variables $(\phi, \psi, B_x, B_y, B_z, E_x, E_y, E_z)$ are continuous across the contact wave. Therefore, we do not expect that precomputing the exact solutions given in (B.5)-(B.8) and then using them as parameters in the rest of the HLLC solver may bring any improvement in the numerical solution of the RRMHD equations in comparison with employing the full HLLC solver as presented in Sec. 5.1 with $\lambda_l = -1$ and $\lambda_r = +1$. Nonetheless, the usage of Eqs. (B.5)-(B.8) as parameters for the rest of the solver may yield a reduced numerical viscosity of the algorithm. The reason

for that is that we are not restricted to use values $\lambda_l = -1$ and $\lambda_r = +1$ as the limitting speeds for the variables $(q, D^*, S_x^*, S_y^*, S_z^*, \mathcal{E}^*)$. For this reduced set of conserved variables, the eigenvalues of the corresponding Jacobian matrix are $\lambda_q = \lambda_{H_0} = v_x$ and $\lambda_{H_\pm}$, Eqs. (3.6)-(3.7), and the maximum and minimum signal speeds can be taken as

$$\lambda_l = \min\{\lambda_{H_-,l}, \lambda_{H_-,r}\},$$
$$\lambda_r = \max\{\lambda_{H_+,l}, \lambda_{H_+,r}\}.$$

We have tested this *hybrid* HLLC solver with all the 1D and 2D tests presented in Sections 5.2 and we have found that it basically provides the same quantitative results as the solver delineated in Sec. 5.1. Nevertheless, this alternative solver introduces less numerical viscosity, which manifests itself in small oscillations arising close to discontinuities in 2D tests, making it a bit less robust to, e.g. accurately predict the growth rate of RITMs (Sec. 7.1).

Appendix C

Collective plasma behaviour

As we have said in the introduction to this thesis, the term *plasma* is used quite generally to refer a *quasi-neutral* assemblies of charged and neutral particles which exhibits collective behavior. This means that the macroscopic result to an external stimulus is the cooperative response of many plasma particles. In this appendix, expand a bit some of the relevant properties of plasmas, which were too detailled to be explicitly spelled in the introductory chapter. Three conditions should be satisfied for collective plasma behaviour (see, e.g. the excellent books of Chen, 1984; Goedbloed and Poedts, 2004):

1. The long-range Coulomb interaction between charged particles should dominate over the short-range binary collisions with neutrals. Indicating typical time scales of collective oscillatory motion by τ ($\sim 1/\omega$ where ω is the angular frequency of the oscillations), this implies that,

$$\tau \ll \tau_n := \frac{\lambda_{\rm mfp}}{v_{\rm th}} = \frac{1}{n_n \sigma_n v_{\rm th}}, \tag{C.1}$$

   where τ_n, $\lambda_{\rm mfp} := (n_n\sigma_n)^{-1}$, $\sigma_n := \pi a^2$ and $v_{\rm th} \simeq \sqrt{k_{\rm B}T/m_p}$ are the mean time between collisions of charged plasma particles with neutrals, the mean free path in a medium with a number density of neutral particles n_n, the cross-section of neutrals with "atomic" radius a and the thermal speed of particles at a temperature T, respectively. In the previous expressions, $k_{\rm B}$ and m_p stand for the Boltzmann constant, the temperature and the proton mass, respectively.

2. The length scale of plasma dynamics (λ) should be much larger than the minimum size over which the condition of *quasi-neutrality* holds. This is, length scales for a quasi-neutral plasma should be larger than the Debye length ($\lambda_{\rm D}$), which is the typical size of a region over which

charge imbalance due to thermal fluctuations may occur. This condition can be written as,

$$\lambda \gg \lambda_{\rm D} \equiv \sqrt{\frac{k_{\rm B}T}{e^2 n}}, \tag{C.2}$$

where e is the electric charge and $n \equiv n_e \simeq Z n_i$ is the number density of electrons (n_e) or of the ions ($Z n_i$) with Z the ion charge number. To clarify the concept of *quasi-neutrality*, we focus our attention on a specific ion, a test-particle, with charge $Q_{\rm T} = Ze$, which we place for convenience at the origin of our coordinate system. This ion attracts electrons toward itself and repels ions. In a steady state, the process will set up an electrostatic potential ϕ_e that satisfies Poisson equation:

$$\nabla^2 \phi_e = -q$$

with q being the charge-density distribution. This distribution includes the ion (test-particle) at the origin as well as a Boltzmann (spatial) distribution of surrounding electrons and ions:

$$q = Q_{\rm T}\ \delta(\mathbf{r}) - e\, n_e\, \exp\left(\frac{e\,\phi_e}{k_B T}\right) + Ze\, n_i\, \exp\left(\frac{-Ze\,\phi_e}{k_B T}\right).$$

In the previous equation, for simplicity, we have assumed that electrons and ions have the same temperature and that there exists only one kind of ions characterized by a charge number Z. Furthermore, because the perturbation due to a single test particle is infinitesimal, we can safely assume that the potential energy is small compared to the thermal energy (i.e; $|Ze\,\phi| \ll k_B T$). Then the Poisson equation becomes,

$$\nabla^2 \phi_e - \frac{1}{\lambda_{\rm D}^2}\phi_e = -Q_{\rm T}\delta(\mathbf{r})$$

where we have used the assumed neutrality of the unperturbed system, $n_e \simeq Z n_i$, and $\lambda_{\rm D}$ as an effective Debye length. The last equation can be solved to give

$$\phi_e(\mathbf{r}) = \frac{Q_{\rm T}}{4\pi r} \exp\left(-r/\lambda_{\rm D}\right),$$

the sometimes called *Yukawa potential* or the *Debye-Hückel potential* after pioneering work of Pieter Debye (1884-1966) and Erich Hückel (1896-1980) on polarization effects in electrolytes (Debye and Hiickel, 1923). For $r \ll \lambda_{\rm D}$ the potential $\phi_e(\mathbf{r})$ is identical to the potential of a test particle in vacuum, whereas for $r \gg \lambda_{\rm D}$ the test charge is completely screened by its surrounding shielding cloud. The nominal radius of the shielding cloud is $\lambda_{\rm D}$. Because the test particle is completely screened

for $r \gg \lambda_D$, the total shielding cloud charge is equal in magnitude to the charge of the test particle and opposite in sign. If the Debye length is a microscopic length, then it is indeed an excellent assumption that plasmas remain extremely close to neutrality, while not being exactly neutral. This tendency to be quasi-neutral occurs because a conventional plasma does not have sufficient internal energy to become substantially non-neutral over distances exceeding a Debye length.

3. The previous test-particle/shielding-cloud analysis is valid only if there is a macroscopically large number of plasma particles (N_D) in the shielding cloud; i.e.,

$$N_D \equiv \frac{4}{3}\pi \lambda_D^3 n \gg 1. \tag{C.3}$$

The dependence of the Debye length on density $\propto n^{-1/2} (n_e^{-1/2} \text{ or } n_i^{-1/2})$ means that an increasing number of shielding particles makes the shielding more efficient and diminishes the size of the perturbed volume.

Appendix D

Heaviside-Lorentz units

We take as our starting point the *generic form* of Maxwell equations (e.g. Jackson, 1999, Eq. (A.8)),

$$\begin{aligned}
\nabla \cdot \mathbf{E} &= 4\pi k_1 q, \\
\nabla \cdot \mathbf{B} &= 0, \\
\nabla \times \mathbf{B} &= 4\pi k_2 \alpha \mathbf{J} + k_2 \alpha k_1^{-1} \partial_t \mathbf{E}, \\
\nabla \times \mathbf{E} &= -k_3 \partial_t \mathbf{B}.
\end{aligned}$$

The various systems of electromagnetic units differ in their choices of the magnitudes and dimensions of the various constants above (e.g. k_1, k_2, k_3, α). Under the constrains,

$$k_1/k_2 = c^2, \qquad k_3 = \alpha^{-1}, \tag{D.1}$$

(e.g. Jackson, 1999, Eq. (A.5) and (A.10)) there are only two constants (e.g. k_2, k_3) that can (and must) be chosen.

The magnitude and dimensions of the electromagnetic constants (D.1) for the Heaviside-Lorentz and Gaussian system of units, are given in Table D.1, where the centimeter, gram and second are used as their fundamental units of length, mass and time (l, m, t).

System	k_1	k_2	α	k_3
Heaviside-Lorentz	$\frac{1}{4\pi}$	$\frac{1}{4\pi c^2}(t^2 l^{-2})$	$c(lt^{-1})$	$c^{-1}\ (tl^{-1})$
Gaussian	1	$\frac{1}{c^2}(t^2 l^{-2})$	$c(lt^{-1})$	$c^{-1}\ (tl^{-1})$

Table D.1: Magnitudes and dimensions of the electromagnetic constants for Heaviside-Lorentz and Gaussian systems of units.

Appendix E

Characteristic velocities in wave damping tests

In Sec. 6.4, we assess the lack of dependence of the results of the MD test on three (out of four) possible candidates to be the characteristic speeds of the system, namely, the sound, the Alfvén and the fast magnetosonic velocities. That brought us to the conclusion that the characteristic speed of the system at hand was the light speed (by discarding the other alternatives). This is a new result that differs significantly from the one obtained by Rembiasz et al. (2017) in classical MHD. In the previous reference, tests involving the propagation of sound waves had the sound speed as characteristic velocity, whereas tests involving either the propagation of Alfvén or fast magnetosonic waves had the fast magnetosonic speed as characteristic velocity. In this appendix we provide a number of figures, which complete our study of the characteristic lengths and velocities for the wave damping tests that were not shown in Chapter 6.

We begin by considering the dependence of the numerical viscosity of the VSL test (Sec. 6.1.1) on the sound speed as potential characteristic speed. As we observe in the right panel of Fig. E.1, ν^* is independent of c_s. Since in this test the magnetic field is zero, there is no need to check the dependence of the results on either v_A or v_fms. Thus, also for the VSL test the characteristic speed is the speed of light ($\mathcal{V} = 1$).

We repeat the previous analysis for the classical and relativistic CPAW tests, finding the same independence of the numerical diffusivity on the sound speed in the classical CPAW test (upper right panel of Figs. E.2 and E.3, corresponding to the MIRK2 and SSP2(332)-LUM time-integrators, respectively) and as in the VSL and MD tests. The relativistic CPAW test shows some scattering in the computed numerical diffusivity as a function of c_s if the models are computed with the MIRK2 time-integrator (Fig. E.4 upper right panel).

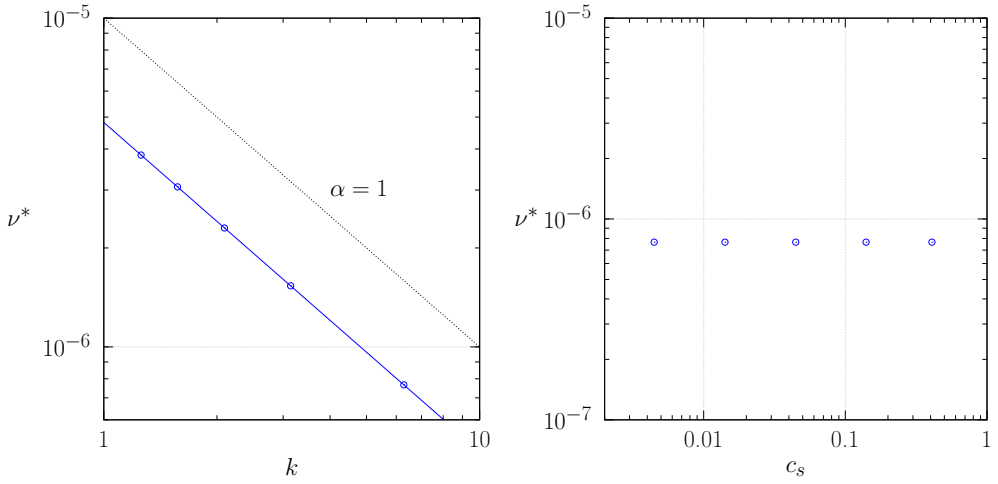

Figure E.1: Numerical viscosity for the **VSL** test. *Left panel*: dependence on the wavenumber $k = 2\pi/\lambda$ (i.e. on the box length, since we fix $\lambda = L_x$). *Right panel*: dependence on the sound speed (c_s). The different values of c_s are set keeping the background density, ρ_0, constant and varying the background pressure p_0 (see setup in Sec. 6.1.1). All the values displayed in this figure are computed using a MIRK2 time-integrator, the HLL Riemann solver and the MP9 reconstruction.

However, the scattering of the results is consistent with an absence of dependence of ξ^* on c_s, since the variations in ξ^* around a mid value $\bar{\xi}^* \sim 10^{-6}$ are smaller than a factor 4 and since for $c_s \gtrsim 0.01$ the relative deviations with respect to $\bar{\xi}^* \sim 10^{-6}$ are less than $\sim 10\%$. Remarkably, the measured numerical diffusivities are negative (note the filled symbols in Fig. E.4 upper right panel). This is a signature of the instability of the MIRK2 scheme for the regime encompassed by relativistic CPAWs. Repeating the test with the SSP2(332)-LUM time-integrator we obtain $\xi^* > 0$ and a reduced scattering (see Fig. E.5)

The absence of a clear (monotonic) trend as well as the (small) scattering about the average value of the measured numerical diffusivity as we vary either the Alfvén speed and or the fast magnetosonic velocity is also consistent with not having any dependence at all between both pairs of variables (see lower panels of Figs. E.2, E.3, E.4 and E.5). Thus, we also conclude that in the CPAW tests, neither the Alfvén speed nor the fast magnetosonic speed are the characteristic velocity of the system. Hence, by discarding the rest of the alternatives, we also conclude that $\mathcal{V} = 1$ in these tests.

For completness, in the left panel of Fig. E.1, we show the variation of the numerical viscosity with the wavenumber. The fact that the slope of the relation $\log \nu^*$ vs $\log k$ (see Eq. (6.48)) is $\alpha = 1$ confirms that the characteristic wavelength is that of sound waves (see Tab. 6.6, where we list the values of α

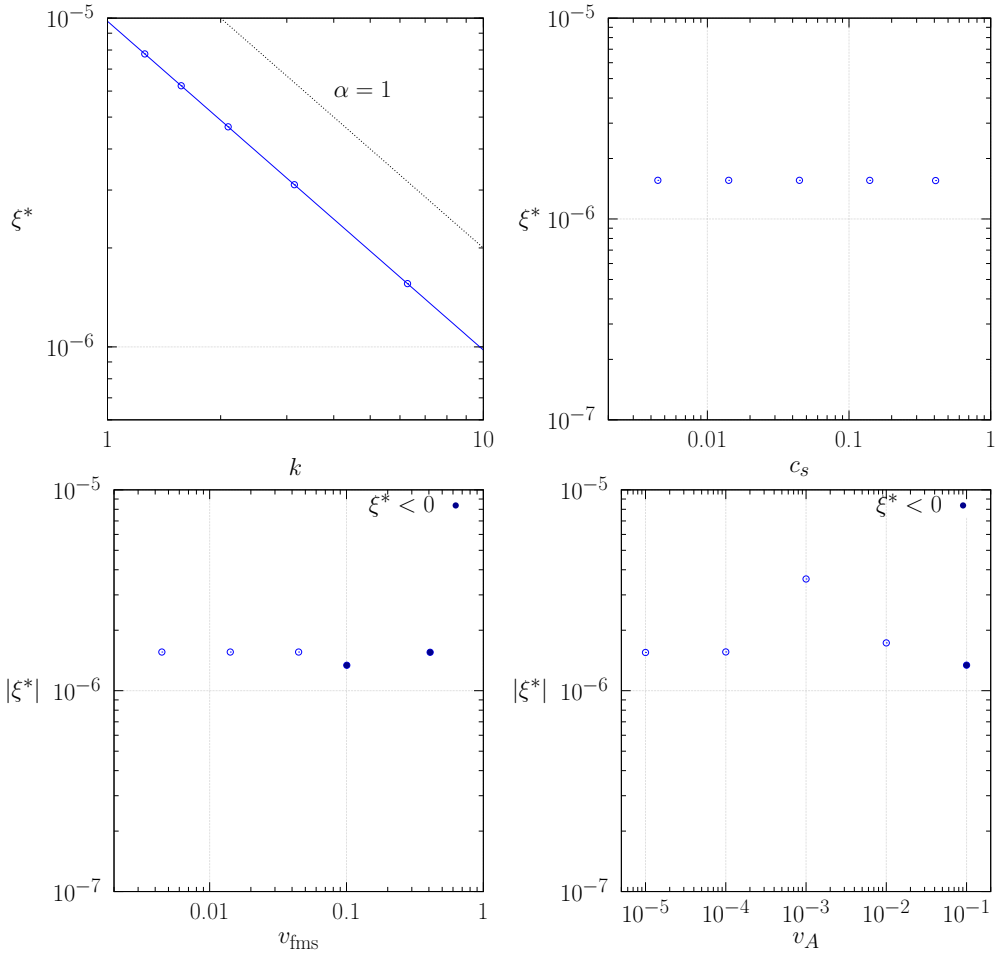

Figure E.2: Same as Fig. 6.13, but for the classical **CPAW** test (see setup in Sec. 6.3.1.1). Filled points correspond to negative values of ξ^*.

obtained from fits to each of the tests). Similar qualitative and quantitative conclusions hold for the classical (Figs. E.2 and E.3 upper left panel) and relativistic (Figs. E.4 and E.5 upper left panel) CPAW tests. However, in these cases the characteristic wavelength is that of the Alfvén waves.

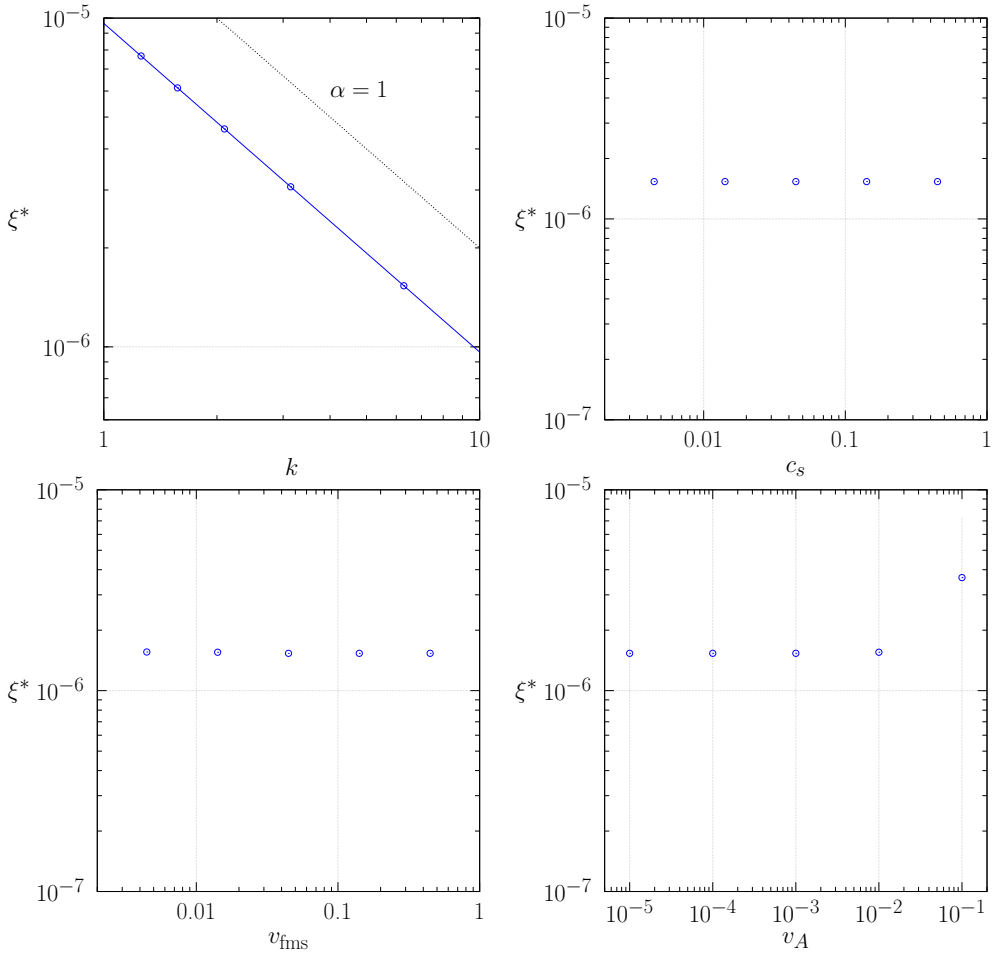

Figure E.3: Same as Fig. E.2, but for SSP2(332)-LUM integrator.

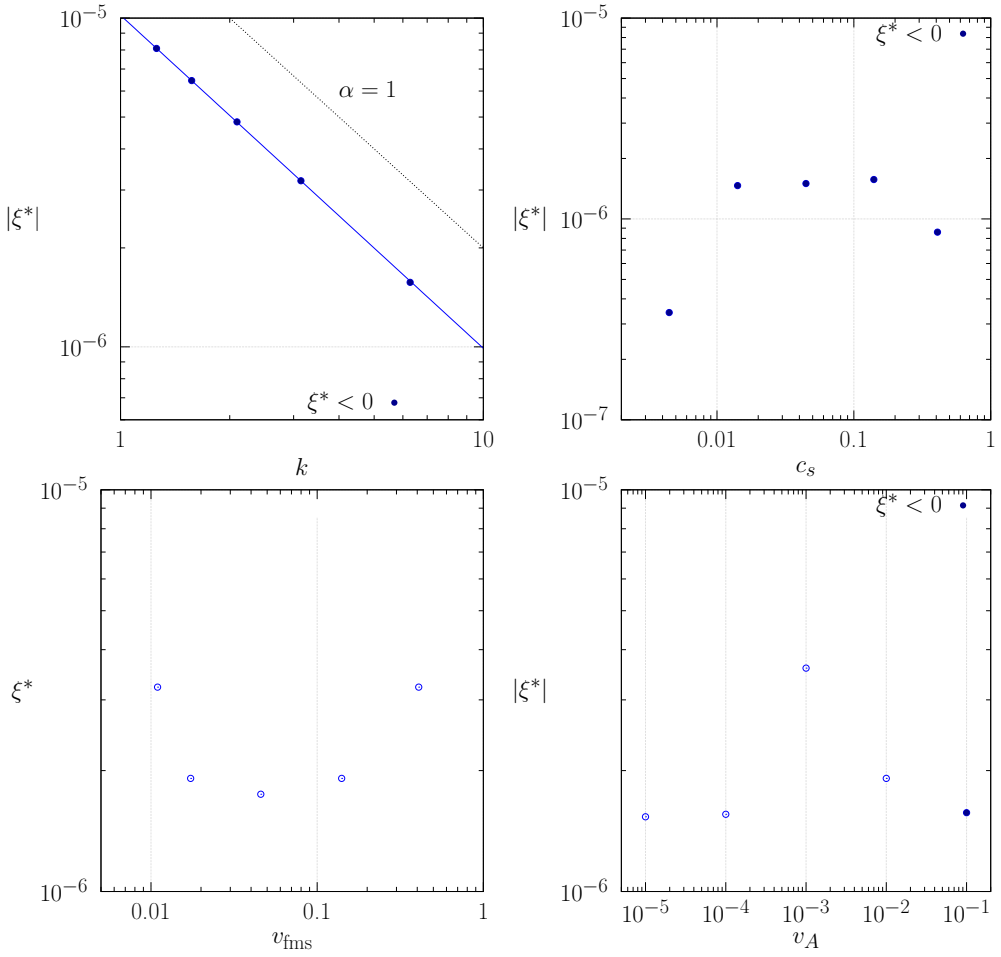

Figure E.4: Same as Fig. 6.13, but for the relativistic **CPAW** test (see setup in Sec. 6.3.1.2).

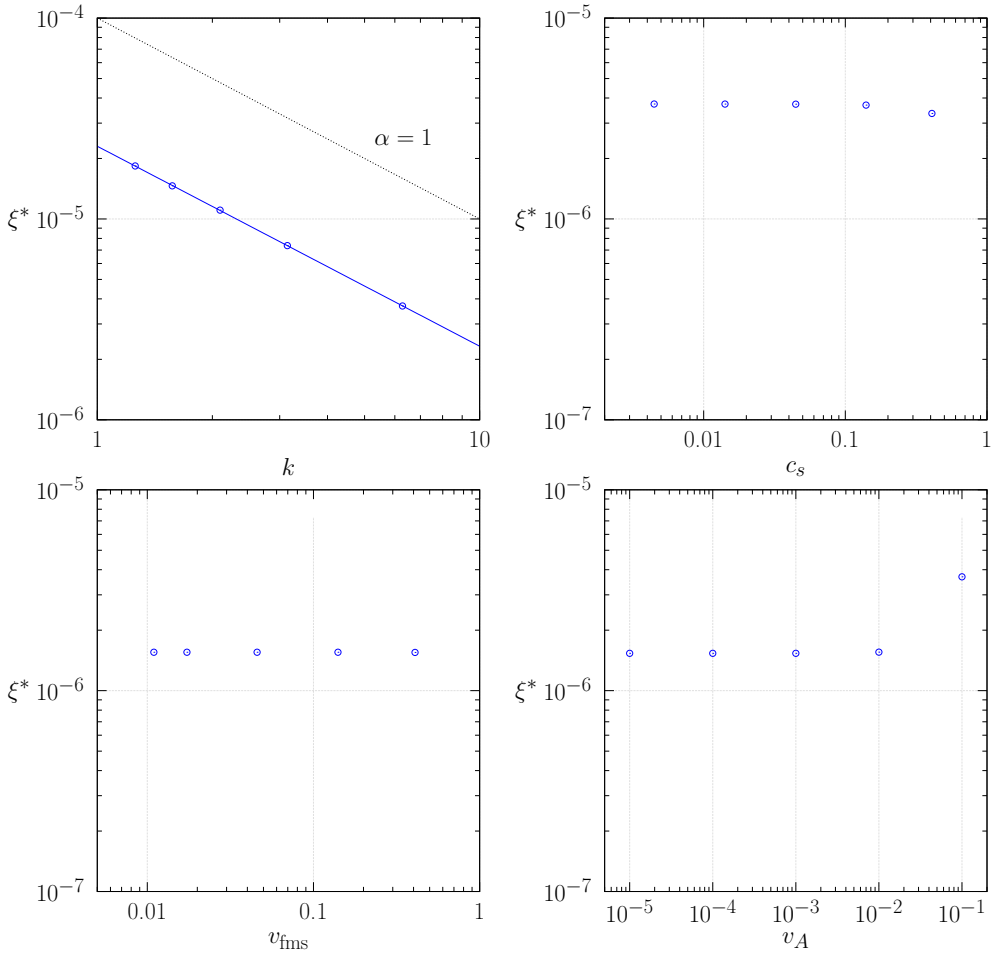

Figure E.5: Same as Fig. E.4 , but for SSP2(332)-LUM integrator.

Abbreviations

This is a list of abbreviations used throughout the text:

1D one dimensional
2D two dimensional
3D three dimensional
BH black hole
CE cylindrical explosion
CFL Courant-Friedrichs-Lewy
CPAW circularly polarized Alfvén wave
CW contact wave
DIRK diagonally implicit Runge-Kutta
DTM double tearing mode
EoS equation of state
FC Ferrari-Cardano
GLM generalized Lagrangian multiplier
GRB gamma-ray burst
HLL Harten-Lax-van Leer
HLLC Harten-Lax-van Leer contact wave
ITM ideal tearing mode
IDTM ideal double tearing mode
LLF Local Lax Friedrichs
MC monotonised center
MCL monotonised central-difference limiter
MD magnetic diffusion
MML monotonised minmod limiter
MHD magnetohydrodynamics
MIRK Minimally Implicit Runge-Kutta
MIRK1 first-order MIRK method
MIRK2 second-order MIRK method
MoC method of characteristics
MoL method of lines
MRI magneto-rotational instability
NR Newton-Raphson
ODE ordinary differential equation
PDE partial differential equation
RITM relativistic ideal tearing mode
RIDTM relativistic ideal double tearing mode
RH Rankine-Hugoniot
RHD relativistic hydrodynamics
RKIMEX Runge-Kutta Implicit-Explicit
RMHD relativistic magnetohydrodynamics
RR resistive rotor
RRMHD resistive relativistic magnetohydrodynamics
RW rotational wave
SBL superbee limiter
SCS self-similar current sheet
SP Sweet-Parker
SSP strong stability preserving
TM tearing mode
TVD total variation diminishing
VSL velocity shear layer

Acknowledgements

Primordialmente mi sincero agradecimiento al profesor Miguel Ángel Aloy, por darme a conocer y guiarme en el área de estudio de la RRMHD. Para él mi admiración por su agudeza e intuición al abordar cada nuevo tema de estudio y mi asombro por su gran capacidad de trabajo multidisciplinar. Valoraré por siempre, sus palabras de ánimo, el ímpetu y las innumerables horas de trabajo que dedicó a este proyecto. El profesor Miguel Ángel, durante todos estos años no solo me acompañó académicamente sino que su candidez humana, lo hacían estar pendiente de todos los pormenores que podían devenir de la vida cotidiana, disposición que profesaba con todos sus estudiantes de doctorado. De él, además de una actitud positiva ante la vida, aprendí a cultivar el rigor científico y llevaré por siempre su vigor y claridad en la labor científica.

Mi agradecimiento a Tomasz Rembiasz, por todas sus exigencias. Cueva, tiene actualmente un desempeño más eficiente, gracias a las pruebas de verificación que realizamos y que él de forma minuciosa revisaba. De él aprendí a ser organizado y pragmático en el trabajo. "Ciñete a los hechos" me decía, como lo haría algún gran filósofo, en los momentos en los cuales empezaban a aparecer resultados no compatibles con la teoría tradicional, en el cálculo de la disipación numérica.

Quisiera agradecer al profesor José María Ibañez, quien me abrió las puertas de su grupo y de un nuevo mundo. No olvidaré las diversas reuniones, que fueron muy enriquecedoras en el comprender la estructura característica de la RRMHD.

Gracias a Isabel Cordero-Carrión, por su trabajo previo en el área de la RRMHD. Tanto su estudio de la estructura característica de la RRMHD como su creación conjunta con el Prof. Miguel Ángel de los métodos MIRK, facilitaron y fueron herramientas de aplicación diaria en mi labor. También agradezco las fructíferas reuniones que tuvimos en la biblioteca del departamento, donde me ayudo a aclarar algunas ideas sobre el funcionamiento de los métodos MIRK, sobre todo teniendo en cuenta que eran después de salir de los que usualmente se convertían en extensos *group meetings*.

Gracias a Carmen Aloy-Torás, por ayudarme en el proceso de paralelización de Cueva, por mantener siempre activos los servidores del grupo y por sus mágicos trucos para salvarme de la hecatombe informática.

Gracias a Martin Obergaulinger, Pablo Cerdá-Durán y Petar Mimica, por estar siempre en disposición de escuchar y orientar.

Mi gratitud con Felicidad Pellicer-Bolufer, Guadalupe Almodovar Gallardo, Manel González del Campo Rodríguez y Enric Marco Soler, por hacer que todas las gestiones administrativas fueran más fáciles.

Mi agradecimiento, por el tiempo y dedicación de quienes fueron revisores de esta tesis, José Antonio Pons Botella, Elena Khomenko, Martin Obergaulinger, José M. Ibáñez Cabanell, Isabel Cordero-Carrión y Mario-Armando Higuera Garzón.

De forma sincera, quiero agradecer a la Universitat de València, a su Servicio de Informática y al Departamento de Astronomía y Astrofísica (DAA), por permitirme desarrollar este trabajo en sus instalaciones y proporcionarme acceso a sus recursos de cálculo.

Al grupo CAMAP, por el soporte recibido a partir de la "Beca de colaboración en el DAA (UV-BC-12-052)" y los proyectos de investigación , AYA2015-66899-C2-1-P, a través del contrato "UV-CI-12-308", "PROMETEOII/2014-069" y CAMAP-259276 a través del contrato "CPI-18-092". Al igual que el facilitarme el acceso a sus recursos computacionales.

Mi agradecimiento por la financiación recibida del gobierno Colombiano, a través de las becas de COLFUTURO (2012) y COLCIENCIAS (conv.679).

Mi agradecimiento al gobierno Español, en particular a la Comunidad Valenciana y al pueblo de Burjassot por cobijarme dentro de su entretejido social.

A nivel personal, quisiera destacar la amistad que forjamos con Jesús Misráyim Rueda-Becerril, siempre serán recordadas aquellas reuniones nocturnas, junto a los más finos caldos.

A mi familia con el cariño y gratitud que siento por todos. A mi madre Alba Aranguren por su dulces palabras, siempre llenas de optimismo. A mi hermana Veronica Miranda-Aranguren, por su constante cariño y apoyo incondicional. A mi hermana Liza Bello-Aranguren, por su perseverancia en ayudarme a cuidar el espíritu y el cuerpo. A mi padre, el poeta Álvaro Miranda por la disciplina y amor por el conocimiento, que me ha inculcado con su ejemplo.

Bibliography

Abdo, A.A., Ackermann, M., Ajello, M., et al., 2011. Gamma-ray flares from the crab nebula. Science 331, 739–742. doi:10.1126/science.1199705.

Abgrall, R., Karni, S., 2001. Computations of Compressible Multifluids. Journal of Computational Physics 169, 594–623. doi:10.1006/jcph.2000.6685.

Acciari, V.A., Beilicke, M., Blaylock, G., et al., 2008. Observation of Gamma-Ray Emission from the Galaxy M87 above 250 GeV with VERITAS. ApJ 679, 397–403. doi:10.1086/587458, arXiv:0802.1951.

Aharonian, F., Akhperjanian, A.G., Bazer-Bachi, A.R., et al., 2006. Fast Variability of Tera-Electron Volt γ Rays from the Radio Galaxy M87. Science 314, 1424–1427. doi:10.1126/science.1134408, arXiv:astro-ph/0612016.

Aharonian, F., Akhperjanian, A.G., Bazer-Bachi, A.R., et al., 2007. An Exceptional Very High Energy Gamma-Ray Flare of PKS 2155-304. ApJL 664, L71–L74. doi:10.1086/520635, arXiv:0706.0797.

Akiyama, S., Wheeler, J.C., Meier, D.L., Lichtenstadt, I., 2003. The Magnetorotational Instability in Core-Collapse Supernova Explosions. ApJ 584, 954–970. doi:10.1086/344135, arXiv:astro-ph/0208128.

Albert, J. Aliu, E., Anderhub, H., Antoranz, P., et al., 2007. Variable Very High Energy γ-Ray Emission from Markarian 501. ApJ 669, 862–883. doi:10.1086/521382, arXiv:astro-ph/0702008.

Albert, J., Aliu, E., Anderhub, H., et al., 2008. Very High Energy Gamma-Ray Observations of Strong Flaring Activity in M87 in 2008 February. ApJL 685, L23. doi:10.1086/592348, arXiv:0806.0988.

Alexander, R., 1977. Diagonally implicit runge-kutta methods for stiff odes. SIAM J. Numer. Anal. 14, 1006–1021. Cited By 319.

Alic, D., Bona, C., Bona-Casas, C., Massó, J., 2007. Efficient implementation of finite volume methods in numerical relativity. Physical Review D 76, 104007. doi:10.1103/PhysRevD.76.104007, arXiv:0706.1189.

Aloy, M.Á., Cordero-Carrión, I., 2016. Minimally implicit Runge-Kutta methods for Resistive Relativistic MHD. Journal of Physics: Conference Series 719, 012015. URL: http://stacks.iop.org/1742-6596/719/i=1/a=012015.

Aloy, M.A., Gómez, J.L., Ibáñez, J.M., Martí, J.M., Müller, E., 2000. Radio Emission from Three-dimensional Relativistic Hydrodynamic Jets: Observational Evidence of Jet Stratification. The Astrophysical Journal 528, L85–L88.

Aloy, M.A., Ibáñez, J.M., Martí, J.M., Müller, E., 1999. GENESIS: A High-Resolution Code for Three-dimensional Relativistic Hydrodynamics. ApJS 122, 151–166. doi:10.1086/313214, arXiv:astro-ph/9903352.

Anile, A.M., 1989. Relativistic fluids and magneto-fluids: with applications in astrophysics and plasma physics. Cambridge University Press.

Antón, L., Miralles, J.A., Martí, J.M., Ibáñez, J.M., Aloy, M.A., Mimica, P., 2010. Relativistic Magnetohydrodynamics: Renormalized Eigenvectors and Full Wave Decomposition Riemann Solver. ApJS 188, 1–31. doi:10.1088/0067-0049/188/1/1, arXiv:0912.4692.

Appl, S., Camenzind, M., 1988. Shock conditions for relativistic MHD jets. Astronomy and Astrophysics (ISSN 0004-6361) 206, 258–268.

Ascher, U.M., Ruuth, S.J., Spiteri, R.J., 1997. Implicit-explicit runge-kutta methods for time-dependent partial differential equations. Appl. Numer. Math. 25, 151–167. doi:10.1016/S0168-9274(97)00056-1.

Bachynski, M.P., 1961. Plasma physics-an elementary review. Proceedings of the IRE 49, 1751–1766. doi:10.1109/JRPROC.1961.287705.

Balbus, S.A., Hawley, J.F., 1991. A powerful local shear instability in weakly magnetized disks. I - Linear analysis. II - Nonlinear evolution. ApJ 376, 214–233. doi:10.1086/170270.

Balbus, S.A., Hawley, J.F., 1998. Instability, turbulence, and enhanced transport in accretion disks. Reviews of Modern Physics 70, 1–53. doi:10.1103/RevModPhys.70.1.

Balsara, D., 2001. Total Variation Diminishing Scheme for Relativistic Magnetohydrodynamics. The Astrophysical Journal Supplement 132, 83–101. doi:10.1086/318941.

Barniol Duran, R., Leng, M., Giannios, D., 2016. An anisotropic minijets model for the GRB prompt emission. MNRAS 455, L6–L10. doi:10.1093/mnrasl/slv140, arXiv:1509.02521.

Baty, H., 2017. Explosive magnetic reconnection in double-current sheet systems: Ideal versus resistive tearing mode. The Astrophysical Journal 837, 74. URL: http://stacks.iop.org/0004-637X/837/i=1/a=74.

Baty, H., Petri, J., Zenitani, S., 2013. Explosive reconnection of double tearing modes in relativistic plasmas: application to the Crab flares. MNRAS 436, L20–L24. doi:10.1093/mnrasl/slt104, arXiv:1308.0906.

Begelman, M.C., 1998. Instability of Toroidal Magnetic Field in Jets and Plerions. ApJ 493, 291–300. doi:10.1086/305119, arXiv:astro-ph/9708142.

Beloborodov, A.M., 2013a. Electron-Positron Flows around Magnetars. ApJ 777, 114. doi:10.1088/0004-637X/777/2/114, arXiv:1209.4063.

Beloborodov, A.M., 2013b. On the Mechanism of Hard X-Ray Emission from Magnetars. ApJ 762, 13. doi:10.1088/0004-637X/762/1/13, arXiv:1201.0664.

Beloborodov, A.M., Thompson, C., 2007. Corona of Magnetars. ApJ 657, 967–993. doi:10.1086/508917, arXiv:astro-ph/0602417.

Beskin, V.S., Kuznetsova, I.V., 2000. On the Blandford-Znajek mechanism of the energy loss of a rotating black hole. Nuovo Cimento B Serie 115, 795. arXiv:astro-ph/0004021.

Bhattacharjee, A., Huang, Y.M., Yang, H., Rogers, B., 2009. Fast reconnection in high-Lundquist-number plasmas due to the plasmoid Instability. Physics of Plasmas 16, 112102.

Bicknell, G.V., Wagner, S.J., 2002. The Evolution of Shocks in Blazar Jets. PASA 19, 129–137. doi:10.1071/AS02009, arXiv:astro-ph/0204439.

Bierwage, A., Benkadda, S., Hamaguchi, S., Wakatani, M., 2005. Fast growing double tearing modes in a tokamak plasma. Physics of Plasmas 12, 082504.

Birk, G.T., Konz, C., Otto, A., 1997. Tearing instabilities in multiple current sheets for current-dependent resistivity models. Physics of Plasmas 4, 4173–4175. doi:10.1063/1.872541.

Blandford, R.D., 2002. To the Lighthouse, in: Gilfanov, M., Sunyeav, R., Churazov, E. (Eds.), Lighthouses of the Universe: The Most Luminous Celestial Objects and Their Use for Cosmology, p. 381. doi:10.1007/10856495_59, arXiv:astro-ph/0202265.

Blandford, R.D., Znajek, R.L., 1977. Electromagnetic extraction of energy from Kerr black holes. MNRAS 179, 433–456. doi:10.1093/mnras/179.3.433.

Bodenheimer, P., Laughlin, G., Laughlin, G., Rozyczka, M., Yorke, H., Plewa, T., Rozyczka, M., Yorke, H., Birkinshaw, M., Silk, J., 2006. Numerical Methods in Astrophysics. CRC Press.

Boris, J.P., Book, D.L., 1973. Flux-Corrected Transport. I. SHASTA, A Fluid Transport Algorithm That Works. Journal of Computational Physics 11, 38–69. doi:10.1016/0021-9991(73)90147-2.

Boscarino, S., 2007. Error Analysis of IMEX Runge–Kutta Methods Derived from Differential-Algebraic Systems. SIAM Journal on Numerical Analysis 45, 1600–1621.

Boscarino, S., Russo, G., 2007. On the Uniform Accuracy of IMEX Runge-Kutta Schemes and Applications to Hyperbolic Systems with Relaxation. Communications to SIMAI Congress 2.

Boscarino, S., Russo, G., 2009. On a Class of Uniformly Accurate IMEX Runge–Kutta Schemes and Applications to Hyperbolic Systems with Relaxation. SIAM Journal on Scientific Computing 31, 1926–1945.

Brackbill, J.U., Barnes, D.C., 1980. The effect of nonzero product of magnetic gradient and B on the numerical solution of the magnetohydrodynamic equations. Journal of Computational Physics 35, 426–430. doi:10.1016/0021-9991(80)90079-0.

Brio, M., Wu, C.C., 1988. An upwind differencing scheme for the equations of ideal magnetohydrodynamics. J. Comp. Phys. 75, 400–422. doi:10.1016/0021-9991(88)90120-9.

Bromberg, O., Tchekhovskoy, A., 2016. Relativistic MHD simulations of core-collapse GRB jets: 3D instabilities and magnetic dissipation. MNRAS 456, 1739–1760. doi:10.1093/mnras/stv2591, arXiv:1508.02721.

Bucciantini, N., Del Zanna, L., 2013. A fully covariant mean-field dynamo closure for numerical 3 + 1 resistive GRMHD. MNRAS 428, 71–85. doi:10.1093/mnras/sts005, arXiv:1205.2951.

Bucciantini, N., Del Zanna, L., Amato, E., Volpi, D., 2005. Polarization in the inner region of pulsar wind nebulae. A&A 443, 519–524. doi:10.1051/0004-6361:20053667, arXiv:astro-ph/0508212.

Butcher, J., 1996. A history of runge-kutta methods. Applied Numerical Mathematics 20, 247–260. doi:10.1016/0168-9274(95)00108-5. cited By 31.

Campos, L.M.B.C., 1999. On the viscous and resistive dissipation of magnetohydrodynamic waves. Physics of Plasmas 6, 57–65. doi:10.1063/1.873257.

Centrella, J., Wilson, J.R., 1984. Planar numerical cosmology. II - The difference equations and numerical tests. ApJS 54, 229–249. doi:10.1086/190927.

Cerdá-Durán, P., Font, J.A., Dimmelmeier, H., 2007. General relativistic simulations of passive-magneto-rotational core collapse with microphysics. A&A 474, 169–191. doi:10.1051/0004-6361:20077432, arXiv:astro-ph/0703597.

Chandrasekhar, S., 1960. The Stability of Non-Dissipative Couette Flow in Hydromagnetics. Proc. of the Nat. Acad. of Science 46, 253–257. doi:10.1073/pnas.46.2.253.

Chen, F., 1984. Introduction to Plasma Physics and Controlled Fusion. Number v. 1 in Introduction to Plasma Physics and Controlled Fusion, Springer.

Chen, G.Q., Levermore, C.D., Liu, T.P., 1994. Hyperbolic conservation laws with stiff relaxation terms and entropy. Communications on Pure and Applied Mathematics 47, 787–830. URL: http://dx.doi.org/10.1002/cpa.3160470602, doi:10.1002/cpa.3160470602.

Cheng, X., Guo, Y., Ding, M., 2017. Origin and Structures of Solar Eruptions I: Magnetic Flux Rope. Science in China Earth Sciences 60, 1383–1407. doi:10.1007/s11430-017-9074-6, arXiv:1705.08198.

Contopoulos, I., Kazanas, D., Papadopoulos, D.B., 2013. The Force-free Magnetosphere of a Rotating Black Hole. ApJ 765, 113. doi:10.1088/0004-637X/765/2/113, arXiv:1212.0320.

Cordero-Carrión, I., Ibáñez, J.M., Aloy, M.Á., 2012. Characteristic structure of the resistive relativistic magnetohydrodynamic equations, in: Beltrán Jiménez, J., Ruiz Cembranos, J.A., Dobado, A., López Maroto, A., De la Cruz Dombriz, A. (Eds.), American Institute of Physics Conference Series, pp. 359–362. doi:10.1063/1.4734434.

Coroniti, F.V., 1990. Magnetically striped relativistic magnetohydrodynamic winds - The Crab Nebula revisited. Astrophysical Journal 349, 538–545.

Cowling, T.G., 1976. Magnetohydrodynamics.

Dai, W., Woodward, P.R., 1998. On the divergence-free condition and conservation laws in numerical simulations for supersonic magnetohydrodynamical flows. The Astrophysical Journal 494, 317. URL: http://stacks.iop.org/0004-637X/494/i=1/a=317.

Daigne, F., Mochkovitch, R., 2002. The expected thermal precursors of gamma-ray bursts in the internal shock model. MNRAS 336, 1271–1280. doi:10.1046/j.1365-8711.2002.05875.x, arXiv:astro-ph/0207456.

Debye, P., Hiickel, E., 1923. Zur theorie der elektrolyte. 2. Das grenzgesetz fir die elektrische leitftihigkeit. Physik 2, 305–325.

Dedner, A., Kemm, F., Kröner, D., Munz, C.D., Schnitzer, T., Wesenberg, M., 2002. Hyperbolic Divergence Cleaning for the MHD Equations. J. Comp. Phys. 175, 645–673. doi:10.1006/jcph.2001.6961.

Del Sarto, D., Pucci, F., Tenerani, A., Velli, M., 2016. "Ideal" tearing and the transition to fast reconnection in the weakly collisional MHD and EMHD regimes. Journal of Geophysical Research: Space Physics 121, 1857–1873.

Del Zanna, L., Bucciantini, N., Londrillo, P., 2003. An efficient shock-capturing central-type scheme for multidimensional relativistic flows. II. Magnetohydrodynamics. A&A 400, 397–413. doi:10.1051/0004-6361:20021641, arXiv:astro-ph/0210618.

Del Zanna, L., Papini, E., Landi, S., Bugli, M., Bucciantini, N., 2016. Fast reconnection in relativistic plasmas: the magnetohydrodynamics tearing instability revisited. MNRAS 460, 3753–3765. doi:10.1093/mnras/stw1242, arXiv:1605.06331.

Del Zanna, L., Zanotti, O., Bucciantini, N., Londrillo, P., 2007. ECHO: a Eulerian conservative high-order scheme for general relativistic magnetohydrodynamics and magnetodynamics. A&A 473, 11–30. doi:10.1051/0004-6361:20077093, arXiv:0704.3206.

Deng, W., Li, H., Zhang, B., Li, S., 2015. Relativistic MHD Simulations of Collision-induced Magnetic Dissipation in Poynting-flux-dominated Jets/outflows. ApJ 805, 163. doi:10.1088/0004-637X/805/2/163, arXiv:1501.07595.

Dimarco, G., Pareschi, L., 2013. Asymptotic preserving implicit-explicit runge–kutta methods for nonlinear kinetic equations. SIAM Journal on Numerical Analysis 51, 1064–1087. doi:10.1137/12087606X.

Dixon, W.G., 1978. Special relativity: the foundation of macroscopic physics. Cambridge Univ. Press.

Dubal, M.R., 1991. Numerical simulations of special relativistic, magnetic gas flows. Computer Physics Communications 64, 221–234. doi:10.1016/0010-4655(91)90033-H.

Dumbser, M., Zanotti, O., 2009. Very high order $P_N P_M$ schemes on unstructured meshes for the resistive relativistic MHD equations. J. Comp. Phys. 228, 6991–7006. doi:10.1016/j.jcp.2009.06.009, arXiv:0903.4832.

Eichler, D., 1993. Magnetic Confinement of Jets. ApJ 419, 111. doi:10.1086/173464.

Evans, C.R., Hawley, J.F., 1988. Simulation of magnetohydrodynamic flows - A constrained transport method. ApJ 332, 659–677. doi:10.1086/166684.

Feng, X., Zhang, M., 2016. A comparative study of divergence cleaning methods of magnetic field in the solar coronal numerical simulation. Frontiers in Astronomy and Space Sciences 3, 6. doi:10.3389/fspas.2016.00006.

Fernández, R., Metzger, B.D., 2016. Electromagnetic signatures of neutron star mergers in the advanced ligo era. Annual Review of Nuclear and Particle Science 66, 23–45. doi:10.1146/annurev-nucl-102115-044819.

Font, J.A., Ibanez, J.M., Marquina, A., Marti, J.M., 1994. Multidimensional relativistic hydrodynamics: Characteristic fields and modern high-resolution shock-capturing schemes. A&A 282, 304–314.

Furth, H.P., Killeen, J., Rosenbluth, M.N., 1963. Finite-Resistivity Instabilities of a Sheet Pinch. Physics of Fluids 6, 459–484. doi:10.1063/1.1706761.

Ghosh, P., 2000. The structure of black hole magnetospheres - I. Schwarzschild black holes. MNRAS 315, 89–97. doi:10.1046/j.1365-8711.2000.03410.x, arXiv:astro-ph/9907427.

Giacomazzo, B., Rezzolla, L., 2006. The exact solution of the Riemann problem in relativistic magnetohydrodynamics. Journal of Fluid Mechanics 562, 223–259. doi:10.1017/S0022112006001145, arXiv:gr-qc/0507102.

Giannios, D., 2013. Reconnection-driven plasmoids in blazars: fast flares on a slow envelope. MNRAS 431, 355–363. doi:10.1093/mnras/stt167, arXiv:1211.0296.

Giannios, D., Spruit, H.C., 2005. Spectra of Poynting-flux powered GRB outflows. A&A 430, 1–7. doi:10.1051/0004-6361:20047033, arXiv:astro-ph/0401109.

Giannios, D., Spruit, H.C., 2006. The role of kink instability in Poynting-flux dominated jets. A&A 450, 887–898. doi:10.1051/0004-6361:20054107, arXiv:astro-ph/0601172.

Giannios, D., Uzdensky, D.A., Begelman, M.C., 2009. Fast TeV variability in blazars: jets in a jet. MNRAS 395, L29–L33. doi:10.1111/j.1745-3933.2009.00635.x, arXiv:0901.1877.

Giannios, D., Uzdensky, D.A., Begelman, M.C., 2010. Fast TeV variability from misaligned minijets in the jet of M87. MNRAS 402, 1649–1656. doi:10.1111/j.1365-2966.2009.16045.x, arXiv:0907.5005.

Godunov, S.K., 1959. A finite difference method for the computation of discontinuous solutions of the equations of fluid dynamics. Matematicheskii Sbornik 47, 357–393.

Goedbloed, J., Poedts, S., 2004. Principles of Magnetohydrodynamics: With Applications to Laboratory and Astrophysical Plasmas. Cambridge University Press.

Goedbloed, J.P., Keppens, R., Poedts, S., 2010. Advanced magnetohydrodynamics : with applications to laboratory and astrophysical plasmas. Cambridge University Press, Cambridge; New York.

Goodman, J., Uzdensky, D., 2008. Reconnection in Marginally Collisionless Accretion Disk Coronae. ApJ 688, 555–558. doi:10.1086/592345, arXiv:0804.4481.

Goodman, J., Xu, G., 1994. Parasitic instabilities in magnetized, differentially rotating disks. ApJ 432, 213–223. doi:10.1086/174562.

Guilet, J., Müller, E., 2015. Numerical simulations of the magnetorotational instability in protoneutron stars - I. Influence of buoyancy. MNRAS 450, 2153–2171. doi:10.1093/mnras/stv727, arXiv:1501.07636.

Guilet, J., Müller, E., Janka, H.T., 2015. Neutrino viscosity and drag: impact on the magnetorotational instability in protoneutron stars. MNRAS 447, 3992–4003. doi:10.1093/mnras/stu2550, arXiv:1410.1874.

Gurski, K.F., 2004. An HLLC-Type Approximate Riemann Solver for Ideal Magnetohydrodynamics. SIAM Journal on Scientific Computing 25, 2165–2187. doi:10.1137/S1064827502407962.

Harten, A., Lax, P.D., van Leer, B., 1983. On Upstream Differencing and Godunov-Type Schemes for Hyperbolic Conservation Laws. SIAM Review 25, 35–61. doi:10.1137/1025002.

Hesse, M., Zenitani, S., 2007. Dissipation in relativistic pair-plasma reconnection. Physics of Plasmas 14, 112102. doi:10.1063/1.2801482.

Higueras, I., Happenhofer, N., Koch, O., Kupka, F., 2012. Optimized Imex Runge-Kutta methods for simulations in astrophysics. Technical Report 14. Institute for Analysis and Scientific Computing, Vienna University of Technology. URL: http://www.asc.tuwien.ac.at/preprint/2012/asc14x2012.pdf.

Hiscock, W.A., Lindblom, L., 1983. Stability and causality in dissipative relativistic fluids. Annals of Physics 151, 466–496. doi:10.1016/0003-4916(83)90288-9.

Hiscock, W.A., Lindblom, L., 1985. Generic instabilities in first-order dissipative relativistic fluid theories. Phys. Rev. D 31, 725–733. doi:10.1103/PhysRevD.31.725.

Honkkila, V., Janhunen, P., 2007. HLLC solver for ideal relativistic MHD. Journal of Computational Physics 223, 643–656. doi:10.1016/j.jcp.2006.09.027.

Hundsdorfer, W., Ruuth, S.J., 2007. IMEX extensions of linear multistep methods with general monotonicity and boundedness properties. Journal of Computational Physics 225, 2016–2042.

Ishihara, O., 2007. Complex plasma: dusts in plasma. Journal of Physics D: Applied Physics 40, R121. URL: http://stacks.iop.org/0022-3727/40/i=8/a=R01.

Izzo, G., Jackiewicz, Z., 2017. Highly stable implicit–explicit Runge–Kutta methods. Applied Numerical Mathematics 113, 71–92.

Izzo, G., Jackiewicz, Z., 2018. Strong stability preserving transformed implicit-explicit DIMSIMs. arXiv.org arXiv:1806.07804.

Jackson, J.D., 1999. Classical electrodynamics. 3rd ed. ed., Wiley, New York, NY.

Janvier, M., Kishimoto, Y., Li, J.Q., 2011. Structure-Driven Nonlinear Instability as the Origin of the Explosive Reconnection Dynamics in Resistive Double Tearing Modes. Physical Review Letters 107, 195001.

Jeffrey, A., Taniuti, T., 1964. in: Non-Linear Wave PropagationWith Applications to Physics and Magnetohydrodynamics. Elsevier. volume 9 of *Mathematics in Science and Engineering*, p. 369. URL: www.sciencedirect.com/science/article/pii/S0076539208624443.

Just, O., Obergaulinger, M., Janka, H.T., 2015. A new multidimensional, energy-dependent two-moment transport code for neutrino-hydrodynamics. Monthly Notices of the Royal Astronomical Society 453, 3386–3413.

Kim, J., Balsara, D.S., 2014. A stable HLLC Riemann solver for relativistic magnetohydrodynamics. Journal of Computational Physics 270, 634–639. doi:10.1016/j.jcp.2014.04.023.

Koide, S., Nishikawa, K.I., Mutel, R.L., 1996. A Two-dimensional Simulation of Relativistic Magnetized Jet. ApJL 463, L71. doi:10.1086/310054.

Kolgan, V.P., 1972. Application of the principle of minimizing the derivative to the construction of finite-difference schemes for computing discontinuous solutions of gas dynamics. Uchenye Zapiski TsAGI 3, 68–77 (In Russian).

Komissarov, S.S., 1999. A Godunov-type scheme for relativistic magnetohydrodynamics. MNRAS 303, 343–366. doi:10.1046/j.1365-8711.1999.02244.x.

Komissarov, S.S., 2002. Time-dependent, force-free, degenerate electrodynamics. Monthly Notice of the Royal Astronomical Society 336, 759–766.

Komissarov, S.S., 2004. Electrodynamics of black hole magnetospheres. MNRAS 350, 427–448. doi:10.1111/j.1365-2966.2004.07598.x.

Komissarov, S.S., 2007. Multidimensional numerical scheme for resistive relativistic magnetohydrodynamics. MNRAS 382, 995–1004. doi:10.1111/j.1365-2966.2007.12448.x, arXiv:0708.0323.

Komissarov, S.S., Barkov, M., Lyutikov, M., 2007. Tearing instability in relativistic magnetically dominated plasmas. MNRAS 374, 415–426. doi:10.1111/j.1365-2966.2006.11152.x, arXiv:astro-ph/0606375.

Koren, B., van der Maarel, H.T.M., 1993. Monotone, higher-order accurate, multidimensional upwinding, in: Thirteenth International Conference on Numerical Methods in Fluid Dynamics: Proceedings of the Conference Held at the Consiglio Nazionale delle Ricerche Rome, CWI. Springer Berlin Heidelberg, Berlin, Heidelberg. pp. 110–114.

Kumar, P., 1999. Gamma-Ray Burst Energetics. ApJL 523, L113–L116. doi:10.1086/312265, arXiv:astro-ph/9907096.

Kumar, P., Narayan, R., 2009. GRB 080319B: evidence for relativistic turbulence, not internal shocks. MNRAS 395, 472–489. doi:10.1111/j.1365-2966.2009.14539.x, arXiv:0812.0021.

Kupka, F., Happenhofer, N., Higueras, I., Koch, O., 2012. Total-variation-diminishing implicit-explicit Runge-Kutta methods for the simulation of double-diffusive convection in astrophysics. J. Comp. Phys. 231, 3561–3586. doi:10.1016/j.jcp.2011.12.031, arXiv:1106.5672.

Landau, L., Lifshitz, E., 1986. Theory of Elasticity. Course of theoretical physics, Butterworth-Heinemann. URL: https://books.google.es/books?id=tpY-VkwCkAIC.

Landau, L., Lifshitz, E., 2013. Fluid Mechanics. v. 6, Elsevier Science.

Landi, S., Del Zanna, L., Papini, E., Pucci, F., Velli, M., 2015. Resistive Magnetohydrodynamics Simulations of the Ideal Tearing Mode. ApJ 806, 131. doi:10.1088/0004-637X/806/1/131, arXiv:1504.07036.

Laney, C.B., 1998. Computational Gasdynamics. Cambridge University Press. doi:10.1017/CBO9780511605604.

Lapenta, G., 2008. Self-Feeding Turbulent Magnetic Reconnection on Macroscopic Scales. Physical Review Letters 100, 235001.

Latter, H.N., Lesaffre, P., Balbus, S.A., 2009. MRI channel flows and their parasites. MNRAS 394, 715–729. doi:10.1111/j.1365-2966.2009.14395.x, arXiv:0901.4712.

Lazar, A., Nakar, E., Piran, T., 2009. Gamma-Ray Burst Light Curves in the Relativistic Turbulence and Relativistic Subjet Models. ApJL 695, L10–L14. doi:10.1088/0004-637X/695/1/L10, arXiv:0901.1133.

Leismann, T., Antón, L., Aloy, M.A., Müller, E., Martí, J.M., Miralles, J.A., Ibáñez, J.M., 2005. Relativistic MHD simulations of extragalactic jets. Astronomy and Astrophysics 436, 503–526. doi:10.1051/0004-6361:20042520.

LeVeque, R.J., 2002. Finite volume methods for hyperbolic problems. Cambridge texts in applied mathematics, Cambridge University Press, Cambridge, New York. URL: http://opac.inria.fr/record=b1100566. autres tirages : 2003, 2005, 2006.

Levinson, A., Segev, N., 2017. On the existence of steady gap solutions in rotating black hole magnetospheres. ArXiv e-prints arXiv:1709.09397.

Li, C., Tang, Y.H., Dai, Y., Fang, C., Vial, J.C., 2007. Flare magnetic reconnection and relativistic particles in the 2003 October 28 event. A&A 472, 283–286. doi:10.1051/0004-6361:20066966, arXiv:0706.3648.

Li, S., 2005. An HLLC Riemann solver for magneto-hydrodynamics. J. Comp. Phys. 203, 344–357. doi:10.1016/j.jcp.2004.08.020.

Liu, T.P., 1987. Hyperbolic conservation laws with relaxation. Communications in Mathematical Physics 108, 153–175. URL: https://doi.org/10.1007/BF01210707, doi:10.1007/BF01210707.

Loureiro, N.F., Schekochihin, A.A., Cowley, S.C., 2007. Instability of current sheets and formation of plasmoid chains. Physics of Plasmas 14, 100703–100703.

Lyubarsky, Y.E., 2005. On the relativistic magnetic reconnection. MNRAS 358, 113–119. doi:10.1111/j.1365-2966.2005.08767.x, arXiv:astro-ph/0501392.

Lyutikov, M., 2006. Did Swift measure gamma-ray burst prompt emission radii? MNRAS 369, L5–L8. doi:10.1111/j.1745-3933.2006.00161.x, arXiv:astro-ph/0601557.

Lyutikov, M., Blandford, R., 2003. Gamma Ray Bursts as Electromagnetic Outflows. ArXiv Astrophysics e-prints arXiv:astro-ph/0312347.

Marinacci, F., Vogelsberger, M., Kannan, R., Mocz, P., Pakmor, R., Springel, V., 2018. Non-ideal magnetohydrodynamics on a moving mesh. MNRAS 476, 2476–2492. doi:10.1093/mnras/sty397, arXiv:1710.10265.

Marrone, D.P., Moran, J.M., Zhao, J.H., Rao, R., 2007. An Unambiguous Detection of Faraday Rotation in Sagittarius A*. ApJL 654, L57–L60. doi:10.1086/510850, arXiv:astro-ph/0611791.

Marscher, A.P., Gear, W.K., 1985. Models for high-frequency radio outbursts in extragalactic sources, with application to the early 1983 millimeter-to-infrared flare of 3C 273. ApJ 298, 114–127. doi:10.1086/163592.

Martí, J.M., 2015. On the correction of conserved variables for numerical RMHD with staggered constrained transport. Computer Physics Communications 191, 100–105. doi:10.1016/j.cpc.2015.02.004, arXiv:1501.02697.

Martí, J.M., Müller, E., 1994. The analytical solution of the riemann problem in relativistic hydrodynamics. Journal of Fluid Mechanics 258, 317–333. doi:10.1017/S0022112094003344.

Martí, J.M., Müller, E., 2015. Grid-based Methods in Relativistic Hydrodynamics and Magnetohydrodynamics. Living Reviews in Computational Astrophysics 1, 3. doi:10.1007/lrca-2015-3.

Martí-Vidal, I., Muller, S., Vlemmings, W., Horellou, C., Aalto, S., 2015. A strong magnetic field in the jet base of a supermassive black hole. Science 348, 311–314. doi:10.1126/science.aaa1784.

McKinney, J.C., 2006. General relativistic force-free electrodynamics: a new code and applications to black hole magnetospheres. MNRAS 367, 1797–1807. doi:10.1111/j.1365-2966.2006.10087.x, arXiv:astro-ph/0601410.

McKinney, J.C., Gammie, C.F., 2004. A Measurement of the Electromagnetic Luminosity of a Kerr Black Hole. ApJ 611, 977–995. doi:10.1086/422244, arXiv:astro-ph/0404512.

McKinney, J.C., Uzdensky, D.A., 2012. A reconnection switch to trigger gamma-ray burst jet dissipation. MNRAS 419, 573–607. doi:10.1111/j.1365-2966.2011.19721.x, arXiv:1011.1904.

Meier, D.L., 2003. The theory and simulation of relativistic jet formation: towards a unified model for micro- and macroquasars. NAR 47, 667–672. doi:10.1016/S1387-6473(03)00120-9, arXiv:astro-ph/0312048.

Mignone, A., Bodo, G., 2005. An HLLC Riemann solver for relativistic flows - I. Hydrodynamics. MNRAS 364, 126–136. doi:10.1111/j.1365-2966.2005.09546.x, arXiv:astro-ph/0506414.

Mignone, A., Bodo, G., 2006. An HLLC Riemann solver for relativistic flows - II. Magnetohydrodynamics. MNRAS 368, 1040–1054. doi:10.1111/j.1365-2966.2006.10162.x, arXiv:astro-ph/0601640.

Mignone, A., Tzeferacos, P., 2010. A second-order unsplit Godunov scheme for cell-centered MHD: The CTU-GLM scheme. J. Comp. Phys. 229, 2117–2138. doi:10.1016/j.jcp.2009.11.026, arXiv:0911.3410.

Mignone, A., Ugliano, M., Bodo, G., 2009. A five-wave Harten-Lax-van Leer Riemann solver for relativistic magnetohydrodynamics. MNRAS 393, 1141–1156. doi:10.1111/j.1365-2966.2008.14221.x, arXiv:0811.1483.

Mimica, P., Aloy, M.A., 2010. On the dynamic efficiency of internal shocks in magnetized relativistic outflows. MNRAS 401, 525–532. doi:10.1111/j.1365-2966.2009.15669.x, arXiv:0909.1328.

Mimica, P., Aloy, M.A., Müller, E., 2007. Internal shocks in relativistic outflows: collisions of magnetized shells. A&A 466, 93–106. doi:10.1051/0004-6361:20066811, arXiv:astro-ph/0611765.

Mimica, P., Aloy, M.A., Müller, E., Brinkmann, W., 2004. Synthetic X-ray light curves of BL Lacs from relativistic hydrodynamic simulations. A&A 418, 947–958. doi:10.1051/0004-6361:20034261, arXiv:astro-ph/0401266.

Mimica, P., Aloy, M.A., Müller, E., Brinkmann, W., 2005. Which physical parameters can be inferred from the emission variability of relativistic jets? A&A 441, 103–115. doi:10.1051/0004-6361:20053218, arXiv:astro-ph/0506636.

Miranda-Aranguren, S., Aloy, M.A., 2013. Building a numerical relativistic non-ideal magnetohydrodynamics code for astrophysical applications, Cambridge University Press. pp. 64–65. doi:10.1017/S1743921314001732.

Miranda-Aranguren, S., Aloy, M.A., Aloy-Torás, C., 2014. Numerical Relativistic Non-ideal Magnetohydrodynamics Code for Astrophysical Applications, in: Pogorelov, N.V., Audit, E., Zank, G.P. (Eds.), 8th International Conference of Numerical Modeling of Space Plasma Flows (ASTRONUM 2013), p. 249.

Miranda-Aranguren, S., Aloy, M.A., Rembiasz, T., 2018. An hllc riemann solver for resistive relativistic magnetohydrodynamics. Monthly Notices of the Royal Astronomical Society 476, 3837–3860. doi:10.1093/mnras/sty419.

Misner, C., Thorne, K., Wheeler, J., 1973. Gravitation. Freeman W. H. and Co. (Eds.).

Mizuno, Y., 2013. The Role of the Equation of State in Resistive Relativistic Magnetohydrodynamics. ApJS 205, 7. doi:10.1088/0067-0049/205/1/7, arXiv:1301.6052.

Mohseni, F., Mendoza, M., Succi, S., Herrmann, H.J., 2015. Lattice Boltzmann model for resistive relativistic magnetohydrodynamics. Phys. Rev. E 92, 023309. doi:10.1103/PhysRevE.92.023309, arXiv:1508.03452.

Mösta, P., Ott, C.D., Radice, D., Roberts, L.F., Schnetter, E., Haas, R., 2015. A large-scale dynamo and magnetoturbulence in rapidly rotating core-collapse supernovae. Nature 528, 376–379. doi:10.1038/nature15755, arXiv:1512.00838.

Mouschovias, T.C., Paleologou, E.V., 1980. Magnetic braking of an aligned rotator during star formation - an exact, time-dependent solution. ApJ 237, 877–899. doi:10.1086/157936.

Nalewajko, K., Giannios, D., Begelman, M.C., Uzdensky, D.A., Sikora, M., 2011. Radiative properties of reconnection-powered minijets in blazars. MNRAS 413, 333–346. doi:10.1111/j.1365-2966.2010.18140.x, arXiv:1007.3994.

Narayan, R., Kumar, P., 2009. A turbulent model of gamma-ray burst variability. MNRAS 394, L117–L120. doi:10.1111/j.1745-3933.2009.00624.x, arXiv:0812.0018.

Narayan, R., Piran, T., 2012. Variability in blazars: clues from PKS 2155-304. MNRAS 420, 604–612. doi:10.1111/j.1365-2966.2011.20069.x, arXiv:1107.5812.

Nathanail, A., Contopoulos, I., 2014. Black Hole Magnetospheres. ApJ 788, 186. doi:10.1088/0004-637X/788/2/186, arXiv:1404.0549.

Noh, W.F., 1987. Errors for calculations of strong shocks using an artificial viscosity and an artificial heat flux. Journal of Computational Physics 72, 78–120. doi:10.1016/0021-9991(87)90074-X.

Obergaulinger, M., 2008. Astrophysical magnetohydrodynamics and radiative transfer: numerical methods and applications. Ph.D. thesis. Technische Universität München. Max-Planck-Institut für Astrophysik. URL: https://mediatum.ub.tum.de/doc/632729/632729.pdf.

Obergaulinger, M., Aloy, M.A., 2012. MUSTA schemes in magnetohydrodynamics and neutrino transfer: application to core-collapse supernovae and gamma-ray bursts. Numerical Methods for Hyperbolic Equations: Theory an Applications. Eds. Vázquez-Cendón , 227–234.

Obergaulinger, M., Aloy, M.Á., 2017. Protomagnetar and black hole formation in high-mass stars. MNRAS 469, L43–L47. doi:10.1093/mnrasl/slx046, arXiv:1703.09893.

Obergaulinger, M., Aloy, M.A., Dimmelmeier, H., Müller, E., 2006. Axisymmetric simulations of magnetorotational core collapse: approximate inclusion of general relativistic effects. A&A 457, 209–222. doi:10.1051/0004-6361:20064982, arXiv:astro-ph/0602187.

Obergaulinger, M., Cerdá-Durán, P., Müller, E., Aloy, M.A., 2009. Semi-global simulations of the magneto-rotational instability in core collapse supernovae. A&A 498, 241–271. doi:10.1051/0004-6361/200811323.

Obergaulinger, M., Just, O., Janka, H.T., Aloy, M.A., Aloy, C., 2014. A New Two-moment Scheme with Algebraic Closure for Energy-dependent Multi-flavor Neutrino Transport in Supernovae. 8th International Conference of Numerical Modeling of Space Plasma Flows (ASTRONUM 2013) ASP Conference Series 488, 255–.

Okamoto, I., 2006. Electromagnetic Extraction of Energy from Kerr Black Holes. PASJ 58, 1047–1071. doi:10.1093/pasj/58.6.1047, arXiv:astro-ph/0506302.

O'Riordan, M., Pe'er, A., McKinney, J.C., 2017. Blazar Variability from Turbulence in Jets Launched by Magnetically Arrested Accretion Flows. ApJ 843, 81. doi:10.3847/1538-4357/aa7339, arXiv:1704.05882.

Otto, A., 1991. The resistive tearing instability for generalized resistivity models: Theory. Physics of Fluids B: Plasma Physics 3, 1739–1745. doi:10.1063/1.859692.

Otto, A., Birk, G.T., 1992. Resistive instability of periodic current sheets. Physics of Fluids B 4, 3811–3813. doi:10.1063/1.860337.

Palenzuela, C., Lehner, L., Liebling, S.L., 2010. Dual Jets from Binary Black Holes. Science 329, 927–930. doi:10.1126/science.1191766, arXiv:1005.1067.

Palenzuela, C., Lehner, L., Reula, O., Rezzolla, L., 2009. Beyond ideal MHD: towards a more realistic modelling of relativistic astrophysical plasmas. MNRAS 394, 1727–1740. doi:10.1111/j.1365-2966.2009.14454.x, arXiv:0810.1838.

Panaitescu, A., Spada, M., Mészáros, P., 1999. Power Density Spectra of Gamma-Ray Bursts in the Internal Shock Model. ApJL 522, L105–L108. doi:10.1086/312230, arXiv:astro-ph/9905026.

Pareschi, L., Russo, G., 2005. Implicit-explicit runge-kutta schemes and applications to hyperbolic systems with relaxation. Journal of Scientific Computing 25, 129–155. doi:10.1007/BF02728986.

Parfrey, K., Giannios, D., Beloborodov, A.M., 2015. Black hole jets without large-scale net magnetic flux. MNRAS 446, L61–L65. doi:10.1093/mnrasl/slu162, arXiv:1410.0374.

Parker, E.N., 1957. Sweet's Mechanism for Merging Magnetic Fields in Conducting Fluids. Journal of Geophysical Research 62, 509–520.

Parker, E.N., 1983. Magnetic Neutral Sheets in Evolving Fields - Part Two - Formation of the Solar Corona. ApJ 264, 642. doi:10.1086/160637.

Pember, R.B., 1993. Numerical methods for hyperbolic conservation laws with stiff relaxation ii. higher-order godunov methods. SIAM Journal on Scientific Computing 14, 824–859. doi:10.1137/0914052.

Penna, R.F., Narayan, R., Sądowski, A., 2013. General relativistic magnetohydrodynamic simulations of Blandford-Znajek jets and the membrane paradigm. MNRAS 436, 3741–3758. doi:10.1093/mnras/stt1860, arXiv:1307.4752.

Pessah, M.E., 2010. Angular Momentum Transport in Protoplanetary and Black Hole Accretion Disks: The Role of Parasitic Modes in the Saturation of MHD Turbulence. ApJ 716, 1012–1027. doi:10.1088/0004-637X/716/2/1012, arXiv:0908.1791.

Petropoulou, M., Giannios, D., Sironi, L., 2016. Blazar flares powered by plasmoids in relativistic reconnection. MNRAS 462, 3325–3343. doi:10.1093/mnras/stw1832, arXiv:1606.07447.

Petschek, H.E., 1964. Magnetic Field Annihilation. NASA Special Publication 50, 425.

Piel, A., 2010. Plasma Physics. doi:10.1007/978-3-642-10491-6.

Pons, J.A., Font, J.A., Ibáñez, J.M., Martí, J.M., Miralles, J.A., 1998. General relativistic hydrodynamics with special relativistic Riemann solvers. A&A 339, 638–642. arXiv:astro-ph/9807215.

Pons, J.A., Martí, J.M., Müller, E., 2000. The exact solution of the Riemann problem with non-zero tangential velocities in relativistic hydrodynamics. Journal of Fluid Mechanics 422, 125–139. arXiv:astro-ph/0005038.

Porth, O., Komissarov, S.S., Keppens, R., 2014. Three-dimensional magnetohydrodynamic simulations of the Crab nebula. Monthly Notices of the Royal Astronomical Society 438, 278–306.

Priest, E., Forbes, T., 2000. Magnetic Reconnection. Cambridge University Press.

Pucci, F., Velli, M., 2014. Reconnection of Quasi-singular Current Sheets: The "Ideal" Tearing Mode. ApJL 780, L19. doi:10.1088/2041-8205/780/2/L19.

Qian, Q., Fendt, C., Noble, S., Bugli, M., 2017. rHARM: Accretion and Ejection in Resistive GR-MHD. ApJ 834, 29. doi:10.3847/1538-4357/834/1/29, arXiv:1610.04445.

Rebhan, E., 2011. Theoretische Physik: Relativitätstheorie und Kosmologie. Theoretische Physik, Spektrum Akademischer Verlag.

Rees, M.J., 1978. The M87 jet - Internal shocks in a plasma beam. MNRAS 184, 61P–65P. doi:10.1093/mnras/184.1.61P.

Rees, M.J., Mészáros, P., 1994. Unsteady outflow models for cosmological gamma-ray bursts. ApJL 430, L93–L96. doi:10.1086/187446, arXiv:astro-ph/9404038.

Rembiasz, T., 2013. Numerical Studies of the Magnetorotational Instability in Core Collapse Supernovae. Ph.D. thesis. Technische Universität München. Max-Planck-Institut für Astrophysik. URL: https://www.imprs-astro.mpg.de/sites/default/files/rembiasz.pdf.

Rembiasz, T., Guilet, J., Obergaulinger, M., Cerdá-Durán, P., Aloy, M.A., Müller, E., 2016a. On the maximum magnetic field amplification by the magnetorotational instability in core-collapse supernovae. MNRAS 460, 3316–3334. doi:10.1093/mnras/stw1201, arXiv:1603.00466.

Rembiasz, T., Obergaulinger, M., Cerdá-Durán, P., Aloy, M.Á., Müller, E., 2017. On the Measurements of Numerical Viscosity and Resistivity in Eulerian MHD Codes. ApJS 230, 18. doi:10.3847/1538-4365/aa6254, arXiv:1611.05858.

Rembiasz, T., Obergaulinger, M., Cerdá-Durán, P., Müller, E., Aloy, M.A., 2016b. Termination of the magnetorotational instability via parasitic instabilities in core-collapse supernovae. MNRAS 456, 3782–3802. doi:10.1093/mnras/stv2917, arXiv:1508.04799.

Rezzolla, L., Giacomazzo, B., Baiotti, L., Granot, J., Kouveliotou, C., Aloy, M.A., 2011. The Missing Link: Merging Neutron Stars Naturally Produce Jet-like Structures and Can Power Short Gamma-ray Bursts. ApJL 732, L6. doi:10.1088/2041-8205/732/1/L6, arXiv:1101.4298.

Rezzolla, L., Zanotti, O., 2001. An improved exact Riemann solver for relativistic hydrodynamics. Journal of Fluid Mechanics 449, 395–411. arXiv:gr-qc/0103005.

Rezzolla, L., Zanotti, O., 2013. Relativistic Hydrodynamics. Oxford University Press. doi:10.1093/acprof:oso/9780198528906.001.0001.

Rezzolla, L., Zanotti, O., Pons, J.A., 2003. An improved exact Riemann solver for multidimensional relativistic flows. Journal of Fluid Mechanics 479, 199–219. doi:10.1017/S0022112002003506, arXiv:gr-qc/0205034.

Roache, P.J., 1997. Quantification of uncertainty in computational fluid dynamics. Annual Review of Fluid Mechanics 29, 123–160. doi:10.1146/annurev.fluid.29.1.123.

Roache, P.J., 1998. Verification and validation in computational science and engineering. Hermosa, Albuquerque, NM.

Roe, P.L., 1985. Some contributions to the modelling of discontinuous flows, in: Engquist, B.E., Osher, S., Somerville, R.C.J. (Eds.), Large-Scale Computations in Fluid Mechanics, pp. 163–193.

Romero, R., Martí, J.M., Pons, J.A., Ibáñez, J.M., Miralles, J.A., 2005. The exact solution of the Riemann problem in relativistic magnetohydrodynamics with tangential magnetic fields. Journal of Fluid Mechanics 544, 323–338. doi:10.1017/S0022112005006701, arXiv:astro-ph/0506527.

Rueda-Becerril, J.M., 2017. Numerical treatment of radiation processes in the internal shocks of magnetized relativistic outflows. Ph.D. thesis. Universitat de València. Valencia, Spain. URL: http://roderic.uv.es/handle/10550/60003.

Rueda-Becerril, J.M., Mimica, P., Aloy, M.A., 2017. On the influence of a hybrid thermal-non-thermal distribution in the internal shocks model for blazars. MNRAS 468, 1169–1182. doi:10.1093/mnras/stx476, arXiv:1612.06383.

Rutherford, P.H., 1973. Nonlinear growth of the tearing mode. Physics of Fluids 16, 1903–1908.

Samtaney, R., Loureiro, N.F., Uzdensky, D.A., Schekochihin, A.A., Cowley, S.C., 2009. Formation of Plasmoid Chains in Magnetic Reconnection. Physical Review Letters 103, 105004.

Sawai, H., Yamada, S., 2016. The Evolution and Impacts of Magnetorotational Instability in Magnetized Core-collapse Supernovae. ApJ 817, 153. doi:10.3847/0004-637X/817/2/153, arXiv:1504.03035.

Sawai, H., Yamada, S., Suzuki, H., 2013. Global Simulations of Magnetorotational Instability in the Collapsed Core of a Massive Star. ApJL 770, L19. doi:10.1088/2041-8205/770/2/L19, arXiv:1303.2856.

Schiesser, W., Griffiths, G., 2009. A Compendium of Partial Differential Equation Models: Method of Lines Analysis with Matlab. Cambridge University Press.

Shu, C.W., Osher, S., 1988. Efficient Implementation of Essentially Non-oscillatory Shock-Capturing Schemes. Journal of Computational Physics 77, 439–471. doi:10.1016/0021-9991(88)90177-5.

Sironi, L., Petropoulou, M., Giannios, D., 2015. Relativistic jets shine through shocks or magnetic reconnection? MNRAS 450, 183–191. doi:10.1093/mnras/stv641, arXiv:1502.01021.

Spada, M., Ghisellini, G., Lazzati, D., Celotti, A., 2001. Internal shocks in the jets of radio-loud quasars. MNRAS 325, 1559–1570. doi:10.1046/j.1365-8711.2001.04557.x, arXiv:astro-ph/0103424.

Spruit, H.C., Daigne, F., Drenkhahn, G., 2001. Large scale magnetic fields and their dissipation in GRB fireballs. A&A 369, 694–705. doi:10.1051/0004-6361:20010131, arXiv:astro-ph/0004274.

Starke, R., Schober, G.A.H., 2016. Relativistic covariance of ohm's law. International Journal of Modern Physics D 25, 1640010. doi:10.1142/S0218271816400101.

Stone, J.M., Norman, M.L., 1992. ZEUS-2D: A Radiation Magnetohydrodynamics Code for Astrophysical Flows in Two Space Dimensions. II. The Magnetohydrodynamic Algorithms and Tests. ApJS 80, 791. doi:10.1086/191681.

Strang, G., 1968. On the construction and comparison of difference schemes. SIAM Journal on Numerical Analysis 5, 506–517. doi:10.1137/0705041.

Suresh, A., Huynh, H.T., 1997. Accurate Monotonicity-Preserving Schemes with Runge Kutta Time Stepping. Journal of Computational Physics 136, 83–99. doi:10.1006/jcph.1997.5745.

Sweet, P.A., 1958. The Neutral Point Theory of Solar Flares. Electromagnetic Phenomena in Cosmical Physics 6, 123–.

T. Birk, G., Otto, A., 1991. The resistive tearing instability for generalized resistivity models - applications 3.

Takamoto, M., 2013. Evolution of Relativistic Plasmoid Chains in a Poynting-dominated Plasma. ApJ 775, 50. doi:10.1088/0004-637X/775/1/50, arXiv:1307.5677.

Takamoto, M., 2014. A New Numerical Scheme for Relativistic Magnetohydrodynamics with Dissipation and Its Application, in: Pogorelov, N.V., Audit, E., Zank, G.P. (Eds.), 8th International Conference of Numerical Modeling of Space Plasma Flows (ASTRONUM 2013), p. 267.

Takamoto, M., Inoue, T., 2011. A New Numerical Scheme for Resistive Relativistic Magnetohydrodynamics Using Method of Characteristics. ApJ 735, 113. doi:10.1088/0004-637X/735/2/113, arXiv:1105.5683.

Taub, A.H., 1948. Relativistic Rankine-Hugoniot Equations. Physical Review 74, 328–334. doi:10.1103/PhysRev.74.328.

Tchekhovskoy, A., Narayan, R., McKinney, J.C., 2010. Black Hole Spin and The Radio Loud/Quiet Dichotomy of Active Galactic Nuclei. ApJ 711, 50–63. doi:10.1088/0004-637X/711/1/50, arXiv:0911.2228.

Tenbarge, J.M., Hazeltine, R.D., Mahajan, S.M., 2010. Relativistic Petschek reconnection with pressure anisotropy in a pair-plasma. MNRAS 403, 335–341. doi:10.1111/j.1365-2966.2009.16116.x.

Tenerani, A., Velli, M., Rappazzo, A.F., Pucci, F., 2015. Magnetic Reconnection: Recursive Current Sheet Collapse Triggered by "Ideal" Tearing. The Astrophysical Journal Letters 813, L32.

Thompson, C., 1994. A Model of Gamma-Ray Bursts. MNRAS 270, 480. doi:10.1093/mnras/270.3.480.

Tonks, L., Langmuir, I., 1929. Oscillations in ionized gases. Phys. Rev. 33, 195–210. doi:10.1103/PhysRev.33.195.

Toro, E.F., 1997. Splitting Schemes for PDEs with Source Terms. Springer Berlin Heidelberg. pp. 497–507. URL: https://doi.org/10.1007/978-3-662-03490-3_15, doi:10.1007/978-3-662-03490-3_15.

Toro, E.F., Spruce, M., Speares, W., 1994. Restoration of the contact surface in the HLL-Riemann solver. Shock Waves 4, 25–34. doi:10.1007/BF01414629.

Tóth, G., 2000. The nabla B=0 Constraint in Shock-Capturing Magnetohydrodynamics Codes. Journal of Computational Physics 161, 605–652. doi:10.1006/jcph.2000.6519.

Tsang, T., 1997. Classical Electrodynamics. Advanced Series on Theoretical Physical Sciences, World Scientific.

Uzdensky, D.A., 2011. Magnetic Reconnection in Extreme Astrophysical Environments. NAR 160, 45–71. doi:10.1007/s11214-011-9744-5, arXiv:1101.2472.

van Leer, B., 1977. Towards the Ultimate Conservative Difference Scheme. IV. A New Approach to Numerical Convection. Journal of Computational Physics 23, 276. doi:10.1016/0021-9991(77)90095-X.

Varnière, P., Rodriguez, J., Tagger, M., 2002. Accretion-ejection instability and QPO in black-hole binaries. II. Relativistic effects. A&A 387, 497–506. doi:10.1051/0004-6361:20020401, arXiv:astro-ph/0203325.

Velikhov, E.P., 1959. Stability of flow of an ideally conducting liquid between rotating cylinders in a magnetic field. Zh. Eksp. Teor. Fiz. 36, 1398–1404.

Vlahakis, N., Königl, A., 2003. Relativistic Magnetohydrodynamics with Application to Gamma-Ray Burst Outflows. II. Semianalytic Super-Alfvénic Solutions. ApJ 596, 1104–1112. doi:10.1086/378227, arXiv:astro-ph/0303483.

Wang, Z.X., Wang, X.G., Dong, J.Q., Lei, Y.A., Long, Y.X., Mou, Z.Z., Qu, W.X., 2007. Fast Resistive Reconnection Regime in the Nonlinear Evolution of Double Tearing Modes. Physical Review Letters 99, 185004.

Watanabe, N., Yokoyama, T., 2006. Two-dimensional Magnetohydrodynamic Simulations of Relativistic Magnetic Reconnection. ApJL 647, L123–L126. doi:10.1086/507520, arXiv:astro-ph/0607285.

Whitham, G.B., 1974. Linear and nonlinear waves. John Wiley & Sons, Ltd, New York.

Wilson, J.R., 1975. Some magnetic effects in stellar collapse and accretion, in: Bergman, P.G., Fenyves, E.J., Motz, L. (Eds.), Seventh Texas Symposium on Relativistic Astrophysics, pp. 123–132. doi:10.1111/j.1749-6632.1975.tb31425.x.

Wilson, J.R., 1977. Magnetohydrodynamics near a black hole., in: Ruffini, R. (Ed.), 1st Marcel Grossmann Meeting on General Relativity, pp. 393–413.

Yokosawa, M., 1993. Energy and angular momentum transport in magnetohydrodynamical accretion onto a rotating black hole. PASJ 45, 207–218.

Zanotti, O., Dumbser, M., 2011. Numerical simulations of high Lundquist number relativistic magnetic reconnection. Monthly Notices of the Royal Astronomical Society 418, 1004–1011.

Zaqarashvili, T.V., Oliver, R., Ballester, J.L., Belvedere, G., 2004. Instability of periodic MHD shear flows, in: MHD COUETTE FLOWS: Experiments and Models. AIP Conference Proceedings, Abastumani Astrophysical Observatory, Al. Kazbegi ave. 2a, 380060 Tbilisi, Georgia. AIP. pp. 201–215.

Zenitani, S., Hesse, M., 2008. Self-Regulation of the Reconnecting Current Layer in Relativistic Pair Plasma Reconnection. ApJ 684, 1477–1485. doi:10.1086/590425, arXiv:0805.4286.

Zenitani, S., Hesse, M., Klimas, A., 2009. Two-Fluid Magnetohydrodynamic Simulations of Relativistic Magnetic Reconnection. ApJ 696, 1385–1401. doi:10.1088/0004-637X/696/2/1385, arXiv:0902.2074.

Zenitani, S., Hesse, M., Klimas, A., 2010. Resistive Magnetohydrodynamic Simulations of Relativistic Magnetic Reconnection. ApJL 716, L214–L218. doi:10.1088/2041-8205/716/2/L214, arXiv:1005.4485.

Zenitani, S., Hoshino, M., 2007. Particle Acceleration and Magnetic Dissipation in Relativistic Current Sheet of Pair Plasmas. ApJ 670, 702–726. doi:10.1086/522226, arXiv:0708.1000.

Zhang, B., Mészáros, P., 2002. An Analysis of Gamma-Ray Burst Spectral Break Models. ApJ 581, 1236–1247. doi:10.1086/344338, arXiv:astro-ph/0206158.

Zhang, B., Pe'er, A., 2009. Evidence of an Initially Magnetically Dominated Outflow in GRB 080916C. ApJL 700, L65–L68. doi:10.1088/0004-637X/700/2/L65, arXiv:0904.2943.

Zhang, B., Yan, H., 2011. The Internal-collision-induced Magnetic Reconnection and Turbulence (ICMART) Model of Gamma-ray Bursts. ApJ 726, 90. doi:10.1088/0004-637X/726/2/90, arXiv:1011.1197.

Zhang, C.L., Ma, Z.W., 2011. Nonlinear evolution of double tearing mode with guiding magnetic field. Physics of Plasmas 18, 052303.

Zweibel, E.G., Yamada, M., 2009. Magnetic reconnection in astrophysical and laboratory plasmas. Annual Review of Astronomy and Astrophysics 47, 291–332. doi:10.1146/annurev-astro-082708-101726.